Carbon nanotubes as nanoreactors for magnetic applications

Xiaojian Li

To cite this version:

Xiaojian Li. Carbon nanotubes as nanoreactors for magnetic applications. Coordination chemistry. Institut National Polytechnique de Toulouse - INPT, 2014. English. NNT : 2014INPT0062 . tel-04557763

HAL Id: tel-04557763
https://theses.hal.science/tel-04557763

Submitted on 24 Apr 2024

THÈSE

En vue de l'obtention du

DOCTORAT DE L'UNIVERSITÉ DE TOULOUSE

Délivré par :

Institut National Polytechnique de Toulouse (INP Toulouse)

Discipline ou spécialité :

Chimie Organométallique et de Coordination

Présentée et soutenue par :

M. XIAOJIAN LI
le jeudi 24 avril 2014

Titre :

CARBON NANOTUBES AS NANOREACTORS FOR MAGNETIC APPLICATIONS

Ecole doctorale :
Sciences de la Matière (SM)

Unité de recherche :
Laboratoire de Chimie de Coordination (L.C.C.)

Directeur(s) de Thèse :
M. PHILIPPE SERP
MME AIKATERINI SOULANTIKA

Rapporteurs :
M. JEAN-CYRILLE HIERSO, UNIVERSITE DE BOURGOGNE
Mme SYLVIE BEGIN COLIN, UNIVERSITE STRASBOURG 1

Membre(s) du jury :
M. EMMANUEL FLAHAUT, UNIVERSITE TOULOUSE 3, Président
Mme AIKATERINI SOULANTIKA, INSA TOULOUSE, Membre
M. PHILIPPE SERP, INP TOULOUSE, Membre
M. YANNICK GUARI, UNIVERSITE MONTPELLIER 2, Membre

Abbreviation list

Reactions

BBA: 2-benzylbenzoic acid

CNT: carbon nanotube

Co: cobalt

Fe: iron

HDA: hexadecylamine

HMDS: hexamethyldisilazane

LA: lauric acid

MMNP: magnetic metallic nanoparticle

NP: nanoparticle

NR: nanorod

NW: nanowire

PA: paltimic acid

PPP: 4-(3-phenylpropyl)pyridine

Pt: platinum

THF: tetrahydrofurane

Techniques

FC: field cooling

HRTEM: high resolution transmission electron microscopy

IR: infrared

NMR: nuclear magnetic resonance

SQUID: superconducting quantum interference device

TEM: transmission electron microscopy

UV-vis: ultraviolet-visible

VSM: vibrating sample magnetometer

WAXS: wide angle X-ray scattering

XRD: X-ray diffraction

ZFC: zero field cooling

Abstract

Carbon nanotubes (CNTs), because of their unique properties and potential use in a variety of applications, are probably the most studied class of nanomaterials. Functionalized CNTs, which can be easily manipulated and modified by covalent or non-covalent functionalization, appear as new tools in biotechnology and biomedicine. Indeed, CNTs have optical, electronic and mechanical properties that can be exploited in biological or biomedical applications. Metallic magnetic nanoparticles (MMNPs) of the 3d series and their alloys exhibit excellent magnetic properties unlike their oxide counterparts, which can be exploited in biomedicine and ultra-high density magnetic recording.

When confined in CNTs nano-materials can have different properties and behaviors compared to bulk materials. Various confinement effects resulting from the interaction between the confined materials and the internal cavities of CNTs provide opportunities for regulating or designing new nanocomposites.

This thesis is devoted to the study of a new approach for the development of nanocomposite materials MMNPs@CNTs and their properties. MMNPs of controlled size and shape of Co and Fe were synthesized with novel aromatic ligands as stabilizers. These MMNPs were then selectively introduced into the cavity of CNTs due to repulsive/attractive interactions between the functionalized multi-walled CNTs and the MMNPs. We were then interested in the protection of these nanoparticles from oxidation by air. Thus, confined iron nanoparticles have been coated with polyisoprene. To do this, the surface of the Fe nanoparticles has been modified with a polymerization catalyst by ligand exchange; then, polymerization of isoprene was conducted inside the channel of CNTs. The protection from oxidation by the polyisoprene was evaluated by magnetic measurements after exposure to air. Quite surprisingly, this study showed that the iron nanoparticles the more resistant to oxidation were those obtained after ligand exchange and without polymerization. In this case only, the original properties of the nanoparticles are maintained after venting. Finally, magnetic bimetallic nanostructures (particles or rods) combining Pt and cobalt or iron were obtained and confined in CNTs. Their chemical structure orderings were also studied by thermal annealing studies.

The work developed in this thesis opens up new perspectives for the production of new MMNPs@NTC nanocomposites resistant to oxidation.

Keywords : carbon nanotubes, magnetic metal nanoparticles, confinement effects; polymerization of isoprene; CoPt and FePt nanowires.

General introduction

Due to their outstanding properties and their potential use in a number of high value applications, carbon nanotubes (CNTs) are one of the most intensively studied nanomaterials (1). CNT composites have the potential for becoming “super-materials”. Indeed, if the unique properties of CNTs were fully exploited in composites, composite materials that are stronger, stiffer, and more thermally and electrically conductive than anything used today, could be obtained. This would require a better control of CNT alignment in the polymer matrix (2, 3). Additionally, functionalized CNTs are emerging as new tools in the field of nanobiotechnology and nanomedicine due to the fact that they can be easily manipulated and modified by bio-polymer encapsulation or by covalent or non-covalent functionalization (4-6). Indeed, CNTs have optical, electronic, and mechanical properties that can be exploited in biological or biomedical applications (7, 8) including, but not limited to, cancer therapeutics (9, 10).

On the other hand, metallic magnetic nanoparticles (MMNPs) of the *3d* series and their alloys are some of the most important targets in nanoscience research. The long and medium term applications targeted range from ultra-high density magnetic recording (11) to multifunctional magnetic probes and transport media for biomedicine (12), which are domains that hold promises of important innovation and therefore economic impact. Presently, iron based magnetic oxides are often preferred (13-15), despite the fact that MMNPs possess advantageous magnetic properties, since they combine a high magnetization that guarantees a more efficient response to magnetic field stimuli, and a tunable anisotropy, which may be optimized depending on the target application. Both advantages, if properly exploited, may open new opportunities (16). However, a major issue in the use of MMNPs in numerous applications is their low biocompatibility (14) coupled with their sensitivity towards oxygen and moisture.

Recently, confinement effects coming from specific interactions of nanoparticles with the internal walls of CNTs have become the object of a research domain that makes use of CNTs as nanoreactors (17-19). Taking advantage of the expertise of the LPCNO in MMNP synthesis and study of their magnetic properties (20-22) as well as of the LCC’s expertise in CNT synthesis and functionalization (17, 23), this thesis focuses on the development of hybrid systems between these two promising materials for high value applications in the field of nanocomposites and biomedecine, and simultaneously on the study of confinement effect arising from the interaction between MMNPs and the inner cavities of multi-walled CNTs. In this respect, the main objective of this thesis is the synthesis of oxidation protected and CNT confined MMNPs of iron, cobalt, Pt-Fe and Pt-Co.

In Chapter I, we provide a comprehensive literature review of confinement in CNTs, for which diverse materials and structures have been involved. We mainly highlight the methods for confining nanomaterials within CNTs, which guides us to perform the confinement study. The different types of confinement effects, presented by confined materials, are also introduced and classified.

Chapter II concerns the confinement of MMNPs (Fe and Co) in CNTs. Different aspect are considered, such as: i) the CNT functionalization, which is required for MMNP confinement through molecular recognition, ii) the synthesis of well-defined Fe and Co MMNPs stabilized with new functional ligands, both of which are critical factors for the selective introduction of guest materials into the CNT cavity; and iv) the confinement of pre-synthesized MMNPs within functionalized CNTs. In this chapter, the main factors that may affect confinement efficiency are discussed.

Based on the confinement results obtained in Chapter II, we describe in Chapter III a study concerning air protection of confined MMNPs *via* polymerization reactions. This may answer to the main drawbacks of the implementation of MMNPs in biological applications such as hyperthermia or transport media for biomedicine. We chose polyisoprene as the polymer coating. Two polymerization methods have been studied, atom transfer radical polymerization (ATRP) and organometallic complex catalyzed polymerization. One of them, the organometallic complex catalyzed polymerization has never been employed before in the literature for the development of a polymer shell around NPs and the resulting MMNP nanohybrids have been characterized by magnetic measurements. The efficiency of the polymer-coating against oxidation has also been investigated.

In Chapter IV, we have produced novel CNT-confined magnetic bimetallic (Pt-Fe and Pt-Co) nanostructures, and have studied their formation. The composition of these bimetallic nanoparticles has been investigated by various techniques. Depending the experimental conditions we have shown that bimetallic confined nanoparticles or nanowires can be selectively produced. Furthermore, phase transformation of these nanostructures has also been studied in order to achieve higher magnetic anisotropic properties.

In Chapter V, we describe the experiments associated to each Chapter in the Experimental section as well as the analytical techniques that we have used to characterize the different samples.

References

1. M. Monthioux, P. Serp, E. Flahaut, M. Razafinimanana, C. Laurent, A. Peigney, W. Bacsa, J.-M. Broto, in *Springer Handbook of Nanotechnology* (Ed.: B. Bhushan), Springer Berlin Heidelberg, **2007**, pp 43-112
2. E. J. García, A. J. Hart, B. L. Wardle, A. H. Slocum, *Advanced Materials,* **2007**, *19*, 2151-2156
3. P.-C. Ma, N. A. Siddiqui, G. Marom, J.- K. Kim, *Composites Part A: Applied Science and Manufacturing,* **2010**, *41*, 1345-1367
4. H. He, L. A. Pham-Huy, P. Dramou, D. Xiao, P. Zuo, C. Pham- Huy, *BioMed Research International* **2013**, *2013*, 12
5. A. M. A. Elhissi, W. Ahmed, I. Ul Hassan, V. R. Dhanak, A. D'Emanuele, *Journal of Drug Delivery,* **2012**, ID 837327
6. P. Liu, *Industrial & Engineering Chemistry Research,* **2013**, *52*, 13517-13527
7. Y. Wenrong, T. Pall, J. J. Gooding, P. R. Simon, B. Filip, *Nanotechnology,* **2007**, *18*, 412001
8. *Carbon Nanotubes for Biomedical Applications*, Springer-Verlag, Berlin, Heidelberg, **2011**
9. E. Heister, V. Neves, S. R. Silva, J. McFadden, H. Coley, in *Carbon Nanotubes for Biomedical Applications* (Eds.: R. Klingeler, R. B. Sim), Springer Berlin Heidelberg, **2011**, pp. 223-245
10. Z. Liu, K. Chen, C. Davis, S. Sherlock, Q. Cao, X. Chen, H. Dai, *Cancer Research,* **2008**, *68*, 6652-6660.
11. N. Weiss, T. Cren, M. Epple, S. Rusponi, G. Baudot, S. Rohart, A. Tejeda, V. Repain, S. Rousset, P. Ohresser, F. Scheurer, P. Bencok, H. Brune, *Physical Review Letters,* **2005**, *95*, 157204.
12. J. Gao, H. Gu, B. Xu, *Accounts of Chemical Research,* **2009**, *42*, 1097-1107.
13. Y.-M. Huh, Y.-w. Jun, H.-T. Song, S. Kim, J.-s. Choi, J.-H. Lee, S. Yoon, K.-S. Kim, J.-S. Shin, J.-S. Suh, J. Cheon, *Journal of the American Chemical Society,* **2005**, *127*, 12387-12391;
14. T. Pedro, M. María del Puerto, V.-V. Sabino, G.-C. Teresita, J. S. Carlos, *Journal of Physics D: Applied Physics,* **2003**, *36*, R182
15. S. Laurent, D. Forge, M. Port, A. Roch, C. Robic, L. Vander Elst, R. N. Muller, *Chemical Reviews,* **2008**, *108*, 2064-2110.
16. L.-Y. Lu, L.-N. Yu, X.-G. Xu, Y. Jiang, *Rare Met.* **2013**, *32*, 323-331
17. P. Serp, E. Castillejos, *ChemCatChem,* **2010**, *2*, 41-47;
18. X. Pan, X. Bao, in *Nanomaterials in Catalysis*, Wiley-VCH Verlag GmbH & Co. KGaA, **2013**,

pp. 415-44

19. X. Pan, X. Bao, *Accounts of Chemical Research,* **2011**, *44*, 553-562
20. C. Desvaux, C. Amiens, P. Fejes, Ph. Renaud, M. Respaud, P. Lecante, E. Snoeck, B. Chaudret, *Nature Mater.,* **2005**, *4*, 750
21. F. Dumestre, B. Chaudret, *Angew. Chem. Int. Ed.* **2002**, *41*, 4286–4289
22. F. Wetz, K. Soulantica, M. Respaud, a. Falqui, B. Chaudret, *Mater. Sci. Eng.: C,* **2007**, *27*, 1162-1166.
23. E. Castillejos, P.-J. Debouttière, L. Roiban, A. Solhy, V. Martinez, Y. Kihn, O. Ersen, K. Philippot, B. Chaudret, P. Serp, *Angew. Chem. Int. Ed.,* **2009**, *48*, 2529-2533.

Chapter I.CNT-confined nanomaterials: a literature survey

CNT-confined nanomaterials: a literature survey

I.1 Nanoscaled porous materials

Hybrid nanomaterial is a rapidly expanding field focusing on innovative combinations of various nanoscaled materials and on the study of their properties. The properties of hybrid nanomaterials depend on the properties of their individual parent building blocks but also on their interfacial characteristics. Confined nanomaterials have been drawing a great interest due: to the specific properties of the confined materials, among which peculiar effects displayed in some reactions in confined spaces by contrast to those in the bulk.

Nanoscaled porous materials, such as silica or zeolites, and hollow carbon-based materials, can be used to adsorb or confine various species. In early studies, in which silica and zeolites were usually involved, it had been shown that the confined materials displayed different physical behaviors from those in the bulk. Schneider *et al.* reported that the density of CO_2 was higher in the mesopores of silica than in the bulk, even under supercritical conditions (1). Chang *et al.* found that confining in zeolites resulted in the modification of heat adsorption of ammonia and some simple amines (2). Surprisingly, water molecules confined in the pores of silica (3), or zeolites (4, 5), were found to form small clusters, whose hydrogen bond network was strongly modified by the confining spaces. Christenson reviewed a series of experimental work on freezing and melting behaviors of confined liquids within various microporous materials. The modifications of these physical behaviors highlight the difficulty of using bulk concepts to define the phase state of a substance confined within nanoscaled pores (6). For example, in a controlled-pore glass sample with a 2 nm pore diameter water remained liquid down to -22 °C.

Due to the modified properties of confined materials that may directly affect the reactivity (7) and selectivity (8-10) of chemical reactions, porous materials have been widely used in heterogeneous catalysis. In these cases, size and structure of pores are essential parameters. Lesthaeghe *et al.* reported in theoretical study that confinement effects within zeolites can influence the reactivity of bulky intermediate molecules in the methanol conversion to olefin (7). Maesen *et al.* showed that shape selectivity, arising from the molecular-range dimensions of the pores, can tune the selectivity of chemical reactions in zeolite catalysis, and argued that a simple thermodynamic analysis of the molecules adsorbed inside the zeolite pores can predict which products will form and guide the identification of zeolite structures (8). Fraile *et al.* estimated that within a three-dimensional structure such as a zeolite possessing well-controlled surfaces and pores, some of the reaction channels might be hindered or even blocked, which consequently modified the selectivity of the reaction (9).

Raja *et al.* reviewed the high surface-area silicas with controllable and adjustable pore diameters in the range of 20-200Å, and the functionalizations of the inner walls of these nanoporous solids with chiral single-site heterogeneous catalysts (10), which opened up the prospect of performing heterogeneous enantioselective conversions in a novel manner under the spatial restrictions imposed by the nanocavities (Figure I.1).

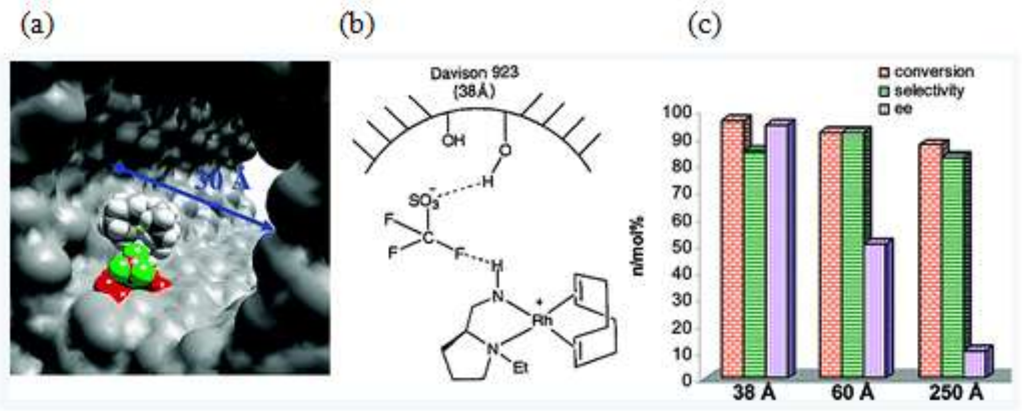

Figure I.1: Enantioselectivity can be induced by anchoring diamine asymmetric ligands onto concave surfaces; (a) Illustration of the inner cavity of a mesoporous silica with a pore diameter of 30 Å and anchored diamine asymmetric ligand; (b) Scheme of non-covalent method for anchoring diamine ligand; (c) Confinement effect of the silica support in facilitating the asymmetric hydrogenation of methyl benzoylformate to methyl mandelate, of which silica support with 38 Å pore size presents best conversion and selectivity (reproduced from ref.10).

In addition to gas molecules, organic molecules, water, organometallic complexes, and metal particles can also be incorporated into porous materials. Carmeron *et al.* reported the synthesis of a novel aerobic oxidation catalyst, a zeolite-confined nanometer sized RuO_2, which presents a two-dimensional structure of independent chains. They reported an extraordinarily high activity and selectivity in the oxidation of both activated and inactivated alcohols to the corresponding aldehydes and ketones due to the spatial restrictions (11).

Fullerenes are one type of the hollow carbon-based nanomaterials, which possess a hollow caged structure. Encapsulating foreign species, such as atoms, ions, or molecules, in the cage of fullerenes, known as endohedral fullerenes, has been extensively studied and reviewed by Dunsch *et al.* (12). Endohedral metallofullerenes (13-15), nitride cluster-fullerenes (14, 16), and oxide cluster-fullerenes (17), which are the main members in the family of endohedral fullerenes, present diverse properties such as electron transfer, stabilization and storage of charge, and intra- or inter-particle magnetic interactions. The principal way to confine foreign species inside fullerenes is the *in situ* direct current arc discharge b r tschmer-Huffman generator (18), in which foreign species are encapsulated during fullerene formation.

Murata *et al.* have successfully confined single H_2 molecule (19), and single H_2O (20, 21) molecules inside fullerene cages *via* a chemical route which involves a closure of the open-cage fullerene as the final step (19, 21) (Figure I.2). It was found that the encapsulated H_2 does not escape even when heated at 500ºC for 10 min (19), and that the single H_2O molecules are electrochemically stable under the hydrophobic environment inside the C_{60} (21). Thus, it is considered that the $H_2O@C_{60}$ molecule allows the study of the intrinsic properties of a single H_2O molecule. Other isolated molecules could be studied in the near future (21).

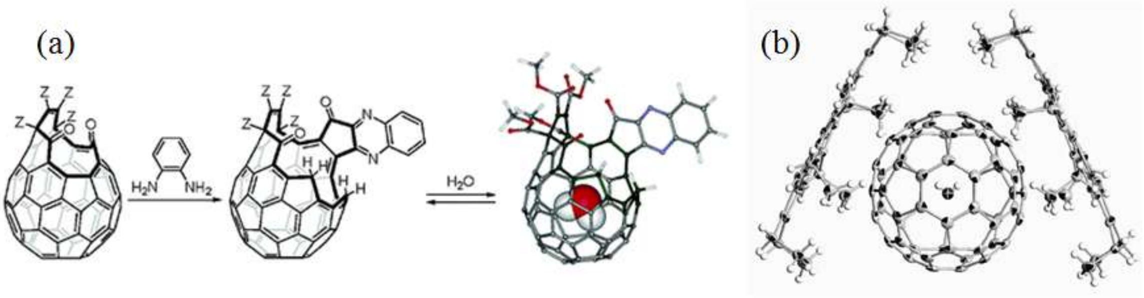

Figure I.2: (a) process of confinement of a single water molecule within the open-caged fullerene (Z=CO_2Me) (20); (b) X-ray structure of the molecular $H_2O@C_{60}\cdot(NiOEP)_2$ (NiOEP= nickel (II) octaethylporphyrin) at the 50% probability level (reproduced from ref.21).

I.2 Confinement effects within CNTs

I.2.1 Basics on CNTs structure

The present thesis deals with the confinement of nanoparticles in carbon nanotubes (CNTs). CNTs, a new type of hollow carbon-based material with a well-defined pore structure, have attracted attentions of researchers all around the world since the first paper published by S. Iijima in 1991 (22), in which graphitic tubular carbon structures were observed by TEM as by-products of fullerene synthesis by an arc-discharge evaporation method. Their unique structure and their properties such as adsorption, reactivity, electronic, optical, mechanical, which make CNTs promising candidates for potential applications in many domains have been subsequently studied and exploited (23).

Three kinds of coaxial CNTs, single-walled CNTs (SWCNTs), double-walled CNTs (DWCNTs) and multi-walled CNTs (MWCNTs), of respectively one, two and more than two graphene layers (Figure I.3), can be obtained depending on the different synthesis techniques, reaction conditions and metal catalysts (23). The diameters of SWCNTs typically range from less than 1 nm to around 2 nm while those of DWCNTs and MWCNTs can be in the range of 2-100 nm or even larger, and their lengths can reach up to several microns. These features make CNTs a nanoscaled porous material with huge aspect ratios.

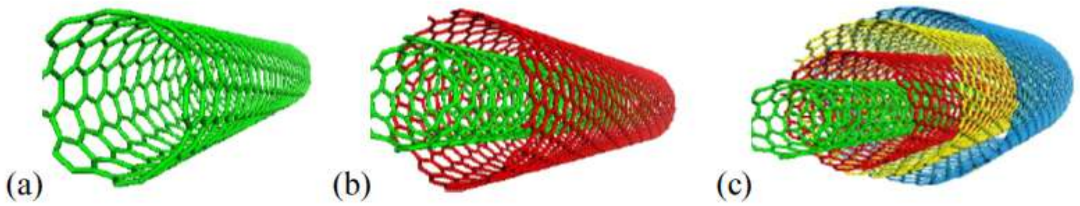

Figure I.3: Representation of (a) SWCNTs, (b) DWCNTs, and (c) MWCNTs (reproduced from ref.24).

CNTs can be considered as rolled-up graphene layers forming a tubular structure with graphitic walls aligned along the tube axis and with two hemispheres capping each ends. In order to understand simply the structure of CNTs, it is relatively easy to imagine a SWCNT. An ideal SWCNT is a perfect graphene sheet, a polyaromatic monoatomic layer possessing sp^2-hybridized carbon atoms arranged in hexagons, rolling into a cylinder. According to the rolling angle of the graphene sheet, SWCNTs may have three conformations: armchair, zigzag and chiral one. The tube conformation is defined by the helical vector $R= ma_1+na_2$, where the integers (m,n) are the number of steps along the unit vectors (a_1 and a_2) of the hexagonal lattice. If m=n, the CNTs are "armchair" (Figure I.4b), for example a (10, 10) SWCNT. If n=0, the CNTs are "zigzag" (Figure I.4a). Otherwise, they are "chiral" (Figure I.4c), called also “helical”. The chiralit of CNTs has considerable impact on their transport properties, especially the electronic properties. For example, considering a given (m, n) CNT, if (2m+n) is a multiple of 3, then the CNT is metallic, otherwise semiconductor. MWCNTs possess multi-layers of graphene, and the interlayer distance is approximately 0.34 nm, as opposed to 0.335 nm in graphite (25). Each layer can have a different chirality. As a result, the prediction of its physical properties is more complicated than that of SWCNTs.

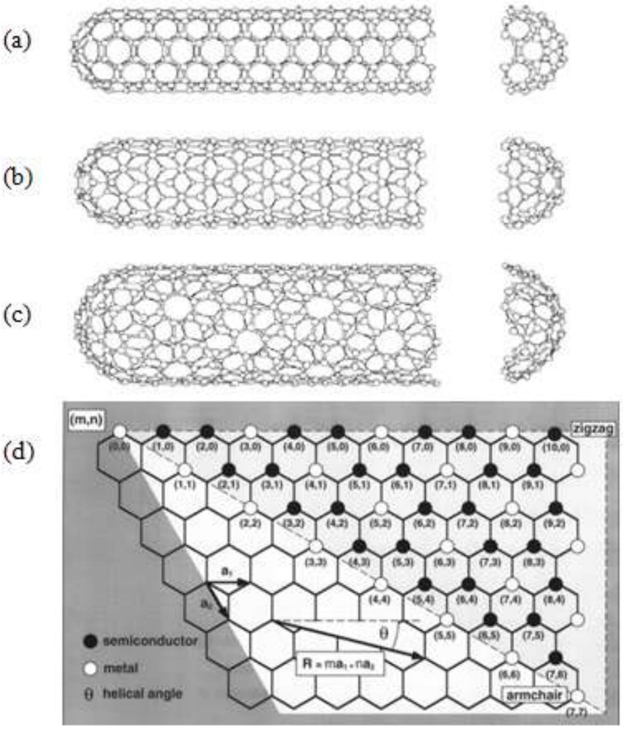

Figure I.4: Sketches of three different SWCNT structures of (a) an armchair-type, (b) a zig-zag-type and (c) a helical type (26). (d) Sketch of the way to make a SWCNT by a graphene sheet (reproduced from ref.27).

Apart from these co-axial CNTs, two other distinct structural types of graphitic filaments, called "nanofibers" instead of "nanotubes", have also been obtained. One has a herringbone structure with the graphitic shells positioned at certain angle with respect to the tube axis (28). The other one has the "bamboo-like" morphology with internal closures that form closed compartments along the tube axis (29) (Figure I.5).

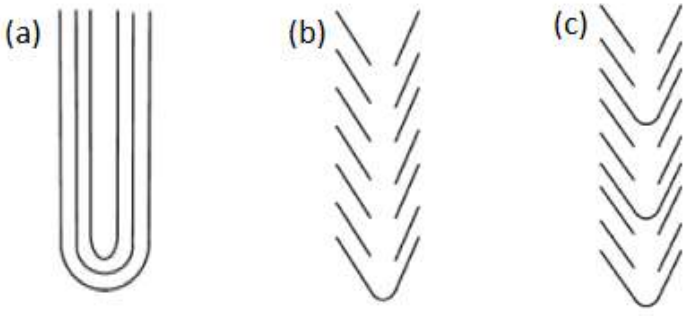

Figure I.5: Simplified representation of (a) multi-walled carbon nanotube, (b) herringbone nanofiber, and (c) bamboo-like nanofiber.

The porous structure of CNTs is suitable for adsorbing or encapsulating foreign species, which makes them an interesting alternative to conventional porous supports for the following reasons: i) their high purity eliminates self-poisoning in chemical reactions; ii) they have impressive mechanical properties, high electrical conductivity and thermal stability; iii) they are characterized by a high surface to mass ratio that allow them to adsorb foreign species; iv) their surface can be easily functionalized of their surfaces (covalent or non-covalent); v) their inner cavity can be used as a template or as a "nanoreactor" for chemical synthesis; vi) they can provide protection of the encapsulated materials from oxidation due to contact with the atmosphere; and vii) they may induce confinement effects in their inner cavity. Thanks to all these advantages, more and more studies focus on filling or confining foreign materials inside CNTs, because confinement in the cavity of CNTs may modify the properties of confined materials compared to those in the bulk or affect chemical reactions with respect to those taking place on the outer surface of CNTs (30, 31).

I.2.2 Stabilization of unstable species

Space restriction in the cavity of CNTs forces encapsulated foreign species to respect the CNT structure, adopting unusual morphologies, or peculiar structures. As a result, CNTs may make possible the synthesis of nanomaterials that could never exist if not encapsulated, and can stabilize unstable species.

An amazing observation concerns the confinement of atom chains inside SWCNTs. The instability of atoms renders them hardly isolable. However, SWCNTs provide a one-dimensional cylindrical cavity that makes encapsulations of atoms possible. Iodine (32, 33) was observed to form a helical chain structure, either single, double, or even triple, rather than to form elongated crystals such as nanowires (Figure I.6).

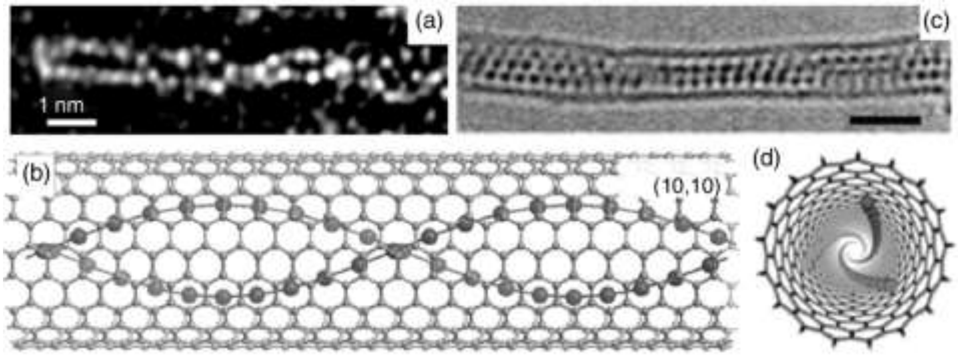

Figure I.6: (a) High-resolution Z contrast TEM of the first example of SWCNTs filled with a double-helix chain of iodine atoms; (b) Side view of a model for the image in (a) considering a (10,10) tube as the containing SWCNT (reproduced from ref.33); (c) High-resolution TEM

image of a I@SWCNT, identified as a triple-helix chain of iodine atoms. The scale bar is 1.5 nm; (d) Top view of a model for the image in (c) (reproduced from ref.32).

Atomically thin nanowires of Eu were also synthesized with different types of CNTs (SWCNTs, DWCNTs, or MWCNTs) (34) (Figure I.7). The magnetization behavior of Eu nanowires is significantly different from that of Eu bulk crystals, especially below 50 K, and the magnetic susceptibility is more than 10 times larger than that of the bulk at 4.25 K. Moreover, the Eu nanowires resist to oxidation and structural disintegration under ambient conditions due to the protection by the CNT sidewalls.

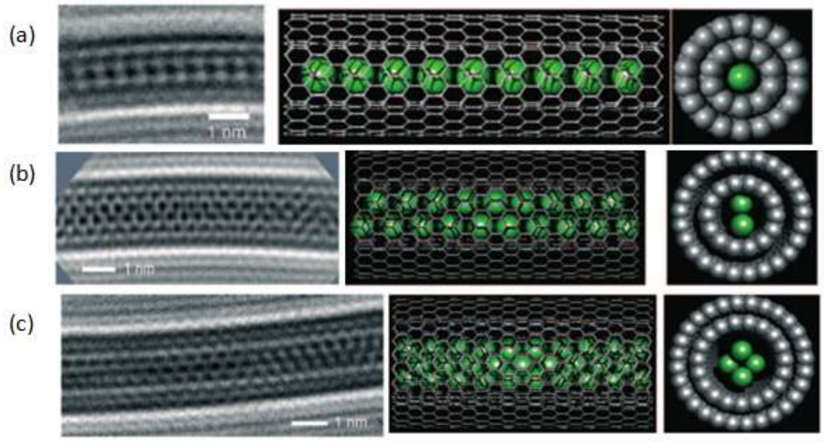

Figure I.7: Observed HRTEM image (left), simulated HRTEM image (middle), and corresponding structure model (right) of a) single, b) two and c) four atomic chains of Eu atoms encapsulated in DWCNTs. Gray carbon, green europium (reproduced from ref.34).

In contrast to confined water molecules that form small clusters within the other porous materials such as silica or zeolites, water molecules confined within CNTs form chain structures. A single-file chain formed in the cavity of the narrowest (6, 6) SWCNT with 8.1 Å diameter (35-37).

Apart from allowing the formation of chain-like or wire-like materials, the cavity of CNTs may stabilize unstable structures of nanoparticles (NPs). For example, γ-Fe NPs with face cubic centered (*fcc*) crystal structure, known to be stable between 912-1394°C in the bulk, retained their stability at room temperature when confined in CNTs (38). Confined cobalt nanorods have adopted a *fcc* structure instead of the stable hexagonal close packed (*hcp*) structure (39).

Space restriction inside CNTs may also hinder aggregation due to high surface energy of the confined NPs, thus enforcing their stability. For example, RhMn NPs were deposited on the inner (RhMn-*in*) and outer (RhMn-*out*) surface of CNTs, and the CNT-confined NPs have served as catalysts for the reaction of CO/H_2 conversion to ethanol (40). RhMn-*in* NPs were found to be in the range of 5-8 nm after 112 hours at 320 °C under 5 MPa, whereas RhMn-*out* NPs were more aggregated with a size of 8-10 nm. A similar effect with confined Fe NPs was also observed in the Fischer-Tropsch reaction (41).

Moreover, a stabilization of Au NPs, deposited respectively on the inner and outer sidewalls of graphitized carbon nanofibers (GNFs) was observed. Two mechanisms responsible for the Au NPs growth were suggested from *in situ* TEM imaging (42), using the electron beam as source of energy to promote the growth of the Au NPs. NPs on the inner surface are supposed to undergo the Ostwald ripening process (43) because the graphitic step-edges forming the internal surface can stabilize them, restricting their migration and thus limiting their aggregative growth. In contrast, NPs on the outer surface are supposed to undergo migration followed by coalescence (Figure I.8). After further heating at 300°C, encapsulated Au NPs exhibited no changes, whereas NPs on the outer sidewall aggregated. In this case, the stabilization of the confined Au NPs is attributed not only to the space restriction, but also to the interaction between Au NPs and the inner sidewall.

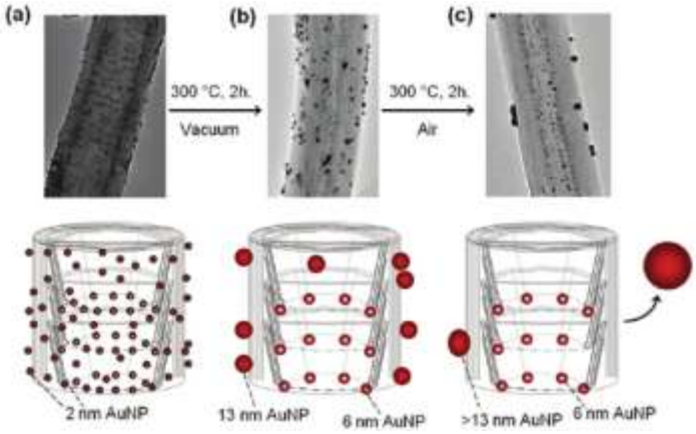

Figure I.8: TEM images and schematic diagrams illustrating the Au NPs adsorbed on the GNF outer surface and anchored at the graphitic step-edges within the GNF (a) immediately after the deposition of 2.3nm Au NPs, (b) after heating the Au NP-GNF composite in vacuum at 300°C for 2h, and (c) after additional heating at 300°C in air for a further 2h, and post-heating in vacuum (reproduced from ref.43).

I.2.3 Modification of confined species properties

Some properties and behavior of confined materials can be changed due to interactions between the confined materials and the inner sidewalls. Bao *et al.* have studied the redox behavior of iron and iron oxide NPs encapsulated within MWCNTs (44). As presented in Figure I. 9, (a) and (b) correspond respectively to the XRD pattern of the oxidation process of Fe-*out*-CNT and Fe-*in*-CNT with 1% O_2 in He. For Fe-*out*-CNT, the intensity of the peak indicative of the Fe phase (110) at $2\theta = 44.1°$ starts to decrease at ∼90°C (T1), and disappears around 290°C (T3) suggesting that the oxidation of Fe is completed. In contrast, the significant decline of the same phase of Fe-*in*-CNT is observed at ∼160°C (T1), and Fe metal fully disappears at 405°C (T3), as displayed in (c). This comparison clearly indicates that Fe NPs confined within CNTs are more difficult to oxidize than those on the outer sidewalls.

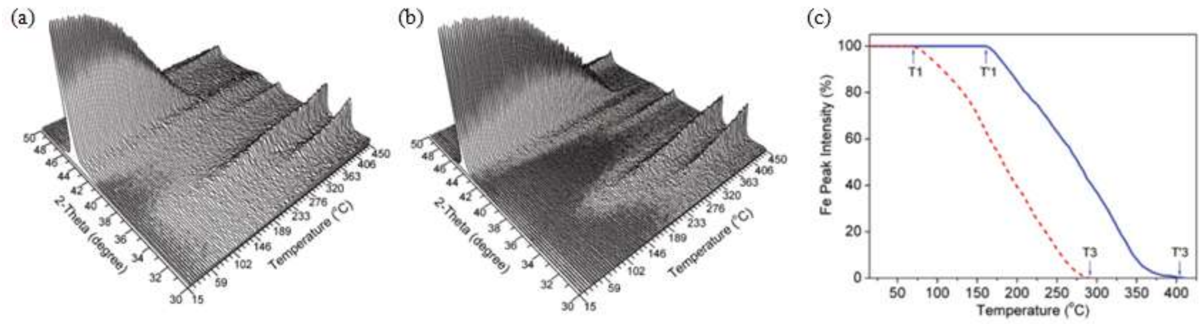

Figure I. 9: *In situ* XRD patterns of (a) Fe-*out*-CNT; (b) Fe-*in*-CNT; (c) the intensity change of the Fe diffraction peaks during temperature programmed oxidation. The dotted red line in (c) denotes Fe-*out*-CNT, and the solid blue line, Fe-*in*-CNT (reproduced from ref.44).

The auto-reduction behavior of Fe_2O_3 NPs has also been studied by monitoring the evolution of CO while heating the samples in a He stream. It has been found that the confined Fe_2O_3 NPs were reduced by carbon at lower temperature than those located on the outer surface (44, 45). Based on the observations, they proposed that an electron deficiency of the inner CNT surface is responsible for the facilitated auto-reduction of the encapsulated Fe_2O_3 (45). The curvature of graphene sheets induces a deviation from sp^2 hybridization to an intermediate between sp^2 and sp^3, and as a result the π electron densit is shifted from the concave inner to the convex outer surface of CNTs (46, 47), causing a deficient electron density on the interior surface while enriched electron density on the outer surface (Figure I. 10). Probably this electron density loss can be partially compensated through interaction with the encapsulated Fe_2O_3 NPs. Apparently this destabilizes the oxide nanoparticles and facilitates the autoreduction of the encapsulates. It is noticeable that the smaller the diameter of CNTs is, the more intense the curvature CNTs, thus the more electron density is shifted from interior to exterior, which is consistent with the observation referring to auto-reduction temperature that became lower with a decrease of the CNT diameter.

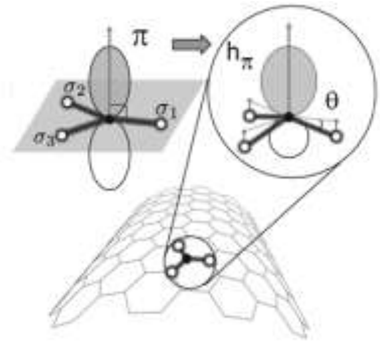

Figure I.10: Schema showing the π orbital in planar graphene and deviation to hybrided π (h_π) under bending together with the pyramidalization angle *θ* that is the angle between σ and π orbitals minus 90 degree and describes the curvature-induced shift in sp^2 hybridization. (0° for the *sp^2* hybridization and 19.5° for the pyramidalization angle for tetrahedral *sp^3* orbital) (reproduced from ref.24).

Khlobystov *et al.* have confined and investigated single-molecule magnets (SMM) within MWCNTs of a mean inner diameter of 6.5 nm (48) (Figure I.11). It was found that the confined $[Mn_{12}O_{12}(O_2CCH_3)_{16}(H_2O)_4]$ ($Mn_{12}Ac$) molecules decomposed at a slightly higher temperature (240°C) than the free molecules (220°C). This indicates that thermal stability and resistance towards air oxidation of the confined SMM molecules are enhanced. Moreover, the $Mn_{12}Ac$ molecule was observed to move within the CNT cavity under the influence of the electron-beam in the microscope, revealing that the molecules are only held by van der Waals forces, with no covalent bonds formed between the SMM and the CNT sidewalls.

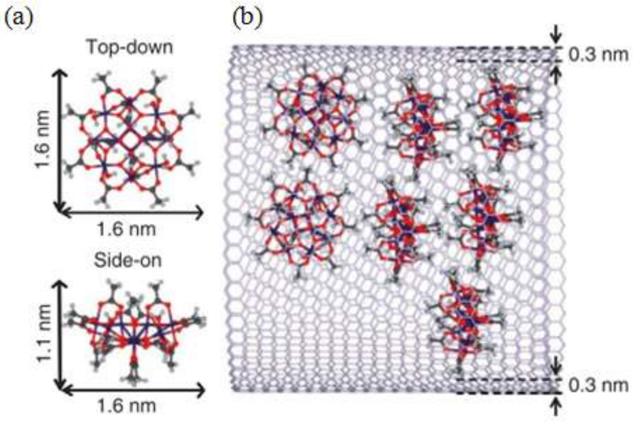

Figure I. 11: (a) Size and structure of a SMM $Mn_{12}Ac$ molecule; (b) Schematic representation of the innermost layer of a CNT hosting $Mn_{12}Ac$ molecules (reproduced from ref.48).

Mn_3O_4 NPs, resulting from the decomposition of $Mn_{12}Ac$ were successively confined within two types of hollow carbon nanofibers, a herringbone carbon nanofiber (CNF) and a graphitized carbon nanofiber (GNF) (49). The confinement affects the magnetic behavior of the resultant hybrid nanomaterials. This effect was observed as a decrease of the ZFC (zero-field-cooled)/FC (field-cooled) blocking temperature in the following order: non-encapsulated Mn_3O_4> Mn_3O_4@CNF > Mn_3O_4@GNF, which is consistent with the decreasing degree of aggregation of the Mn_3O_4 NPs as observed by TEM (Figure I.12). In addition, the encapsulated Mn_3O_4 NPs presented lower coercivity values than free NPs as a result of the confinement. These magnetic property modifications may be attributed to the precisely controlled arrangement of NPs connected to the internal structure of the host.

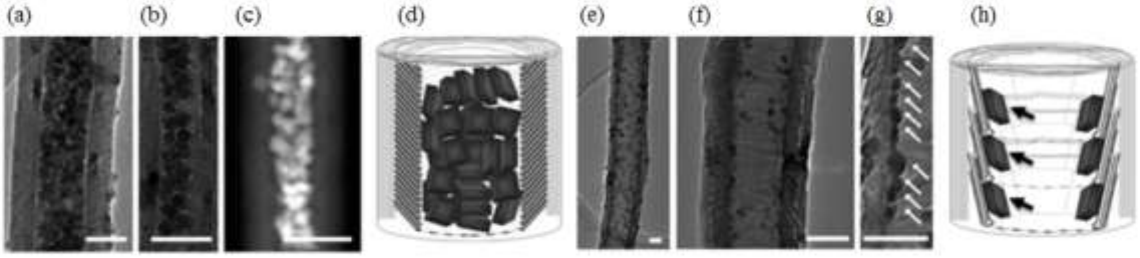

Figure I. 12: Dense packing of NPs in Mn_3O_4@CNF, as revealed by bright field TEM (a-b) and high-angle annular dark-field scanning TEM (HAADF-STEM) (c). Bright-field TEM images of Mn_3O_4 nanobricks adsorbed on the step-edges of GNF (e–g). The scale bars are 40 nm. Schematic diagrams illustrating Mn_3O_4 nanobricks densely packed in a CNF (d) and sparsely distributed within a GNF through anchoring to the graphitic step-edges (h) (reproduced from ref.49).

Diffusion of gas or liquids in CNTs has also been theoretically studied because of potential applications in separation, chemical reactions, drug delivery and sensing. A faster diffusive behavior of the confined phase has been frequently reported (50-52). The diffusivity of N_2 was predicted to be faster in SWCNTs with diameters ranging from 0.86 to 1.6 nm than that outside (50). Water confined in infinitely long CNTs with diameter 1.08 nm diffused faster due to the long-lasting hydrogen bonds in narrow CNTs (51). The diffusion of *n*-heptane inside individual SWCNTs was also more than 30 times faster than the bulk diffusion at the same temperature (52).

I.2.4 Chemical reactivity and catalysis

Up to now, relatively few experimental studies have provided reliable insight into confinement effects in CNTs due to synthetic difficulties. Nevertheless, an increase of the catalytic activity and/or selectivity when using confined catalysts has been often reported. CNTs have been used to confine catalysts for reactions such as syngas conversion (40, 53), hydrogenation (54-58), and ammonia decomposition (59).

Confined catalysts inside CNTs have been employed for syngas reactions, such as Fischer–Tropsch synthesis, and methanol, or higher alcohol synthesis. An interesting reaction in this category is syngas conversion to ethanol, acetaldehyde, acetic acid and C_2 oxygenates. When a RhMn catalyst was confined into the CNT channel, much higher conversions were reported than that for RhMn dispersed on the outer CNT surface (40). For the Fischer–Tropsch synthesis, the confinement of 4–8 nm Fe NPs inside MWCNTs allowed a significant increase in the activity and selectivity towards C_{5+} hydrocarbons in comparison to 6–10 nm Fe NPs deposited on the external surface of CNTs, or to 8–12 nm Fe NPs deposited on activated carbon. These results can be explained by considering the modified redox properties of the confined catalyst, for which higher amounts of iron carbide are present (53).

Hydrogenation is used to form a wide variety of commercial products. For the selective hydrogenation of cinnamaldehyde, an improvement in C=O-selective hydrogenation was detected when 5 nm Pt NPs were located inside large diameter MWCNTs rather than 2–5 nm NPs deposited on the external surface of small diameter MWCNTs (54).

Serp *et al.* reported that 2 nm Pt–Ru NPs confined inside MWCNTs of 40 nm internal diameter showed a higher selectivity towards cinnamyl alcohol formation in the selective hydrogenation of cinnamaldehyde than their counterparts deposited on the convex surface (55).

In the case of 5 nm Pd NPs located mostly inside CNTs with internal diameters ranging from 20 to 40 nm, very high selectivity towards C=C bond hydrogenation was obtained, which could be attributed to changes in the metal surface adsorption properties due to the special support morphology (56).

Li *et al.* encapsulated Pt NPs modified by cinchonidine (CD) within CNTs and found out that the encapsulated Pt NPs were very active and could lead to the highly enantioselective hydrogenation of α-ketoesters (57). The high activity and enantioselectivity were attributed mainly to the unique properties of the nanochannels of the CNTs as they can be readily enriched in both CD and the reactants. The chiral modifier CD that is adsorbed onto Pt surface not only induces the enantioselectivity of the reaction, but also accelerates the reaction rate of Pt catalysts for the asymmetric hydrogenation of α-ketoesters (Figure I. 13).

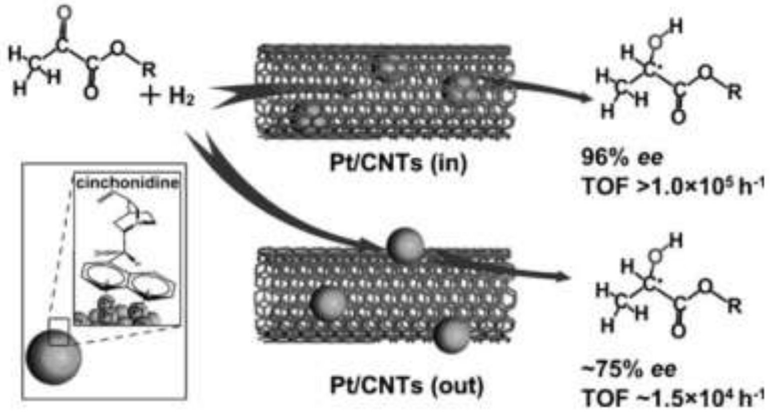

Figure I.13: Asymmetric hydrogenation of α-ketoesters on Pt NPs encapsulated within CNTs (Pt/CNTs (in)) and adsorbed onto CNTs (Pt/CNTs (out)) with CD as a chiral modifier (reproduced from ref.57) (TOF= turnover frequency).

In the NH_3 decomposition reaction for hydrogen production, 14 nm alloyed FeCo NPs located within CNTs with an inner diameter of 20–50 nm gave higher conversion (48%) than 15 nm FeCo NPs deposited on the external surface of the same CNTs (24%) (59). The confinement effect improved the thermal stability rather than the TOF and the sintering of NPs inside CNTs was reduced.

In conclusion, the studies referring to the confinement effects in the cavity of CNTs have opened opportunities for developing novel hybrid nanomaterials that may exhibit novel structures, novel properties, and novel behaviors. Hence, methods for selective filling of CNTs with foreign materials should be developed to take advantage of confinement effect.

I.3 Filling CNTs

I.3.1 The early experiments

The earliest attempts of introducing foreign materials inside CNTs began in 1993, two years after the first comprehensive and detailed characterization of MWCNTs published by S. Iijima (22). Four publications reported fillings of MWCNTs with metal oxides (PbO (60) and Bi_2O_5 (61)), carbides (Y_3C and TiC (62)), and metals (Ni (63)) in order to obtain inorganic nanowires. Encouraged by these first results, filling of the inner cavity of MWCNTs with various foreign species was widely and enthusiastically studied by physicists, chemists and even mathematicians. At the beginning, researchers worked on filling arc-produced MWCNTs *via* an "*in situ* filling" route, where compounds were introduced during the CNT growth process. The first results were not really successful due to low filling yields. Later on, SWCNTs (64, 65) renewed the enthusiasm and attracted a great interest (66, 67) due to their extreme stability and their quasi one-dimensional morphology. Five years later, in 1998 the first studies on filling SWCNTs appeared, including the filling of pre-opened SWCNTs with $RuCl_3$ (68) reported by Sloan *et al.* and the so-called "peapod" (69) reported by Monthioux *et al.*, where fullerenes were encapsulated and packed in the cavity of SWCNTs (Figure I. 14). Since then, more and more studies on filling SWCNTs and MWCNTs have appeared and a new field of CNT-based hybrid nanomaterials has emerged.

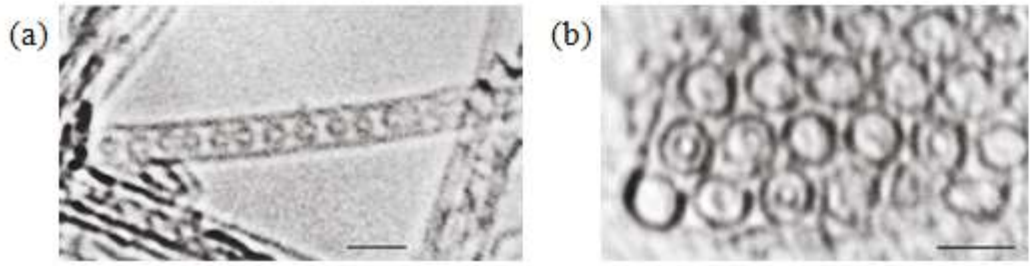

Figure I.14: (a) The first image showing a row of encapsulated fullerenes; (b) Cross-sectional image of the C_{60} fullerene peapods. Scale bar 2 nm (reproduced from ref.69).

I.3.2 Filling materials

Up to now, a wide variety of species such as atoms, molecular compounds and nanomaterials (nanoparticles, nanorods and nanowires) have been encapsulated into the inner cavity of CNTs.

—Atoms

Iodine (32, 33) was the first substance introduced in the cavity of CNTs, as presented in the previous section. Later on, a similar chain structure in which cesium atoms were also observed encapsulated within SWCNTs was reported (70). In a more recent work it was found that Cs (71) or K (72, 73) atoms attached on fullerenes may remain isolated when they were encapsulated within CNTs.

—Molecular compounds

Fullerenes@SWCNTs have become significantly popular since the first insertion of C_{60} fullerenes into SWCNTs (69) forming the so-called nanopeapods, symbolized as C_{60}@SWCNTs (74). The confinement of a large number of fullerenes, including higher members until C_{90} (75), and endohedral fullerenes (76-82) has been studied. Khlobystov *et al.* have developed the methods of filling SWCNTs with fullerene-encapsulated materials, and have studied the interactions between SWCNTs and these encapsulated materials (83-93).

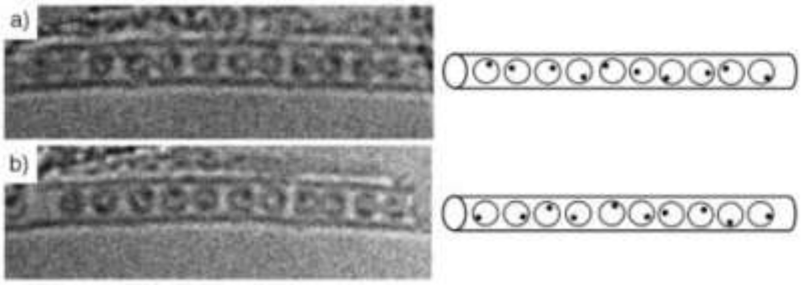

Figure I.15: A series of successive HRTEM images of (Ce@C_{82})@SWNT and their schematic representation (a and b) (reproduced from ref.84).

In addition to fullerene-encapsulated molecules, organic molecules such as *o*-carborane (94, 95), octasilasesquioxane (96), dyes (97), and metallocenes (98-104) have been encapsulated within SWCNTs as well. Besides the molecules mentioned above, filling work with gaseous molecules at room temperature has also been carried out. The most widely investigated gas is hydrogen because of the interest in its storage. Adsorption of hydrogen (105) and other gas molecules such as O_2, N_2 (106) and Xe (107) by CNTs for storage purposes is an active research area. However, lack of direct evidence renders impossible the demonstration of the filling, or the adsorption on the exterior of CNTs that is one of four distinct adsorption sites (108).

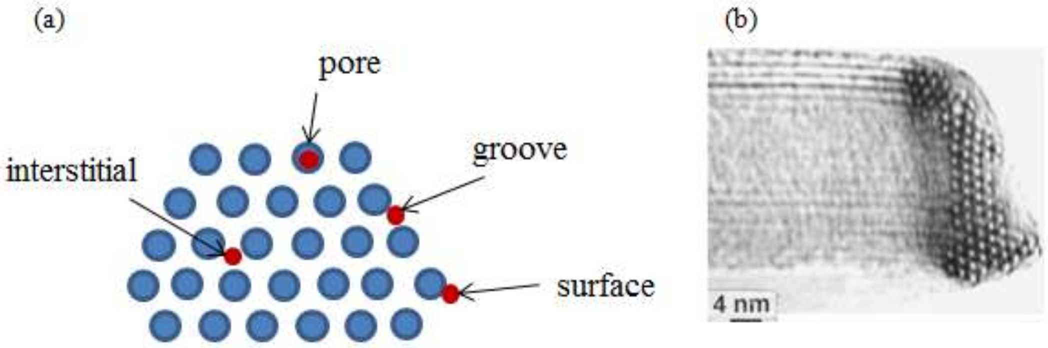

Figure I. 16: (a) Sketch of a SWCNT bundle, illustrating the four different adsorption sites (108). (b) cross-sectional of a SWCNT rope (reproduced from ref.109).

Compounds filled inside CNTs include principally inorganic salts. Among them, halides, involving Cl, Br, I and F, are the most utilized due to their wide ranges of melting temperatures and good solubility in common solvents. Hence, many studies on filling CNTs with different halides have been carried out with MWCNTs (110-112), SWCNTs or DWCNTs (68, 113-122). Nitrates are also popular salts that can be easily introduced into CNTs, as for example, iron (44) and silver nitrate (113, 123). Moreover, oxides such as CrO_3 (123), Sb_2O_3 (124), Re_xO_y (125) and PbO (126) were also introduced into SWCNTs. Filling CNTs with compounds is widely used, usually as an intermediate step, in order to encapsulate NPs within CNTs, which will be discussed in the following section.

—Nanomaterials

In contrast to confined atoms, and molecular compounds mentioned above, nanomaterials, including NPs, nanorods (NRs) and nanowires, can be formed inside CNTs *via* the decomposition of a confined precursor, such as thermal decomposition or reduction by hydrogen or other reducing agents, of molecular compound containing CNTs.

Nanowires of several crystalline transition metals with diameter around 1 nm, including Ru (68), Au (113), Pt (113), Ag (113, 127, 128), Pd (113), and Fe (98, 129), were formed in the cavity of SWCNTs as a result of the tube template effect. Cobalt ferrite ($CoFe_2O_4$) nanowires (130) with an average diameter of 50 nm and single crystalline Mg_3N_2 nanowires (131) were also synthesized using large MWCNTs as template. Interestingly, well-defined preformed NPs, sometimes possessing well-controlled size, morphology and structure, can be also directly encapsulated within CNTs, although examples are quite few (42, 49, 56, 132-140).

Rao *et al.* managed to produce large aligned-nanotube bundles encapsulating Fe_3O_4 NPs (132), which were initially suspended in water- or organic-based solvents, called "ferrofluids". Chang *et al.* introduced Ag NPs, with diameters ranging from 2 to 20 nm, inside CNTs in supercritical water (133). Coalescence of the encapsulated NPs and formation of NRs were observed in that case. Kim *et al.* studied experimentally and theoretically the filling of CNTs with fluorescent polystyrene beads (134) with 50 nm diameter (Figure I. 17a). Similar fluorescent polystyrene NPs were encapsulated using a self-sustained diffusion mechanism by Bazilevsky *et al.* (135) (Figure I. 17b). Interestingly, the fluorescent signals emitted by the NPs were visible through the sidewalls of CNTs.

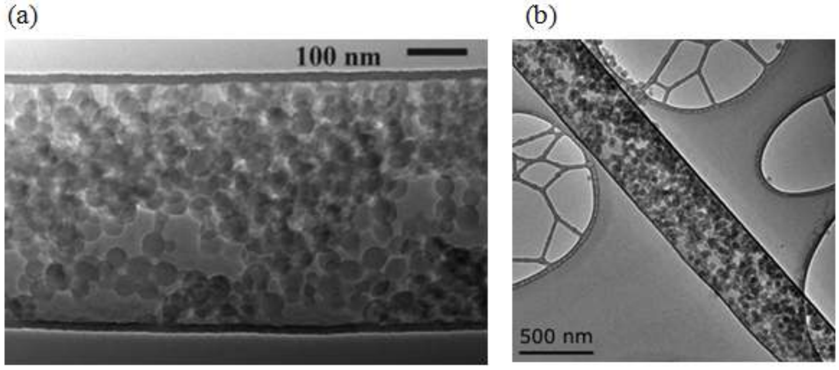

Figure I.17: TEM images of the encapsulated fluorescent NPs (a) within 500 nm diameter CNTs (reproduced from ref.134) and (b) within 200-300 nm diameter CNTs (reproduced from ref.135).

Recently, Khlobystov *et al.* introduced preformed Rh (136), Au (42,137), and Mn_3O_4 (49) NPs into the cavity of CNTs by mixing them with a suspension of targeted NPs in n-hexane or with a mixture of n-hexane and supercritical CO_2 ($scCO_2$).

Furthermore, the self-assembly of a sulfur-terminated graphene nanoribbons (GNRs) within SWCNTs was generated by decomposing confined fullerenes at high temperature (1000°C) or under an e-beam radiation (138, 139) (Figure I.18), which gave birth to a novel hybrid nanomaterial GNR@SWCNT.

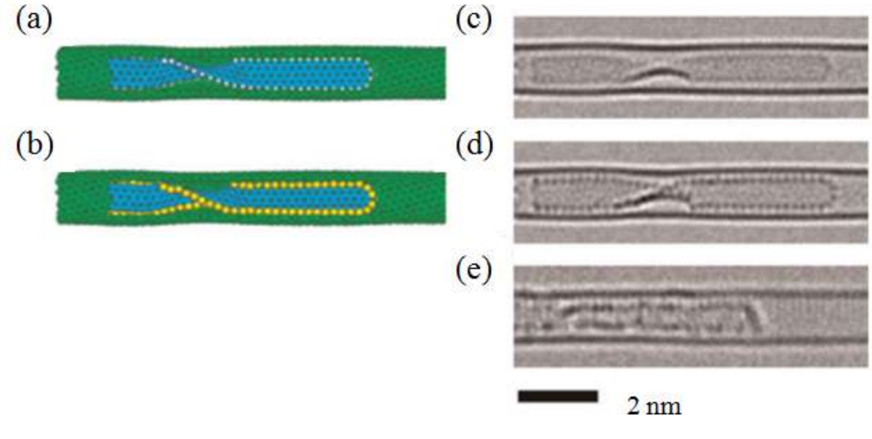

Figure I.18: Calculated HRTEM images of (c) H- and (d) S-terminated GNRs inside a SWNT and the corresponding models (a) and (b). The experimental image (e), presented for visual comparison, shows that the contrast of the nanoribbon edge matches the model with sulfur atoms (b and d) closer than the model with hydrogen atoms (a and c) (reproduced from ref.139).

Serp *et al.* reported a simple and efficient method for the selective confinement of preformed and monodispersed PtRu NPs in the inner cavity of MWCNTs (Figure I. 19a).

Then, they also efficiently and selectively confined preformed Au NPs within CNTs (140) (Figure I. 19b).

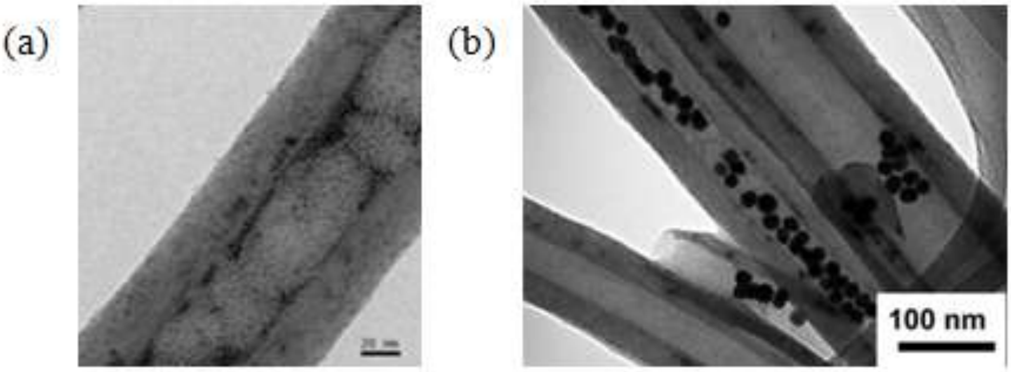

Figure I. 19: TEM images of (a) the preformed PtRu NPs and (b) the preformed Au NPs confined within MWCNTs (reproduced from ref.140).

Pham-Huu *et al.* encapsulated monodispersed Co-based NPs (~50 nm) (141) and $Fe_{3-x}O_4$ NPs (~13 nm) (142) within MWCNTs *via* an *in situ* thermal decomposition method.

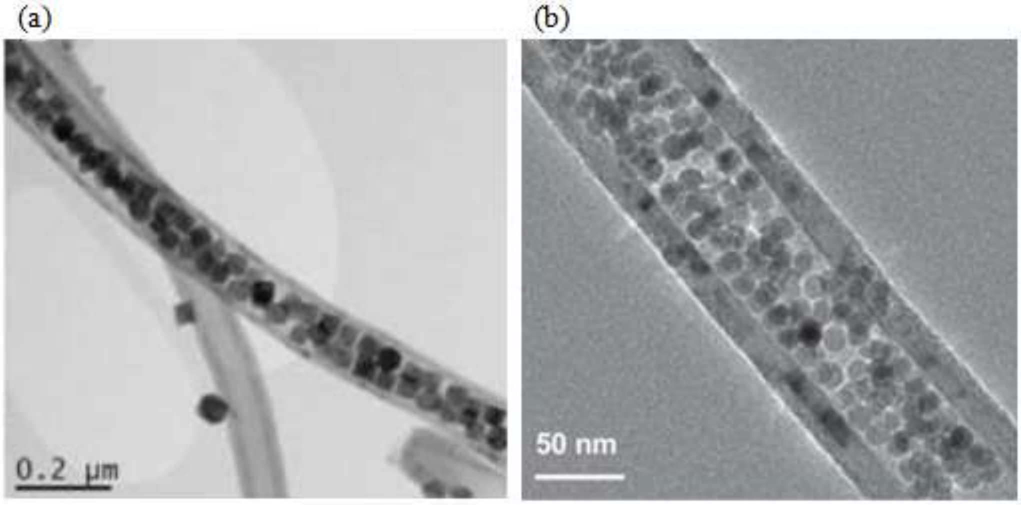

Figure I.20: TEM images of the MWCNT-encapsulated Co-based NPs (141) and $Fe_{3-x}O_4$ NPs (142) (reproduced from ref. 141 and 142).

I.3.3 **Filling methods**

Various methods of filling CNTs have been developed, depending in particular on the physical properties of the encapsulated material, the internal diameter of CNTs, and the capabilities of the methods themselves, which should be all considered as important parameters in a filling strategy. Figure I. 21 summarizes the filling routes that will be described in this section.

Materials in the vapor, liquid, or solid phases can be introduced into CNTs cavities. Therefore, physical properties of the materials filling the CNTs, such as boiling point, melting point, surface tension, and solubility, should be firstly considered. The inner diameter of CNTs is obviously an important parameter because it will determine the ultimate diameter of the filling species (vapor or melting phase) or transport media (solution or suspension) that are able to enter the cavity of CNTs.

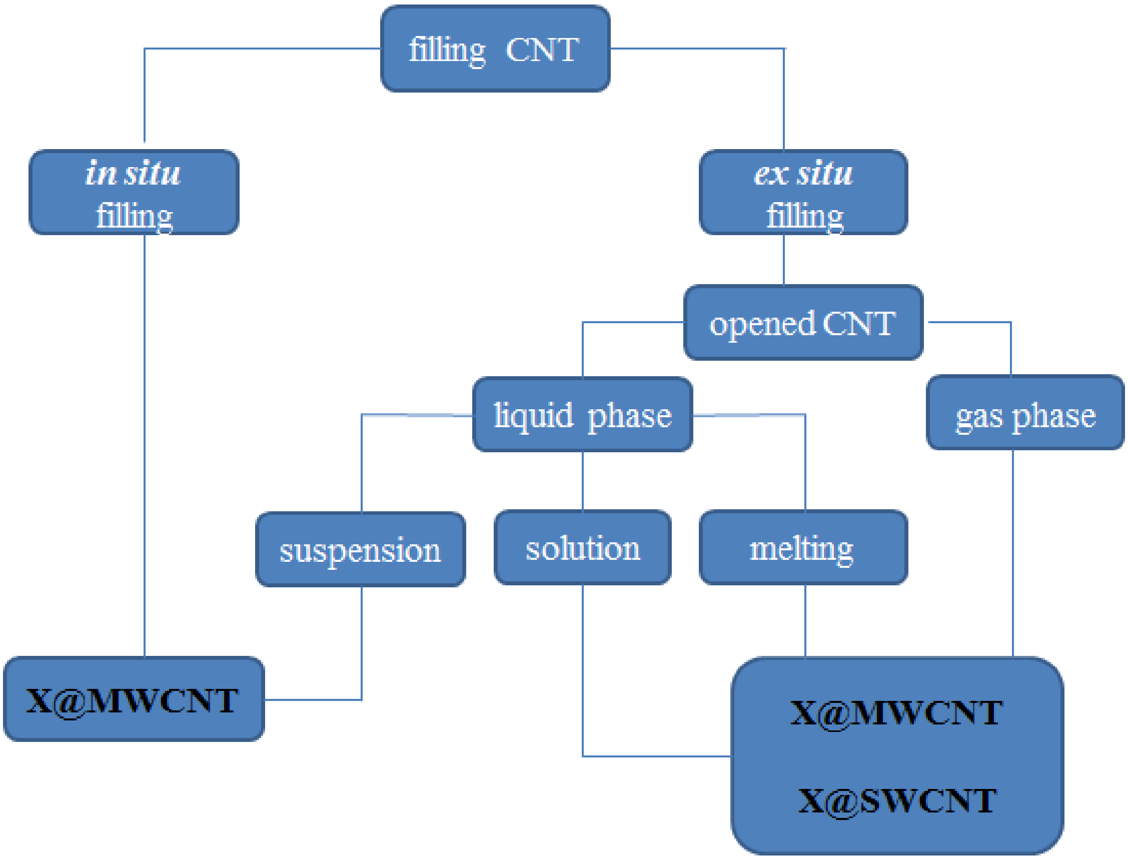

Figure I.21: Schematic representation of main filling routes for CNT-based hybrid nanomaterials (X represents foreign materials).

I.3.3.1 In situ filling processes

The *in situ* filling process is a one-step synthesis procedure and it is the earliest filling method. Foreign species can be introduced into the cavity of MWCNTs during the nanotube synthesis by the catalytic chemical vapor deposition process (CCVD) (143) (Figure I.22) or by the electric arc process (144).

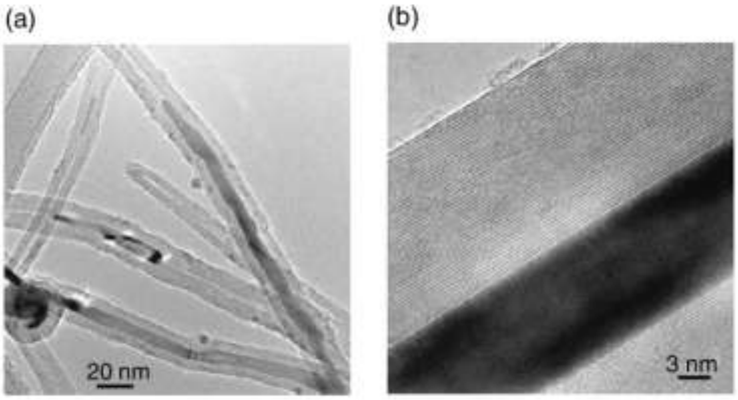

Figure I.22: (a) TEM image of in situ filled MWCNTs obtained via a CCVD-related process. The filling material is pure α-Fe (bcc Fe crystals). (b) High resolution of one of the Fe@MWCNTs in (a) (reproduced from ref.143).

The CCVD process is a method that was limited to species that catalyzed CNTs formation, typically transition metals such as Fe, Co and Ni. For example, ferromagnetic nanowires were formed in the cavity of CNTs *via* pyrolysis of ferrocene (132) or of toluene/ferrocene mixtures at different temperatures (145). Iron/nickel sulfide nanostructure-filled CNTs were also produced. They are composed of two-component Fe_7S_8 and $Ni_{17}S_{18}$ (146). Two modified CVD processes have also been developed: i) a microwave plasma chemical vapor deposition (MPCVD) was used to obtain nickel and cobalt single-crystalline NRs inside MWCNTs (147) and ii) a pulse-injection CVD was employed to produce freestanding multifunctional ferromagnetic CNT arrays (148).

The electric arc plasma process consists firstly in drilling a coaxial hole within the graphite anode and filling it with the desired elements. Then the electric arc is produced under conditions similar to that used to produce fullerenes, and finally the MWCNTs are found partially filled with the desired elements. However, the efficiency and control of the filling process is lower than for the CCVD-related method, probably because of the huge temperature gradients that are typical of the plasma zone in arc-related processes, which are also responsible for the heterogeneity in the diameter distribution of the MWCNTs synthesized that way (149,150). Contrary to the CCVD methods, the electric arc method is hardly able to fill MWCNTs filling with transition metals such as Fe, Ni, or Co, because when such transition metals are used, the growth of empty SWCNTs is promoted (64, 65). This is in fact the reason of the accidental discovery of SWCNTs, as by-products of filling MWCNTs with these transition metals.

The CCVD and the electric arc processes can complement each other because the former is mainly able to produce MWCNTs encapsulating transition metals, whereas the latter is able to produce MWCNTs filled with many other elements. However, *in situ* filling that includes these two mentioned processes is limited to fill MWCNTs but not SWCNTs. Moreover, the size, the loading and the morphology of the encapsulated materials cannot be controlled, forming CNT-templating nanowires or NRs. Therefore, new filling methods for SWCNTs were needed, and the *ex situ* filling processes were subsequently used and fully developed.

I.3.3.2 Ex situ filling processes

Ex situ filling processes have been extensively exploited and can be used to introduce almost any species into SWCNTs, DWCNTs and MWCNTs. CNTs should be firstly opened and shortened via suitable methods depending on filling materials and filling strategies. Two principal types of processes are involved: gas phase processes and liquid phase processes, which may include one or several steps, where post-treatments are involved, with sometimes a final cleaning step in order to remove undesired materials.

I.3.3.2.1. Opening and purification of CNTs

CNTs can be open-ended or closed by a hemispherical fullerene-type cap, depending on their synthesis process (151). Opening end tips of CNTs can be achieved through two main pathways: thermal treatments in an oxidizing gaseous phase (air or O_2) (61), or reactions with strong acids such as HNO_3, H_2SO_4, HNO_3/H_2SO_4 or H_2O_2 (110, 116). Both oxidation pathways are efficient to open SWCNTs and MWCNTs. In fact, the graphene lattice is relatively more inert toward chemical oxidation than the structural defects, typically five- or seven-member carbon rings, which are located on the tips and on the sidewalls as well. Obviously, carbon atoms on the tips are more reactive, because of the important curvatures of C-C bonds compared to those on the sidewall. As a consequence, damages from oxidation take place easily on the tips. Besides opening CNT tips, purifications procedures of CNTs, including removal of metal catalyst or carbon residues, as well as the introduction of functional groups, have been intensively studied (152-154). Table I.1 presents a summary of common purification techniques for CNTs (155).

Table I.1: Summary of common purification techniques for CNTs (155) (● represents accessibility).

	Metal residues	Carbon residues	Functional group
Heating in air/O_2		●	●
HCl	●		
HNO_3/H_2SO_4	●	●	●
Microwave		●	
Ar@ 2000°C	●	●	

As shown in Table I.1, all oxidative treatments can remove carbon residues, except HCl that can only remove metal residues without damaging the carbon skeleton. On the contrary, microwave-assisted purification can remove only amorphous carbon around metal particles (153). Gaseous oxidation cannot remove metal residues, and often damages CNT surfaces, especially at high temperature or combined with ultrasonication (156). It should be noted that metal residues may act as an oxidation catalyst, which decrease the oxidation temperature. Liquid oxidation with strong acids not only removes metal and carbon residues, but also introduces organic functional groups, consequently modifying the CNT surface and thus allowing further covalent functionalizations of the outer surface. In contrast to the oxidative treatments mentioned above, annealing at high temperature under vacuum or under inert gas allows to remove both metal residues and amorphous carbon without damaging CNT surface. This treatment also decreases the number of structural defects and therefore enhances the degree of graphitization of CNTs (157, 158).

I.3.3.2.2. Gas phase processes

Filling CNTs through gas phase processes required contacting opened CNTs with the vapor of the targeted filling materials. Hence, the filling temperature should correspond either to the vaporization or sublimation temperature of the target materials, or should be slightly higher. Materials can be divided into two types. One type possesses high affinity with the sidewall of CNTs as fullerenes (159-161, 164) (Figure I.23), whose filling process was proven to be a surface diffusion-driven mechanism (159), highly depending on temperature and heating time. The other type possesses relatively low affinity with the sidewall, and includes salts (162), oxides (125) or pure elements (34, 163). In these cases, filling involves capillary condensation due to increasing of van der Waals interactions between vapor phase molecules in the confined cavity of CNTs. Filling materials are expected to exhibit high vapor pressure in order to reach high filling yields (163).

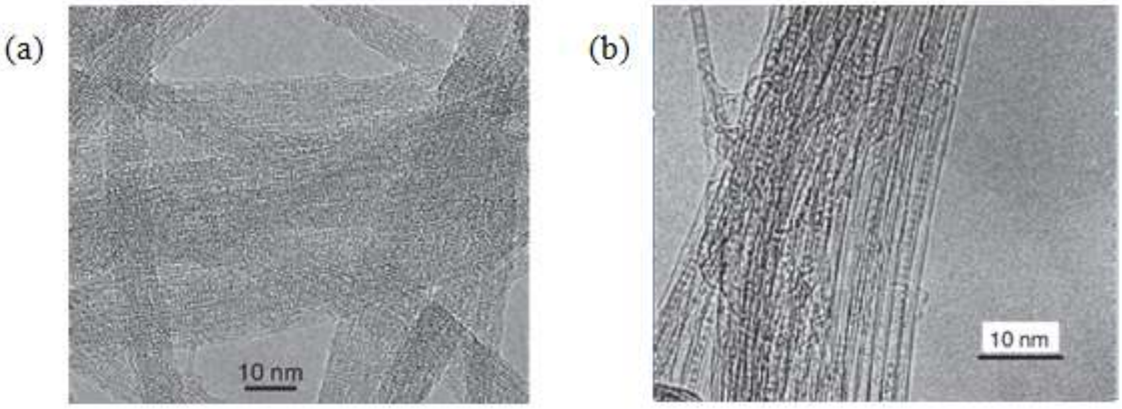

Figure I.23: TEM (a) and HRTEM (b) images of C_{60}@SWCNT (peapods) material prepared by the sublimation method at 450°C (reproduced from ref.164).

The advantages of gas phase processes include simplicity, high filling rate and high purity of the filling materials. However, the filling materials have to possess a relatively low vaporization or sublimation temperature in order to avoid reactions with carbon. This is the main drawback of gas phase processes for filling salts or oxides because of their high sublimation temperature.

I.3.3.2.3. Liquid phase processes

In contrast to *in situ* and gas phase *ex situ* filling processes, liquid phase processes are the main filling techniques by which a wide range of materials can be introduced in CNTs. Liquid phase processes can be divided into molten phase, solution, and suspension methods. All of them depend principally on the interaction between the filling liquid (organic or inorganic solvent, molten species) and CNTs. When a liquid or a solution is involved, a molten or dissolved material is used. The surface tension of the inserted liquid or solution becomes a significant parameter in order to wet the cavity of CNTs. It is considered that any liquid that has a surface tension below 100-200 mNm^{-1} should wet spontaneously the inner cavity of opened MWCNTs at atmospheric pressure (165). This is due to the Young-Laplace law and equations, which describe the capillarity-driven mechanism. For SWCNTS, it is more precisely defined as 130-170 mNm^{-1} (166). In most cases, especially for the solution and the suspension methods, "wettability" is not likely to be a problem because surface tensions of the common solvents are all below 80mN m^{-1}. However, viscosity is probably another factor that play an important role due to transport resistance of the filling liquid inside the cavity of CNTs. Furthermore, interactions between foreign target materials and host CNTs may also affect filling of CNTs, which are rarely discussed in the literature. Table I.2 presents surface tensions and viscosities of various solvents.

Table I. 2: Surface tensions and viscosities of certain liquids ordered by viscosity (reproduced from ref.167).

liquid	Surface tension (mN/m) at 25°C	Viscosity (centipoise) at 25°C
Diethyl ether	16.7	0.22
Acetone	23.0	0.31
n-Heptane	19.8	0.39
Dichloromethane	27.8	0.41
Tetrahydrofuran	26.7	0.46
Methanol	22.1	0.54
Toluene	27.9	0.56
Benzene	28.2	0.60
Pyridine	36.7	0.88
Cyclohexane	24.7	0.89
Water	72.7	0.89
Anisole	36.2 (15°C)	1.05 (20°C)
Acetic acid	27.0	1.06
Ethanol	22.0	1.07
Benzonitrile	38.8	1.27
1,3,5-trimethylbenzene	28.8 (20°C)	6.92 (20°C)
Cyclohexanol	33.4	57.5

I.3.3.2.3.a. Molten phase method

The molten phase method is a simple process whose operation is usually as easy as that of gas phase processes. The opened CNTs need to come in contact with the filling materials in a quartz vessel sealed under vacuum, and then be heated at a temperature above the melting point of the filling materials. Some examples, such as KI (118), PbO (126), CoI_2 (122), and SnTe (168), can be found in the literature. Post-treatments are sometimes used in order to transform the filling material to the aimed one. For example, opened SWCNTs were impregnated with molten CoI_2 at 550 °C for 24h. Then, the CoI_2-filled SWCNTs were annealed in H_2/Ar atmosphere at 400 °C for 24h. Finally, Co NPs were formed and encapsulated within SWCNTs (122).

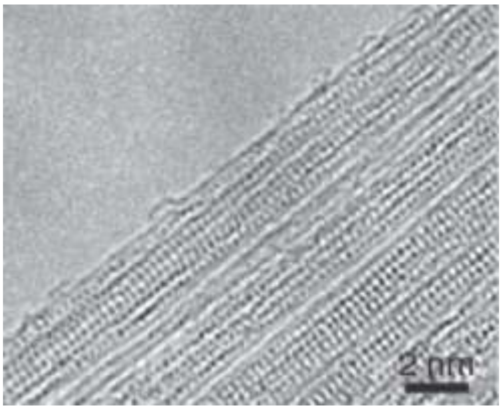

Figure I.24: High resolution TEM image illustrating the high filling yield obtained for KI@SWCNT using the molten phase method (reproduced from ref.118).

The molten phase method is relative easy to apply, and as for the gas phase process only the desired filling material is entering the cavity of CNTs, in the absence of solvent. However, a main limit is that filling material has to exhibit a low melting point, not to react with CNTs, and its molten phase has to exhibit low surface tension (165). As a result, many metals and salts possessing high melting points and high surface tensions cannot be introduced in CNTs by this method (67).

I.3.3.2.3.b. Solution method

Application of the solution method requires taking into account the solubility of the filling materials in the filling solvent. Examples of one-step filling of the desired material are very rare because the filling salt or precursor solution inside CNTs is just an intermediate step, and subsequent steps, such as post-treatments (thermal treatment and/or reduction), and washing procedures, are usually required to obtain the filling of the desired materials, in most cases, NPs. The main advantage of this method is that it is suitable for filling all types of CNTs.

The first example of the solution method was the filling of SWCNTs with Ru *via* reduction of $RuCl_3$ (68). Bao *et al.* confined Fe_2O_3 NPs within small inner diameter MWCNTs, in the range of 2-12 nm, by using an aqueous $Fe(NO_3)_3$ solution under stirring and ultrasonication, then followed by slow water evaporation at room temperature and calcination under He (44, 169). TEM images have shown that 80±5% Fe_2O_3 NPs were located inside the tubes. The same group also confined Ru NPs within shortened small MWCNTs *via* filling with a $RuCl_3$/acetone solution (112, 170). Ultrasonic treatment and extended stirring were employed to increase the capillary forces because the trapped air and the dynamics of filling in the opened CNT channels hinder migration of the solution by capillary forces, as pointed out by Ebbesen *et al.* (171). It was also considered that slow evaporation of the solvent results in a concentration gradient of the filling salt between the interior and the exterior of CNTs. That means that the solution outside the tubes is more concentrated and salt will migrate into the cavity of CNTs, where the solution concentration is lower (112). Consequently, subsequent slow drying at 110 °C in air resulted in most Ru NPs (over 80%) being introduced into CNT channels (Figure I.25).

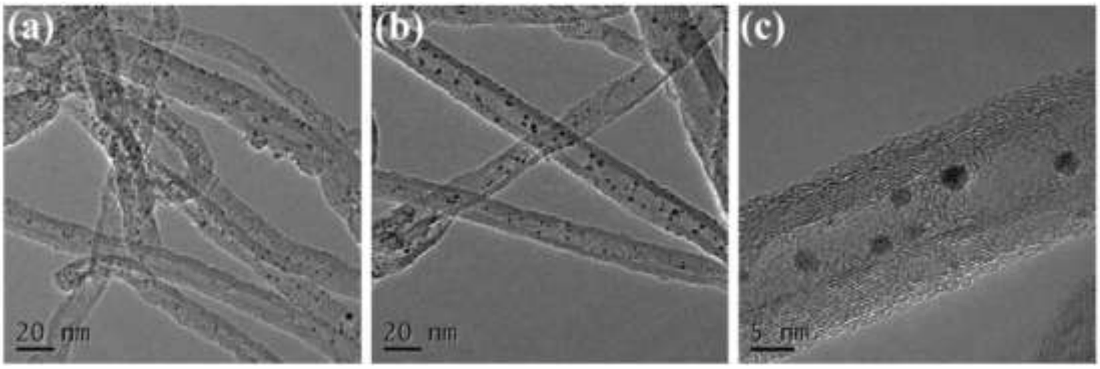

Figure I. 25: Dispersion of Ru NPs inside the CNT channels using the wet chemistry method: (a) sample obtained without being aided by ultrasonic treatment and extended stirring; (b and c) different magnification images of sample obtained with the aid of ultrasonic treatment and extended stirring (reproduced from ref.112).

Nguyen *et al.* studied the effect of several parameters that include carbon nanotube (CNT) pretreatment and diameter, and the nature of the metal (Co, Ru, Pd), the metal precursor (nitrate, chloride, organometallic complexes), and the solvent on the filling yield of metallic NPs in CNT channels (172). The obtained results show that it is possible to modulate the filling yield between 10 and 80 % by controlling the CNT opening and playing on the molecular recognition of the inner/outer surfaces by the metal molecular precursor. Interestingly, the best filling yields have been obtained on nitric acid oxidized nanotubes, a treatment often used for the preparation of most CNT-supported metal catalysts. The confined NPs systematically show a smaller particle size than those supported on the external surface.

Tessonnier *et al.* improved the solution method for decorating CNTs with Ni NPs (173). Their approach is based on the difference in the liquid-solid interface energies of an aqueous and an organic solvent with the CNT surface. This method allowed selective localization of Ni NPs inside (75% of NPs in the inner cavity) or on the outer surface of CNTs (Figure I.26).

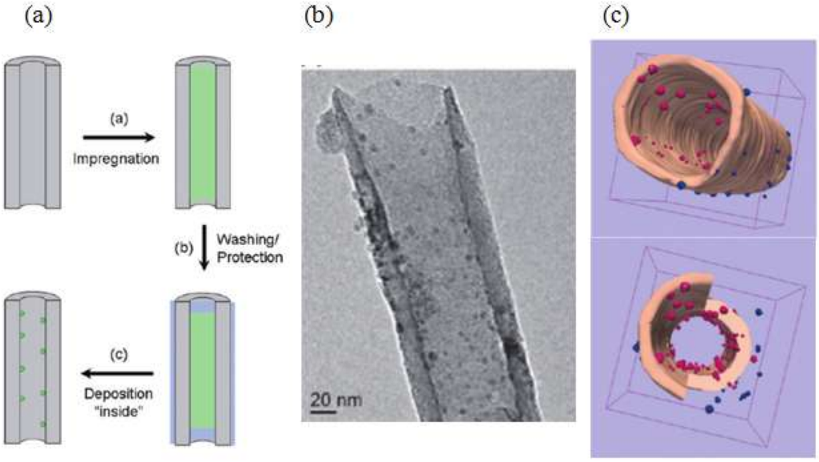

Figure I.26: (a) Schematic view of a longitudinal cross section of a CNT during the different steps for the selective deposition of NPs inside CNTs; (b) Typical 2D-TEM image of the sample "metal inside"; (c) Modeling of the reconstructed volume: (pink) CNT, (red) Ni NPs inside the tube, (blue) Ni NPs on the external surface (reproduced from ref.173).

In spite of high selective deposition achieved, 20-25% of the Ni NPs are still attached on the outer surface of CNTs. For some specific applications, such as magnetic applications, it is critical to ensure that all the targeted NPs are located inside CNTs. Consequently, a selective procedure for the removal of the NPs on the outer surface, without affecting the encapsulated NPs, is highly desirable.

Cleaning treatments have been developed in order to remove species located on the outer surface. These cleaning treatments can be carried out after (174-176) or before (177-179) post-treatments steps. W. Chen *et al.* confined TiO_2 NPs with diameters in the range 3-8 nm inside MWCNTs (inner diameter 4-8 nm) by the hydrolysis of titanium salt solution (174). Then, they treated the dry sample with HF to remove titanium species from the outer surface and washed with deionized water until the filtrate reached pH value of about 7. The loading of TiO_2 was determined to be 20wt% by element analysis. Z. Chen *et al.* filtered and washed with deionized water their Pt NPs-confined CNTs obtained by reduction of a Pt salt with a sodium formate solution (175), to finally reach 5wt% Pt located inside CNTs.

Cleaning before post-treatments has been also employed (177-179), although cleaning efficiencies were not comparable due to the lack of reliable data. Moreover, it is unclear whether washing remove simultaneously or not part of the desired confined materials.

Capobianchi *et al.* have developed a controlled, adaptable cold wet chemical procedure (Figure I.27), consisting in a lyophilization process to fill MWCNTs, followed by a washing step to clean the outer surface without removing the encapsulated materials (111).

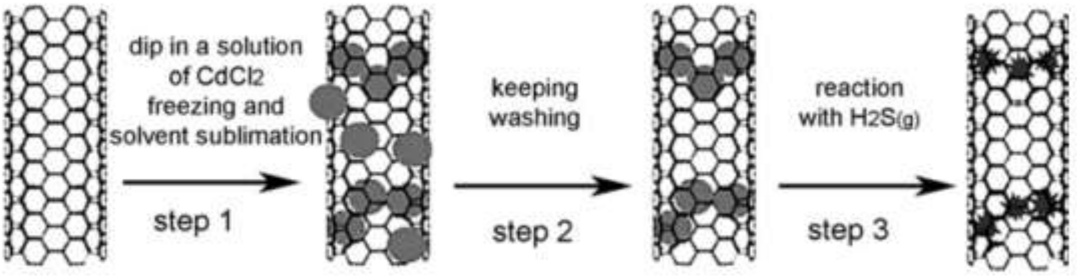

Figure I.27: Schematic representation of the cleaning procedure employed for the synthesis of CdS nanocrystals inside MWCNTs (reproduced from ref.111).

First, an aqueous solution of $CdCl_2$ is introduced into the opened tube channels only by capillary force at room temperature under vacuum. After ultra-sonication and stirring, the mixture is frozen at a temperature just below the solution freezing point. Then solvent sublimation is carried out at a pressure close to 10^{-2} mmHg for 2 days. During this step $CdCl_2$ clusters or particles are deposited both inside and on the external surface of CNTs. In a second step, benzene is used to fill the CNTs in order to protect the encapsulated $CdCl_2$ inside. Then, the mixture is washed by water to remove the $CdCl_2$ outside. $CdCl_2$ should be insoluble in the protecting solvent, benzene. On the contrary, the washing solvent has to be able to dissolve $CdCl_2$, while being immiscible with benzene. In a final step, the encapsulated $CdCl_2$ reacts with H_2S to generate CdS crystals.

The main difference between the lyophilization process and the other wet method used by Bao *et al.*, where the solvent is eliminated by evaporation has been discussed. It was proposed that neither a fast nor a slow evaporation process can control the amount of filling materials. That was tested by using a conventional slow evaporation method with solutions at different concentrations. The resulting cluster size was about the same for all concentrations as well as the amount of material filled inside the cavity (111).

With this specific filling and cleaning procedure, Astinchap *et al.* produced a FePt @MWCNTs/Ru nanocomposite, in which 2-5 nm FePt NPs were selectively encapsulated within CNTs, and subsequently 5 nm Ru NPs were deposited on the outer surface (180). The filling with magnetic NPs should easily allow magnetic separation and recycling of the catalyst. In addition, magnetic NPs would allow heating the catalyst by means of an alternate external magnetic field. In this way, only the catalytic NPs would be heated, enhancing selectively their reactivity and saving the energy needed to heat the entire reactor. On the contrary, without a lyophilisation protecting step, the presence of Ru NPs and FePt/Ru core-shell NPs were simultaneously observed inside MWCNTs instead of FePt NPs. However, no detailed result concerning the filling yield was mentioned in this work.

In conclusion, the solution method is such a powerful technique that a large range of materials can be introduced into the cavity of CNTs. Based on this method, several cleaning treatments have been developed in order to remove the species on the outer surface. The use of a solvent for dissolving and transporting filling materials is undoubtedly a big advantage.

I.3.3.2.3.c. Suspension method

The suspension method was used to fill CNTs with preformed NPs, although so far only MWCNTs have been involved. In related experiments, opened MWCNTs were immerged into a suspension of targeted NPs, and then the mixture was evaporated and/or washed. As presented in the section I.2.2, Fe_3O_4 (132), Ag (133), polystyrene (134, 135), Rh (136), Au (42, 137), Mn_3O_4 (49), and PtRu (56) NPs have been encapsulated within MWCNTs either from conventional solvents or from *sc*CO_2. In contrast to common solvents used as transport medium, *sc*CO_2 is a valuable alternative since it allows a high penetrability in nanopores due to its almost zero surface tension and low viscosity. Khlobystov *et al.* have successfully encapsulated many kinds of materials by this method, including NPs, and molecules such as fullerenes (83, 86), octasilasesquioxane (96), and $Mn_{12}Ac$ (48).

Besides common cleaning treatment like washing and filtration, La Torre *et al.* have developed a three-step cleaning procedure aiming at the selective removal of non-encapsulated Au NPs, whereas retaining the ordered arrays of encapsulated NPs (Figure I. 28) (137). First, the AuNP-GNF composite was immersed in benzene (or cyclohexane) initially under reduced pressure before the atmospheric pressure was restored rapidly. Under these processing conditions, liquid benzene fills up the channels of GNFs due to a combination of capillary action and a favorable pressure gradient. In a second step, by lowering the temperature to 0°C, the solvent in the internal channels of the nanofibers becomes solidified, thus protecting the encapsulated NPs, while the NPs on the outer GNF surface remain exposed to the environment. Finally, either KI/I_2 (181) or "organic *aqua regia*" (182) was employed to dissolve the gold core of the externally adsorbed NPs, followed by removal of the solvent.

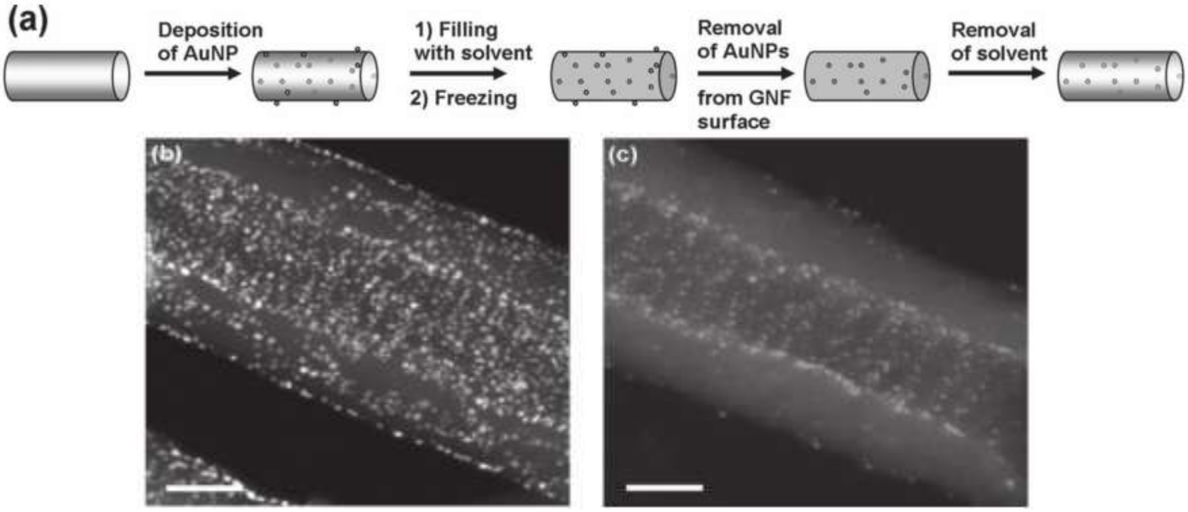

Figure I.28: (a) Schematic representation of the selective removal of Au NPs from the outer surface of GNFs; HAADF STEM images of AuNP-GNF composites before (b), and after (c), the washing procedure. Scale bars are 20 nm (reproduced from ref.137).

Serp *et al.* recently reported a simple and selective procedure to confine preformed NPs, which involved the use of surface chemistry to favor interaction of NPs with the inner surface of the tubes and repulsion between NPs and the outer surface of the tubes (56). For comparison, three MWCNTs with an average inner diameter of 40 nm, possessing different outer surface chemistry, were used: opened CNTs without functional group on the outer surface (CNT_1), oxidized CNTs with -COOH as the main functional group (CNT_2), and long alkyl chain covalently functionalized CNTs (CNT_3). As shown in Figure I. 29a, the repulsive interaction between the outer surface of CNT_3 and the NPs hinders the attachment of NPs on the outer surface, whereas the π-π stacking interaction between the NPs ligands and the tube internal surface drives the NPs inside the tubes. Three-dimensional TEM analyses have shown that this procedure allows the confinement of 80% of PtRu NPs (2 nm average diameter) in the inner cavity of 40 nm internal diameter CNT_3, even at metal loadings as high as 40 wt% (Figure I.29b and c). Without this recognition for CNT_1 and CNT_2, the selectivity of confinement was quite poor.

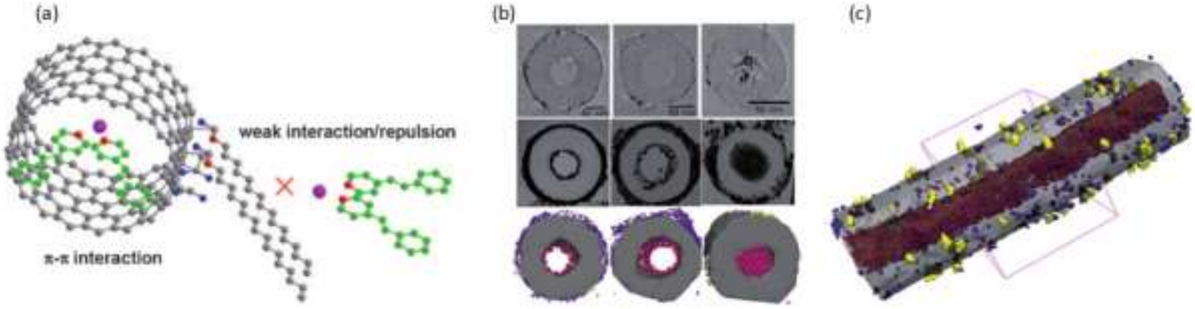

Figure I.29: (a) Strategy adopted to drive NPs into CNTs, PtRu NPs pink, N red, O blue, C gray and green; (b) Top: examples of transverse sections extracted from the reconstruction, middle: minimum-intensity projections of all sections on the same plane to highlight the contribution of the NPs, and bottom: modeling of the reconstruction of 5 wt% PtRu@CNT$_2$ (left), 11 wt% PtRu@CNT$_1$ (middle), and 23 wt% PtRu@CNT$_3$ (right); (c) Modeling of the reconstructed nanoreactor volume (b right) by 3D TEM, with blue PtRu NPs outside, red PtRu NPs inside, and yellow Au NPs deposited on the CNT surface for image reconstruction (reproduced from ref.55).

In conclusion, the highlight of this suspension method is that the introduced preformed NPs can be well defined in size, structure and morphology, which is critical for confinement effect studies and productions of well-defined nanocomposites. However, this method is presently limited to MWCNTs, unless cluster smaller than 1 nm in diameter can be synthesized for filling SWCNTs.

I.4 Magnetic nanoparticles confined within CNTs

Magnetic nanoparticles (MNPs) are potential candidates for catalysis, biotechnology and biomedicine applications (183-185). In catalysis, MNPs or functionalized MNPs can serve as catalyst, and additionally they can be useful to separate other catalysts, nuclear waste, biochemical products, and cell (186-188). In biotechnology and biomedicine, MNPs have been used for protein (189) and gene separation (190, 191) due to their high separation efficiency. Other biomedical applications, such as magnetic drug-targeting and/or delivery (192, 193), magnetic resonance imaging (MRI) (192, 194), and hyperthermia treatment combined as a supplementary treatment with chemotherapy, radiotherapy and surgery in cancer therapy (195-197). In spite of some considerable achievements have been reached in these *in vivo* applications, many fundamental issues have to be solved, such as well size controlled MNPs, their stability and biocompatibility, and drug-particle binding (195, 198).

CNT-confined MNPs may be good alternatives for the magnetic applications due to the specific properties of CNTs which have recently been proposed as alternative multifunctional nanostructures in nanomedicine for imaging (199, 200), tissue engineering (201) and drug-delivery (202-204). A number of *in vitro* and *in vivo* studies have been reported toward the understanding of the toxicity of CNTs (205). It has been found that long (>5 µm) pristine CNTs can induce cytotoxicity and inflammatory responses if inhaled, whereas intravenous or intratumoral administration of short (<500 nm) or exohedrall functionalized CNTs revealed to be non-toxic (206) and to be expelled in urine (207) and fecal excretions (208). In addition, the cavity of CNTs may provide protection for confined materials and present surprising confinement effects as described in the previous part of this chapter. Therefore, the MNPs@CNTs combined the magnetic properties of the confined MNPs and the stability of the CNTs may become promising nanoreactors.

For confining magnetic materials within CNTs, the most used method is CVD in which catalysts (Fe, Co and Ni) can be embedded inside the CNTs during the synthesis process (132, 143, 145-148, 209, 210). From this method, magnetic nanowires or nanorods are often obtained, and their sizes cannot be controlled, which makes it impossible for tuning magnetic properties of the nanocomposites.

Compared to the magnetic nanomaterials produced by CVD process, size controlled MNPs have been selectively encapsulated within CNTs *via* the suspension method and the solution method. Table I.3 cited the articles concerning the confined MNPs within CNTs.

Table I.3: Examples of the confined MNPs within CNTs.

MNPs (size)	CNTs inner diameters	Method	Additional treatment	Application or advantage	Ref
Fe_3O_4 (10 nm)	300 nm	Ferrofluid suspension	Washing	CNT orientation	211
Fe_3O_4 (~6 nm)	200-300 nm	Ferrofluid suspension	Filtration and Washing	Enhanced magnetic property	212
Fe_2O_3 (3-8nm)	2-12 nm	Solution		Redox property study	44
Fe_2O_3 and Fe (4-8nm)	4-8 nm	Solution	H_2 reduction	Fischer-Tropsch catalysis	53

Ni **(3-7 nm)**	20-50 nm	Solution	Washing	Selective NP deposition	173
Co/CoO **(50±5nm)**	80±30 nm	Solution		High filling density	141
Fe_3O_4 **(4-8nm)**	1-5 nm	Solution	HCl washing	Enzyme recycling	176
Co **(4.4±0.9 nm)**	10-20 nm	Solution	Filtration	Fischer-Tropsch catalysis	179
Fe_3O_4 **(6-8nm)**	6-8 nm	Solution	Filtration washing	Imaging and drug delivery	177
$Fe_{3-x}O_4$ **(13±3nm)**	40-60 nm	Solution		Selective NP deposition	142

Magnetic metallic nanoparticles (MMNPs) present much better magnetic properties compared to their oxides. However there is no example of studies concerning the effect of the confinement of MMNPs in CNTs. This is probably due to the difficulty to produce non-oxidized MMNPs in general, and more particularly confined in CNTs. A recent work reported the encapsulation of Fe NPs within a pea-pod like CNT (Pod-Fe) through an one-step synthesis at 350°C in N_2 using ferrocene and sodium azide as the precursors (213). Interestingly, the Fe NPs outside the carbon shell can be removed by washing with acid solution without affecting the NPs trapped inside. The Fe NPs are completely isolated within the compartments of CNTs and each compartment usually contain 1-2 Fe particles (Figure I.30).

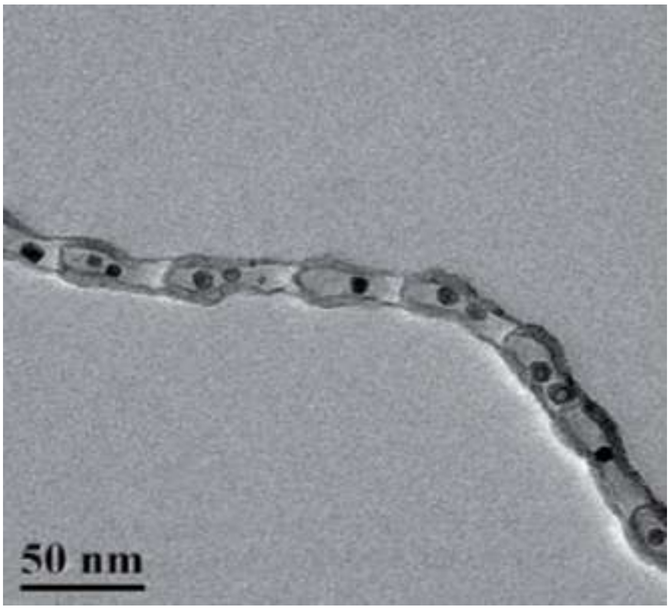

Figure I.30: TEM image of the Pod-Fe (reproduced from ref.213).

This nanocomposite has been tested for the oxygen reduction reaction (ORR) and has presented a high activity and long-term stability even in the presence of SO_2 poison. Although nanoscaled Fe particles are susceptible to oxidation, situ XANES reveals an intact metallic Fe in Pod-Fe after running for 7 h. However, well-defined MMNPs are needed since magnetic properties of NPs are very size- and shape-dependant. Therefore, a new method should be developed in order to confine size and shape controlled MMNPs within CNTs and to protect them from oxidation.

I.5 Conclusion

New morphologies, new structures, and new properties of the confined materials, as well as enhanced reactivity and selectivity of chemical reactions in the cavity of CNTs have attracted our interests in developing new CNT-based nanocomposites. In this thesis, the work is focused on i) filling CNTs with MMNPs, ii) protecting the air-sensitive confined MMNPs from oxidation and also iii) producing CNT-as nanoreactors for encapsulating or templating magnetic nanostructures in order to study their magnetic properties.

Based on the bibliographic results mentioned above, in order to fill CNTs with foreign materials, we must consider some essential factors that could determine or impact the filling feasibility and efficiency, such as i) the availability of CNTs with opened end tips allowing foreign materials to enter into their inner cavity; ii) the inner diameter of CNTs and the physical size and shape of the filling materials; iii) the wettability of the inner surface of CNTs; and iv) the interactions between CNTs and the filling materials, as well as the interactions among the filling materials. The confinement approach that we have followed in the present work is based on a molecular recognition strategy which operates through the creation of attractive/repulsion interactions of the MMNPs or MMNP precursor with the inner/outer surface of CNTs, respectively. This method, reported by Serp *et al.* (55), requires functionalization of both CNTs and MMNPs, which are described in the following chapters.

I.6 Reference

1. M.S. Schneider, J.-D. Grunwaldt , A. Baiker, *Langmuir*, **2004**, *20*, 2890–2899.
2. E. G. Derouane, C. D. Chang, *Microporous Mesoporous Mater*., **2000**, 35-36, 425-433.
3. P. Gallo, M. Rapinesi, M. Rovere, *J. Chem. Phys.*, **2002**, *117*, 369−375.
4. N. Floquet, J. P. Coulomb, N. Dufau, G. Andre, *J. Phys. Chem. B*, **2004**, *108*, 13107−13115.
5. P. Demontis, J. ul n- onz l ez, M. Masia, G. B. Suffritti, *J. Phys.: Condens. Matter.,* **2010**, *22*, 284106−284118.
6. H. K. Christenson, *J. Phys.:Condens. Matter*, **2001**,*13*, R95-R133.
7. D. Lesthaeghe, V. V. Speybroeck, M. Waroquier, *Phys.Chem. Chem. Phys.*, **2009**, *11*, 5222-5226.
8. B. Smit, T.L.M. Maesen, *Nature*, **2008**, *451*, 671-678.
9. J. M. Fraile, J. I. García, C. I. Herrerías, J. A. Mayoral, E. Pires, *Chem. Soc. Rev.*, **2009**, *38*, 695-706.
10. J. M. Thomas, R. Raja, *Acc. Chem. Res*., **2008**, *41*, 708-720.
11. B.-Z. Zhan, M. A. White, T.-K. Sham, J. A. Pincock, R. J. Doucet, K. V. R. Rao, K. N Robertson, T. S. Cameron, *J. Am. Chem. Soc*., **2003**, *125*, 2195-2199.
12. A. Popov, S. Yang, L. Dunsch, *Chem. Rev.*, **2013**, *113*, 5989−6113.
13. Y. Maeda, T. Tsuchiya, X. Lu, Y. Takano, T. Akasaka, S. Nagase, *Nanoscale*, **2011**, *3*, 2421-2429.
14. M. N. Chaur, F. Melin, A. L. Ortiz, L. Echegoyen, *Angew. Chem. Int. Ed*., **2009**, *48*, 7514-7538.
15. X. Lu, L. Feng, T. Akasaka, S. Nagase, *Chem. Soc. Rev.*, **2012**, *41*, 7723-7760.
16. L. Dunsch, S. Yang, *Small*, **2007**, *3*, 1298-1320.
17. S. Yang, F. Liu, C. Chen, M. Jiao, T. Wei, *Chem. Commun*., **2011**, *47*, 11822-11839.
18. . r tschmer, L. D. Lamb, K. Fostiropoulos, D. R. Huffman, *Nature*, **1990**, *347*, 354-358.
19. K. Komatsu, M. Murata, Y. Murata, *Science.*, **2005**, *307*, 238–240.
20. S. Iwamatsu, T. Uozaki, K. Kobayashi, S. Re, S. Nagase, S. Murata, *J. Am. Chem. Soc*., **2004**, *126*, 2668–2669.
21. K. Kurotobi, Y. Murata, *Science*, **2011**, *333*, 613-616.
22. S. Iijima, *Nature*, **1991**, *354*, 56-58.
23. M. Monthioux, P. Serp, E. Flahaut, C. Laurent, A. Peigney, M. Razafinima- nana, W. Bacsa, J.-M. Broto in Springer *Handbook of Nanotechnology*, 2nd revised and extended edition (Ed. B. Bhushan), Springer-Verlag, Heidelberg, Germany, **2007**, pp. 43–112.
24. X. Pan, X. Bao, *Confinement Effects in Nanosupports, in Nanomaterials in Catalysis*, **2013**, First Edition (eds P. Serp and K. Philippot), Wiley-VCH Verlag GmbH & Co. KGaA, Weinheim, Germany.
25. P-C. Ma, N.A. Siddiqui, G. Marom, J-K. Kim, *Composites: Part A*, **2010**, *41*, 1345-1367.

26. M.S. Dresselhaus, G. Dresselhaus, R. Saito, *Carbon*, **1995**, *33*, 883-891.

27. P.M. Ajayan, T.W. Ebbesen, *Rep.Prog.Phys*., **1997**, *60*, 1025-1062.

28. K.P. De Jong, J.W. Geus, *Catal. Rev.-Sci. Eng*., **2000**, *42*, 481-510.

29. C.J. Lee, J.H. Park, J. Park, *Chem. Phys. Lett*., **2000**, *323*, 560-565.

30. P. Serp, E. Castillejos, *ChemCatChem*, **2010**, *2*, 41-47.

31. X. Pan, X. Bao, *Acc. Chem. Res*., **2011**, *44*, 553-562.

32. X. Fan, E.C. Dickey, P.C. Eklund, K.A. Williams, L. Grigorian, R. Buczko, S.T. Pantelides, S.J. Pennycook, *Phys. Rev. Lett*., **2000**, *84*, 4621–4624.

33. L. Guan, K. Suenaga, S. Zujin, Z. Gu, S. Iijima, *Nano Lett*., **2007**, *7*, 1532–1535.

34. R. Kitaura, R. Nakanishi, T. Saito, H. Yoshikawa, K. Awaga, H. Shinohara, *Angew. Chemie*, **2009**, *121*, 8448–8452.

35. M. S. P. Sansom, P. C. Biggin, *Nature*, **2001**, *414*, 156−159.

36. G. Hummer, J.C. Rasaish, J.P. Noworyta, *Nature*, **2001**, *414*, 188-190.

37. Hanasaki, A. Nakamura, T. Yonebayashi, S. Kawano, *J. Phy.: Condens. Matter*, **2008**, *20*, 015213.

38. H. Kim, W. Sigmund, *Journal of Crystal Growth*, **2005**, *276*, 594-605.

39. S. Liu, J. Zhu, Y. Mastai, I. Felner, A. Gedanken, *Chem. Mater*., **2000**, *12*, 2205-2211.

40. X. Pan, Z. Fan, W. Chen, Y. Ding, H. Luo, X. Bao, *Nat. Mater*., **2007**, *6*, 507–511.

41. R.M.M. Abbaslou, A. Tavassoli, J. Soltan, A. K. Dalai, *Appl. Catal. A: Gen*., **2009**, *367*, 47-52.

42. M. W. Fay, G. A. Rance, A. La Torre, C. Gime, W. A. Solomonsz, T. W. Chamberlain, P. D. Brown, A. N. Khlobystov, *ACS Nano*, **2012**, *6*, 2000–2007.

43. L. Ratke, P. W. Voorhees, *Growth and Coarsening: Ostwald Ripening in Material Processing*. Springer, **2002**, pp.117–118.

44. W. Chen, X. Pan, X. Bao, *J. Am. Chem. Soc*., **2007**, *129*, 7421–7426.

45. W. Chen, X. Pan, M. G. Willinger, D. S. Su, X. Bao, *J. Am. Chem. Soc*., **2006**, *128*, 3136-3137.

46. R. C. Haddon, *Science*, **1993**, *261*, 1545-1550.

47. D. Ugarte, A. Chatelain, W. A. De Heer, *Science*, **1996**, *274*, 1897-1899.

48. M. D. C. Giménez-López, F. Moro, A. La Torre, C. J. Gómez-García, P. D. Brown, J. van Slageren, A. N. Khlobystov, *Nat. Commun.* **2011**, *2*, 407-413.

49. M. D. C. Gimenez-Lopez, A. La Torre, M. W. Fay, P. D. Brown, A. N. Khlobystov, *Angew. Chem. Int. Ed.*, **2013**, *52*, 2051–2054.

50. G. Arora, N.J. Wagner, S.I. Sandler, *Langmuir*, **2004**, *20*, 6268-6277.

51. Striolo, *Nano lett*., **2006**, *6* (4), 633-639.

52. P. Kondratyuk, Y. Wang, J. Liu, J. K. Johnson, J. T. Yates, *J. Phys.Chem. C*, **2007**, *111*, 4578-4584.

53. W. Chen, Z. L. Fan, X. L. Pan, X. Bao, *J. Am. Chem. Soc*., **2008**, *130*, 9414– 9419.

54. H. Ma, L. Wang, L. Chen, C. Dong, W. Yu, T. Huang, Y. Qian, *Catal. Commun.*, **2007**, *8*, 452–456.

55. E. Castillejos, P.-J. Debouttière, L. Roiban, A. Solhy, V. Martinez, Y. Kihn, O. Ersen, K. Philippot, B. Chaudret, P. Serp, *Angew. Chem. Int. Ed.* **2009**, *48*, 2529–33.

56. J.-P. Tessonier, L. Pesant, G. Ehret, M. J. Ledoux, C. Pham-Huu, *Appl. Catal. A: Gen.*, **2005**, *288*, 203–210.

57. Z. Chen, Z. Guan, M. Li, Q. Yang, C. Li, *Angew. Chem. Int. Ed.*, **2011**, *50*, 4913–4917.

58. M. Zhang, J. L. Dong, Q. H. Xu, H. K. Rhee, X. L. Li, *Catal. Today*, **2004**, *93–95*, 347–352.

59. J. Zhang, J-O Müller, W. Zheng, D. Wang, D. Su, R. Schlögl, *Nano Lett.*, **2008**, *8*, 2738–2743.

60. P.M. Ajayan, S. Iijima, *Nature*, **1993**, *361*, 333–334.

61. P.M. Ajayan, T.W. Ebbesen, T. Ichihashi, S. Iijima, K. Tanigaki, H. Hiura, *Nature*, **1993**, *362*, 522–525.

62. S. Seraphin, D. Zhou, J. Jiao, J.C. Withers, R. Loufty, *Nature*, **1993**, *362*, 503.

63. Y. Saito, T. Yoshikawa, *J. Cryst. Growth*, **1993**, *134*, 154–156.

64. S. Iijima, T. Ichihashi, *Nature*, **1993**, *363*, 603–605.

65. D.S. Bethune, C.H. Kiang, M.S. De Vries, G. Gorman, R. Savoy, J. Vasquez, R. Breyers, *Nature*, **1993**, *363*, 605–607.

66. M. Monthioux, *Carbon,* **2002**, *40*, 1809–1823.

67. M. Monthioux, E. Flahaut, J. P. Cleuziou, *J. Mater. Res.*, **2006**, *21*, 2774-2793.

68. J. Sloan, J. Hammer, M. Zwiefka-Sibley, M.L.H. Green, *Chem. Commun.*, **1998**, 347–348.

69. B.W. Smith, M. Monthioux, D.E. Luzzi, *Nature*, **1998**, *396*, 323–324.

70. G-H. Jeong, R. Hatakeyama, T. Hirata, K. Tohji, K. Motomiya, T. Yaguchi, Y. Kawazoe, *Chem. Commun.*, **2003**, 152–153.

71. B.-Y. Sun, Y. Sato, K. Suenaga, T. Okazaki, N. Kishi, T. Sugai, S. Bandow, S. Iijima, H. Shinohara, *J. Am. Chem. Soc.*, **2005**, *127*, 17972–17973.

72. T. Pichler, A. Kukovecz, H. Kuzmany, H. Kataura, Y. Achiba, *Phys. Rev. B*, **2003**, *67*, 125416.1–125416.7

73. M. Kalbac, L. Kavan, M. Zukalova, L. Dunsch, *J. Phys. Chem. B*, **2004**, *108*, 6275–6280.

74. Burteaux, A. Claye, B.W. Smith, M. Monthioux, D.E. Luzzi, J.E. Fischer, *Chem. Phys. Lett.*, **1999**, *310*, 21–24.

75. T. Shimada, Y. Ohno, T. Okazaki, T. Sugai, K. Suenaga, S. Kishimoto, T. Mizutani, T. Inoue, R. Taniguchi, N. Fukui, H. Okubo, H. Shinohara, *Physica E*, **2004**, *21*, 1089–1092.

76. F. Simon, H. Kuzmany, H. Rauf, T. Pichler, J. Bernardi, H. Peterlik, L. Korecz, F. Fülöp, A. Jànossy, *Chem. Phys. Lett.*, **2004**, *383*, 362–367.

77. K. Suenaga, M. Tence, C. Mory, C. Colliex, H. Kato, T. Okazaki, H. Shinohara, K. Hirahara, S. Bandow, S. Iijima, *Science*, **2000**, *290*, 2280–2282.

78. P.W. Chiu, G. Gu, G.T. Kim, G. Philipp, S. Roth, S.F. Yang, S. Yang, *Appl. Phys. Lett.*, **2001**, *79*, 3845–3847.

79. T. Okazaki, K. Suenaga, K. Hirahara, S. Bandow, S. Iijima, H. Shinohara, *J. Am. Chem. Soc.*, **2001**, *123*, 9673–9674.

80. T. Okazaki, K. Suenaga, K. Hirahara, S. Bandow, S. Iijima, H. Shinohara, *Physica B*, **2002**, *323*, 97–99.

81. K. Suenaga, T. Okazaki, C.-R. Wang, S. Bandow, H. Shinohara, S. Iijima, *Phys. Rev. Lett.*, **2003**, *90*, 055506/1–4.

82. K. Suenaga, R. Taniguchi, T. Shimada, T. Okazaki, H. Shinohara, S. Iijima, *Nano Lett.*, **2003**, *3*, 1395–1398.

83. D. A. Britz, A. N. hlob stov, J. a ng, A. S. O'Neil, M. Poliakoff, A. Ardavan, . A. D. Briggs, *Chem. Commun.* **2004**, *61*, 176–177.

84. N. Khlobystov, K. Porfyrakis, M. Kanai, D. a Britz, A. Ardavan, H. Shinohara, T. J. S. Dennis, G. A. D. Briggs, *Angew. Chem. Int. Ed.,* **2004**, *43*, 1386–1389.

85. N. Khlobystov, D. a Britz, G. A. D. Briggs, *Acc. Chem. Res.* **2005**, *38*, 901–909.

86. D. A. Britz, A. N. Khlobystov, K. Porfyrakis, A. Ardavan, G. A. D. Briggs, *Chem. Commun.,* **2005**, 37–39.

87. D. A. Britz, A. N. Khlobystov, *Chem. Soc. Rev.*, **2006**, *35*, 637–659.

88. G. Pagona, G. Rotas, A. N. Khlobystov, T. W. Chamberlain, K. Porfyrakis, N. Tagmatarchis, *J. Am. Chem. Soc.*, **2008**, *130*, 6062–6063.

89. M. Ashino, D. Obergfell, M. Haluska, S. Yang, A. N. Khlobystov, S. Roth, R. Wiesendanger, *Nat. Nanotechnol.*, **2008**, *3*, 337–341.

90. Á. Botos, A. N. Khlobystov, B. Botka, R. Hackl, E. Székely, B. Simándi, K. Kamarás, *Phys. Status Solidi* (B), **2010**, *247*, 2743–2745.

91. T. W. Chamberlain, A. M. Popov, A. a Knizhnik, G. E. Samoilov, A. N. Khlobystov, *ACS Nano,* **2010**, *4*, 5203–5210.

92. M. D. C. Gimenez-Lopez, A. Chuvilin, U. Kaiser, A. N. Khlobystov, *Chem. Commun.,* **2011**, *47*, 2116–2118.

93. T. W. Chamberlain, J. C. Meyer, J. Biskupek, J. Leschner, A. Santana, N. a Besley, E. Bichoutskaia, U. Kaiser, A. N. Khlobystov, *Nat. Chem.*, **2011**, *3*, 732–737.

94. D.A. Morgan, J. Sloan, M.L.H. Green, *Chem. Commun.*, **2002**, 2442–2443.

95. M. Koshino, T. Tanaka, N. Solin, K. Suenaga, H. Isobe, E. Nakamura, *Science*, **2007**, *316*, 853–855.

96. J. Wang, M. K. Kuimova, M. Poliakoff, G. A. D. Briggs, A. N. Khlobystov, *Angew. Chem. Int. Ed.,* **2006**, *45,* 5188–5191.

97. K. Yanagi, K. Iakoubovskii, H. Matsui, H. Matsuzaki, H. Okamoto, Y. Miyata, Y. Maniwa, S. Kazaoui, N. Minami, H. Kataura, *J. Am. Chem. Soc.*, **2007**, *129*, 4992–4997.

98. Y.F. Li, R. Hatakeyama, T. Kaneko, T. Izumida, T. Okada, T. Kato, *Appl. Phys. Lett.*, **2006**, *89*, 083117.
99. L. Guan, Z. Shi, M. Li, Z. Gu, *Carbon*, **2005**, *43*, 2780–2785.
100. L.-J. Li, A.N. Khlobystov, J.G. Wiltshire, G.A.D. Briggs, R.J. Nicholas, *Nature Mater.*, **2005**, *4*, 481–485.
101. D. M. Guldi, M. Marcaccio, D. Paolucci, F. Paolucci, N. Tagmatarchis, D. Tasis, E. Vasquez, M. Prato, *Angew. Chem. Int. Ed.*, **2003**, *42*, 4206–4209.
102. H. Qiu, Z. Shi, Z. Gu, J. Qiu, *Chem. Commun.*, **2007**, 1092–1094.
103. L. Guan, K. Suenaga, S. Iijima, *Nano Lett.*, **2008**, *8*, 459–462.
104. H. Shiozawa, T. Pichler, A. Grüneis, R. Pfeiffer, H. Kuzmany, Z. Liu, K. Suenaga, H.Kataura, *Adv. Mater.*, **2008**, *20*, 1443–1449.
105. D. M. Kammen, T.E. Lipman, A.B. Lovins, P.A. Lehman, J.M. Eiler, T.K. Tromp, R.-L. Shia, M. Allen, Y.L. Yung, *Science*, **2003**, *302*, 226–229.
106. Fujiwara, K. Ishii, H. Suematsu, H. Kataura, Y. Maniwa, S. Susuki, Y. Achiba, *Chem. Phys. Lett.*, **2001**, *336*, 205–211.
107. Kuznetsova, J.T. Yates Jr., J. Li, R.E. Smalley, *J. Chem. Phys.*, **2000**, *112*, 9590–9598.
108. K.A. Williams, P.C. Eklund, *Chem. Phys. Lett.*, **2000**, *320*, 352–358.
109. M. Monthioux, B. W. Smith, B. Burteaux, A. Claye, J. E. Fischer, D. E. luzzi, Carbon, 2001, *39*, 1251-1272.
110. S.C. Tsang, Y.K. Chen, P.J.F. Harris, M.L.H. Green, *Nature*, **1994**, *372*, 159–162.
111. Capobianchi, S. Foglia, P. Imperatori, A. Notargiacomo, M. Giammatteo, T. Del Buono, E. Palange, *Carbon,* **2007**, *45*, 2205–2208.
112. Wang, S. Guo, X. Pan, W. Chen, X. Bao, *J. Mater. Chem.* **2008**, *18*, 5782.
113. Govindaraj, B.C. Satishkumar, M. Nath, C.N.R. Rao, *Chem. Mater.*, **2000**, *12*, 202–205.
114. E. Borowiak-Palen, E. Mendoza, A. Bachmatiuk, M.H. Rummeli, T. Gemming, J. Nogues, V. Skumryev, R.J. Kalenczuk, T. Pichler, S.R.P. Silva, *Chem. Phys. Lett.*, **2006**, *421*, 129–133.
115. J. Sloan, A.I. Kirkland, J.L. Hutchison, M.L.H. Green, *Chem. Commun.*, **2002**, 1319–1332.
116. B.C. Satishkumar, A. Govindaraj, J. Mofokeng, G.N. Subbanna, C.N.R. Rao, *J. Phys. B*, **1996**, *29*, 4925–4934.
117. Guerret-Piécourt, Y. Le Bouar, A. Loiseau, H. Pascard, *Nature*, **1994**, *372*, 761–765.
118. G. Brown, S.R. Bailey, M. Novotny, R. Carter, E. Flahaut, K.S. Coleman, J.L. Hutchison, M.L.H. Green, J. Sloan, *Appl. Phys. A*, **2003**, *76*, 1–6.
119. P.M.F.J. Costa, S. Friedrichs, J. Sloan, M.L.H. Green, *Chem. Mater.*, **2005**, *17*, 3122–3129.
120. J. Sloan, S.J. Grosvenor, S. Friedrichs, A. Kirkland, J.L. Hutchison, M.L.H. Green, *Angew. Chem., Int. Ed.*, **2002**, *41*, 1156–1159.
121. J.S. Bendall, A. Ilie, M.E. Welland, J. Sloan, M.L.H. Green, *J. Phys. Chem.*, **2006**, *110*, 6569–6573.

122. J.-P. Cleuziou, W. Wernsdorfer, T. Ondarçuhu, M. Monthioux, *ACS Nano,* **2011**, *5*, 2348–55.

123. P. Corio, A.P. Santos, P.S. Santos, M.L.A. Temperini, V.W. Brar, M.A. Pimenta, M. S. Dresselhaus, *Chem. Phys. Lett*., **2004**, *383*, 475–480.

124. S. Friedrichs, R.R. Meyer, J. Sloan, A.I. Kirkland, J.L. Hutchison, M.L.H. Green, *Chem. Commun*., **2001**, 929–930.

125. P.M.F.J. Costa, J. Sloan, T. Rutherford, M.L.H. Green, *Chem. Mater*., **2005**, *17*, 6579–6582.

126. M. Hulman, H. Kuzmany, P.M.F.J. Costa, S. Friedrichs, M.L.H. Green, *Appl. Phys. Lett*., **2004**, *85*, 2068–2070.

127. J. Sloan, D.M. Wright, H.G. Woo, S. Bailey, G. Brown, A.P.E. York, K.S. Coleman, J.L. Hutchison, M.L.H. Green, *Chem. Commun*., **1999**, 699–700.

128. P. Corio, A.P. Santos, P.S. Santos, M.L.A. Temperini, V.W. Brar, M.A. Pimenta, M. S. Dresselhaus, *Chem. Phys. Lett*., **2004**, *383*, 475–480.

129. E. Borowiak-Palen, E. Mendoza, A. Bachmatiuk, M.H. Rummeli, T. Gemming, J. Nogues, V. Skumryev, R.J. Kalenczuk, T. Pichler, S.R.P. Silva, Chem. *Phys. Lett*., **2006**, *421*, 129–133.

130. Pham-Huu, N. Keller, C. Estourn?s, G. Ehret, M. J. Ledoux, *Chem. Commun*., **2002**, 1882–1883.

131. J. Hu, Y. Bando, J. Zhan, C. Zhi, D. Golberg, *Nano Lett*., **2006**, *6*, 1136– 1140.

132. C.N.R. Rao, R. Sen, *Chem. Commun*., **1998**, 1525–1526.

133. J.-Y. Chang, F.-D. Mai, B. Lo, J.-J. Chang, S.-H. Tzing, A. Ghule, Y.-C. Ling, *Chem. Commun.*, **2003**, *1*, 2362–2363.

134. M. Kim, S. Qian, H. H. Bau, *Nano Lett.*, **2005**, *5*, 873–878.

135. V. Bazilevsky, K. Sun, A. L. Yarin, C. M. Megaridis, *J. Mater. Chem*., **2008**, *18*, 696–702.

136. W. A. Solomonsz, G. A. Rance, M. Suyetin, A. La Torre, E. Bichoutskaia, A. N. Khlobystov, *Chem.Eur.J*., **2012**, *18*, 13180–13187.

137. La Torre, M. W. Fay, G. a Rance, M. Del Carmen Gimenez-Lopez, W. A. Solomonsz, P. D. Brown, A. N. Khlobystov, *Small*, **2012**, *8*, 1222–1228.

138. A Chuvilin, E. Bichoutskaia, M. C. Gimenez-Lopez, T. W. Chamberlain, G. A. Rance, N. Kuganathan, J. Biskupek, U. Kaiser, a N. Khlobystov, *Nat. Mater*., **2011**, *10*, 687–692.

139. T. W. Chamberlain, J. Biskupek, G. a Rance, A. Chuvilin, T. J. Alexander, E. Bichoutskaia, U. Kaiser, A. N. Khlobystov, *ACS Nano*, **2012**, *6*, 3943–3953.

140. Castillejos, R. Chico, R. Bacsa, S. Coco, P. Espinet, M. Pérez-Cadenas, A. Guerrero-Ruiz, I. Rodríguez-Ramos, P. Serp, *Eur. J. Inorg. Chem.,* **2010**, 5096-5012.

141. W. Baaziz, S. Begin-Colin, B. P. Pichon, I. Florea, O. Ersen, S. Zafeiratos, R. Barbosa, D. Begin, C. Pham-Huu, *Chem. Mater.* **2012**, *24*, 1549–1551.

142. W. Baaziz, X. Liu, I. Florea, S. Begin-Colin, B. P. Pichon, *J. Mater. Chem. A,* **2013**, *1*, 13853–13861.

143. P.C.P. Watts, W.K. Hsu, V. Kotzeva, G.Z. Chen, *Chem. Phys. Lett*., **2002**, *366*, 42–50.

144. Loiseau, H. Pascard, *Chem.Phys. Lett*., **1996**, *256*, 246-252.

145. Morelos-Gómez, F. López-Urías, E. Muñoz-Sandoval, C. L. Dennis, R. D. Shull, H. Terrones, M. Terrones, *J. Mater. Chem*,. **2010**, *20*, 5906-5914.

146. Q. Su, J. Li, G. Zhong, G. Du, B. Xu, *J. Phys. Chem. C*, **2011**, *115*, 1838–1842.

147. P. K. Tyagi, A. Misra, M. K. Singh, D. S. Misra, J. Ghatak, P. V. Satyam, F. Le Normand, *Appl. Phys. Lett.* **2005**, *86*, 253110-1-253110-3.

148. V. Gupta, R. K. Kotnala, *Angew. Chem. Int. Ed.*, **2012**, *51*, 2916–2919.

149. N. Demoncy, O. Stéphan, N. Brun, C. Colliex, A. Loiseau, H. Pascard, *Eur. Phys. J. B*, **1998**, *4*, 147–157.

150. Loiseau, F. Willaime, *Appl. Surf. Sc*i., **2000**, *164*, 227–240.

151. P.J.F. Harris, *Carbon Nanotubes and Related Structures*; Cambridge University Press: Cambridge, U.K., **2003.**

152. S. Banerjee, T. Hemraj-Benny, M. Balasubramanian, D. A. Fischer, J. A. Misewich, S. S. Wong, *ChemPhysChem*, **2004**, *5*, 1416-1422.

153. T. J. Park, S. Banerjee, T. Hemraj-Benny, S. S. Wong, *J. Mater. Chem*., **2006**, *16*, 141-154.

154. Fei, H. Lu, Z. Hu, J. H. Xin, *Nanotechnology*, **2006**, *17*, 1589.

155. Eder, *Chem. Rev*,. **2010**, *110*, 1348–1385.

156. P.-X. Hou, C. Liu, H.-M. Cheng, *Carbon*, **2008**, *46*, 2003-2025.

157. R. Andrews, D. Jacques, D. Qian, E. C. Dickey, *Carbon*, **2001**, *39*, 1681-1687.

158. D. Eder, A. H. Windle, *Adv. Mater*., **2008**, *20*, 1787-1793.

159. B.W. Smith, D.E. Luzzi, *Chem. Phys. Lett*., **2000**, *321*, 169–174.

160. W. Mickelson, S. Aloni, W.-Q. Han, J. Cumings, A. Zettl, *Science*, **2003**, *300*, 467–469.

161. T. Fröhlich, P. Scharff, W. Schliefke, H. Romanus, V. Gupta, C. Siegmund, O. Ambacher and L. Spiess, *Carbon*, **2004**, *42*, 2759–2762.

162. Brown, S. Bailey, J. Sloan, C. Xu, S. Friedrichs, E. Flahaut, K.S. Coleman, J.L. Hutchison, R.E. Dunin-Borkowski , M.L.H. Green, *Chem. Commun*., **2001**, 845–846.

163. J. Chancolon, F. Archaimbault, A. Pineau, S. Bonnamy, *J. Nanosci. Nanotechnol*., **2006**, *6*, 1-5.

164. M. Monthioux, *Carbon Meta-Nanotubes : Synthesis, Properties and Applications*, 2nd edition, John Wiley & Sons, **2011**, pages 225-271.

165. E. Dujardin, T.W. Ebbesen, H. Hiura, K. Taginaki, *Science*, **1994**, *265*, 1850–1852.

166. E. Dujardin, T.W. Ebbesen, A. Krishnan, M.M.J. Treacy, *Adv. Mater*., **1998**, *10*, 1472–1475.

167. http://www.dynesonline.com/visc_table.html

168. L. V. Yashina, A. A. Eliseev, M. V. harlamova, A. A. ol khov, A. . g orov, S. . Savilov, A. . Lukashin, . P ttner, A. I. Belogorokhov, *J. Phys. Chem. C* , **2011**, *115*, 3578–3586.

169. W. Chen, Z. Fan, X. Pan, X. Bao, *J. Am. Chem. Soc.*, **2008**, *130*, 9414–9419.

170. S. Guo, X. Pan, H. Gao, Z. Yang, J. Zhao, X. Bao, *Chem.Eur.J.* **2010**, *16*, 5379–5384.

171. T. W. Ebbesen, *J. Phys. Chem. Solids*, **1996**, *57*, 951-955.

172. T.T. Nguyen, P. Serp, *ChemCatChem*, **2013**, *5*, 3595-3603.

173. J. Tessonnier, O. Ersen, G. Weinberg, C. Pham-huu, D. S. Su, R. Schlögl, *ACS Nano*, **2009**, *3*, 2081–2089.

174. W. Chen, Z. Fan, B. Zhang, G. Ma, K. Takanabe, X. Zhang, Z. Lai, *J. Am. Chem. Soc.,* **2011**, *133*, 14896–9.

175. Z. Chen, Z. Guan, M. Li, Q. Yang, C. Li, *Angew. Chem. Int. Ed.*, **2011**, *50*, 4913–4917.

176. W. J. Goh, V. S. Makam, J. Hu, L. Kang, M. Zheng, S. L. Yoong, C. N. B. Udalagama, G. Pastorin, *Langmuir,* **2012**, *28*, 16864–16873.

177. M.-L. Chen, Y.-J. He, X.-W. Chen, J.-H. Wang, *Langmuir,* **2012**, *28*, 16469–16476.

178. Zhang, H. Song, X. Chen, J. Zhou, *Phys. Chem. C*, **2012**, *116*, 22774-22779.

179. Y. Zhu, Y. Ye, S. Zhang, M. E. Leong, F. F. Tao, *Langmuir*, **2012**, *28*, 8275–8280.

180. Astinchap, R. Moradian, A. Ardu, C. Cannas, G. Varvaro, A. Capobianchi, *Chem. Mater.,* **2012**, *24*, 3393-3400.

181. Y. Lee, M. Angel Garcia, N. A. F. Huls, S. Sun, *Angew. Chem. Int. Ed.*, **2011**, *49*, 1271-1274.

182. W. Lin , R. W. Zhang , S. S. Jang , C. P. Wong , J. I. Hong , *Angew. Chem. Int. Ed.*, **2010**, *49*, 7929-7932.

183. H. Lu , E. L. Salabas , F. Schuth , *Angew. Chem. Int. Ed.* **2007**, *46* , 1222-1244

184. H. Zeng , S. Sun , *Adv. Funct. Mater.*, **2008** , *18* , 391-400.

185. Y. W. Jun , J. S. Choi , J. Cheon , *Chem. Commun.*, **2007** , 1203-1214.

186. S. Giri, B. G. Trewyn, M. P. Stellmaker, V. S.-Y. Lin, *Angew. Chem. Int. Ed.*, **2005**, *44*, 5038-5044.

187. C. Bergemann, D. Muller-Schulte, J. Oster, L. Brassard, A. S. Lubbe, *J. Magn. Magn. Mater.*, **1999**, *194*, 45-52.

188. L. Nunez, M. D. Kaminski, *J. Magn. Magn. Mater.*, **1999**, *194*, 102-107.

189. Xu, K. Xu, H. Gu, R. Zheng, H. Liu, X. Zhang, Z. Guo, B. Xu, *J. Am. Chem. Soc.*, **2004**, *126*, 9938-9939.

190. H. Gu, K. Xu, C. Xu, B. Xu, *Chem. Commun.*, **2006**, 941-949.

191. I. Safarik, M. Safarikova, *J. Chromatogr. B*, **1999**, *722*, 33-53.

192. O. Veiseh , J. W. Gunn , M. Zhang , *Adv. Drug Deliv. Rev.*, **2010**, *62* , 284-304.

193. B. Polyak , G. Friedman , *Expert Opin. Drug Deliv.*, **2009**, *6* , 53-70.

194. C. Sun , J. S. H. Lee , M. Zhang , *Adv. Drug Deliv. Rev.*, **2008** , *60* , 1252-1265.

195. K. Gupta, M. Gupta, *Biomaterials*, **2005**, *26*, 3995-4021.

196. C. Berry, A. S. G. Curtis, *J. Phys. D*, **2003**, *36*, R198-R206.

197. S. Mornet, S. Vasseur, F. Grasset, E. Duguet, *J. Mater. Chem.*, **2004**, *14*, 2161-2175.

198. T. Neuberger, B. SchPpf, H. Hofmann, M. Hofmann, B. von Rechenberg, *J. Magn. Magn. Mater.*, **2005**, *293*, 483-496.

199. H. Hong , T. Gao , W. Cai , *Nano Today*, **2009** , *4* , 252-261.

200. T. Al-Jamal, H. Nerl , K. H. Müller , H. Ali-Boucetta , S. Li , P. D. Haynes , J. R. Jinschek, M. Prato , A. Bianco , K. Kostarelos , A. E. Porter , *Nanoscale*, **2011** , *3* , 2627-2635.

201. S. L. Edwards , J. A. Werkmeister , J. A. M. Ramshaw , *Expert Rev. Med. Dev.*, **2009** , *6* , 499-505.

202. G. Pastorin , W. Wu , S. Wieckowski , J. P. Briand , K. Kostarelos, M. Prato , A. Bianco , *Chem. Commun.*, **2006** , 1182-1184.

203. W. Wu , S. Wieckowski , G. Pastorin, M. Benincasa , C. Klumpp , J. P. Briand , R. Gennaro , M. Prato, A. Bianco , *Angew. Chem. Int. Ed.*, **2005** , *44* , 6358-6362.

204. S. K. Vashist, D. Zheng , G. Pastorin , K. Al-Rubeaan , J. H. T. Luong , F. S. Sheu, *Carbon*, **2011** , *49* , 4077-4097.

205. Y. Liu, Y. Zhao, B. Sun, C. Chen, *Acc. Chem. Res.,* **2013**, *46*, 702–713.

206. H. Dumortier , S. Lacotte , G. Pastorin , R. Marega , W. Wu, D. Bonifazi , J. P. Briand , M. Prato , S. Muller , A. Bianco , *Nano Lett.*, **2006** , *6* , 1522-1528.

207. Lacerda , M. A. Herrero , K. Venner , A. Bianco , M. Prato, K. Kostarelos , *Small*, **2008** , *4* , 1130-1132.

208. A. Herrero , L. Lacerda , A. Bianco , K. Kostarelos , M. Prato, *Int. J. Nanotechnol.*, **2011** , *8* , 885-895.

209. R. Lv, S. Tsuge, X. Gui, K. Takai, F. Kang, T. Enoki, J. Wei, J. Gu, K. Wang, D. Wu, *Carbon,* **2009**, *47*, 1141–1145.

210. R. Marega, F. De Leo, F. Pineux, J. Sgrignani, A. Magistrato, A. D. Naik, Y. Garcia, L. Flamant, C. Michiels, D. Bonifazi, *Adv. Funct. Mater.,* **2013**, *23*, 3173–3184.

211. G. Korneva, H. Ye, Y. Gogotsi, D. Halverson, G. Friedman, J.-C. Bradley, K. G. Kornev, *Nano Lett.,* **2005**, *5*, 879–884.

212. S. Pal, S. Chandra, M.-H. Phan, P. Mukherjee, H. Srikanth, *Nanotechnology,* **2009**, *20*, 485604-485611.

213. D. Deng, L. Yu, X. Chen, G. Wang, L. Jin, X. Pan, J. Deng, G. Sun, X. Bao, *Angew. Chem. Int. Ed,.* **2013**, *52*, 371–375.

Chapter II. Confinement of iron and cobalt metallic magnetic nanoparticles within functionalized multi-walled carbon nanotubes

Confinement of iron and cobalt metallic magnetic nanoparticles within functionalized multi-walled carbon nanotubes

II.1 Introduction

Iron and cobalt pure metallic NPs are the most common metallic magnetic nanoparticles (MMNPs). They are potentially interesting for application in magnetic hyperthermia (1). Magnetic hyperthermia is based on the fact that magnetic nanoparticles, when subjected to an appropriate alternating magnetic field, produce heat. Indeed, many magnetic materials display a magnetic hysteresis when subjected to a magnetic field that alternates direction. The power dissipated by a magnetic material subjected to an alternating magnetic field is often called the "Specific Absorption Rate" (SAR); it is commonly expressed in W/g of NPs. This energy is used in magnetic hyperthermia. As a consequence, if magnetic NPs are introduced in a tumour and the patient is placed in an alternating magnetic field of well-chosen amplitude and frequency, the tumour temperature would rise and the tumour will be destroyed. The most widely used magnetic NPs for hyperthermia are iron oxide NPs, which have recently been employed for hyperthermia on humans by the Jordan group at the Charité Hospital in Berlin (2, 3). These oxide NPs show good bio-compatibility and display physical properties necessary for both imaging and hyperthermia (4). However, the intrinsic properties of the material (maghemite) coupled to a broad size dispersion require the use of a high concentration of particles and a long treatment. The higher magnetization of metallic NPs of Co and Fe compared to iron oxide increases the maximum SAR values, thus exhibiting better magnetic performance than oxides, which makes them ideal alternatives for hyperthermia treatment of cancer. However, it is worth mentioning that due to their air-sensitivity, much fewer reports concern the potential application of MMNPs in hyperthermia treatment compared to their oxide counterparts (5-7).

Co nanorods (NRs) are of interest for applications in which "hard" magnetic materials are required. Compared to their oxide counterparts, Co NRs present a higher magnetic moment and high magnetic anisotropy that are critical features for ultra-high density magnetic recording and for their use as permanent magnets. As for other metallic NPs, a main issue with respect to Co NRs concerns also their protection against oxidation.

For the same reason no reports concern the magnetic properties of MMNPs confined in nanoscaled spaces such as the inner cavity of CNTs, and only very few concern their catalytic behavior (8, 9). Their confinement inside MWCNTs could constitute a first step towards their protection from oxygen, but also the study of their magnetic properties which can be modified due to the confinement. This chapter concerns the synthesis of MMNPs@MWCNT composites by confinement of Fe and Co MMNPs within functionalized MWCNTs.

II.2 MWCNT functionalization and characterization

Two commercial MWCNTs, Pyrograf®-III from Applied Science and Nanocyl-3100 from Nanocyl have been used in our work. The pristine MWCNTs with large diameter (Pyrograf), named **CNT$_1$** present a specific surface area of 38 m^{2}g^{-1}. Their inner diameters, essential for filling CNTs, mainly ranged from 20 nm to 100 nm as observed from TEM images. Some CNTs with an inner diameter of about 200 nm also exist. Figure II.1 displays TEM micrographs of CNT$_1$. Pyrograf®-III stacked-cup CNTs, also known as carbon nanofibers, possess a unique morphology not encountered in other nanomaterials. Pyrograf®-III nanofiber has a tubular structure with the sidewalls composed of angled graphite sheets.

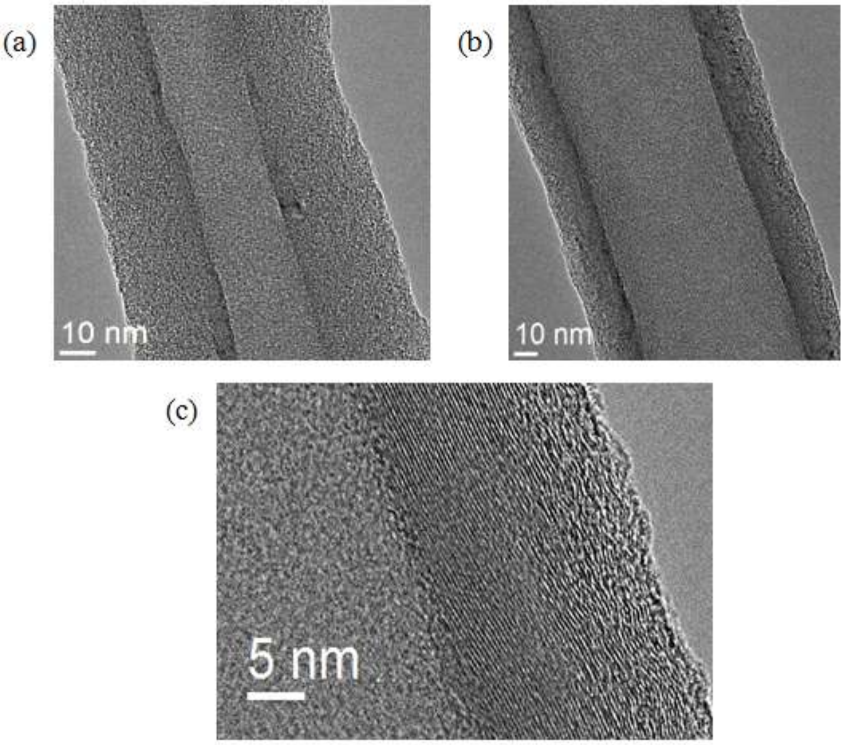

Figure II.1: HRTEM images of (a) a CNT$_1$ with d$_{inner}$ ~ 20-25 nm and d$_{outer}$~ 75-80 nm, and (b) a CNT$_1$ with d$_{inner}$ ~ 60 nm and d$_{outer}$~ 95-100 nm. (c) is magnification of part of the CNT$_1$ in (b) indicating its graphite layers.

This morphology called “stacked-cup” CNTs generates a fiber with exposed edge planes along the entire surface of the fiber. These edge sites are highly reactive and allow chemical modification of the fiber surface.

A bamboo-like structure has also been observed (Figure II.2a-b). The tips of the CNT_1 are all almost closed. At the tips of these CNTs, few iron catalyst particles are embedded and protected by graphite, as detected by EDX (Figure II.2c-d).

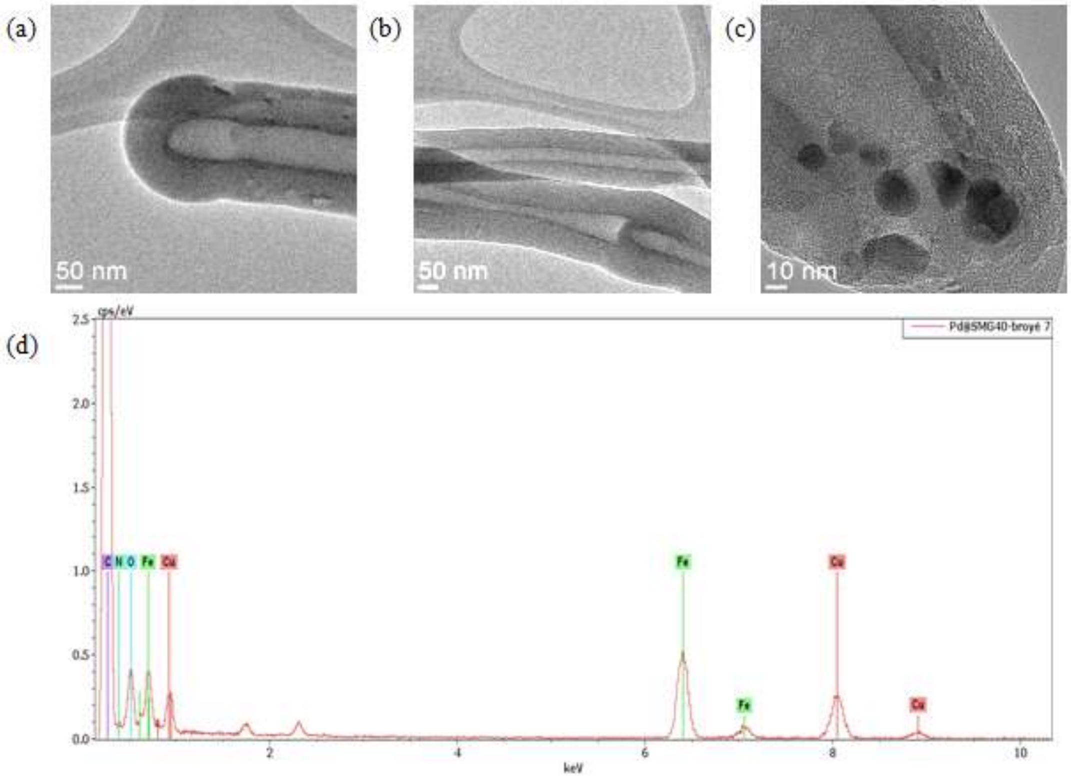

Figure II.2: (a-b) TEM micrographs showing a bamboo-like structure; (c) iron catalysts; (d) Energy-dispersive X-ray spectroscopy (EDX) analysis of the catalysts in (c).

The pristine MWCNTs with small diameter (Nanocyl-3100), named $\mathbf{CNT_2}$ (TEM and HRTEM in Figure II.3), present a specific surface area of 240 m^2g^{-1}, and a mean inner diameter of 6.5 nm. They are bundled and in their majority closed at the tips, possessing 5-11 walls and inner diameters between 3-10 nm.

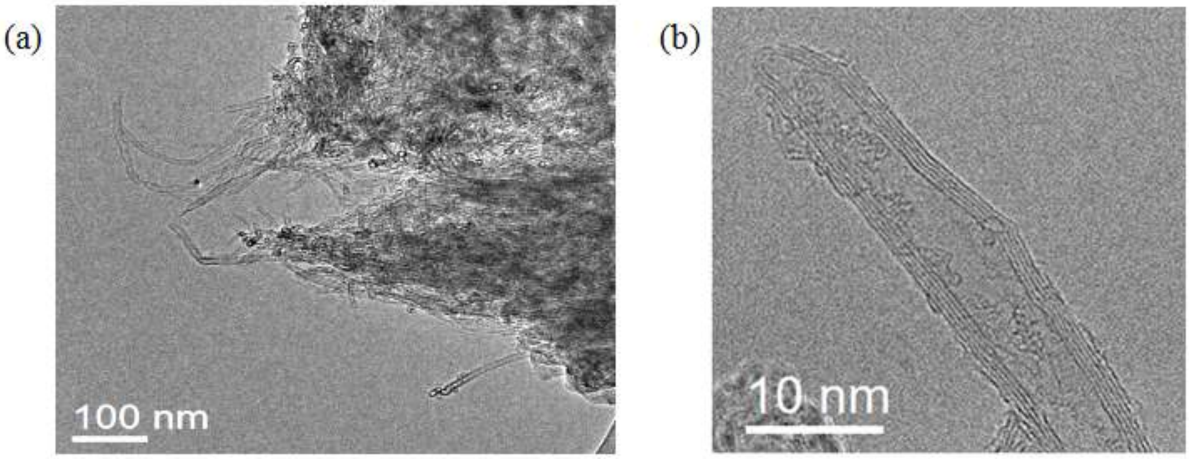

Figure II.3: TEM micrographs of (a) the bundles of CNT_2 and (b) a closed CNT_2 with 5 walls.

Since these CNTs are closed, bundled, and even trap residual magnetic catalyst particles, they need to be opened, purified and functionalized before filling. For opened CNTs, the outer and the inner surfaces are both available for hosting foreign materials. A functionalization that consists in the grafting of long alkyl chains on the outer surface of CNTs can create a repulsive interaction with host materials, thus leaving only the inner surface, accessible for interaction with the host materials (see Figure II.4) (10).

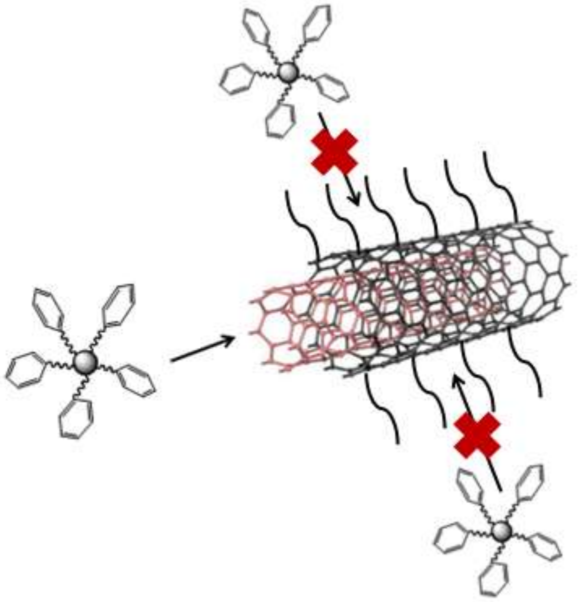

Figure II.4: Schematic illustration of the attractive/repulsive interactions between the MMNPs and inner/outer surface of the f-MWCNT.

Among the different methods available for opening CNTs, the treatment with concentrated nitric acid has been chosen as the most appropriate, since it can open the tips, remove metal residues, and simultaneously introduce oxygenated groups on the external surface, which allows the subsequent covalent functionalization (see experimental section) (11). The oxygenated hydrophilic groups include carboxylic acid, phenol, carbonyl, and quinone (12). Mainly the carboxylic acid groups react with hexadecylamine (HDA), forming an amide with a long alkyl chain. The Figure II.5 schematically presents the functionalization procedure.

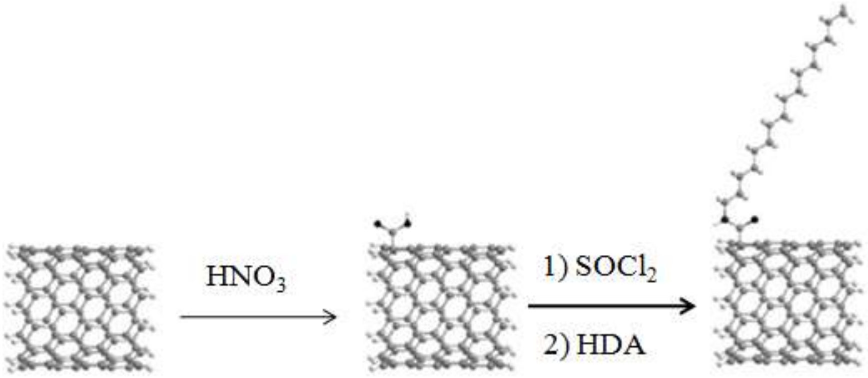

Figure II.5: Functionalization process of pristine MWCNTs to produce f-MWCNTs (10).

After functionalization (see Figure II.6), almost all the **CNT_1** and **CNT_2** are opened except the bamboo-like nanofibers within **CNT_1** and some **CNT_2**. An amorphous layer can also be observed on the outer surface of the f-**CNT_1**. It has been shown that the amorphous carbonaceous fragments that may be present on the SWCNT surface are very reactive towards oxidation, and produce carboxylated debris (13).

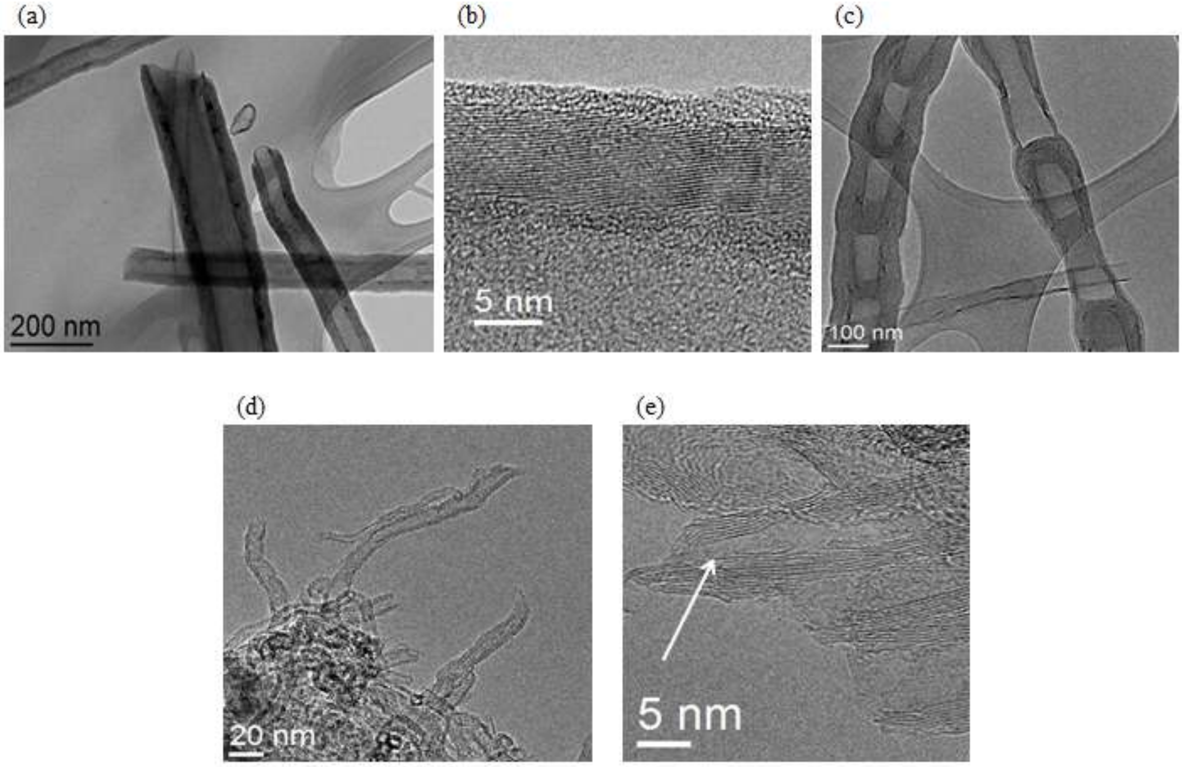

Figure II.6: (a) TEM image of f-CNT$_1$ with various diameters; (b) HRTEM image of an amorphous structure on the outer surface of a f-CNT$_1$; (c) presence of bamboo-like nanofibers after functionalization; HRTEM images of (d) all the opened f-CNT$_2$ and (e) a closed f-CNT$_2$ (white arrow).

The infra-red (IR) spectra (Figure II.7) confirmed the alkyl chain functionalization. For both f-**CNT$_1$** and f-**CNT$_2$**, the bands at 2915 and 2847 cm^{-1} correspond to the aliphatic C-H stretch of the alkyl chain. The band at 1634 cm^{-1} is attributed to C=O stretch of the amide, formed during the functionalization. These bands determine the grafted alkyl long chain on the surface of the CNTs *via* the formation of a covalent amide bond. However, the band at 1714 cm^{-1}, attributed to C=O stretch of the carboxylic acid group is still present, which indicates that only parts of the acetyl chloride groups hydrolyzed to carboxylic acid and the functionalization is incomplete in both cases. Besides the residual carboxylic acid groups, hydroxyl groups provide also a function that can connect MMNPs (14). These oxygenated groups on the outer surface of the CNTs are therefore potential obstacles for confinement selectivity. However, in the literature (10), the confinement of RuPt NPs presented a significant selectivity with similarly functionalized CNT$_1$ despite the presence of these oxygenated groups. Therefore, we decided to carry on our study with these f-CNTs.

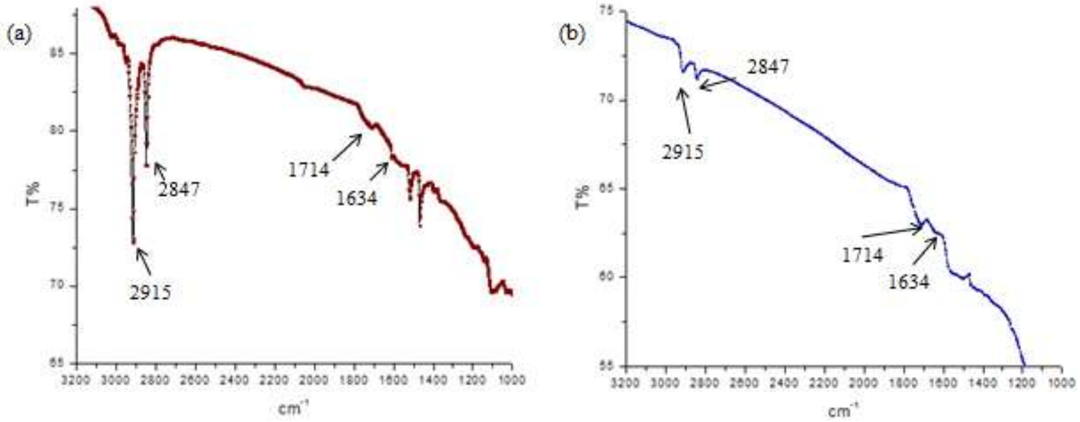

Figure II.7: IR spectra of (a) the f-CNT_1 and (b) the f-CNT_2.

After opening and functionalization of the MWCNTs, two different strategies have been followed for the confinement: the first is to introduce pre-formed MMNPs *via* an *ex situ* suspension filling method, in which pre-synthesized NPs are introduced in the f-MWCNTs; the second is to generate directly MMNPs in the cavity of the f-MWCNTs *via* an *in situ* method.

II.3 Synthesis of MMNPs and their confinement *via* the *ex-situ* suspension method

The Fe and Co NPs have been synthesized by the "organometallic method", through procedures routinely used in the LPCNO . Two silyl amide complexes $[Fe\{N(SiMe_3)_2\}_2]_2$ and $[Co\{N(SiMe_3)_2\}_2(THF)]$ (Me = methyl; THF = tetrahydrofuran) (see Figure II.8) have been chosen as precursors for the synthesis of pre-formed MMNPs. It is known that monodispersed and monocrystalline Co NRs and Fe NPs can be synthesized by reduction of the corresponding precursors under H_2 in the presence of long chain acid and amine ligands that act as stabilizers (15-19). Tuning the size and shape can be realized by varying the reaction conditions such as reaction temperature, pressure, reactant concentration, as well as the ratio of stabilizing agents with respect to the metal.

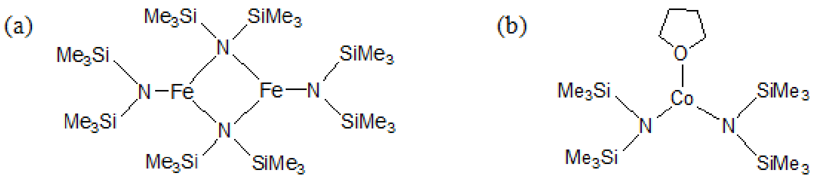

Figure II.8: Schematic representation of (a) $[Fe\{N(SiMe_3)_2\}_2]_2$ and (b) $[Co\{N(SiMe_3)_2\}_2(THF)]$.

All the prepared samples have been named as indicated in Figure II.9, allowing the visualization of the reaction parameters. For example, "Fe_1PA:2HDA_Mes_150°C_48h" indicates the reduction of 1 equivalent of Fe atom stabilized by 1 equivalent of PA (paltimic acid) and 2 equivalents of HDA (hexadecylamine), carried out in mesitylene at 150 °C during 48 hours.

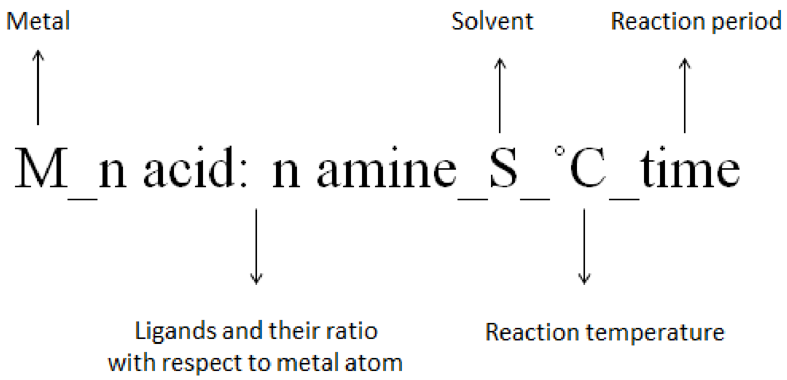

Figure II.9: Nomenclature of the experiments carried out.

The whole synthesis procedure of NPs consists in: i) the preparation of a solution containing the metal precursor and the stabilizing ligands in a glove box, and ii) the metal reduction by heating under 3 bars of H_2 pressure. The preparation of the starting solution is a crucial part of the synthesis that can determine the reaction outcome. Thus, besides the usual reaction parameters such as reduction temperature and H_2 pressure, reactant concentrations and relative ratios, other parameters, including mixing order at room temperature of the reactants before reduction and mixing rate also play an important role (20). In this section, these parameters are kept constant in all the subsequent reactions, unless otherwise stated. Details for each experiment are given in the experimental section.

II.3.1 Synthesis of Fe and Co NPs with classic long chain ligands and their confinements

Long chain acid and amine ligands (Figure II.10) are the usually employed ligands for the synthesis of Fe and Co NPs in LPCNO (15-19). It is therefore known that these syntheses are very sensitive to small variations of the experimental conditions. Indeed, the size and the shape of NPs can change considerably by modifying the amounts of the stabilizers, and the way of preparing the stating solutions (20). We have tried to modulate the NPs size not only by modifying the ratio M/acid/amine but also by changing the addition order or addition rate of the ingredients. Despite the fact that this thesis had not as an objective the study of the effect of the reaction conditions on the NPs growth, we have varied the reaction conditions in order to obtain in a reproducible way NPs of an appropriate size and size distribution for the subsequent confinement in CNTs. For instance we have slightly modified the M/Acid/amine ratio or/and the order of mixing the reactants in the starting solution. This can be explained by the formation of different species in the two solutions prepared by the two different protocols. These species have different reactivity and they participate to a different degree to the nucleation and growth steps during the formation of the NPs, finally leading to NPs with the different characteristics.

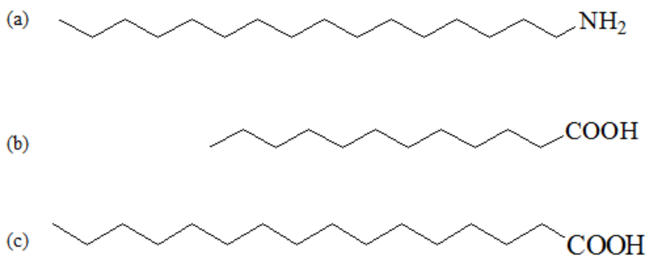

Figure II.10: (a) Hexadecylamine (HDA); (b) Lauric acid (LA) (c) Palmitic acid (PA).

Based on the study of Liakakos *et al.,* we have observed a remarkable difference in terms of size and shape of Co and Fe NPs which can result from delicate changes in the addition rate of the precursor to the mixture of the ligands during preparation of the stock solution before subsequent reduction (20). The Fe and Co precursors react readily with the acid forming metal carboxylates, which are very stable towards reduction and do not participate in the nucleation process. When the acid is in excess with respect to the amine and when the addition of the precursor is slow, the coordination of the acid to the silyl amide precursor liberates the amine $HN(SiMe_3)_2$ (HMDS) (Me = methyl), which can react subsequently with the excess of acid to form a silyl ester in a side reaction. This part of the acid that is “trapped” by the silyl ester is not able to coordinate to the metal and form stable carboxylates. Therefore the last quantity of precursor that enters the ligand mixture, when we add it slowly, does not have available enough acid for stabilization. It is therefore easy to decompose, and during reduction it forms numerous nuclei, on which a small amount of carboxylate, that was formed at the very beginning of the addition, is added during the growth stage. On the other hand, when the precursor solution is added rapidly, the silyl ester is formed in very small quantities, because the acid "prefers" to coordinate to the metal than to react with the liberated HMDS. Very little acid is consumed in the side reaction, thus more stable species, such as bis(carboxylate) complexes, are formed in the solution. The small quantity of unstable metal species forms only a few primary nuclei during the nucleation step. The majority of the metal participates to the growth of these nuclei, leading eventually to larger NPs. This effect is illustrated by the Figure II.13. The different addition rates of the solution of Fe precursor result in a significant difference of the morpholog of the NPs formed: “dropwise” addition produces NPs with a mean size of about 10 nm, whereas “fast addition” gives rise to NPs with a mean size of about 130 nm.

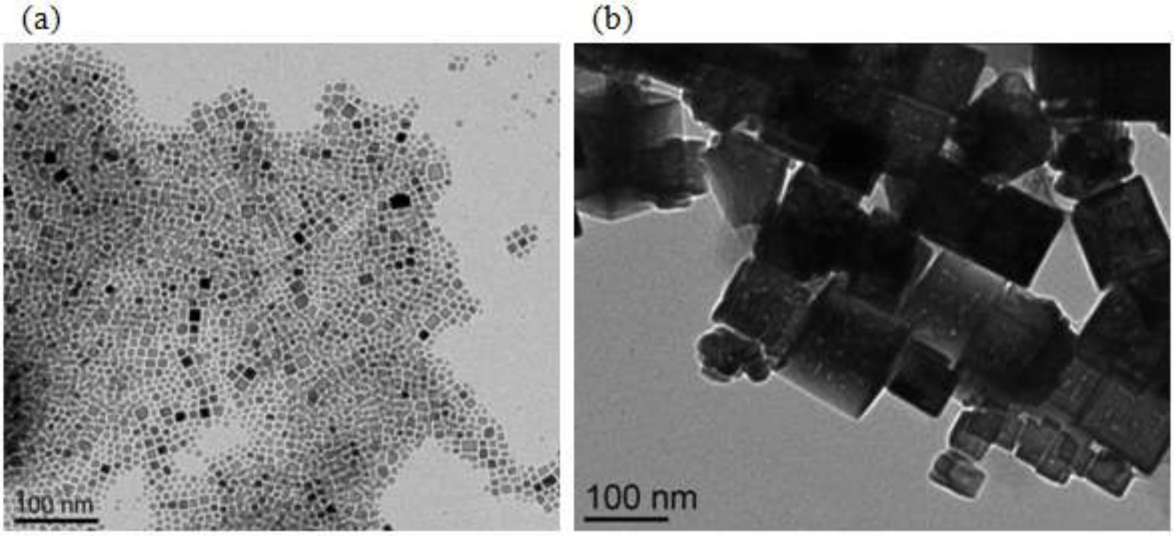

Figure II.13: TEM images of the reactions " Fe_2LA:0.36HDA_ Ani_150°C_24h" with the adding rate (a) slow and (b) fast (19).

Two more examples of the effect that small differences of the reaction conditions can have on the final NPs obtained, are given below. One concerns a modification of the ligand ratio, and the other the modification of the addition order of the reactants during the preparation of the starting solutions.

Thus, we compared two syntheses of Co NPs, in which only the amount of one ligand was changed. For these reactions, the two ligands were mixed in solution, followed by adding drop-wise the Co precursor solution. In Figure II.11a, we can see spherical Co NPs with scarce nanorods for the reaction "Co_1.2LA:1.2HDA_Mes_150°C_24h". By increasing by 0.2 the equivalents of acid, short Co NRs were obtained as shown on Figure II.11b. Adding more carboxylic acid gave rise to short rod morphology instead of spherical NPs,. since acid ligands promote the anisotropic growth of Co nanoparticles (20).

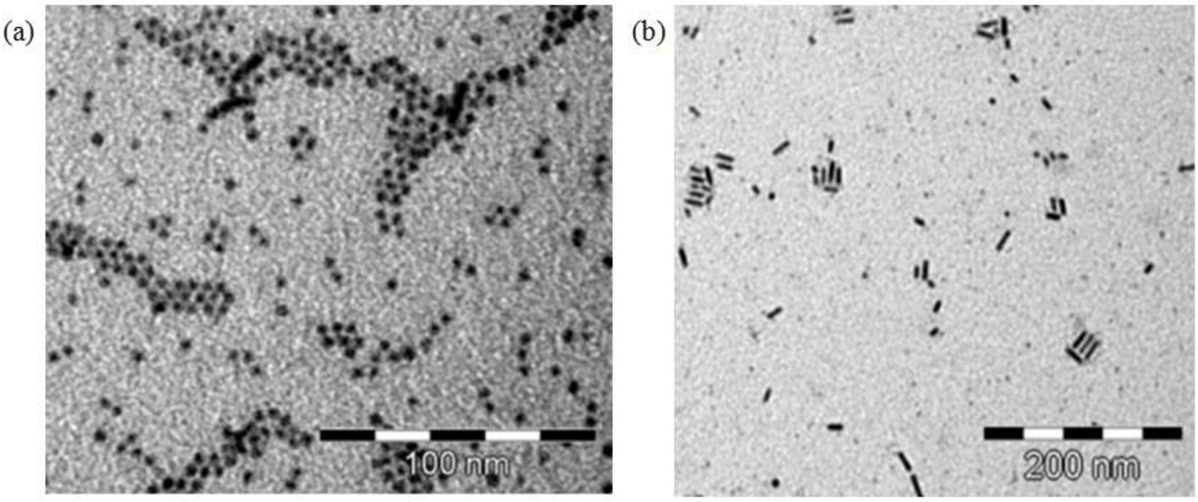

Figure II.11: TEM images of (a) Co_1.2LA:1.2HDA_Mes_150°C_24h; (b) Co_1.4LA:1.2HDA_ Mes_150°C_24h.

In another series of experiments, two reactions "Fe_1PA:2HDA_Mes_150°C_48h" were carried out, but the adding orders for starting solution preparations were different. For the reaction in Figure II.12a, the Fe precursor was added drop-wise to the acid, giving rise to a lemon yellow and clear solution. After 30 min, the amine was added to the Fe-acid mixture, and the mixture became immediately brown.

In the second experiment (Figure II.12b), the acid and the amine were mixed together and formed a white emulsion. Then, the Fe precursor was added drop-wise to the mixture, giving rise to a dark brown solution. These two experiments produced NPs of similar cubic-like shapes but two different size distributions, 8.8±1.9 nm in Figure II.12a and 13.7±2.1 nm in Figure II.12b. We believe that the formation of smaller NPs in the first experiment is due to the deactivation of part of the stabilizing ligand PA by its reaction with the initial ligands of the Fe precursor. The dropwise addition must have let the time for the PA to react with the liberated HDA of the entering precursor. The ligands $^{-}N(SiMe_3)_2$ are displaced as an amine (HMDS) upon reaction with SA in the first step. This reaction is less important in the second experiment probably because the SA forms a ion pair with HDA and it is less available for reaction with the HMDS.

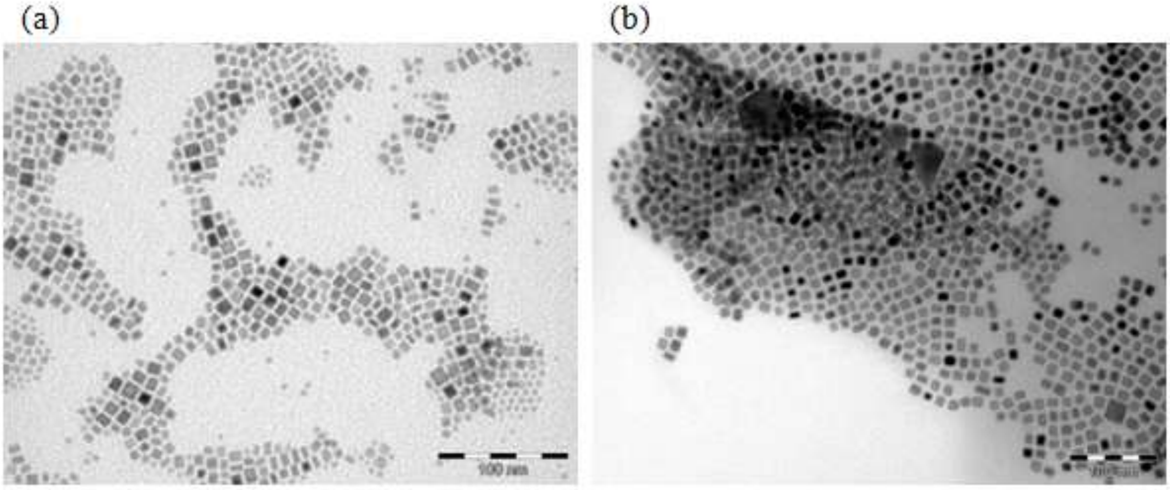

Figure II.12: TEM images of "Fe_ 1PA:2HDA_ Mes_150°C_48h" with different adding order: (a) Fe+ acid+ amine; and (b) acid+ amine+ Fe.

The encapsulation of pre-formed Fe and Co NPs stabilized by long alkyl chain ligands within the f-**CNT₁** was attempted in order to confirm the decisive role played by the ligand nature on the possibility to introduce these NPs in f-CNTs. The f-CNT$_1$ was respectively introduced into the colloidal solutions of these two NPs in THF. After ultra-sonication for 20 min and subsequent stirring during 2 hours, TEM grids were prepared by diluting the suspension in THF.

As expected, no NPs were unequivocally encapsulated although some NPs seem to be in the interior of the CNTs due to the superposition of the CNTs and the NPs on the TEM grid (Figure II.14).

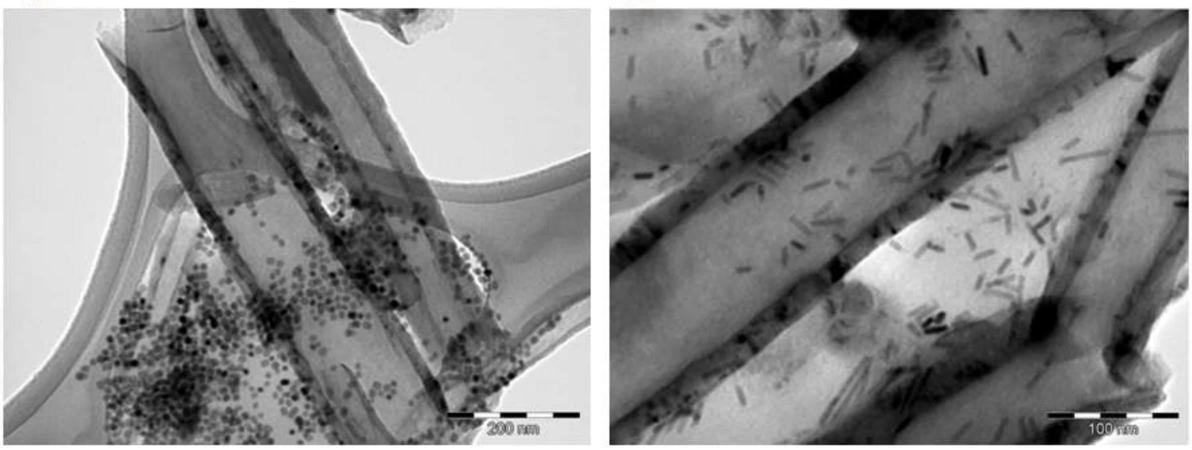

Figure II.14: TEM image presenting that (a) Fe and (b) Co NPs stabilized with long alkyl chains are outside the CNTs.

From these experiments we have confirmed that the long chain ligands are not well adapted for the introduction of the NPs in the CNTs, which must be due to the lack of affinity between the inner surface of the CNTs and the NPs with long alkyl chain on their surfaces. We have also seen that the reaction conditions for the NP synthesis have to be very rigorously controlled in order for the NPs to be synthesized in a reproducible way. We have therefore decided to use aromatic ligands susceptible to allow the introduction of the NPs in the CNTs by favoring an interaction with the interior walls of the f-CNT via π-π interaction. These aromatic ligands were used either *in situ* during the NPs synthesis, as alternative ligands instead of long chain ones, or in a ligand exchange step for the displacement of the initial ligands from preformed NPs, which, as described above, were obtained by the classical long-chain acids and amines.

II.3.2 Synthesis of MMNPs with new aromatic ligands and their confinement

We have synthesized Fe and Co NPs in the presence of new acid/amine ligands possessing aromatic groups (Figure II.15) as stabilizing agents, instead of the classic long chain ligands. These aromatic group bearing ligands MMNPs can establish π-π interaction with the inner surface of the f-MWCNTs.

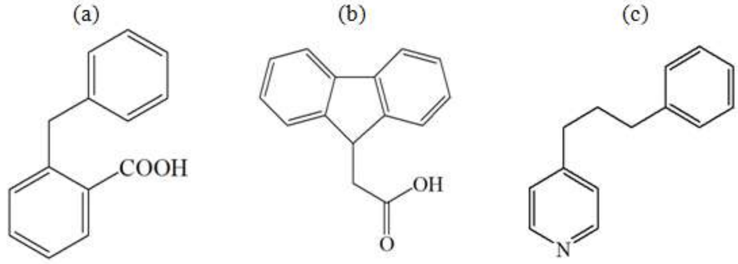

Figure II.15: (a) 2-benzylbenzonic acid (BBA); (b) 9-fluoreneacetic acid (FAA); and (c) 4-(3-phenylpropyl)pyridine (PPP).

II.3.2.1 Synthesis of Fe NPs with new aromatic ligands

Monodispersed Fe NPs were synthesized by the following procedure: a solution of 0.125 mmol of $[Fe\{N(SiMe_3)_2\}_2]_2$ was added dropwise into a mixture of 0.25mmol of BBA and 0.5 mmol of PPP. Then the Fischer-Porter bottle was charged with 3 bars H_2 and heated at 150 °C. After 48 hours, a colloidal solution of Fe NPs was obtained. The spherical Fe NPs are monodispersed with mean diameter centered 4.5 nm as measured by TEM (Figure II.16).

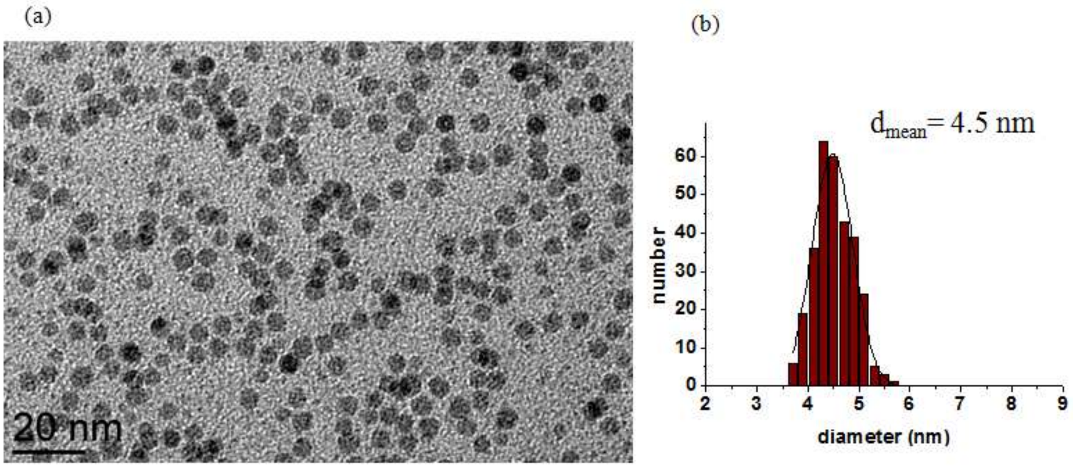

Figure II.16: Reaction "Fe_1BBA:2PPP_ Mes_150°C_48h". (a) TEM image of the pre-formed Fe NPs; and (b) particle size distribution with d= 4.5±0.4 nm.

Another synthesis was carried out by changing the addition order of ingredients,:, mixing BBA with Fe precursor was followed by PPP addition instead of mixing BBA with PPP and then adding the precursor. In this case, almost no change was observed either in the color of the starting solution or for the Fe NPs obtained at the end. Therefore, changing the addition order seems to have no influence on Fe NPs formation in this reaction, in contrast to the observation from the reaction of the Fe NPs in the presence of the long chain ligands where different addition orders resulted in different NP size. The difference between the behaviors of the system in the presence of the aromatic compared to long chain ligands might be attributed to interactions between the acid and amine, in each case. The long chain acid and amine can generate an ion pair, displayed by the equation below, due to the p*Ka* of primary amine (10.7 for the conjugated acid of ethylamine) indicating a relative high basicity (21). The formation of ion pair could be associated with the observed white emulsion. That ion pair formation may affect the coordination between metal and acid, affecting therefore the NP formation.

$$\text{R-NH}_2 + \text{HOOC-} \rightarrow \text{-NH}_3^+ \ {}^-\text{OOC-R}$$

On the other hand, PPP is a pyridine possessing a much lower p*Ka* (5.25 for the conjugated acid of pyridine) compared to primary amine (22). We believe that the salt formation is less favored in this case and the BBA and PPP act more as isolated molecules and their behavior in the presence of precursor resembles more to the situation where the ligands are added one by one to the precursor. That's why no difference was observed by modifying the addition order.

However for this same reaction, when the addition rate of the precursor was increased, by injecting the entire precursor in one time, supercrystals were formed directly in solution by assembly of NPs (Figure II.17). In this case the Fe NPs that could be measured presented a diameter of 8.1±0.9 nm. These assemblies of NPs are strongly ferromagnetic and attach on the stirring magnetic bar. They were therefore not appropriate for introduction in the CNTs, which demands well dispersed NPs.

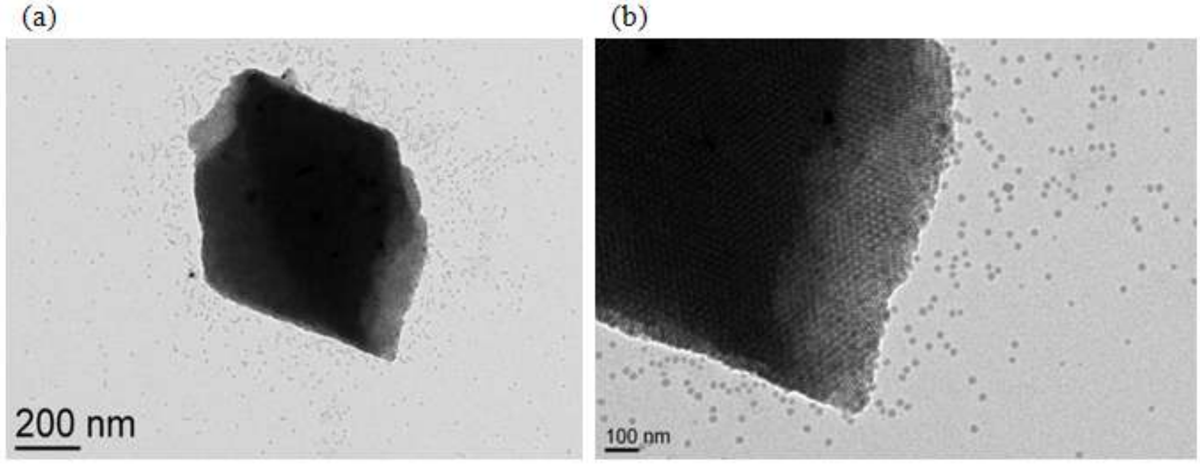

Figure II.17: Reaction "Fe_1BBA:2PPP_ Mes_150°C_48h" with fast adding rate.

Using FAA instead of BBA to synthesize the Fe NPs and by a slow addition of the precursor to the ligand mixture, the NPs were slightly bigger, with main diameter of 5.3±0.4 nm. Due to the high price of FAA, for the rest of the study we have decided to use BBA.

In conclusion, the synthesis of monodispersed Fe NPs is very sensitive, also when aromatic ligands are used. Minor modifications of the starting solution preparation, such as the addition rate of the precursor, in this case also can affect the final products. More precisely, fast addition rate of Fe precursor results in supercrystal structures, which hinder the subsequent confining step. On the other hand, the order of mixing does not seem to influence the reaction outcome.

II.3.2.2 Synthesis of Co NPs with new aromatic ligands

In our group, spherical Co NPs and well defined Co NRs have been synthesized with long chain ligands by modification of the Co/acid/amine ratio (15, 23, 24). Since the introduction of Co NPs prepared by long chain ligands was not possible as we showed before, we focused our attention on the synthesis of Co NPs stabilized by the new aromatic ligands. We were mostly interested in forming NRs in the presence of aromatic ligands, and introduce them into CNTs. There are no examples in the literature of CNTs in which pre-formed NRs have been confined.

As in the case of Fe, the mixing procedure during the preparation of the starting solution also affects the size of the Co NPs. In Figure II.18, we present the resulting Co NPs from a drop by drop addition of the Co precursor to the mixture of the acid and amine ligands. “Co_1.2BBA:1.2PPP_Mes_150°C_24h” (Figure II.18a) gave rise to Co NPs with diameter in the range of 1-5 nm. With the other aromatic acid “Co_1.2FAA:1.2PPP_Mes_150°C_24h” (Figure II.18b) Co NPs with diameter in the range of 1-3.5 nm are obtained. The large size distribution may result from an insufficient separation between the nucleation and growth steps, *i.e.* a long period of nuclei formation during which growth of NPs takes place simultaneously, therefore resulting to an inhomogeneous growth of the nuclei.

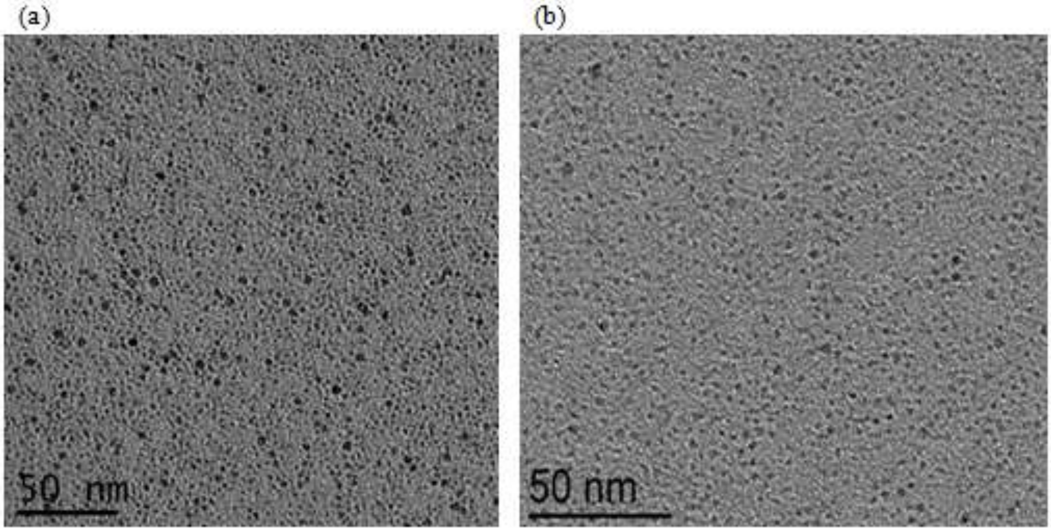

Figure II.18: TEM images of (a) "Co_1.2BBA:1.2PPP_Mes_150°C_24h", and (b) "Co_ 1.2FAA: 1.2PPP_ Mes_150°C_24h".

Another reaction was carried out by adding fast the Co precursor to the solution containing the mixture of the new aromatic ligands. When comparing Figure II.19 with Figure II.18a, a fast addition rate results in little larger Co NPs ranging from 2 to 6 nm, not very monodisperse in size. Interestingly while for the a fast addition of Co precursor to a mixture of a long chain amine and a long chain acid, and for a Co/acid/amine ratio of 1/1.2/1.2 we obtain NRs, with the aromatic ligands we have not been able to obtain NRs of a high aspect ratio even by applying the fast addition method.

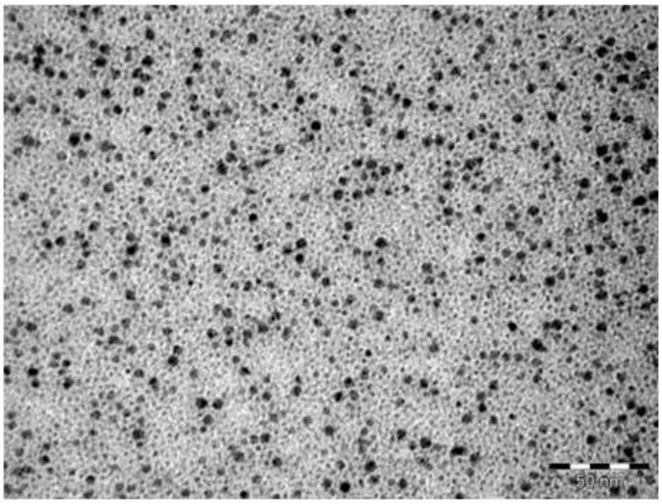

Figure II.19: TEM image of " Co_1.2BBA:1.2PPP_Mes_150°C_24h" with fast addition rate.

We have also tried to see whether one of the long chain ligands was responsible for the NR formation. Thus, we combined one long chain ligand (acid) and an aromatic one (amine). The reaction "Co_1.2LA:1.2PPP_Mes_150°C_24h", in which BBA replaced by LA, produced small monodispersed Co NPs (Figure II.20a). However, decreasing the reaction temperature to 120 °C, some elongated NPs were found (Figure II.20b). By keeping the reaction temperature at 150°C but working in anisole, monodispersed Co NPs, a little larger than those obtained in mesitylene, were formed without any elongated NPs (Figure II.20c). When we replaced the aromatic amine PPP by HDA and we used an aromatic acid ("Co_1.2BBA:1.2HDA_Ani_ 150°C_ 24h"), many short Co NRs were formed (Figure II.20d), indicating that HDA might play a role in Co NR formation. Further investigation on the effect of the ligand structure on the synthesis of Co NRs was not in the center of our subject. However, this study has shown that the replacement of the long chain ligands by aromatic ones has as a result the formation of either spherical NPs or very short NRs. We have therefore decided to use for the confinement Co NRs produced by the classical introduced long chain ligands after ligand exchange, which will be described below (part II.3.3).

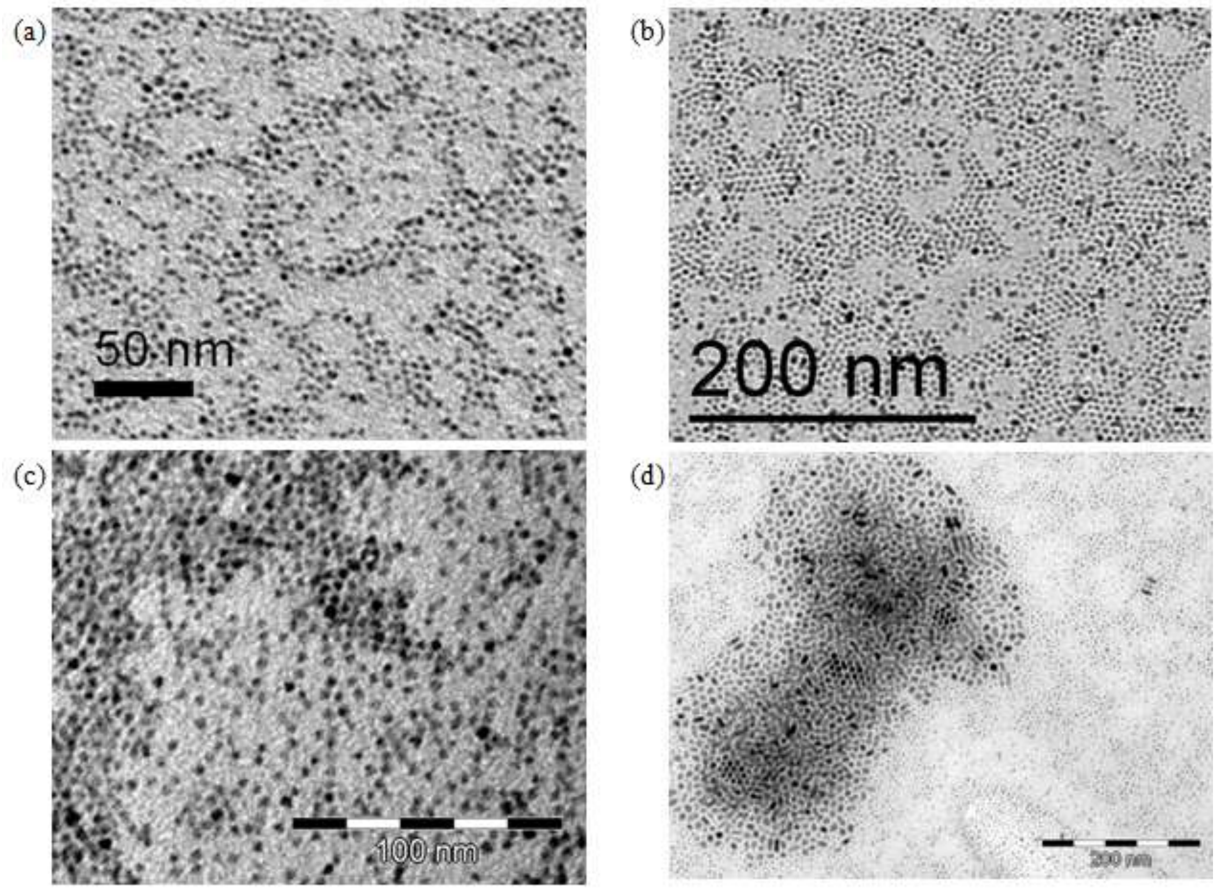

Figure II.20: TEM images of (a) Co_1.2LA:1.2PPP_ Mes_150°C_24h, (b) Co_1.2LA:1.2PPP_ Mes_120°C_24h, (c) Co_1.2LA:1.2PPP_Ani_150°C_24h, and (d) Co_1.2BBA:1.2HDA_ Ani_150°C_24h with "one injection" adding rate.

II.3.2.3 Confinement of pre-formed MMNPs by suspension method in the presence of f-CNT1

The monodispersed Fe NPs synthesized in the presence of the aromatic ligands ("Fe_1BBA:2PPP_Mes_150°C_48h"), after washing for removal of the reaction side-products and the excess of ligands and dying, have been suspended in an organic solvent in the presence of the functionalized MWCNTs (f-MWCNTs).

All the solvents for synthesis, dispersion, or washing of MMNPs, have a surface tension low enough for wetting the CNTs channel (25, 26).

Table II.1: Relevant physical properties of solvents involved in this thesis. (cP is the abbreviation for centipoise).

Solvent	Boiling point (°C)	Surface tension (mN/m)	Viscosity (cp) at 20°C
Toluene	110.6	27.9 (25°C)	0.59
Tetrahydrofuran (THF)	65-67	26.7 (25°C)	0.55
Pentane	35-36	15.5 (25°C)	0.24
1,3,5-trimethylbenzene (mesitylene)	165	28.8 (20°C)	6.92
Anisole	154	36.2 (15°C)	1.05

According to the literature relative to the liquid phase filling methods, ultra-sonication treatment is always used to introduce the liquid phase into the CNTs. A test to evaluate the resistance of Fe NPs under ultra-sonication was carried out. Compared to the initial NPs, the NPs had almost no size change after sonication during 20 min using a common ultra-sonication bath.

The goal was to obtain solid samples of the filled CNTs for characterizations by X-ray diffraction, and SQUID, and if possible evaluate their potential in hyperthermia. Two methods have been applied for obtaining a solid sample after confinement: i) solvent evaporation and ii) separation from the colloidal solution by filtration.

II.3.2.3.1. Solvent evaporation after confinement

As a first approach, we tried a relatively easy method that consists in wetting the CNT channel with a colloidal solution in an appropriate solvent, of pre-formed Fe NPs that is introduced in the CNTs by capillary forces. This step is followed by solvent evaporation as described in the literature (10). This could help the filling, thanks to the difference of concentration of the filling materials between the interior and the exterior of the channel. During this procedure, we first dispersed the preformed Fe NPs with diameter 4.5 nm in a solvent, and then introduced the f-CNT$_1$ into this colloidal solution. Then the mixture was ultra-sonicated for 20 min and subsequently stirred. Finally the solvent was evaporated.

Toluene or THF were chosen as solvents for preparing the Fe NPs colloidal solution, because both CNTs and NPs can be well dispersed in these solvents upon sonication. The main differences between these two solvents are: i) that THF is likely to be a coordinating solvent that might modify NPs under certain conditions, and ii) that toluene is evaporated more slowly than THF at room temperature. In addition, toluene is an aromatic molecule that may compete with the aromatically functionalized MMNPs and adsorb on the inner sidewall of CNTs.

The initial concentration of Fe NPs in the colloidal solution after their formation reaction is roughly 3mg/mL, *i.e.* 6mg of solid NPs in 2 mL of solvent. This concentration was the first to be used for filling. The large-diameter f-**CNT$_1$** was added into the colloidal solution (3 mg/mL in THF) in a Schlenk tube. After ultra-sonication for 20 min and subsequent stirring for 1 hour, the black colloidal solution, in which no precipitate was present, was evaporated to dryness under vacuum. A part of the final black solid was re-dispersed in THF in order to prepare a TEM grid (Figure II.21).

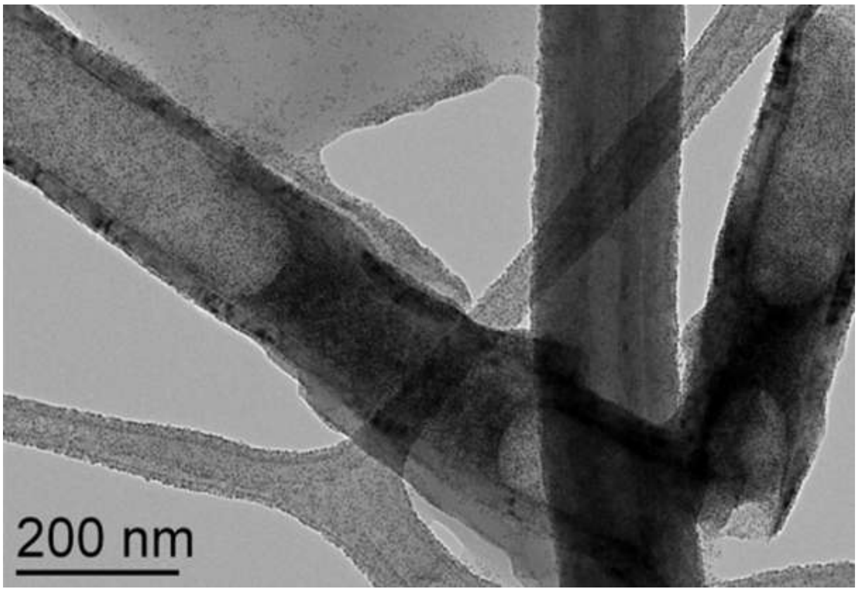

Figure II.21: TEM image that display the position of the pre-formed Fe NPs and the liquid-gas interfaces near the tip of f-CNT$_1$.

From TEM observations we see that a number of Fe NPs are attached on the outer surface covering the CNTs. Fe NPs deposited on the TEM grid were also present. Some parts of the CNTs present an increased contrast area, which is defined by two menisci. We believe that this phenomenon is due to the evaporation of the THF from the colloidal solution trapped in the CNTs, which can be clearly discerned by the meniscus formed. In these parts, the contrast is higher than in other areas, and corresponds to the presence of a high concentration of NPs in this area of the cavity. These areas can be found often near the tip of CNTs, in spite of some exceptions as shown below, in which the NPs rich areas are located in the middle rather than at the tip (Figure II.22). Most of the CNTs are empty, especially those with small diameter and thick sidewalls.

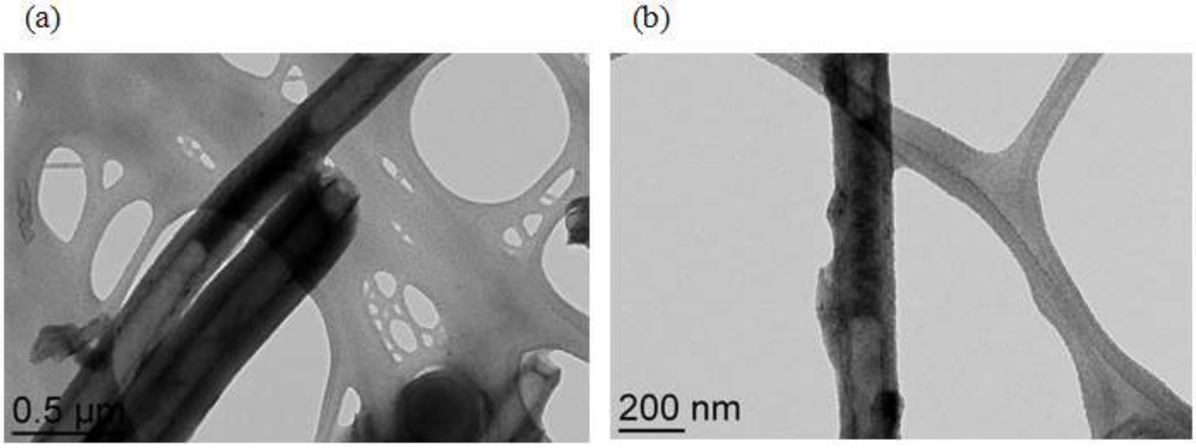

Figure II.22: TEM micrograph of the interface found in the middle of f-CNT$_1$.

From these results, we can conclude that the cavity of f-**CNT$_1$** can be wet by the colloidal solution of Fe NPs in THF, and NPs can be encapsulated within CNTs after evaporation of the solvent. However, no evidence of selective encapsulation of NPs is obtained, due to the high amount of NPs attached on the outer sidewall.

The poor selectivity observed might be due to the fast evaporation under vacuum. Thus, the same mixture was slowly evaporated in a glove-box. A similar result was obtained, except that some discontinue NPs rich areas were found (Figure II.23).

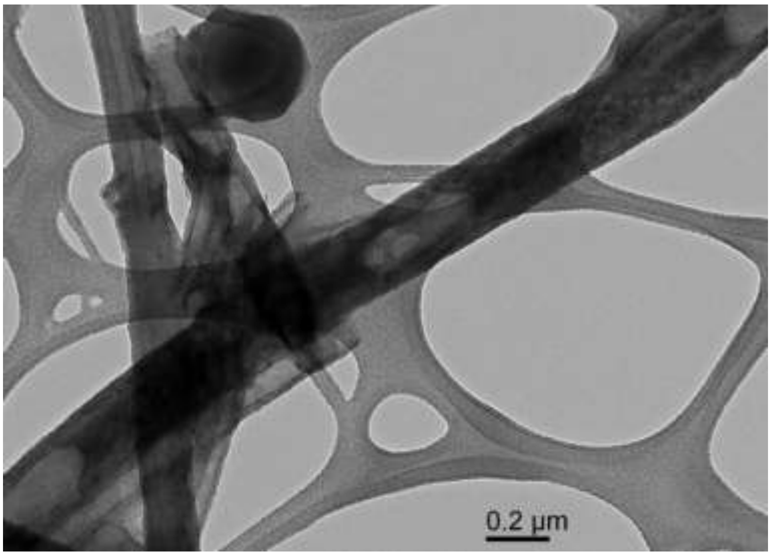

Figure II.23: The discontinue areas found in the middle of f-CNT1.

In Figure II.24, we show schematically some phenomena that may take place during solution evaporation and may account for the observed results. At the beginning, NPs are dispersed in the colloidal solution that wets the CNT channels and parts of the NPs are confined. When the solvent is evaporated, the concentration outside CNTs increases. However, instead of stimulating a NP migration into the CNT channel, where the concentration is lower than outside, as supposed by Bao *et al.* in the case of salts or compounds in the solution filling method (27), magnetic NPs tend to agglomerate in solution due to their low solubility or magnetic dipole interactions among them (28). Agglomeration may hinder the continuous entering of NPs into the CNT channel. This effect could also be the reason of the impossibility of filling CNTs with small diameter. On the other hand, the evaporation makes NPs agglomerating outside CNTs and forces them to attach on the outer surface regardless of the functionalized long chain that may prevent NPs from approaching the outer surface. The continuous evaporation of solvent in CNT channels drives the encapsulated NPs sliding along the smooth inner sidewall of CNTs, and finally the encapsulated NPs appear packed together at certain parts of the CNT channel.

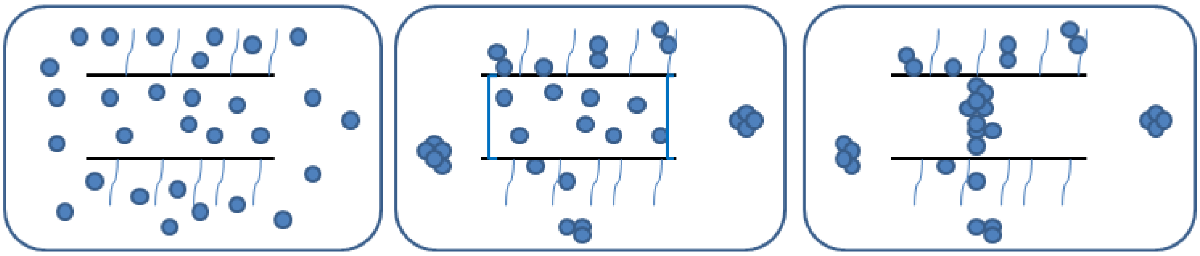

Figure II.24: Proposed phenomena occurring during the evaporation of solvent in the colloidal solution.

When the solid is re-dispersed in a solvent by sonication for preparing the TEM grid, the agglomerated NPs could also be re-dispersed and then deposited on the grid, as observed from TEM images. It should be noticed that the CNTs obtained after evaporation are more difficult to disperse in the solvent than those before evaporation. It is not clear whether the sonication treatment in this step affects the filling of NPs. In order to avoid any misinterpretation of the results due to this effect, grids were prepared in another way without dispersing in solvent. However, this method damages the carbon film on the grid, and entangled CNTs were found rather than individual ones, which makes the observation difficult. As a result, the former re-dispersing method was preferred in most cases having however in mind that the final results could be affected by the TEM grid preparation.

In order to reach 100% selectivity of Fe NPs within CNTs, NPs present outside the tubes have to be removed by washing. Three concentrations of NPs for filling were tested in order to see whether the concentration of the colloidal solution in NPs was affecting the yield in encapsulated NPs: 1.5 mg/mL (T1), 3 mg/mL (T2) and 6mg/mL (T3) with the same quantity of CNTs. After the treatments by sonication and stirring as described above, three black solids were obtained after slow evaporation in the glove-box, named T1, T2, and T3 respectively (Figure II.25).

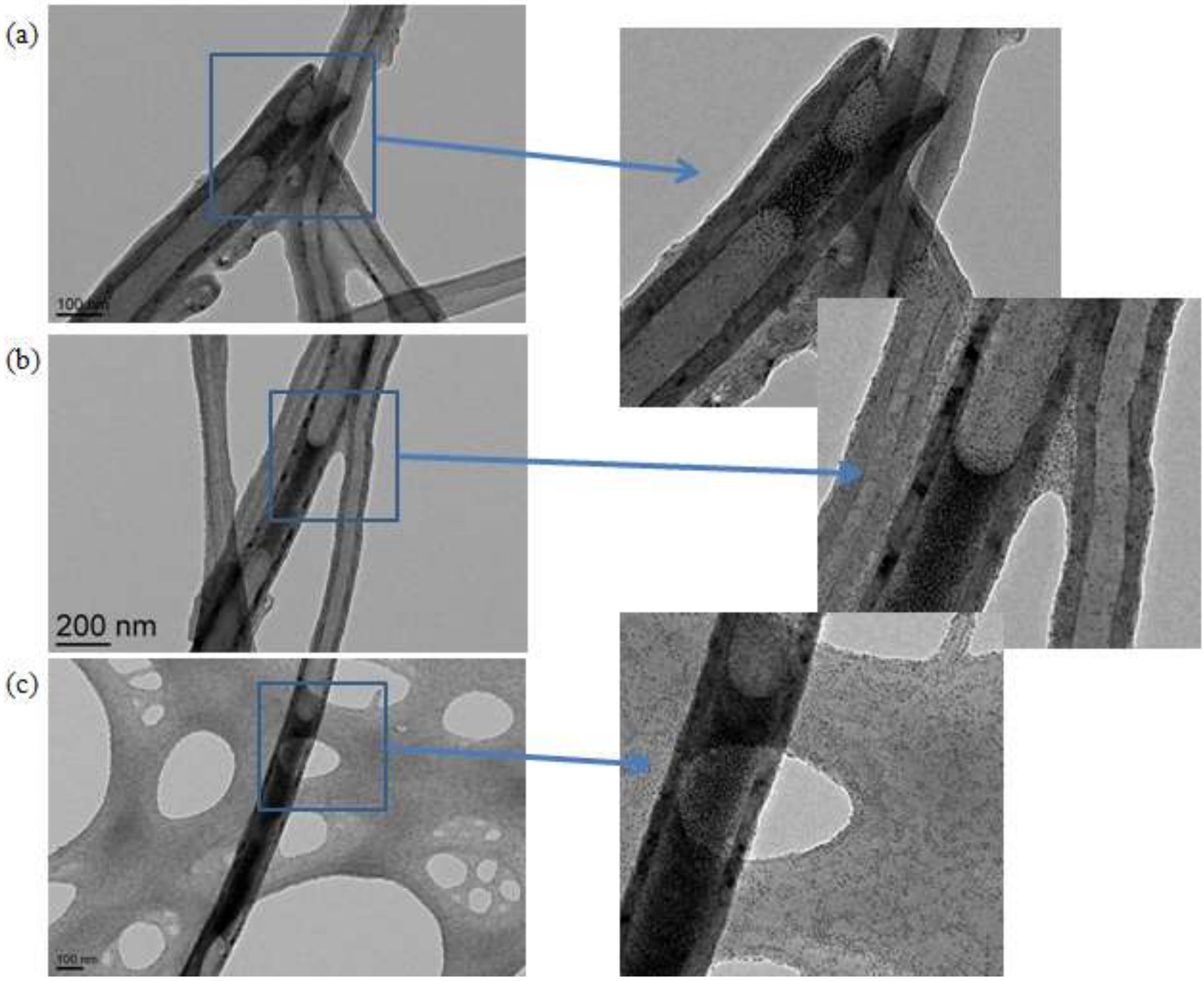

Figure II.25: TEM images of (a) T1, (b-c) T2, and (d-e) T3.

As expected, the higher the concentration, the more the encapsulated NPs observed from TEM images, but more NPs are also located on the outer CNT surface as well as on the grid. These three samples were washed with pentane. After filtration, free NPs were no more observed on the grid support. However, many NPs still remain attached on the outer surface of CNTs (Figure II.26).

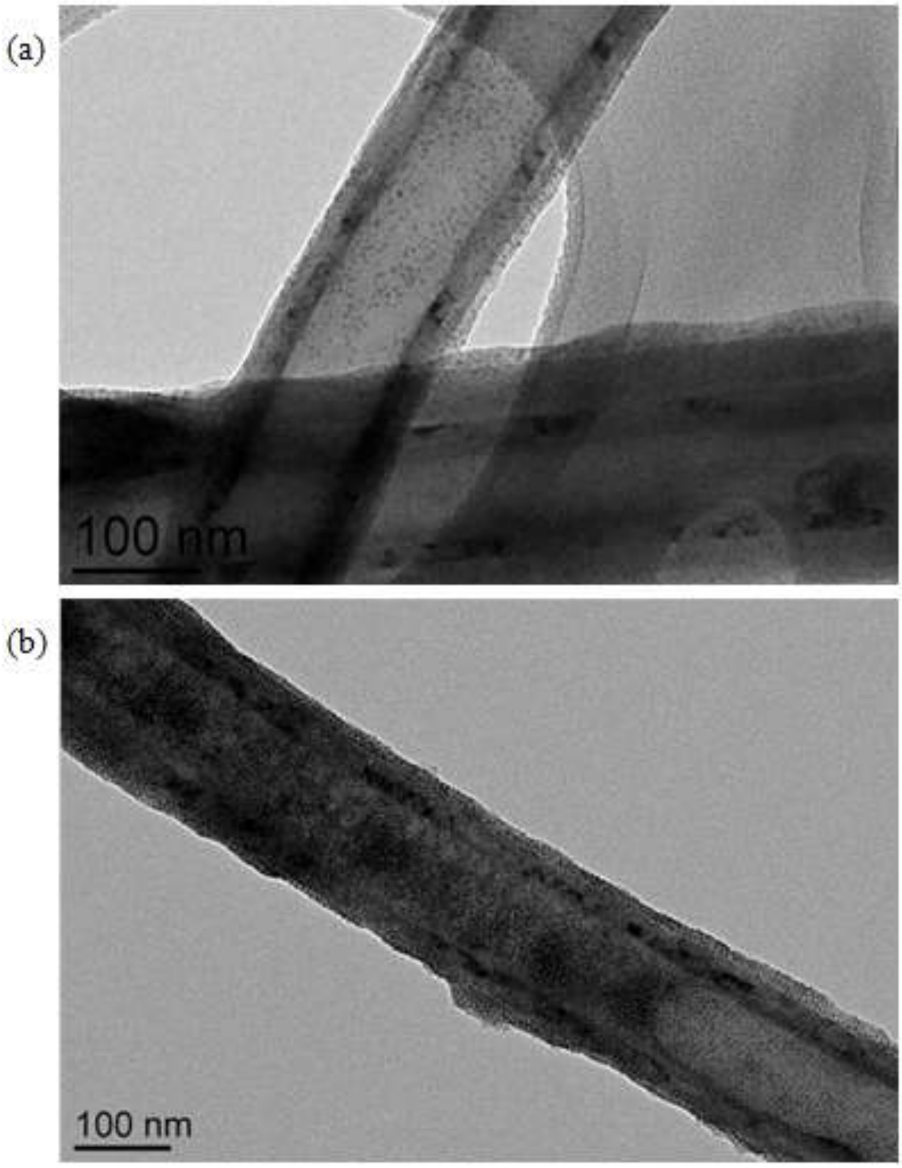

Figure II.26: TEM images (a) T2 and (b) T3 washed respectively with pentane.

Subsequently, another washing with THF was performed. After this washing, part of NPs attached on the outer surface was removed; however, an unexpected loss of the encapsulated NPs was noticed as well. More precisely for T1 almost all of the tubes seem to have lost the encapsulated NPs.

Tomography was used to examine the filling for T2 and T3 after THF washing (Figure II.27). Both of them have a significant amount of NPs on the outer surface, which indicates that the cleaning method *via* washing with solvent, pentane or THF, is not successful in this case.

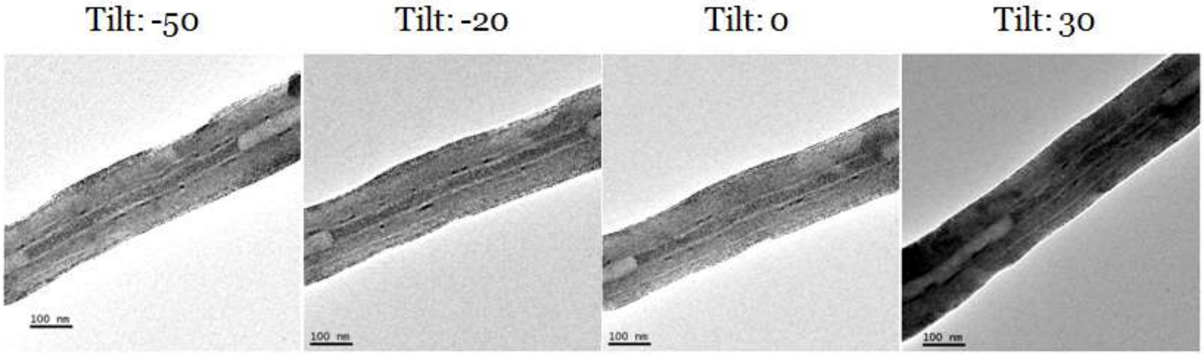

Figure II.27: Tomography of TEM images of T3 washed with THF.

In conclusion, solvent evaporation of colloidal solution containing the Fe NPs and the f-**CNT$_1$** gave rise to NP-filled CNTs, which are also decorated with NPs on their outer surface. These cannot be entirely removed by simple washing with a solvent. Further sonication and washing may induce the removal of the confined NPs from the inner cavity of CNTs. These problems render impossible the study of the magnetic properties of the encapsulated NPs since the decorating NPs on the outer surface would make unreliable any conclusion on the effect of the confinement on the magnetic properties. Hence, another confining method, instead of solvent evaporation, needs to be explored in order to drive the majority of NPs population into the CNT cavity or remove successfully the NPs from the external surface.

II.3.2.3.2. Filtration and washing after confinement

Several filling tests have been performed with different colloidal solutions.

—Direct filling with the as-synthesized crude colloidal solution

The pre-formed Fe NPs were synthesized in mesitylene, a solvent possessing a high boiling point and a high viscosity compared to THF and toluene. We tried to wet the cavity of f-**CNT$_1$** with this as-synthesized colloidal solution, followed by ultra-sonication for 20 min and stirring for one hour. The TEM grids were then prepared with a dilution of the mixture in toluene (Figure II.28) rather than with the dried solid after solvent evaporation and re-dispersion in a solvent (see previous method).

From the TEM images, the Fe NPs are clearly encapsulated within the CNTs and they are concentrated close to their tips. The liquid-gas interface forming a meniscus can also be seen where the NPs are concentrated. In contrary to what was observed in the evaporation method, in this case there are fewer NPs attached on the outer surface. Since no effect from evaporation is present, these observations may be attributed to the selective attraction/repulsion interactions between the inner or outer sidewall of CNTs and the functionalized NPs.

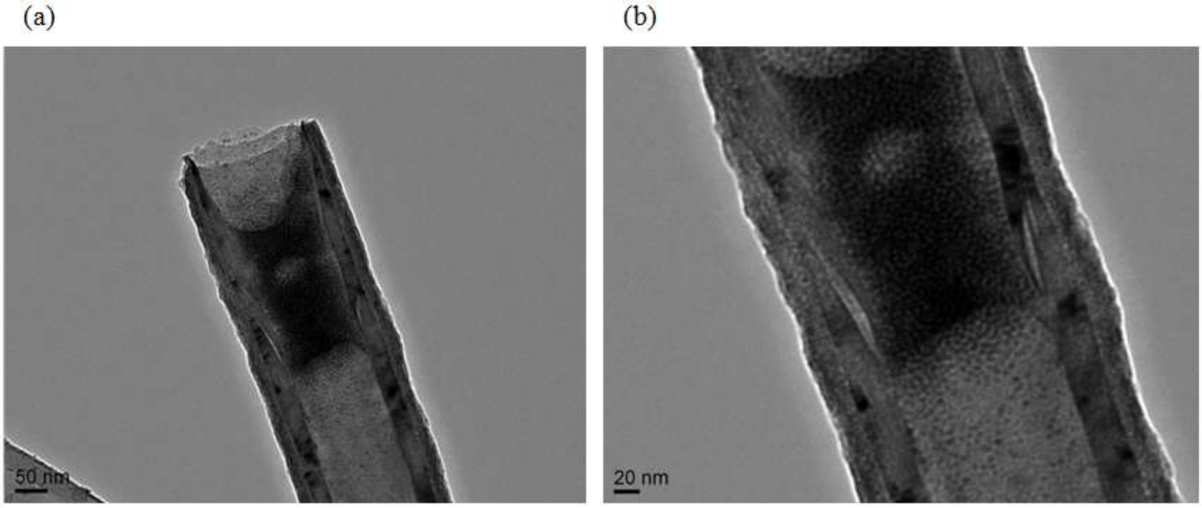

Figure II.28: Encapsulated Fe NPs within f-CNT$_1$.

Although the pre-formed Fe NPs were successfully confined within **CNT$_1$** and, importantly, very few NPs were observed on the outer surface, only a few CNTs contained NPs. Furthermore, a small part of the CNTs was filled with concentrated NPs, and the liquid-gas interface was always seen. A longer stirring period (24 hours) seems to improve the filling (Figure II.29). However further extension of the stirring period to 7 days did not improve the filling any further. Thus, a period of 24 hours of stirring has been fixed for the rest of suspension confinement experiments.

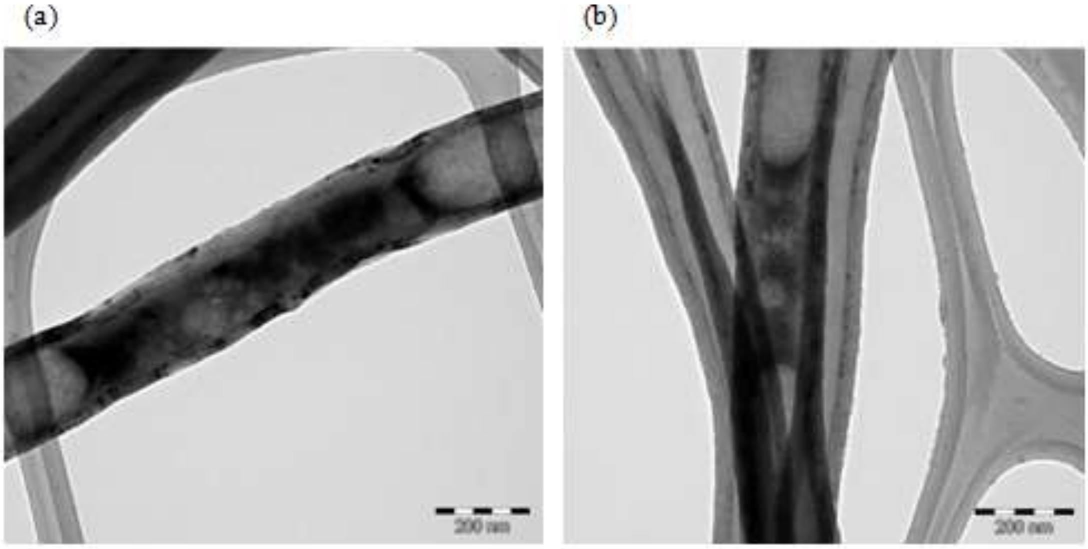

Figure II.29: TEM images of the f-CNT$_1$ encapsulating the Fe NPs (24-hours stirring).

It is known that solvated species may increase the viscosity of fluids. Not only Fe NPs present in colloidal solution, but also residues such as organic ligands and Fe complexes that have not been decomposed after the reaction, could play such a role. These solvated species may contribute to the high viscosity of the solution. In addition, mesitylene molecules may occupy part of the CNT channel the sites available for the interaction with NPs. All these reasons are unfavorable to confinement of NPs. Hence, the filling with the as-synthesized colloidal solution was probably not the best choice.

We therefore chose to use purified NPs in order to avoid the presence of impurities in the solution and use a less viscous solvent than mesitylene, which could favor the entrance of the NPs in the CNTs.

—Filling of colloidal solution in solvents possessing low viscosities

Toluene, THF, and pentane are solvents with relative low viscosities. The f-**CNT$_1$** and pre-formed MMNPs are hardly dispersed in pentane, and even precipitate rapidly after sonication. Toluene and THF can be used to disperse the f-**CNT$_1$** and the pre-formed MMNPs using an ultra-sound bath. Especially the pre-formed MMNPs can disperse easily in toluene just by simple shaking. However, toluene has an aromatic structure like mesitylene that may compete with the NP ligand through the π-π interaction with the inner sidewall of CNTs. Consequently, THF was used in a first approach as transport medium.

The f-**CNT$_1$** was immersed into a colloidal solution of a 3 mg/mL concentration of the pre-formed MMNPs in THF. Then, the mixture was treated by ultra-sonication for 20 min and stirred for 24 hours. The TEM grids were prepared by diluting the final colloidal solution in THF (Figure II.30a-b).

From the TEM images, much more NPs were encapsulated within CNTs than those by the filling approach which used mesitylene solutions, which demonstrates that the viscosity of the filling colloidal solution is a critical factor. In addition, only few NPs are observed on the outer surface of CNTs.

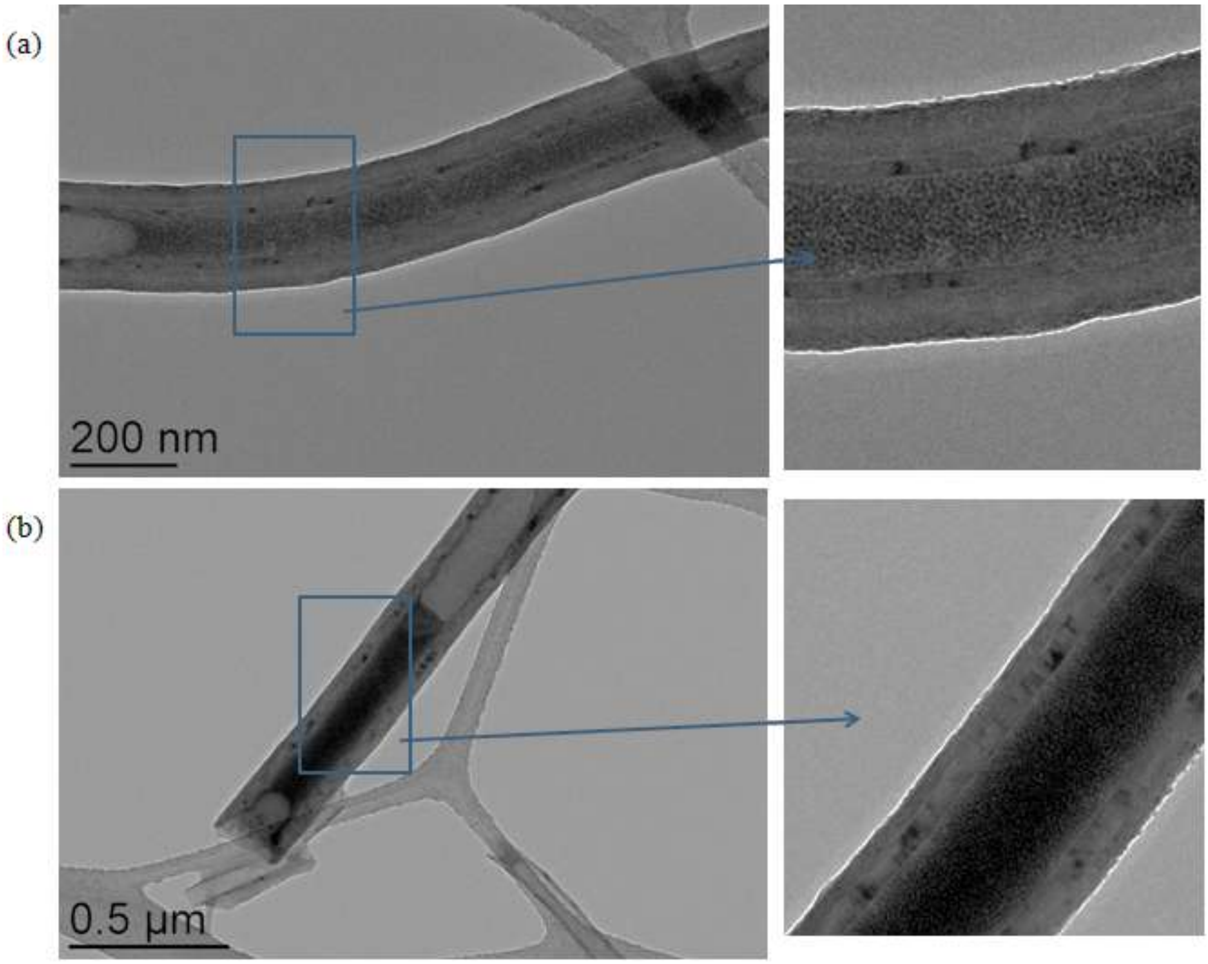

Figure II.30: TEM images of the filled f-MWCNTs with the Fe NPs in THF colloidal solution.

The inner diameter of CNTs is likely to play an important role in the filling with magnetic NPs that could form aggregates. A statistical analysis on the inner diameters of the filled CNTs was performed based on the TEM images, which indicates that the inner diameters of the filled CNTs are mostly ranged from about 35 to 160 nm but the CNTs with smaller and larger inner diameters are scarcely filled. The non-encapsulation for the small diameter CNTs (~35 nm) might result from the high viscosity of the filling solution, or the difficulty of migration of the MMNPs aggregates, while for the large diameter CNTs (>160 nm) that might be due to the weak interactions between the inner sidewall of CNTs and MMNPs with the limited surface contact.

Khlobystov *et al.* have discussed noncovalent interactions between molecules and SWCNTs based on a simplified Lennard-Jones potential (LJP) model, that describes the binding energy of an atom or a small molecule with the inner and outer surface of CNTs *via* van der Waals interactions (29). It is considered that when the CNT diameter D is inclined to infinite, the atom's binding energ in the interior of the CNT would be equal to the binding energy on planar graphene (Figure II.31e). As D is decreased, the binding energy increases, and then reaches a maximum at an ideal CNT diameter for that atom (Figure II.31b), called "snap-fit". This condition occurs when $D = d + 2 \times r_{vdW}$, where d is the diameter of the atom or molecule and r_{vdW} is the thickness of the p orbital of CNT. As the CNT diameter decreases further, the repulsive component of the LJP becomes dominant due to the large overlap of the atom and the CNT orbital (Figure II.31a). This model is suitable for the CNT–molecule interactions where van der Waals forces are dominant.

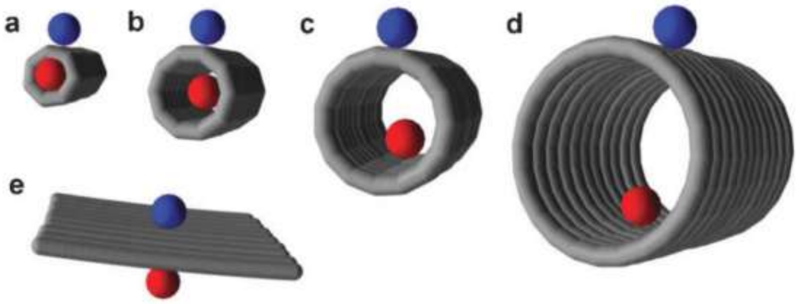

Figure II.31: Schematic diagrams of small molecules adsorbed on the outer (blue) and inner (red) surface of CNTs with different diameters ($d_{molecule}$ is van der Waals diameter of molecule, and d_{CNT} is internal van der Waals diameter of CNT): (a) $d_{CNT}<d_{molecule}$, (b) $d_{CNT}\sim d_{molecule}$, (c) $d_{CNT} > d_{molecule}$, (d) $d_{CNT} >> d_{molecule}$, (e) d_{CNT} infinite (15).

In our case, the situation is more complicated. First, the inner diameter of the f-**CNT₁** (20-200 nm) is much larger than that of the pre-formed Fe NPs (4-5 nm). Second, the viscosity of the filling colloidal solution (determined by the viscosity of the used solvent and the concentration of the MMNPs), and the π-π interactions are likely to play an important role. Finally, the π-π interactions and the magnetic dipole interactions among the MMNPs may be factors that should not be ignored. Those interactions among the MMNPs may result in an aggregation of the NPs in the colloidal solution, which hinder their entering and migration in the cavity of CNTs. As a result, CNTs with smaller diameters are hard to be filled with MMNPs.

For CNTs with larger diameters, the interactions of MMNPs with the inner sidewall of CNTs might be dominant for the confinement. In a study on the encapsulation of Au NPs, Khlobystov *et al.* mentioned the geometric fit with the step-edge of graphite nanofibers (GNFs) *via* van der Waals interactions (30). It was considered that the area of surface contact was critical, leading to different affinities for NPs attachment on the inner sidewall. In Figure II.32a, the small Au NPs **1** at the step-edge has a significantly larger area of surface contact with the GNF as compared with NPs **2** on a flat area. However, for larger Au NPs in Figure II.32b, the energetic difference between NPs **1** and **2** is less pronounced, due to a poorer geometric fit with the step-edge.

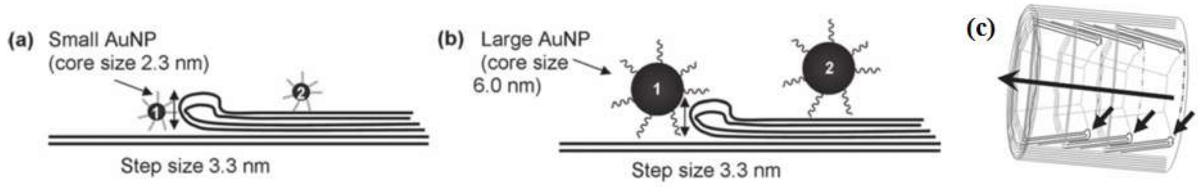

Figure II.32: Schematic representation of Au NPs of different sizes, (a) smaller and (b) larger, residing at internal step-edges of a GNF; (c) schematic representation of GNF step-edges (reproduced from ref.30).

Although the CNTs used in our study do not have such step-edge structure, the point of view about the area of surface contact may help us to interpret our observations. Imagine one Fe NP or an aggregate of NPs, supposed to be of spherical shape, attached to the inner surface of a CNT. The curvature of CNT and the NP diameters are both critical for the area of surface contact. The larger the diameter of CNTs, the lower is the curvature, thus the smaller is the contact area with a same NP. The larger the diameter of the NP, the smaller is the contact area with a same CNT. Both cases result in a weaker interaction between NPs and the CNT inner surface. That might be the reason why few large CNTs were filled. This could also explain why in the literature (10) the 2 nm RuPt NPs stabilized by the aromatic ligands were better encapsulated than our 4.5 nm Fe NPs within f-CNTs of similar diameter as ours.

Other attempts have been made to improve the filling yield. For example, by increasing the concentration of NPs to 12 mg/mL, very low filling yield was obtained presumably due to a too high viscosity of the solution or even an aggregation of the NPs. Heating can be used to decrease the viscosity and to promote the fluidity. A test was carried out by heating at 60 °C and stirring for 24 hours. However, this had as result, the modification of our NPs from spherical to bigger cubic (Figure II.33). In addition, the extended stirring for 7 days resulted in a size evolution of NPs outside the CNTs and a lower filling yield.

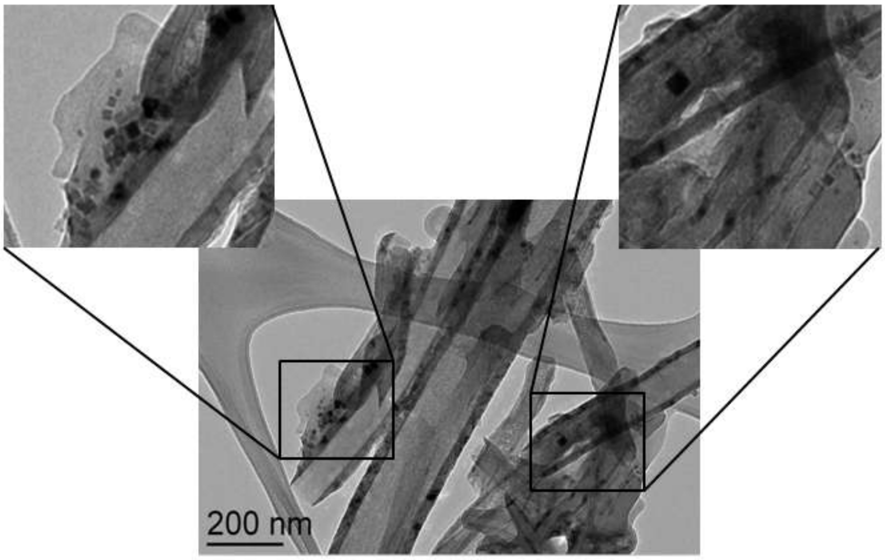

Figure II.33: TEM image of the growth from spherical to bigger cubic NPs, highlighted by magnifications.

Furthermore, we supposed that the gas trapped in the CNTs may hinder the filling with fluid of the CNT cavity. Thus, another method was attempted, consisting in the removal of air within CNTs under vacuum by heating, and then piercing the septum of the stoppered flask under vacuum by a syringe containing the colloidal solution of NPs. However, no improvement of the yield was observed by this method.

After various attempts for filling f-$\mathbf{CNT_1}$ with the colloidal solution of the pre-formed Fe NPs, the "3 mg/mL in THF 24 hours" condition gives the best result. Under the same conditions, the preformed Co NPs with the aromatic ligands ("Co_1.2BBA_1.2PPP_Mes _150°C_24h") were also encapsulated within the $\mathbf{CNT_1}$ (Figure II.34).

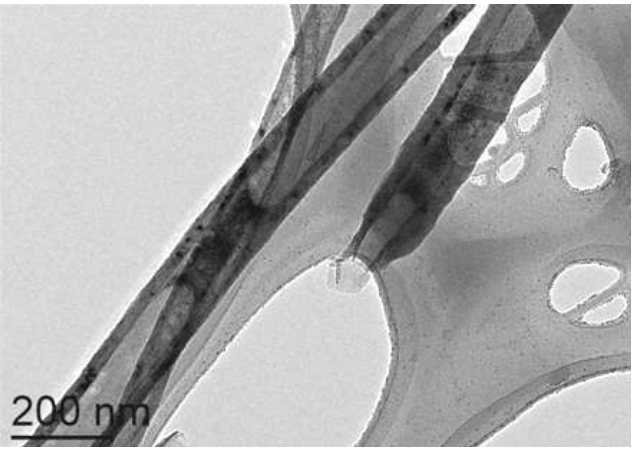

Figure II.34: TEM image of filled f-$\mathbf{CNT_1}$ with the pre-formed Co NPs ("Co_1.2BBA_1.2PPP_Mes_150°C_24h").

For the small diameter f-**CNT$_2$**, the filling attempt was made with only the as-synthesized colloidal solution of Fe NPs. None of the Fe NPs is confined as shown in Figure II.35. Many Fe NPs are attached on the outer surface of the f-**CNT$_2$**. The difficulty of introduction of the Fe NPs into the f-**CNT$_2$** channel may be attributed to the small difference of diameter between the NPs (4-5 nm) and the f-**CNT$_2$** inner diameter (3-10 nm). This is consistent with the results we obtained with the f-**CNT$_1$** of smaller diameters, as described in the previous paragraph.

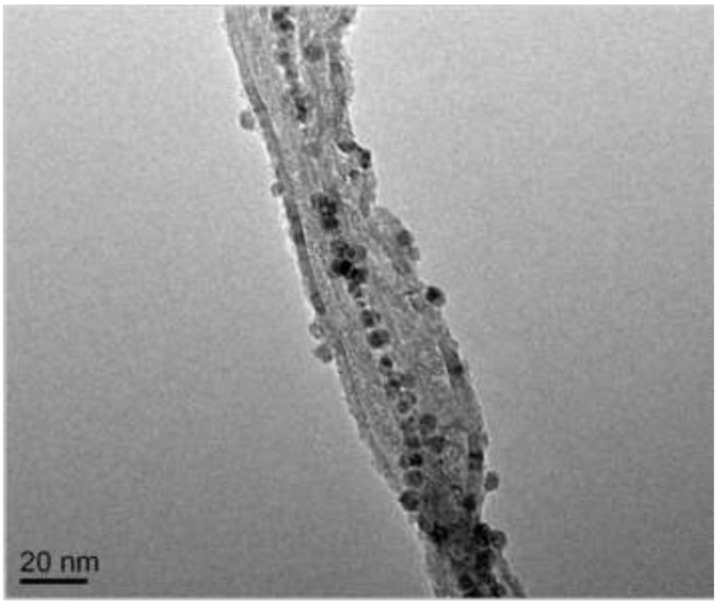

Figure II.35: TEM image of the f-CNT$_2$ attached by the Fe NPs on its outer surface.

—Separation of the filled CNTs from the colloidal solution

We have successfully confined the aromatic ligand stabilized Fe NPs within the f-**CNT$_1$**, which has been confirmed by TEM observation. Yet, that is the situation in the colloidal solution. However, in order to study the magnetic properties of the FeNP@CNT nanohybrid, a dried solid sample is necessary. Apart from solvent evaporation, centrifugation, precipitation, and filtration are techniques that may allow separating the filled CNTs from the NPs in the colloidal solution.

The black colloidal solution in THF was let to decant during a week, but the solution was invariably not clear. The supernatant was carefully removed and subsequently examined by TEM, in which both NPs and CNTs were observed. When pentane was added for precipitation, the supernatant became clear and transparent, indicating that both NPs and CNTs were precipitated. When THF or toluene was added, a black colloidal solution was reformed. Therefore, none of these solvents can selectively separate the filled CNTs from the free NPs in the colloidal solution *via* precipitation.

Centrifugation was also attempted with the same colloidal solution in THF. The interface could be seen more easily, although the mixture was always black. The dark supernatant was removed, and then THF was added to wash the precipitate. After an additional centrifugation, the supernatant was clearer. The washing centrifugation step was repeated until a clear supernatant was obtained. Unfortunately, almost no confined NPs were observed in the final precipitate by TEM. Hence, too much washing and centrifugation are inappropriate for isolating filled CNTs, since the solvents which dissolve the NPs outside the CNTs, seem to displace them form the inner cavity also.

Alternatively, a filtration by cannula was attempted in order to realize the separation. Purified THF for washing can be added by a glass syringe under Ar. The main drawback is the difficulty of detaching the CNTs from the filter paper. In addition, the filter paper is obstructed very easily by the CNTs, which renders the filtration difficult. Finally, we used a Schlenck type filter that allows separating the CNTs from the colloidal solution under inert atmosphere.

After filtration and washing with THF, the black solid, denoted FeNP@**CNT$_1$**, can be removed from the filter with a spatula. The grids were either prepared by re-dispersing the solid in a solvent (Figure II.36), or directly by contacting the TEM grid with the dry solid (Figure II.37). From the TEM images of both grids, we see that very few NPs are attached on the **CNT$_1$** outer surface and no NPs were deposited on the grid, indicating that most of the NPs are confined within **CNT$_1$**. The confined Fe NPs possess nearly the same diameter (4.7nm) as the pre-formed ones (4.5 nm). It was also found out that the washing process can remove the NPs outside the tubes as well as those inside, which is hard to avoid.

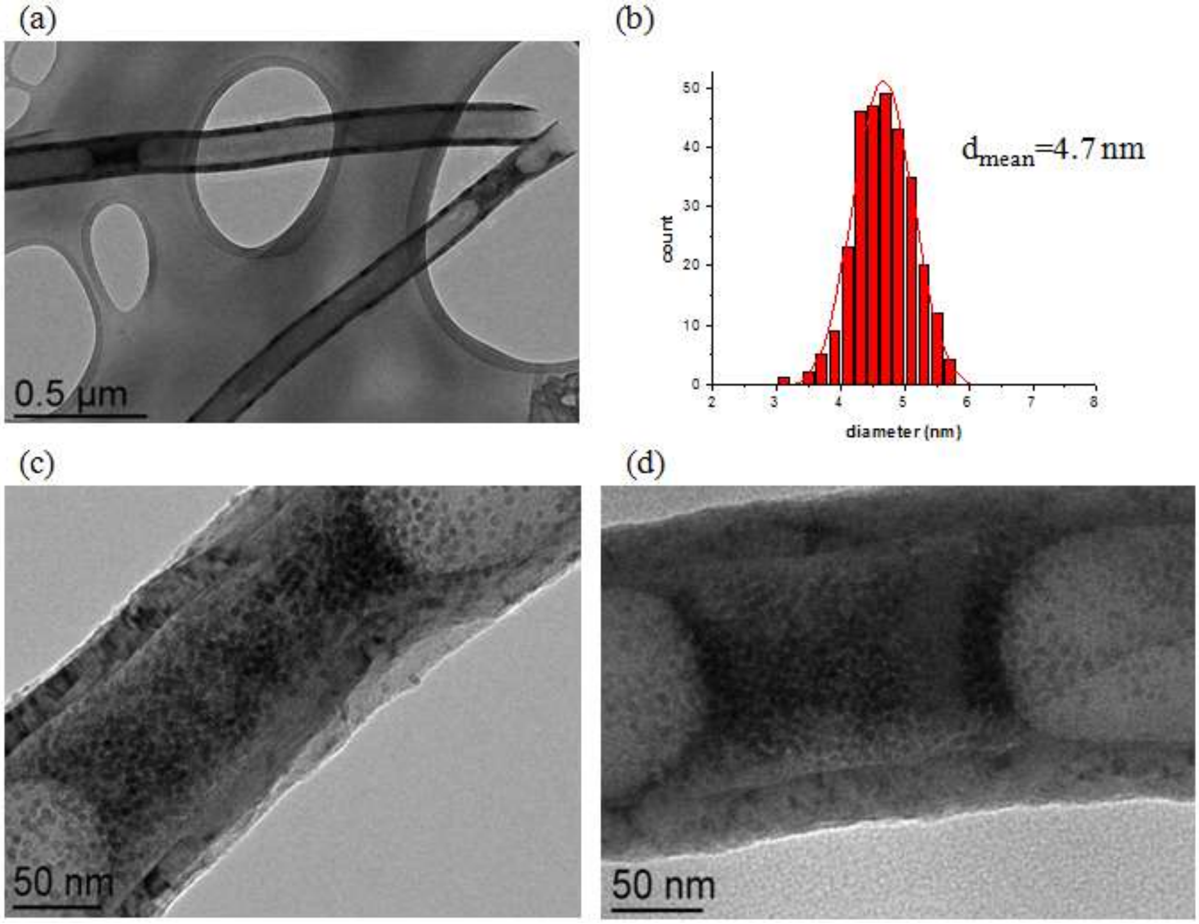

Figure II.36: TEM images from the grid prepared by dispersing. (c) and (d) are magnifications of (a); (c) the size distribution d=4.7±0.5 nm.

There is a difference between the TEM images from the grids prepared by two methods. On the grid prepared directly with the solid (Figure II.37), the confined NPs are homogeneously deposited in the cavity of **CNT$_1$**, whereas after re-dispersing in a solvent and evaporation (Figure II.36), the confined NPs are agglomerated. This comparison may indicate that solvent wetting of the CNT channel followed by solvent evaporation contributes to agglomeration of the confined NPs in the cavity. The sample FeNP@**CNT$_1$** constitutes the first sample we have produced that is clean enough to perform magnetic measurements.

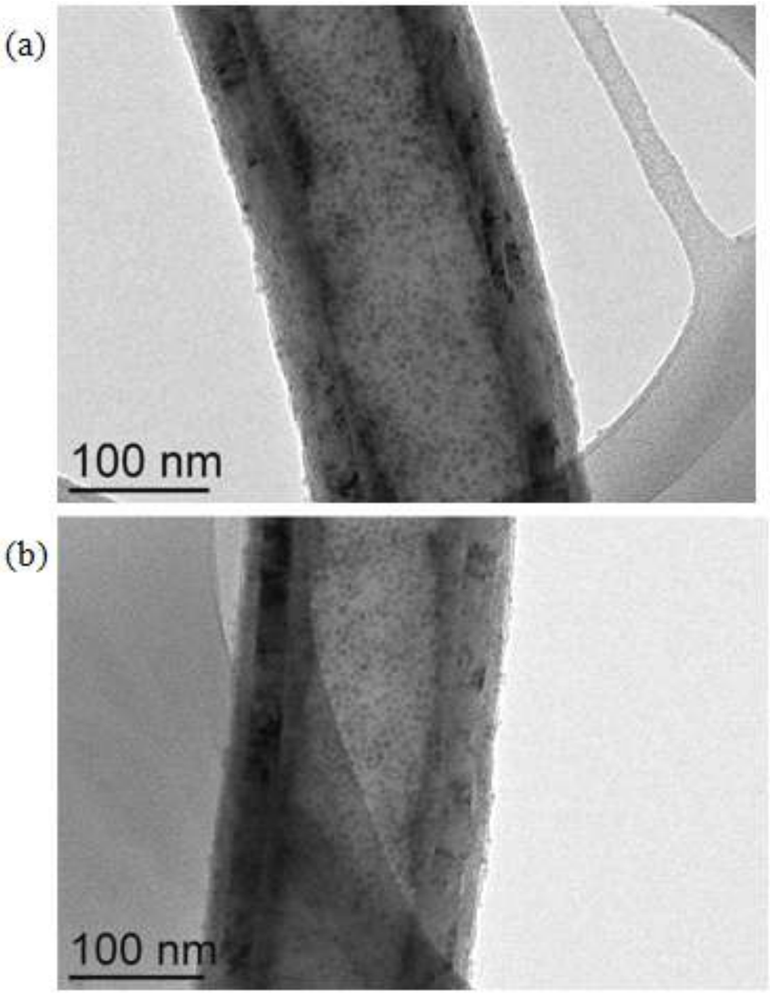

Figure II.37: TEM images from the grid prepared directly with the solid FeNP@CNT_1.

Hysteresis loops were performed by superconducting quantum interference device (SQUID) at 2K for both the pre-formed Fe NPs and the solid FeNP@**CNT_1**. In Figure II.38, we see that there is no shift of the coercive field, resulting from exchange bias effect (31) between ferromagnetic core and antiferromagnetic shell, for both of them (see Annex II.B), indicating the absence of oxide in these two samples. This means that the two samples are metallic and no oxidation is presented during the synthesis of the Fe NPs and the confinement of the NPs inside the CNTs. The coercive field increases from 579 Oe for the pre-formed Fe NPs (Figure II.38a) to 859 Oe for the CNT-confined ones (Figure II.38b), which is probably due to different dipolar interactions among the NPs in the samples (32). In the sample of the Fe NPs, metal fraction is higher than that in the FeNP@**CNT_1** nanohybrid. As a result, dipolar interaction is stronger in the Fe NPs sample than in the FeNP@**CNT_1** nanohybrid, which results in smaller coercive field presented in the Fe NPs sample.

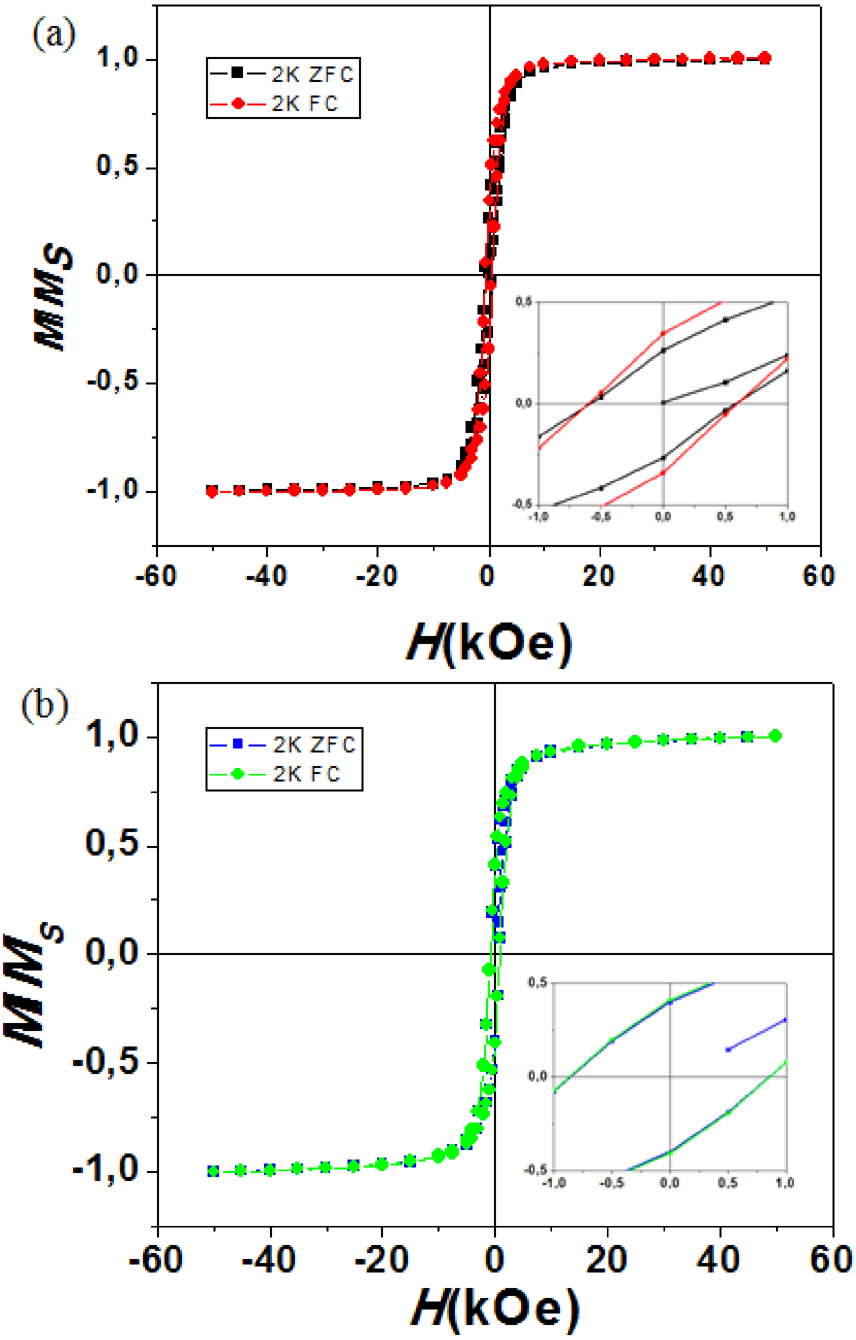

Figure II.38: Hysteresis loops of (a) the pre-formed Fe NPs and (b) the FeNP@CNT$_1$ at 2K performed by SQUID.

In conclusion, the pre-formed monodispersed Fe or Co NPs have been successfully confined within the large f-MWCNTs as a result of the selective interactions between the NPs and the inner/outer surface of CNTs *via* the suspension method. Both the CNT diameter and the viscosity of the filling colloidal solution play a critical role. By washing and filtering, the filled CNTs can be isolated from the colloidal solution. By investigating the TEM images, we have observed that the concentration of the confined Fe NPs in the solid FeNP@**CNT$_1$** was higher than that observed by dispersing in solvent, which reveals that during washing the solvent can move the confined Fe NPs along the inner surface, leading to inhomogeneous filling along the CNTs cavity. In addition, extensive washing with low viscosity solvent, such as THF, induces the expulsion of the NPs from the inner cavity, and therefore should be avoided.

In perspective, washing with a solvent that possesses a high viscosity in order not to enter easily in the cavity but which can well disperse the NPs should be attempted.

II.3.3 Confinement of pre-formed MMNPs *via* ligand exchange

Co NRs stabilized by long alkyl chain ligands have been synthesized and studied by Wetz *et al.* by using $Co\{N(SiMe_3)_2\}_2(THF)$ as a precursor (15). These Co NRs do not enter the f-$\mathbf{CNT_1}$. When they were suspended in toluene in the presence of the f-$\mathbf{CNT_1}$, no confined NRs were found and all the NRs were aggregated outside the CNTs.

Under the same experimental conditions that yield Co NRs, the aromatic ligands employed in our work do not form anisotropic NPs. We therefore, decided to use Co NRs prepared by LA and HDA ligands in order to confine them in $\mathbf{CNT_1}$, after an exchange procedure of the long chain ligands by the aromatic ones.

The as-synthesized Co NRs are shown in Figure II.39a. Small Co NPs are also formed during this synthesis. The Co NRs possess a length $l = 52 \pm 3.5$ nm (Figure II.39b) and a diameter about 4-5 nm. After precipitation and washing, the Co NRs can be separated from the Co NPs (Figure II.39c). The washed Co NRs were mixed with a solution of BBA in toluene, followed by a vigorous stirring during one hour. Nearly all Co NRs were quickly precipitated and stuck on the magnetic stirrer, and then the supernatant was removed. This washing with BBA solution and separating cycle was repeated three times. Finally, the new ligand-functionalized Co NRs were washed with pentane. Compared to the as-synthesized Co NRs, the functionalized Co NRs exhibit the same length and diameter.

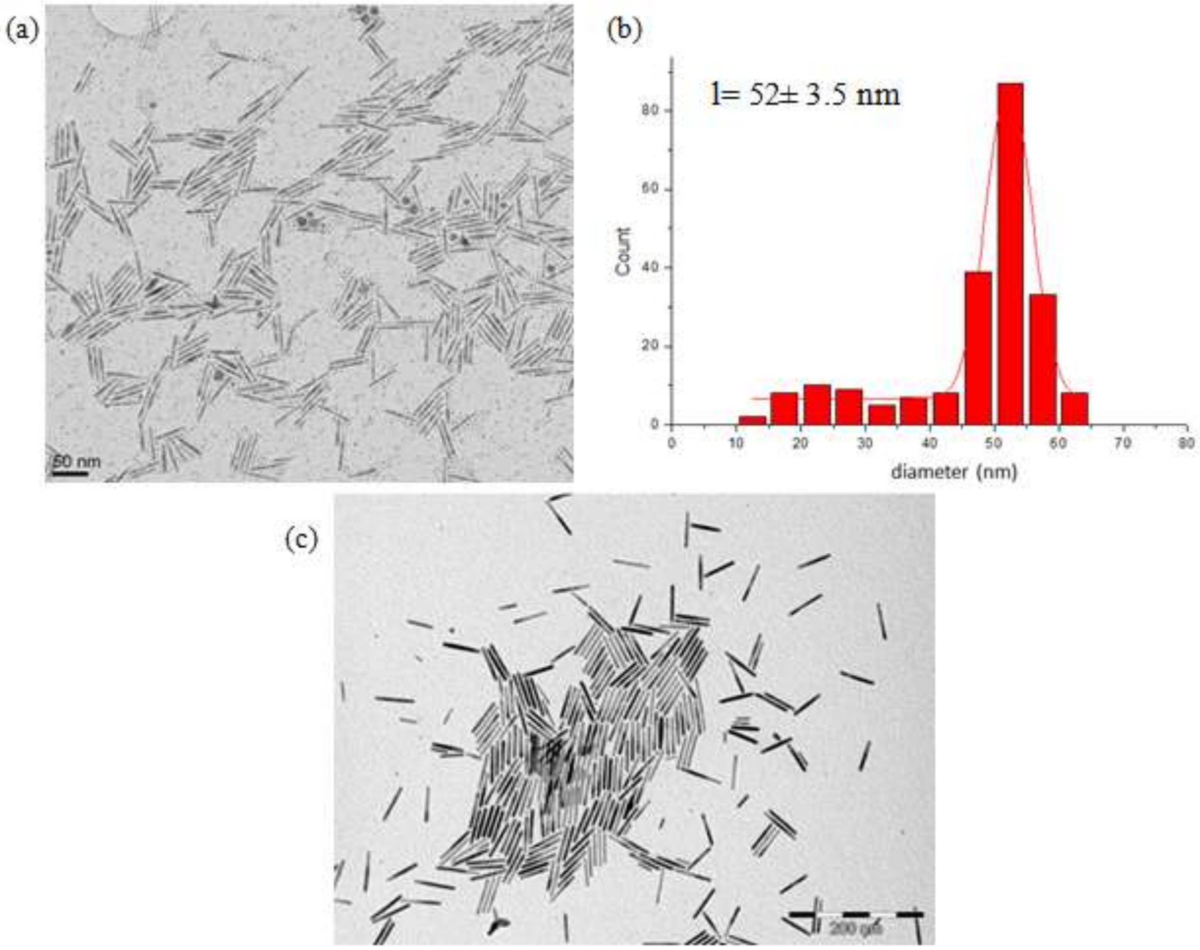

Figure II.39: TEM images of (a) the as-synthesized Co NRs before exchange and (c) the Co NRs after washing; (b) length distribution l =52±3.5 nm.

Very strong magnetic dipole interactions among the Co NRs render them hard to disperse in most common solvents. Compared to other solvents, toluene can disperse relatively easily the NRs. Thus, toluene was chosen as a transport solvent for introducing the NRs into the f-$\mathbf{CNT_1}$. After sonication of a mixture containing 10 mg of the Co NRs in 5mL of toluene (2 mg/mL) and 30 mg of the f-$\mathbf{CNT_1}$, the mixture was stirred vigorously with a magnetic bar during 24 hours. A grid was prepared after dilution of the mixture in toluene.

In Figure II.40, groups of partially organized Co NRs are clearly observed in the cavity of CNTs, either near the tips or in the middle of CNTs. The liquid-gas meniscus is also present in this case. Interestingly, the confinement of the NRs depends on the diameter of the CNTs. The CNTs with smaller and larger diameters are rarely filled. Most of the filled CNTs present diameters in the range of 100-150 nm.

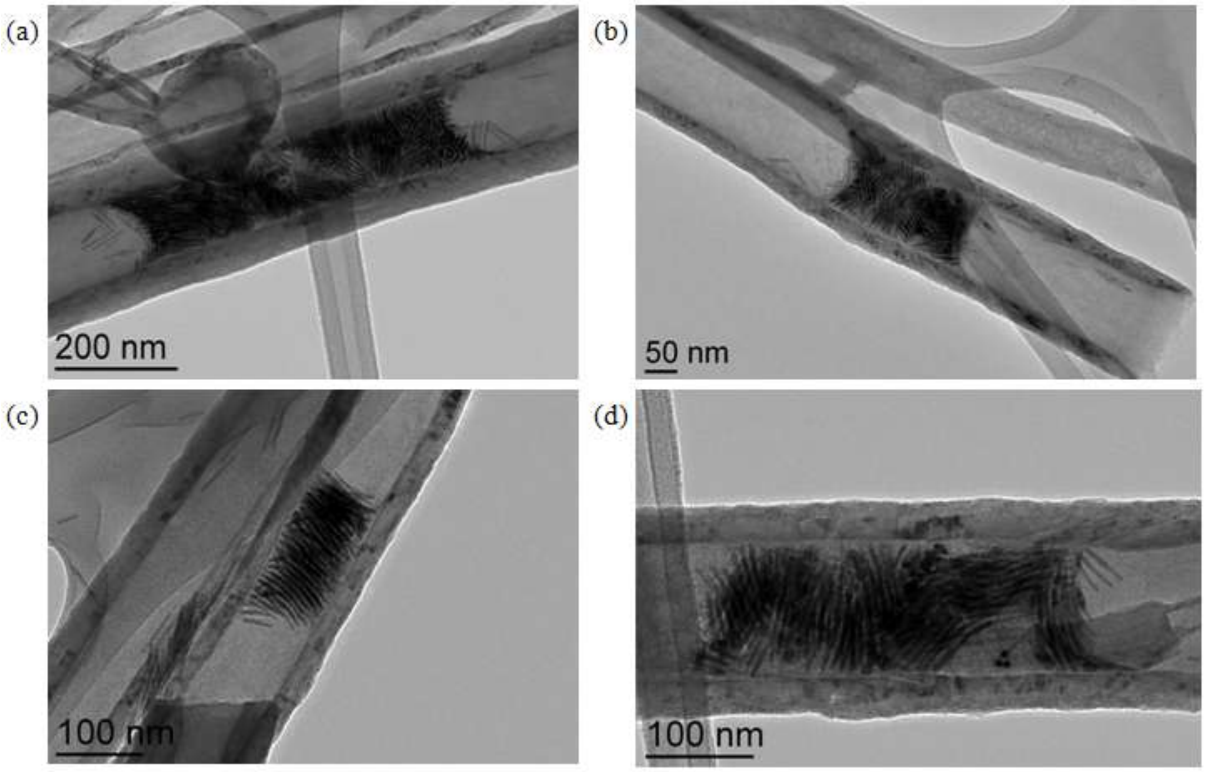

Figure II.40: (a-d) TEM images of the functionalized Co NRs confined within the f-CNT$_1$.

Tomography images demonstrate that the CNTs are filled with the Co NRs (Figure II.41). Some isolated NRs are also observed on the outer surface.

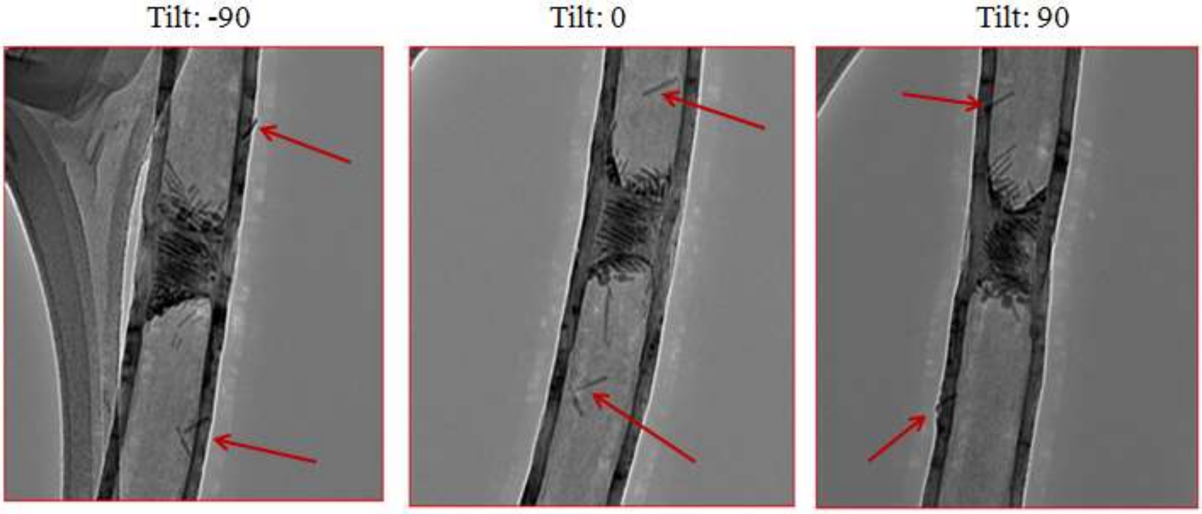

Figure II.41: Tomography images of the confined Co NRs within f-CNT$_1$. The NRs on the outer surface are highlighted by the red arrows.

From the TEM images, the confined Co NRs seem to be organized in groups in the CNT channel. These groups have an orientation axis that is often aligned perpendicularly to the tube axis (Figure II.40). Some isolated NRs inside the channel are randomly oriented.

However, other images (Figure II.42) show that the confined Co NRs exhibit an alignment along the CNT channel as well. Hence, the confined Co NRs seem to have no preference of orientation.

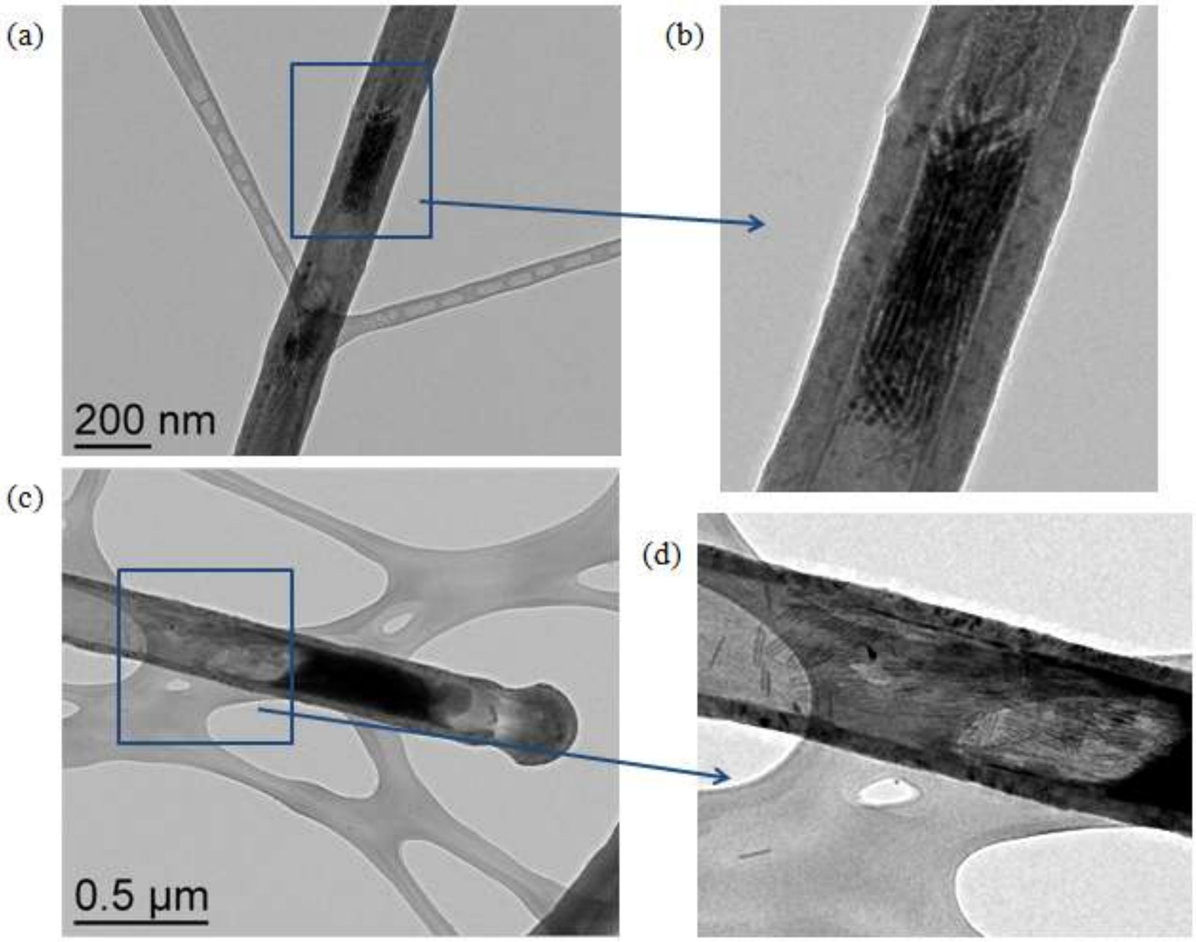

Figure II.42: TEM images of the confined Co NRs exhibiting the alignment along the CNT channel. (b) and (d) are respectively local magnifications of (a) and (c).

These observations are surprising because normally the alignment along the tube axis should give rise to a bigger area of surface contact. It should be noticed that solvent may drive the NRs to move along the CNT channel. Therefore, the π-π interactions between the NRs and the inner surface seem not to be dominant compared to the dipolar interactions among the NRs.

Some TEM images are likely to reflect a possible filling process. It seems that the NRs enter as bundles and not as isolated NRs in the CNTs. In Figure II.42a, a group of Co NRs is halfway in the interior of a **CNT$_1$**. It is possible that this pre-organized bundle is entering in the CNT. If it is the case, we have to note that only the bundles that are smaller than the diameter of the CNTs can enter the channel. Since at least one of the dimensions of the bundles is around 50 nm (the length of a single NR) it becomes obvious why smaller diameter **CNT$_1$** do not contain any NRs. Thus, we could suppose that the Co NRs enter into the tube channel in the form of pre-organized bundles. This could explain also the fact that some bundles are oriented with the long NR axis parallel to the CNT channel and other bundles with the long NR axis perpendicular to the CNT channel. It is in fact the whole bundle dimensions that determine the possibility of entering as well as the entering orientation and subsequently the orientation of the individual NRs with respect to the CNT channel.

It is however possible that Figure II.43a shows a bundle going out of the CNT. In that case we cannot conclude about how entering takes place but we have to think that the confined NRs can be driven out of the CNTs due to the weak interaction with the inner surface or the good fluidity of the suspension. The three images in Figure II.43b demonstrate the good fluidity of the suspension and the good migration of the confined Co NRs in the **CNT$_1$** channel, which have reached the closed end of some one side-opened **CNT$_1$**. The closed ends probably prevent the NRs from driving out of the CNTs.

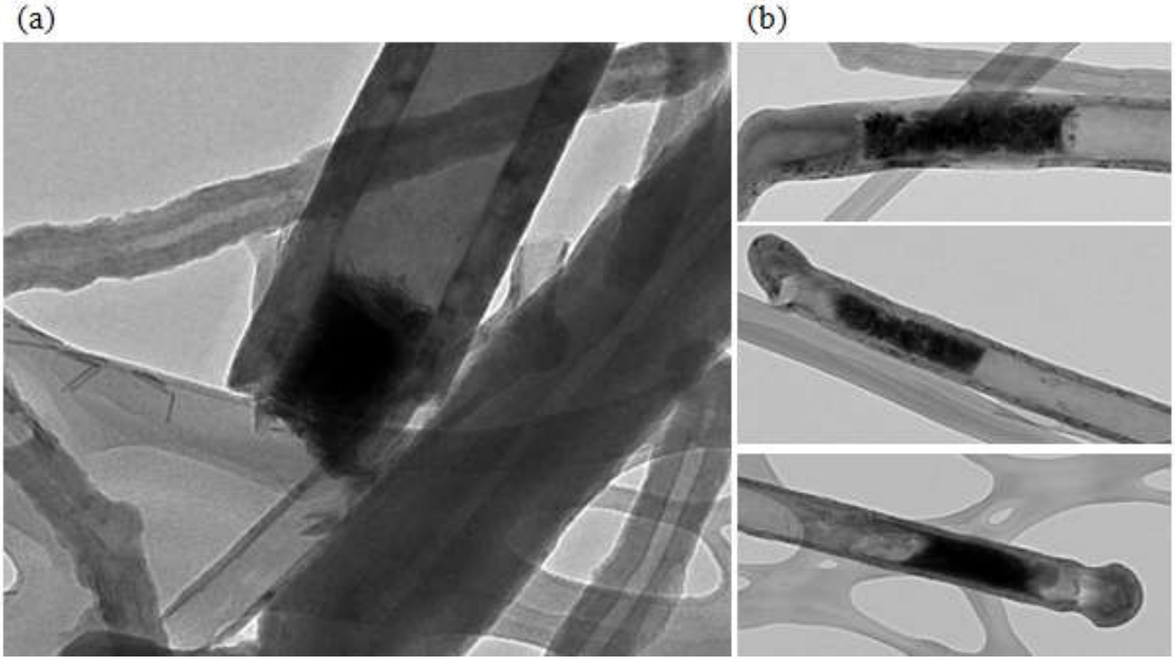

Figure II.43: TEM images of (a) Co NRs blocked at the open tip of CNT$_1$ and (b) packed at the closed tip of CNT$_1$.

Unfortunately, besides the Co NRs encapsulated within the CNTs, most of Co NRs are found outside the CNTs (Figure II.44), and they are difficult to separate from the CNTs filled or empty.

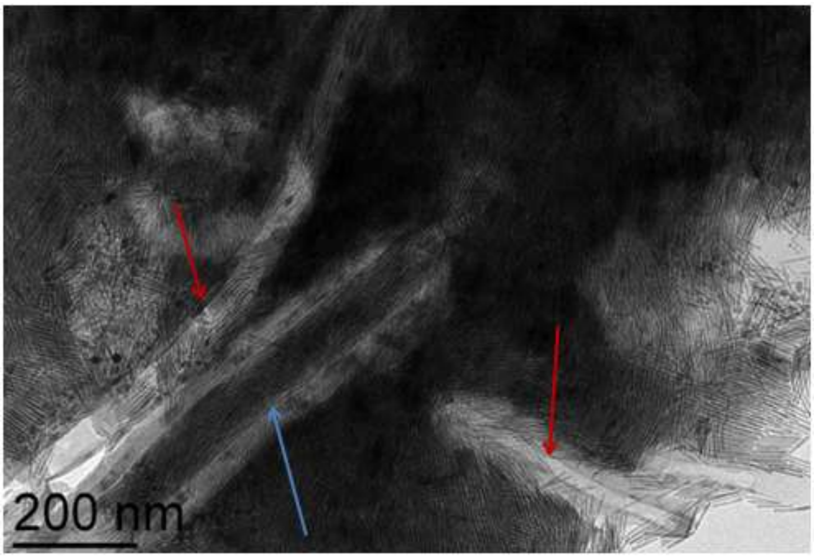

Figure II.44: TEM image of the bundled Co NRs in the suspension. The blue arrow highlights a well filled CNT, and the red arrows highlight the empty CNTs, all of them are covered with NRs.

In order to separate the Co NRs in solution from the Co NR-filled CNTs, filtration and washing step under Ar were performed. However, due to the weak dispersion in toluene or THF, the aggregated NRs could not be washed away. This means that since the dispersion in toluene is not good enough, we have to reject the possibility that individual NRs enter in the cavity. Adding amine can aid the dispersion of the NRs in toluene, so a solution of 3 mg/mL of PPP or HDA in toluene was used to clean the CoNR@**CNT$_1$**. Unfortunately, this treatment was unsuccessful.

In conclusion, the filling of CNTs *via* the suspension method depends significantly on the state of the NPs. The aromatically functionalized Co NRs can be encapsulated within the f-**CNT$_1$**, as confirmed by TEM and tomography images. We believe that the NRs enter in pre-organized bundles. This pre-organization in bundles of several NRs prevents the efficient removal by filtration of the rest of the bundles that are suspended in solution outside the CNTs. Thus, large amounts of the aggregated composed of groups of NRs, which cannot be dispersed and removed by washing treatment; prevent further analysis of the magnetic properties of the NRs confined in the CNTs.

II.4 Confinement of as-synthesized MMNPs by an in situ solution method

II.4.1 Confinement with f-CNT$_1$

Although the preformed Fe NPs, Co NPs, and Co NRs have been confined within the f-**CNT$_1$** *via* the suspension method, only the clean and solid nanohybrid FeNP@**CNT$_1$**, with monodispersed Fe NPs confined within the f-**CNT$_1$**, has been reproducibly obtained. In order to compare to the suspension method, the filling of CNTs *via* the *in situ* solution method was also explored. The f-**CNT$_1$** were immersed into the prepared starting solution containing the metallic precursors and the aromatic stabilizing ligands, followed by thermo decomposition and/or reduction under H_2 and heating.

A similar reaction was performed under the same reaction condition as for the synthesis of "Fe_1BBA:2PPP_Mes_150°C_48h" with fast addition rate, except that now the f-**CNT$_1$** were present. It was found that many CNTs were well filled with densely packed Fe NPs. Some of them are completely filled with NPs, which sometimes overflow out of the CNTs (Figure II.45). The Fe NPs exhibit a cubic shape with diameter around 8-9 nm.

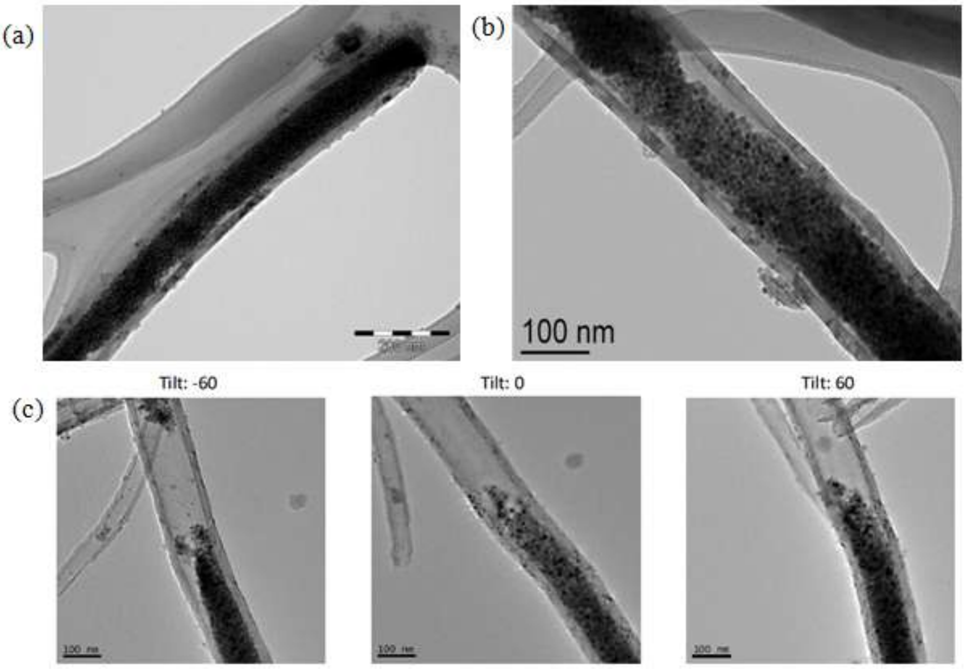

Figure II.45: TEM images of (a-b) an almost completely filled f-CNT$_1$ in the condition "Fe_1BBA:2PPP_ Mes_150°C_ 48h" with fast adding rate; (c) tomography images of a filled f-CNT$_1$.

It was also found out that similar cubic Fe NPs were generated on the outer surface of the CNTs, forming a thick-layer covering the CNTs (Figure II.46a). Abundant agglomerated Fe NPs were observed as well from the TEM image (Figure II.46b).

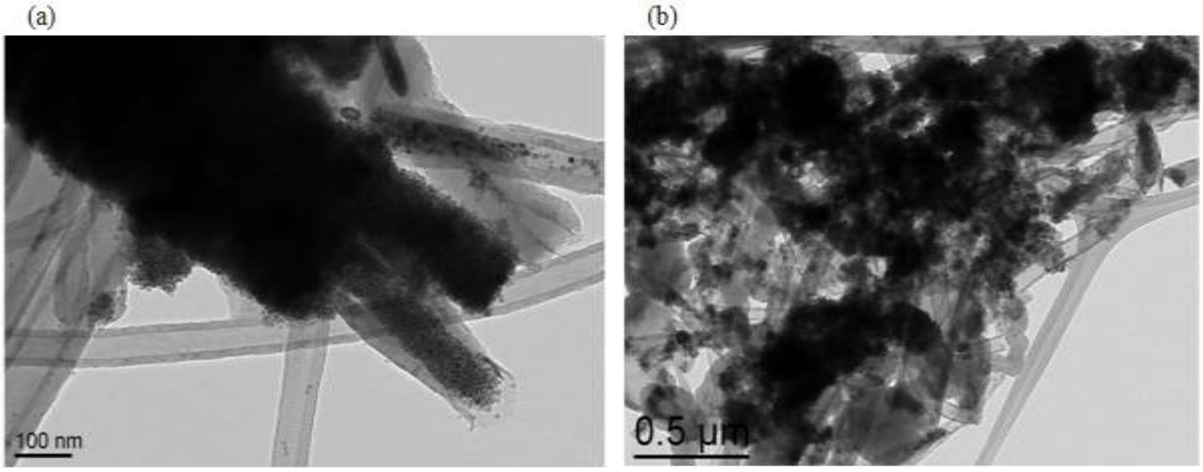

Figure II.46: TEM images of the divers states of the Fe NPs generated outside the CNTs.

Similarly, the reaction "Fe_1BBA:2PPP_Mes_150°C_48h" from a starting solution prepared by dropwise addition rate in the presence of the CNTs gave rise to NPs with a larger distribution of diameter (5-15 nm), encapsulated within the CNTs as well as attached on the outer sidewall of the CNTs (Figure II.47).

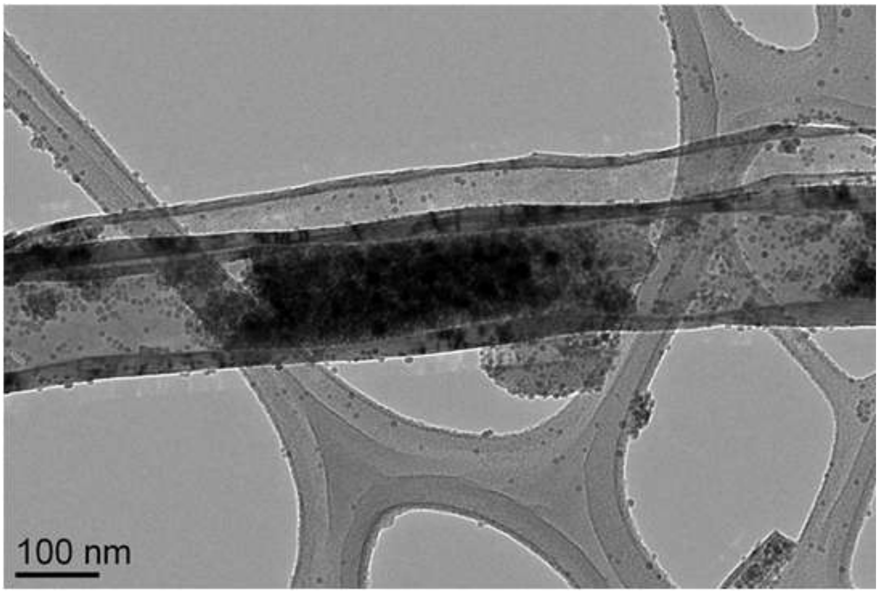

Figure II.47: TEM image of the polydispersed Fe NPs confined within the CNTs or deposited outside in the reaction "Fe_1BBA:2PPP_Mes_150°C_48h" with a dropwise addition rate.

Washing and filtration were attempted in order to remove the Fe NPs deposited outside the CNTs in these two cases. However, the Fe NPs attached on the outer surface resist to this treatment. Indeed, they were generated *in situ* and they are presumably grafted on the outer surface. This disadvantage makes the purification by washing inefficient and prevents any further measurements of the magnetic properties.

Under the same reaction conditions of the synthesis of Co NRs with the long chain ligands, a reaction was carried out in the presence of the f-**CNT**$_1$ ("Co_1.2LA_1.2HDA_Ani_150°C_24h"). Instead of the expected long NRs, many very short NRs and small NPs were observed inside and outside the tubes (Figure II.48), which indicates that the presence of the CNTs affects significantly the NR formation, probably due to its surface and the different groups on it.

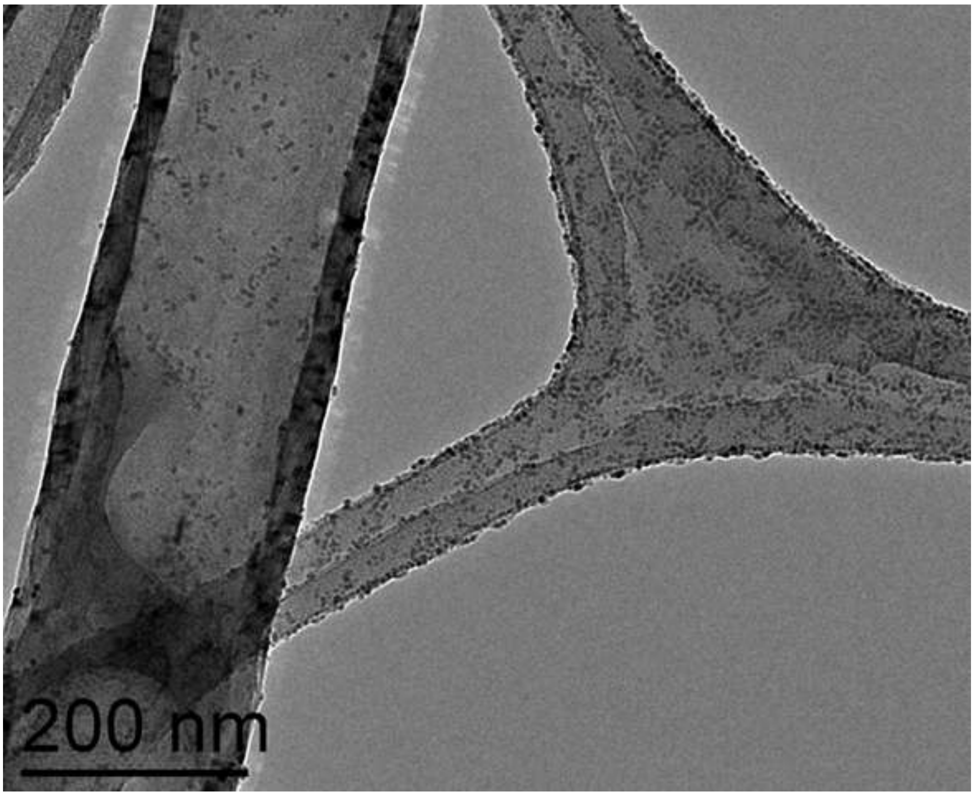

Figure II.48: TEM image of the synthesis of Co NRs ("Co_1.2LA_1.2HDA_Ani_150°C_24h") in the presence of the f-CNT$_1$.

Besides the reactions described above *via* the *in situ* solution method, the reactions in absence of stabilizing ligands were also carried out. In the reaction "Co_THF_50°C_24h" in the presence of the f-**CNT**$_1$, the Co NPs (4 to 10 nm) were encapsulated within the CNTs (Figure II.49).

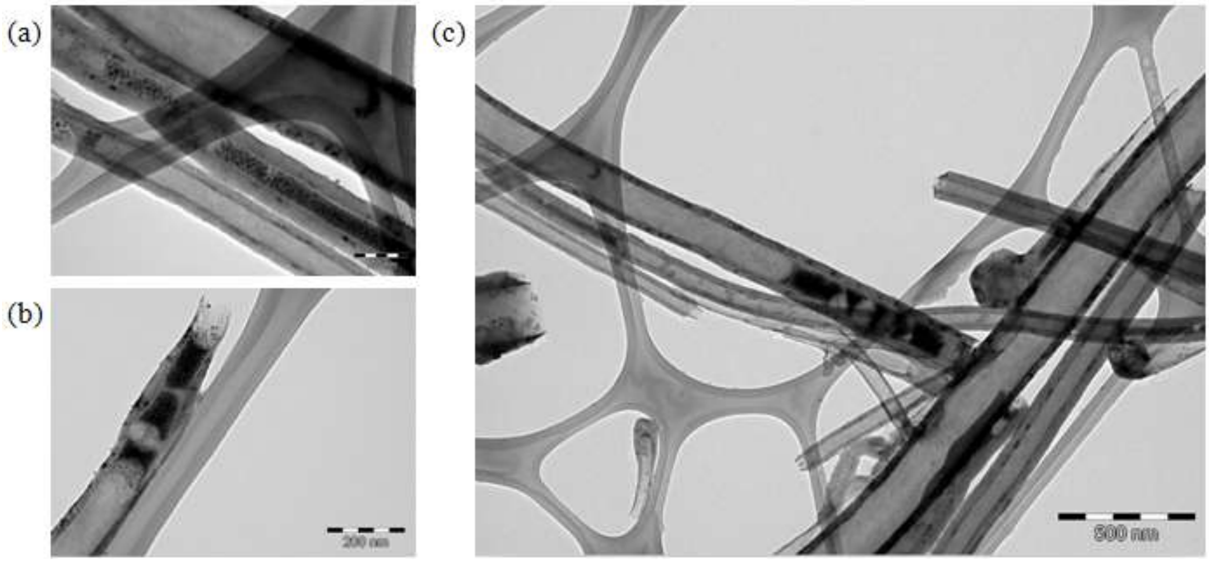

Figure II.49: TEM images of Co NPs encapsulated within the f-CNT$_1$ in absence of the stabilizing ligands *via* the *in situ* solution method.

In Figure II.49a, a CNT with inner diameter of 38 nm is well filled with the Co NPs, which might be due to the low viscosity of the solution in the absence of organic ligands. After washing with solvent, the Co NPs were found aggregated inside the CNTs (Figure II.50b), and massive agglomerations outside the tubes occurs (Figure II.50a), which may be arising from the lack of stabilization of the NPs and the weak interactions with the inner surface of the CNTs.

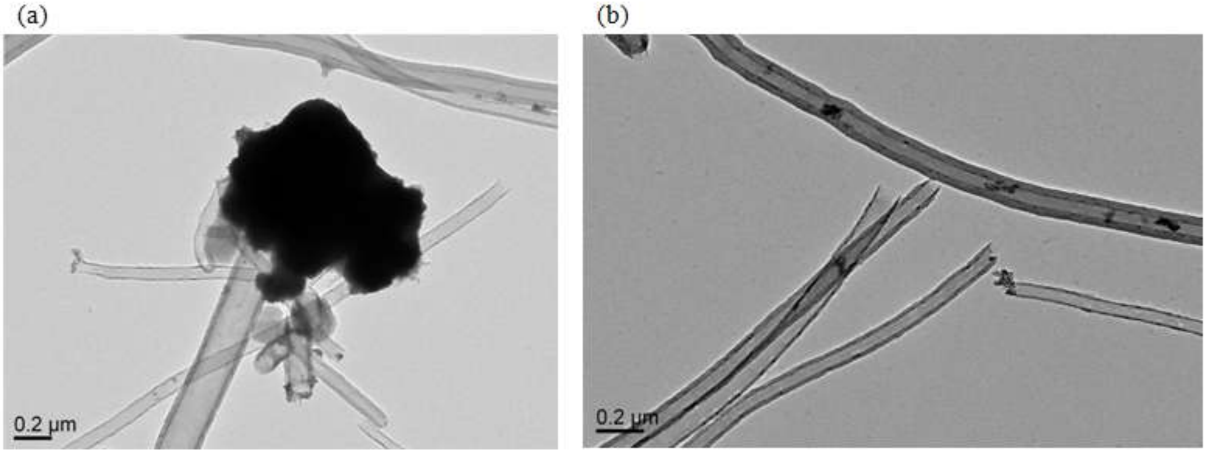

Figure II.50: TEM images of (a) the massive agglomeration outside the tube and (b) the coalescences of the Co NPs inside the tubes.

For the reactions in THF with the Fe precursor, Fe NPs were not formed even after heating at 60 °C for 48 hours, indicating that decomposition of the Fe complex did not take place, even though extending the reaction during four days. Therefore, it is supposed that tiny

Fe clusters were formed due to the difficulty of the decomposition of the Fe complex in solution. This observation can be explained by the formation of the stable [Fe{N(SiMe$_3$)$_2$}$_2$(THF)] complex upon [Fe{N(SiMe$_3$)$_2$}$_2$]$_2$ dissolution in THF (17, 33).

II.4.2 Confinement with f-CNT$_2$

Due to the comparable dimensions of the NPs and the channels of **CNT$_2$**, it is almost impossible to encapsulate the pre-formed MMNPs within the f-**CNT$_2$** *via* the suspension method. Therefore, we attempted to introduce the NPs in solution through the *in situ* method. At first, the reactions were carried out in absence of added ligands at 100°C in toluene. In Figure II.51, the TEM images correspond respectively to the reaction with (a) [Fe{N(SiMe$_3$)$_2$}$_2$]$_2$, (b) [Co{N(SiMe$_3$)$_2$}$_2$(THF)] and (c) [Co(COD)(COT)].

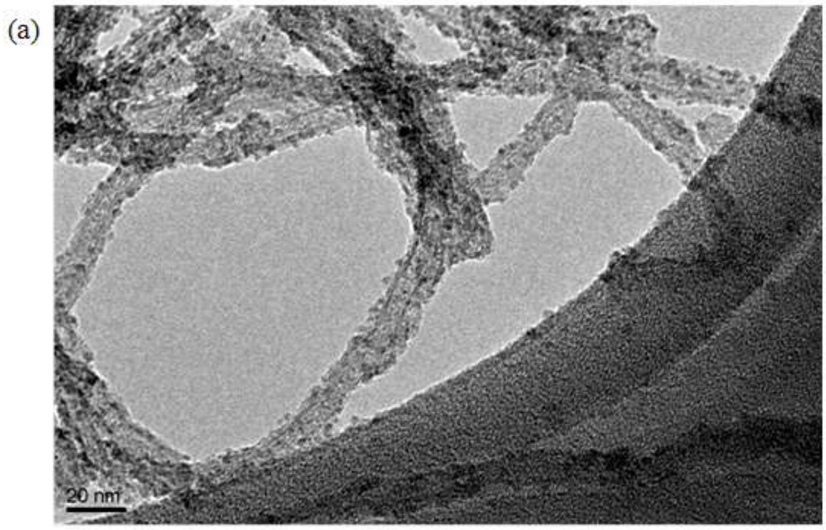

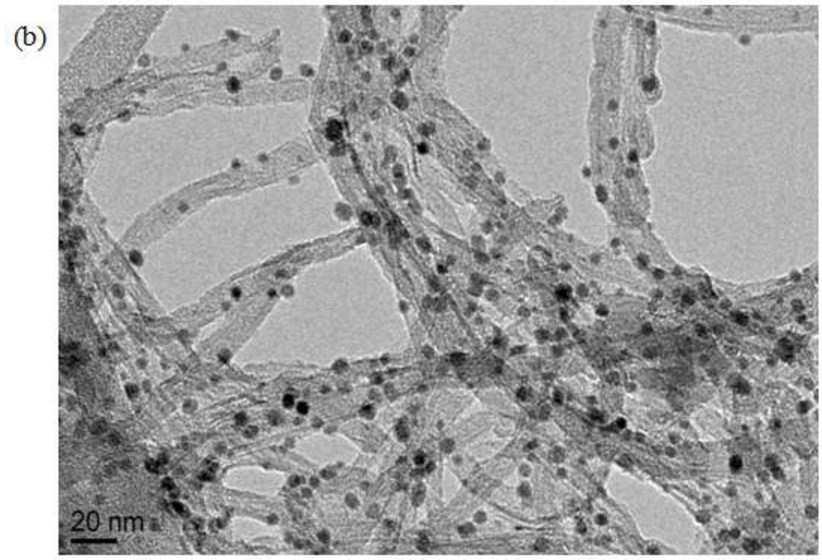

(c)

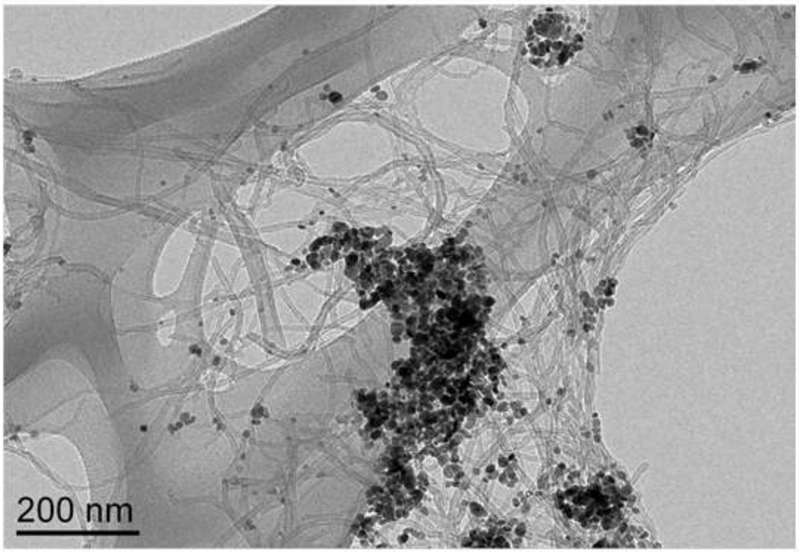

Figure II.51: Reactions with (a) [Fe{N(SiMe$_3$)$_2$}$_2$]$_2$, (b) (b) [Co{N(SiMe$_3$)$_2$}$_2$(THF)] and (c) [Co(COD)(COT)].

For (a) and (b), HMDS liberated from the reduction of silyl amide ligands in the precursor could serve as a stabilizing agent after reduction, so in these two reactions, small NPs are generated (2-3 nm in (a); 3-9 nm in (b)) . On the contrary, [Co(COD)(COT)] does not contain any stabilizing agents after reduction, which results in very polydispersed NPs. In all these cases, almost no NPs are found confined within the f-**CNT$_2$**. It seems that the solution of the precursor cannot enter into the tube channel and therefore the NPs are formed only outside the tube, or that although the NPs can be generated inside the tube, they are not capable to stay inside due to the lack of attractive interactions in the absence of any aromatic ligands.

Other reactions were carried out in the presence of the aromatic ligands under the same conditions at 100ºC in toluene, but only [Fe{N(SiMe$_3$)$_2$}$_2$]$_2$, and [Co{N(SiMe$_3$)$_2$}$_2$(THF)] were used. When 4 equivalents of BBA were added for both precursors, no NP was observed by TEM, indicating that some stable complexes were formed and did not decompose under these conditions. However, when 4 equivalents of PPP were used instead of BBA, polydispersed Fe or Co NPs were formed outside the tube. Two reactions for [Co{N(SiMe$_3$)$_2$}$_2$(THF)] with, respectively, 2BBA+2PPP and BBA+PPP did not allow successful confinement of NPs within f-**CNT$_2$** (see Experimental section).

To summarize, *via* either the pre-formed NP suspension method or the *in situ* solution method, confinement works only with the large f-**CNT$_1$**. This selectivity derives possibly from the nature of the CNTs, for example its inner diameter and surfaces, or the species formed in the starting solution. However, the preliminary data obtained during the experiments performed with the f-**CNT_2** do not allow us to arrive to a safe conclusion.

II.5 Conclusion

The confinement strategy has been designed by taking advantage of an attractive/repulsive interaction between the MMNPs and the f-MWCNTs (10). This selective interaction results from the functionalization of the external surface of the MWCNTs and of the MMNPs surface. Fe and Co MMNPs have been successfully encapsulated within the large diameter f-**CNT_1** *via* either suspension method or *in situ* solution method.

In the former method, the pre-formed MMNPs, directly synthesized with the aromatic ligands as stabilizers or indirectly modified by ligand exchange, have been confined inside the CNT channel by mixing in the colloidal solution. During the confinement study of the monodispersed Fe NPs, the factors that may impact the filling of CNTs, such as viscosity of the filling colloidal solution, have also been considered. Various approaches have been attempted to remove the NPs from the outer sidewall as well as to separate the filled CNTs from the free NPs in the colloidal solution, and thus to finally obtain the dried solid nanohybrid for further magnetic analysis. A FeNP@**CNT_1** nanohybrid, free from NPs on the external CNTs walls, has been obtained after confinement of filtrated and washed pre-formed Fe NPs. The CoNR@f-**CNT_1** has been achieved by using NRs after exchanging the long chain ligands with the aromatic ones. However, the CoNR@f-**CNT_1** composites have not been separated from the free bundles of Co NRs in solution, due to their inefficient dispersion in solvent.

In the later *in situ* method, the as-synthesized Fe and Co NPs have been confined within the f-**CNT_1** during the reaction in solution. However, the confinement selectivity is not high, making it impossible to obtain a clean sample appropriate for magnetic measurements.

For the confinement in the thinner f-**CNT_2**, both of the filling methods have been attempted. However, only MMNPs attached on the outer surface have been formed. For the *ex situ* method, this result could be explained by the size of the preformed NPs that is close to the one of the CNT inner cavity. For the *in situ* method, this could be explained by a steric hindrance induced by the long alkyl chain that prevents the confinement of the molecular complexes. Indeed, the functionalization with long alkyl chain is effective not only on the sidewall but also at the open extremities of CNTs that possess reactive carbon atoms. This steric hindrance should be determinant for small diameter CNTs but should not affect the entrance of molecular species in large diameter nanotubes.

To summarize, the confinement has worked for many experiments. However, what we were trying to achieve in the present thesis was not just the efficient confinement but also an efficient isolation of the resulting composites from free nanoparticles, in order to be able to measure the properties of the NPs inside the CNTs, without any masking coming from NPs outside. The only samples that were clean enough for further studies were the FeNP@$\mathbf{CNT_1}$. We have chosen to use FeNP@$\mathbf{CNT_1}$ in order to study their magnetic properties which indicates a higher coercive field for the confined Fe NPs in the FeNP@$\mathbf{CNT_1}$ than that for the pre-formed ones. This confinement effect is probably due to the smaller dipolar interaction among the CNT-confined NPs. Importantly, the magnetic measurements have confirmed the absence of oxidation in both the pre-formed Fe NPs and the FeNP@$\mathbf{CNT_1}$ nanohybrid. This means that no oxidation is presented during the synthesis of the Fe NPs and the confinement of the NPs inside the CNTs.

The protection from oxidation *via* polymerization of the FeNP@$\mathbf{CNT_1}$ will be discussed in the next chapter.

II.6 Reference

1. R. Hergt, S. Dutz, R. Müller, M. Zeisberger, *J. Phys. Condens. Matter.,* **2006**, *18*, S2919–S2934.
2. M. Johannsen, U. Gneveckow, L. Eckelt, A. Feussner, N. WaldöFner, R. Scholz, S. Deger, P. Wust, S. A. Loening, A. Jordan, *Int. J. Hyperth.,* **2005**, *21*, 637–647.
3. M. Johannsen, U. Gneveckow, K. Taymoorian, B. Thiesen, N. Waldöfner, R. Scholz, K. Jung, A. Jordan, P. Wust, S.A. Loening, *Int. J. Hyperthermia*., **2007**, *23*, 315–323.
4. A. Natarajan, R. Sundrarajan, S. J. DeNardo, **2011**. Magnetic Nanoparticles for Cancer Imaging and Therapy. Nanotechnologies for the Life Sciences.
5. L.-M. Lacroix, R. B. Malaki, J. Carrey, S. Lachaize, M. Respaud, G. F. Goya, B. Chaudret, *J. Appl. Phys.,* **2009**, *105*, 023911 (1-4).
6. M. Zeisberger, S. Dutz, R. Müller, R. Hergt, N. Matoussevitch, H.Bönneman, *J. Magn. Magn. Mater.,* **2007**, *311*, 224-227.
7. B. Mehdaoui, A. Meffre, L.-M. Lacroix, J. Carrey, S. Lachaize, M. Respaud, M. Gougeon, B. Chaudret, *J. Magn. Magn. Mater*., **2010**, *322*, L49–L52
8. Y. Zhu, Y. Ye, S. Zhang, M. E. Leong, F. F. Tao, *Langmuir,* **2012**, *28*, 8275–80.
9. D. Deng, L. Yu, X. Chen, G. Wang, L. Jin, X. Pan, J. Deng, G. Sun, X. Bao, *Angew. Chem. Int. Ed. Engl.,* **2013**, *52*, 371–375.
10. E. Castillejos, P.-J. Debouttière, L. Roiban, A. Solhy, V. Martinez, Y. Kihn, O. Ersen, K. Philippot, B. Chaudret, P. Serp, *Angew. Chem. Int. Ed.,* **2009**, *48*, 2529–2533.
11. A. Solhy, B. F. Machado, J. Beausoleil, Y. Kihn, F. Gonçalves, M. F. R. Pereira, J. J. M. Orfao, J. L. Figueiredo, J. L. Faria, P. Serp, *Carbon*, **2008**, *46*, 1194–1207.
12. T. I. T. Okpalugo, P. Papakonstantino, H. Murphy, J. McLaughlin, N. M. D. Brown, *Carbon*, **2005**, *43*, 153–161.
13. C. G. Salzmann, S. A. Llewellyn, G. Tobias, M. A. H. Ward, Y. Huh, M. L. H. Green *Adv. Mater.,* **2007**, *19*, 883-887.
14. N. T. K. Thanh, L. A. W. Green, *Nano Today,* **2010**, *5*, 213–230.
15. F. Wetz, K. Soulantica, M. Respaud, A. Falqui, B. Chaudret, *Mater. Sci. Eng., C*, **2007**, *27*, 1162-1166.
16. N. Cordente, M. Respaud, F. Senocq, M.-J. Casanove, C. Amiens, B. Chaudret, *Nano Lett*., **2001**, *1*, 565-568.
17. F. Dumestre, B. Chaudret, C. Amiens, P. Renaud, P. Fejes, *Science*, **2004**, *303*, 821-823.
18. C. Desvaux, C. Amiens, P. Fejes, P. Renaud, M. Respaud, P. Lecante, E. Snoeck, B. Chaudret, *Nat. Mater*., **2005**, *4*, 750-753.
19. L.-M. Lacroix, S. Lachaize, A. Falqui, M. Respaud, B. Chaudret, *J. Am. Chem. Soc*., **2009**, *131*, 549-557.

20. N. Liakakos, B. Cormary, X. Li, P. Lecante, M. Respaud, L. Maron, A. Falqui, A. Genovese, L. Vendier, S. Koïnis, B. Chaudret, K. Soulantica, *J. Am. Chem. Soc.,* **2012**, *134*, 17922–17931.
21. *Wilson and Gisvold's Textbook of Organic Medicinal and Pharmaceutical Chemistry, 9th Ed.* (1991), (J. N. Delgado and W. A. Remers, Eds.) p.878, Philadelphia: Lippincott.
22. R. Milcent, F. Chau: *Chimie organique hétérocyclique: Structures fondamentales*, pp. 241–282, EDP Sciences, **2002**, ISBN 2-86883-583-X
23. F. Dumestre, B. Chaudret, C. Amiens, M. Respaud, P. Fejes, P. Renaud, P. Zurcher, *Angew. Chem., Int. Ed.*, **2003**, *42*, 5213-5216.
24. F. Dumestre, B. Chaudret, C. Amiens, M.-C. Fromen, M.-J. Casanove, P. Renaud, P. Zurcher, *Angew. Chem., Int. Ed.*, **2002**, *41*, 4286-4289.
25. E. Dujardin, T.W. Ebbesen, H. Hiura, K. Taginaki, *Science*, **1994**, *265*, 1850–1852.
26. E. Dujardin, T.W. Ebbesen, A. Krishnan, M.M.J. Treacy, *Adv. Mater.*, **1998**, *10*, 1472–1475.
27. W. Chen, X. Pan, M. G. Willinger, D. S. Su, X. Bao, *J. Am. Chem. Soc.,* **2006**, *128*, 3136-3137.
28. S. Mørup, M. F. Hansen, C. Frandsen, *Beilstein J. Nanotechnol.,* **2010**, *1*, 182–90.
29. D. a Britz, A. N. Khlobystov, *Chem. Soc. Rev.* **2006**, *35*, 637–659.
30. A. La Torre, M. W. Fay, G. a Rance, M. Del Carmen Gimenez-Lopez, W. a Solomonsz, P. D. Brown, A. N. Khlobystov, *Small,* **2012**, *8*, 1222–1228.
31. J. Nogués, I.K. Schuller, *J. Magnet. Magnet. Mater.*, **1999**, *192*, 203-232.
32. R. K. Das, S. Rawal, D. Norton, a. F. Hebard, *J. Appl. Phys.,* **2010**, *108*, 123920 (1-4).
33. O. Margeat, F. Dumestre, C. Amiens, B. Chaudret, P. Lecante, M. Respaud, *Prog. Solid. State. Chem.*, **2005**, *33*, 71-79.

Chapter III Polymer-coated nanohybrid MMNP@MWCNT and their magnetic study

Chapter III Polymer-coated nanohybrid MMNP@MWCNT and their magnetic study

III.1 Introduction

A major issue in the use of MMNPs in numerous applications is their low biocompatibility coupled with their sensitivity towards oxidation. Many approaches to protect MMNPs from air and water have been reported, including: i) a controlled oxidation of the pure metal core, a technique long known for the passivation of air sensitive supported catalysts (1, 2); which however, may negatively influence the desired magnetic properties; ii) a coating of the metallic core by a noble metal like gold (3); however, many of the reported metallic shells do not provide sufficient protection of the magnetic core because of non-uniform coating (4); iii) carbon encapsulation (5); however this technique requires in most of the cases harsh reaction conditions that can affect MMNPs size (6); iv) the formation of alloys (7); however, controlling the composition of magnetic alloy NPs can be difficult when they are produced from two or more precursors; or v) the coating of the metal core with surfactants or polymer (8); however, weak polymer-MMNP interactions are generally prevailing (9), and robust synthetic routes to controllably functionalize metallic magnetic colloids remains an important challenge.

In recent years, polymer-coated NPs as nanohybrids have received considerable interest since an appropriate polymer layer can be chosen so that it provides solubility, long-term stability and a substrate for further functionalization (10). These nanohybrids can be generally produced through four methods (11): i) *in situ* preparation, ii) “grafting to” method, iii) “grafting through” method, and iv) the “grafting from” method, as shown in Figure III.1. For the *in situ* preparation, the NP synthesis is performed in the presence of pre-formed polymer chains, leading directly to NP@polymer nanohybrid. Simplicity is the advantage of this method, and the polymer chains can be tailored to afford the desired properties and functionality. However, this method is limited to some polymers due to their solubility or chemical stability under the conditions used for NP synthesis. Moreover, the presence of polymer chains may result in a broad distribution of NP size, which influences significantly their properties (12). For the “grafting to” method, the polymer chains are coated on the pre-formed NPs by mixing them together. It is considered that the polymer is grafted to the NP surface by either physical adsorption, or covalent interaction, or a combination of both. This method allows using well-controlled nanostructures and well-defined polymer. However, this method yields usually low grafting density that cannot ensure homogeneous polymer coating. The “grafting through” method, in which the polymerization is performed in the presence of NPs functionalized with polymerizable moieties (13, 14), has been rarely used for coating NPs. Compared to the three former methods, the “grafting from” method has been more widely used (15-17). In this method, the NP surface is functionalized with an initiator, a catalyst or a chain transfer agent (CTA) and then polymerization of the targeted monomer is performed. The advantage compared to physisorption, for which van der Waals forces are in action, is the formation of stronger covalent bonds, preventing desorption of the polymer from the NPs, and more importantly, well defined nanostructures are used, and controlled polymerization can be realized by tailoring surface initiators.

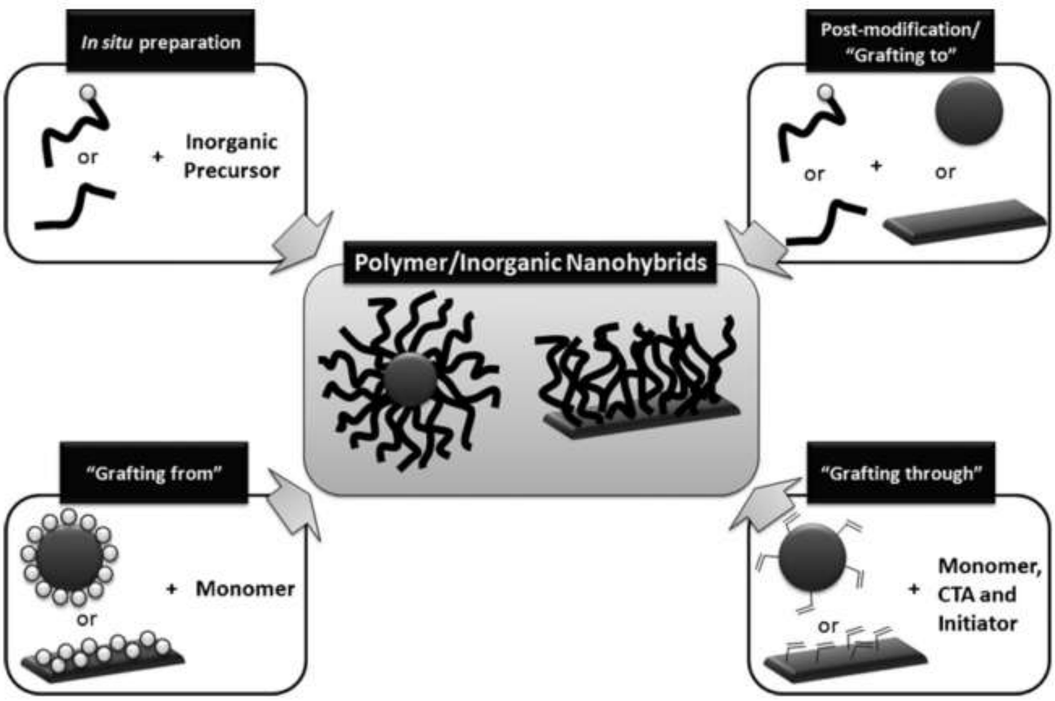

Figure III.1: Methods for NP@polymer nanohybrids preparations (11).

The formation of polymeric shells is of high interest for biomedical applications of magnetic NPs, such as magnetic targeting drug delivery and magnetic resonance imaging (MRI) contrast enhancement, since polymer coating can enhance NP biocompatibility and also prevent their aggregation (11). In earlier studies, *in situ* preparations of polymer-coated magnetic nanohybrids led to polydispersed NP cores (18-20). Later, surface-initiated polymerization through "graft from" pathway has been employed for the core/shell magnetic nanohybrid synthesis *via* atom transfer radical polymerization (ATRP) (15-17). Other polymer-coated iron oxide nanohybrids were also reported via reversible addition-fragmentation chain transfer (RAFT) polymerization (21-23).

Among these polymer coating methods, ATRP has been used for coating magnetic NPs. $MnFe_2O_4$@polystyrene core/shell (core ~9nm, and core/shell <15 nm) NPs were synthesized (Figure III.2) by grafting 3-chloropropionic acid as initiator to the $MnFe_2O_4$ NPs surface, followed by styrene polymerization (15). The same procedure was also used for production of Fe_3O_4@PMEMA (poly(2-methoxyethyl methacrylate)) NPs with 2-bromo-2-methylpropionic acid as initiator (16). In these studies, the initiators are multi-functional which can graft on the NP surface through covalent binding and can also serve as an initiator for polymerization.

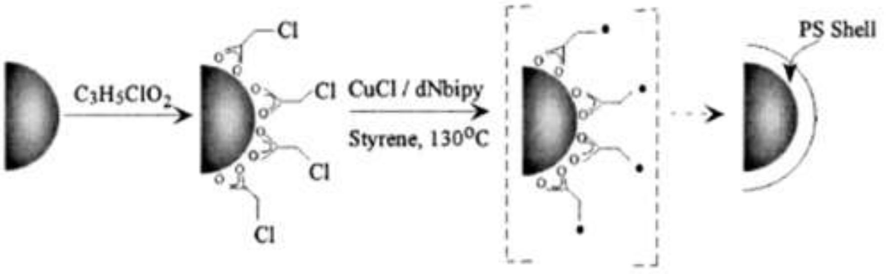

Figure III.2: Procedure of $MnFe_2O_4$@polystyrene core/shell NPs synthesis (reproduced from ref.15).

Additionally, ring-opening polymerization (ROP) has also been used for coating Co NPs (17). Hydroxyl-functional cobalt cores can be obtained in a single step by thermal decomposition of $[Co_2(CO)_8]$ in the presence of ricinolic acid as a functional surfactant (Figure III.3). The role of ricinolic acid is multifold: i) it serves as micelle-forming pre-stabilizing amphiphile for the precursor decomposition, ii) it allows a permanent attachment on the particle surface oxide layer by means of the carboxylic function, iii) it provides an effective steric stabilization due to the aliphatic chain, and iv) it enables subsequent surface-initiated ROP of lactones by using the hydroxyl group.

However, only oxide magnetic NPs are involved in these studies and air-protection with polymer-coating is not considered.

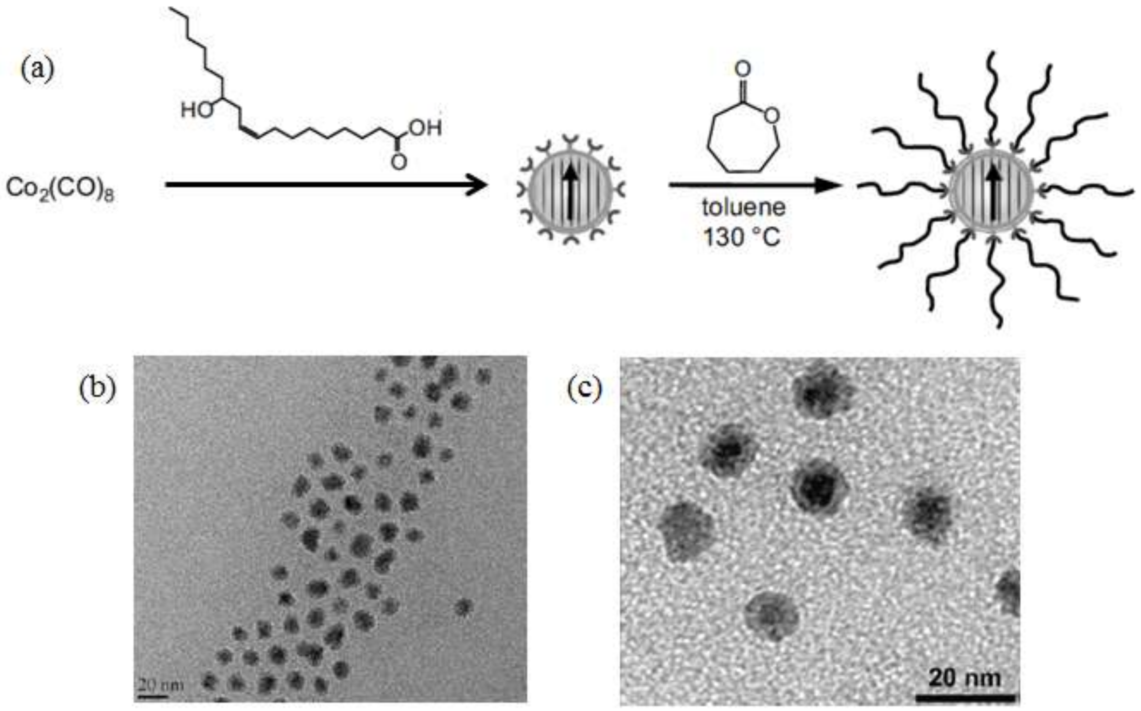

Figure III.3: (a) Procedure of Co@PCL (PCL= poly(3-caprolactone)) following a ROP mechanism; (b-c) TEM images of the Co@PCL NPs (reproduced from ref.17).

Natural rubber is one of the best known natural polymers, coming from latex of *Hevea Brasiliensis* tree. Natural rubber is a polymer of isoprene (2-methyl-1,3-butadiene) with a molecular weight of 100,000 to 1,000,000. Most often the polyisoprene (~99%) consists almost completely of the *cis*-1,4-isomer. Typically a few percent of other materials (proteins, fatty acids, resins and inorganic materials) are found in high quality natural rubber. Natural rubber is resistant to many chemical solvents and displays high-performance mechanical properties (24). It has been used as barrier against water and air such as gloves for glove-box. This barrier property may make natural rubber a good candidate for protecting MMNPs from oxidation. Polyisoprenes are synthetic, predominantly stereoregular polymers that closely resemble natural rubber in molecular structure as well as in properties (25). It can be therefore a good alternative to natural rubber.

Polymerization of isoprene can afford four polyisoprene isomers (Figure III.4). Selective polymerization is critical since the identity of the isomer influences the properties of the resulting polymer (25).

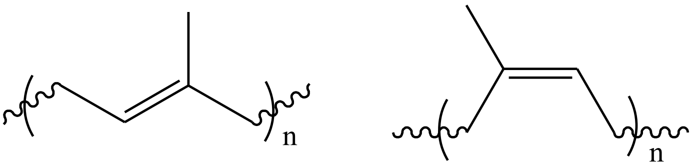

trans-1,4-polyisoprene

cis-1,4-polyisoprene

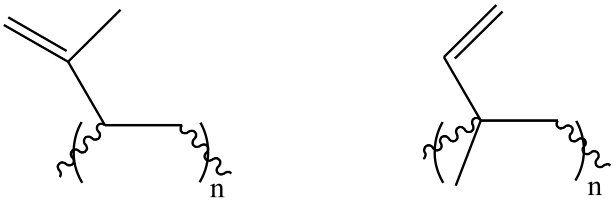

3,4-polyisoprene

1,2-polyisoprene

Figure III.4: Four isomers of polyisoprene.

We aimed at coating the confined monodispersed Fe NPs *via* "graft from" polymerization of isoprene and study its protection from air oxidation by measuring the magnetic properties of this nanocomposite (Figure III.5). We will start on the basis of the result of FeNP@**CNT₁** described in the previous chapter. To achieve this goal, two approaches have been followed: the ATRP, and coordination polymerization.

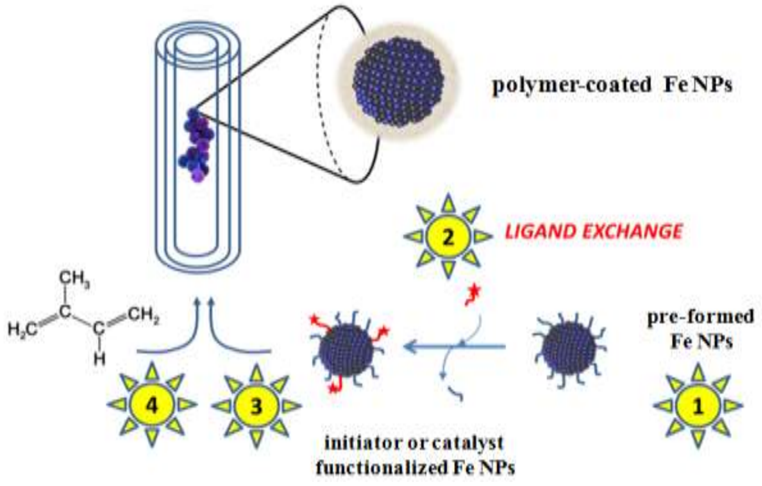

Figure III.5: Bottom-up approach to produce air-protected Fe NPs confined in f-CNT$_1$: (1) synthesis of Fe NPs; (2) surface-modification on the Fe NPs with an initiator or a catalyst; (3) selective confinement of the surface-modified Fe NPs in f-CNT$_1$; and (4) polymerization of isoprene in a confined space to produce FeNP@polyisoprene/ f-CNT$_1$.

III.2 Atom transfer radical polymerization - ATRP

ATRP is a preferred “grafting-from” method in surface-initiated polymerization from colloidal particles (26-29), since it offers the advantage of a “living”/controlled mechanism leading to linear chains with low polydispersity and good control over the molecular weight and a fairly good resistance to additional reaction components and impurities.

Matyjaszewski *et al*. have studied the ATRP process in detail (30, 31). The general process of ATRP is outlined in Figure III.6 (31).

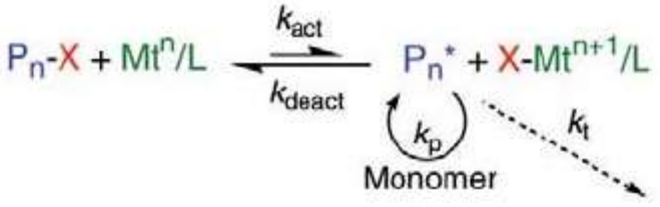

Figure III.6: Global process of ATRP (reproduced from ref.31).

The catalyst includes a transition metal species (Mt^n), which can expand its coordination number and increase its oxidation number by one electron, a coordination ligand (*L*), and a counter-ion, which can form a covalent or ionic bond with the metal center.

$$\mathbf{Mt^n + L \rightarrow Mt^n/\mathit{L}}$$

The transition metal complex (Mt^n/L) is responsible for the homolytic cleavage of an alkyl halogen bond R-X, which generates the corresponding higher oxidation state metal halide complex $Mt^{n+1}X/L$ (with a rate constant k_{act}) and an organic radical $R^\bullet$ (32).

$$\mathbf{Mt^n/\mathit{L} + R\text{-}X \rightarrow Mt^{n+1}X/\mathit{L} + R^\bullet}$$

$R^\bullet$ can then propagate by addition of a monomer (M) (rate constant k_p), terminate as in conventional free radical polymerization by either coupling or disproportionation (rate constant k_t), or be reversibly deactivated (rate constant k_{deact}) in this equilibrium by $Mt^{n+1}X/L$ to form a halide-capped dormant polymer chain.

$$\mathbf{R^\bullet + M \rightarrow RM^\bullet;\ RM^\bullet + Mt^{n+1}X/\mathit{L} \rightarrow RMX + Mt^n/\mathit{L}}$$

ATRP has been successfully mediated by a variety of metals, including Ti, Mo, Re, Fe, Ru, Os, Rh, Co, Ni, Pd, and Cu (30). Complexes of Cu have been found to be the most efficient catalysts in the ATRP of a broad range of monomers in diverse media (30). One advantage of ATRP is the commercial availability of all necessary ATRP reagents (alkyl halides, ligands and transition metals). Commonly employed nitrogen-based ligands used in conjunction with Cu ATRP catalysts include derivatives of bidentate bipyridine (bpy), and multidentate ligands such as tridentate diethylenetriamine (DETA) and tetradentate tris[2-aminoethyl]amine (TREN). The counter-ion is very often a halide ion, and others such as carboxylates, triflate and hexafluorophosphate anions have also been used in the literature (33, 34). Thus, we have chosen the copper (I) bromide (CuBr)/bipyridine (bpy) system to form a transition metal complex that actives polymerization. For the initiator, we chose 12-bromododecanoic acid (BDA), possessing a carboxylic acid group on one side and a Br on the other side, which may therefore attach on the Fe NPs with its carboxylic acid group and serve as an ATRP reagent.

Therefore, the total reaction of the system can be described as equilibrium in Figure III.7.

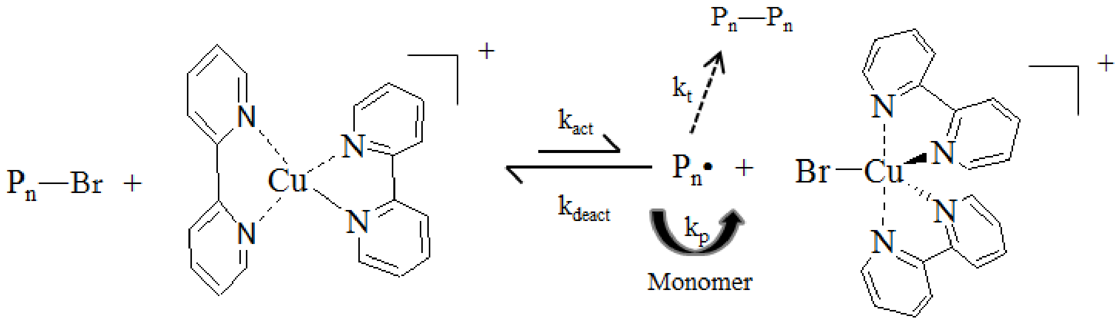

Figure III.7: Equilibrium of the polymerization in our system (reproduced from ref. 30).

In the literature, ATRP has been used for isoprene polymerization (35, 36) with low product yield. However, our target is to coat the Fe NPs via a controllable polymerization, thus high yield is not mandatory. From this point of view, ATRP may be an appropriate choice for our study.

III.2.1 Isoprene polymerization with an initiator in the absence of Fe NPs

In a first step, the polymerization was carried out in the presence of the initiators. THF and toluene were first used because they can disperse well the Fe NPs and serve the next step of polymerization in the presence of the Fe NPs. However, CuBr is difficult to dissolve in these solvents. We chose therefore another more polar solvent DMF (dimethylformamide) that can also disperse the Fe NPs. A solution of 0.3 mmol CuBr and 0.75 mmol bpy in 3 mL of distilled DMF was mixed with a solution of 0.15 mmol BDA in 6 mL of isoprene (monomer/initiator ratio 400:1) in a glove-box. The reaction mixture was stirred at room temperature for 24 hours. A very small amount of white precipitate appeared. It was washed with methanol to remove the Cu complex and the initiator. The dried white precipitate was collected (4 mg, conversion 0.1%) and dissolved in $CDCl_3$ for NMR analysis. Table III.1 presents the main peaks in ^{1}H NMR and ^{13}C NMR spectra (see Annex I) and their attributions.

Table III.1: Chemical shifts in NMR spectra and their corresponding polyisoprene isomers.

^{1}H NMR		**^{13}C NMR**	
δ (ppm)	proton	δ (ppm)	carbon
1.53	$\mathrm{C}H_3$-trans-1,4-motif	15.01	$C\mathrm{H}_3$-trans-1,4-motif
1.61	$\mathrm{C}H_3$-cis-1,4-motif	25.70	$C\mathrm{H}_3$-cis-1,4-motif
1.97	$\mathrm{C}H_2$	38.73	$C\mathrm{H}_2$
5.05	$\mathrm{C}H$	77.16	$CDCl_3$
7.26	$CDCl_3$	123.20	$C\mathrm{H}$
		133.93	Quaternary C

Besides the main product 1,4-polyisoprene, some other isomers in trace amounts were also detected, corresponding to 1,2- or 3,4-polyisoprene. Using the equations below, we can calculate the polymerization selectivity (Table III.2).

$$[\%1{,}4-\text{motif}] = \frac{\text{A}(\sim CH = \text{CMe} - 1{,}4 - \text{motif})}{\text{A}(\sim CH = \text{CMe} - 1{,}4 - \text{motif}) + \frac{\text{A}(CH_2 = \text{CMe} - 3{,}4 - \text{motif})}{2}}$$

$$[\%trans - 1{,}4 - \text{motif}] = \frac{\text{A}(C\text{H}_3 - trans - 1{,}4 - \text{motif})}{\text{A}(C\text{H}_3 - trans - 1{,}4 - \text{motif}) + \text{A}(C\text{H}_3 - cis - 1{,}4 - \text{motif})}$$

$$[\%cis - 1{,}4 - \text{motif}] = \frac{\text{A}(C\text{H}_3 - cis - 1{,}4 - \text{motif})}{\text{A}(C\text{H}_3 - cis - 1{,}4 - \text{motif}) + \text{A}(C\text{H}_3 - trans - 1{,}4 - \text{motif})}$$

Reactions (presented in Table III.2) with different monomer/initiator ratio were performed in order to improve conversion of the polymerization, in which only the initiator amount changed and the other reagents were kept the same as the previous one.

Table III.2: Polymerization with different monomer/initiator ratio and their selectivity.

Monomer/initiator ratio	Polymer weight (mg)	Conversion (%)	Selectivity	
			trans-1,4	*cis*-1,4
200	<1	/	/	/
400	4	0.097	52.43	42.51
800	3	0.073	55.24	44.75
1200	5	0.122	53.47	41.17

The results reveal that by modifying the amount of initiator, the conversion has almost no improvement, presenting very low conversion. The polymerization selectivity is not significantly affected by the modification of the monomer/initiator ratio, yielding more than 95% of 1,4-polyisoprene (less than 5% of 1,2-polyisoprenes) out of which more than 50% is *trans*-1,4-polyisoprene.

Reactions were also carried out at different temperatures (presented in Table III.3) by keeping the monomer/initiator ratio at 400. At 30°C, 4 mg of polymer were obtained. When reactions were performed at 50°C or 70°C in addition to the low yield, the polymer became very viscous, and was hard to collect from the Schlenk tube.

Moreover, 4 mg of polymer were produced after one hour reaction, and the conversion did not increase even when the reaction time was prolonged to 24 hours, which revealed that the polymerization stopped after one hour reaction.

Table III.3: Polymerizations at different temperatures and reaction periods.

	Temperature (monomer/initiator ratio at 400, 24 h)		
	30°C	50°C	70°C
Product weight	5 mg	Very viscous	Very viscous
	period (monomer/initiator ratio at 400, 30°C)		
	1 h	3 h	6 h
Product weight	4 mg	4 mg	4 mg

In conclusion, the polymerization of isoprene *via* ATRP results in non-selective polyisoprene isomers, mainly 1,4-polyisoprene, with very low conversion (around 0.1%). It has not been possible to promote the conversion by modifying monomer/initiator ratio and reaction temperature. In spite of the low conversion, we attempted the coating of Fe NPs by this method.

III.2.2 Isoprene polymerization with an initiator grafted on the surface of Fe NPs

Fe NPs stabilized by BBA (2-benzylbenzoic acid), on which the 12-bromododecanoic acid initiator has been grafted on their surface were prepared *via* a ligand exchange procedure followed by a washing treatment (see Experimental section).

In order to confirm the ligand exchange an IR characterization was performed. First, the pre-formed Fe NPs were analyzed by IR and compared to free BBA (Figure III.8).

For BBA, the band at 1689 cm^{-1} is attributed to the aromatic conjugated C=O stretching vibration. The bands at 1600, 1575, 1494 and 1452 cm^{-1} correspond to the aromatic C=C stretching. The bendings of O-H are at 1415 and 931 cm^{-1}. The C-O stretching vibrations are between 1320 and 1280 cm^{-1}.

For the pre-formed Fe NP, the aromatic C=C stretching bands do not change position with respect to the free acid. However, the bands of $\nu_{C=O}$, $\delta_{O\text{-}H}$, and $\nu_{C\text{-}O}$ are absent, which suggests that BBA ligands are chemically bound to the Fe NPs surface rather than simply adsorbed. Instead, the bands at 1535 and 1386 cm^{-1} correspond respectively to the carboxylate anion asymmetric (ν_{as}) and symmetric (ν_s) stretches coordinated on the surface of the NPs (26, 27). The binding mode of the carboxylic acid to the NPs can be deduced by the separation $\Delta\nu_{a\text{-}s}$ between ν_{as} and ν_s. Generally, the band separation is 350-500 cm^{-1} for monodentate binding, 150-180 cm^{-1} for bidentate bridging, and 60-100 cm^{-1} for bidentate chelating (28) (Figure III.9). In our case, the value $\Delta\nu_{a\text{-}s}$ is 149 cm^{-1}, which implies a bidentate bridging.

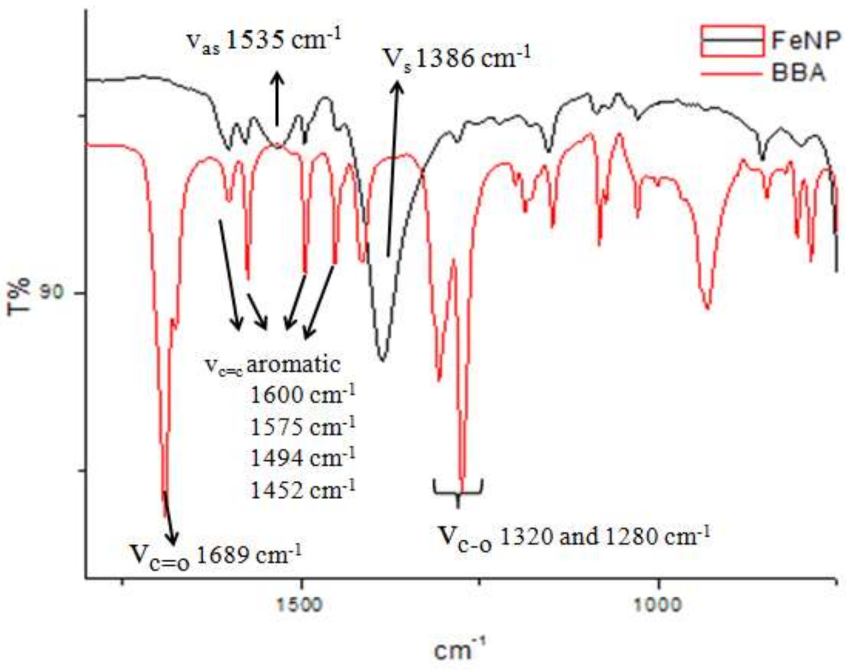

Figure III. 8: IR spectrum comparison between BBA and Fe NPs.

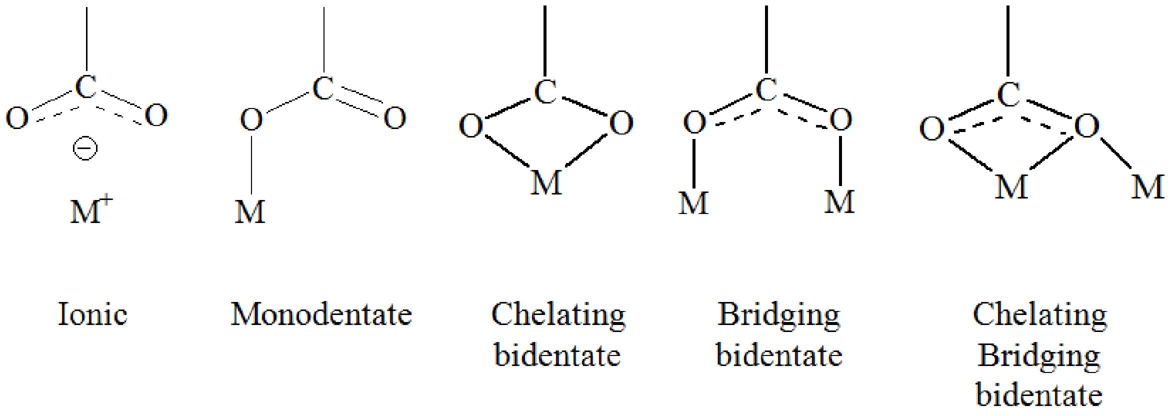

Figure III.9: Carboxylate binding modes.

The IR spectrum of 12-bromododecanoic acid (BDA) presents C-H stretching band at 2918 and 2850 cm^{-1}, C=O stretching band at 1708 cm^{-1}, C-H bending band at 1468 cm^{-1}, O-H bending band at 1407 cm^{-1} and C-O stretching vibrations are between 1320 and 1280 cm^{-1} (Figure III. 10).

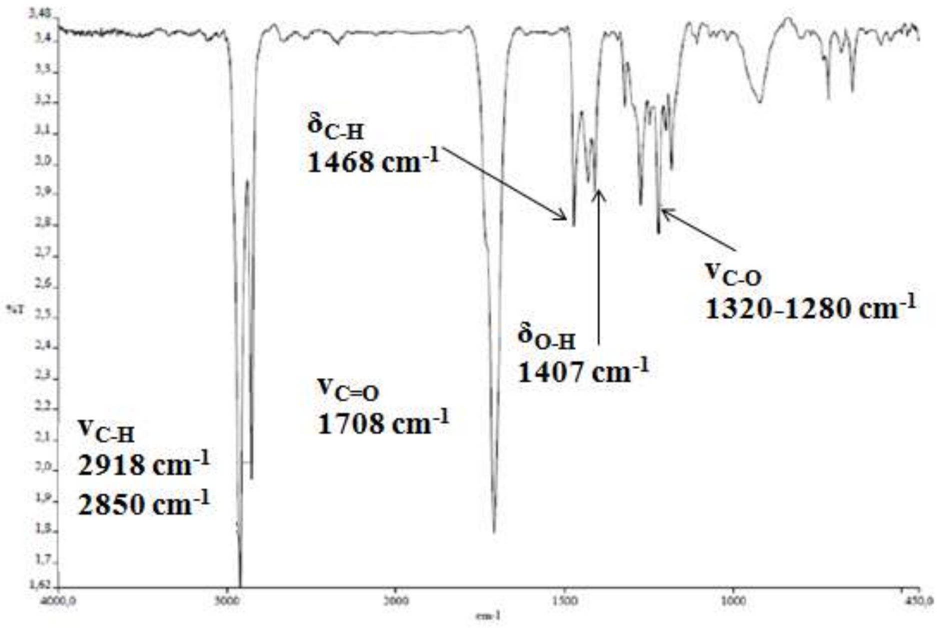

Figure III.10: IR spectra of 12-bromododecanoic acid.

After ligand exchange with BDA, the surface-exchanged FeNPs were compared to the starting ones. In Figure III.11, the absence of the aromatic C=C stretching vibration and of the corresponding carboxylate ν_s stretch reveal the displacement of the aromatic stabilizer from the Fe NPs, replaced by the new carboxylate, which presents a ν_s stretch vibration at 1402 cm^{-1} with a $\Delta\nu_{a\text{-}s}$=133 cm^{-1}, a value between bidentate bridging and bidentate chelating. Thus we propose a chelating bridging bidentate mode for the incoming ligand. In addition, the C-H stretching vibration between 2950 and 2850 cm^{-1} implies the presence of long alkyl chains of BDA. The weak band at 1708 cm^{-1} indicates that a small amount of free BDA is presented in the sample. Therefore, the BDA initiator is successfully grafted on the Fe NPs surface. It is not certain whether the exchange is complete since the peaks are quite broad and those from the initial NPs may be overlapped with the new ones. On the other hand, a complete exchange may not be favourable to further confinement if the aromatic ligands are completely absent.

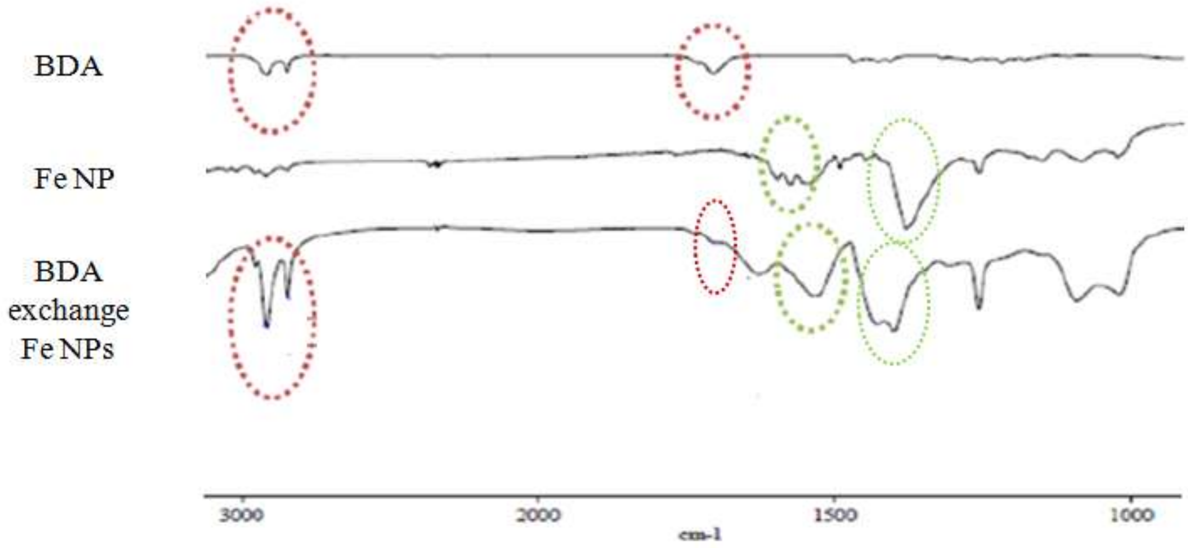

Figure III.11: IR spectra comparison among BDA, the pre-formed Fe NPs and the BDA modified Fe NPs. C-H stretching vibration (left red cycle); C=O stretching vibration (middle red cycle); modifications for the different carboxylates on the Fe NPs (green cycles).

After ligand exchange, the NP size presents no difference compared to the initial ones from the TEM micrographs (Figure III.12).

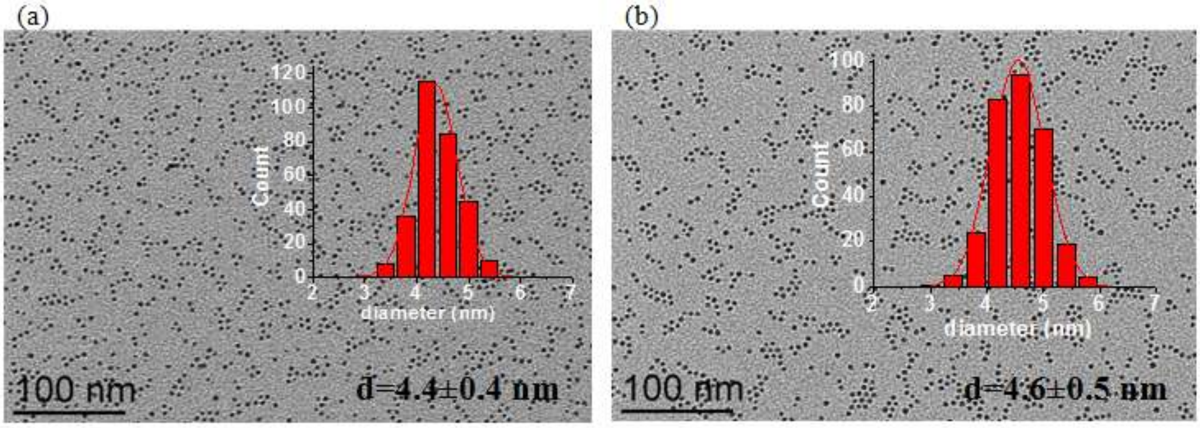

Figure III.12: TEM images and size distributions of (a) the pre-formed Fe NPs and (b) the initiator-modified Fe NPs.

In order to see whether the surface grafting of the BDA on the NPs can induce the polymerization of isoprene around the Fe NPs, three parallel polymerization tests were carried out, which are presented in Table III.4.

Table III.4: Polymerization tests under different conditions[a].

	Fe NPs	Solvent	Reactants and conditions
1	Non-grafted NPs	/	isoprene; 24h; RT
2	Non-grafted NPs	DMF	Initiator+ CuBr/bpy+ isoprene; 24h; RT
3	Initiator-grafted NPs	DMF	CuBr/bpy+ isoprene; 24h; RT

[a] Reaction conditions: isoprene (6 mL); BDA (0.15 mmol); CuBr (0.3 mmol)/bpy (0.75 mmol) in 3 mL of distilled DMF; RT= room temperature.

In the first reaction, the non-grafted Fe NPs were suspended in isoprene. This reaction, as expected, did not produce any polymer (Figure III.13a), which indicates that the Fe NPs cannot catalyze polymerization of isoprene under the conditions employed. Furthermore from the TEM image, we see that Fe NPs are badly dispersed in isoprene.

In the second reaction, the non-grafted Fe NPs were introduced into a mixture of monomer/initiator (ratio 400), which led to uncoated NPs and formation of polymer in the solution (Figure III.13b). In this case, Fe NPs are well dispersed due to the presence of DMF in the solution.

In the third reaction, the initiator-grafted Fe NPs were involved under the same conditions as for the second reaction, which led to polymer-coated NPs (Figure III.13c and d). However, agglomeration of NPs is also observed (Figure III.13d). No formation of polymer in the solution was noted.

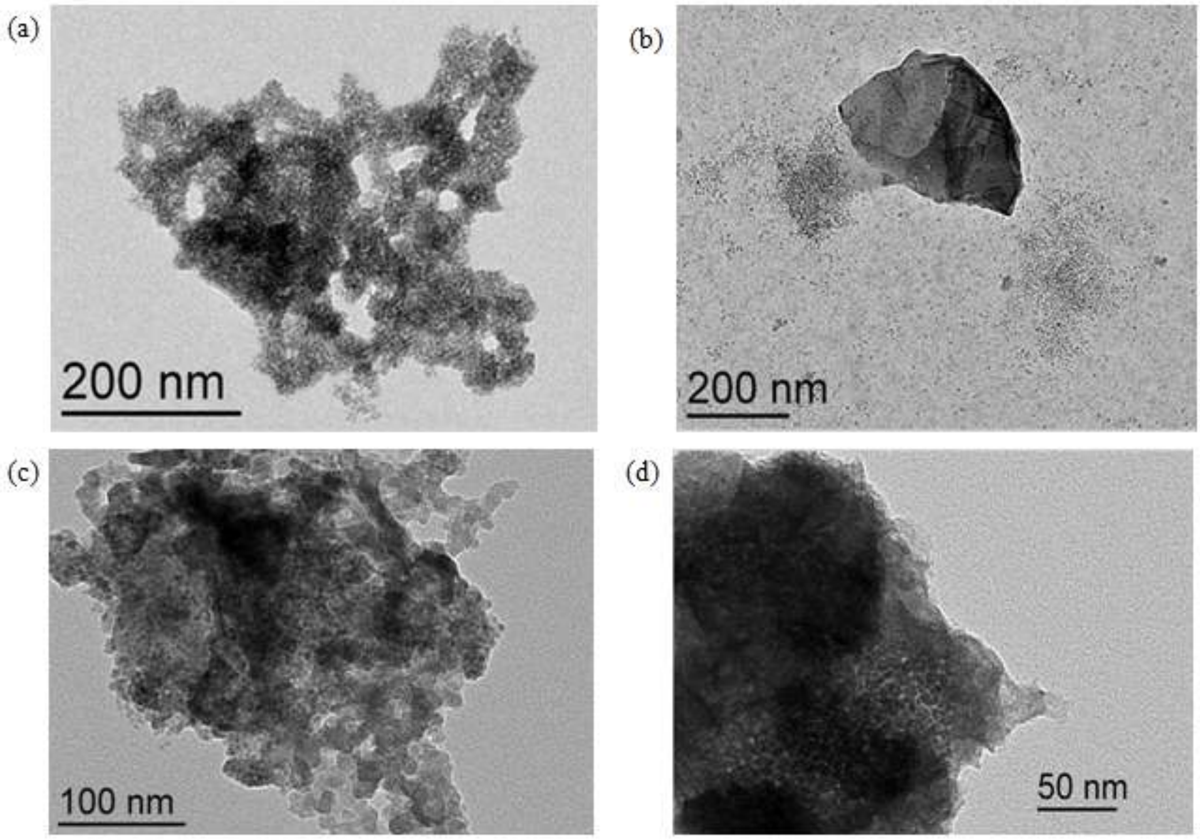

Figure III.13: TEM images of the polymerizations: (a) non-grafted Fe NPs +isoprene; (b) non-grafted Fe NPs + BDA + isoprene; (c-d) BDA-grafted Fe NPs + isoprene.

Therefore we have been able to polymerize isoprene around the Fe NPs after grafting of an initiator on the Fe NPs by ligand exchange. It was therefore interesting to attempt to polymerize isoprene around the Fe NPs after their introduction into the CNTs. However, we have to note that the NPs were found agglomerated in DMF, in which the polymerization works.

III.2.3 Isoprene polymerization within Fe NPs confined within f-CNT1

The initiator-grafted Fe NPs were introduced into the f-**CNT$_1$** according to the filling method described in chapter II. From the TEM images, the nanotubes are much less filled than in the case of the starting Fe NPs synthesized in the presence of aromatic ligands (Figure III.14a), indicating that the functionalization on the NP surface with the initiator hinders their entrance in CNTs. This is not unexpected since the modification of the NPs surface by BDA grafting reduces the number of aromatic functions on the NPs, therefore the favourable interaction with the CNT channel surface. Similarly to the polymerization without the CNTs, many NPs are agglomerated, and some polymer is observed on the CNT surface (Figure III.14b and c).

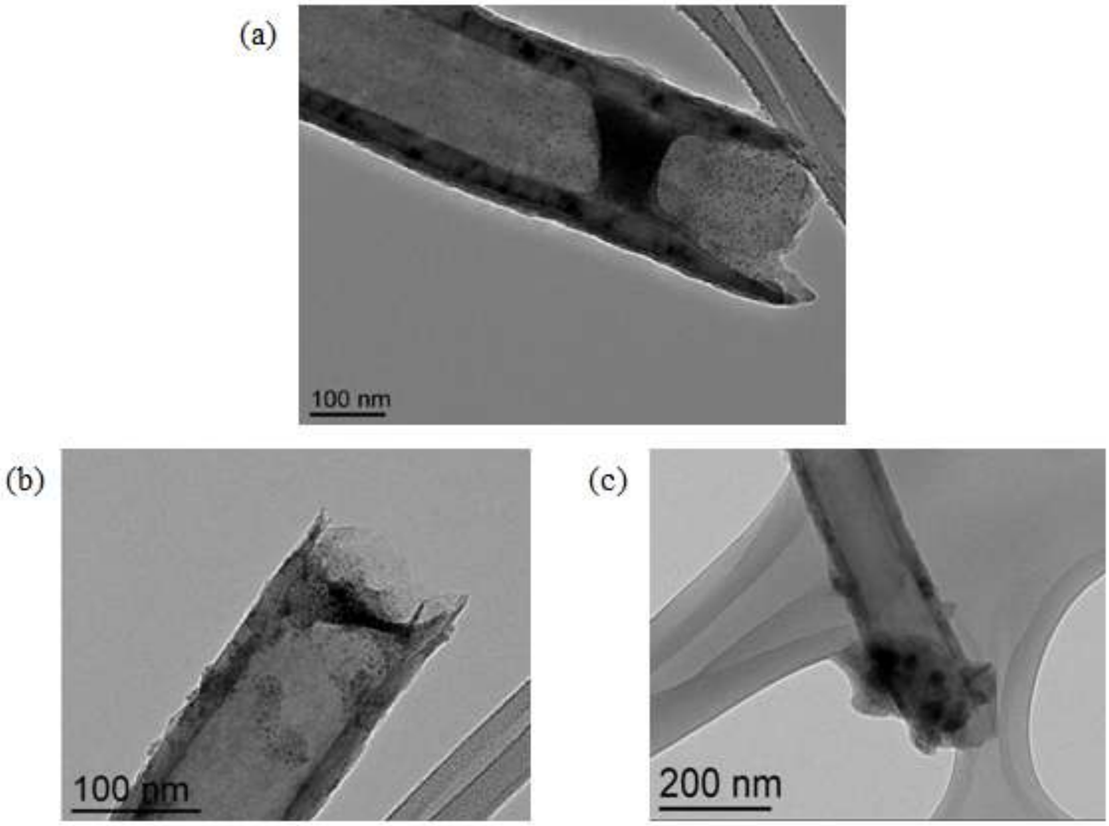

Figure III.14: TEM images of (a) confinement of the surface-modified Fe NPs in the f-CNT_1 and (b-c) polymerization of isoprene with the f-CNT_1-confined surface-modified Fe NPs.

In conclusion, the ATRP presents several drawbacks for our application. First, the isoprene polymerization *via* ATRP presents very low conversion, which can be an issue for the oxidation protection. Second, the surface modification with the initiator renders more difficult the introduction of the surface modified Fe NPs into the CNTs. Last but not least, the agglomeration of Fe NPs takes place during this polymerization. Therefore, another strategy of polymerization on the Fe NPs confined within the f-**CNT**$_1$ is definitely needed.

III.3 Coordination polymerization

III.3.1 Synthesis of a polymerization catalyst and polymerization of isoprene

If ATRP has been used to coat magnetic NPs with a polymer, no report has been found employing coordination compounds as catalysts. According to a recent study reported by Ritter *et al.* (37), iron iminopyridine complexes displayed high activity for the isoprene polymerization and produced various high-performance rubbers through effectively controlled polymerization conditions. For our study, we have decided to use a new iron complex $[Fe(C_{17}H_{14}N_2)_2Cl_2]$ (38) developed independently in the LCC containing an iminopyridine functional group (Figure III.15), which can be grafted on the surface of the Fe NPs *via* π-π interactions. We anticipated that such a grafting, involving a weak complex/nanoparticle interaction, should not perturb the catalytic activity.

The derived iminopyridine ligand was synthesized based on a procedure described in the literature (38) (Figure III.15). Then, the iron complex $[Fe(C_{17}H_{14}N_2)_2Cl_2]$ was prepared by reacting $FeCl_2$ with two equivalents of the ligand in ethanol under inert atmosphere. The isolated blue solid is air-stable. Compared to the IR spectra of the free ligands, the C=N stretching vibrations in the complex are shifted to lower frequency (1596 cm^{-1}), indicating an effective coordination of the imino nitrogen atoms on the iron center. Single crystals of this complex were obtained by by L. Zhang (39), who also elucidated its structure through X-ray diffraction analysis.

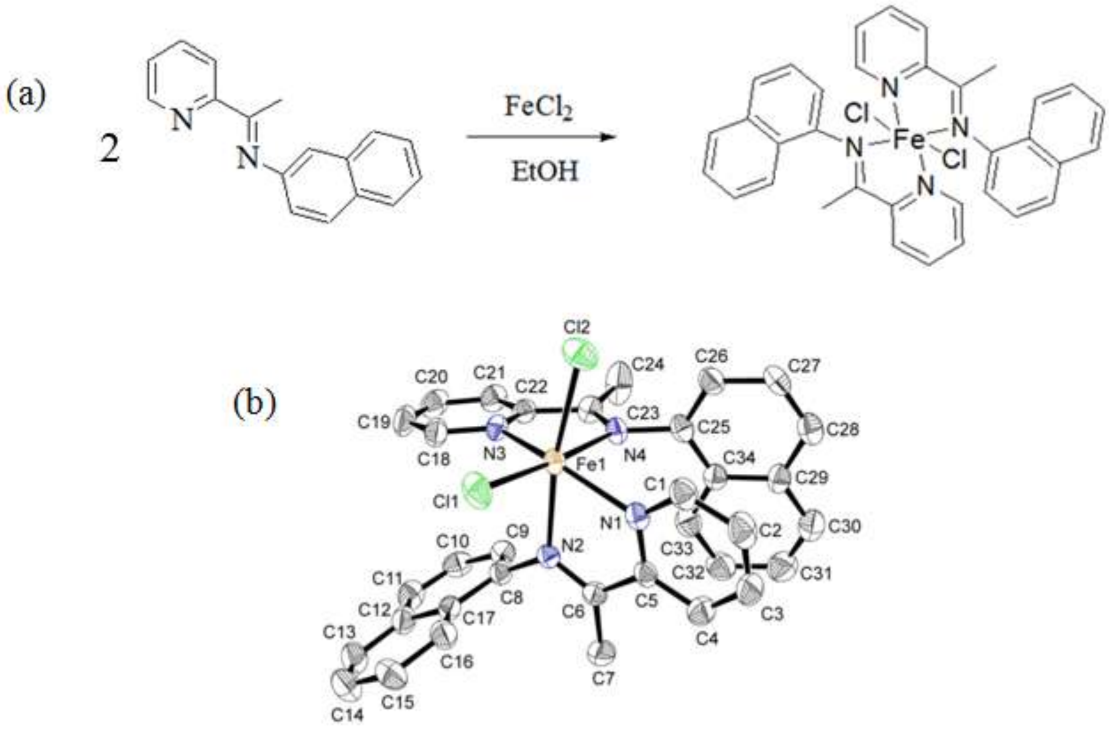

Figure III.15: (a) Schematic representation of the synthetic procedure of the Fe complex. (b) Molecular structure of the Fe complex. Thermal ellipsoids are shown at 30 % probability.

Isoprene polymerization catalyzed by this iron complex was performed in a glove-box under argon. Triisobutylaluminum served as a co-catalyst to abstract the chloride from the dichloride iron complexes and to produce the active species. In the absence of this co-catalyst no polymer was formed. Moreover, trityl tetrakis(pentafluorophenyl)borate can be used as the dealkylating reagent and increase the reaction rate (39).

In Table 5, we see that more than 99% of the isoprene is converted into polyisoprene in half an hour at room temperature. According to the ^{1}H NMR data, the selectivity (calculated by the equations shown in the previous section) between 1,4-polyisoprene and 3,4-polyisoprene is slightly in favor of the 1,4-polyisoprene, and is not much affected by reaction temperature variations. Moreover, the *cis*-1,4-polyisoprene content is raised up to more than 99% at ≤ 0°C.

Table 5: Comparison of a series of polymerizations with the Fe complex [a].

	T (°C)	t (min)	Conv. (%)	1,4/3,4	1,4 (%) *cis/trans*
1	25	30	>99	11:9	19:1
2	0	30	96	57:43	>99
3	-33	30	78	14:11	>99
4	25	15	86	11:9	24:1

[a] Reaction conditions: 3 μmol Fe complex; 7.5 mL isoprene (M), $[Al]/[Ph_3C^+]/[M]/[Fe]$ = 1:12: 25000:1; 100 mL toluene.

Thus, this complex is a very good isoprene polymerization catalyst. By grafting it on the surface of the Fe NPs we could induce the polymerization on the surface of the Fe NPs. Indeed, the naphthalene ring of the ligand should be able interact with the surface of Fe NPs through π-π interaction.

III.3.2 Surface-functionalized FeNP@Fe

The surface-functionalized FeNP@Fe was prepared by stirring a colloidal solution of the pre-formed Fe NPs in the presence of the Fe complex, in THF under inert conditions, during 1 day (see Experimental section). From the TEM images (Figure III.16), we can conclude that the procedure does not modify the size of the Fe NPs (d=4.6±0.4 nm and d=4.5±0.4 nm for the pre-formed NPs and the modified NPs, respectively). The elemental analysis indicates contain respectively 71.7% and 67.5% by weight Fe in the pre-formed Fe NPs and the surface-functionalized FeNP@Fe samples.

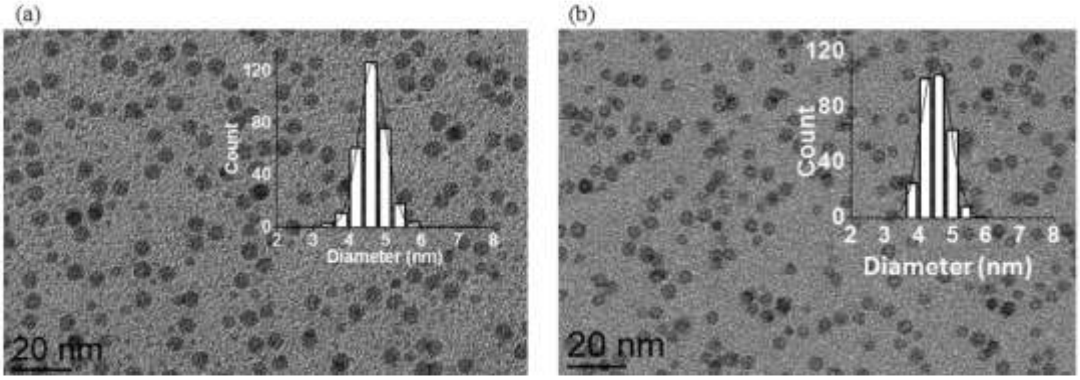

Figure III.16: (a) the pre-formed Fe NPs and (b) the FeNP@Fe.

Comparison of the IR spectra of the FeNP@Fe with the pre-formed Fe NPs (Figure III.17) evidenced an additional vibration at 1615 cm^{-1} belonging to the C=N of the Fe complex. Compared to the C=N vibration for free Fe complex (1596 cm^{-1}), this shift indicates an effective interaction the Fe complex and the NP surface. We can therefore conclude that the Fe complex is present on the surface of the NPs.

Figure III.17: IR Spectra of the preformed Fe NPs (bottom) and FeNP@Fe (top).

III.3.3 Nanohybrid FeNP@ Fe@PI@CNT$_1$

The new surface-functionalized Fe NPs can be confined within f-**CNT$_1$** *via* the suspension filling method. TEM observations confirmed the confinement (Figure III.18). Very few NPs can also be found on the outer surface of CNTs. The size of the confined Fe NPs (4.6±0.6 nm) remains the same as the one before filling. No agglomeration of NPs was observed. The elemental analysis indicates 4.8% by weight of Fe in this FeNP@ Fe@**CNT$_1$**.

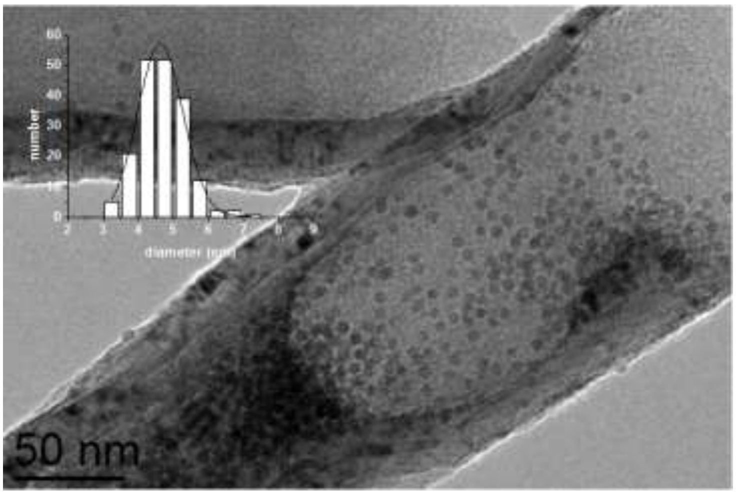

Figure III.18: TEM image of the FeNP@Fe@CNT$_1$.

Before attempting to polymerize the FeNPs@Fe after introduction in the CNTs we checked the activity of the grafted complex in the absence of CNTs. This was a very important step, since a failure of the iron complex to catalyze the polymerization when grafted on the Fe NPs would be a very negative indication for the polymerization of the FeNP@Fe once in the interior of the CNTs.

The catalytic polymerization of isoprene was therefore investigated with the FeNP@Fe. In a Schlenk tube, the FeNP@Fe, $Al(^{i}Pr)_{3,}$ trityltetrakis(pentafluorophenyl)borate and isoprene were mixed in toluene (see Experimental section). The mixture was intensively stirred during 30 min at 25°C. Then the solvent was removed under vacuum. At the end, a gum-like product was obtained. For the FeNP@Fe@PI, the color is dark brown. From TEM observations, this gum-like product was dissolved in toluene with the aid of ultra-sonication at 60ºC. After one hour, a gel-like solution was formed, with which TEM grids were prepared.

The FeNP@Fe@PI sample after partial dissolution in toluene, as shown in Figure III.19, corresponds to a film composed of NPs and the polymer. The polymer coating is not as well controlled as in some literature reports, in which single NPs or groups of a few NPs are coated by a thin layer of polymer separately (15-17). This should be the result of the high activity of our Fe catalyst. The displacement of the complex from the surface of the NPs to the colloidal solution during the reaction, which may lead to polymer generated not only around the functionalized NPs but also in the solution, can be discarded since we have not observed the formation of free polymer. There is nearly no modification for the size distribution (d= 4.6±0.4 nm) after the polymerization, and there is 0.39% by weight of Fe in FeNP@Fe@PI according to the elemental analysis.

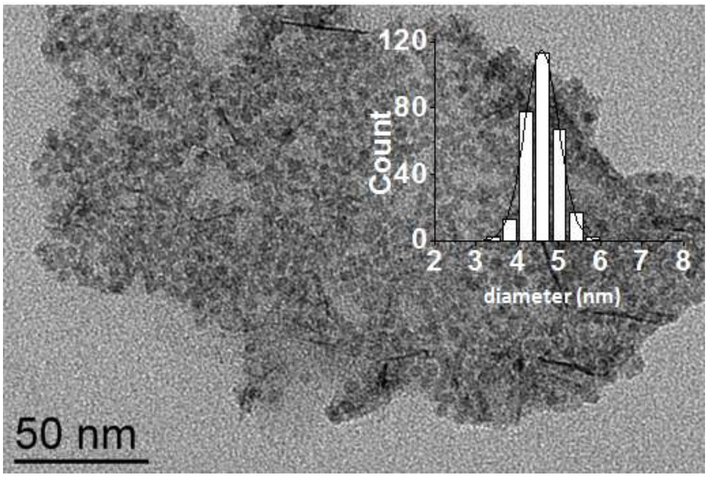

Figure III.19: TEM image of the FeNP@Fe@PI.

Once the polymerization around the FeNP@Fe verified, we performed the polymerization reaction with FeNP@Fe@CNT$_1$. The polymerization followed the same procedure as used for FeNP@Fe@PI (see Experimental section). At the end, a black gum-like product was obtained.

For the FeNP@Fe@PI@CNT$_1$, as shown in Figure III.20, the NPs are confined within the CNTs and surrounded by polymer. Electron tomography was used to study the three-dimensional structure of this nanohybrid (Figure III.21). The polymer-coated and confined Fe NPs can be visualized by the 3D animation of the reconstructed series of tomography available images.

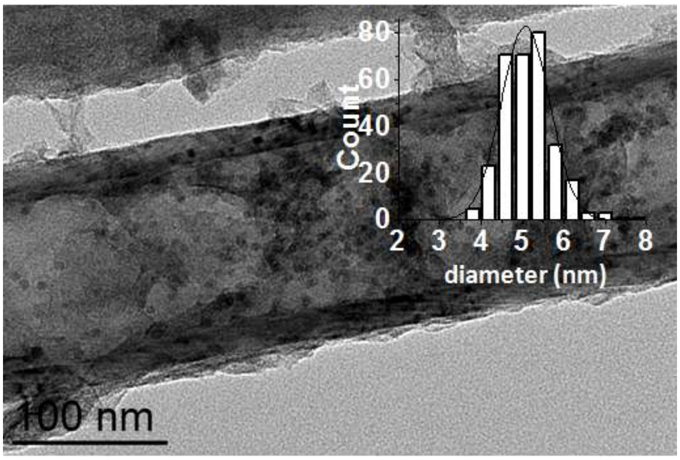

Figure III.20: TEM image of the FeNP@Fe@PI@CNT$_1$.

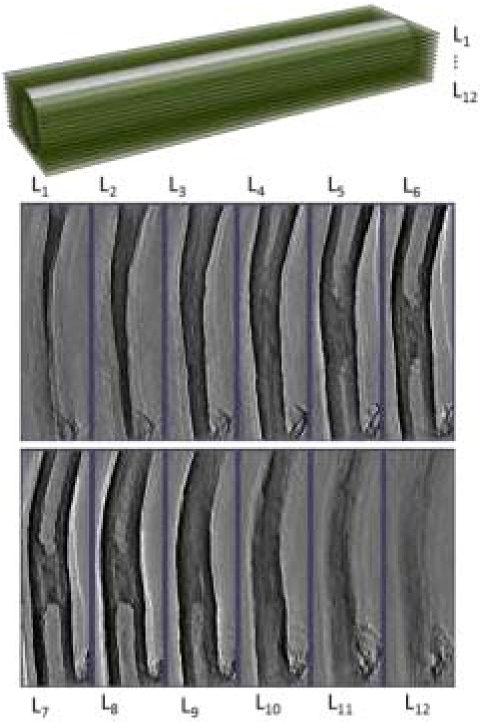

Figure III.21: Electron tomography analysis of the FeNP@Fe@PI@CNT$_1$ nanohybrid. Sequential cuts in the Z direction extracted from the reconstruction of the electron tomogram. The upper inset gives a schematic view of the position of the volume cuts represented in the lower insets. The hollow structure of the nanotube and the partial filling is clearly visible from the cuts.

However, it is of course difficult to confirm that all the NPs are coated with polymer. It is also possible that part of the coating polymer may be dissolved during the grid preparation. The gum-like aspect reveals that polymer is also generated outside the CNTs, as observed by TEM images, arising either from the very few surface-functionalized NPs outside the CNTs or/and Fe complex, which may have been displaced from the NP surface. This complex can indeed attach itself on the outer surface of the CNTs *via* the π-π interaction despite the functionalization of the external surfaces with long chain moieties. It can therefore catalyze the polymerization at the exterior of the CNTs. Considering the very high polymer conversion with the Fe catalyst, the production of a high amount of polymer around the CNTs, and therefore the gum-like aspect, is comprehensible. The size of the confined NPs are a little larger (d=5.1±0.6 nm) than those measured in the former samples. The amount of Fe in the FeNP@Fe@PI@CNT$_1$ nanohybrid decreases to 0.12% by weight as verified by elemental analysis.

In conclusion, we have successfully produced nanobybrids based on the initial Fe NPs after ligand exchange, confinement and polymerization steps. They are the catalyst-modified Fe NPs, CNT$_1$-confined Fe NPs, polyisoprene-coated Fe NPs and CNT$_1$-confined and polyisoprene-coated Fe NPs, denoted respectively as FeNP@Fe, FeNP@Fe@CNT$_1$, FeNP@Fe@PI, FeNP@Fe@PI@CNT$_1$. This study constitutes the first example of confined polymerization inside CNTs.

In order to investigate the magnetic properties of each of these Fe NP samples and to evaluate the protection from oxidation, magnetic measurements have been performed for all these samples by superconducting quantum interference device (SQUID) and vibrating sample magnetometer (VSM).

III.4 Magnetism study

The protection from oxidation has been studied by $M(H)$ hysteresis loops performed by SQUID or VSM. In a $M(H)$ hysteresis loop, the saturation magnetization (M_S) and the coercivity (H_C) are critical values that can give information about the oxidation degree of samples based on the modification of M_S and the shift of H_C with respect to a non-oxidized sample (see Annex II, part B). For instance, a decrease of the M_S may result from oxidation of a pure magnetic metal into its oxide. Moreover, oxidation may cause a shift of the hysteresis loop across the magnetic field H axis, called the exchange bias effect (40), due to interactions at the interface between ferromagnetic core and antiferromagnetic shell.

The Fe NPs used for our study are monodomain NPs with a size distribution 4.6±0.4 nm, synthesized from the reaction "Fe_1BBA_2PPP_Mes_150ºC_48h". They are superparamagnetic at room temperature, and thus no H_C is measured, as shown by the curve of the magnetization with respect to the applied field (Figure III.22). Below the blocking temperature (T_B) of the NPs, measured from susceptibility ZFC/FC curves, the NPs are in the blocked state where the energy barrier becomes more important than thermal fluctuations. Therefore, H_C can be displayed from hysteresis loops.

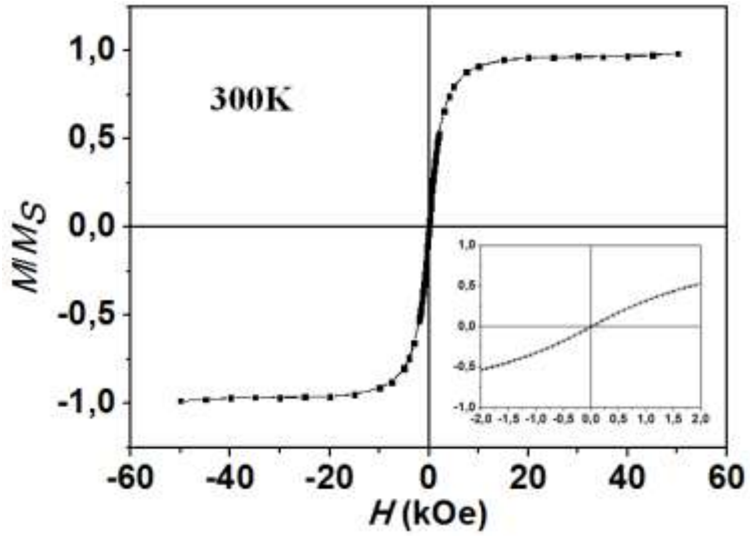

Figure III.22: Hysteresis loop of Fe NPs at 300K performed by SQUID with an inset magnification.

At 4K, The bare Fe NPs exhibit a magnetization at saturation $M_S = 125$ emu/g at 4 K (see Figure III.23), a value which is lower than for bulk iron (~ 220 emu/g). This decrease can be explained by the influence of the PPP or BBA ligands, which can modify the surface magnetic properties of NPs, especially small NPs, for which a great percentage of the atoms is found on the surface and interacts directly with them (41, 42). Additionally, hysteresis loops performed after a ZFC and FC (5T) protocol did not present any shift (see Figure III.23), suggesting that the NPs are metallic.

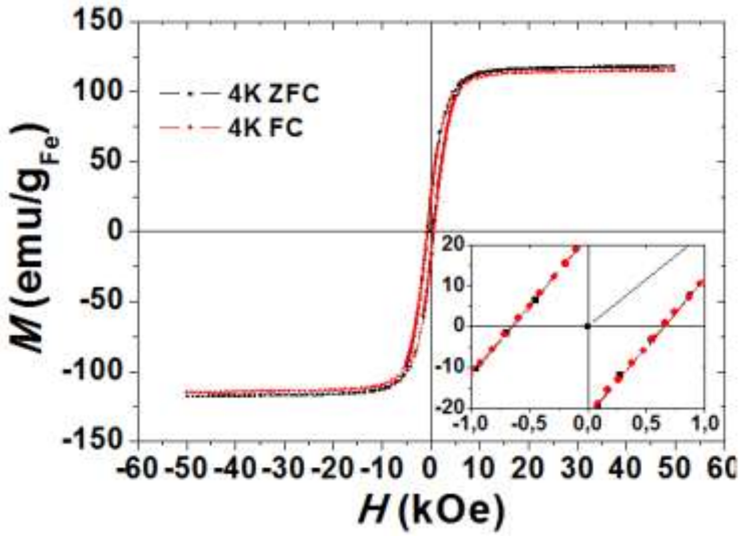

Figure III.23: Hysteresis loop of the Fe NPs at 4K performed by VSM with an inset magnification.

The zero field-cooled (ZFC) and field-cooled (FC) magnetic susceptibility, measured under a field of 10 Oe on a sample of Fe NPs diluted in a wax matrix, indicates a blocking temperature T_B = 38 K (see Figure III.24). The fitting of these curves leads to an effective anisotropy K_{eff} = (6.0±0.1) 10^5 erg/cm^3, considering the size distribution obtained by TEM. This slight increase of K_{eff} compared to the bulk value (~ 5 10^5 erg/cm^3 for *bcc* Fe) is attributed to the contribution of enhanced surface anisotropy due to the reduced size of the NPs (43).

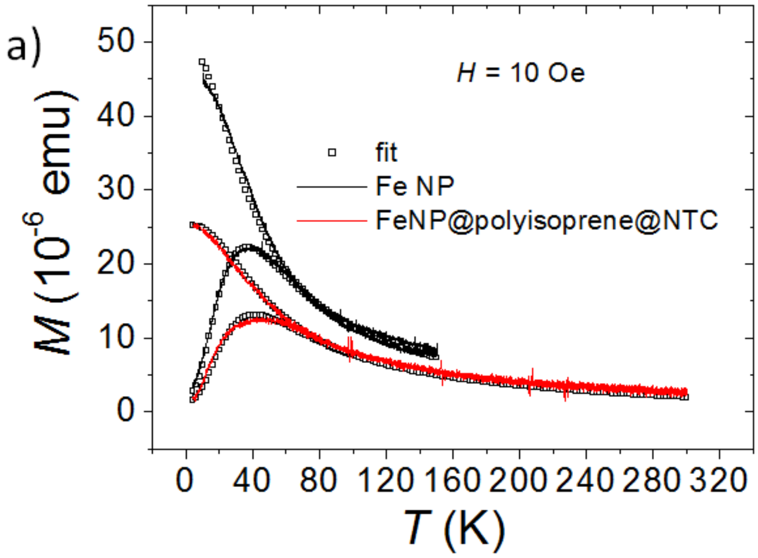

Figure III.24: Magnetic susceptibility measurement under 10 Oe for the Fe NPs and the FeNP@Fe@PI@CNT$_1$.

The magnetic characterizations of FeNP@Fe@PI and FeNP@Fe@PI@CNT$_1$ are delicate. In fact, both processes lead to very low Fe NPs loading (0.1- 0.5 % w/w), rendering a precise estimation of the magnetization value difficult. However, careful analyses of the high temperature hysteresis loops in the superparamagnetic regime and of the temperature dependence of the magnetic susceptibility unambiguously show that there was no significant change on the magnetic properties (same magnetic moment) of the Fe NPs after all processes. Indeed, the magnetization curves plotted as a function of the ratio H/T in the superparamagnetic regime are presented in Figure III.25. Their adjustments are obtained using the integration of Langevin function weighted by the magnetic moment distribution, deduced from the size distribution (44). This scaling and the superposition of the curves of both samples, as well as the adjustment of the ZFC/FC curves, show that the magnetic properties of the Fe NPs are not modified after all steps of encapsulation.

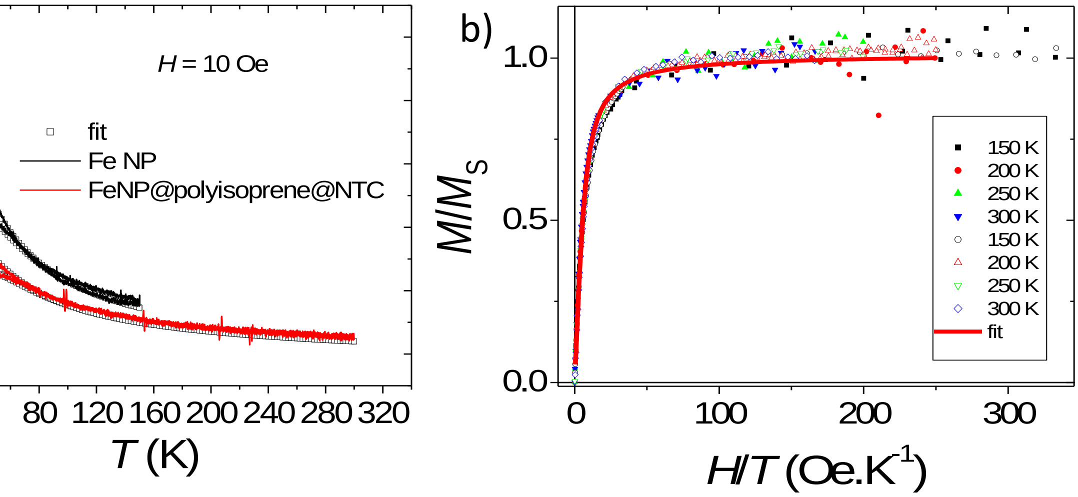

Figure III.25: Scaling of magnetization curves of samples FeNPs (solid symbols) and FeNP@Fe@PI@CNT (open symbols).

This constitutes a positive result since it is usually found in the literature that coating Fe NPs with polymers lead to a reduction of the magnetization. This phenomenon has already been reported for PVP (Ms ~ 180 emu/g$_{Fe}$ for 15-65 nm NPs) (45), PMMA (Ms ~ 115 emu/g$_{Fe}$ for 20 nm NPs) (46), biscarboxyl-terminated PEG (Ms = 70 emu/g$_{Fe}$ for 10 nm NPs) (47) or polyisobutene (Ms = 8-140 emu/g$_{Fe}$ for 20 nm NPs) (9) coated Fe nanoparticles. In our case, a single dead magnetic layer at the surface of the NPs would lead to a reduction of ~ 30 % of M_S due to the small size of the NPs.

In order to evaluate the efficiency of the polymer coating as an oxygen barrier, we have examined the magnetic hysteresis curves of the same samples exposed to air for different time intervals (see Figure III.26 and 27). For the discussion that follows, the magnetization at saturation before *air exposure* will be defined as $M_S^{(t=0)}$. For all samples, an oxidation takes place after exposition to air during 15 min. Indeed, the hysteresis curves show a decrease of the *Ms* and a displacement of the cycle with respect to the one of the non-oxidized sample, characteristic of an exchange bias between the ferromagnetic core of Fe and an antiferromagnetic oxide layer. As expected, the bare Fe NPs are the most sensitive to oxygen. After only 15 min (Figure III.26a), the hysteresis loop recorded after a FC (5T) is strongly shifted and evidences an exchange bias (defined as $H_{EB} = (H_C^+ - H_C^-)/2$ with H_C^+ and H_C^- the positive and negative coercive field, respectively) H_{EB} = 122 Oe. The oxidation is also well illustrated by the large drop of M_S down to 31 % of $M_S^{(t=0)}$, which corresponds to an oxidation of ~ 3 atomic layers. Exposition of the FeNP@Fe@PI@CNT leads to similar results (Figure III.26c), but with a slower rate of oxidation, where H_{EB} presents quite small values (~35 Oe) after 15 min, while M_S decreases to 64% of $M_S^{(t=0)}$. This decrease of the magnetization corresponds to a volume of Fe atoms occupying 1 atomic surface layer. At last, the sample composed of FeNP@Fe@PI shows the best resistance against oxygen diffusion (Figure III.26b). It has to be noted that the hysteresis loops present a small exchange bias before exposition to air (H_{EB} = 35 Oe) presumably due to an accidental exposition of the sample to air during the transfer to the chamber of the SQUID. However, even after 1 hour of exposition, H_{EB} only increases to 83 Oe, while M_S only drops to 83%. The fact that the Fe NPs at this step are less affected than the ones encapsulated in CNTs can be explained by a more efficient polymerization on free Fe NPs in solution. Indeed, the diffusion of isoprene inside the CNTs and between the confined NPs can be reduced, resulting in the formation of fewer polymers around the NPs.

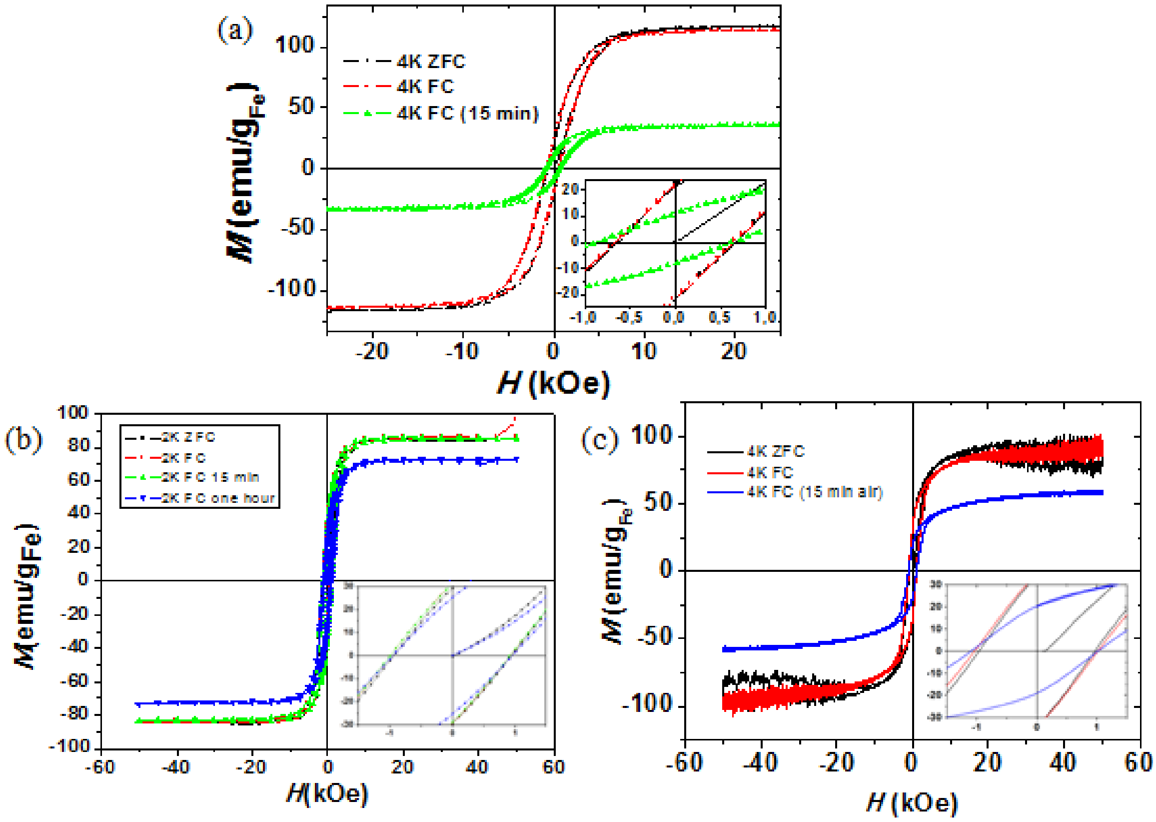

Figure III.26: Comparisons of hysteresis loops of (a) FeNP, (b) FeNP@Fe@PI and (c) FeNP@Fe@PI@CNT (before and after exposition).

The most surprising result during this study concerns the behavior of the FeNP@Fe sample. Figure III.27 shows the hysteresis loops corresponding to the FeNP@Fe before air exposition, and after 15 min and one hour air exposition. Examination of the curves shows no modification for both M_S and H_{EB} after 15 min exposure to air. Extended to one hour, only a 3 emu/g decrease for M_S is detected. This very efficient protection has not been understood because only the surface of the Fe NPs are modified with the Fe complex, and their shape do not change importantly, as presented by the TEM images (Figure III.16). We can evoke that the Fe complex bearing aromatic groups interacts with the Fe NPs stabilized by the aromatic ligands, and that it might form a protective layer preventing oxygen from penetrating through them. Further studies are definitely necessary in order to confirm this surprising result and to determine the reasons for this unexpected effect. This constitutes however a very interesting result that can offer many perspectives for the protection of MMNPs from air oxidation.

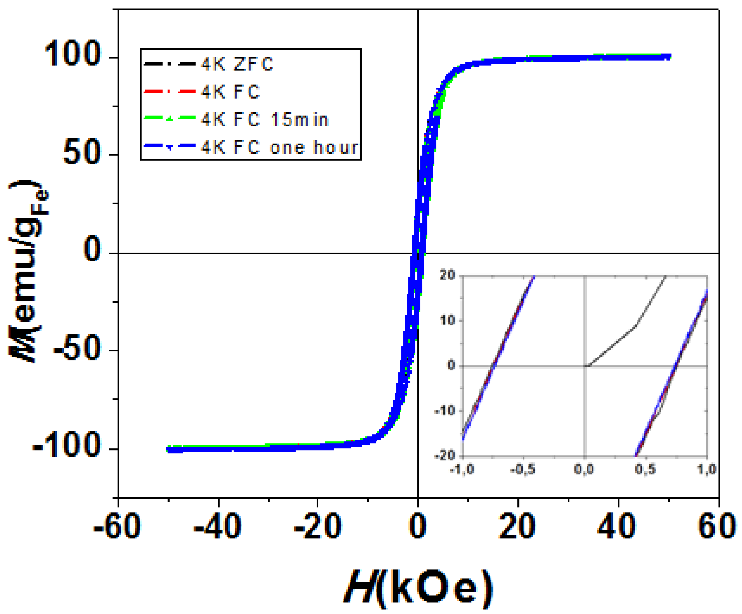

Figure III.27: Hysteresis loops of the FeNP@Fe (before and after exposition).

In conclusion, the magnetic studies of air-protection of the polyisoprene-coated Fe NPs indicate that the polymer that we have chosen can clearly delay the oxidation although it cannot prevent the slow diffusion of oxygen to the Fe NP core. The polymerization is more efficient when the Fe NPs are not confined, as evidenced by comparing the oxidation monitoring of the FeNP@Fe@PI and the FeNP@Fe@PI@CNT$_1$, which may be attributed to the reduced diffusion of isoprene in the CNT channel. In addition, the Fe complex-modified Fe NPs present surprisingly very good stabilization against oxidation, which is significantly worthy to further study.

III.5 Conclusion

Two different polymerization methods have been investigated for coating the monodispersed Fe NPs. For the ATRP method, the initiator-modified Fe NPs have been confined within the f-**CNT**$_1$ following the filling method as developed and described in the Chapter II. Polymerization of isoprene has been carried out on both the free modified NPs and the confined ones. However, both of them have been found aggregated after being coated by polyisoprene *via* ATRP, which hinders further magnetic measurement.

Polymerization of isoprene catalyzed by the Fe complex presents a very high conversion. The Fe complex-modified Fe NPs have been also confined within the f-**CNT**$_1$. Polymerization of isoprene has been carried out on both the free modified NPs and the confined ones. No aggregation has been observed in this case. Finally, the FeNP@Fe@PI and the FeNP@Fe@PI@CNT$_1$ nanohybrids have been obtained.

The resistance to air-oxidation of these nanohybrids has been studied by magnetic measurements. The polyisoprene coating delays the air oxidation. The polymerization is more efficient when the Fe NPs are not confined within CNTs, which may be attributed to more polymer coating on the free Fe NPs than on the confined ones. In order to optimize the air-protection, the selectivity of the polymerization of isoprene has to be improved, because only 50-60% of proportion for *cis*-1,4-polyisoprene was achieved in our polymerization, which is far from nature rubber (>99%). Nevertheless, this proof of concept suggests that this strategy could be used with other polymers that are more efficient air and moisture barriers and to other air-sensitive nanoparticles. Further experiments could be performed with polyethylene coatings on Fe NPs.

Furthermore, the reason why the Fe complex-modified Fe NPs present good stabilization against oxidation should be further studied.

III.6 Reference

1. H. Bönnemann, W. Brijoux, R. Brinkmann, N. Matoussevitch, N. Waldöfner, N. Palina, H. Modrow, *Inorg. Chim. Acta*, **2003**, *350*, 617-624.
2. C. Dobbrow, A. M. Schmidt, *Beilstein Journal of Nanotechnology*, **2012,** *3,* 75-81.
3. S.-J. Cho, J.-C. Idrobo, J. Olamit, K. Liu, N. D. Browning, S. M. Kauzlarich, *Chem. .Mater.*, **2005,** *17,* 3181-3186.
4. M. Chen, S. Yamamuro, D. Farrell, S. A. Majetich, *J. Appl. Phy.*, **2003,** *93,* 7551-7553.
5. B. I. Kharisov, H. V. Rasika Dias, O. V. Kharissova, V. Manuel Jimenez-Perez, B. Olvera Perez, B. Munoz Flores, *RSC Advances*, **2012,** *2,* 9325-9358.
6. J. Qiu, Y. Li, Y. Wang, Y. An, Z. Zhao, Y. Zhou, W. Li, *Fuel Processing Technology*, **2004,** *86,* 267-274.
7. I. Robinson, S. Zacchini, L. D. Tung, S. Maenosono, N. T. K. Thanh, *Chem. Mater.*, **2009**, *21*, 3021-3026.
8. J. Pyun, *Polym. Rev.*, **2007**, *47*, 231–263.
9. N. A. D. Burke, H. D. H. Stöver, F. P. Dawson, *Chem. Mater.,* **2002,** *14,* 4752-4761.
10. Goesmann H, Feldmann C., *Angew. Chem. Int. Ed.*, **2010**, *49*, 1362–1395.
11. M. Beija, J.-D. Marty, M. Destarac, *Prog. Polym. Sci.,* **2011**, *36*, 845–886.
12. J. Shan, H. Tenhu. *Chem Commun.*, **2007**, *43*, 4580–4598.
13. P.S. Chinthamanipeta, S. Kobukata, H. Nakata, D.A . Shipp, *Polymer*, **2008**, *49*, 5636–5642.
14. V.G. Ngo, C. Bressy, C. Leroux, A. Margaillan., *Polymer*, **2009**, *50*, 3095–3102.
15. C. R. Vestal, Z. J. Zhang, *J. Am. Chem. Soc.*, **2002**, *124*, 14312-14313.
16. T. Gelbrich, M. Feyen, A. M. Schmidt, *Macromolecules*, **2006**, *39*, 3469-3472.
17. C. Gürler, M. Feyen, S. Behrens, N. Matoussevitch, A. M. Schmidt, *Polymer,* **2008**, *49*, 2211–2216.
18. H. Srikanth, R. Hajndl, C. Chirinos, J. Sanders, A. Sampath, T. S. Sudarshan, *Appl. Phys. Lett.*, **2001**, *79*, 3503-3505.
19. S. Lo´pez, I. Cendoya, F. Torres, J. Tejada, C. Mijangos, *Polym. Eng. Sci.*, **2001**, *41*, 1845-1852.
20. N.A.D. Burke, H.D.H. Sto¨ver, F. P. Dawson, J. D. Lavers, P.K. Jain, H. Oka, *IEEE Trans. Magn.*, **2001**, *37*, 2660-2662.
21. Z.-P. Xiao, K.-M. Yang, H. Liang, J. Lu, *J. Polym. Sci. Part A Polym. Chem.,* **2010**, *48*, 542–550.
22. Y. Tsujii, M. Ejaz, K. Sato, A. Goto, T. Fukuda, *Macromolecules*, **2001**, *34*, 8872–8878.
23. C. Boyer, V. Bulmus, P. Priyanto, W.Y. Teoh, R. Amal, T.P. Davis, *J. Mater. Chem.*, **2009**, *19*, 111–123.
24. S. . De, J. . hi te, ubber technologist's handbook, rapra technolog limited, shawbur , **2001**, 49–51.

25. Desmond Threadingham, Werner Obrecht, Wolfgang Wieder, Gerhard Wachholz, Rüdiger Engehausen, "Rubber, 3. Synthetic Rubbers, Introduction and Overview" in Ullmann's Encyclopedia of Industrial Chemistry, **2011**, Weinheim.
26. T. von Werne, T. E. Patten, *J. Am. Chem. Soc.,* **2001**, *123*, 7497-7505.
27. K. Ohno, K. Koh, Y. Tsujii, T. Fukuda, *Angew. Chem. Int. Ed.,* **2003**, *42*, 2751-2754.
28. H. Duan, M. Kuang, D. Wang, D. G. Kurth, H. Mo¨hwald, *Angew. Chem., Int. Ed.,* **2005**, *44*, 1717-1720.
29. X. Chen, D. P. Randall, C. Perruchot, J. F. Watts, T. E. Patten, T. von Werne,; S. P. Armes, *J. ColloidInterface Sci.,* **2003**, *257*, 56-64.
30. W. a. Braunecker, K. Matyjaszewski, *Prog. Polym. Sci.,* **2007**, *32*, 93–146.
31. K. Matyjaszewski, *Macromolecules*, **2012**, *45*, 4015-4039.
32. K. Matyjaszewski, J. Xia, *Chem. Rev*., **2001**, *101*, 2921–2990.
33. B.E. Woodworth, Z. Metzner, K. Matyjaszewski, *Macromolecules*, **1998**, *31*, 7999-8004.
34. K.A. Davis, H-j. Paik, K. Matyjaszewski, *Macromolecules*, **1999**, *32*, 1767-1776.
35. J. Li, J. EI harfi, S. M. Howdle, K. Carmichael, D. J. Irvine, *Polym.Chem*., **2012**, *3*, 1495-1501.
36. J. Wootthikanokkhan, M. Peesan, P. Phinyocheep, *European Polymer Journal*, **2001**, *37*, 2063-2071.
37. J. Raynaud, J. Y. Wu, T. Ritter, *Angew. Chem. Int. Ed.,* **2012**, *51*, 11805–11808.
38. L. Zhang, E. Yue, B. Liu, P. Serp, C. Redshaw, W.-H. Sun, J. Durand, *Catal. Commun.*, **2014**, *43*, 227–230.
39. L. Zhang, *Immobilization of molecular late-transition metal polymerization catalysts on nanomaterials*, thesis of University of Toulouse, **2014**.
40. J. Nogués, I.K. Schuller, *J. Magn. Magn. Mater*., **1999**, *192*, 203-232.
41. T. C. Monson, Q. Ma, T. E. Stevens, J. M. Lavin, J. L. Leger, P. V. Klimov, D. L. Huber, *Particle & Particle Systems Characterization,* **2013,** *30,* 258-265.
42. O. Margeat, F. Dumestre, C. Amiens, B. Chaudret, P. Lecante, M. Respaud, *Progress in Solid State Chemistry,* **2005,** *33,* 71-79.
43. J. P. Chen, C. M. Sorensen, K. J. Klabunde, G. C. Hadjipanayis, *Phys. Rev. B*, **1995**, *51*, 11527-11532.
44. G.F. Goya, *Solid State Commun.*, **2004**, *130*, 783-787.
45. Y.-L. Hou, S. Gao, *Journal of Alloys and Compounds*, **2004**, *365*, 112-116.
46. J. L. Wilson, P. Poddar, N. A. Frey, H. Srikanth, K. Mohomed, J.P. Harmon, S. Kotha, J. Wachsmuth, *J. Appl. Phys*., **2004**, *95*, 1439-1443.
47. C. G. Hadjipanayis, M. J. Bonder, S. Balakrishnan, X. Wang, H. Mao, G. C. Hadjipanayis, *Small*, **2008**, *4*, 1925-1929.

Chapter IV. Platinum-based magnetic nanomaterials confined in CNTs

Chapter IV. Platinum-based magnetic nanomaterials confined in CNTs

IV.1 Introduction

Magnetic Pt-based *3d*-transition nanomaterials are of great interest in many domains, such as electrocatalysis for the oxygen reduction reaction (ORR) (1-4), biomedical applications (5-7) and information storage media (5, 8). For the ORR used in fuel cells and metal-air batteries for renewable energy applications, Co-Pt (2) and Fe-Pt (4) catalysts are less expensive alternatives to the classic Pt catalysts, and present enhanced activity and stability. For biomedical applications, these nano-alloys are interesting candidates that exhibit better stability than pure metals as Fe or Co, and also possess higher magnetic moment than commonly used oxides (5, 7).

For information storage media, magnetic storage has played a key role in audio, video and computer developments since its invention by IBM, who built the first magnetic hard disk drive (HDD) displaying a total storage capacity of 5 MB at a recording density of 2 kbit/in^2 in 1956. Presently, after 50 years, modern HDD have capacities superior to 1 TB and storage densities of about 200 Gbit/in^2. In order to increase the capacity of storage, increasing storage density is mandatory. The smaller the grain size and the more the grains present per unit surface, the higher the capacity is. However, when the grain size decreases below a critical value, the grains become superparamagnetic and they are demagnetized spontaneously due to thermal fluctuation, destroying the stored data. Due to this superparamagnetic effect, hard disk technology with traditional longitudinal recording has a limit of 100 to 200 Gbit/in^2.

It has been predicted that density higher than 1 Tbit/in^2 could be reached with perpendicular recording media, for which materials with strong perpendicular anisotropy, high coercive field (>0.4 T) and small grain size (<10 nm) are required.

Fe-Pt and Co-Pt alloys have attracted much attention since some of their crystalline phases present very high uniaxial magnetocrystalline anisotropy constant, as high as 7×10^6 J/m^3 for FePt (8), and good chemical stability (9). Indeed these bimetallic alloys are known to possess a chemically disordered *fcc* structure or a chemically ordered face-centered tetragonal (*fct*) structure (Figure IV.1). The *fcc* structure is characterized by small magnetocristalline anisotropy and coercive field. In contrary, the fully ordered *fct* structure presents a large coercivity and is magnetically hard, and can be viewed as alternating atomic layers of Fe (or Co) and Pt stacked along the (001) direction (the *c*-axis in Figure IV.1b), which is also described as the $L1_0$ phase (10).

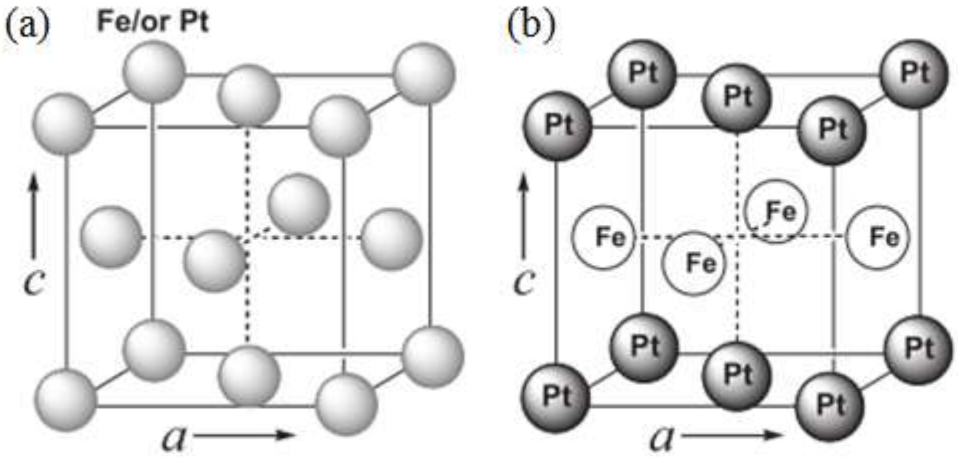

Figure IV.1: Schematic illustration of the unit cell of (a) chemically disordered *fcc* (atoms represent Fe or Pt), and (b) chemically ordered *fct* FePt (adapted from ref.11).

Apart from the $L1_0$ structure for which the magnetic metal and platinum are present in ratio close to 1 (FePt and CoPt), $L1_2$ is another ordered structure, which corresponds to different ratios between the magnetic metal and platinum ($FePt_3$, Fe_3Pt, $CoPt_3$ and Co_3Pt) (12, 13). The $L1_2$ structure is less studied for magnetic applications due to its much lower magnetocrystalline anisotropy (14-18).

Up to now, FePt or CoPt NPs have been usually synthesized *via* wet chemistry (5, 19-22), by which only the disordered *fcc* phase can be directly obtained. A post-annealing process is required to transform the magnetically "soft" *fcc* phase into the "hard" *fct* one. Sun *et al.* have synthesized monodispersed FePt NPs with diameter 4 nm ($\sigma \leq 5$ %) *via* thermal decomposition and reduction of metal precursors in the presence of oleic acid and oleyl amine as stabilizers and a polyalcohol as reducing agent (polyol process) (19). As observed from TEM images, the FePt NPs can self-assemble into an *hcp* 3D super-lattice. After deposition on a thermally oxidized Si substrate and further annealing at 560°C for 30 min, no agglomeration was found, and more importantly the *fct* phase was obtained. This phase transition was indicated by: i) the XRD pattern, from which it was shown that the (111) plane with a lattice spacing of 2.20 Å, is shifted with respect to its position before annealing, and ii) b an evolution of the (001) and (110) peaks (Figure I .2). However, further annealing at T ≥ 600°C resulted in the coalescence of the NPs (20, 21).

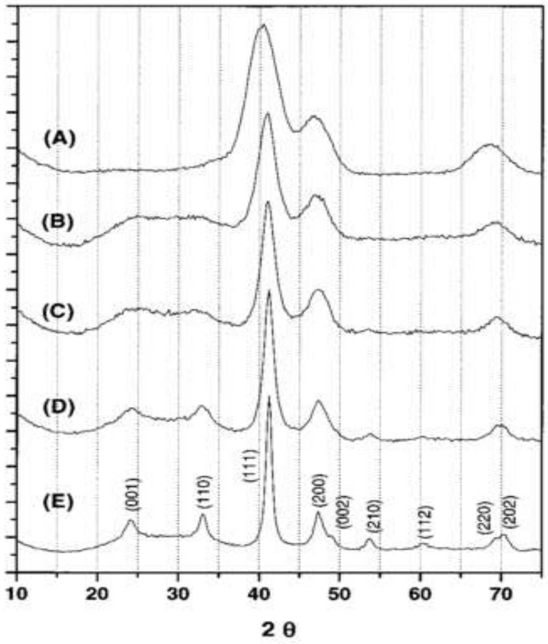

Figure IV.2: Evolution of the FePt phase during annealing. XRD pattern of (a) as-synthesized 4 nm $Fe_{52}Pt_{48}$ particle assemblies, and a series of similar assemblies annealed under N_2 for 30 min at temperature of (b) 450°C, (c) 500°C, (d) 550°C and (e) 600°C (reproduced from ref 19).

Yang *et al.* described another approach for obtaining *fct* FePt NPs from Pt/Fe_2O_3 core-shell NPs (23). The core-shell NPs deposited on a thin amorphous carbon support were converted to *fct* FePt NPs through a reduction under H_2 at 550ºC. Efforts have been also devoted to prevent coalescence during the post-annealing process (24-26). Liu *et al.* mixed the as-synthesized *fcc* FePt NPs with NaCl powders and annealed them at 700ºC (24). The NaCl was then removed by washing with water. The monodispersed *fct* FePt NPs exhibited a coercivity up to 30 kOe at room temperature, and retained their initial size and shape, in spite of the observation of a polycrystalline morphology. Sun *et al.* protected the FePt NPs from sintering at high temperature by coating them with MgO (25). The robust MgO coating could limit atom mobility thus preventing coalescence. However the conversion from *fcc* into *fct* FePt NPs required a high temperature annealing and this was more difficult than for the non-coated NPs. Finally, the *fct* FePt NPs obtained from the annealing at 750ºC for 6h show a coercivity of 10 kOe at room temperature and a magnetization of 56.4 emu/g. The MgO can be removed by acid washing, causing a small reduction in the Fe content of the alloy.

Alternatively, silica-coated ordered FePt NPs (4-20 nm) were reported by Ramanath *et al.* (26). Organized assemblies formed from the FePt/silica core-shell NPs present a coercivity of 8500 Oe upon annealing to 650ºC for 1h, without notable changes to the overall size and shape of the NPs. Operating in a high viscosity solvent, PEG-600 (polyethylene glycol), Migliori *et al.* obtained monodispersed *fcc* FePt NPs (5.7 nm), which were trapped into an amorphous matrix, derived from solvent condensation/decomposition, without aggregation (27). A further thermal treatment at 650ºC for 3h leads to the structural properties of the $L1_0$ FePt NPs with a coercivity of 2500 Oe. However, heat treatments at higher temperatures result in a significant reduction of the coercive field.

In addition to the *fct* magnetic bimetallic NPs, magnetic nanowires (NWs) have also attracted great attention due to their high shape anisotropy that can lead to high coercivity as well. Porous alumina templates have been used for the preparation *via* electrodeposition of transition metal NWs, such as Fe, Co, Ni, and their alloys (28-39), by which metals and alloys are electrochemically deposited into the templates and adopt the template morphology. Among them, FePt and CoPt NWs are ideal candidates due to their potential in ultrahigh-density magnetic data storage devices, since they can present high magnetocrystalline as well as high shape anisotropy. Furthermore, the alumina templates allow keeping the shape of the NWs during thermal treatment during phase transformation. The alumina template can be simply removed by dissolving in NaOH aqueous solution in order to obtain NWs. By this process, CoPt (38), FePt (38) and $CoPt_3$ (39) NPs with diameter of around 60 nm have been produced.

It is known that the crystallographic structure, chemical composition, diameter, and aspect ratio of the NWs affect their magnetic properties (33). Reducing the diameter raises the coercivity.

CNTs possess hollow cavities of various diameters, which can serve as templates for producing magnetic NWs and NRs (40-47). However, Pt-based magnetic NWs have not yet been formed inside CNTs. Therefore, in our study, we focus on the possibility to form CNT-confined Pt-based bimetallic nanostructures. In addition confinement may give the opportunity to directly form elongated forms of these materials and allow annealing in a template that may guarantee the shape conservation. Furthermore an interaction with the CNT walls may modify the phase transition temperature.

IV.2 Pt-based magnetic nanostructures

Our previous results from the confinement of monometallic Fe and Co nanoparticles in CNTs have clearly shown that the presence of aromatic ligands was necessary for the confinement to succeed. In a preliminary step we have examined the possibility of forming Co-Pt NPs in the presence of the aromatic ligands, by the co-decomposition of two monometallic precursors, namely $[Pt(CH_3)_2(COD)]$ (COD=1,5-cyclooctadiene) and $[Co\{N(SiMe_3)_2\}_2(THF)]$.

The same nomenclature as the one used in the previous chapters will be used throughout this one also. The starting solution was prepared as described in the experimental part. As we have seen in Chapter II, the addition order and the addition rate of the reactants during the preparation of the starting solution can influence the reaction outcome. We have therefore added the reactants in the same order and we added the metal precursors to the solution by a dropwise addition in all the experiments unless otherwise stated. The addition order "BBA+Pt+PPP+M (Co or Fe)", means that a Pt precursor solution was added dropwise to a solution of BBA. To this solution a solution of PPP was fast added and the magnetic metal precursor solution was finally added dropwise to the mixture.

For cobalt, the target alloy was the CoPt. Therefore, in a first approach, the Pt/Co ratio was meant to be fixed to 1. However, at that time, we did not know that the Co precursor contained a THF molecule. In fact, it was only towards the end of the thesis that we have realized that the Co precursor contained a molecule of THF (48). This error has been taken into account and the ratios presented throughout the thesis are the real ones.

The first reaction performed was the reaction "Pt_0.84Co_BBA_PPP_Mes_150°C_ 24h". After heating for 24h under 3 bar of H_2, big aggregates (> 100 nm) of NPs and very small NPs (about 1 nm) were obtained (Figure IV.3a). The former were stuck on the surface of the stirring bar and the latter were in the suspension. The formation of the aggregates indicates an insufficient stabilization or too much heating. The aggregates were isolated from the colloidal solution and washed with toluene. The XRD pattern of the aggregate displays a phase very similar to Pt, but with a slight shift to high angles, indicating the presence of a small amount of Co in the sample (Figure IV.3b). Thus, the reaction with a higher amount of stabilizing ligands "Pt_0.84Co_2BBA_2PPP_Mes_150°C_24h" was performed, producing less aggregates and more NPs (Figure IV.3c).

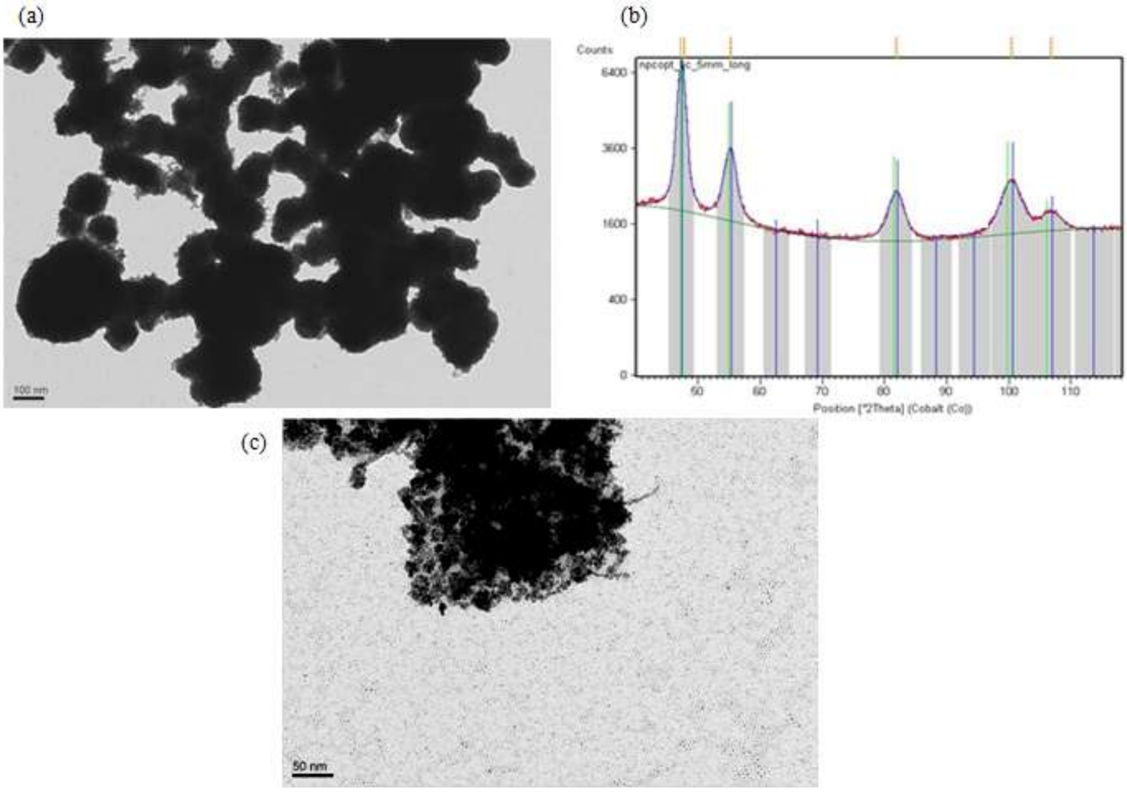

Figure IV.3: (a) TEM image of "Pt_0.84Co_BBA_PPP_Mes_150°C_24h" and (b) XRD pattern of (a); (c) TEM image of "Pt_0.84Co_2BBA_2PPP_Mes_150°C_24h".

By decreasing the reaction temperature to 100°C, we succeed to avoid the formation of aggregates, and small NPs (d= 2.5±0.2 nm) were formed (Figure IV.4a). Compared to the previous aggregates, the NPs are much smaller, corresponding to very broad peaks in the XRD pattern (Figure IV.4b), in spite of which, the sample seems to be still close to Pt as in the previous aggregates. EDX analysis of the toluene washed NPs shows that the Co composition is not homogenous, ranging from 19-66% (Figure IV.4c).

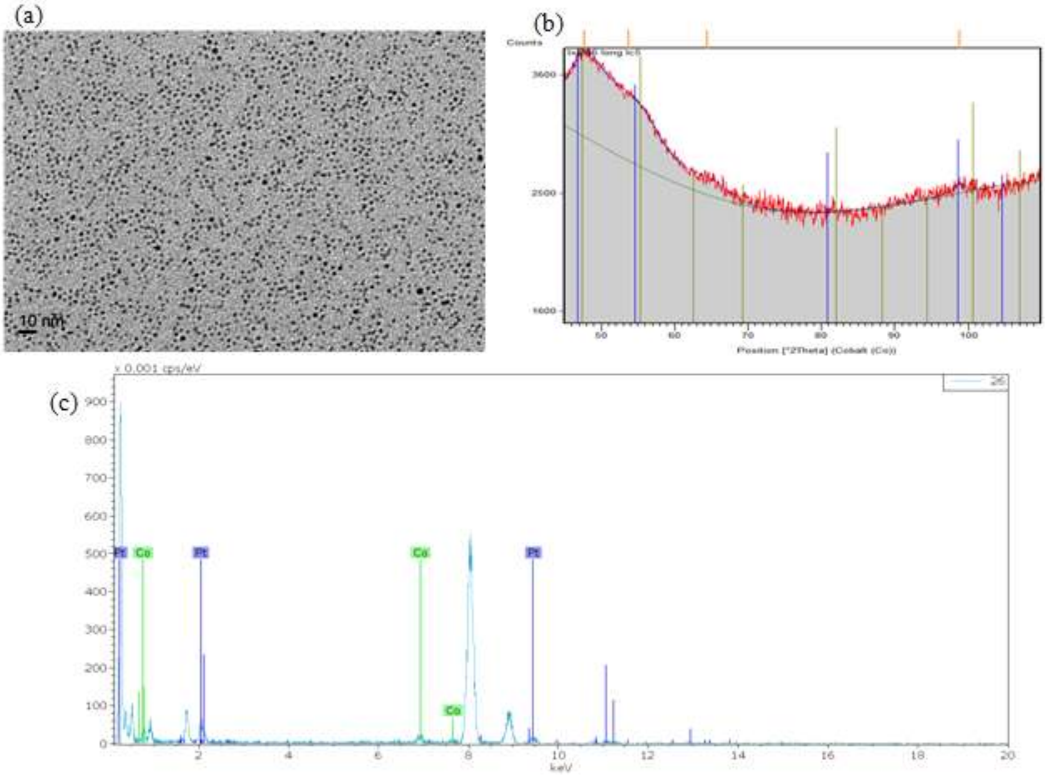

Figure IV.4: (a) TEM image of "Pt_0.84Co_2BBA_2PPP_Tol_100°C_24h"; (b) XRD pattern of the NPs in (a); (c) EDX analysis of the washed NPs.

IV.3 Pt-based magnetic nanostructures confined within f-CNT1

The confinement of the above mentioned pre-formed Co-Pt NPs has not been attempted in f-**CNT$_1$** because of the large diameter of these tubes that will negatively influences the possible confinement effects. The confinement of preformed Co-Pt NPs was attempted only in f-**CNT$_2$**. These results will be presented in section IV.3. In order to explore the *in situ* confinement of NPs in the presence of the f-**CNT$_1$** we have decided to use the same reaction conditions, as for the synthesis of Co-Pt NPs in the absence of CNTs ("Pt_0.84Co_2BBA_2PPP_Tol_100°C_24h"). Interestingly, it was found that small NPs (2-4 nm) were present in some large diameter CNTs (Figure IV.5a-b), whereas big NPs formed by coalescence are present inside the thinner CNTs (Figure IV.5c-d). These latter tend to aggregate and /or coalesce towards wire like structures. STEM (scanning transmission electron microscopy) analysis indicates that the regions where coalescence occurs are Pt-rich, while the small NPs are Co-rich (Figure IV.5e). EDX analysis shows a composition of 22%/78% Co/Pt for the coalesced NPs and a composition of 75%/25% Co/Pt for the small NPs. According to the TEM observations and the EDX results, different nanostructures seem to be preferentially formed depending on the environment, *i.e.* the CNT cavities with different diameters. In the large cavity (d_{inner}=170 nm) (Figure IV.5a,b) the environment is similar to that outside the tube. Consequently, the confinement effect is negligible, resulting in confined NPs having the same aspect as those outside the tube in terms of size and composition. In contrast, the confinement effect seems to play an important role in smaller nanotubes, which favor the compact wire-like morphology. Interestingly, it is not only the NP size that is affected by the CNT diameter, but the composition as well. The reason why different compositions are obtained depending on the CNTs diameter is hard to explain based on these results. However, we may think that this could be connected to the affinity of the precursors towards the CNT channels. Since Pt is found to be in excess with respect to Co in the small CNTs, this means that Pt species are able to enter the channel easier than Co.

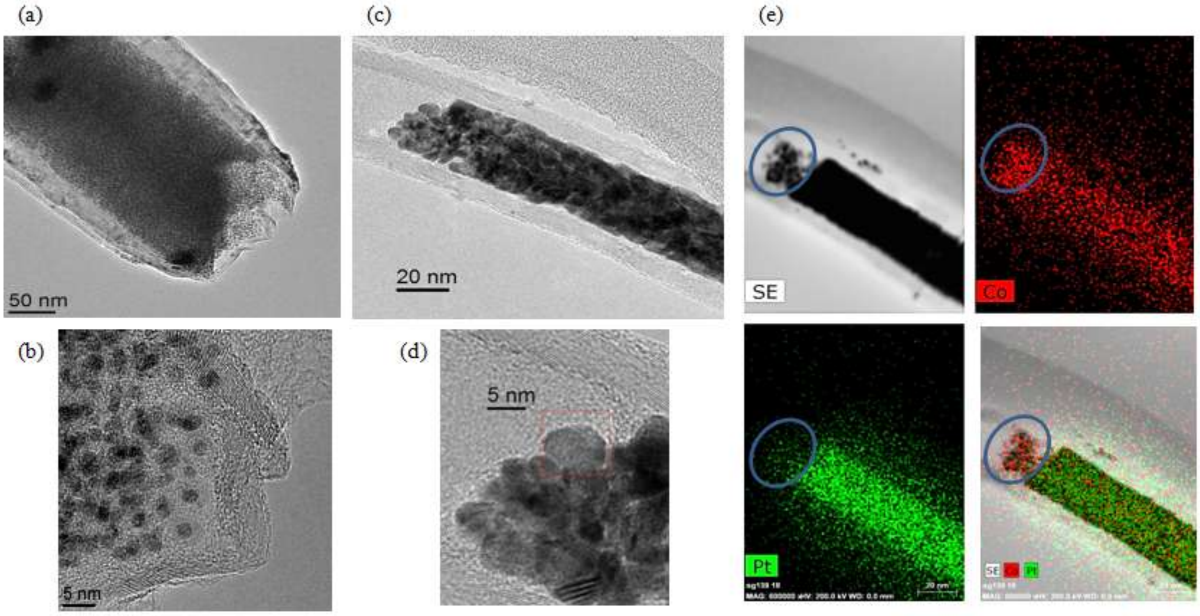

Figure IV.5: (a-b) TEM images of the confined NPs within the f-CNT$_1$ of larger diameter; (c-d) TEM images of coalesced NPs within the f-CNT$_1$ of smaller diameter; (e) STEM analysis of the content of a tube containing both kinds of NPs (blue cycle highlight the small confined NPs rich in Co).

We will see later on that dimeric cobalt species can form in solution. The size and the stability of these species could be an explanation of the low Co/Pt ratio of the nanostructures confined in small diameter CNTs.

Some CNTs were also coated by a layer of metal around their outer surface (Figure IV.6). The presence of these metal-coated CNTs rendered useless any further analysis of the sample, because they cannot be removed or separated from the targeted CNT-confined NPs.

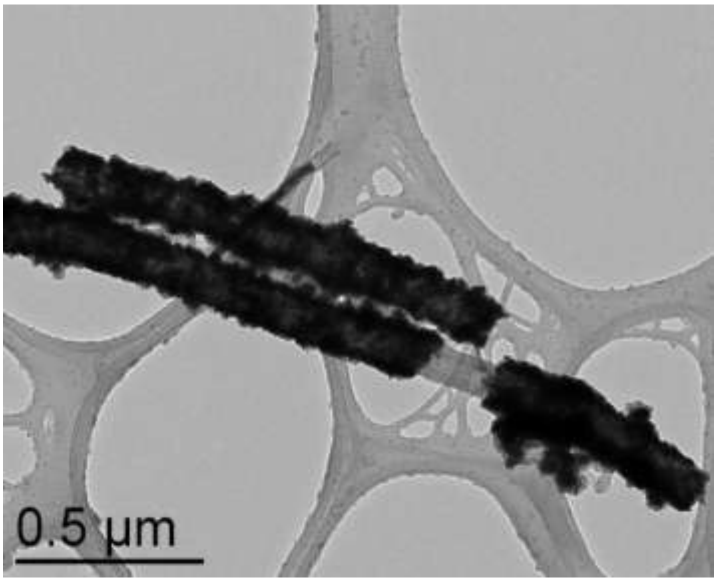

Figure IV.6: TEM image of the metal-coated f-CNT$_1$.

In conclusion, we have synthesized Co-Pt NPs (~1.5 nm) under mild conditions "Pt_0.84Co_ 2BBA_2PPP_Tol_100°C_24h", which seem to adopt a structure close to Pt. Under the same conditions, but in the presence of the f-**CNT$_1$**, the morphology and composition of the confined nano-objects depends on CNT diameter. Within large diameter CNTs, small Co-rich NPs (2-4 nm) are formed both inside and outside the tubes. These NPs are bigger than the NPs synthesized in the absence of the CNTs (1.5 nm). On the other hand, coalescence of Pt-rich NPs occurs inside the CNTs with small diameters. These Pt-rich coalesced particles tend to form NW-like objects, which may be attributed to a confinement effect. This preliminary experience reveals that CNT diameter contributes considerably to confinement effect, and thus affects directly the morphology and the composition of the confined materials. This inhomogeneity of the material within the same sample, which is due to the inhomogeneity of the f-**CNT$_1$** diameters was clearly an obstacle to the exploration of the magnetic properties of the material. Thus, we decided not to apply the *in situ* method for the formation of Fe-Pt NPs f-**CNT$_1$**. We have chosen to focus our efforts on the f-**CNT$_2$**, which have more homogeneous and smaller diameters, therefore we would expect a more homogeneous compositions of the resulting nanomaterials.

IV.4 Pt-based magnetic nanostructures confined within f-CNT2

First, encapsulation of the pre-formed Co-Pt NPs within the f-**CNT$_2$** was attempted *via* the suspension method. From the TEM images, it is difficult to determine the confinement efficiency since the NPs are too small and most them seem to be deposited on the outer surface of the CNTs.

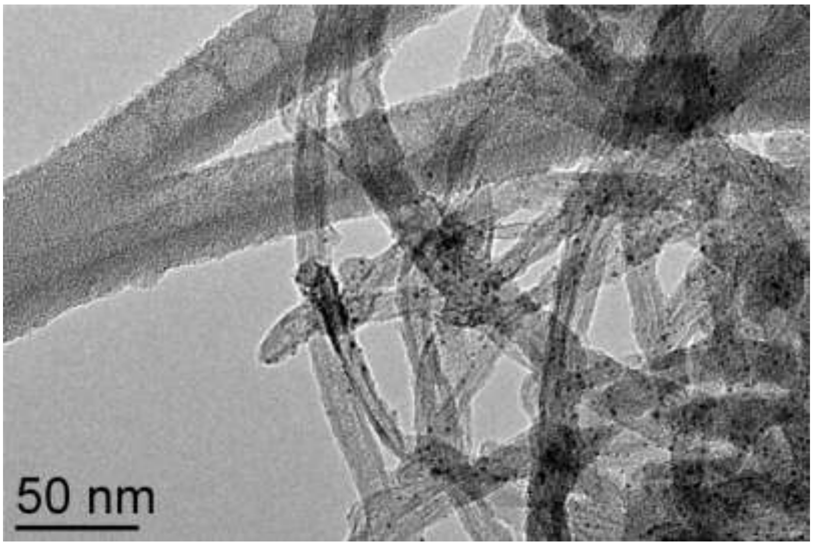

Figure IV.7: TEM image of the pre-formed Co-Pt NPs attached on the f-CNT$_2$.

Therefore, we have decided to synthesize directly the NPs in the CNTs through the *in situ* solution method.

IV.4.1 Co-Pt nanowires templated within f-CNT2

IV.4.1.1 Preliminary experiments

The reaction "Pt_0.84Co_2BBA_2PPP_Tol_100°C_24h" was carried out in the presence of the f-**CNT$_2$** by mixing a colloidal solution of f-**CNT$_2$** in toluene with the starting solution prepared as described in the experimental section. The addition order and rate were kept as described in the previous section. The mixture was then charged with 3 bars of H_2 under rapid stirring. After 24 h at 100°C, a TEM grid was prepared with the as-synthesized colloidal solution, which contained the CNTs. In Figure IV.8, several kinds of nanostructures can be observed. We observe the presence of long NWs in the interior of the CNTs, empty CNTs, and polydispersed NPs (2.5-7 nm) attached on the CNTs external surface. The presence of long NWs in the small diameter f-**CNT$_2$** confirms the confinement effect previously observed for **f-CNT$_1$**.

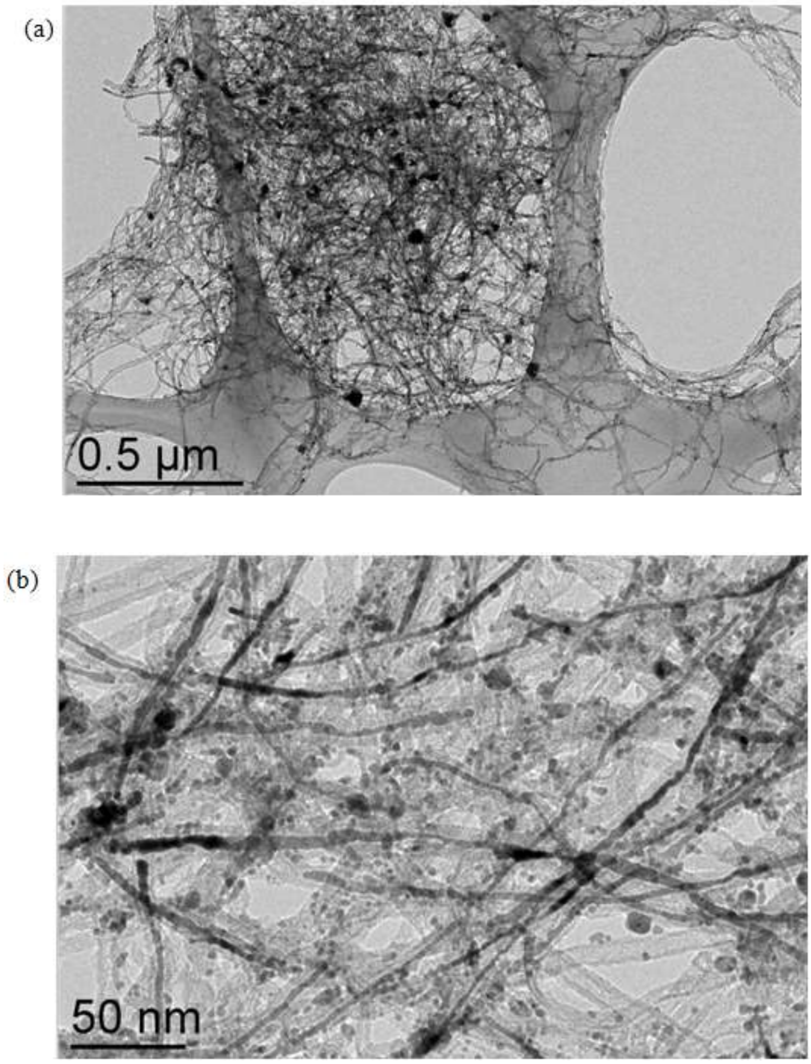

Figure IV.8: (a-b) TEM images of the CNT-templated Co-Pt NWs and the polydispersed NPs attached on the outer surface of the f-CNT$_2$.

The precipitate was then separated with the aid of a permanent magnet from the as-synthesized colloidal solution, and washed with toluene and pentane. The precipitate presents the same features as the colloidal solution as verified from TEM images, while in the supernatant the existing CNTs seem to be less filled than those in the precipitate.

Consequently, the solvent-washed and dried precipitate was analyzed by HRTEM, STEM-EDX, and XRD (Figure IV.9, IV.10 and IV.11). As observed by HRTEM (Figure IV.9), the NWs are well crystallized with crystal parameters that are close to the ones of Pt. It has to be noted that HRTEM cannot unambiguously confirm the presence of Co since the lattice parameters of Pt and Co-Pt alloys are very similar.

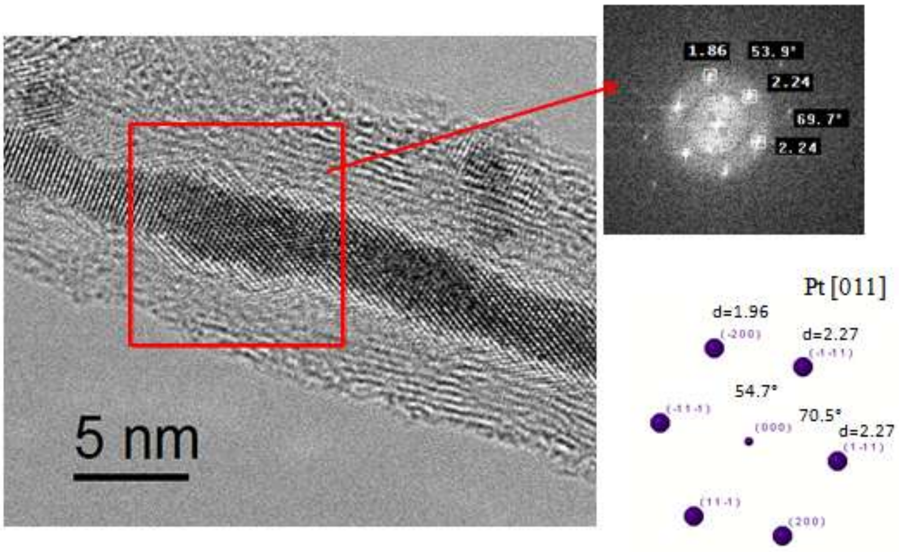

Figure IV.9: HRTEM image of a continuous Co-Pt NW; fast Fourier transform (FFT) indicates a structure close to Pt.

STEM-EDX analysis shows that the NWs are Pt-rich with a Co content around 18% (at), and that the NPs outside the tubes contain more Co with varied compositions (55-75%) (Figure IV.10).

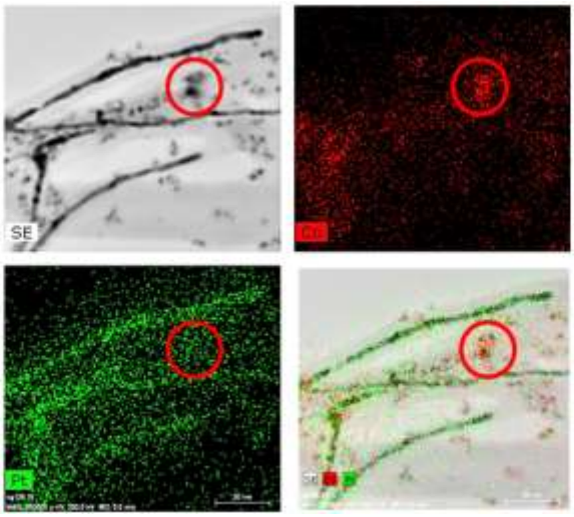

Figure IV.10: STEM analysis of the sample on a TEM grid. The zone highlighted by the red cycles corresponds to a coalescence of NPs that is rich in Co, whereas the NW zones are rich in Pt.

In the XRD pattern, the principle peaks are attributed to a structure that is almost identical to Pt (Figure IV.11). The broad peaks on the left side correspond to the kapton (a polyimide film) from the XRD sample holder and the CNTs in the sample. In addition, two peaks of small intensity can also be observed, corresponding to a phase similar to the cubic Co phase.

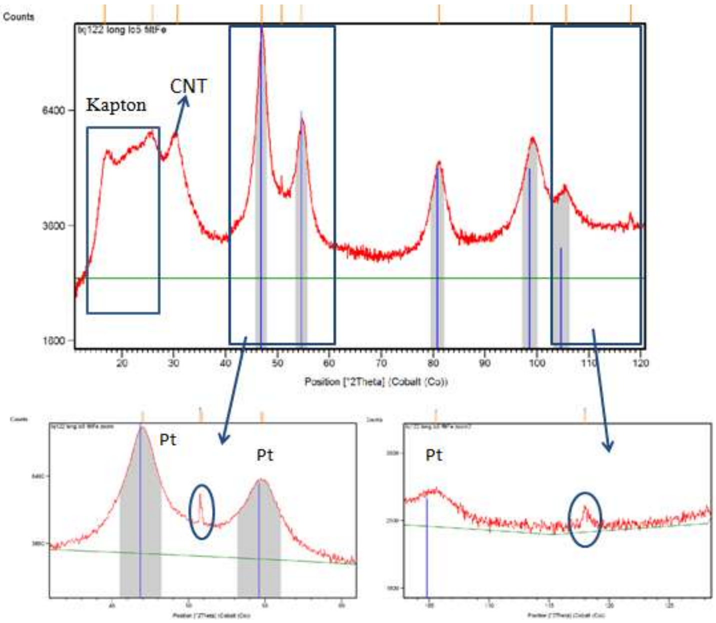

Figure IV.11: XRD patterns of the Co-Pt NW, with two magnifications of the zones where peaks of a Co-rich phase are indicated.

Based on these analyses, this sample consists of a Pt-rich Co-Pt phase that corresponds to the NWs inside f-**CNT$_2$**, and Co-rich NPs and their aggregates outside. The NPs and the aggregates outside the CNTs prevent further study and analysis of the magnetic properties of the NWs. Thus, subsequent removals by washing treatments were attempted.

The sample was re-dispersed in toluene and sonicated, before removal of the supernatant. This treatment was repeated three times. However, TEM images showed that the NPs are always present, indicating that they are not simply adsorbed on the outer surface of the CNTs *via* van de Waals forces.

The sample was then washed with a HCl/ether solution accompanied by ultra-sonication. The supernatant developed a blue color, which can be related to Co soluble species formed in solution by HCl etching. The washing was repeated until the supernatant was nearly colorless. After washing with ether and dried, the HCl-washed sample still presented a weak magnetism as verified by permanent magnet. In the XRD pattern, the low intensity peaks present before HCl washing are absent (Figure IV.12a). Meanwhile, as seen by TEM most of the small NPs disappeared, however the bigger NPs are still present (Figure IV.12b).

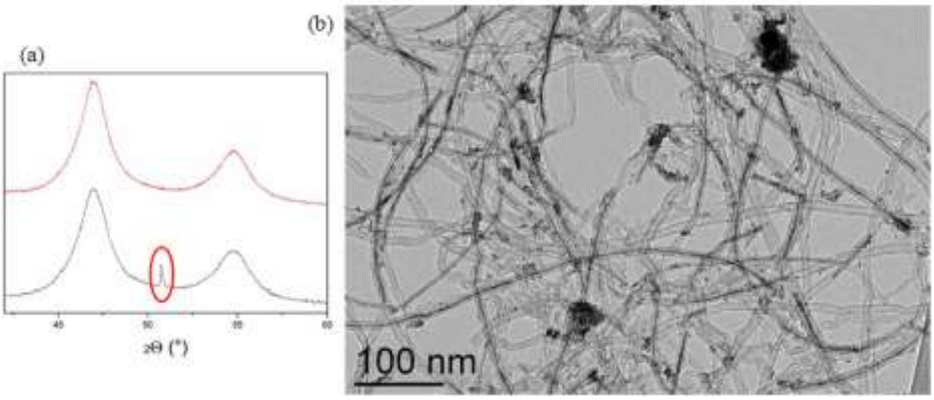

Figure IV.12: (a) XRD pattern of the sample after HCl washing (red) and before washing (black). We can note the absence of the Co phase (red cycle); (b) TEM image of the HCl washed CNT-templated Co-Pt NWs.

The STEM-EDX analysis shows that the Co compositions in both NWs NPs decreases compared to those before HCl washing, from 18% to 12-17% for the NWs and from 56-76% to 24-68% for the NPs (Figure IV.13). We can therefore conclude that HCl washing removes part of the Co content in the entire sample. However, many large NPs are still present as shown by TEM.

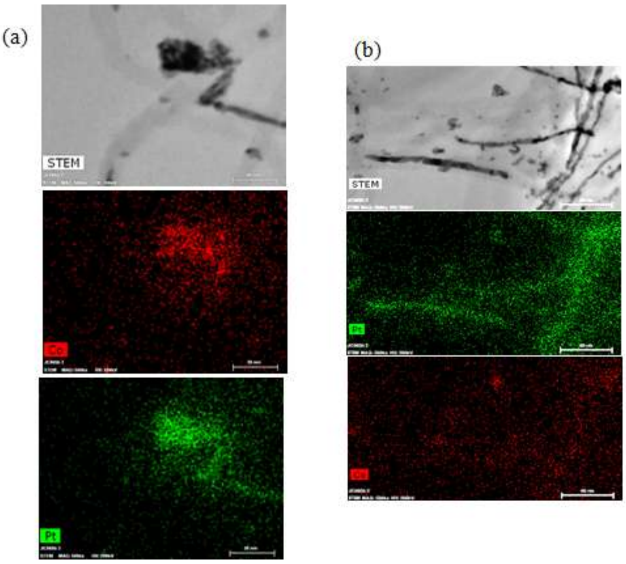

Figure IV.13: STEM-EDX analysis of HCl washing sample.

Another washing was tried with an *aqua regia* solution. After 2 min, the solid was rinsed with distilled water and ether, then dried in air. We observed that the residue was not attracted by a magnet anymore. From the TEM images (Figure IV.14a), the NPs are completely removed. It seems that the NWs are well protected by the CNTs since they are still crystallized as observed by HRTEM (Figure IV.14b). Nevertheless, the Co content is reduced to only 1-7% on the basis of the EDX analysis (Figure IV.14c).

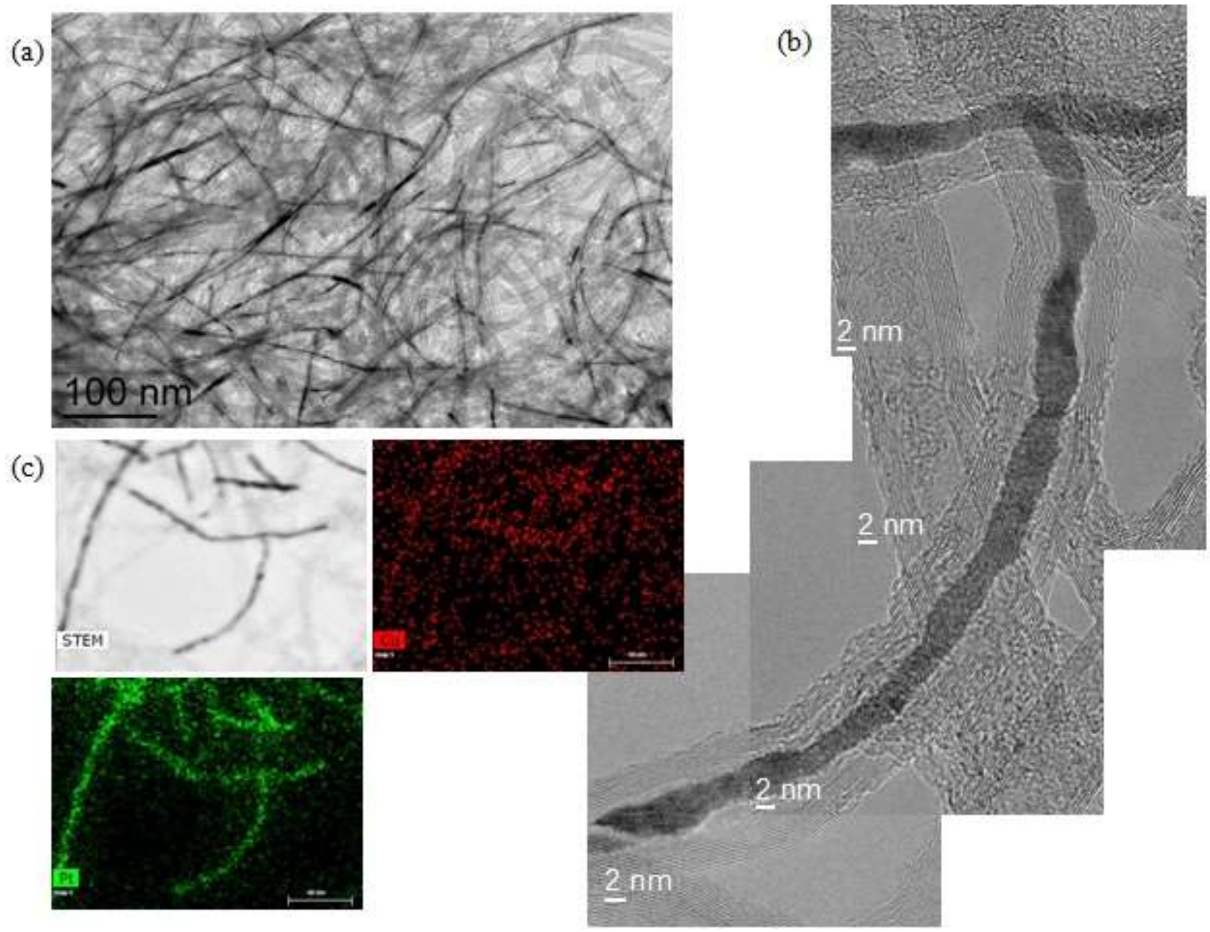

Figure IV.14: (a) TEM image of the CoPt NWs washed with *Aqua regia* solution; (b) combination of HRTEM images of a continuous Co-Pt NW inside the CNT; (c) STEM-EDX analysis of this sample.

The removal of the NPs outside the CNTs is expected since they come into direct contact with the strong acid. However the NWs should be protected from the acid by the CNT templates. The NW structure remains as that before washing as confirmed by HREM (Figure IV.14b), indicating that the *aqua regia* solution does not destroy its structure after 2 min. Even though, part of the Co, that was supposed to be inside the CNTs by the EDX analysis, seems to have been removed by the acid treatment. The decrease of the Co content after acid washing could be explained by two phenomena: i) either a selective removal of Co from the alloyed nano-objects, or ii) an overestimation of the Co content in the NWs. Selective leaching due to acid washing in bimetallic nanoparticles (PtNi, PdNi, PtCo) has already been reported (49-51).

The initial overestimation could be due to the fact that some molecular Co species could be attached on the outer surface of the CNTs. The NW formation monitoring was carried out by modifying the reaction time. Reactions were performed during 1 h, 3 h, 24 h and 48 h. The results are presented in the TEM images of Figure IV.15. We see that only a few NWs are formed after 1h reaction, and more NWs are presented after 3 h. At the end of 24 h, more NWs are observed than after 3 h. Extended to 48 h, the filling is not improved compared to a 24 h reaction, while more NPs are presented outside the CNTs. Therefore, we suggest that the NW formation is terminated after 24 h or even earlier. Extending reaction time to 48 h does not favor more NW formation but results in more undesired NPs outside the CNTs.

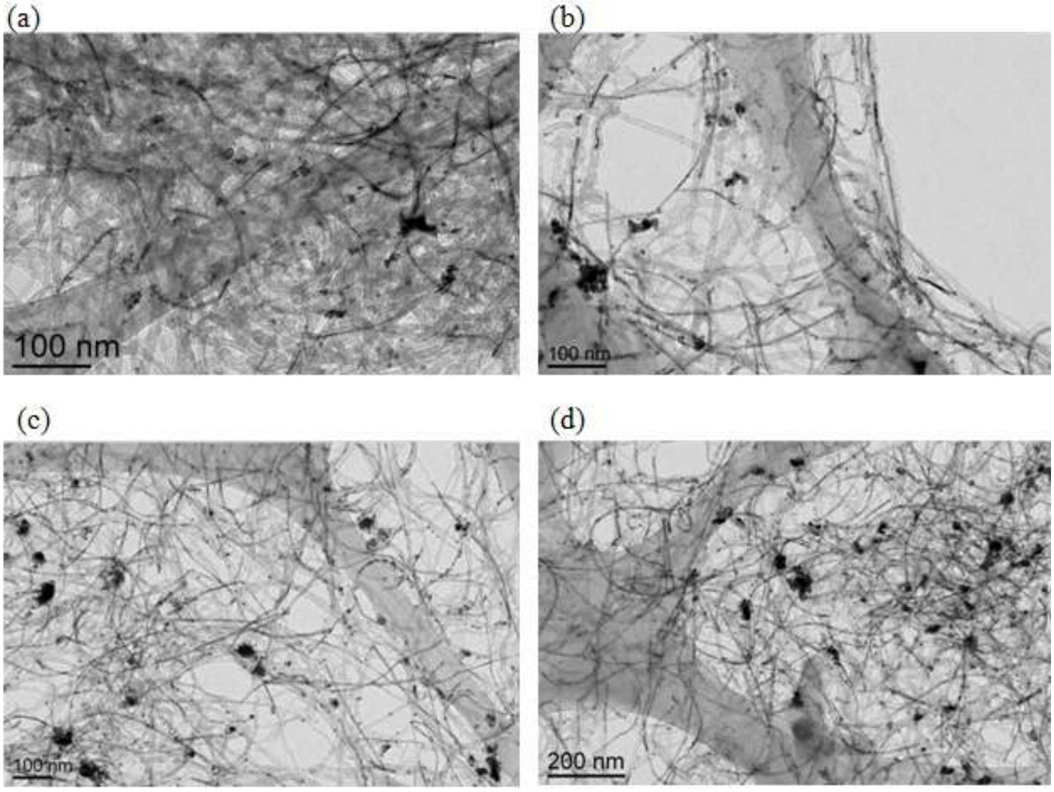

Figure IV.15: TEM images of "Pt_0.84Co_2BBA_2PPP_Tol_100°C" during (a) 1h, (b) 3h, (c) 24h and (d) 48h.

The formation of Co-Pt NWs by taking advantage of the CNT template effect *via* the *in situ* solution method was a very interesting result and has never been reported before in the literature. Indeed, apart from the fact that undesired NPs and aggregates were generated simultaneously outside the CNTs, the metal contents of the structures formed inside and outside the CNTs are not the same. This phenomenon is very intriguing. We have already observed in the case of f-**CNT$_1$** that the composition and the shape of the Co-Pt NPs depend on the CNT diameter. More importantly, a Pt-rich material is formed in the interior of the CNTs, whereas cobalt prefers to stay outside. Figure IV.16 show the evolution of the atomic Co content (in %) in the confined NWs according to CNT mean inner diameter (from f-**CNT$_1$** and f-**CNT$_2$**. An almost linear correlation is obtained.

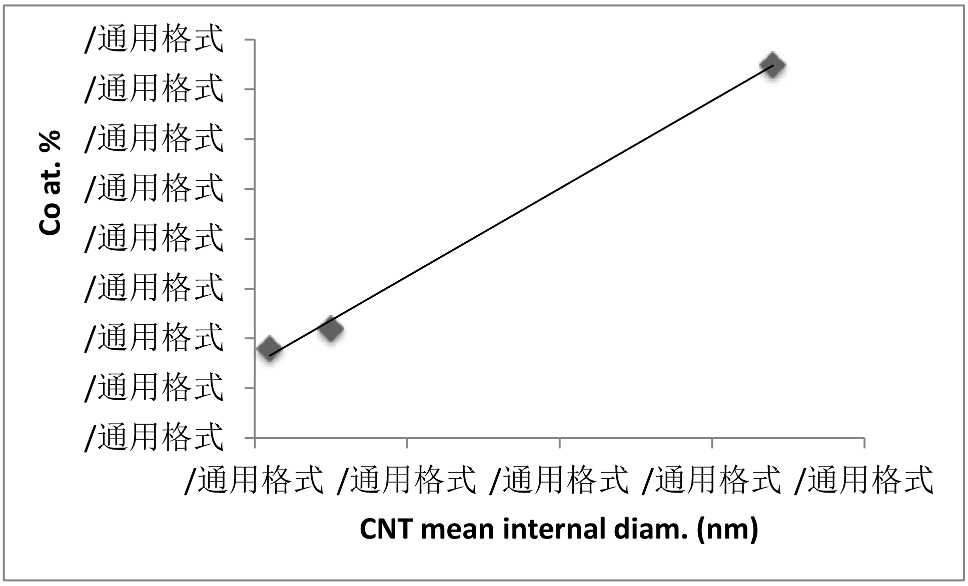

Figure IV.16: Evolution of the atomic Co content in the Co-Pt NWs accordant to CNT mean inner diameter.

It has to be noted that the magnetic properties of the ordered phase $L1_0$ are optimized when the atomic composition is close to 50:50 M/Pt (M= Co, Fe) (52), presenting the highest anisotropic feature. It was therefore of interest i) to increase the Co content in the NWs and ii) to produce NWs selectively without NPs being present in the same sample. For this, it would be important to try to understand how the formation of the NWs takes place. We have therefore studied the impact of several experimental parameters on the formation of the NWs in order to detect the parameters that affect the reaction outcome.

The experiment "Pt_0.84Co_2BBA_2PPP_Tol_100°C_24h" was chosen as a basis for this study, and we varied successively the conditions of this reaction.

IV.4.1.2 Effect of the modification of the reaction parameters

In this section, we present the effect of the variation of certain reaction parameters on the reaction outcome. Our objective was to try to understand why the two metals are not homogeneously distributed in the NWs and whether we can modify the reaction parameters towards an increased Co content in the confined Co-Pt NWs. From what we have seen up to now we could attribute this effect to different reasons. One possibility is that all the Co does not enter in the CNTs because it forms species that have not a good affinity with the CNTs channels. Another possibility is that at least a part of Co enters but in a form that is not easily reduced. If the latter hypothesis is valid, it means that different forms of Co are present in the solution, because, as we have seen in our preliminary experiments, Co is mainly present on the material at the exterior of the CNTs, which means that this part of Co, which stays outside can be as easily reduced as the Pt (inside or outside the CNTs).

—Experiments without Co

Cobalt let aside, we know that Pt does enter the CNTs. We therefore examined the possibility of forming pure Pt NWs by using only Pt either as a pure precursor or with the same ligands as the ones used in the preliminary experiment that gave rise to NWs. We present the results below.

For "1Pt_Tol_100ºC_24h", very large NPs are found outside the CNTs due to the absence of ligands. Nothing is observed inside the CNTs.

<table>
<tr><td colspan="2">1Pt_Tol_100ºC_24h</td></tr>
<tr><td>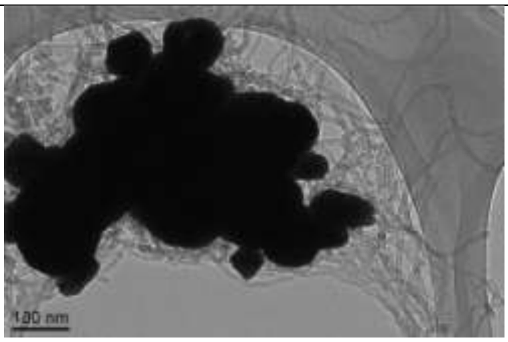
</td><td>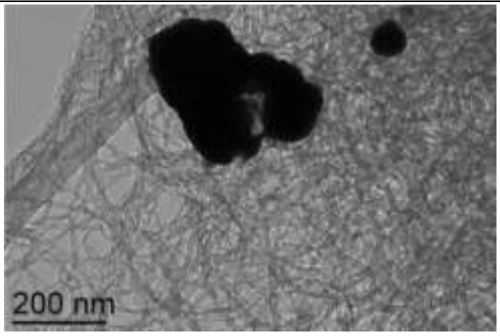
</td></tr>
</table>

This means that the aromatic ligands are necessary for the introduction of the Pt in the CNTs.

Pt has a very good affinity towards amine ligands. It is possible then that a PPP containing Pt complex is able to enter in the CNTs. So we have added 4 PPP equivalents to the Pt precursor and we performed the experiment.

1Pt_4PPP_Tol_100ºC_24h	
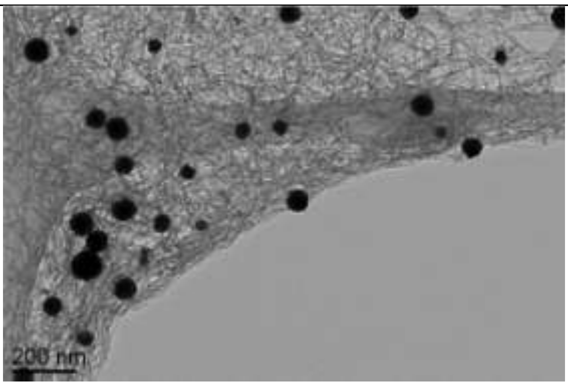	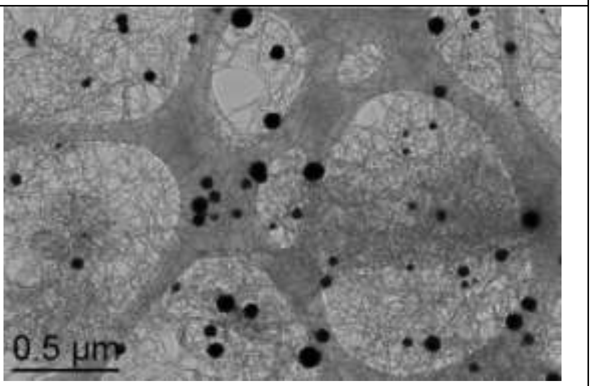

Therefore the addition of 4 equivalents of PPP gives rise to polydispersed NPs (55-100 nm) outside the CNTs while the CNTs remained empty. The NPs are smaller that in the absence of ligands but this experiment apart from the failure of complexes containing only PPP to enter and/or to be reduced into the CNTs, also indicates that PPP alone cannot stabilize small Pt NPs.

The next step was to use the other aromatic ligand BBA. Once again no NWs or NPs were formed in the interior of CNTs.

1Pt_4BBA_Tol_100ºC_24h	
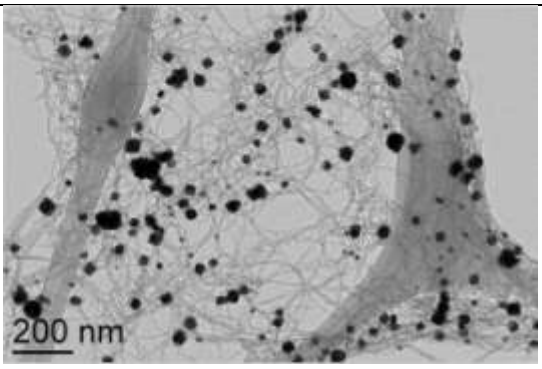	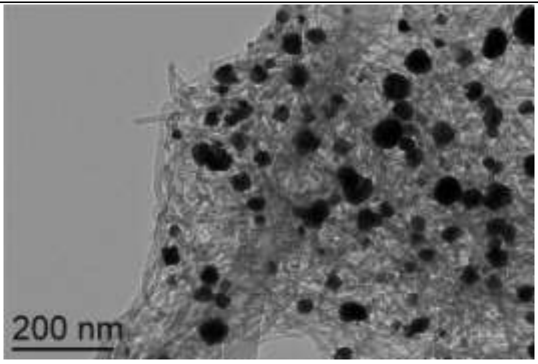

The NPs formed outside the CNTs are more polydispersed (15-100 nm), which indicates that neither BBA is able to stabilize small Pt NPs.

The reaction "Pt_2BBA_2PPP_Tol_100°C_24h" gave rise to irregular Pt NPs (10-37 nm) but no trace of NWs.

<table>
<tr><th colspan="2">1Pt_2BBA_2PPP_Tol_100ºC_24h</th></tr>
<tr><td>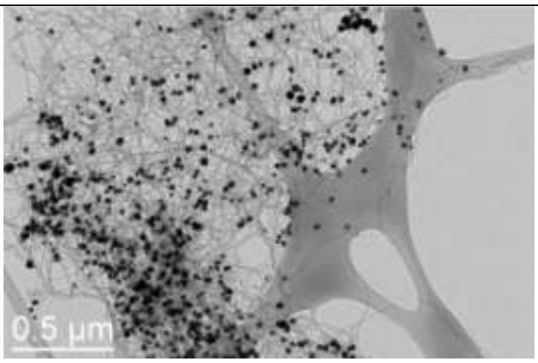
</td><td>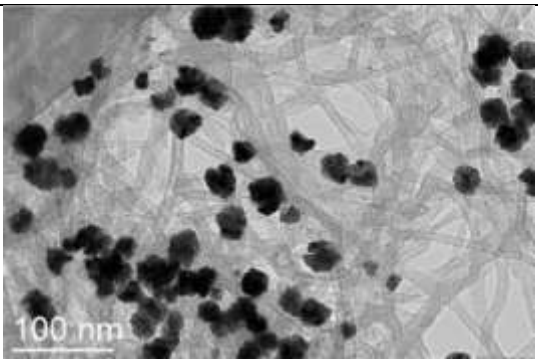
</td></tr>
</table>

Finally reducing the amount of the two ligands as "Pt_1BBA_1PPP_Tol_100°C_24h" leads also to Pt NPs (6-50 nm) outside the CNTs.

<table>
<tr><th colspan="2">1Pt_1BBA_1PPP_Tol_100ºC_24h</th></tr>
<tr><td>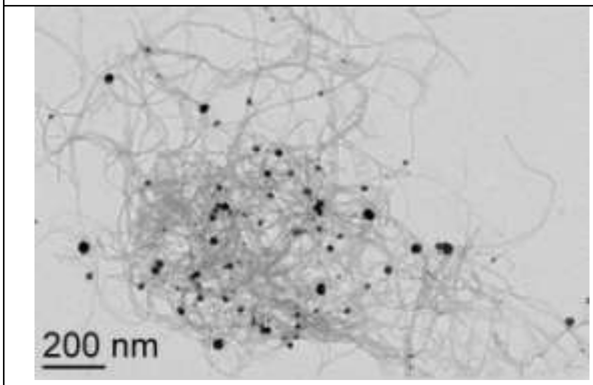
</td><td>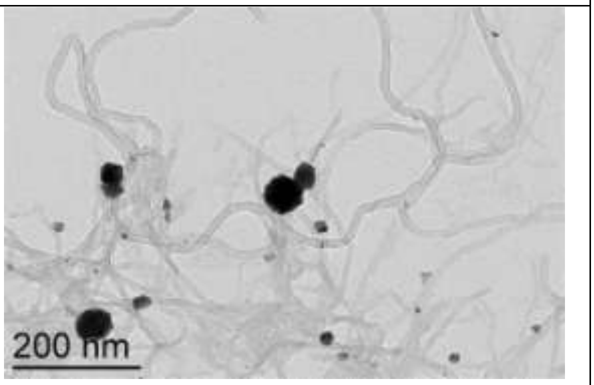
</td></tr>
</table>

Based on this series of reactions, we can say that BBA and PPP alone or in combination cannot give rise to any confined structure inside the CNTs. This means that something related to the presence of Co assists the entrance of Pt in the CNTs and the formation of NWs, since in its absence the CNTs are always empty. In addition none of these ligands favors the stabilization of small Pt NPs.

—Experiments without Pt

The same series of reactions were carried out without adding Pt but with Co only. The reaction without any stabilizing ligands (precursor alone) gives rise to NPs (4-6 nm) outside the CNTs. Nothing was observed in the interior of CNTs. The Co NPs can be stabilized with the amine HMDS liberated from the reduction of the [Co{N(SiMe$_3$)$_2$}$_2$(THF)] (53). However it is obvious that the HMDS alone cannot transfer Co in the interior of CNTs.

0.84Co_Tol_100ºC_24h

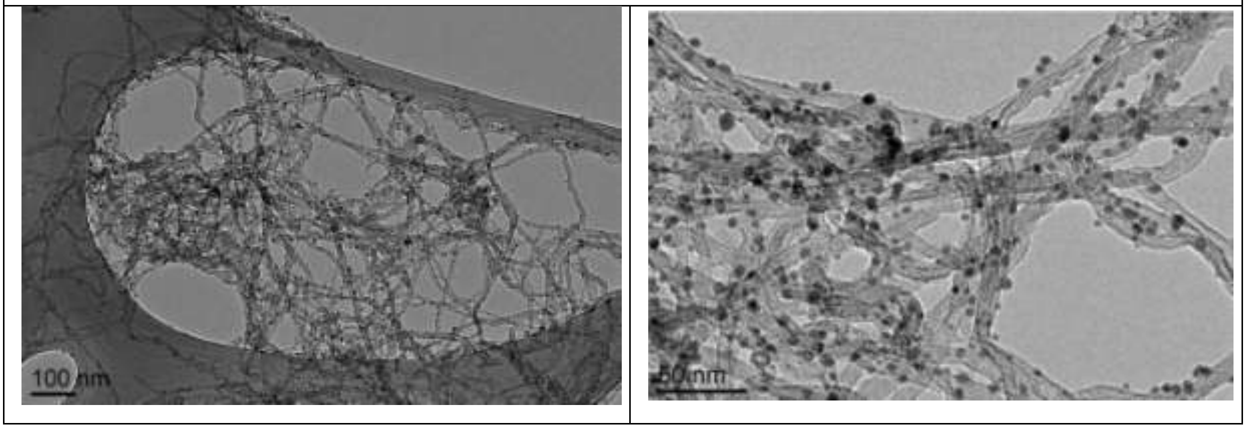

In the presence of 4 equivalents of BBA no nano-objects are detected inside or outside the CNTs. This may be due to the stability of Co carboxylates that cannot be decomposed at 100°C.

0.84Co_4BBA_Tol_100ºC_24h

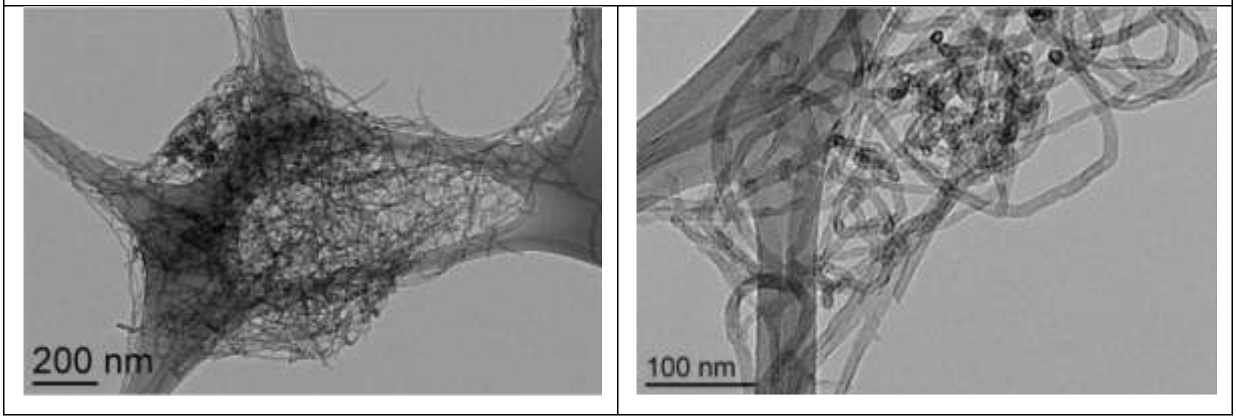

The presence of 4 equivalents of PPP results in NPs (5-15 nm) located outside the CNTs. This result is similar to the one obtained in the absence of any aromatic ligands. The HMDS alone seems to be able to stabilize Co NPs of a smaller size than the PPP and the HMDS together.

0.84Co_4PPP_Tol_100ºC_24h

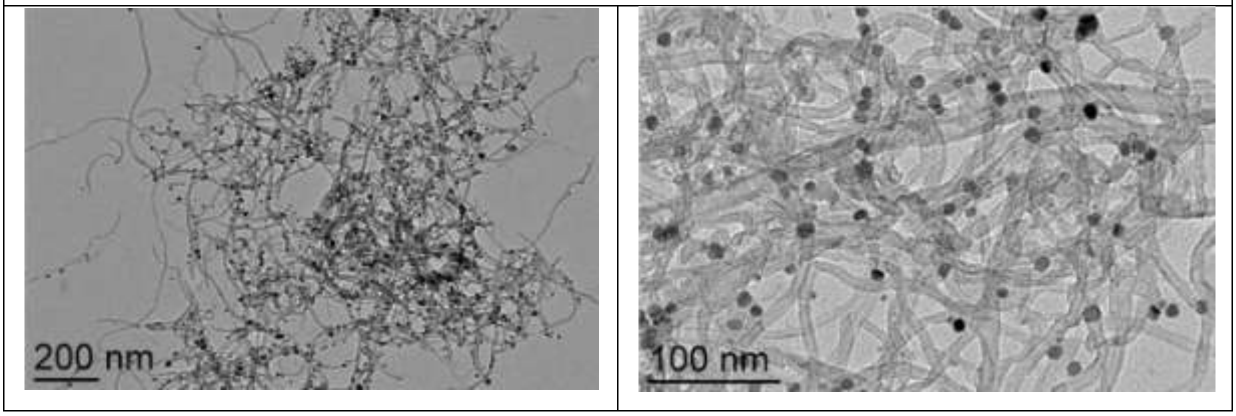

The reaction with 2 equivalents of BBA and PPP gives rise to the same observation as the case with only 4 equivalents of BBB, which implies that stable BBA carboxylates are the compounds formed even in the presence of 2 only equivalents of BBA and additional PPP.

0.84Co_2BBA_2PPP_Tol_100ºC_24h

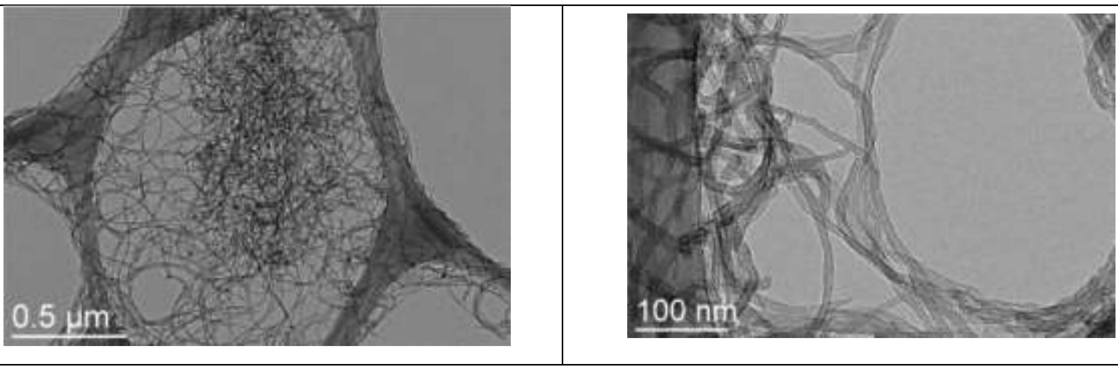

In the presence of 1 BBA and 1 PPP, nothing was observed in the interior of CNTs, however the cobalt particles formed outside are big and ill-shaped.

0.84Co_1BBA_1PPP_Tol_100ºC_24h

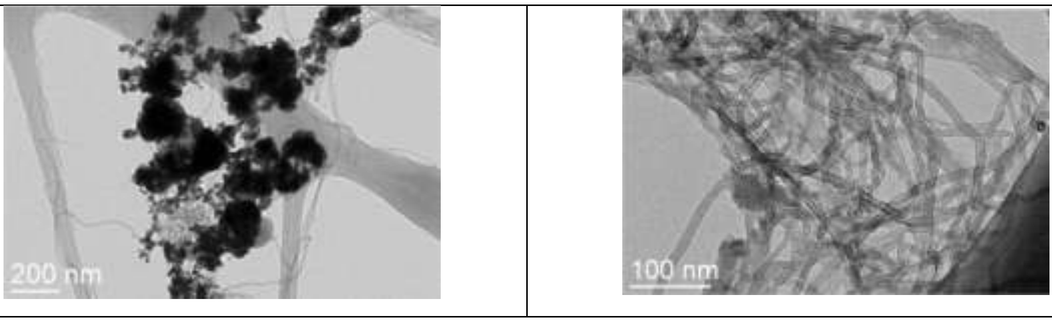

From the observations in this series of experiments, we can say that no nanostructure can be formed inside the CNTs when only Co is present. Indeed, Co in the presence of BBA and PPP alone or in combination or even in the presence of HMDS cannot enter and/or decompose in the CNTs cavity. In addition, Co has a very good affinity towards the aromatic acid ligands, presumably forming stable carboxylates that cannot be reduced at 100°C.

Taken together, the experiments performed up to now, point towards a necessary interaction between the two metal systems, in order for the NWs to be formed.

—Influence of the Pt/Co ratio

The Pt/Co ratio was decreased in order to promote the increase of the Co content in the NWs. We adjusted first the Pt:Co ration to 1:1. No significant difference is observed by TEM. Unfortunately no EDX or XRD analyses were possible for this series. However, when the Co amount raises to 1.7 equivalents, much less NWs are formed inside the CNTs, and much more numerous NPs are formed outside the tubes. This indicates that simply increasing the Co amount hinders the NW formation.

1Pt	2BBA	1Pt_1Co_2BBA_2PPP_Tol_100ºC_24h
1Co	2PPP	
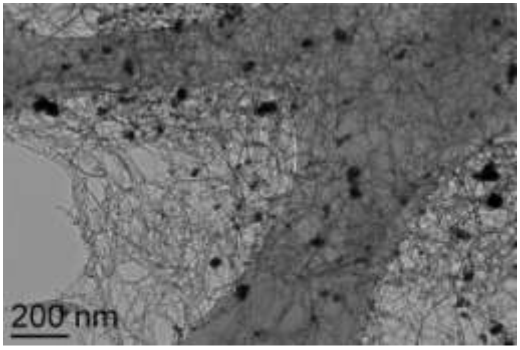		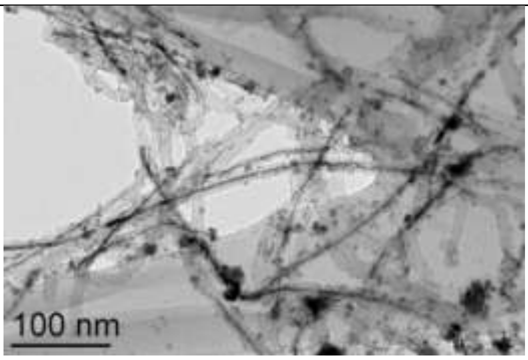
1Pt	2BBA	1Pt_1.7Co_2BBA_2PPP_Tol_100ºC_24h
1.7Co	2PPP	
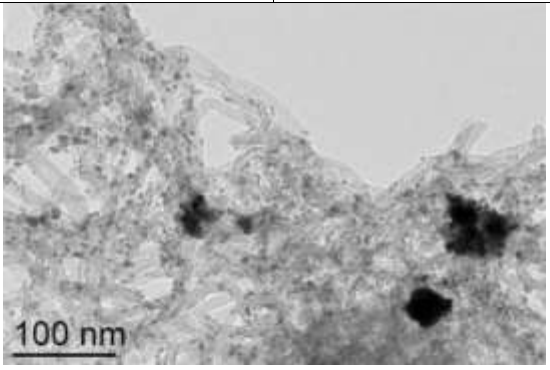		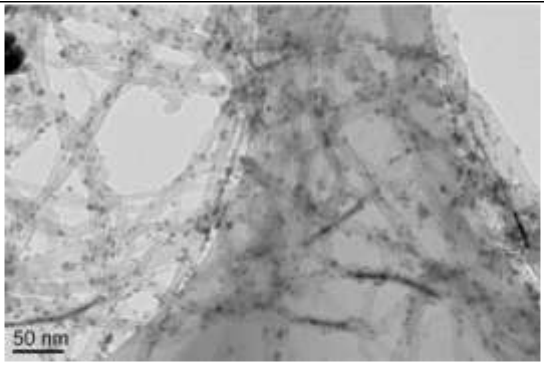

—Effect of temperature

We think that certain stable Co species (carboxylate-rich compounds) were harder to decompose than Pt compounds. It was possible that some Co-BBA species were able to enter the CNTs, but remained in a molecular formed, un-reduced due to their increased stability. In order to verify this, we have increased the reduction temperature in order to favor the reduction of these stable compounds. Two reactions were respectively performed at 120ºC and 150ºC. Much more NPs and aggregates of NPs are presented at 120°C and at 150ºC, which make the sample impossible to perform a reliable analysis by EDX .

<table>
<tr><td>1Pt</td><td>2BBA</td><td rowspan="2">1Pt_0.84Co_2BBA_2PPP_Tol_120ºC_24h</td></tr>
<tr><td>0.84Co</td><td>2PPP</td></tr>
<tr><td colspan="2">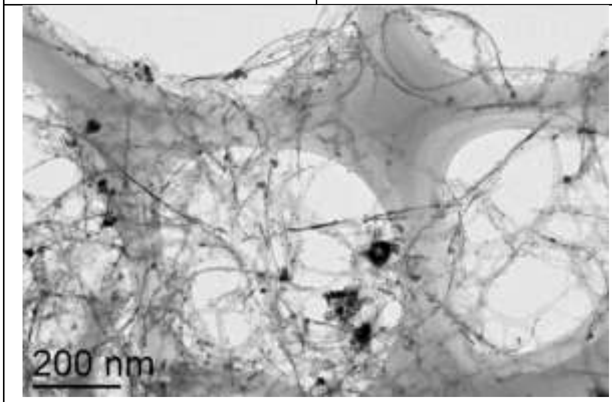
</td><td>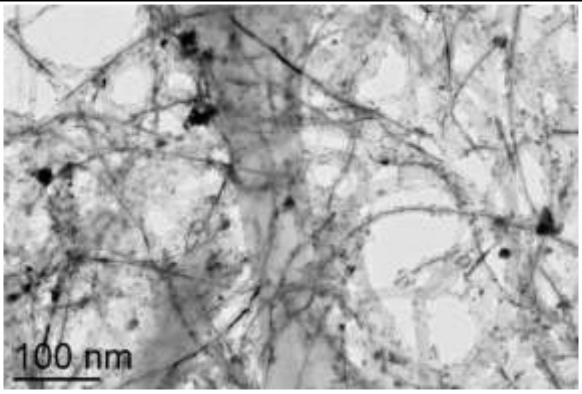
</td></tr>
<tr><td>1Pt</td><td>2BBA</td><td rowspan="2">1Pt_0.84Co_2BBA_2PPP_Tol_150ºC_24h</td></tr>
<tr><td>0.84Co</td><td>2PPP</td></tr>
<tr><td colspan="2">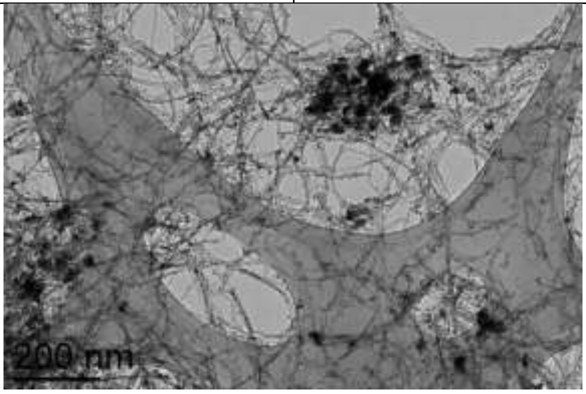
</td><td>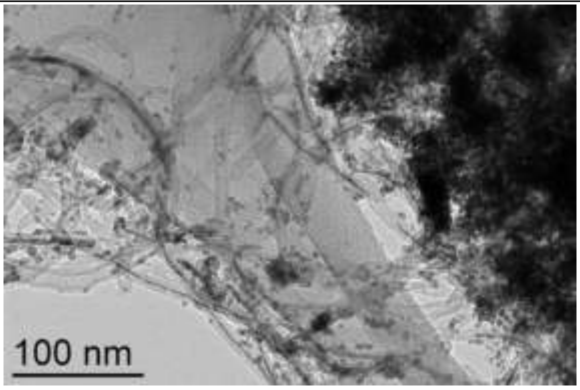
</td></tr>
</table>

—Effect of ligands

In order to confirm that the aromatic ligands were indispensable in order to obtain the confined NWs we performed the experiment by using the classic long chain ligands instead of the aromatic ones. "1Pt_0.86Co_2LA_2HDA_Tol_100°C_24h" led to only NPs (12-18 nm) outside the tube. This observation indicates that our aromatic ligands are critical for the NW formation within the tube. In another experiment we have introduced only one of the two aromatic ligands, the BBA. "1Pt_1Co_2BBA_Tol_100ºC_24h", gave rise to a few NWs. However, the amount of nanoparticles formed outside the CNTs was considerably increased.

Nevertheless this experiment showed that BBA alone can form the NWs. The presence of several NPs outside rendered the EDX analysis difficult.

<table>
<tr><td>1Pt</td><td>1LA</td><td rowspan="2">1Pt_0.84Co_1LA_1HDA_Tol_100ºC_24h</td></tr>
<tr><td>0.84Co</td><td>1HDA</td></tr>
<tr><td colspan="2">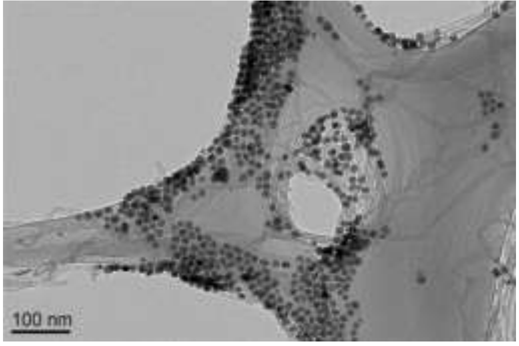
</td><td>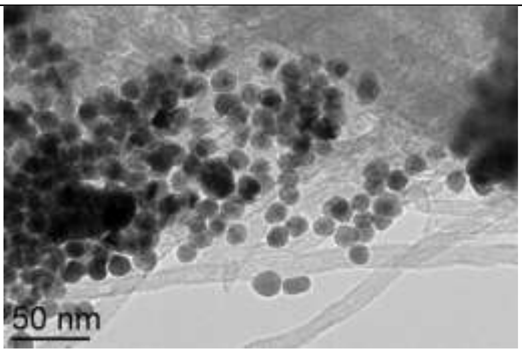
</td></tr>
<tr><td>1Pt</td><td>2BBA</td><td rowspan="2">1Pt_1Co_2BBA_Tol_100ºC_24h</td></tr>
<tr><td>1Co</td><td>/</td></tr>
<tr><td colspan="2">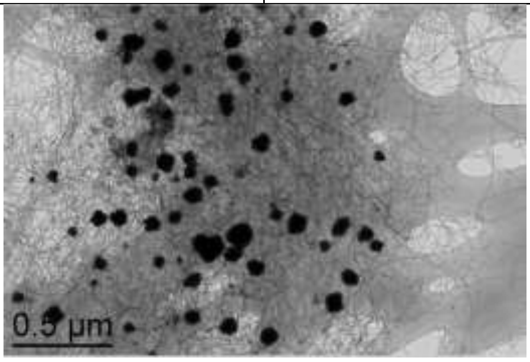
</td><td>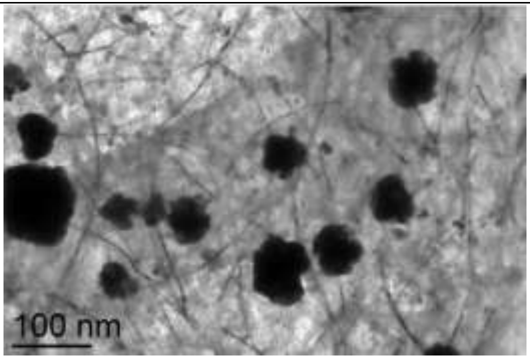
</td></tr>
</table>

Finally we have confirmed that in the absence of added ligands no NWs were formed.

<table>
<tr><td>1Pt</td><td>/</td><td rowspan="2">1Pt_1Co_Tol_100ºC_24h</td></tr>
<tr><td>1Co</td><td>/</td></tr>
<tr><td colspan="2">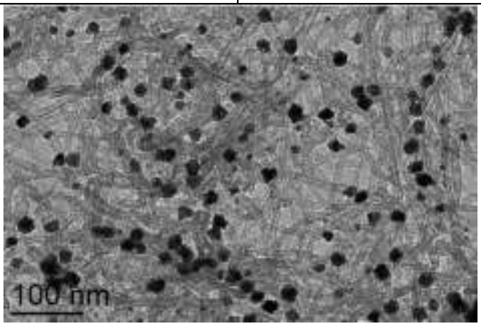
</td><td>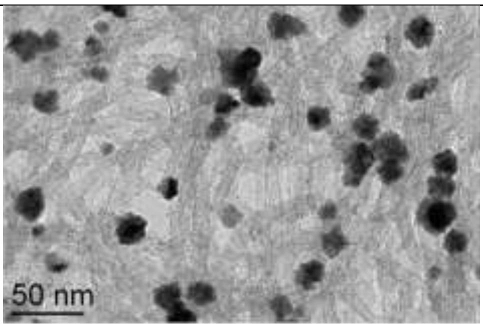
</td></tr>
</table>

From these results, it seems that the role of the aromatic ligands is important to form NWs, especially the presence of BBA. We have not examined the effect of the PPP alone in order to see whether its presence is enough to form NWs.

—Effect of precursors

In another effort, in which the aromatic ligands were conserved, we have modified, the nature of the metal precursors. The Co precursor $[Co(\eta^3\text{-}C_8H_{13})(\eta^4\text{-}C_8H_{12})]$ ([Co(COD)(COT)]) was used instead of $[Co\{N(SiMe_3)_2\}_2(THF)]$. For this reaction, very few NWs were presented as well as many aggregates.

<table>
<tr><td>1Pt</td><td>2BBA</td><td rowspan="2">1Pt_1Co(COD)(COT)_2BBA_2PPP_Tol_100ºC_24h</td></tr>
<tr><td>1Co(COD)(COT)</td><td>2PPP</td></tr>
<tr><td colspan="2">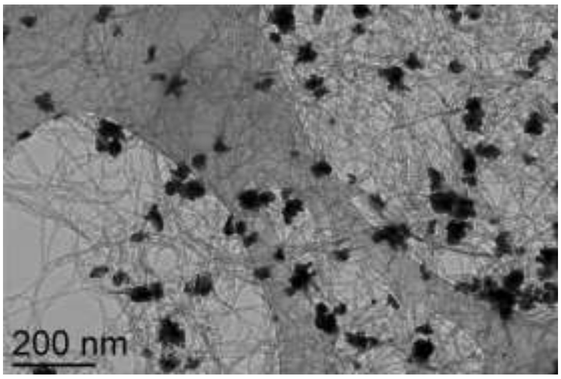
</td><td>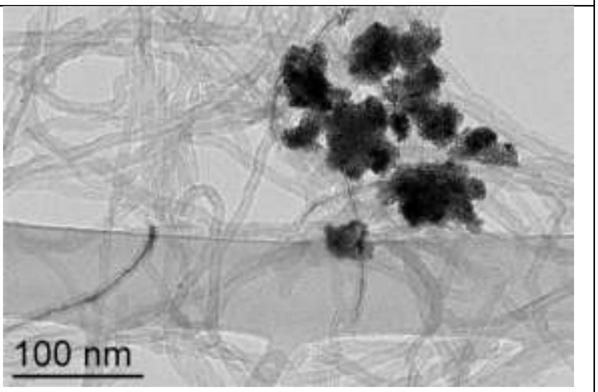
</td></tr>
</table>

Notably, $[Co\{N(SiMe_3)_2\}_2(THF)]$ upon reaction with acid ligands can give rise to 2 equivalents of HMDS that may play a favorable role for the formation of NWs since a simple replacement of the HMDS generating precursor severely reduces the NW formation. Thus, 2 equivalents of HMDS were added to the starting solution, which contained the [Co(COD)(COT)] precursor. This reaction resulted in very few NWs as in the absence of HMDS but many polydispersed NPs and their aggregates, which indicates that with the [Co(COD)(COT)] precursor HMDS does not play a decisive role in the formation of NWs .

1Pt	2BBA	1Pt_1Co/2HMDS_2BBA_2PPP_Tol_100ºC_24h
1Co(COD)(COT)/2HMDS	2PPP	
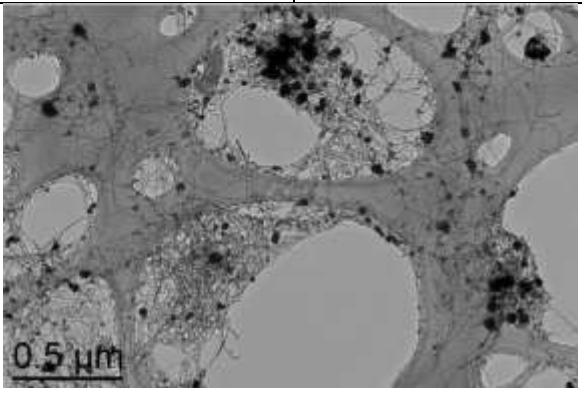		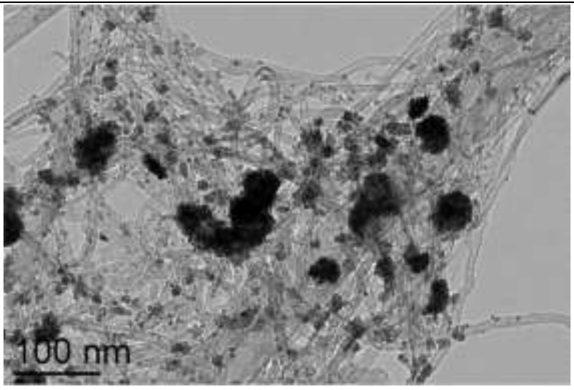

Under these reaction conditions we have modified only the Co precursor. The Pt precursor has been modified however in another experiment, in which the CNTs were also different in the sense that they were functionalized differently. Therefore no direct comparison can be made between this experiment and the rest, which are all performed with **CNT$_2$**. These results are described later.

—Effect of preparation procedure of the starting solution

As already noted in the Chapter II the preparation of the starting solution can be very important. We have to remind that the addition rate of the $[Co\{N(SiMe_3)_2\}_2(THF)]$ or $Fe[Fe\{N(SiMe_3)_2\}_2]_2$ precursors to a mixture of acid and amine had been shown to influence the composition of the starting solution when the acid ligand was in excess compared to the amine (54). The results obtained up to now do not allow to understand how the formation of NWs takes place. Nevertheless, it seems that some specific compounds can enter in the interior of the CNTs while others cannot. It is therefore possible that the preparation procedure may have an impact on the formation of NWs, since different preparation procedures may result in different starting solution compositions.

The Co addition rate was therefore changed from "dropwise" to "fast injection", which however led to no significant difference compared to the standard dropwise addition employed in the rest of the experiments. Thus, the addition rate seems to have no influence towards the NW formation. In this experiment the acid is not in excess compared to the amine and this may be the reason why the rate addition had no effect on the reaction outcome.

1Pt	2BBA	1Pt_0.84Co_2BBA_2PPP_Tol_100ºC_24h; fast Co addition rate
0.84Co	2PPP	
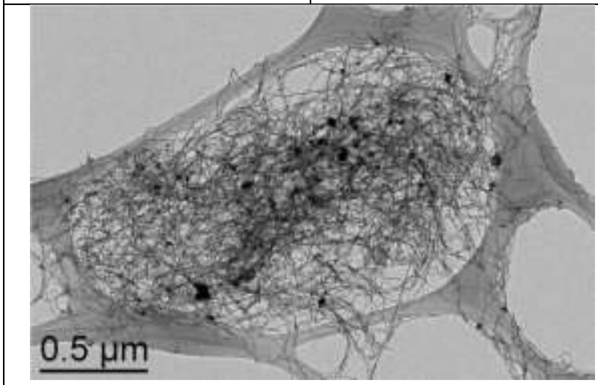		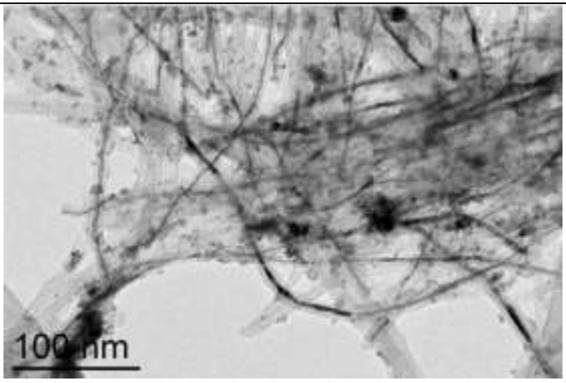

In another experiment we changed the preparation procedure of the starting solution by modifying the addition order: Co was mixed first with the acid, then the amine was added to them and finally Pt was added to the mixture. (BBA+Co+PPP+Pt) compared to the order "BBA+Pt+PPP+Co" in all other reactions. This modification led to more NPs and aggregates outside the CNTs.

1Pt	2BBA	1Pt_0.84Co_2BBA_2PPP_Tol_100ºC_24h; addition order: BBA+Co+PPP+Pt
0.84Co	2PPP	
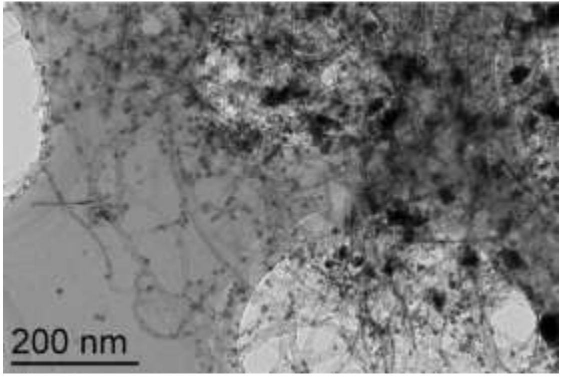		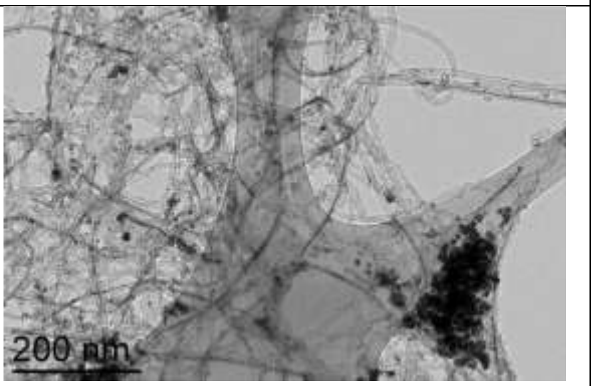

UV-vis spectroscopy was used to compare the starting solutions (Figure IV.17) resulting from these two different ways of preparation. Each solution was tested immediately after preparation. We see that the composition of the two solutions generated following a different addition order is not the same. The formation of different species should account for the different results observed.

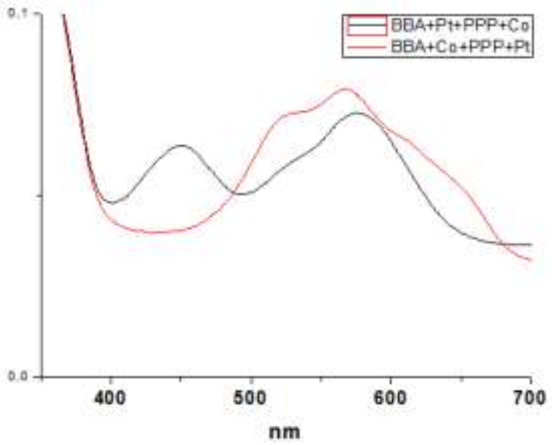

Figure IV.17: Comparison of UV-vis spectra between the addition order "BBA+Pt+PPP+Co" (black) and "BBA+Co+PPP+Pt".

Finally, the prepared starting solution was kept for one day before mixing with the CNTs , and then the reaction was performed, resulting in much more aggregates. It seems that the reaction after mixing is not completed and that evolution towards equilibrium is slow. Therefore we may conclude that the equilibrium composition does not favor the formation of NWs.

<table>
<tr><td>1Pt</td><td>2BBA</td><td rowspan="2">1Pt_0.84Co_2BBA_2PPP_Tol_100ºC_24h;
starting solution long kept</td></tr>
<tr><td>0.84Co</td><td>2PPP</td></tr>
<tr><td colspan="2">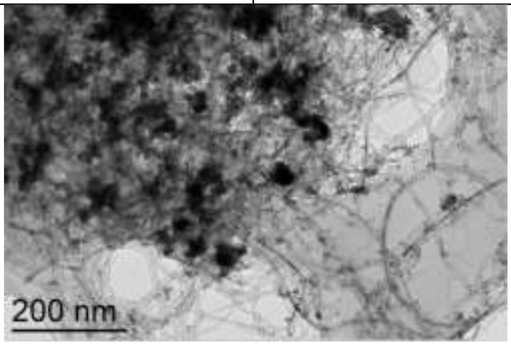
</td><td>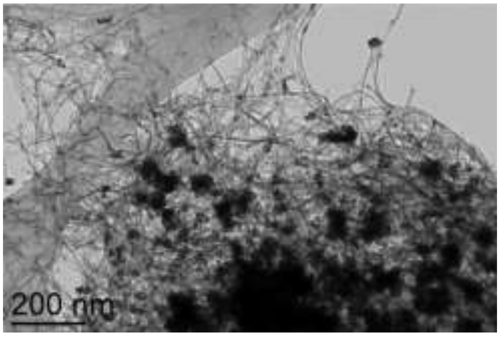
</td></tr>
</table>

—Other effects

We supposed that the oxidized groups on the surface of CNTs may coordinate with the Co species, which hinders entrance of Co into the CNT channel. Thus, the f-**CNT_2** was pre-washed with a [$Co\{N(SiMe_3)_2\}_2(THF)$] solution in toluene, and then the CNTs was washed with toluene. After decomposition of a standard "1Pt_0.84Co_2BBA_2PPP_ Tol_100ºC_24h" solution, no improvement was obtained. On the contrary, much more NPs and aggregates were presented on the outer surface of CNTs.

1Pt	2BBA	1Pt_0.84Co_2BBA_2PPP_Tol_100ºC_24h; Tubes pre-washed by Co solution
0.84Co	2PPP	
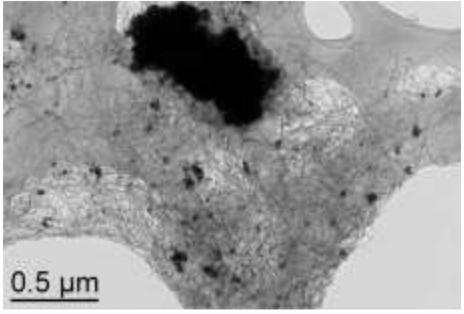 		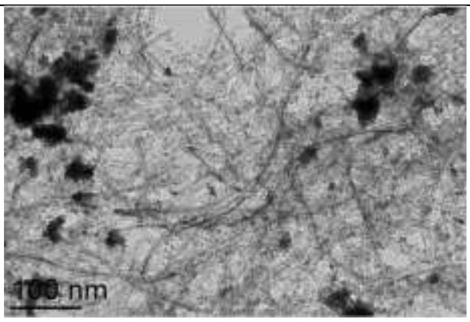

Another type of CNTs, the Nanocyl treated with HNO_3 but without the long alkyl chain functionalization, denoted **CNT_3** were also used because of the good confinement selectivity reported in the literature (55). In spite of the presence of oxidized groups on the outer surface of the **CNT_3** that may interact with species like MMNPs, as a result, attaching on its outer surface, in this case of the *in situ* decomposition the carboxylate-coordinated Co complex is very stable in the solution and would not interact with the oxidized groups. Thus, using the **CNT_3** may improve confinement selectivity.

We tried a reaction in which [Pt(CH_3)$_2$(COD)] was replaced by [Pt(acac)$_2$] (acac = acetylacetonate), giving rise to small confined NPs (1.5-2.2 nm) and bigger NPs (3-6 nm) attached on the outer surface of the CNTs. This result reveals that different precursors modify the nature of the starting solution, resulting in different confined morphologies as well as NPs outside.

1Pt(acac)$_2$	2BBA	1Pt(acac)$_2$_1Co_2BBA_2PPP_Tol_100ºC_24h; **CNT_3**
1Co	2PPP	
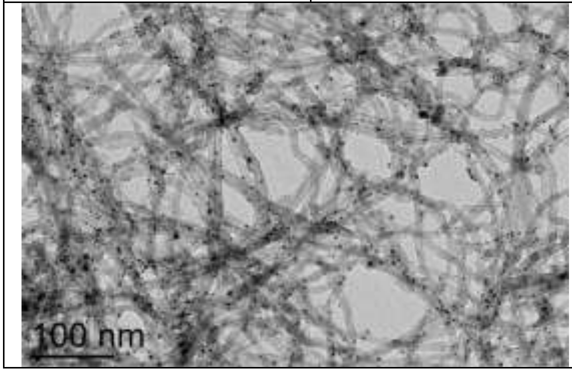 		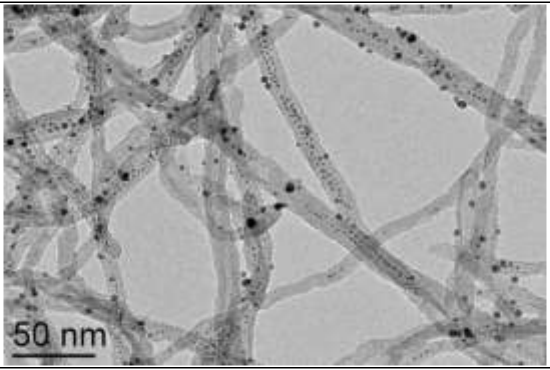

The above exploration showed that the presence of all Co, Pt and aromatic ligands are necessary for the formation of NWs. The absence of any of these components is detrimental to their formation. We have also seen that BBA alone is able to induce a limited formation of NWs, but only when both metals are present. The effect of PPP alone in the presence of the two metals has not been examined. The results obtained point towards a synergy between all these components. We suspected that the participation of certain ploynuclear complexes including aromatic ligands played an important role in this process. We have explored this possibility and we will present the results later (see IV.3.3). We cannot discarded a possible involvement of the HMDS ligand in the [$PtMe_2$(COD)] - [Co{$N(SiMe_3)_2$}$_2$(THF)] system. Concerning the Co content modification in the NWs, brought about by the modification of the reaction conditions, a clear conclusion cannot be made, due to the fact that all modifications produced more NPs in solution, which persisted after cleaning, rendering EDX analysis not very reliable.

IV.4.2 Fe-Pt nanowires templated within f-CNT2

Fe-Pt alloys are as interesting as the Co-Pt ones and both of them have high uniaxial magnetocrystalline anisotropy constant, as high as 7×10^6 J/m^3 for FePt (8). We have therefore explored the possibility to confine Fe-Pt NPs in CNTs.

Under similar conditions that gave rise to Co-Pt NWs, but using [Fe{$N(SiMe_3)_2$}$_2$]$_2$ instead of [Co{$N(SiMe_3)_2$}$_2$(THF)], we obtained very similar results to the ones obtained with Co. It has to be noted that the Pt/Fe ratio in the starting solution in this case was 1 (in comparison to the Pt/Co ratio on the comparable experiment where it was 1/0.84 because of the stoichiometry error induced by the presence of THF in the Co precursor). "1Pt_1Fe_2BBA_2PPP_Tol_100°C_24h" gave rise to more CNT-templated NWs and interestingly in this case, very few NPs and small aggregates on the outer surface of the f-**CNT$_2$** are present, compared to the one with Co precursor (Figure IV.18). In addition by the magnified TEM images, we can see that the majority of the CNTs are filled with wire-like nano-objects. Some of them almost completely filled, and some others partially filled, by discontinue NWs. Very few small NPs are attached on the external sidewall.

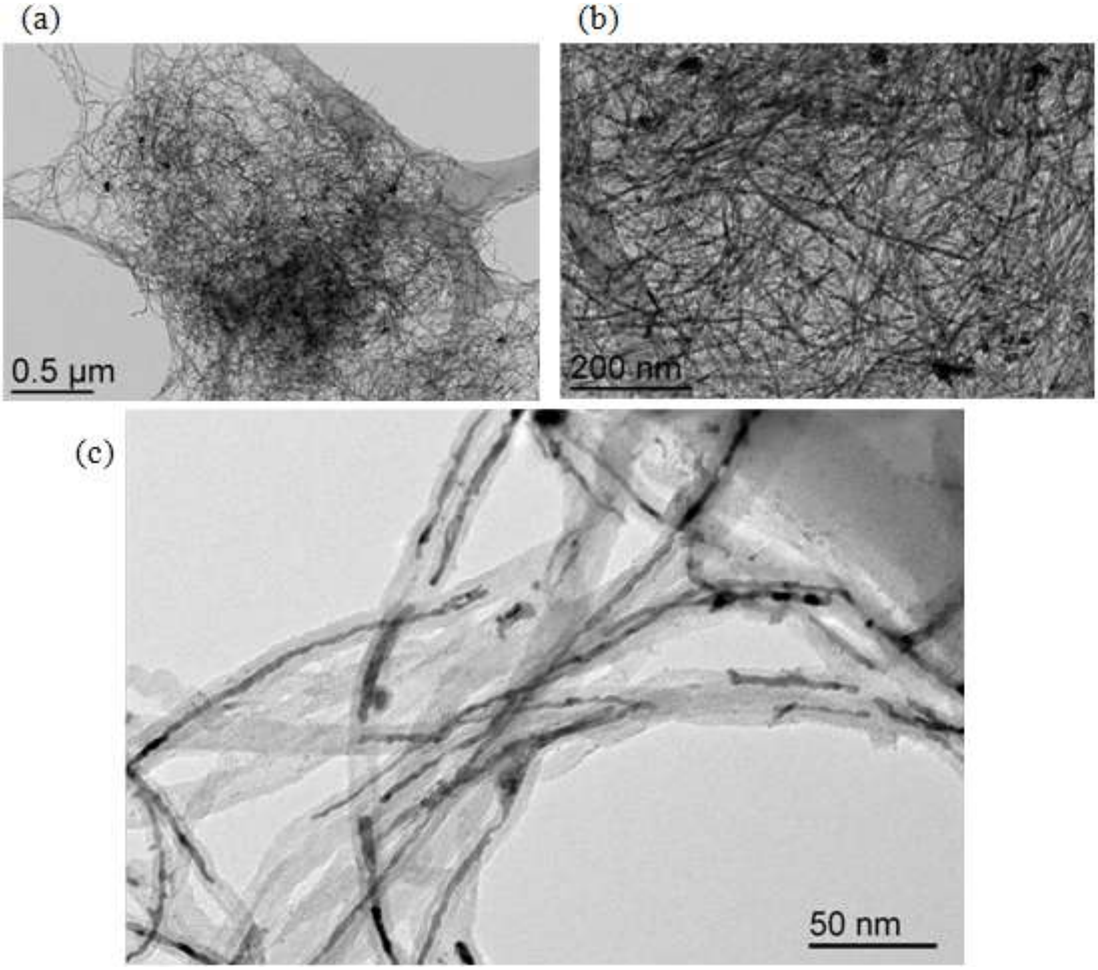

Figure IV.18: TEM images of the Fe-Pt NWs from "1Pt_1Fe_2BBA_2PPP_Tol_100°C_24h".

In the supernatant, we saw also the filled CNTs and numerous small NPs generated during the reaction and dispersed in the colloidal solution (Figure IV.19). The small NPs are around the CNTs probably due to solvent evaporation on the TEM grid.

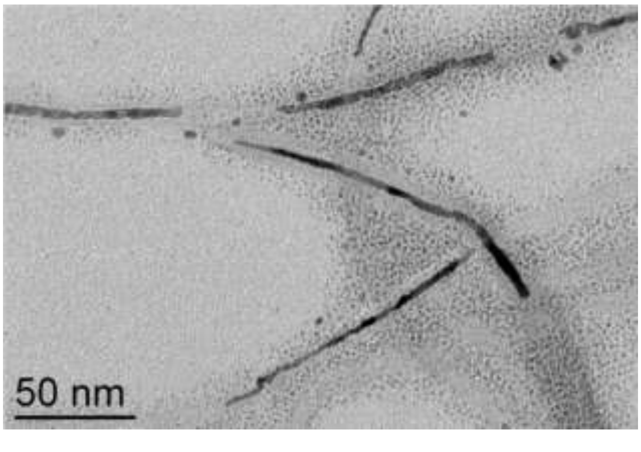

Figure IV.19: TEM image of the supernatant of "1Pt_1Fe_2BBA_2PPP_Tol_100°C_24h".

The solvent-washed and dried sample was analyzed by XRD, HRTEM and STEM-EDX. In the XRD pattern (Figure IV.20), a structure close to Pt is also found. Unlike the case of Co-Pt NW sample were a Co peak was present, no peak corresponding to Fe was detected in the diffractogram.

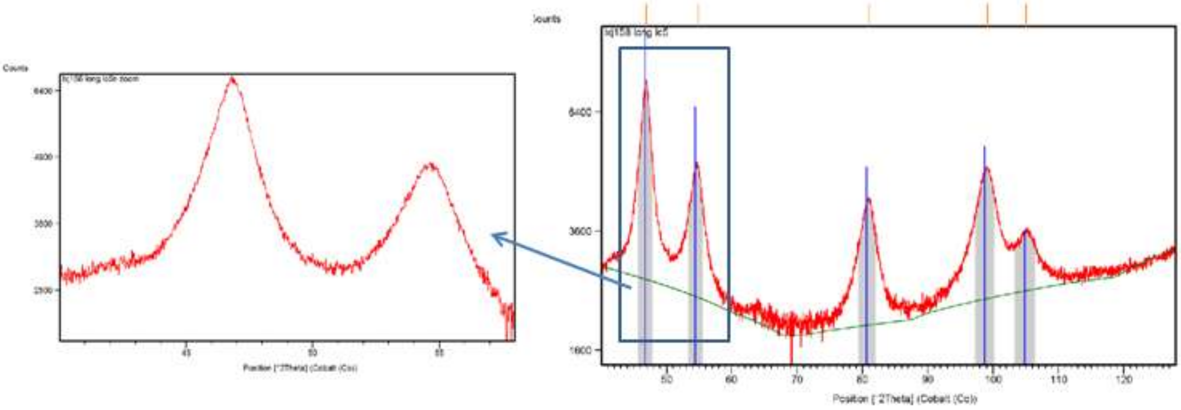

Figure IV.20: XRD pattern of the CNT-templated Fe-Pt NWs.

From HRTEM, the NWs seem to possess a homogeneous well-crystallized structure that is closely related to the one of Pt (Figure IV.21).

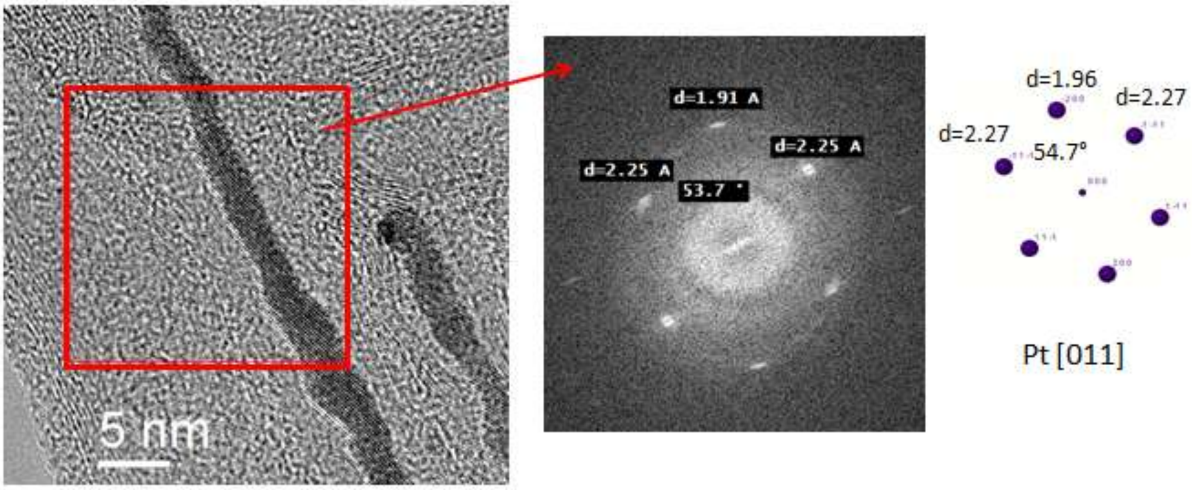

Figure IV.21: HRTEM image of Fe-Pt NWs; FFT indicates a structure close to Pt.

STEM-EDX analysis shows a result similar to the Co-Pt NWs: the NWs are Pt-rich (Figure IV.22). The EDX analysis on NWs indicates that they consist of 17-25% Fe, whereas on larger zones, the Fe composition raises to 30-35%. The increased Fe content in the zones far away from the CNTs may be due to the small NPs and/or certain Fe species on the external surface of the CNTs that were not removed by washing.

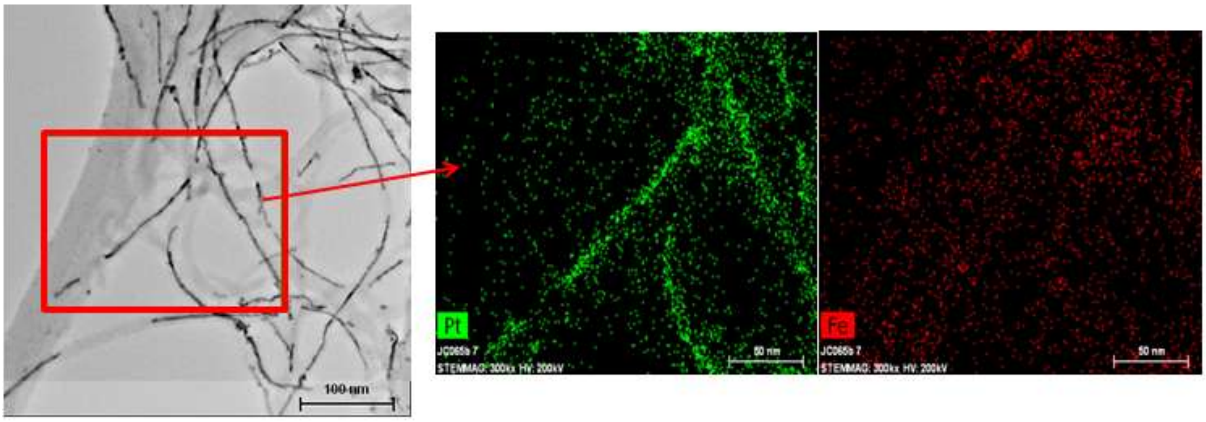

Figure IV.22: STEM-EDX analysis of the Fe-Pt NWs.

After HCl washing, there are no small NPs left any more, while some NPs are always present (Figure IV.23). The Fe composition of the NWs is decreased to around 5-13%, (on NPs from 42% to 15%). This HCl effect is similar to the effect on the Co-Pt NWs, and both result from the selective removal of Fe.

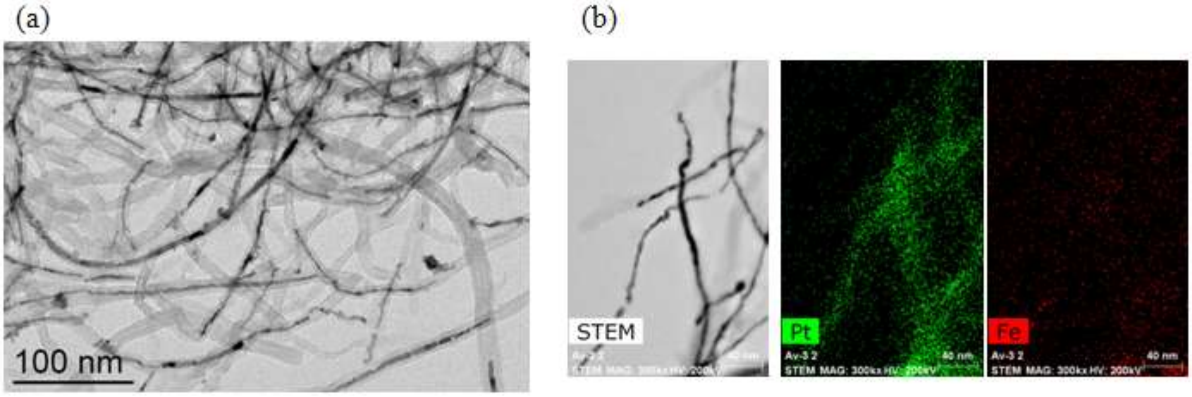

Figure IV.23: (a) TEM image and (b) STEM-EDX analysis of the HCl washed Fe-Pt NWs.

IV.4.2.1 Study of effects from variation of reaction condition

There also, we have performed additional experiments although less numerous than in the case of Co-Pt. The reaction conditions were varied with respect to "1Pt_1Fe_2BBA_2PPP_Tol_100°C_24h".

—Influence of the Pt/Fe ratio

In the reaction "0.5Pt_1.5Fe_2BBA_2PPP_Tol_100ºC_24h", the Pt amount was decreased to 0.5 equivalent but Fe was increased to 1.5 equivalents, where 1 equivalent is equal to 0.1 mmol. Not surprisingly, much less NWs are observed from TEM, while more aggregates are presented. This variation demonstrates that the amount of Pt-rich NWs decreases with the decreasing Pt amount in the starting solution, and that the increasing amount of Fe in the starting solution without adding more ligands tends to increase the formation of aggregates outside the CNTs.

<table>
<tr><td>0.5Pt</td><td>2BBA</td><td rowspan="2">0.5Pt_1.5Fe_2BBA_2PPP_Tol_100ºC_24h</td></tr>
<tr><td>1.5Fe</td><td>2PPP</td></tr>
<tr><td colspan="2">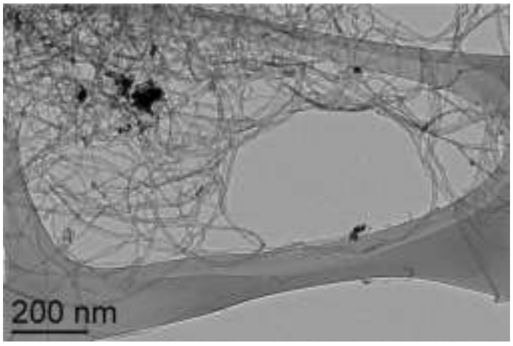 </td><td>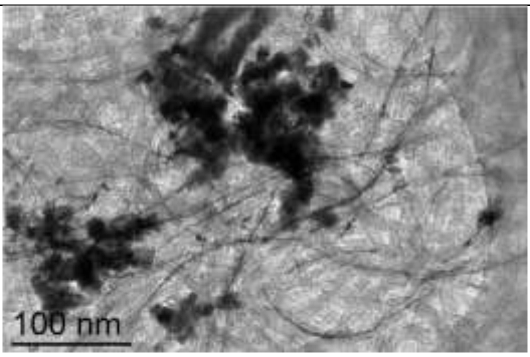 </td></tr>
</table>

Therefore in another reaction, we kept one equivalent of Pt in order to maintain the amount of NWs, while we doubled the Fe content and the ligands in the starting solution in order to avoid the formation of aggregates. From TEM, the amount of NWs seems to be the same as that in the reference reaction "1Pt_1Fe_2BBA_2PPP_Tol_100ºC_24h", whereas the big aggregates are still present.

<table>
<tr><td>1Pt</td><td>4BBA</td><td rowspan="2">1Pt_2Fe_4BBA_4PPP_Tol_100ºC_24h</td></tr>
<tr><td>2Fe</td><td>4PPP</td></tr>
<tr><td colspan="2">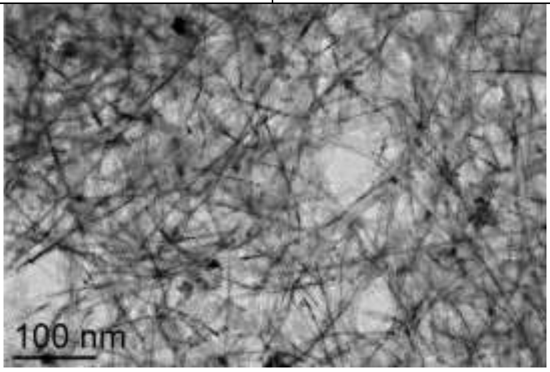 </td><td>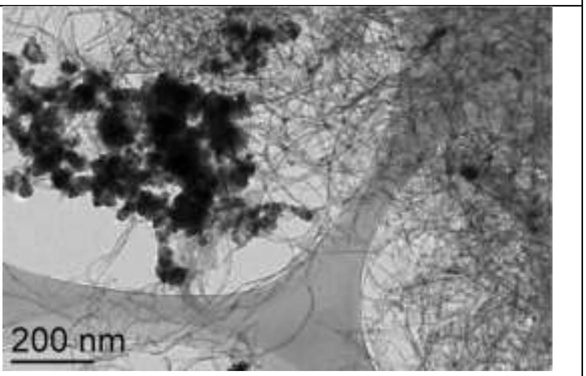 </td></tr>
</table>

STEM-EDX analysis was used for this sample that was washed with toluene (Figure IV.24). In the large zones measured comprising both NWs and aggregates, the Fe composition (33%-36%) is similar to that in the reference reaction (30%-35%), which indicates that the toluene washing has efficiently removed the excess of Fe from the sample, since theoretically the Fe content is doubled compared to the reference experiment one. Local measurements show that the Fe content is around 30% on the NWs and 32%-49% on the aggregates.

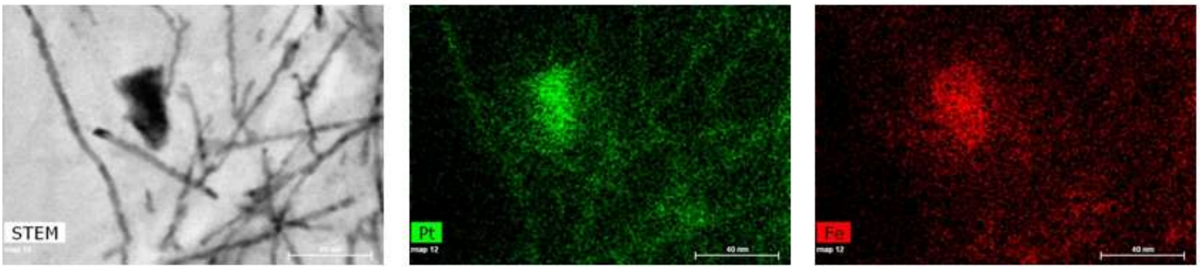

Figure IV.24: STEM-EDX analysis of the washed "1Pt_2Fe_4BBA_4PPP_Tol_100ºC_24h" sample.

As a result, we conclude that increasing the Fe content in the starting solution does not raise significantly the Fe content in the NWs while the formation of aggregates is more pronounced. A similar results was obtained with Co.

—Effect of temperature

Raising the reaction temperature to 150°C results in many small NPs outside besides the NWs inside the CNTs. As for Co, an increase of the temperature should favor the decomposition of stable, carboxylate containing Fe species.

<table>
<tr><td>1Pt</td><td>2BBA</td><td rowspan="2">1Pt_Fe_2BBA_2PPP_Tol_150ºC_24h</td></tr>
<tr><td>1Fe</td><td>2PPP</td></tr>
<tr><td colspan="2">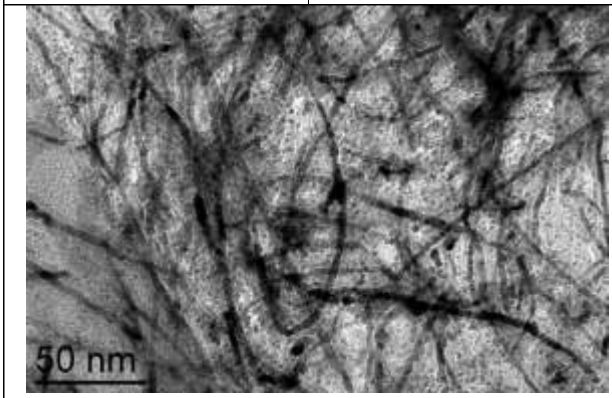
</td><td>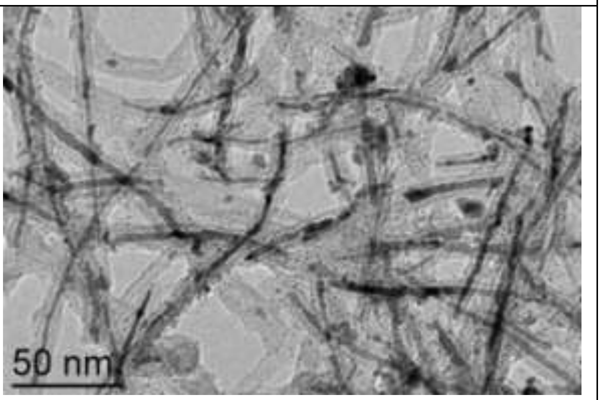
</td></tr>
</table>

—Effect of ligands

Compared to "1Pt_1Fe_2BBA_2PPP_Tol_100°C_24h", in which we have both aromatic ligands, "1Pt_1Fe_2BBA_Tol_100°C_24h" with only BBA led to no obvious modification in terms of confinement selectivity and filling yield. Since very few NPs and coalescences were observed, this sample seems to be a good candidate for further study, which will be described in the next section. This result shows that BBA alone is enough to induce the introduction of the metals in the CNTs, as shown also in the case of Co.

<table>
<tr><td>1Pt</td><td>2BBA</td><td rowspan="2">1Pt_1Fe_2BBA_Tol_100ºC_24h</td></tr>
<tr><td>1Fe</td><td>/</td></tr>
<tr><td colspan="2">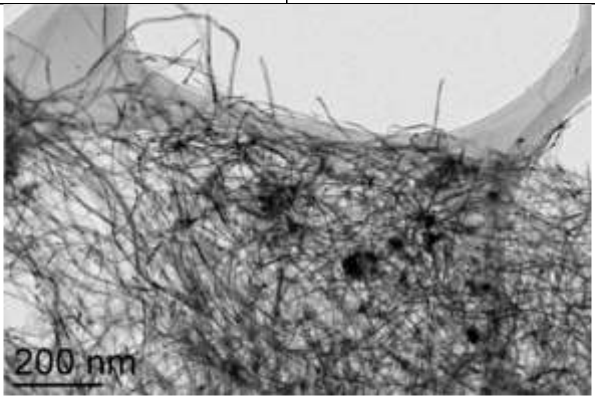 </td><td>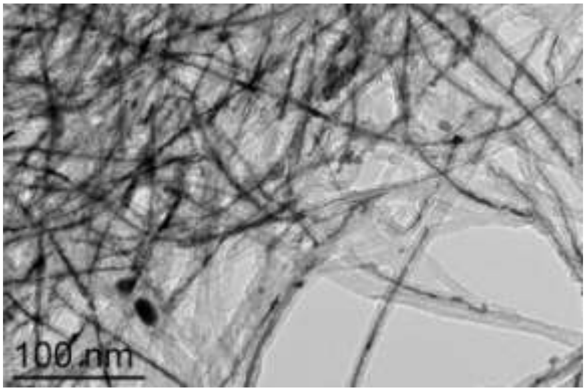 </td></tr>
</table>

The reduction of the BBA content in the starting solution and without PPP, "1Pt_1Fe_1BBA_Tol_100ºC_24h" gave rise to core/shell NPs (12-35 nm) outside the CNTs instead of the CNT-templated NWs.

<table>
<tr><td>1Pt</td><td>1BBA</td><td rowspan="2">1Pt_1Fe_1BBA_Tol_100ºC_24h</td></tr>
<tr><td>1Fe</td><td>/</td></tr>
<tr><td colspan="2">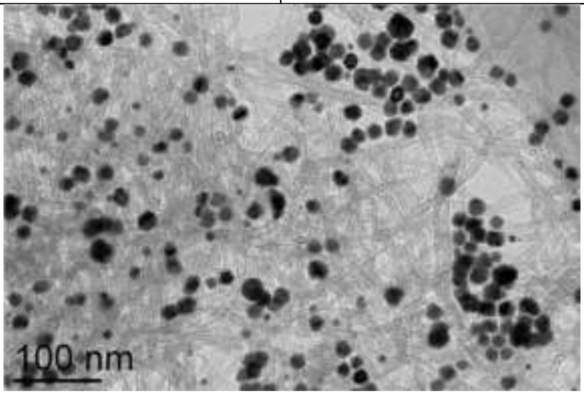 </td><td>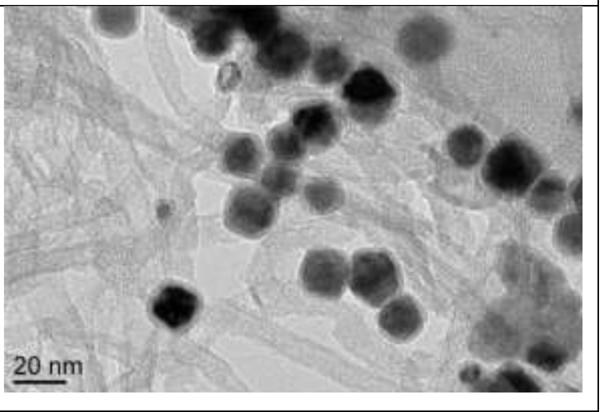 </td></tr>
</table>

The toluene washed core/shell sample was analyzed by HRTEM and STEM-EDX. From HRTEM, the core possesses a structure close to Pt and the shell presents a Fe_3O_4 structure (Figure IV.25). STEM-EDX analysis shows that the Fe/Pt composition is around 50%/50% on both the large zones and locally on the NPs (Figure IV.26). This experiment suggests that Pt is reduced first, followed by a slower reduction of Fe. This could be due to the selective coordination of the BBA to Fe, which is stabilized and is reduced after the reduction of Pt has taken place. However, the lower amount of BBA does not allow the formation of NWs. This points towards the necessity of having a sufficiently large amount of BBA in order for the metals to enter in the CNTs. Even Pt that seems to enter more easily seems to need the BBA in order to do so.

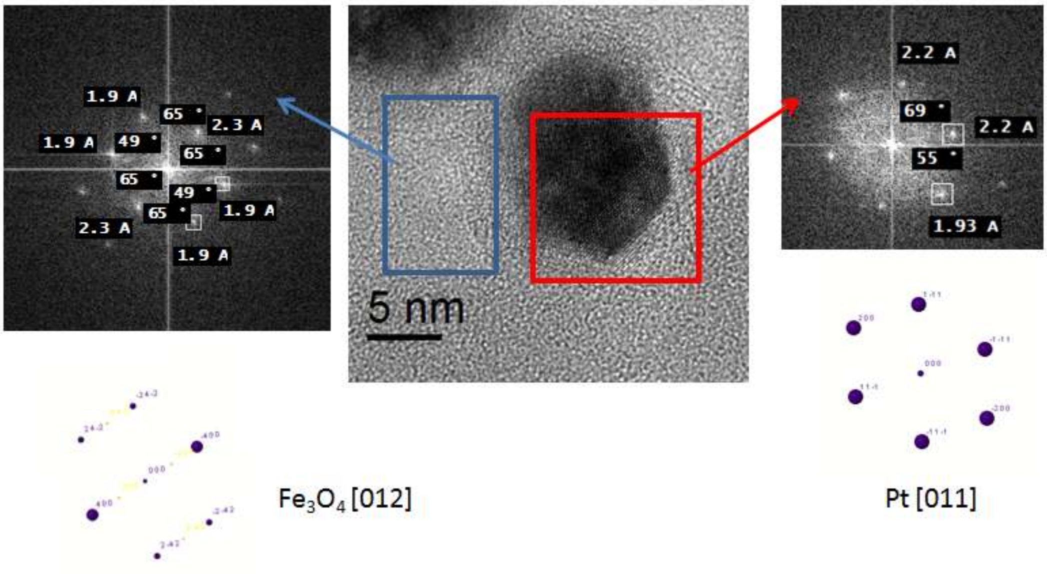

Figure IV.25: HRTEM analysis of the core/shell nanostructure.

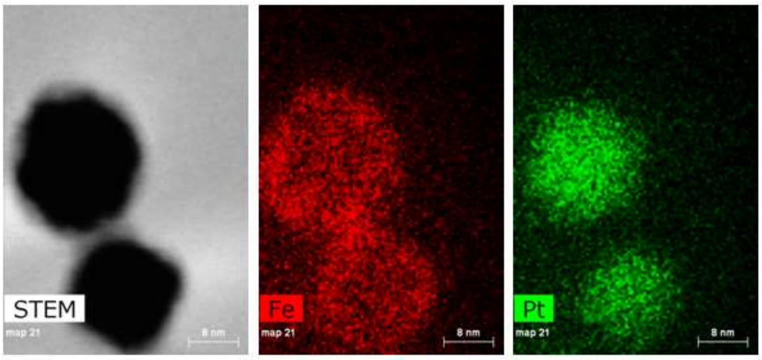

Figure IV.26: STEM-EDX analysis of the core/shell nanostructure.

When the temperature was raised to 150°C, "1Pt_1Fe_1BBA_Tol_150ºC_24h" led also to core/shell structure but with a larger size ranging (6-40 nm).

<table>
<tr><td>1Pt</td><td>1BBA</td><td rowspan="2">1Pt_1Fe_1BBA_Tol_150ºC_24h</td></tr>
<tr><td>1Fe</td><td>/</td></tr>
<tr><td colspan="2">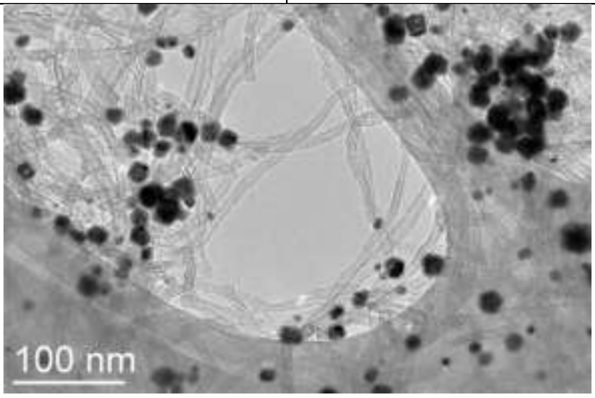 </td><td>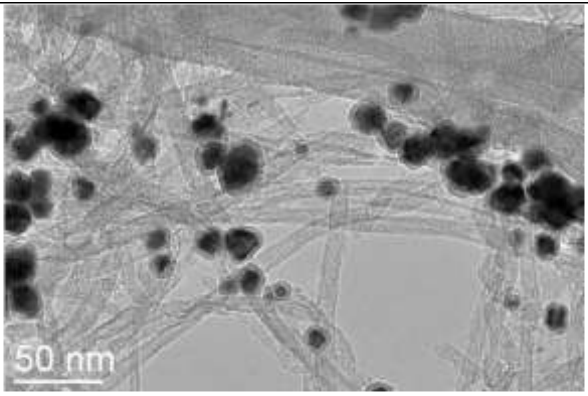 </td></tr>
</table>

The addition of PPP alone, "1Pt_1Fe_2PPP_Tol_100°C_24h" results in almost no formation of NWs but few short NRs inside the CNTs and big aggregates outside. This confirms that the NW formation requires the presence of BBA.

<table>
<tr><td>1Pt</td><td>/</td><td rowspan="2">1Pt_2Fe_2PPP_Tol_100ºC_24h</td></tr>
<tr><td>1Fe</td><td>2PPP</td></tr>
<tr><td colspan="2">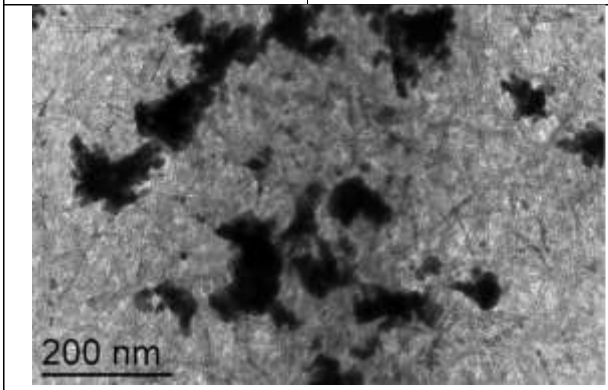 </td><td>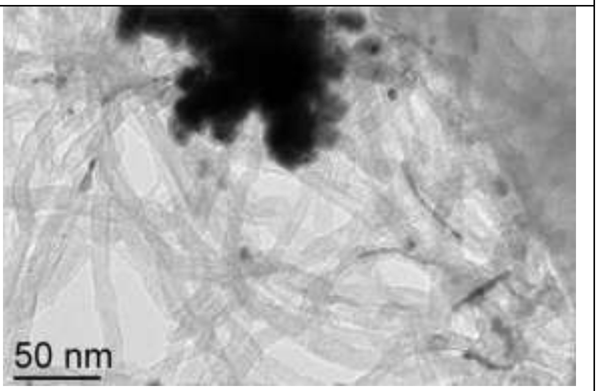 </td></tr>
</table>

When 2 equivalents of PPP and 1 equivalent of BBA were added to the starting solution the core/shell structure was absent but some NWs and several aggregates were present. Therefore PPP plays a role for the NW formation when only one BBA is present. It is possible that in the presence of PPP, the BBA is not completely consumed by the Fe, and some of it can participate to the formation of species that can enter in the CNTs.

1Pt	1BBA	1Pt_1Fe_1BBA_2PPP_Tol_100ºC_24h
1Fe	2PPP	
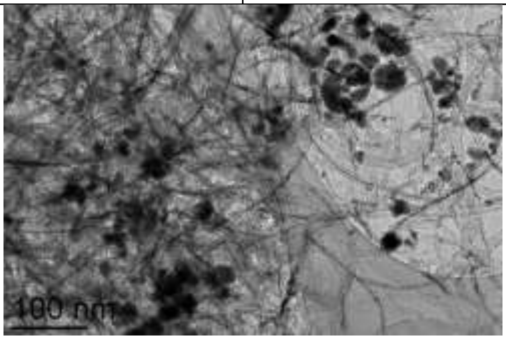		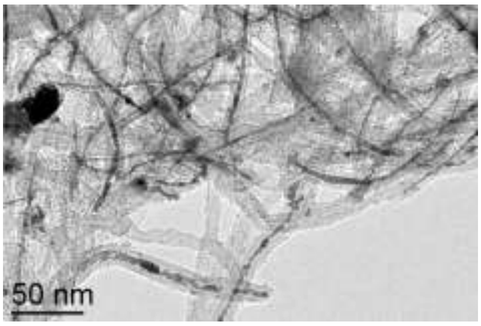

—Effect of precursors

In order to increase the Fe content in the NWs we have changed the Pt precursor. We saw that when [Pt(Me)$_2$COD] is used as a starting precursor the decomposition gives rise to NWs with high Pt content. This could be due to a much faster reduction of the Pt species formed in solution starting from this precursor. We have also seen a faster reduction of the Pt compared to Fe when only BBA is present, resulting to the Pt@Fe core@shell NPs. Consequently, Fe species, which are much more stable does not incorporate at the same rate in the nanomaterial formed. Thus we hoped that replacement of the [Pt(CH$_3$)$_2$COD] precursor by a more stable one would slow down the reduction of Pt.

When [Pt(acac)$_2$] was used instead of [Pt(CH$_3$)$_2$COD]under the standard reaction conditions, many small NPs confined within the f-**CNT$_2$**, as well as some NPs attached on the outer surface of the CNTs were observed. There is not size difference between the NPs inside and outside the tube (1-3 nm), whereas some coalesced and/or aggregated NPs are found inside the CNTs.

1[Pt(acac)$_2$]	2BBA	1[Pt(acac)$_2$]_1Fe_2BBA_2PPP_Tol_100ºC_24h
1Fe	2PPP	
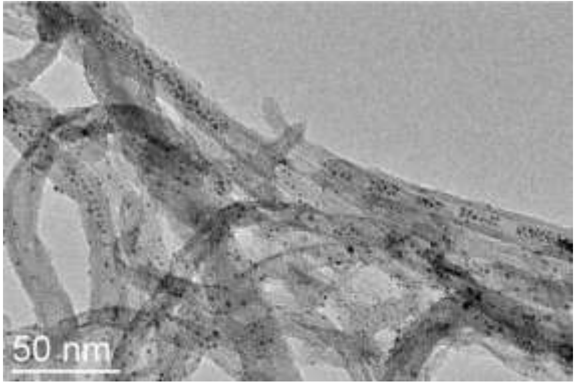		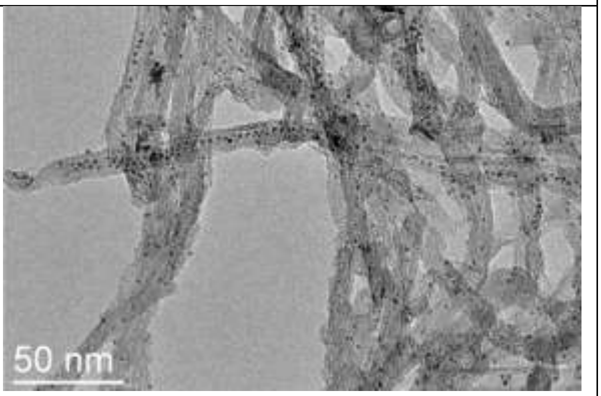

The toluene washed sample was analyzed by HRTEM and STEM-EDX. From HRTEM, we see clearly the confined NPs and those attached on the outer surface (Figure IV.27a-b). Inside the tube, the NPs tend to coalescence and form CNT-templated structure. The individual NPs were very small to be analyzed individually by STEM-EDX but analysis over a large area shows a Fe composition between 22% to 32% (Figure IV.27c).

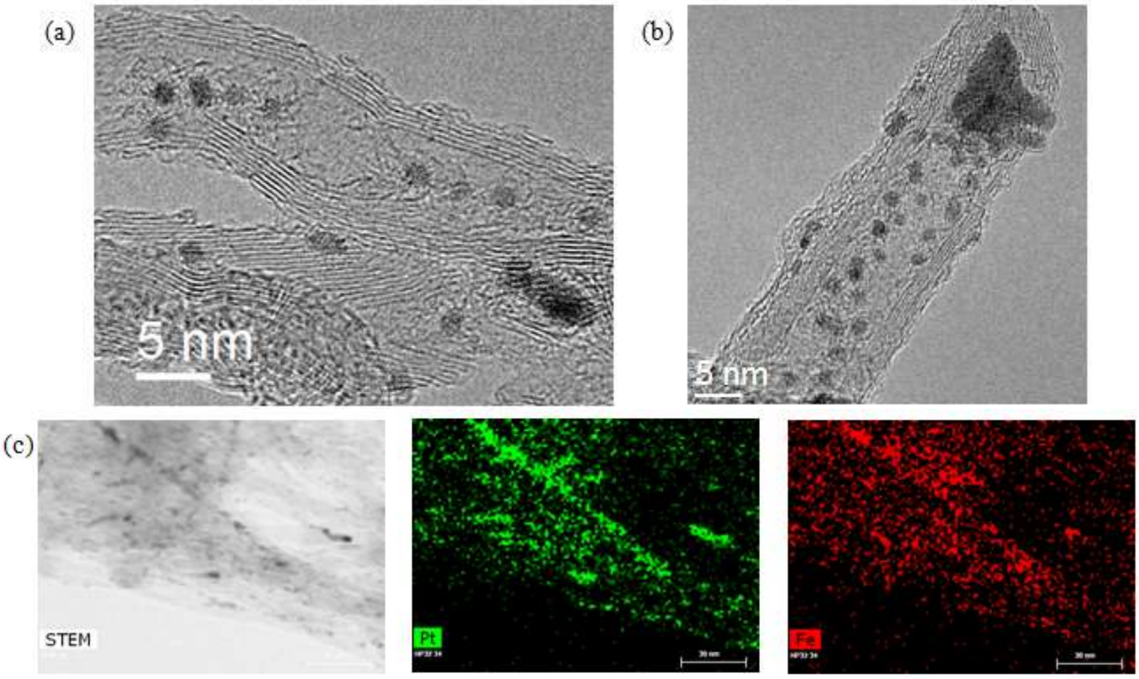

Figure IV.27: (a-b) HRTEM images and (c) STEM-EDX analysis of the washed sample in "1[Pt(acac)$_2$]_1Fe_2BBA_2PPP_Tol_100ºC_24h".

For the same reaction with [Pt(acac)$_2$], when reaction temperature was raised to 150°C, some short NWs were presented while much more NPs were also found on the outer surface of the CNTs.

1[Pt(acac)$_2$]	2BBA	1[Pt(acac)$_2$]_1Fe_2BBA_2PPP_Tol_150ºC_24h
1Fe	2PPP	
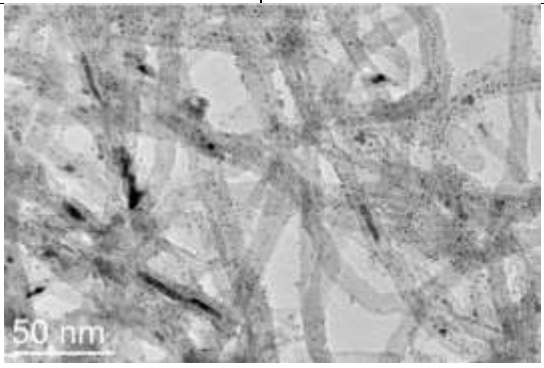 50 nm		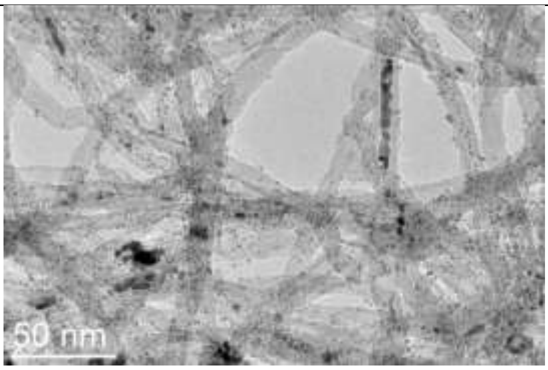 50 nm

STEM-EDX analysis shows that the Fe composition is around 21-32% on the NW zones (Figure IV.28).

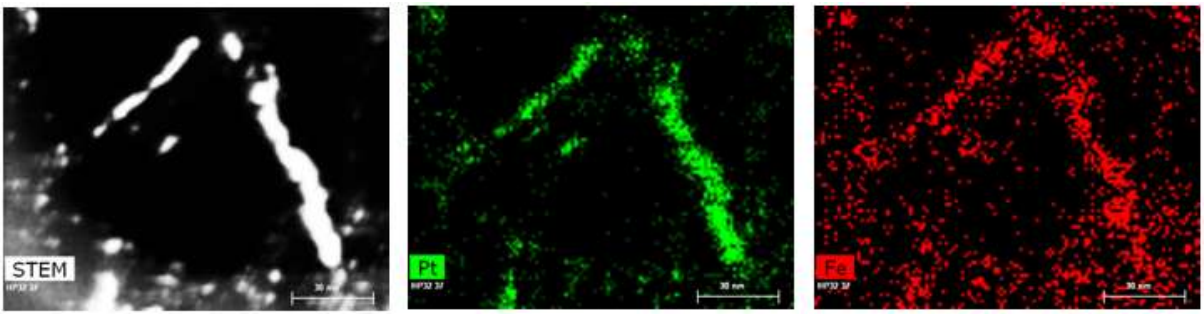

Figure IV.28: STEM-EDX analysis of the washed sample in "1[Pt(acac)$_2$]_1Fe_2BBA_2PPP_Tol_150ºC_24h".

In order to improve the confinement selectivity, the reaction "1[Pt(acac)$_2$]_1Fe_2BBA_2PPP_ Tol_100ºC_24h" was carried out in the presence of **CNT$_3$** instead of **CNT$_2$**. Compared to the former reaction with the f-**CNT$_2$**, much less NPs were found outside the tubes. The mean size of the NPs is around 1.7 nm, and the length of some NRs can reach 12 nm. The NPs tend to coalescence along the tube channel forming rod-like particles (Figure IV.29).

<table>
<tr><td>1[Pt(acac)$_2$]</td><td>2BBA</td><td rowspan="2">1[Pt(acac)$_2$]_1Fe_2BBA_2PPP_Tol_100ºC_24h;
CNT$_3$</td></tr>
<tr><td>1Fe</td><td>2PPP</td></tr>
<tr><td colspan="2">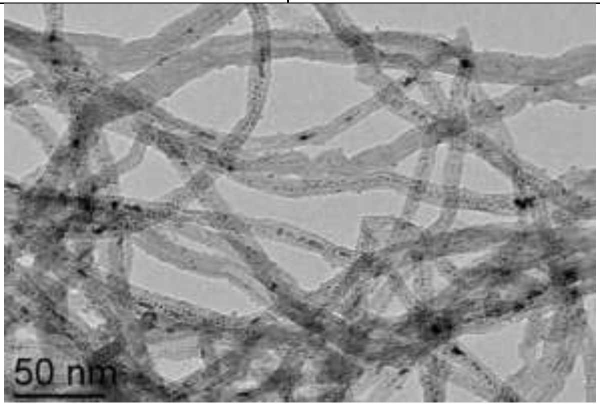
</td><td>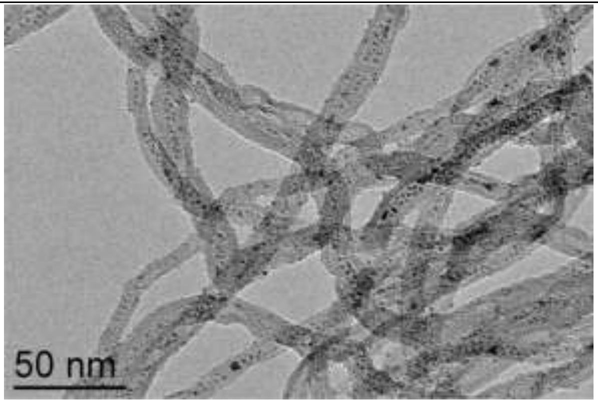
</td></tr>
</table>

Due to its good confinement selectivity of the NPs, the toluene washed sample is of great interest for futher study, which will be described in the next section.

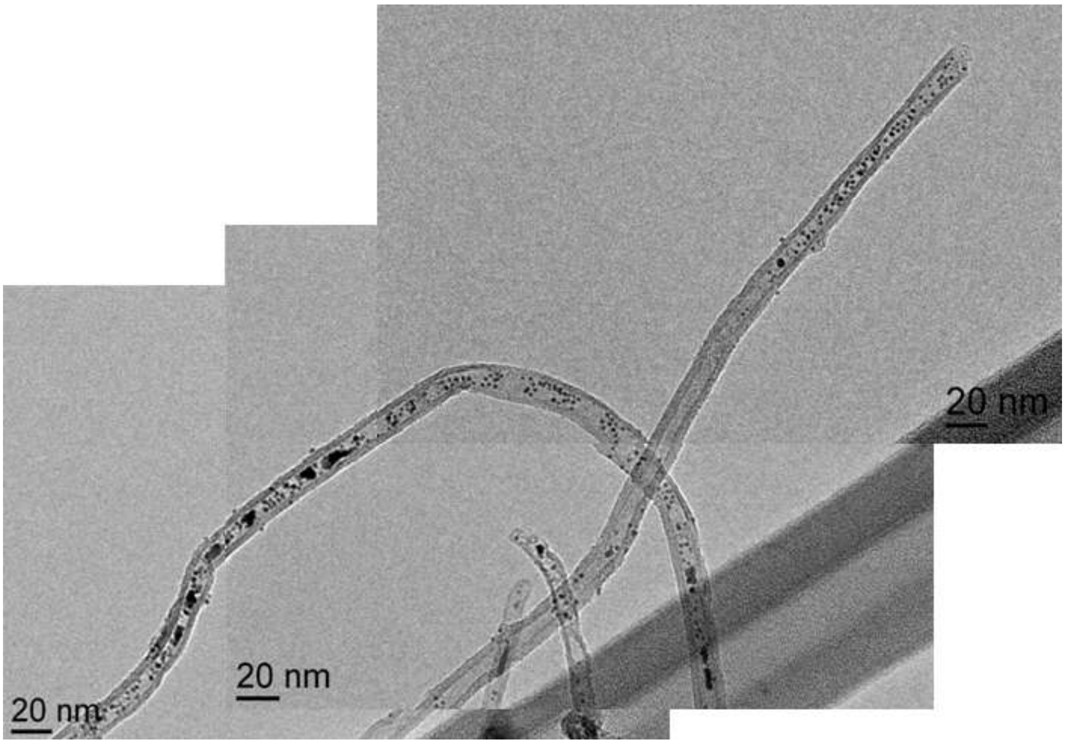

Figure IV.29: TEM image of a well filled CNT_3 in which both small NPs and coalescences are formed.

In another experiment $[Pt(CH_3)_2(COD)]$ was replaced by a less stable precursor, the $[Pt(dba)_2]$ (dba = dibenzylideneacetone). Under the reference condition “Pt_Fe_2BBA_2PPP_Tol_ 100°C_24h”, onl ver small NPs (~1 nm) were presented attached on the outer surface of the CNTs. It has to be pointed out that $[Pt(dba)_2]$ contains a ligand that can interact with the **CNT_2** channel. Once liberated after displacement by the BBA and PPP it can be in competition with the newly formed species for the occupation of the channels.

$1[Pt(dba)_2]$	2BBA	$1[Pt(dba)_2]$_1Fe_2BBA_2PPP_Tol_100ºC_24h
1Fe	2PPP	
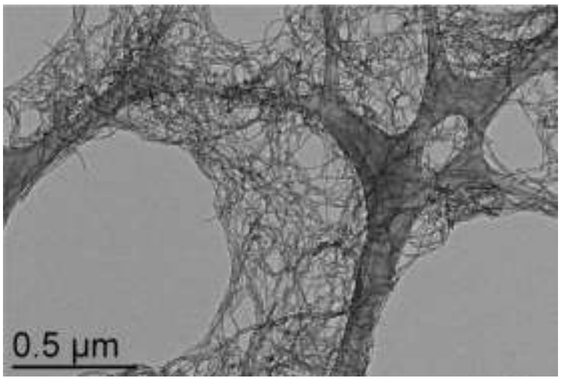 0.5 µm		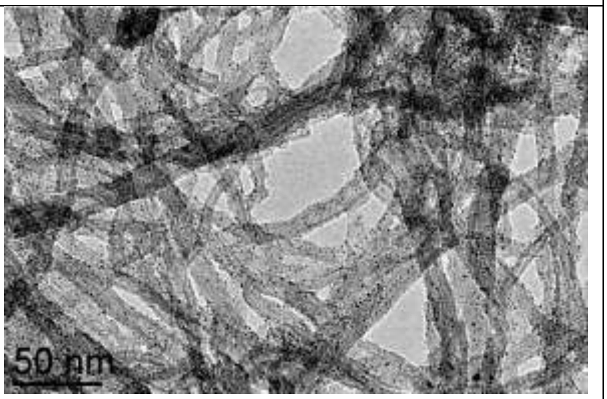 50 nm

From this series of experiments it seems that the nature of the precursor is a very important parameter that can completely change the reaction outcome. Apart for the stability towards reduction, the reactivity towards the added ligands can be completely altered by changing the starting precursor. [Pt(acac)$_2$] seems to yield better stabilized small nanoparticles, but less molecular species that can enter the CNTs cavity.

—Other effects

In all the experiments presented above, the CNT amount was kept constant. In order to see whether the CNT amount played a role on the reaction outcome, we kept the solution composition as "1Pt_Fe_2BBA_2PPP_Tol_100°C_24h" but we doubled the quantity of CNTs. This experiment presented much more NPs outside the CNTs, indicating that the f-**CNT$_2$** may play also an important role, which could involve both their channels as templates and the grafted groups on their outer surface as reactants.

1Pt	2BBA	1Pt_1Fe_2BBA_2PPP_Tol_100ºC_24h; double f-**CNT$_2$**
1Fe	2PPP	
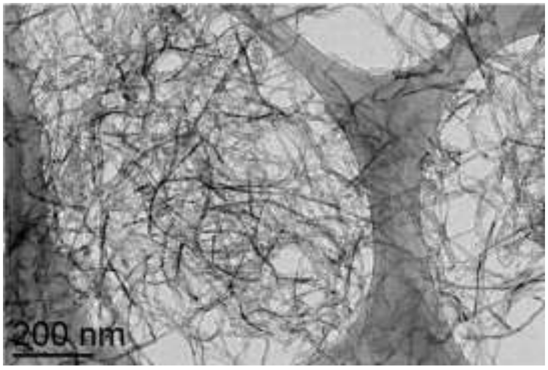		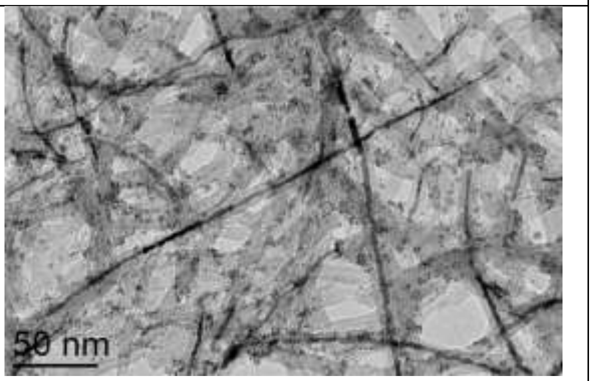

Additional experiments are needed with a decreasing amount of CNTs to see if the amount of NWs increases. In conclusion, this parametric study on the Pt-Fe system shows similar tendencies than with the Pt-Co system. However, cleaner nano-objects were obtained with the Pt-Fe system.

IV.4.2.2 Study of the confined Fe-Pt NPs

From the reaction "1[Pt(acac)$_2$]_1Fe_2BBA_2PPP_Tol_100ºC_24h", we obtained the **CNT$_3$**-confined Fe-Pt NPs. In order to obtain more structural information on these confined NPs (**C-NPs**) (Figure IV.30a), wide angle X-ray scattering (WAXS) was used. X-Ray Fluorescence (XRF) could also be performed on the same samples.

The NPs in the supernatant were also collected for comparison with the confined ones. These NPs, denoted **S-NPs** possess a mean size of 1.6 nm very close to the one of the confined ones (Figure IV.30b). Moreover, the NPs synthesized in absence of the CNTs were also obtained with a mean size of 1.4 nm, denoted as **AS-NPs** (Figure IV.30c).

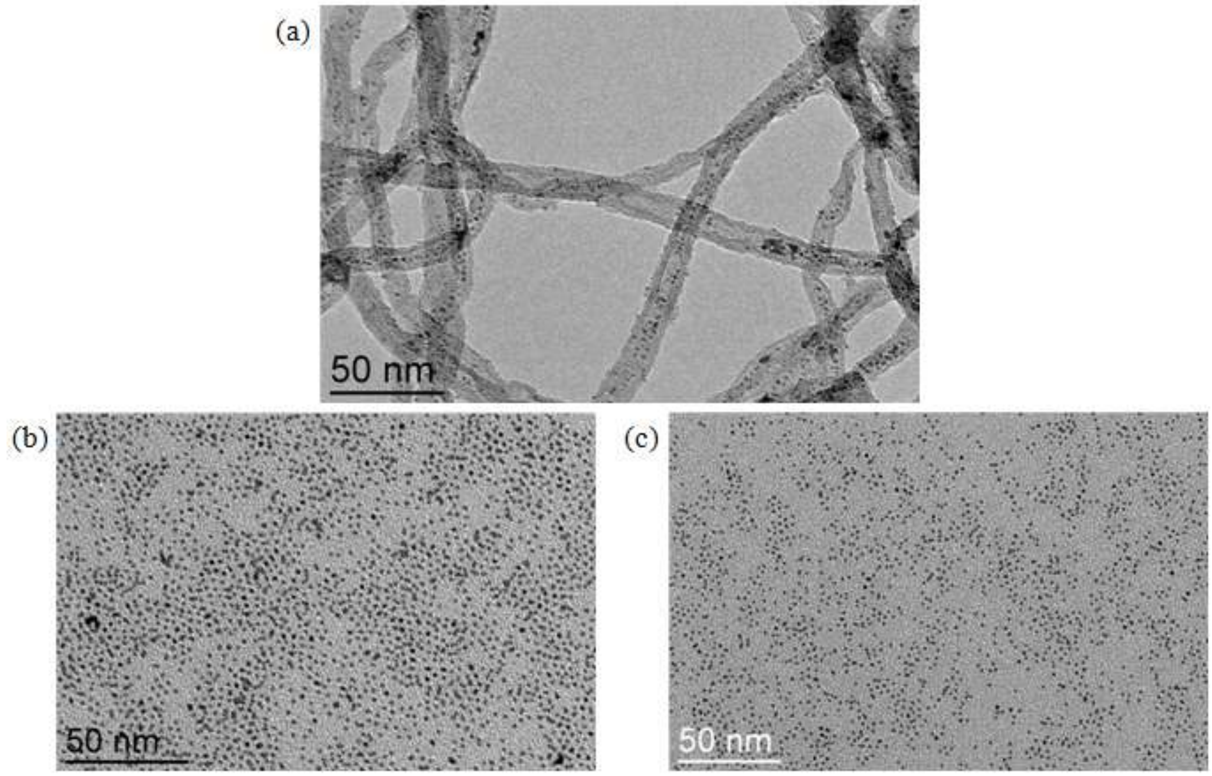

Figure IV.30: TEM images of (a) C-NPs; (b) S-NPs; (c) AS-NPs.

First of all, the **C-NPs** and **AS-NPs** were analyzed by XRF (Figure IV.31). Three mixtures, which contain respectively the Fe and Pt complexes (Fe/Pt in stoichiometric ratios 40/60, 50/50 and 60/40) have been used for calibration. From the sample analysis we found that the **C-NPs** and **AS-NPs** samples present a small difference in composition, but they were both close to Fe$_{40}$Pt$_{60}$. The XRF results are almost consistent with those obtained by ICP elemental analysis ($Fe_{43}Pt_{57}$ for **C-NPs** and $Fe_{46}Pt_{54}$ for **AS-NPs**). Additionally, the **S-NPs** possess also a similar composition as the other two NPs according to XRF.

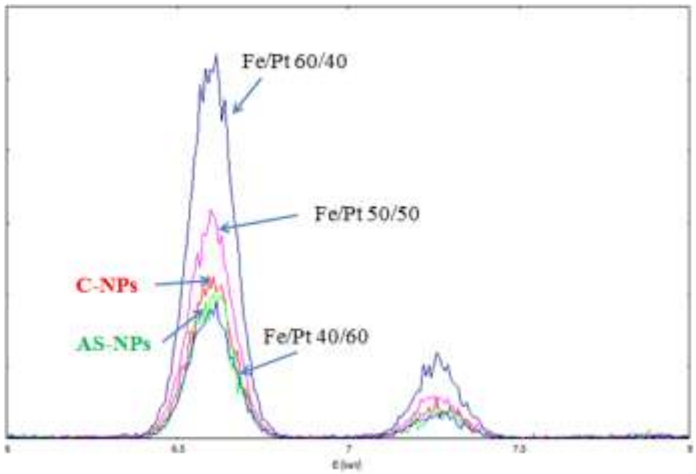

Figure IV.31: XRF Fe Kα and Fe Kβ patterns of the comparison of the C-NPs (red) and AS-NPs (green) with the standard Fe/Pt composition prepared with organometallic complexes. (Amplitudes are normalized on the Pt L pattern).

Second, we have exposed the **C-NPs** to air and compared them with the ones without exposition in order to know whether the NPs were oxidized. The WAXS diffractograms in reciprocal space, in which the **CNT₃** and the bulk FePt diffractograms were added for comparison are shown on Figure IV.34. It was found that both pristine **C-NPs** and air-exposed **C-NPs** show a very similar structure. For the NPs structure, no more detailed information was obtained in the diffractogram (Figure IV.32).

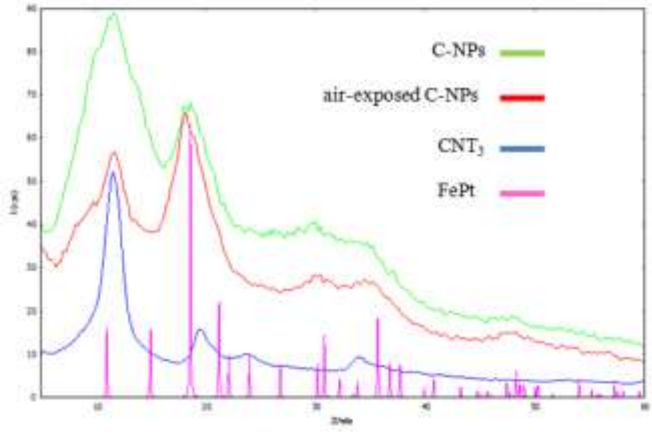

Figure IV.32: WAXS pattern of comparison among the C-NPs (green), air-exposed C-NPs (red), CNT₃ (blue) and standard FePt (pink).

Thus, we applied Fourier transform to the diffractogram from reciprocal space to real space for further comparison between the **C-NPs** and the "oxidized" **C-NPs** (Figure IV.33). The radical distribution function (RDF) shows that the metal-oxygen distance is not observed for any of them, and the short distance is probably attributed to C-C from the CNTs. That means that there is no oxidation of the sample after exposition in the air.

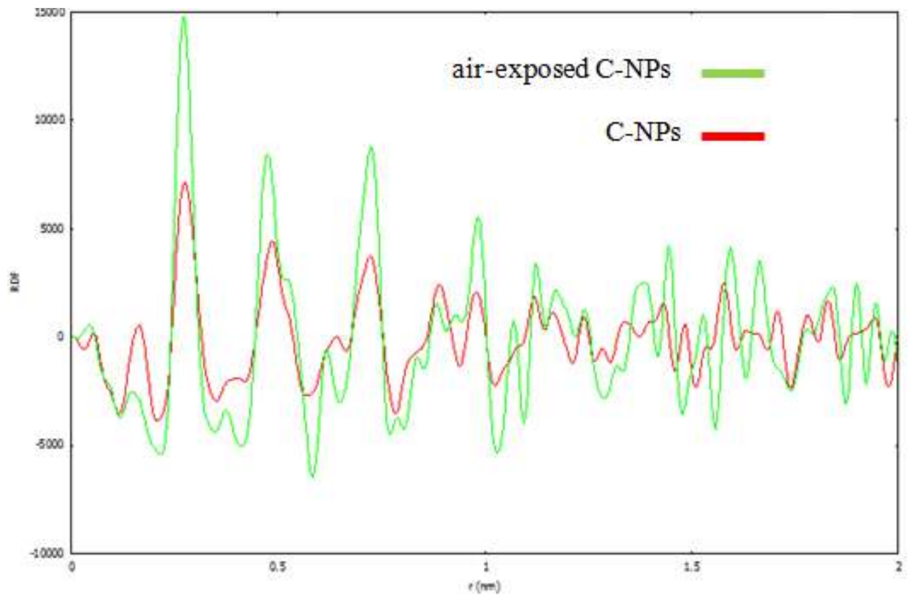

Figure IV.33: RDF of air exposed C-NPs (green) and C-NPs (red).

Subsequently, we compared the **C-NPs** and the **AS-NPs** with a FePt bulk simulation (Figure IV.34). We found that the **C-NPs** are better crystallized than the **AS-NPs** synthesized in the absence of **CNT$_3$**. The first bonding distance for both NPs is identical (0.275 nm) and slightly longer than that of FePt (0.272 nm), which indicates both C-NPs and AS-NPs present a structure closer to bulk Pt (0.275 nm) than to FePt. in contrast to the XRF and elemental analysis results. This may result from certain Fe molecular species attached on the crystallized structure, which can be detected by XRF and elemental analysis but not by WAXS or XRD.

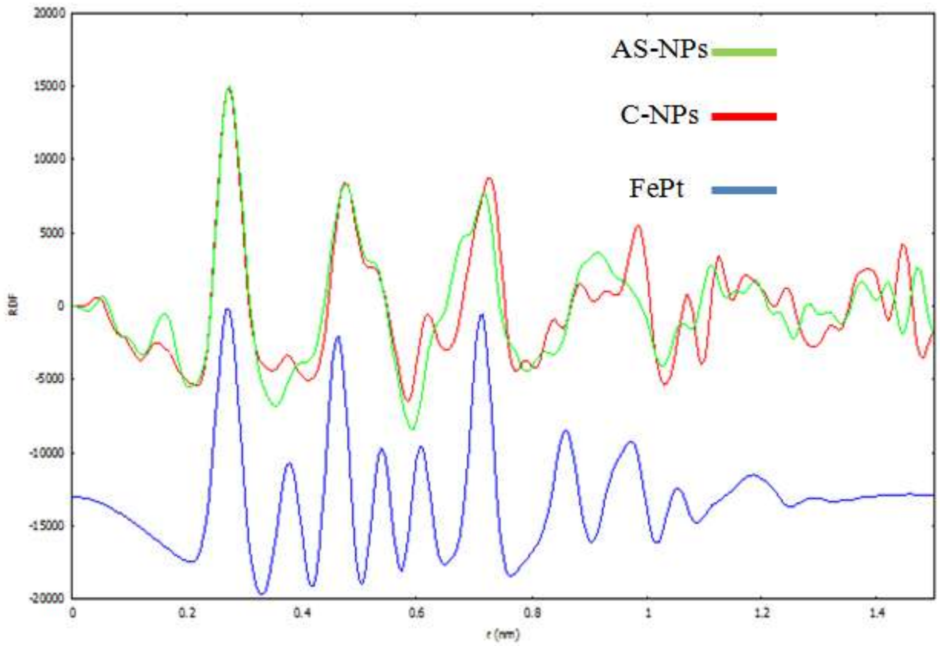

Figure IV.34: RDF among the AS-NPs (green), C-NPs (red) and FePt bulk (blue).

Comparing the **C-NPs** with the **S-NPs** by WAXS (Figure IV.35), the **C-NPs** were found to be better crystallized that the **S-NPs**. That means that confinement in the **CNT_3** facilitates the crystallization of the NPs since the NPs formed in the colloidal solution (**AS-NPs**) and the ones isolated from the supernatant of a reaction that contained CNTs (**S-NPs**) do not undergo this confinement effect.

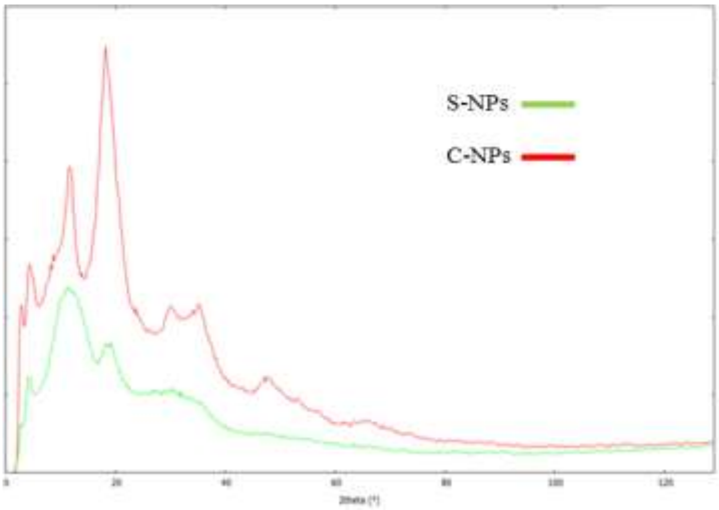

Figure IV.35: WAXS pattern between the C-NPs (red) and the S-NPs (green).

To summarize, Fe-Pt NPs have been confined within CNTs (**C-NPs**) after reduction of a "[Pt(acac)$_2$]_1Fe_2BBA_2PPP_Tol_100°C_24h" starting solution in the presence of **CNT_3**.

The **C-NPs**, and similar size NPs isolated from the supernatant (**S-NPs**) as well as NPs synthesized in the absence of the **CNT_3** (**AS-NPs**) have been studied in order to see whether the confinement had an impact on **C-NP** structure. We have studied the composition and the structure of these three different Fe-Pt NPs by XRF and WAXS. From elemental analysis and XRF results, we show that the composition of the **C-NPs** and the **AS-NPs** are very similar and both close to $Fe_{43}Pt_{57}$. However, WAXS analyses have shown that they possess a structure very rich in Pt rather than the $Fe_{43}Pt_{57}$. These results may indicate that some other species of Fe exist in the samples, which increase the Fe content but do not crystallize in the structure of the NPs. It has to be mentioned that similar results were obtained in the case of the NWs. In that case, the Fe content varies based on the EDX (around 30%) and XRD (almost no Fe) results; while after annealing (see **IV.4**) both analyses present a similar result, around 30% from EDX and a structure close to $FePt_3$ (25%) from XRD. That supports our hypothesis that some non-decomposed Fe species that might be coordinated to CNTs by the aromatic ligands, can be attached on the sidewall of the CNTs *via* π-π interaction, or that some metallic species deposited on the inner sidewall do not contribute to the crystallized structure. We also found that confinement in CNTs facilitates the crystallization of the NPs, which may due to the interactions between the confined species and the inner surface of CNT.

IV.4.3 Isolated Co and Fe complexes from starting solutions and UV-visible study

From our previous results, we saw that the presence of both Pt and Co (or Fe) is mandatory to form the NWs at 100°C and 3 bar H_2. The presence of BBA at least is also necessary. The metallic species that are able to enter into the CNTs should be some complexes with the aromatic ligands and most probably with BBA. Therefore, we attempted to isolate and characterize compounds that are present in the starting solution.

In general, and even for simple NPs composed of only one metal, the starting solutions, that we heat under H_2 in order to obtain the NPs are systems, in which several species are formed in the presence of the stabilizing ligands. These species have different reactivity under hydrogen, and can be reduced at different rates. The ones that are easily reduced form the first seeds (nucleation step), on which, more stable compounds will be subsequently attached (growth step), as the reaction continues. To this process we may add several equilibriums that may be established between species in solution, either from the beginning or at any moment during the reaction. These are therefore very complex systems difficult to study and to understand. In the case of bimetallic NPs, things become even more complicated, since we have two different metals that can react very differently with the two added ligands. In addition the CNTs can also alter the course of the reactions by creating local concentration gradients (in *vs* out). We were interested in isolating any complex formed in the initial solution that yields to Co-Pt or Fe-Pt after heating under H_2. The nature of the complex could give a hint about the possible interactions with the CNTs.

The first system from which we tried to isolate relevant complexes was the the starting solution of "1Pt_0.84Co_2BBA_2PPP_Tol_100°C_24h". After mixing all the ingredients as usually, it was concentrated by evaporation under vacuum. Then, the concentrated solution was conserved in the freezer of the glove-box at -40°C. Some purple crystals, which were formed together with a pink solid, were carefully collected and washed with pentane. The structure of the crystals was determined by single-crystal X-ray study. Its molecular structure is shown in Figure IV.36. We can see that two Co (II) centers coordinate to four molecules of BBA and two molecules of PPP. Each BBA coordinates with two Co by bridging bidentate binding mode. The two Co centers are connected by a bond, so that both have 18 electrons.

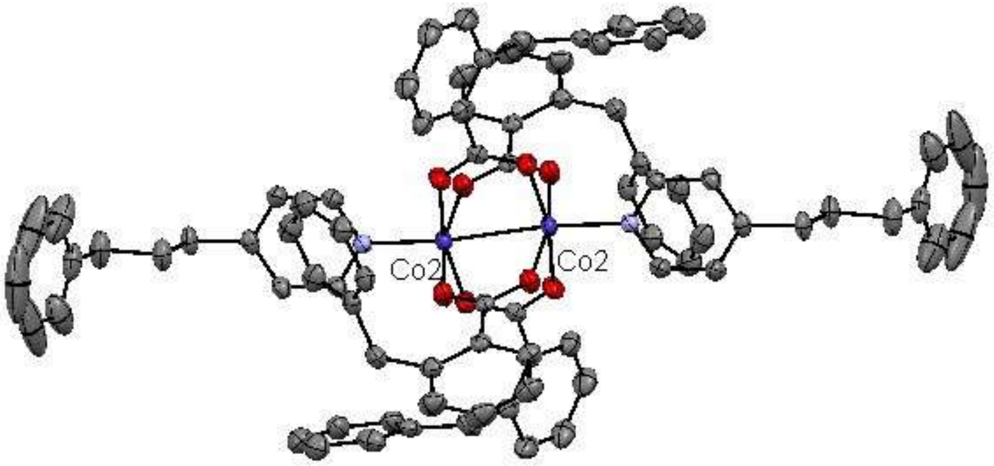

Figure IV.36: Schematic representation of the structure of the purple Co crystal.

A UV-visible spectrum of the crude solution just after mixing all the compounds in toluene is shown in Figure IV.37 (left) (green line) The black line corresponds to the Pt precursor in toluene, presenting nearly no absorption in the visible zone, which is consistent with its almost colorless solution. After adding the two aromatic ligands, the solution becomes slightly yellow, presenting nearly no absorption (red line). The addition of the Co precursor provokes a very significant difference (green line), corresponding to a purple color. An additional blue line is displayed for comparison, which corresponds to a Co precursor solution in toluene alone.

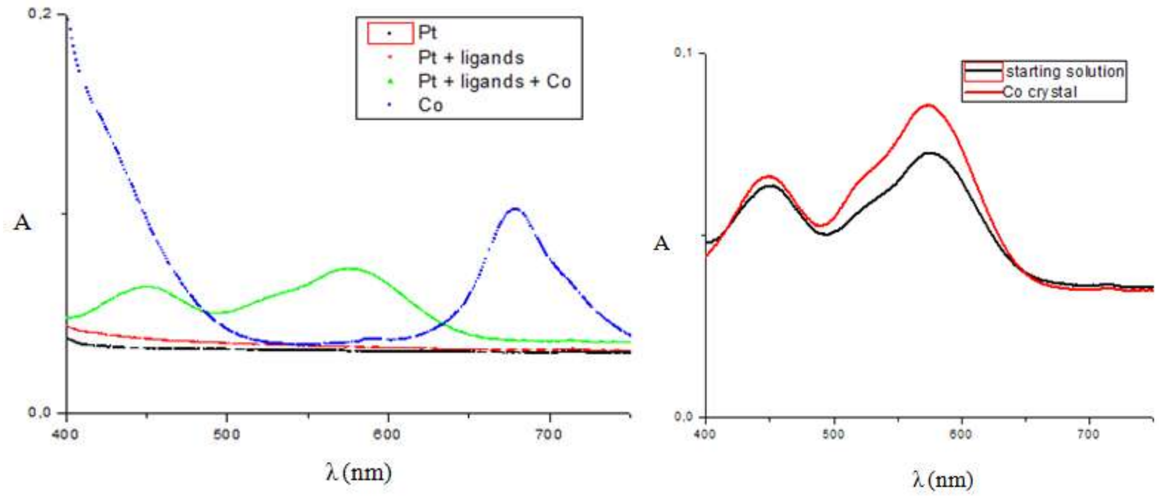

Figure IV.37: UV-visible spectrum. (left) The preparation of the starting solution of "Pt_0.84Co_2BBA_2PPP_Tol_100°C_24h"; (right) Comparison between the starting solution and the Co crystal in toluene.

By comparing the UV-visible spectra of each step during the preparation of the starting solution, the evolution indicates that the addition of the Co precursor obviously modifies the solution composition. The UV-visible spectrum of the isolated Co crystals was then compared to the one of the whole starting solution and they are found very similar (Figure IV.37 (right)).

The purple solid was isolated by adding pentane to the concentrated starting solution. It was then washed and analyzed by elemental analysis. The results (C 74.44%; H 5.26%; N 2.21%) are very close to those calculated theoretically for the purple crystal molecule (C 74.33%; H 5.49%; N 2.06%). Then, the purple solid was compared to the crystals and the starting solution by UV-visible spectroscopy (Figure IV.38). The starting solution (black line), presents two main peaks (445 nm and 575 nm) and a shoulder (525 nm). These peaks are also present in the spectrum of the crystal as well as in the one of the pink powder. They correspond to the isolated Co species. However the ratio between these peaks is not exactly the same in the three cases. This could mean that the complexes present in the pink powder as well as in the starting solution could have some structural differences between them,. Two additional peaks between 300 and 400 nm that are present in the starting solution but absent from the spectra of the crystal and of the pink powder, should correspond to Pt species (blue line) and to the rest of the cobalt.

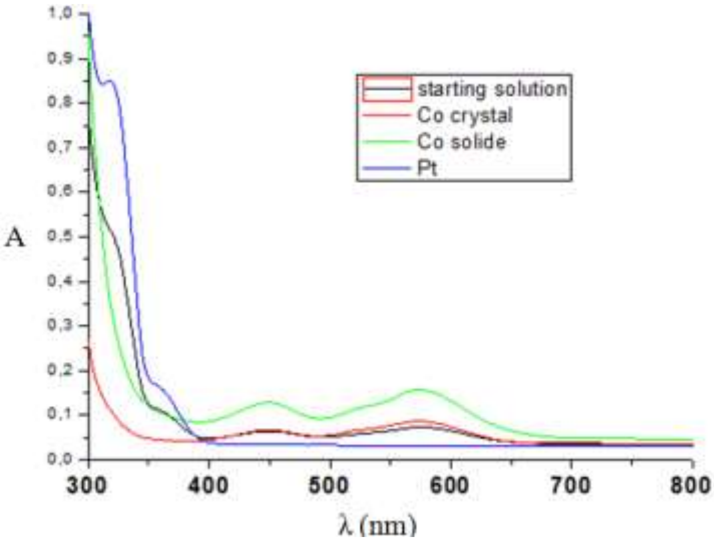

Figure IV.38: Comparison of UV-visible spectra among the starting solution, the Co crystal the Co solid, and the Pt precursor in toluene.

The presence of this Co dimer in the starting solution is therefore unambiguous. Although the exact quantity has not been measured due to the loss during its isolation and washing treatment, the final amount obtained corresponds to more than 60% of the total Co in the starting solution, which indicates its majority among the Co species. However, as already mentioned the peak ratios in the pure complex and the solid are not the same. This could indicate that they could be some differences between the two. One possibility is that the structure of the solid is slightly different than the one of the crystal, or even that the solid is composed of a mixture of the crystal compound and another compound that has a more intense peak at 445 nm.

Through the same procedure, a dark yellow crystal and a yellow solid were isolated from the starting solution of "Pt_Fe_2BBA_2PPP_Tol_100°C_24h". The single-crystal X-ray study (Figure IV.39) show a structure that contains three Fe (II) centers coordinated by six BBA and four PPP ligands. The two terminal Fe centers bind to two molecules of PPP each, and each one shares three bridging BBA molecules with the central Fe. However the three BBA molecules are not equivalent since two of them are normal bidentate bridges, whereas the third one is tri-dentate (acting as a chelate for the terminal Fe and as a bridge between the terminal and the central Fe). The central Fe is therefore coordinated to 6 different BBA molecules, which form three bridges with the terminal Fe centers. All the Fe centers have 18 electrons.

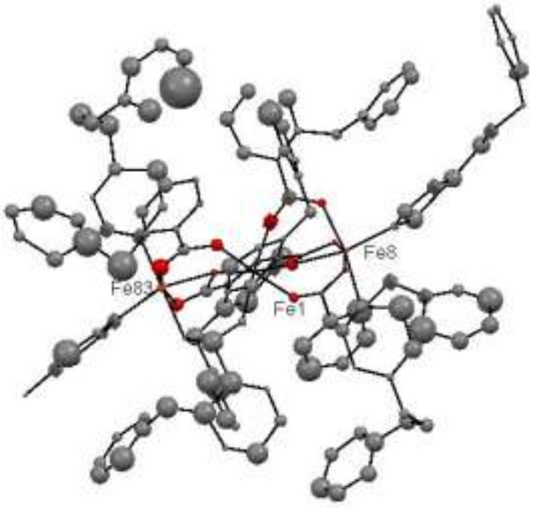

Figure IV.39: Schematic representation of the structure of the yellow Fe crystal.

The elemental analysis for the isolated yellow solid is similar (C 75.40%; H 5.43%; N 2.35%) than that of the Fe crystal molecule (C 75.61%; H 5.71%; N 2.52%). The comparison by UV-spectrometry indicates that the yellow crystal and the solid present in the starting solution (Figure IV.40) have also very similar spectra and both resemble to the one of the starting solution, which however seems to have much more intense absorption in the UV region.

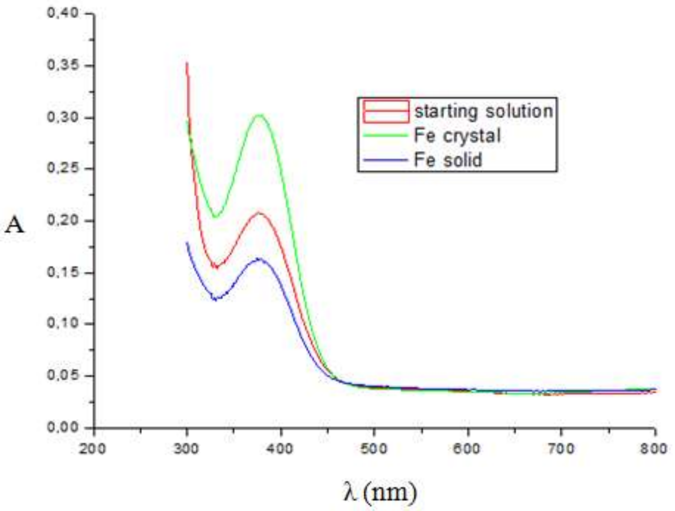

Figure IV.40: UV-visible spectra comparison among the starting solution of "Pt_Fe_2BBA_2PPP_Tol_100°C_24h", the Fe crystal and the Fe solid.

The isolated complexes comprise aromatic ligands that could interact with the internal walls of the CNTs. However they do not contain platinum. Pt species remain in solution and we have not been able to have information concerning their nature. Nevertheless, we have used the isolated powders of the Co and Fe bi and tri-nuclear compounds, respectively, in order to see whether the presence of these ligands could favor their confinement in the CNTs. Two reactions were carried out, one for each metal, in the presence of-**CNT$_2$** under the conditions "complex_Tol_100°C_24h". From TEM, nothing was observed except empty CNTs in both reactions, which implies that these complexes did not decompose under these conditions. Having in mind that the magnetic metal content is low in the NWs, this result was not unexpected. However this result can be interpreted in two different ways. The most straightforward interpretation is that the isolated complexes do not enter in the CNTs despite the favorable interactions that their ligands could establish with the CNTs internal walls. However we have to keep in mind that the Co and Fe carboxylate-rich complexes are very stable, so we may also think that even if these compounds were able to enter in the CNTs cavity, they could probably not be reduced under the conditions employed. It would be interesting to repeat this experiment at an increased reaction temperature in order to see where Fe is located once reduced. However this experiment has not been performed for the moment. If the first hypothesis was true, this would mean that it is what it is left in the solution that is the material that gives rise to the NWs. Thus, instead of using the isolated complexes, we have then used the residual solution after removing the Fe tri-nuclear complex. This concentrated residual solution was decomposed in the presence of the f-**CNT$_2$** under the same conditions as "residue_100°C_24h". We have to note that we cannot have any quantitative information about the metal content of this residual mixture, however we can be quite confident that it contains some Fe and the total amount of Pt used for the initial solution. From the TEM image of Figure IV.41, we see several big nanocrystals formed outside the CNTs. Some rare short NWs are also found inside the CNT. It has to be noticed that although most of the known complex was isolated, there should be still some traces in the residual solution, which may play a role. Moreover, the volume of the concentrated residual solution was not the same as the initial starting solution. This variation of the concentration may also influence the result.

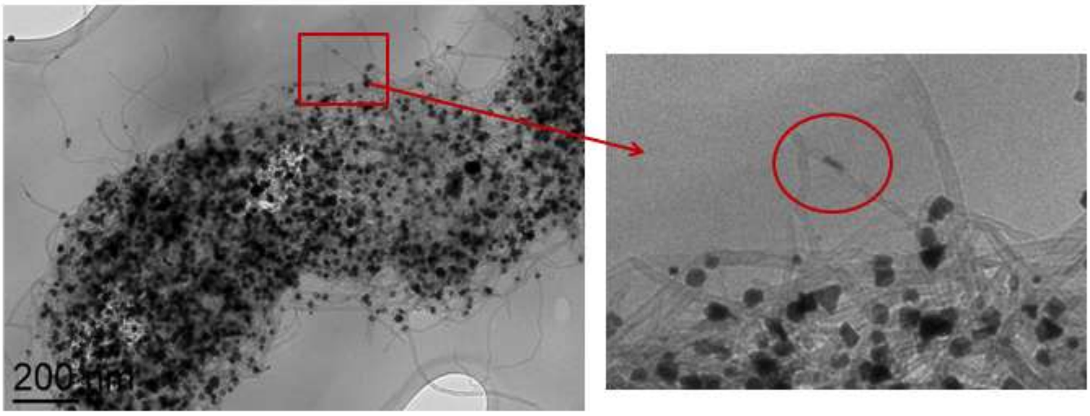

Figure IV.41: TEM images of the reaction with the supernatant isolated from the initial starting solution ("residue_100°C_24h") after removing the Fe tri-nuclear complex.

Finally, we tried to "recompose" the starting solution from its constituents, after having separated the Fe tri-nuclear compound from the rest of the reactants. We have re-dissolved the isolated Fe powder and added it to the rest of the reactants, we have added the normal amount of CNTs and we performed a reduction as before. While some NWs were formed (Figure IV.42), lots of big NPs and aggregates were also observed. These aggregates are not present in the standard "Pt_Fe_2BBA_2PPP_Tol_100°C_24h" experiment. We suppose that the procedure for isolating the complex has as a consequence the modification of other species. These "other species" are probably playing a key-role in the formation of NWs. However, we have to note that the concentration of Pt is higher than usually, due to the fact that a smaller volume of solvent was used for this experiment. This could have provoked the faster than usual formation of Pt NPs and a perturbation of the equilibrium between the species in the rest of the solution. Nevertheless it is also clear that in the presence of the Fe tri-nuclear complex the amount of NWs is increased. It therefore plays a role even if this role is not clear at the moment.

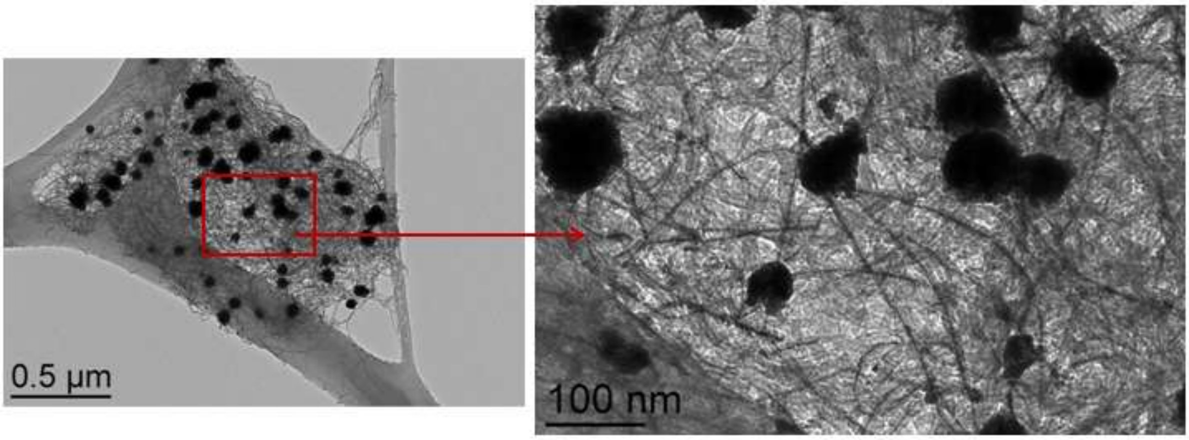

Figure IV.42: TEM images of the reaction in which the supernatant was decomposed in the presence of the Fe complex.

In conclusion, two complexes have been respectively isolated from their starting solutions, and two crystal structures have been solved, showing that monometallic bi- and tri-nuclear complexes are the major Co and Fe compounds formed, respectively, in the initial solutions that give rise to NWs in CNTs. The presence of these complexes in the as prepared initial solutions that give rise to NWs has been proved by UV-visible studies. It has been also found that alone they cannot be reduced at the reaction temperature employed to produce NWs. We can also say that their formation induces the accumulation of HMDS in the medium that can coordinate on platinum. We may say that Pt is the metal by which reduction begins, since the magnetic metals were found not to give rise to any NPs when used alone. The formation of Pt nuclei may facilitate the reduction of Fe and Co. Thus, we suppose that the two monometallic bi- and tri-nuclear complexes constitute a "reservoir" of Co and Fe. The seem to be critical species that assist the NW formation. This has been indirectly proved by control reactions with the Fe complex.

IV.5 Study of phase transition by annealing

IV.5.1 Annealing study for the CNT2-confined Fe-Pt NWs

The Fe-Pt NWs from the reaction "1Pt_Fe_2BBA_Tol_100°C_24h" constitute a good candidate for transformation study since they possess a relative high Fe concentration (about 30%). The obtained f-**CNT_2**-confined Fe-Pt NWs are magnetically "soft", which is characteristic of a chemically disordered phase and possesses a low coercivity (93 Oe) at room temperature (Figure IV.43). In order to transform the disordered structure to the ordered one, thermal annealing is often used to obtain the magnetically hard ordered phases (11).

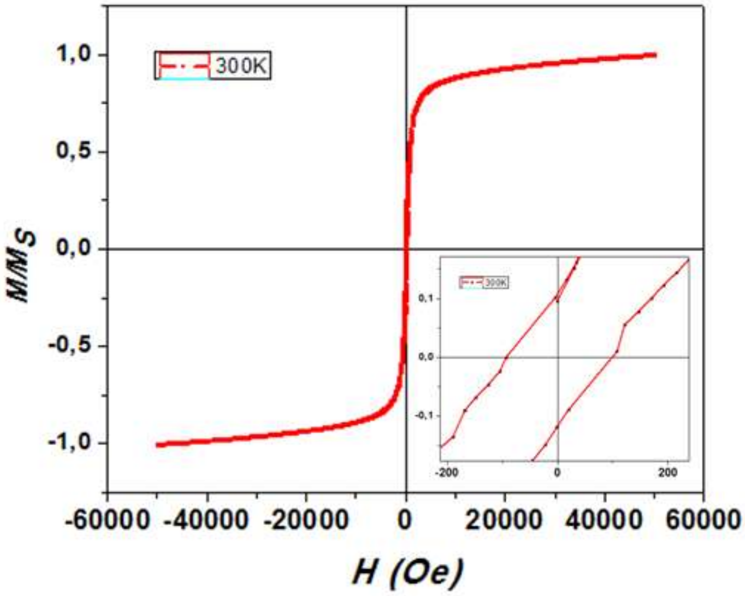

Figure IV.43: Hysteresis loop of the non-annealed Fe-Pt NWs at 300K. Inset is a magnification close to zero point.

It is known that for isolated NPs, simple annealing treatment results in coalescence. To prevent this uncontrolled aggregation, NPs have been embedded in thick organic (56) or robust inorganic (57-61) matrices, or immobilized on the surface of a robust -Si-O- network to limit the mobility of NPs at high temperature (62). Sun *et al.* have found that the onset of the structure change occurs at around 500°C for a $Fe_{52}Pt_{48}$ particle assemblies, and the maximum value of coercivity is reached at about 650°C (11). Higher annealing temperatures can destroy the nanocrystalline structure of the NPs, leading to the formation of multi-domain aggregates and to a decrease in the coercivity (63).

For our samples, the Fe-Pt NWs are confined within the f-**CNT_2**. Due to the template effect, the confined Fe-Pt NWs might retain their shape during annealing. We considered that the CNTs would act as a robust template that could guarantee the conservation of the NW shape during annealing. One of the effects of the confinement could be the modification of the phase transition temperature with respect to the non-confined material. This effect could facilitate or hamper the transition and we are not able to predict whether it will happen at lower or higher temperatures with respect to the bulk material.

The sample was first annealed under N_2. We have followed the reaction by thermogravimetric analysis (TGA) (Figure IV.44), in which heat flow may indicate the onset of structure conversion. However, the heat flow does not present the temperature point where the conversion occurs, because no obvious endothermic process is detected.

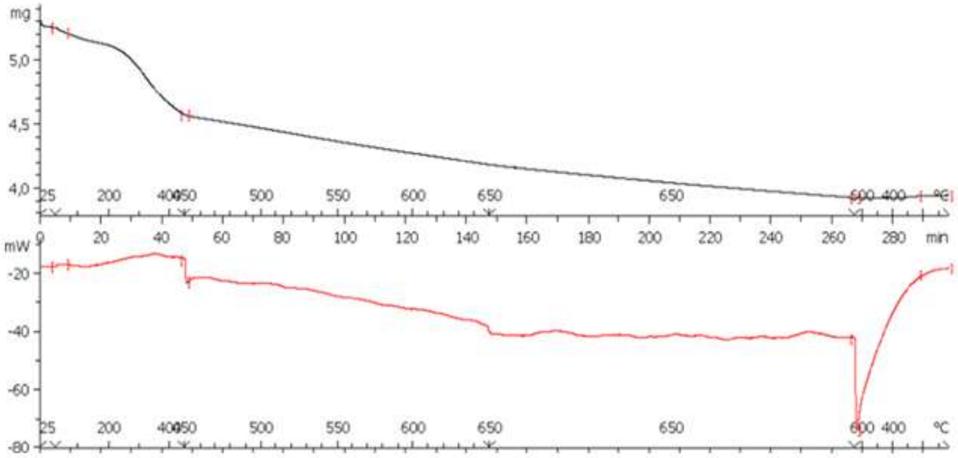

Figure IV.44: (top) TGA performed under N_2 from RT to 650°C for 2 hours with the Fe-Pt NWs; (bottom) heat flow detected during the annealing.

After annealing for 2 hours at 650°C, the temperature at which Fe-Pt has been reported to retain crystalline order (11), the sample was easily and strongly attracted by a strong magnet. XRD analysis indicated the presence of a structure that could be attributed to $FePt_3$, and at the same time another structure appeared as indicated by the development of shoulders on the peaks that correspond to Pt (Figure IV.45). These shoulders correspond to the ordered $FePt_3$ phase.

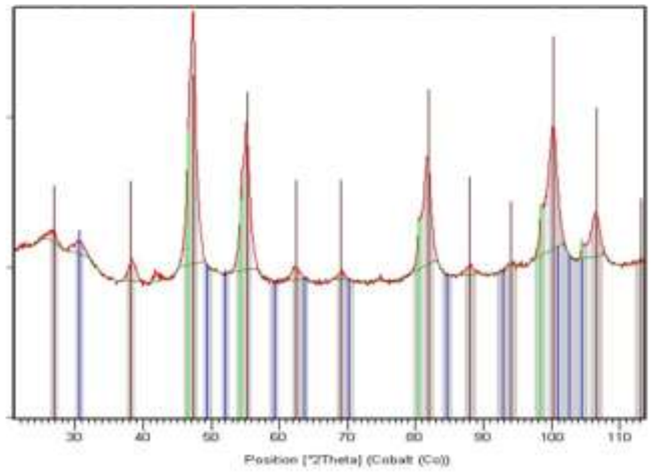

Figure IV.45: XRD pattern of the TGA annealed Fe-Pt NWs that presents a phase associated to CNTs (blue), a ordered $FePt_3$ phase (brown) and a phase close to Pt (green).

The TEM observations revealed that during the annealing parts of the NWs had been extracted from the tubes and had coalesced outside (Figure IV.46). Inside the channels of the CNTs, the NWs were broken into discontinuous NRs of various lengths.

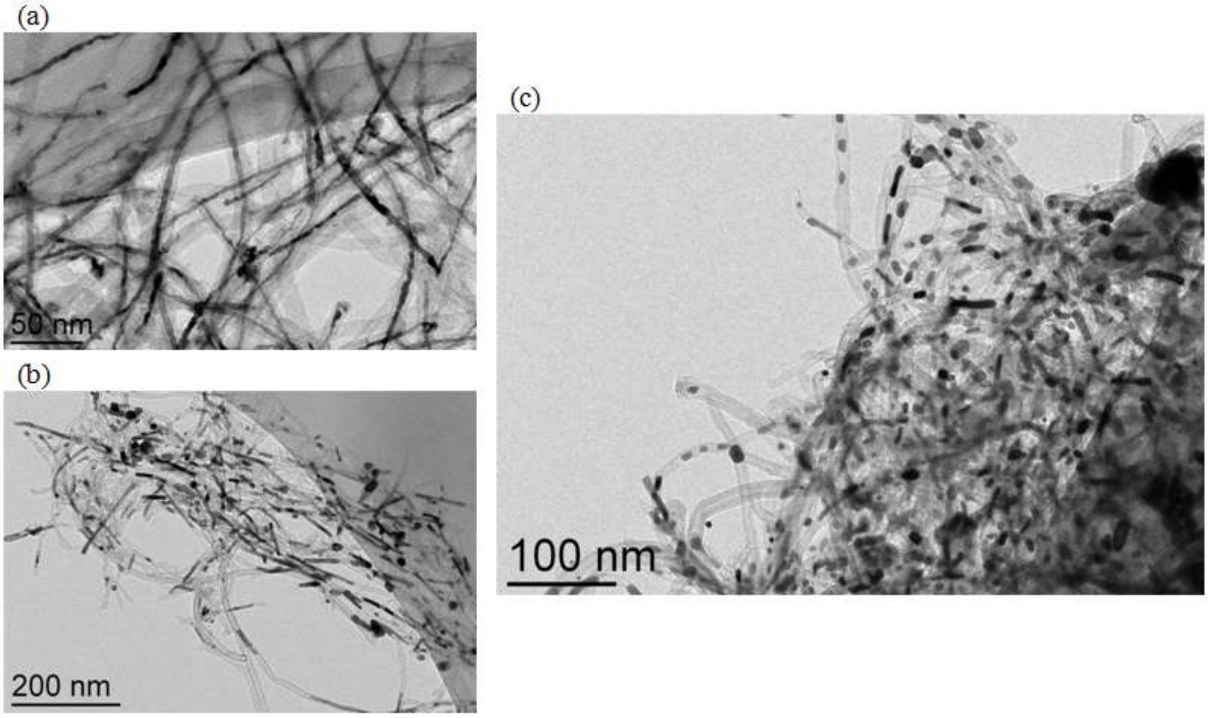

Figure IV.46: TEM images of (a) the Fe-Pt NWs before annealing and (b-c) after annealing.

The higher magnification images show that many tips of the CNTs are clogged by material that seems to be moving outwards (Figure IV.47).

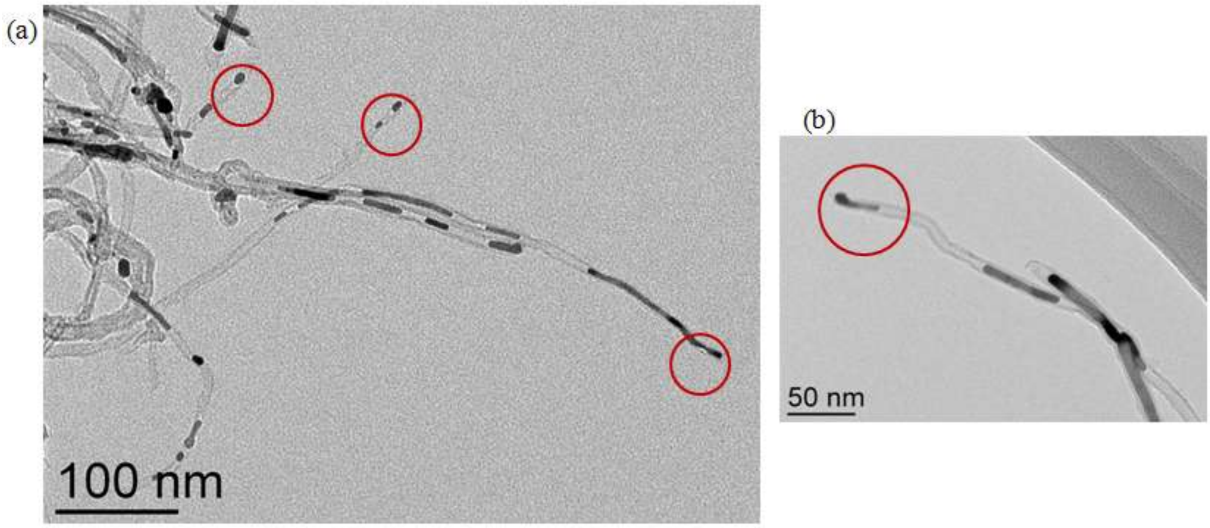

Figure IV.47: TEM images focusing on some tips of the CNTs.

STEM-EDX analyses indicate a homogenous composition of Fe (30-34%) on the NWs (Figure IV.48).

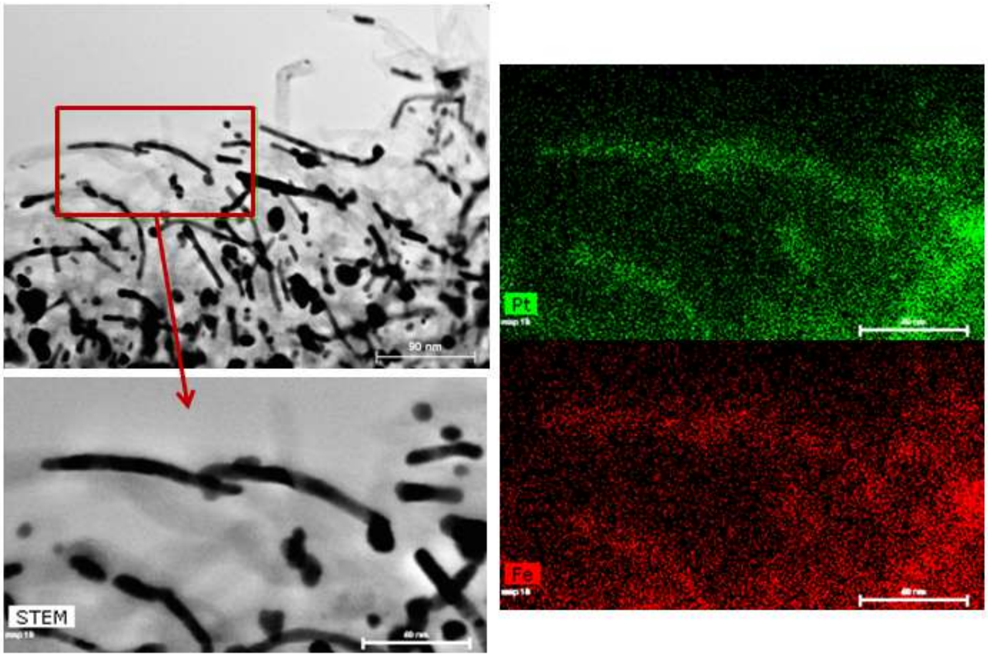

Figure IV.48: STEM analysis of the annealed sample.

The first test showed that annealing at 650°C for 2 hours results in the conversion of the disordered structure into the ordered structure. However, it is not certain that the conversion is complete. Nevertheless, the annealing treatment drove the confined NWs outside of the tube, resulting in a coalescence forming irregular nano-objects. It is known that thermal annealing can cause a re-arrangement of atoms in the materials. Nano-objects are known to exhibit lower melting points that their bulk counterparts. When the temperature increases, the confined metallic NWs become quasi-liquid, a state that presents a high surface tension (64). It seems that in our case the high surface tension drives the liquid to agglomerate in order to decrease its surface tension and thus to decrease its global energy. Moreover, the inner surface of the CNTs is constituted of smooth graphene layers, so friction or other resistances are relative low. These two effects favor the exit and subsequent coalescence.

With the aim to avoid this undesirable effect we have reduced the annealing temperature. We had to determine the low temperature limit at which the phase transformation can take place without however extracting the material from the tube. For this, an *in situ* annealing monitored by XRD under Ar was performed. The diffractograms were recorded at different temperatures as shown in Figure IV.49. At each isotherm, the temperature was maintained for one hour, except at 650 °C for 3 hours. The temperature was increased from 25 to 700 °C (rate 10°C/min) with isotherms of 1 hour at 200, 400, 450, 500, 550, 600, 650 and 700 °C. At the end of each isotherm, a diffractogram was recorded. At the end of the annealing, the sample was cooled to room temperature and a last diffractogram was obtained. The structure evolution is presented in Figure IV.49. The area between 20° and 75° angle is displayed magnified on the left part of the figure. The characteristic peaks associated to the ordered phase $FePt_3$, at 26.8° and 38.1° corresponding to the (100) and (110) planes with the distances 3.85Å and 2.73Å, respectively, start to appear at about 450°C. Upon increasing the temperature, these peaks become sharper and more intense, indicating an increase of the size of the crystallites. After cooling down to room temperature, we see an ordered $FePt_3$ phase in the sample, but also a phase close to Pt, which may reveal that the phase transformation was not terminated even after annealing at 650 °C for 3 hours and at 700 °C.

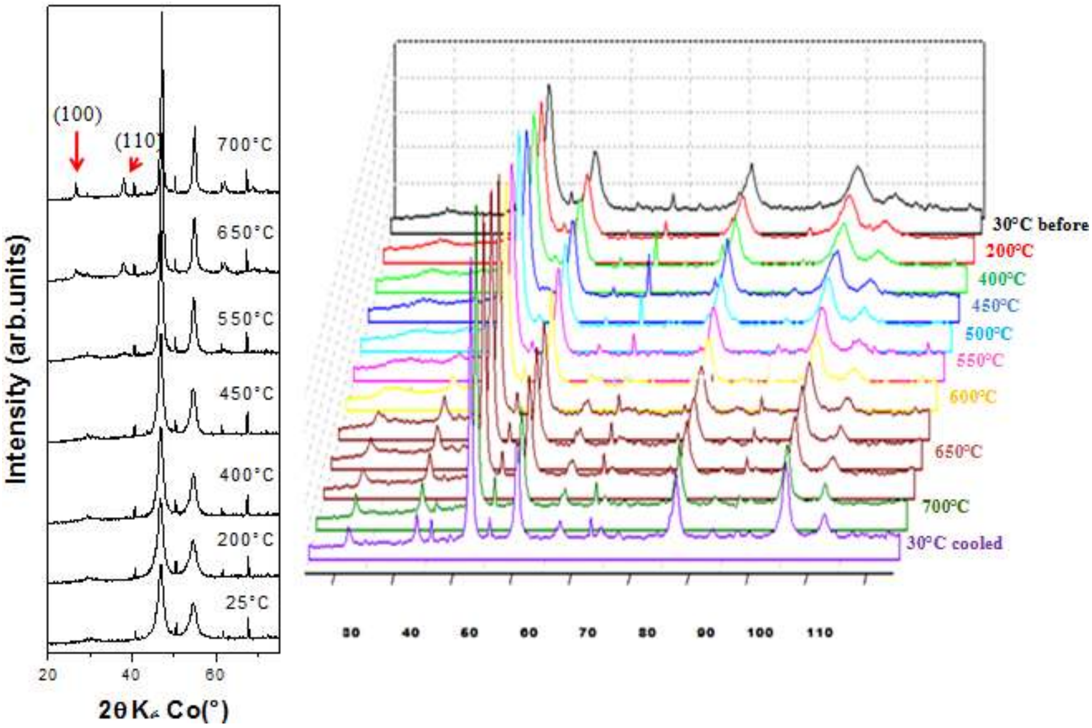

Figure IV.49: XRD pattern for the *in situ* annealing until 700 °C. The new (100) and (110) planes are indicated by red arrows on the left longitudinal comparison.

Calculation of the average crystallite size by the Scherrer method, showed an important increase of the size after the end of the annealing. The sample presents crystallites of 4.8 nm mean size before annealing and 17.7 nm after annealing and cooling down to room temperature. This evolution indicates that coalescence occurred during annealing, which is in agreement with TEM observations (Figure IV.50).

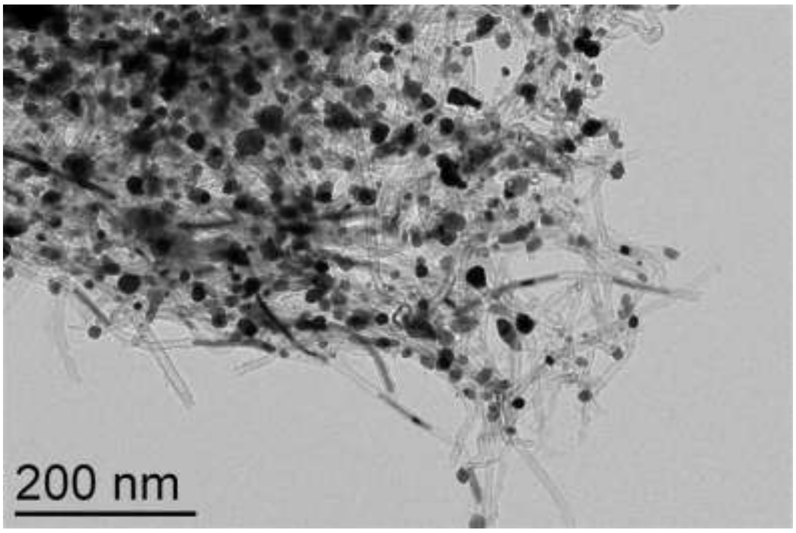

Figure IV.50: TEM image of the sample after the *in situ* annealing.

The hysteresis loop of the annealed sample presents a higher coercivity (1551 Oe) than that before annealing (93 Oe), indicating that the disordered phase of the Fe-Pt NWs before annealing has been transformed into a more ordered phase (Figure IV.51).

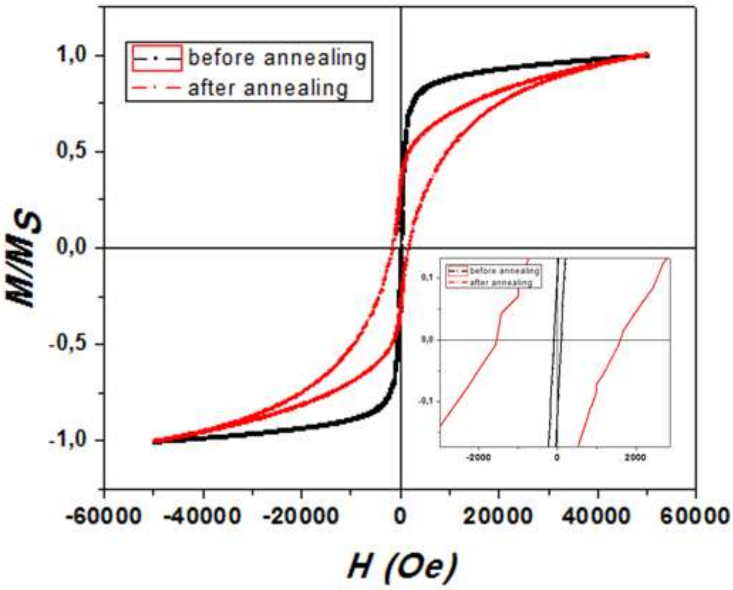

Figure IV.51: Comparison of the hysteresis loops at 27 °C for the Fe-Pt sample (black) before annealing and (red) after annealing at 700 °C.

Although the onset of the transformation occurs at about 450°C, we do not know whether coalescence takes place before this temperature or not. If the coalescence starts at higher temperature than 450 °C, an extended period of annealing at 450 °C could finally lead to the desired ordered structure. Thus, a series of annealing at different temperatures were carried out during one hour at 200, 300, 400 and 500 °C. From TEM, we found out that the NWs already started to escape from the templates after one hour at 200 °C (Figure IV.52) and that some small aggregates are already formed at that temperature. The observations reveal that coalescence occurs before the phase transformation.

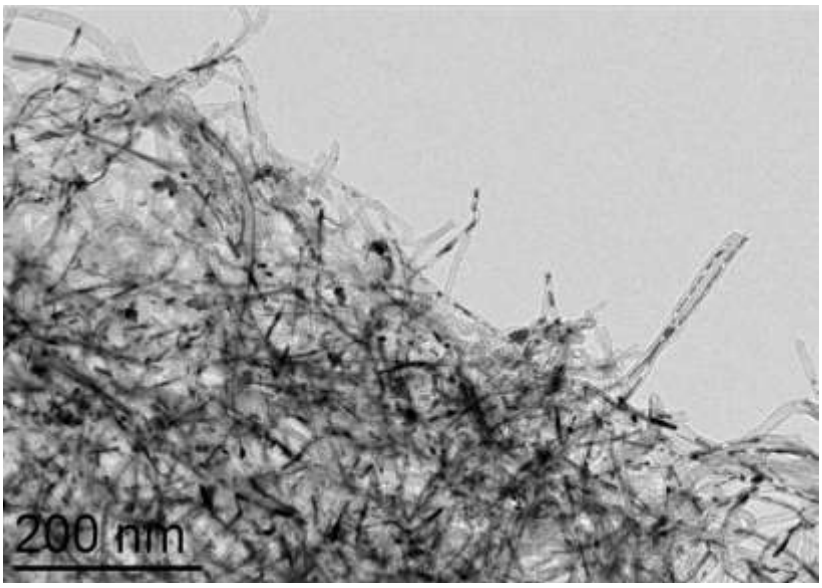

Figure IV.52: TEM image of the sample after annealing at 200 °C for one hour.

In order to avoid coalescence we tried to reduce the annealing time, while at the same time increase the temperature. We thought that with a relatively short micro-wave treatment we could rapidly attain a high local temperature in the metal, avoiding its exit from the CNTs. Thus, the sample was micro-wave annealed for one hour under 800W. However neither a modification of the NW morphology from TEM, nor a structure evolution was observed by XRD.

Another idea was to coat the whole tube with polymer and then anneal it. It was expected that the polymer, which would also block the tube extremities would form a carbon coating upon annealing at high temperatures and prevent the exit of the NWs. The sample was completely and homogenously packed with polyisoprene synthesized by the polymerization of isoprene in the presence of the CNT-templated Fe-Pt NWs. The black gum-like product was washed with ethanol in order to remove the residual reactants and the catalyst, followed by drying under vacuum. Finally, the product was annealed under Ar at 650 °C for one hour. TEM analyses revealed many big NPs and aggregates outside the tubes and CNTs surrounded by amorphous carbon arising from the decomposition of polyisoprene (Figure IV.53).

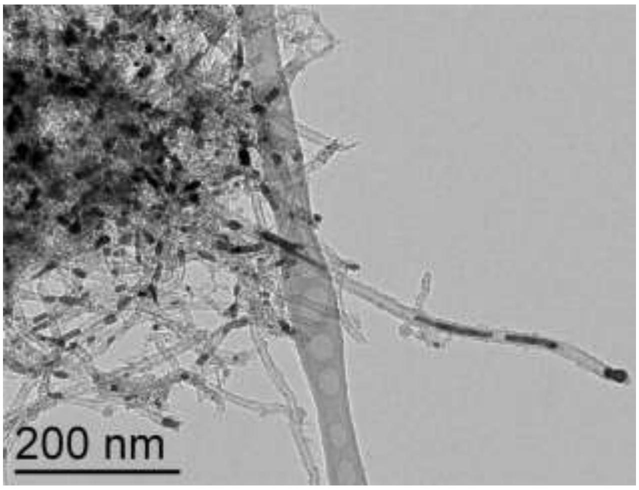

Figure IV.53: TEM image of the annealed Fe-Pt NWs which were pre-coated with polyisoprene before annealing.

XRD pattern shows that after annealing at 600 °C for one hour, an evolution was observed, which is associated with the appearances of some new peaks at 26.8° and 38.1°, corresponding to (100) and (110) planes of ordered $FePt_3$ phase (Figure IV.54). However, careful analysis for the four principal broad peaks shows that two species are presented, one is very close to the Pt phase, the other is very close to ordered $FePt_3$ phase, indicating either an incomplete phase transition or a very Pt-rich composition in the sample, or both.

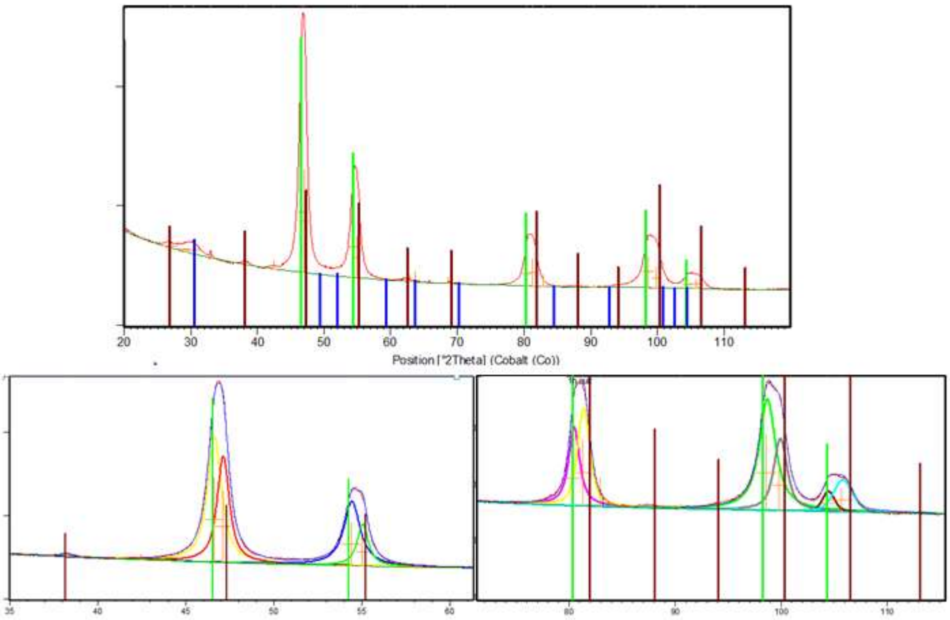

Figure IV.54: XRD pattern of the polyisoprene-coated Fe-Pt NWs at 600°C for one hour. Blue, green and brown lines correspond respectively to carbon, Pt and ordered $FePt_3$ phases.

In conclusion, the CNT-templated Fe-Pt NWs migrate outside the CNTs and coalesce losing their form at about 200 °C, a temperature well inferior to the phase transition temperature (onset at about 450 °C). Further efforts should be focused on improving the annealing, for example by polymer coating that could provide an efficient blocking.

IV.5.2 Annealing study for the CNT3-confined Fe-Pt NPs

The **CNT3**-confined Fe-Pt NPs were annealed at 500 °C for one hour under Ar, and were then examined by TEM. In Figure IV.55, the annealed sample was compared with that before annealing. Before annealing (Figure IV.55a), most of the NPs were confined within **CNT$_3$**, and presented a mean size of 1.7 nm. We observed a very limited coalescence that gave rise to scarce rod-like particles. After annealing at 500 °C, we observed a considerable difference in size. The confined NPs grow to a size as large as 5 nm, and at the same time some NPs with sizes up to 8 nm are present outside the tubes (Figure IV.55b). The TEM observation indicates that thermal annealing makes the NPs coalesce and may drive some confined NPs out of the CNTs, which subsequently coalesce without their size being limited by the channel restriction.

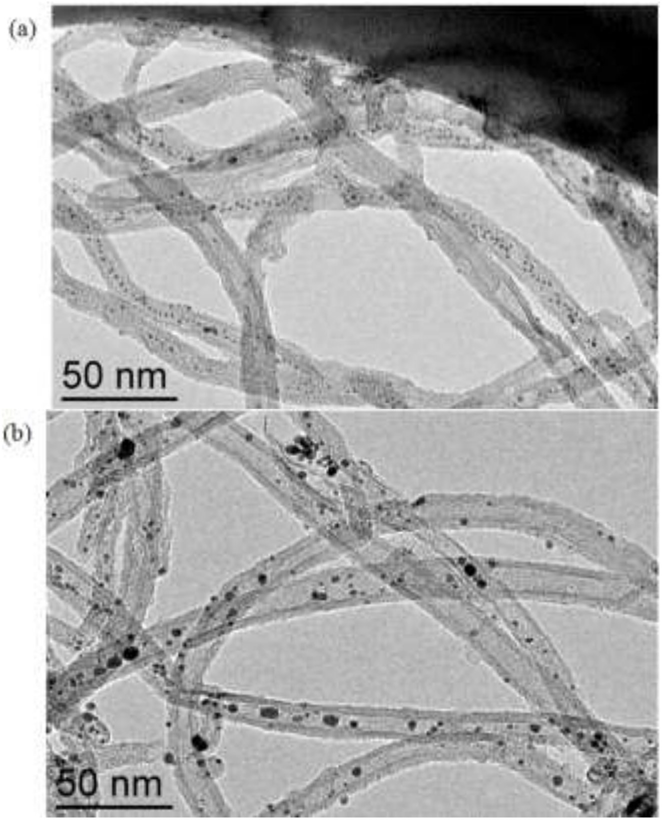

Figure IV.55: TEM images of the sample of the CNT$_3$-confined Fe-Pt NPs (a) before and (b) after annealing.

Another comparison was performed between the XRD patterns of the sample before and after annealing (Figure IV.56). The patterns on the top correspond to the sample before annealing and that on the bottom corresponds to the one after annealing. In the top pattern, the structure of the CNTs (blue) and a structure close to Pt (green) are present. The shift of the peaks with respect to the peaks of Pt could be attributed to the presence of Fe atoms. In the bottom pattern, the structure of the CNTs is still present (blue), whereas a structure associated to $FePt_3$ (brown) is observed instead of the former one. The magnification of the diffractogram of the annealed sample shows better the $FePt_3$ structure (brown) located between the Pt (green) and the FePt (pink) structures.

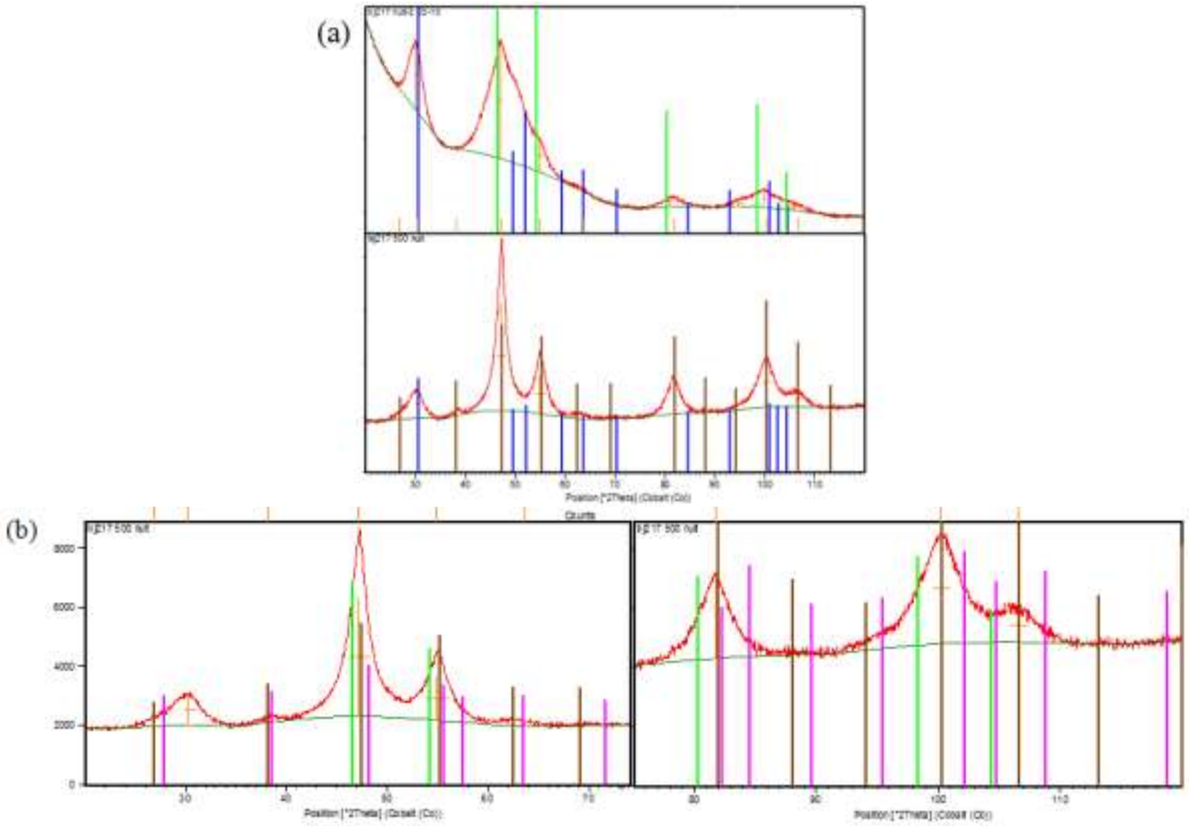

Figure IV.56: (a) Comparison of XRD patterns between the samples before annealing (top) and after annealing (bottom); (b) magnifications of the bottom diffractogram in (a) (blue line: carbon, green line: Pt; brown line: $FePt_3$; pink line: FePt).

In order to see the evolution of the Fe-Pt NPs phase during annealing, an *in situ* annealing monitoring by XRD under Ar was performed. The sample was annealed from 25 to 700°C (rate 10°C/min). The temperature was directly raised from 25 to 500°C. The diffractograms were recorded at 500, 600, 650 (twice) and 700°C (twice). The first two isotherms were maintained during 1 hour and the other two during two hours. The structure evolution is presented in Figure IV.57. Before annealing, the most intense peaks correspond to the Al_2O_3 sample holder (indicated by four red sticks at the bottom of the left patterns). We see that below 600 °C, the peaks corresponding to Pt-like phase become more and more intense ($2\theta = 47°$ and $55°$). At 600 °C, the peak at $2\theta = 47°$, begins to be dissociated into two peaks, one attributed to an ordered $FePt_3$ phase ("$FePt_3$" peak) at $2\theta = 47.3°$, the other is a phase close to Pt ("Pt" peak) $2\theta = 46.8°$. At 650 °C, some small peaks are emerging at 26.8° and 38.1° consistent with the (100) and (110) planes of the ordered $FePt_3$ phase. The "$FePt_3$" peak and the "Pt" peak have almost the same intensity. Surprisingly, after one more hour annealing at 650 °C, the "$FePt_3$" peak decreases while the "Pt" peak increases. When the temperature is increased to 700°C, all the four "$FePt_3$" peaks at $2\theta = 26.8°$, 38.1°, 47.3°and 55.2°, highlighted with four red sticks in the row "$FePt_3$" in Figure IV.57 (left), reach to a maximum while the "Pt" peaks, highlighted with two red sticks in the row "Pt", almost disappears. However, further annealing at 700 °C inverses the situation again, whereby the "$FePt_3$" peaks are nearly absent, replaced by intense "Pt" peaks.

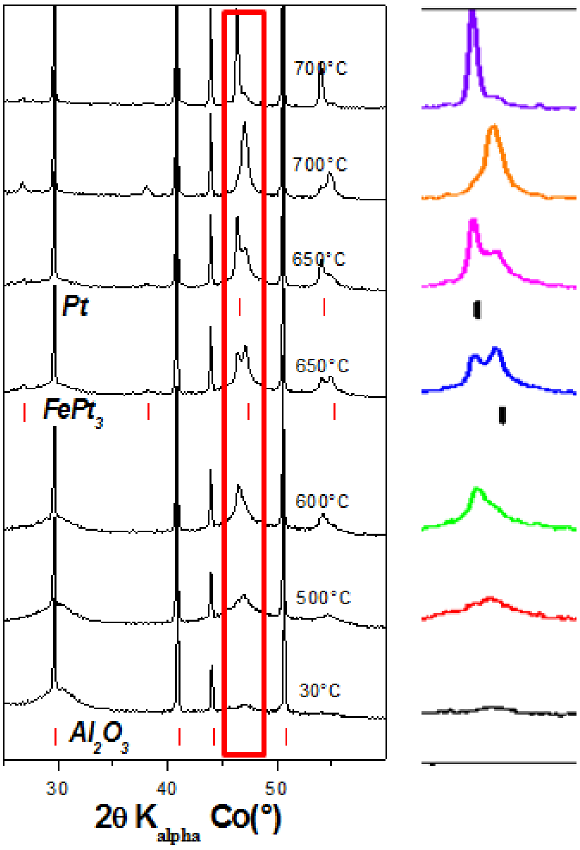

Figure IV.57: (left) Evolution of the phases detected by XRD during the *in situ* annealing; (right) magnifications of the peaks at $2\theta = 47°$ for all the XRD patterns.

This oscillating appearance and disappearance of the $FePt_3$ phase during the annealing, is accompanied by a continuous decrease of the peak at $2\theta = 29.5°$ associated to the CNTs (Figure IV.58), which implies a consumption of CNT during the annealing. We think that oxygen traces in the Ar fluid consume the CNTs completely during annealing. We suppose therefore that the temperature increase favors the transformation to the ordered $FePt_3$ phase at the beginning of the annealing, whereas with prolonged heating at 650°C, oxygen may oxidize the Fe in the $FePt_3$ phase and generate iron oxide and pure Pt as indicated by the increased intensity of the Pt-pure peak. The iron oxide is then reduced back to Fe by oxidizing the CNTs. Subsequently, Fe reforms the $FePt_3$ phase and so on, until complete oxidation of the CNTs, after which the $FePt_3$ phase completely disappears. At the end of the measurement, the CNTs are used up as shown in the Figure IV.58 (brown), and so the "$FePt_3$" phase is oxidized by oxygen, forming the "Pt" phase again. Unfortunately, the iron oxide phase was not detected during the annealing, which may due to the presence of peaks that mask it.

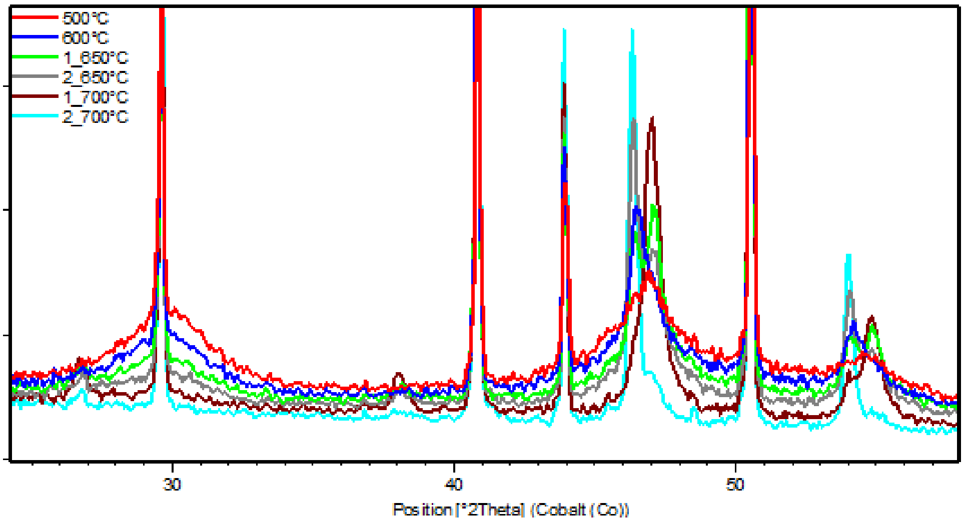

Figure IV.58: Comparison among the XRD patterns by overlapping them.

In conclusion, we have studied phase transformation by thermal annealing with two samples: the CNT-templated Fe-Pt NWs from the reaction "1Pt_1Fe_2BBA_2PPP_Tol_100°C_24" in the presence of the f-$\mathbf{CNT_2}$ and the CNT-confined Fe-Pt NPs from the reaction "1[$Pt(acac)_2$]_1Fe_2BBA_2PPP_Tol_100°C_24" in the presence of the $\mathbf{CNT_3}$.

In the case of Fe-Pt NWs, thermal annealing by TGA, *in situ* XRD or in oven resulted in the formation of the ordered $FePt_3$ phase, which co-exists with a Pt-pure phase. The Fe content in the crystallized structure, is lower than ~30% as measured by EDX analysis for the samples before and after annealing. Based on this comparison, we suppose that some Fe species in the form of molecules or non-crystallized metal may be confined within the CNTs, which can be detected by EDX but not by XRD before annealing. The thermal annealing drive the confined NWs out of the CNTs, and provoke their aggregation into NPs outside the tubes. The tests with different annealing temperatures indicate that the NWs have already started to move out at temperatures as low as 200°C, much lower than the temperature where the phase transformation begins (450°C). Efforts have been made in order to avoid the aggregation outside the CNTs. By using a relatively less "violent" annealing process with micro-wave, no ordered phase took place. Coating the CNTs with polymer, did not function since the NWs still moved out and the aggregates were observed as usual. The hysteresis loop of the annealed sample presents a higher coercivity (1551 Oe) than that before annealing (93 Oe).

In the case of Fe-Pt NPs, the situation is better since less NPs leaching has been observed after annealing. The XRD experiments for both NPs and NWs showed that the Fe content is inferior to 30% in the confined materials, since both $FePt_3$ and pure Pt were present.

IV.6 Conclusion

Different Pt-based bimetallic nanostructures have been confined within different CNTs. Based on the results of a reference reaction "Pt_0.84Co_2BBA_2PPP_Tol_100°C_24h" performed from [$PtMe_2$(COD)] and [Co{$N(SiMe_3)_2$}$_2$(THF)] in the presence of the f-**CNT_1**, we have shown that different CNT diameters result in different confined morphologies. Inside the large inner diameter f-**CNT_1**, small NPs are formed, while the NPs tend to coalesce and form wire-like morphology in the small diameter CNTs. Additionally, a difference in the metal composition between the NPs in small diameter (75%/25% Co/Pt) and large diameter CNTs (22%/78% Co/Pt) indicates an easier entrance of the magnetic metal in the larger diameter CNTs. Under the same reaction conditions, when the inner diameter decreases to less than 10 nm (f-**CNT_2)**, bimetallic Co-Pt NWs are formed. The confined wire-like structures contain more Pt than Co according to EDX analysis. Very similar Fe-Pt NWs have been also formed under the comparable conditions "Pt_1Fe_2BBA_2PPP_Tol_100°C_24h.

The Co or Fe composition in the toluene-washed sample decreases when acid solution washing is used, which indicates that some Co or Fe species can be selectively removed by acid solution. However, after acid washing, the continuous NW structures seems to persist.

Many efforts have been devoted in order to increase the Co or Fe content in the NWs and also to understand the NW formation by variations of the reaction conditions. It can be concluded that the simultaneous presences of Pt and Co (or Fe) and acid ligand (BBA) are necessary to form the NWs. Changing various reaction parameters, such as the nature of the Pt precursor, the metal ratio, the temperature, the ligand type and ratio, as well as the preparation of the starting solution, results in different morphologies of nanostructures outside the CNTs and influences significantly the NW yield.

Two organometallic complexes and their single crystals have been isolated from the concentrated starting solutions. By comparing the UV-vis spectra of these compounds with the ones of the corresponding starting solutions, we can confirm their existence in the starting solution. In fact they seem to be the major Co (Fe) containing species formed in the starting solution. These complexes while they are not the ones that preferentially enter in the CNTs cavities, seem to be indispensable for the entrance of other species in the CNTs.

Using **CNT_3** that possess –COOH groups on their surface instead of **CNT_2** that possess long alkyl chain, and using [$Pt(acac)_2$] as precursor in the presence of PPP and BBA ligands, we have been able to produce small Pt-Co and Pt-Fe NPs selectively confined in the inner cavity of **CNT_3** by the *in situ* method. These NPs are also Pt-rich. This is an interesting result since no confinement was obtained with f-**CNT_2**. This confirms the steric hindrance induced by the long alkyl chain that prevents the confinement of the molecular complexes mentioned above. For **CNT_3**, the presence of the –COOH groups can be detrimental for the confinement of preformed NPs, which can interact easily with such groups. However, for the *in situ* preparation method, in which molecular species are involved, if these complexes are "stable" enough, they will not react with the –COOH groups and will be able to enter the inner cavity and to interact with the inner sidewalls *via* π-π interactions thanks to their ligands.

The structures of the as-prepared CNT-templated Co-Pt or Fe-Pt NWs have been studied by XRD, and that of the CNT-confined Fe-Pt NPs has been studied by WAXS. Taken altogether, the results show that the NPs formed in the interior of CNTs are better crystallized than the NPs formed outside.

The transformation from disordered structure to ordered structure has also been attempted by thermal annealing of the confined Fe-Pt NWs and Fe-Pt NPs. For the NWs it has been found that migration along the CNT tube walls results in coalescence and expulsion from the CNT cavity at low temperatures, well before the phase transition starts. The attempts to avoid this aggregation by decreasing the annealing temperature, using micro-wave heating, and coating protection with polyisoprene have failed. The NPs, suffer less from the thermal annealing, although a limited coalescence of NPs outside the CNTs has also been found. The annealing has led to two phases for both NWs and NPs, one is the ordered $FePt_3$ phase, the other is a Pt phase, which may indicate that the Fe content is less than 25% in the crystallized structures of both Fe-Pt NWs and Fe-Pt NPs. This could be related to the nature of the species that are able to enter in the CNTs.

Further efforts should be focused on: i) increasing the Co or Fe composition of the confined nanostructures aiming at a Pt/Co ratio of 1; ii) searching the critical species that are responsible for the NW formation; and iii) searching an appropriated method for phase transformation by annealing.

IV.7 Reference

1. S.-I. Choi, S.-U. Lee, W. Y. Kim, R. Choi, K. Hong, K. M. Nam, S. W. Han, J. T. Park, *ACS Appl. Mater. Interfaces*, **2012**, *4*, 6228–6234.
2. D. Wang, H. L. Xin, R. Hovden, H. Wang, Y. Yu, D. a Muller, F. J. Disalvo, H. D. Abruña, *Nat. Mater.*, **2013**, *12*, 81–87.
3. S. Guo, S. Zhang, D. Su, S. Sun, *J. Am. Chem. Soc.*, **2013**, *135*, 13879–13884.
4. S. Guo, D. Li, H. Zhu, S. Zhang, N. M. Markovic, V. R. Stamenkovic, S. Sun, *Angew. Chem. Int. Ed. Engl.* **2013**, *52*, 3465–3468.
5. N. a Frey, S. Peng, K. Cheng, S. Sun, *Chem. Soc. Rev.*, **2009**, *38*, 2532–2542.
6. S. Mornet, S. Vasseur, F. Grasset, E. Duguet, *J. Mater. Chem*., **2004**, *14*, 2161–2175.
7. Q. A. Pankhurst, J. Connolly, S. K. Jones, J. Dobson, *J. Phys. D: Appl. Phys*., **2003**, *36*, R167.
8. K. Inomata, T. Sawa, S. Hashimoto, *J. Appl. Phys*., **1988**, *64*, 2537-2540.
9. D. Weller, A. Moser, *IEEE Trans. Magn*., **1999**, *35*, 4423-4439.
10. D. E. Laughlin, K. Srinivasan, M. Tanase, L. Wang, *Scr. Mater.,* **2005**, *53*, 383–388.
11. S. Sun, *Adv. Mater.,* **2006**, *18*, 393–403.
12. Z. R. Dai, S. Sun, Z. L. Wang, *Nano Lett*., **2001**, *1*, 443–447.
13. X. Sun, Z. Y. Jia, Y. H. Huang, J. W. Harrell, D. E. Nikles, K. Sun, L. M. Wang, *J. Appl. Phys.,* **2004**, *95*, 6747-6749.
14. C. -b. Rong, D. Li, V. Nandwana, N. Poudyal, Y. Ding, Z. L. Wang, H. Zeng, J. P. Liu, *Adv. Mater.,* **2006**, *18*, 2984–2988.
15. M. Albrecht, M. Maret, A. Majer, F. Treubel, B. Riedlinger, U. Mazur, G. Schatz, S. Anders, *J. Appl. Phys*., **2002**, *91*, 8153-8155.
16. M. Maret, M. C. Cadeville, R. Ponsot, A. Herr, E. Beaureparie, C. Monier, *J. Magn. Magn. Mater*., **1997**, *166*, 45.
17. P. W. Rooney, A. L. Shapiro, M. Q. Tran, F. Hellman, *Phys. Rev. Lett*., **1995**, *75*, 1843-1846.
18. G. R. Harp, D. Weller, T. A. Rabedeau, R. F. C. Farrow, M. F. Toney, *Phys. Rev. Lett*., **1993**, *71*, 2493-2496.
19. S. Sun, C. B. Murray, D. Weller, L. Folks, A. Moser, *Science*, **2000**, *287*, 1989-1991.
20. Z. R. Dai, S. Sun, Z. L. Wang, *Nano Lett*., **2001**, *1*, 443-447.
21. S. Sun, S. Anders, T. Thomson, J. E. E. Baglin, M. F. Toney, H. F. Hamann, C. B. Murray, B. D. Terris, *J. Phys. Chem. B*, **2003**, *107*, 5419-5425.
22. J. Zhang, J. Fang, *J. Am. Chem. Soc.,* **2009**, *131*, 18543–18547.
23. X. Teng, H. Yang, *J. Am. Chem. Soc.,* **2003**, *125*, 14559–14563.
24. K. Elkins, D. Li, N. Poudyal, V. Nandwana, Z. Jin, K. Chen, J. P. Liu, *J. Phys. D. Appl. Phys.,* **2005**, *38*, 2306–2309.
25. B. J. Kim, C. Rong, J. P. Liu, S. Sun, *Adv. Mater.,* **2009**, *21*, 906–909.

26. B. Q. Yan, A. Purkayastha, T. Kim, R. Kröger, A. Bose, G. Ramanath, *Adv. Mater.,* **2006**, *18*, 2569–2573.
27. M. Solzi, C. Pernechele, G. Calestani, M. Villani, M. Gaboardi, A. Migliori, *J. Mater. Chem.,* **2011**, *21*, 18331-18338.
28. S.-Z. Chu, K. Wada, S. Inoue, S.-I .Todoroki, Y. K. Takahashi, K. Hono, *Chem. Mater*., **2002**, *14*, 4595-4602.
29. F. Tian, J. Zhu, D. Wei, Y. T. Shen, *J. Phys. Chem. B*, **2005**, *109*, 14852-14854.
30. H. Pan, B. Liu, J. Yi, C. Poh, S. Lim, J. Ding, Y. Feng, C. H. A. Huan, J. Lin, *J. Phys. Chem. B*, **2005**, *109*, 3094-3098.
31. J. Qin, J. Nogues, M. Mikhaylova, A. Roig, J. S. Munoz, M. Muhammed, *Chem.Mater*., **2005**, *17*, 1829-1834.
32. Y.-G. Guo, L.-J. Wan, C.-F. Zhu, D.-L. Yang, D.-M. Chen, C.-L. Bai, *Chem. Mater*., **2003**, *15*, 664-667.
33. G. Ji, J. Cao, F. Zhang, G. Xu, H. Su, S. Tang, B. Gu, Y. Du, *J. Phys. Chem. B*, **2005**, *109*, 17100-17106.
34. S.-Z. Chu, S. Inoue, K. Wada, K. Kurashima, *J. Phys. Chem. B*, **2004**, *108*, 5582-5587.
35. J.-r . Choi, S. J. Oh, H. Ju, J. Cheon, *Nano Lett*., **2005**, *5*, 2179-2183.
36. F. Liu, J. Y. Lee, W. Zhou, *J. Phys. Chem. B*, **2004**, *108*, 17959-17963.
37. G. B. Ji, S. L. Tang, B. X. Gu, Y. W. Du, *J. Phys. Chem. B*, **2004**, *108*, 8862-8865.
38. Y. Dahmane, L. Cagnon, J. Voiron, S. Pairis, M. Bacia, L. Ortega, N. Benbrahim, a Kadri, *J. Phys. D. Appl. Phys.,* **2006**, *39*, 4523–4528.
39. H. M. Chen, C. F. Hsin, P. Y. Chen, R.-S. Liu, S.-F. Hu, C.-Y. Huang, J.-F. Lee, L.-Y. Jang, *J. Am. Chem. Soc.,* **2009**, *131*, 15794–801.
40. C.N.R. Rao, R. Sen, *Chem. Commun*., **1998**, 1525–1526.
41. P.C.P. Watts, W.K. Hsu, V. Kotzeva, G.Z. Chen, *Chem. Phys. Lett*., **2002**, *366*, 42–50.
42. A. Morelos-Gómez, F. López-Urías, E. Muñoz-Sandoval, C. L. Dennis, R. D. Shull, H. Terrones, M. Terrones, *J. Mater. Chem.,* **2010**, *20*, 5906-5914.
43. Q. Su, J. Li, G. Zhong, G. Du, B. Xu, *J. Phys. Chem. C*, **2011**, *115*, 1838–1842.
44. P. K. Tyagi, A. Misra, M. K. Singh, D. S. Misra, J. Ghatak, P. V. Satyam, F. Le Normand, *Appl. Phys. Lett.,* **2005**, *86*, 253110-1-253110-3.
45. V. Gupta, R. K. Kotnala, *Angew. Chem. Int. Ed.*, **2012**, *51*, 2916–2919.
46. R. Lv, S. Tsuge, X. Gui, K. Takai, F. Kang, T. Enoki, J. Wei, J. Gu, K. Wang, D. Wu, *Carbon,* **2009**, *47*, 1141–1145.
47. R. Marega, F. De Leo, F. Pineux, J. Sgrignani, A. Magistrato, A. D. Naik, Y. Garcia, L. Flamant, C. Michiels, D. Bonifazi, *Adv. Funct. Mater.,* **2013**, *23*, 3173–3184.
48. B. Cormary, F. Dumestre, N. Liakakos, K. Soulantica, B. Chaudret, *Dalton Transactions*, **2013**, *42*, 12546-12552.

49. K. Lee, S. W. Kang, S-U. Lee, K-H. Park, Y. W. Lee, S. W. Han, *ACS Appl. Mater. Inter*, **2012**, *4*, 4208–4214.

50. C. Cui, L. Gan, M. Heggen, S. Rundi, P. Strasser, *Nat. Mater*, **2013**, *12*, 765–771.

51. E. Antolini, J. R.C. Salgado, E. R. Gonzalcz, *J. Power Sources*, **2006**, *160*, 957–968.

52. T. J. Klemmer, N. Shukla, C. Liu, X. W. Wu, E. B. Svedberg, O. Mryasov, R. W. Chantrell, D. Weller, M. Tanase, D. E. Laughlin, *Appl. Phys. Lett.*, **2002**, *81*, 2220-2222.

53. Thesis of Lise-Marie Lacroix, *Nanoparticules de fer de taille contrôlée pour l'hyperthermie : Synthèse par voie organométallique, caractérisations magnétiques et mesures de puissance dissipée*, **2008.**

54. N. Liakakos, B. Cormary, X. Li, P. Lecante, M. Respaud, L. Maron, A. Falqui, A. Genovese, L. Vendier, S. Koïnis, B. Chaudret, K. Soulantica, *J. Am. Chem. Soc.* **2012**, *134*, 17922–31.

55. N. Trang , P. Serp, *ChemCatChem*, **2013**, *5*, 3595–3603.

56. S. Momose, H. Koroyoshi, N. Ihara, T. Uzumaki, A. Tanaka, *Jpn. J. Appl. Phys., Part 2*, **2003**, *42*, 1252-1254.

57. M. Chen, J. P. Liu, S. Sun, *J. Am. Chem. Soc.*, **2004**, *126*, 8394-8395.

58. H. Zeng, J. Li, Z. L. Wang, J. P. Liu, S. Sun, *Nano Lett.*, **2004**, *4*, 187-190.

59. C. Liu, X. Wu, T. Klemmer, N. Shukla, D. Weller, *Chem. Mater.*, **2005**, *17*, 620-625.

60. K. Elkins, D. Li, N. Poudyal, V. Nandwana, Z. Jin, K. Chen, J. P. Liu, *J. Phys. D: Appl. Phys.*, **2005**, *38*, 2306-2309.

61. M.-P. Chen, K. Kuroishi, Y. Kitamoto, *IEEE Trans. Magn.*, **2005**, *41*, 3376-3378.

62. M. Mizuno, Y. Sasaki, A. C. C. Yu, M. Inoue, *Langmuir*, **2004**, *20*, 11305-11307.

63. H. Zeng, S. Sun, T. S. Vedantam, J. P. Liu, Z. R. Dai, Z. L. Wang, *Appl. Phys. Lett.*, **2002**, *80*, 2583-2585.

64. B. J. Keene, *Int. Mat. Rev.*, **1993**, *38*, 157-192.

Conclusions and perspectives

In this thesis, we have studied the confinement of magnetic metallic nanostructures inside multi-walled carbon nanotubes of various diameters. Such hybrid nano-objects could find applications in hyperthermia or for the magnetic alignment of CNTs in composites. Several characterization techniques have been used in order to study the properties and structure of the confined nanostructures. The work is divided into two main topics:

- The selective confinement of well-defined monometallic (Fe, Co) MMNPs within functionalized MWCNTs and their protection from oxidation by polymerization; and

- The study of Pt-based bimetallic (CoPt and FePt) magnetic nanostructures inside CNTs and their phase transformation by thermal annealing.

It has to be noted that in order to be able to study the confinement effect on the magnetic properties, we had not only to suppress the growth of magnetic nanomaterials on the external surface of the CNTs, but also to efficiently separate any free NPs formed in solution from samples containing CNTs with confined NPs. Various approaches have been attempted toward this goal in order to finally obtain the dried solid nanohybrid for further magnetic measurements.

By taking advantage of attractive/repulsive interactions between the MMNPs and surface functionalized-MWCNTs, Fe and Co MMNPs (both spherical nanoparticles and nanorods) have been successfully confined within the large diameter f-**CNT$_1$** (inner diameter 20-200 nm) *via* either the *ex situ* suspension method or the *in situ* solution method. For the suspension method, the MMNPs, directly synthesized with aromatic ligands (PPP and BBA) as stabilizer or indirectly modified by ligand exchange, have been confined inside the CNT channel by simply mixing the CNTs in the colloidal solution. Ligand exchange has allowed modifying the surface of Co NRs, thus allowing introducing superlattices of Co NRs in the interior of f-**CNT$_1$**. To the best of our knowledge there are no examples in the literature of NRs introduced in CNTs. In this case, a great effort has been devoted to the separation of the CNT-confined nanoparticles from the colloidal mixture. However, we have not been able to study the magnetic properties of the confined NRs because the separation was not efficient. Different solvents should be used in the future in order to “break” the superlattices formed in solution without affecting the superlattices in the interior of the CNTs.

A FeNP@**CNT$_1$** nanohybrid, practically free from Fe NPs on the CNT external surface has been obtained after filtration and washing treatment. This material has been obtained by the *in situ* synthesis of Fe NPs in the presence of the aromatic ligands. The magnetic measurements have shown the absence of oxidation for both pre-formed Fe NPs and the FeNP@**CNT$_1$** nanohybrid. The measurement of the magnetic properties had revealed a confinement effect (higher coercive field for the confined NPs). Additionally, we have performed polymerization *via* two different methods (ATRP and metal-catalyzed polymerization) in order to coat the confined Fe NPs and protect them from air oxidation. In the ATRP method, the initiator-modified Fe NPs have been confined within the f-**CNT$_1$**. Isoprene polymerization has been performed with both the free modified NPs and the confined ones. However, both of them have been found aggregated after being coated by relatively few amounts of polyisoprene (PI), which hinders further magnetic measurement. For the organometallic catalyzed polymerization method, a naphthalene-modified Fe iminopyridine complex has been developed, which presented a very high activity for isoprene polymerization. The Fe complex-modified Fe NPs (FeNP@Fe) have been also confined within the f-**CNT$_1$**. Polymerization has been carried out on both the free modified NPs and the confined ones. No aggregation has been observed in this case. Finally, the PI-coated FeNP@Fe@PI and the FeNP@Fe@PI@CNT$_1$ nanohybrids have been obtained. Although several catalytic reactions have been performed in the inner cavity of CNTs, to the best of our knowledge polymerization inside their cavity has never been reported. We have then evaluated the resistance to air oxidation of the polymer coated confined Fe NPs by magnetic measurements. The non-exposed Fe NPs, FeNP@Fe@PI and FeNP@Fe@PI@CNT$_1$ nanohybrids have been confirmed to be non-oxidized. We have found that the PI coating can delay the air oxidation. It has also been found that the polymerization is more efficient when the Fe NPs are not confined within CNTs, which may be attributed to the presence of higher amounts of polymer on the free Fe NPs than on the confined ones. Nevertheless, this proof of concept suggests that this strategy could be used with other polymers that are more efficient air- and moisture-barriers and to other air-sensitive NPs. Moreover, we have discovered that the Fe complex-modified Fe NPs presented a very good resistance towards air oxidation. Indeed, even a one hour air exposition does not influence its magnetic properties. This latter result is very interesting and surprising, and offers very exciting perspectives for the protection from oxidation of MMNPs. Of course, this result has to be confirmed and studied in more detail.

In the *in situ* method, the as-synthesized Fe and Co NPs have been confined within the f-**CNT$_1$** during the reaction in solution. However, the confinement selectivity is not high, making it impossible to obtain a clean sample appropriate for magnetic measurements. For the confinement in the thinner f-**CNT$_2$**, both of the filling methods have been attempted. However, only MMNPs attached on the outer surface have been formed. For the *ex situ* method, this result could be explained by the size of the preformed NPs that is close to the one of the CNT inner cavity. For the *in situ* method, this could be explained by a steric hindrance induced by the long alkyl chain that prevents the confinement of the molecular complexes. Indeed, the functionalization with long alkyl chain is effective not only on the sidewall but also at the open extremities of CNTs that possess reactive carbon atoms. This steric hindrance should be determinant for small diameter CNTs but should not affect the entrance of molecular species in large diameter nanotubes.

In the second part of this thesis, the template effect of the CNTs has been exploited and different Pt-based bimetallic nanostructures have been confined within CNTs of different diameter and surface composition. From the results of the preliminary reaction in the presence of the f-**CNT$_1$**, we have found out that different CNT diameters result in different confined bimetallic Co-Pt morphologies as well as different ratios of the two metals in the confined nanomaterials. Inside the large inner diameter **CNT$_1$** (~ 100 nm), small NPs are formed, while the NPs tend to coalescence and to form wire-like morphology in the small diameter **CNT$_1$** (~ 20 nm). A difference in the metal composition between the NPs in smaller diameter and the larger diameter CNTs indicates an easier entrance of the magnetic metal in the larger CNTs. Under the same reaction conditions, bimetallic Co-Pt and Fe-Pt NWs have been formed in the presence of the f-**CNT$_2$** with inner diameters less than 10 nm. The confined wire-like structures contain more Pt than Co or Fe. In an effort to detect the species that enter in the CNTs channels and produce the confined material after reduction, two coordination complexes, one of Co (dimeric) and one of Fe (trimeric), have been isolated from the corresponding starting solutions. Their structure has been elucidated by single-crystal X-ray analysis. Their presence in the starting solutions has been confirmed by UV-vis spectroscopy. However the structure of the species present in solution, can deviate from their structure in the solid state. This means that the dimer and trimer structures found in the solid state could be monomers in solution. Whatever their structure in solution, these are the major species formed by each magnetic metal in the starting solution. These complexes do not decompose under the standard reaction conditions however they are indispensable for the confinement to take place, as it can be expected due to the fact that they contain several aromatic ligands that can interact with the CNT sidewalls via π-π interaction. Further on, we performed a parametric study in order to try to understand the mechanism of confinement of the NWs, both for cobalt and for iron. The mechanism of the reaction should be very complex, and up to now we are not able to propose any convincing hypothesis. We note however some similarities between the cobalt and the iron behavior. First, the presence of all the $[Co\{N(SiMe_3)_2\}_2(THF)]$ (or $[Fe\{N(SiMe_3)_2\}_2]_2$) precursor, $[PtMe_2(COD)]$ precursor and aromatic ligands are necessary for the formation of the NWs. The absence of any of these components is detrimental to their formation. We have also seen that BBA alone is able to induce a limited formation of NWs, but only when both metals are present. The results obtained point towards a synergy between all these components. Second, we also suspect that the Pt precursor is the first one to decompose under the optimal condition for NWs formation. We cannot discard a possible involvement of the HMDS ligand, released in the starting solution during the formation of the Co dimer and Fe trimer, in the stabilization of the primary mono- or bimetallic Pt containing species. It is not clear however if the low amounts of magnetic metal incorporated in the NWs arise from the stable Co dimer and Fe trimer, or from the remaining (and still unknown) Co and Fe species. Considering the fact that 60-70% of the Co (or Fe) species in the starting solution consists in the stable Co dimer (or Fe trimer), and that approximately 20-30% of Co (or Fe) is present in the final NWs, a value in good balance with the amount of unknown Co (or Fe) species present in the starting solution, the association of this latter species to Pt could be proposed.

Finally, when using $\mathbf{CNT_3}$ that possess –COOH groups on their surface and not long alkyl chains (f-$\mathbf{CNT_2}$), and using $[Pt(acac)_2]$ as precursor in combination with PPP and BBA ligands, we have been able to very selectively produce, by the *in situ* method, small Pt-Co and Pt-Fe NPs confined in the inner cavity of $\mathbf{CNT_3}$. These NPs are also Pt-rich. This is an interesting result since no confinement was obtained with f-$\mathbf{CNT_2}$. This confirms the steric hindrance induced by the long alkyl chain that prevents the confinement of the molecular complexes mentioned above. For $\mathbf{CNT_3}$, the presence of the –COOH groups can be detrimental for the confinement of preformed NPs, which can interact easily with such groups. However, for the *in situ* preparation method, in which molecular species are involved, if these complexes are "stable" enough, they will not react with the –COOH groups and will be able to enter the inner cavity and to interact with the inner sidewalls *via* π-π interactions thanks to their ligands. This confirm also that the chemistry involved is very complex since changing the nature of the Pt precursor modifies significantly the course of the reaction and the final morphology of the confined nano-objects.

Further work concerning this first part should focuses on: i) developing the filling method in order to confine more MMNPs within the CNTs; ii) improving the selectivity of the polymerization of isoprene for a better air-protection; iii) performing other polymerization like polyethylene coating on the MMNPs for a better air-protection; iv) an in-depth study of the air protection of MMNPs by the grafted iron complex; and v) further studies on the confined NW *vs* NP formation in thin MWCNTs.

Transformation from disordered structure to ordered structure has also been attempted by thermal annealing of the confined Fe-Pt NWs and Fe-Pt NPs. For the NWs it has been found that migration along the CNT walls results in coalescence and expulsion from the CNT cavity at low temperature (200°C) well before the phase transition starts. The attempts to avoid this unexpected aggregation by decreasing the annealing temperature, using micro-wave heating, and coating protection with as-synthesized polymer have failed. For the NPs, thermal annealing gives rise to less influence than for the NWs, although the growth of the NPs outside the CNTs has also been found. The annealing has led to two phases for both NWs and NPs, one is ordered $FePt_3$ phase, the other is a close to Pt phase, which may indicate that the Fe content is $\leq 25\%$ in the crystallized structures of both Fe-Pt NWs and Fe-Pt NPs.

For perspective in this part, further efforts should be focused on: i) raising the Co or Fe composition in the confined nanostructures aiming at a stoichiometry of 50% compared to Pt; ii) searching the species that are responsible for the NW formation; and iii) searching an appropriated method for phase transformation by annealing.

To summarize, a very complex nanochemistry has been performed inside CNTs, and various hybrid nanostructures have been obtained, characterized and studied in this thesis. More effort should be made in the future for developing new nanohybrids with novel properties in the CNT-confined nano-space.

Appendix I- Experimental part

Experimental part

I. Glassware

The glassware used for all the reactions was washed with an aqua regia to remove any metal trace, and then immersed in an alcoholic solution of hydroxylic potassium for about 30 min. After rinsing with water and acetone (technical grade) several times, the glassware was dried at 110°C in a oven for at least one day.

II. Reactants

II.1 Synthesis gases

For the glove-box and the vacuum line, Argon 4.5 (>99.995% purity) purchased from Linde was used without further purification.

The dihydrogen used in the reactions is generated from a commercial dihydrogen generator (Parker Hannifin ltd, Domnick Hunter, Model 40H).

II.2 Synthesis solvents

The solvents, mesitylene (1,3,5-trimethylbenzene), toluene, THF (tetrahydrofuran) and pentane, were collected from a solvent purification system (PureSolv MD 7 from Innovative Technology, Inc.), degassed by freeze- pump-thaw three times and kept under activated molecular sieves in the glove-box. Anisole (methoxybenzene), anhydrous 99.7%, is purchased from Sigma-Aldrich, and dried under activated molecular sieves.

II.3 Metallic precursors

Table V.1: Metal precursors used for the experiments.

Metal	Formula	Supplier	Purity	M_w (g/mol)
Fe	$[Fe\{N(SiMe_3)_2\}_2]_2$	Nanomeps		376.62
Co	$[Co\{N(SiMe_3)_2\}_2(THF)]$	Nanomeps		452.03
	$[Co(\eta^3\text{-}C_8H_{13})(\eta^4\text{-}C_8H_{12})]$	Nanomeps		276.31
Pt	$[Pt(CH_3)_2(C_8H_{12})]$	Nanomeps		333.33
	$[Pt(C_5H_7O_2)_2]$	STREM	98%	393.29
	$[Pt(C_6H_5CH{=}CHCOCH{=}CHC_6H_5)_2]$	Nanomeps		663.68

II.4 Reaction products

Table V.2: Organic and inorganic products used for the experiments.

Name	Formula	Supplier	Purity	M_w (g/mol)
Paltimic acid	$CH_3(CH_2)_{14}COOH$	Aldrich	99%	256.42
Lauric acid	$CH_3(CH_2)_{10}COOH$	Acros organics	99.5%+	200.32
Hexadecylamine	$CH_3(CH_2)_{15}NH_2$	Aldrich	98%	241.46
4-(3-phenylpropyl)pyridine	$C_{14}H_{15}N$	Alfa Aesar	98%	197.28
2-benzylbenzoic acid	$C_{14}H_{12}O_2$	Aldrich	97%	212.24
9-fluoreneacetic acid	$C_{15}H_{12}O_2$	Alfa Aesar	99.5%+	224.25
Thionyl chloride	$SOCl_2$	Fluka	99%	118.97
2-methyl-1,3-butadiene	$CH_2{=}CHC(CH_3){=}CH_2$	Aldrich	≥99%	68.12
12-bromododecanoic acid	$BrCH_2(CH_2)_{10}COOH$	Aldrich	97%	279.21
Copper (I) bromide	CuBr	Aldrich	≥98%	143.45
2,2'-bipyridyl	$C_{10}H_8N_2$	Aldrich	≥99%	156.18
Hexamethyldisilazane	$HN(Si(CH_3)_2)_2$	Alfa Aesar	98%	161.4
Isoprene	$CH_2{=}C(CH_3)CH{=}CH_2$	Aldrich	≥99%	68.12
Triisobutylaluminum	$Al(^{i}Pr)_3$	Aldrich	≥99%	198.32
Trityltetrakis(pentafluorophenyl)borate		Strem	97 %	922.36

III. Analytical techniques

III.1. Transmission Electron Microscopy (TEM)

The TEM micrograph were obtained with a JEOL JEM-1011 microscope equipped with a W thermionic electron source and a Mega-View Olympus CCD camera and working at an acceleration voltage of 100 kV, or with a JEOL JEM 1400 microscope equipped with a LaB_6 thermionic electron source and a Gatan Ultrascan 1000 CCD camera working at an acceleration voltage of 120 kV. The samples were prepared by drop casting of the solution on a carbon coated copper grid. Prior to observation the grids were dried under vacuum (10^{-5} torr) overnight. Both of the microscopes are located in the TEMSCAN service of the Université Paul Sabatier at Toulouse.

III.2. High Resolution Transmission Electron Microscopy (HRTEM)

The HRTEM images were obtained with a JEOL JEM-2100F (Temscan, Université Paul Sabatier), operating at 200 kV. The JEOL microscopes are equipped with a Field Emission Gun (FEG) Gatan Ultrascan 1000 CCD camera. The samples were prepared by drop casting of the solution on a carbon coated copper grid. Prior to observation the grids were not dried further to avoid possible oxidation.

III.3. Electron tomography

The electron tomogram has been obtained using a JEOL 2100 electron microscope installed in the METi platform. A Gatan High-Tilt specimen holder and the Gatan Tomography extension for Digital Micrograph were used for the serial image acquisition. Reconstruction and visualization of the results has been performed using the IMOD software. Tomogram alignment has been performed using a patch tracking procedure while the volume reconstruction was obtained using a SIRT algorithm.

Electron tomography has been used to study the three-dimensional structure of the object. A series of TEM images has been acquired by tilting the specimen between -65° and 70°.

III.4. Magnetic measurements

The ZFC/FC measurements were performed between 2 K and 300 K under a magnetic field of 10^{-3} T. The hysteresis loops were recorded at different temperatures under a magnetic field ranging from -5 to +5 T.

The samples of powders were prepared in a gelatin capsule. The product, in solid form, was introduced in the capsule and then it is capped with an amount of silicon grease or with tetracosane (n-$C_{24}H_{50}$), which served as the immobilization matrices for the powder. A second, smaller capsule is introduced in order to immobilize the sample and then the sample is closed with the gelatin cap. If tetracosane is used, the sample is heated above the melting point of tetracosane (*Tm* = 52°C) and the powder is dispersed with the aid of an ultrasounds bath.

The $M(H)$ hysteresis loops are presented normalized with respect to the saturation magnetization of the sample (M/M_S), or when an elementary analysis has been performed they are presented with respect to the mass of the metal (emu/g units).

III.5. Elemental Analysis

The mass analysis of C, H, and N was carried out by the service of elemental microanalysis of the Laboratoire de Chimie de Coordination (LCC) in Toulouse. The analyses were performed under argon after having conditioned the samples in glass-sealed vials.

The mass analysis of metals was carried out by Mikroanalytisches Labor Pascher in Germany (http://www.mikrolabor.info). The technique used for this determination was the ICP-AES under inert gas.

III.6. UV-visible spectroscopy

The electronic spectra were recorded with a Perkin Elmer Lambda 35 spectrometer. The scanning rate was set to 240 $nm{\cdot}min^{-1}$. The quartz cells used are purchased from Hellma Analytics.

III.7. Infrared spectroscopy

The infrared spectra were recorded on a Thermo-Scientific Nicolet 6700 FT-IR Instrument in an ATR (Attenuated Total Reflectance) mode (diamond window).

The IR spectra were also recorded on a Perkin Elmer Spectra One spectrometer using KBr salt for solid pellet analysis.

III.8. X-ray Diffraction (XRD) and Wide-angle X-ray Scattering (WAXS)

The XRD measurements were carried out in the Laboratoire de Physique et Chimie de Nano-Objets (LPCNO) on a Panalytical Empyrean instrument operating with a Co cathode source (Ka = 1.789010 Å). The samples were prepared from dried powders enclosed by two Kapton foils to avoid possible air-contamination. The analysis of the diffractograms obtained was done with the aid of the Highscore software (version 2) and the crystallite size was calculated using the Scherrer equation and the same software:

$\beta = C\ \lambda / L\ cos\theta$ (Scherrer Equation)

β is the angular breadth of a diffraction line, C is a constant, λ is the wavelength of the X-Rays source, L is the volume-averaged size of the cr stallites and θ is the Bragg angle. The constant C was calculated by a Si crystal reference.

The WAXS measurements were carried out at the CEMES by Dr. Pierre Lecante. The samples were sealed in 1 mm diameter Lindemann glass capillaries. Data collection was performed using a dedicated two-axis diffractometer with graphite-monochromated Mo K_α radiation ($K_\alpha = 0.07107$ nm).

III.9. Nuclear Magnetic Resonance (NMR)

NMR spectra for the polyisoprene were recorded on an Bruker 300 MHz instrument. The solvent used for the NMR experiments was $CDCl_3$.

IV. Functionalization of CNTs

4g of **CNT_1** (Pyrograph III, Applied Science, 98% purity) were treated with 170 mL of a HNO_3 solution (69%) at 120°C during 3 hours under magnetic stirring. The black mixture was cooled to room temperature, and then filtered. The black solid was washed with distilled water until pH=6, and dried in an oven at 110°C during 48 hours.

2 g of oxidized **CNT_1** were further refluxed in a solution of thionyl chloride (70 mL) for 24 hours at 70°C under Ar. Then the solvent was evaporated under vacuum. Chlorinated **CNT_1** were reacted with HDA (2 g, XX mol) in THF (80 mL) at 70°C for 24 hours. Finally, THF was evaporated and the f-**CNT_1** were washed with ethanol (200 mL) to remove excess amine, and dried at 100°C for 24 hours under vacuum.

The functionalization procedure for **CNT_2** (Nanocyl, 95+% purity) is similar to that for **CNT_1** except that the HNO_3 treatment was carried out at 140°C for 5 hours in the first oxidation step.

V. Synthesis of MMNPs

Due to the air-sensitivity of the metal precursors and the nanoparticles produced, all experiments were performed under inert conditions, either by using Schlenk techniques or in of a glove-box. All glassware was carefully dried and introduced in the glove-box before use.

For the reaction "Fe_1BBA_2PPP_Mes_150°C_48h", 0.125 mmol of $[Fe\{N(SiMe_3)_2\}_2]_2$ (94.4 mg) was dissolved in 1.5 mL of mesitylene. 0.25 mmol of BBA (2-benzylbenzoic acid) (54.7 mg) was dissolved in 2 mL of mesitylene. 0.5 mmol of PPP (4-(3-phenylpropyl)pyridine) (100.6 mg) was dissolved in 1.5 mL of mesitylene. The solution of BBA was first transferred to a Fischer-Porter tube, and then the solution of PPP was fast added to the Fischer-Porter tube. After 5 min under stirring, the green solution of Fe precursor was dropwise added with a Pasteur pipette in 5 min. The solution turned more and more yellow, and finally presented a cider color. The addition order in this reaction is denoted as "BBA+PPP+Fe" indicating the order that reactant solution is transferred to the Fischer-Porter tube, and the addition rate is "slow addition rate" indicating the addition rate of the metal precursor solution (slow addition rate=dropwise, ~1 mL/min; fast addition rate= one injected addition).

When the preparation of starting solution is finished, the Fischer-Porter tube is connected to the vacuum line and also to the hydrogen generator. After 3 cycles of H_2/vacuum for purging the circuit, the Fischer-Porter tube is charged with 3 bar of H_2 for 10 min during which the starting solution is magnetically stirred at room temperature. Finally, the Fischer-Porter tube is disconnected from the H_2 source and introduced in an oil bath, which is pre-heated to the desired temperature. It is left to react under stirring for 24 or 48 hours.

After the end of the reaction, the Fischer-Porter tube is cooled down by immersion in a water bath and then transferred in the glove-box. Hydrogen is released in the glove-box. A TEM sample is prepared by drop casting of the diluted solution (in toluene) on a carbon-coated copper grid.

The colloidal solution is transferred from the Fischer-Porter tube to a glass bottle. volume mL of pentane are added in order to assist the precipitation of the NPs. The turbid supernatant is removed, and then the precipitate is washed 5 times with volume mL of pentane. Finally, the sample is dried in the glove-box and conserved in freezer for further use.

V.1 Synthesis of MMNPs with long chain ligands

Details of the experiments for synthesis of MMNPs with long chain ligands are given in Tables V.3.

Table V.3: Experiments for synthesis of MMNPs with long chain ligands.

Ref	Metal atom (mmol)	Metal (mg)	Acid (mg)	Amine (mg)	TEM image
Fe_1PA:2HDA_ Mes_150°C_48h; Order: PA + Fe + HDA Slow adding rate **Lxj004**	0.25	94.2	64.4	121.0	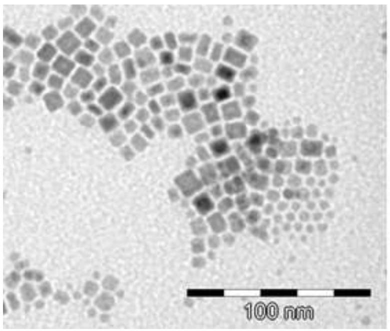
Co_1.2PA:1.2HDA_ Mes_150°C_24h; Order: PA + HDA + Co Slow adding rate **Lxj005**	0.21	94.9	50.8	60.5	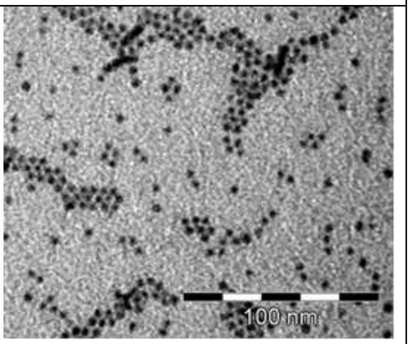
Co_1.4PA:1.2HDA_ Mes_150°C_24h; Order: PA + HDA + Co Slow adding rate **Lxj006**	0.21	94.8	60.5	60.5	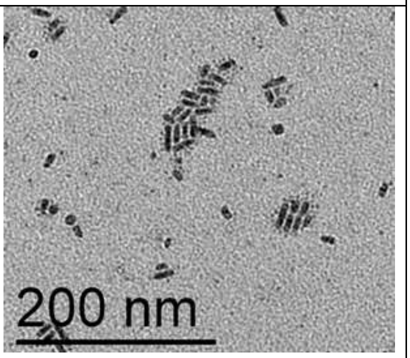

Fe_1PA:2HDA_ Mes_150°C_48h; Order: PA + HDA + Fe Slow adding rate **Lxj007**	0.25	94.4	64.4	120.9	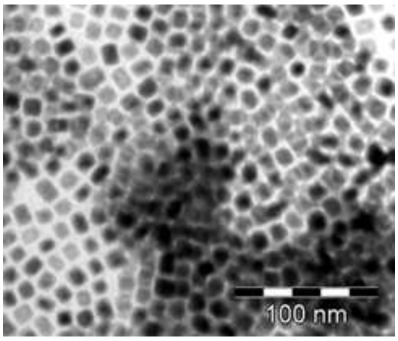
Co_1.2LA:1.2HDA_ Ani_150°C_24h; Order: LA + HDA + Co Fast adding rate **Lxj048**	0.21	94.9	50.4	60.5	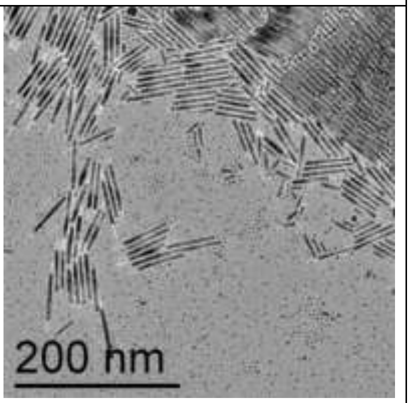
Co_1.2LA:1.2HDA_ Ani_150°C_24h; Order: LA + HDA + Co Fast adding rate **Lxj065a**	0.21	94.9	50.4	60.5	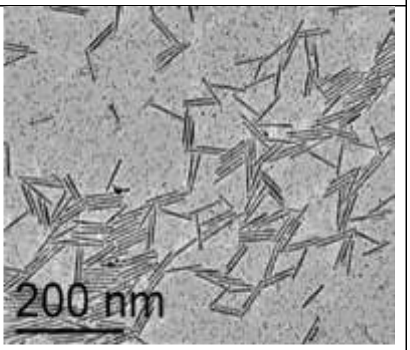
Fe_2LA:0.5HDA_ Mes_150°C_48h; Order: LA + HDA + Fe Fast adding rate **Lxj116a**	0.5	188.3	200.4	60.4	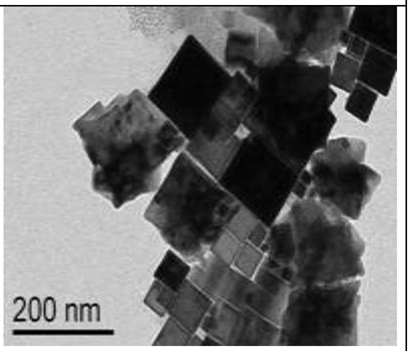

Fe_2LA:0.5HDA_ Mes_150°C_48h; Order: LA + HDA + Fe Slow adding rate **Lxj116b**	0.5	188.3	200.4	60.4	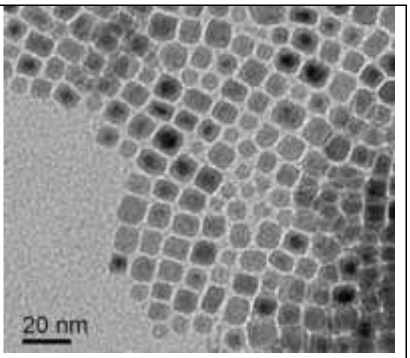
Fe_2LA:0.36HDA_ Ani_150°C_24h; Order: LA + HDA + Fe Fast adding rate **Lxj118**	0.42	158.1	170.2	36.2	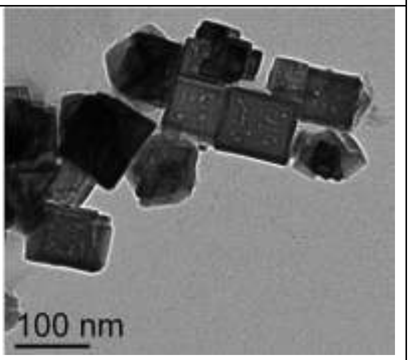
Fe_2LA:0.36HDA_ Ani_150°C_24h; Order: LA + HDA + Fe Slow adding rate **Lxj120**	0.42	158.1	170.2	36.2	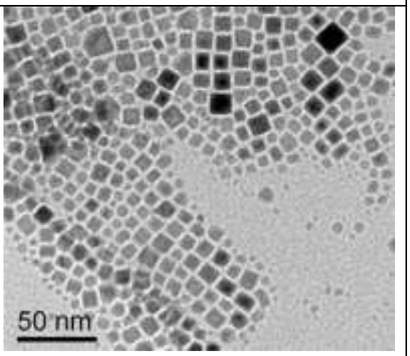

V.2 Synthesis of MMNPs with aromatic ligands

Details of the experiments for synthesis of Co and Fe NPs with aromatic ligands are given in Tables V.4 and V.5, respectively.

Table V.4: Details of the experiments for synthesis of Co NPs with aromatic ligands.

Ref	Metal (mmol)	Metal (mg)	Acid (mg)	Amine (mg)	TEM image
Co_1.2BBA:1.2PPP_ Mes_150°C_24h; Order: BBA + PPP + Co Slow adding rate **Lxj015**	0.21	94.9	54.7	50.3	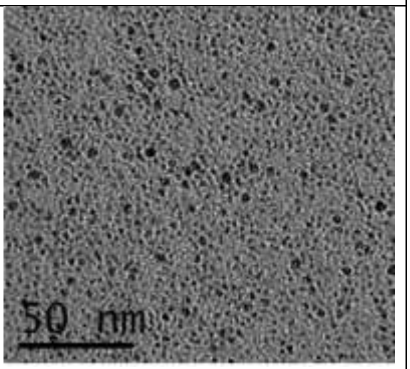
Co_1.2FAA:1.2PPP_ Mes_150°C_24h; Order: FAA + PPP + Co Slow adding rate **Lxj017**	0.21	94.8	56.2	50.7	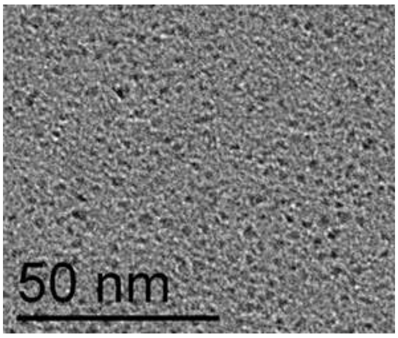
Co_1.4BBA:1.2PPP_ Mes_150°C_24h; Order: BBA + PPP + Co Slow adding rate **Lxj020**	0.21	94.8	65.9	50.4	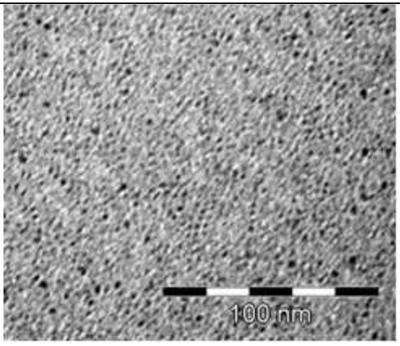

Co_1.7BBA:1.2PPP_ Mes_150°C_24h; Order: BBA + PPP + Co Slow adding rate **Lxj021**	0.21	94.8	76.5	50.3	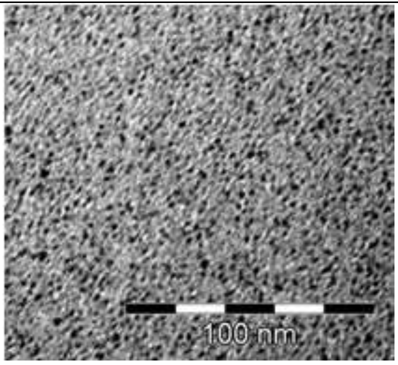
Co_1.2BBA:1.2PPP_ Mes_150°C_24h; Order: BBA + PPP + Co Fast adding rate **Lxj037**	0.21	95.0	54.5	50.3	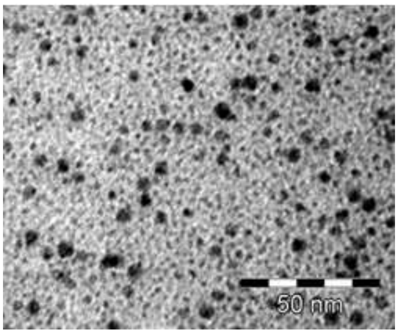
Co_1.2LA:1.2PPP_ Mes_150°C_24h; Order: LA + PPP + Co Fast adding rate **Lxj043**	0.21	94.9	50.8	50.3	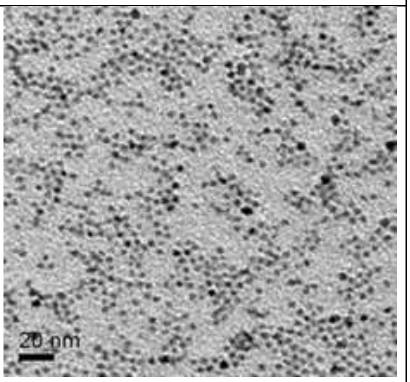
Co_1.2BBA:1.2HDA_ Mes_150°C_24h; Order: BBA + HDA + Co Fast adding rate **Lxj044**	0.21	94.9	54.5	60.5	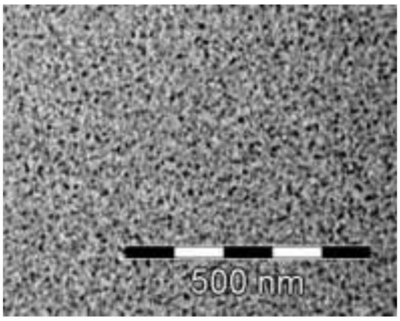

Co_1.2LA:1.2PPP_ Mes_120°C_24h; Order: LA + PPP + Co Fast adding rate **Lxj051**	0.21	94.9	50.8	50.3	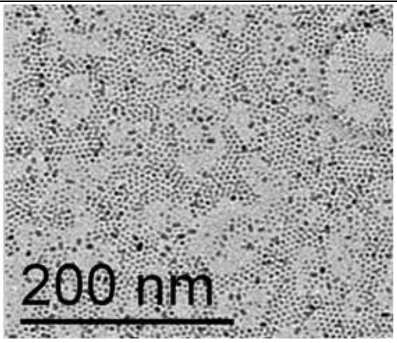
Co_1.2BBA:1.2HDA_ Ani_150°C_24h; Order: BBA + HDA + Co Fast adding rate **Lxj053**	0.21	94.9	54.5	60.5	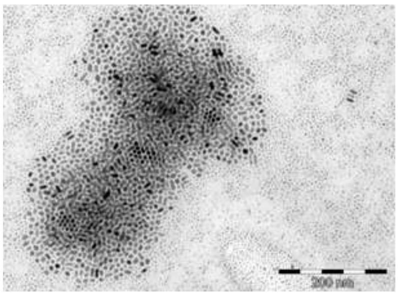
Co_1.2LA:1.2PPP_ Ani_150°C_24h; Order: LA + PPP + Co Fast adding rate **Lxj054**	0.21	94.9	50.8	50.6	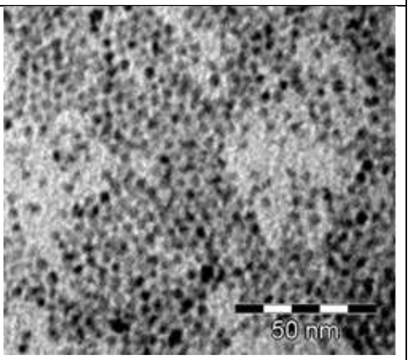
Co_1.2BBA:1.2HDA_ Ani_150°C_48h; Order: BBA + HDA + Co Fast adding rate **Lxj072**	0.21	94.9	54.5	60.5	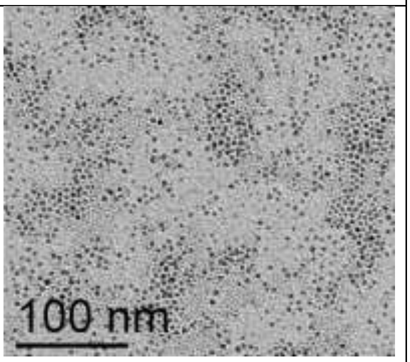

Table V. 5: Details of the experiments for synthesis of Fe NPs with aromatic ligands.

Ref	Metal (mmol)	Metal (mg)	Acid (mg)	Amine (mg)	TEM image
Fe_1BBA:2PPP_ Mes_150°C_48h; Order: BBA + PPP + Fe Slow adding rate **Lxj016**	0.25	94.4	54.7	100.6	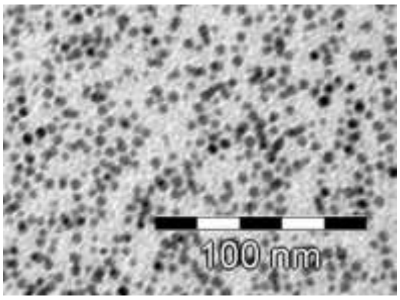
	d= 4.4±0.6 nm				
Fe_1BBA:2PPP_ Mes_150°C_48h; Order: BBA + Fe + PPP Slow adding rate **Lxj023**	0.25	94.4	54.7	100.6	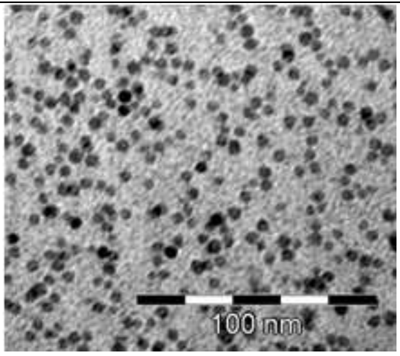
	d=4.5±0.6 nm				
Fe_1FAA:2PPP_ Mes_150°C_48h; Order: FAA + Fe + PPP Slow adding rate **Lxj024**	0.25	94.4	56.2	100.6	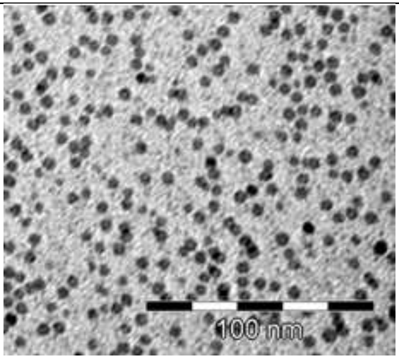
	d=5.3±0.4 nm				
Fe_1BBA:2PPP_ Mes_150°C_48h; Order: BBA + PPP + Fe Fast adding rate **Lxj075**	0.25	94.4	54.7	100.6	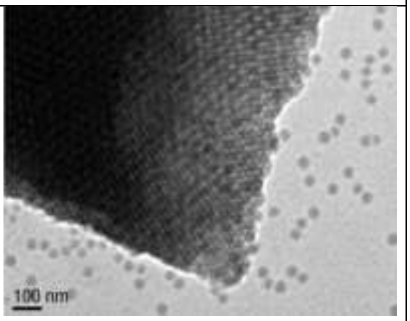
	d=8.1±0.9 nm				

Fe_1BBA:2PPP_ Mes_150°C_48h; Order: BBA + PPP + Fe Slow adding rate **Lxj078**	0.5	188.8	109.4	201.2	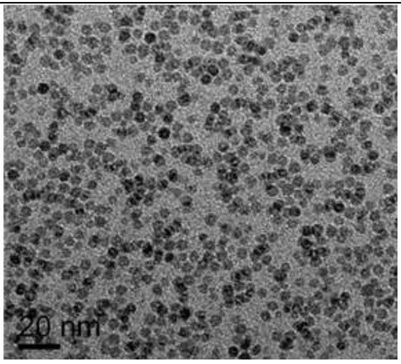
	d=4.7±0.6 nm				
Fe_1BBA:2PPP_ Mes_150°C_48h; Order: BBA + PPP + Fe Slow adding rate **Lxj100**	1.0	377.6	218.8	402.4	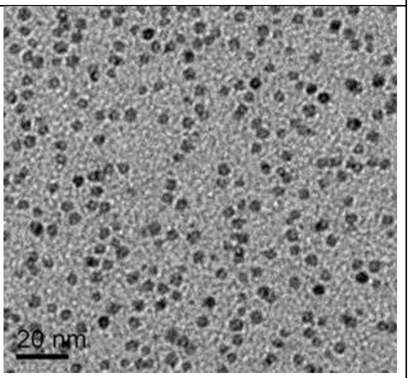
	d=4.3±0.4 nm				
Fe_1BBA:2PPP_ Mes_150°C_48h; Order: BBA + PPP + Fe Slow adding rate **Lxj239**	1.0	377.6	218.8	402.4	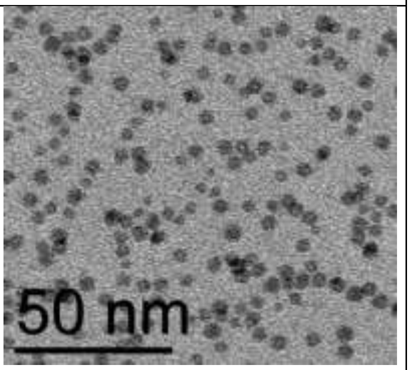
	d=4.5±0.4 nm				

V.3 Functionalization of MMNPs *via* ligand exchange

V.3.1 Functionalization of Co NRs with aromatic ligand

The solvent-washed Co NRs (Co_1.2LA:1.2HDA_Ani_150°C_24h) (10 mg) were added to 5 mL of a solution of BBA in toluene (1mg/mL). The mixture was magnetically stirred for 24 hours. Then, the NRs were separated with the aid of a strong magnet, and the supernatant was removed. The ligand exchange procedure was repeated for 3 times. Subsequent washing with pentane (5 mL) was carried out and repeated for 3 times. Finally, the NRs were dried in the glove-box for 24 hours.

V.3.2 Functionalization of Fe NPs with the ATRP initiator

1 mg of the pre-formed Fe NPs (Fe_1BBA:2PPP_Mes_150°C_48h) was added to 1 mL of the solution of BDA (12-bromododecanoic acid) (20 mg/mL in THF), and then the mixture was magnetically stirred. After 30 min, the NPs were separated with the help of strong magnet and washed by addition of 5 mL of pentane. The washing treatment was repeated for 3 times. Finally, the NPs were dried in the glove-box for 24 hours.

V.3.3 Functionalization of Fe NPs with the Fe complex

8 mg of the Fe complex (see its synthesis in **VII.2.1**) were dissolved in 5 mL of THF. 40 mg of the preformed Fe NPs (Fe_1BBA:2PPP_Mes_150°C_48h) were added to the solution, and then the mixture was sonicated for 5 min. The colloidal solution was continuously stirred for 24 hours. The NPs were separated with the aid of a magnet, and then the supernatant was removed. The solid was washed with 5 mL of THF and further 2x5 mL of pentane. Finally, a black solid was obtained after drying.

VI. Confinement of MMNPs within the f-CNTs

VI.1 Confinement of pre-formed or functionalized MMNPs

The pre-formed or functionalized MMNPs were dispersed in solvent (THF, toluene or pentane) in order to form colloidal suspensions with concentrations indicated in Table V.6. Then, the CNTs (f-$\mathbf{CNT_1}$ or f-$\mathbf{CNT_2}$) were mixed with the suspension of MMNPs in amounts that result to a final CNT concentration of 10mg of CNTs/mL. The mixture was treated with ultra-sonication for 20 min and subsequently stirred for the periods indicated in Table V.6. In the solvent evaporation method, the colloidal solution was slowly evaporated in the glove-box. In the filtration method, the colloidal solution was filtrated under Ar/reduced pressure, and then washed with a volume of THF equal to the initial solution volume for at least 3 times, and the last traces of solvent were evaporated in the glove-box. In Table 6, we summarize the conditions used for each experiments types of NPs and CNT, concentration of NP colloidal solution, and post-treatments are presented.

Table V.6: Confinement of pre-formed or functionalized MMNPs *via* the *ex situ* suspension method.

Ref		NP Concentration (mg/mL $_{solvent}$)	Treatments	TEM image
Lxj012	Co_1.4PA:1.2HDA_ Mes_150°C_24h; $\mathbf{CNT_1}$	1.5 in THF	Sonication; stirring 2h	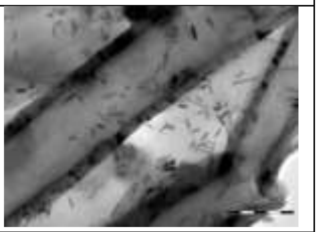
Lxj013	Fe_1PA:2HDA_ Mes_150°C_48h; $\mathbf{CNT_1}$	1.5 in THF	Sonication; stirring 2h	
Lxj035	Fe_1BBA:2PPP_ Mes_150°C_48h; $\mathbf{CNT_1}$	3 in Mes	Sonication; stirring 1h	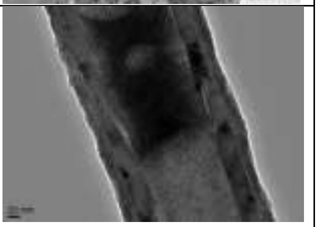

Lxj039	Co_1.2LA:1.2HDA_ Ani_150°C_24h; **CNT$_1$**	3 in Mes	Sonication; stirring 24h	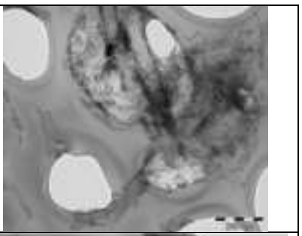
Lxj040	Fe_1BBA:2PPP_ Mes_150°C_48h; **CNT$_1$**	3 in Mes	Sonication; stirring 24h	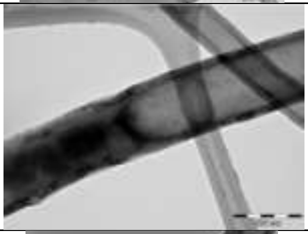
Lxj050	Co_1.2LA:1.2PPP_ Mes_150°C_24h; **CNT$_1$**	3 in Mes	Sonication; stirring 24h	
Lxj052	Co_1.2LA:1.2HDA_ Ani_150°C_24h; BBA exchange; **CNT$_1$**	2 in Tol	Sonication; stirring 24h	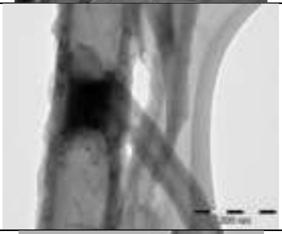
Lxj056	Co_1.2LA:1.2HDA_ Ani_150°C_24h; BBA exchange; **CNT$_1$**	2 in Tol	Sonication; stirring 24h	
Lxj061	Fe_1BBA:2PPP_ Mes_150°C_48h; **CNT$_2$**	3 in Mes	Sonication; stirring 24h	
Lxj063	Fe_1BBA:2PPP_ Mes_150°C_48h; **CNT$_1$**	3 in Mes	Sonication; stirring 7 days	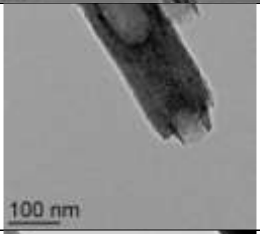
Lxj064	Fe_1BBA:2PPP_ Mes_150°C_48h; **CNT$_1$**	3 in pentane	Sonication; stirring 24h	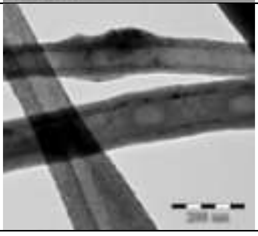

Lxj078	Fe_1BBA:2PPP_ Mes_150°C_48h; **CNT$_1$**	3 in Tol	Sonication; stirring 24h; evaporation	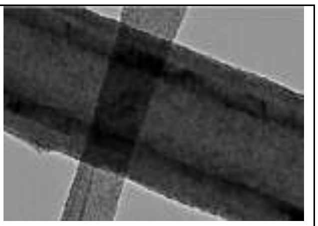
Lxj093a	Fe_1BBA:2PPP_ Mes_150°C_48h; **CNT$_1$**	1.5 in THF	Sonication; stirring 24h; evaporation	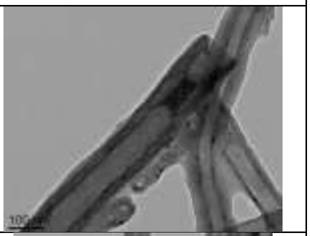
Lxj093b	Fe_1BBA:2PPP_ Mes_150°C_48h; **CNT$_1$**	3 in THF	Sonication; stirring 24h; evaporation	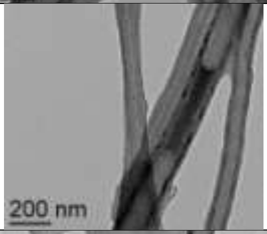
Lxj093c	Fe_1BBA:2PPP_ Mes_150°C_48h; **CNT$_1$**	6 in THF	Sonication; stirring 24h; evaporation	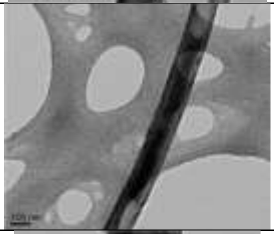
Lxj106	Fe_1BBA:2PPP_ Mes_150°C_48h; **CNT$_1$**	3 in THF	Sonication; stirring 24h; evaporation	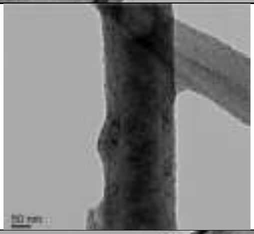
Lxj107	Fe_1BBA:2PPP_ Mes_150°C_48h; **CNT$_1$**	12 in THF	Sonication; stirring 24h; evaporation; THF washing	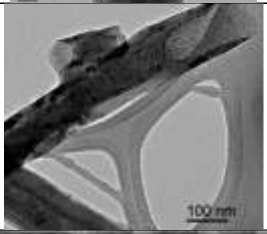
Lxj111	Co_1.2BBA:1.2PPP_ Mes_150°C_24h; **CNT$_1$**	3 in THF	Sonication; stirring 24h; filtration; THF washing	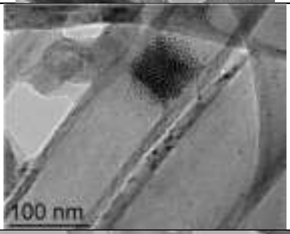
Lxj139	Co_1.2LA:1.2HDA_ Ani_150°C_24h; BBA exchange; **CNT$_1$**	2 in Tol	Sonication; stirring 18h; filtration; Tol washing	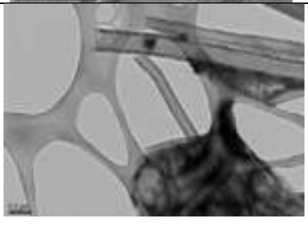

Lxj178	Fe_1BBA:2PPP_ Mes_150°C_48h; **CNT$_1$**	3 in THF	Sonication; stirring 24h; filtration; Tol washing	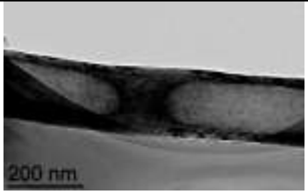
Lxj 184	Fe_1BBA:2PPP_ Mes_150°C_48h; **CNT$_1$**	3 in THF	Sonication; stirring 24h; filtration; THF washing	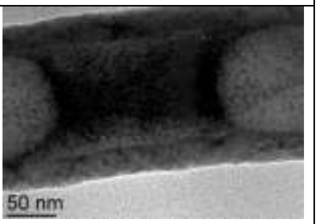
Lxj193	Co_1.2LA:1.2HDA_ Ani_150°C_24h; BBA exchange; **CNT$_1$**	0.25 in THF	Sonication; stirring 24h; filtration; HDA washing	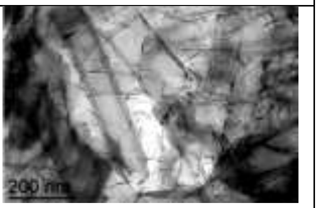
Lxj235	Fe_1BBA:2PPP_ Mes_150°C_48h; Fe complexe exchange; **CNT$_1$**	3 in THF	Sonication; stirring 24h; filtration; THF washing	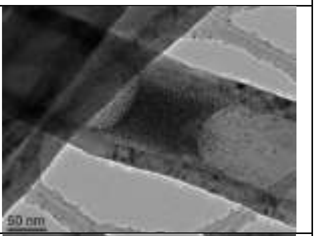
Lxj239	Fe_1BBA:2PPP_ Mes_150°C_48h; Fe complexe exchange; **CNT$_1$**	3 in THF	Sonication; stirring 24h; filtration; THF washing	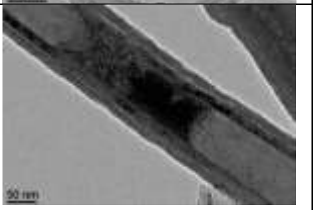
lxjT005	Fe_1BBA:2PPP_ Mes_150°C_48h; BDA exchange;**CNT$_1$**	3 in THF	Sonication; stirring 24h; filtration; THF washing	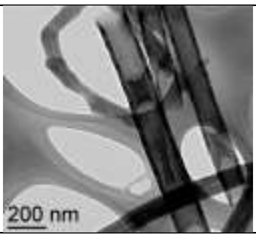

VI.2 Confinement of MMNPs *via* the *in situ* method

The starting solution was prepared following the same procedure as the one described in part V. The CNTs were then immersed into the starting solution, and then the mixture was treated with ultra-sonication for 20 min. The subsequent H_2 charging and the thermal reduction in oil bath followed the same procedure as described in part V.

Table.V.7: Confinement *via* the *in situ* solution method in the presence of CNTs.

Ref	Metal (mmol)	Metal (mg)	Acid (mg)	Amine (mg)	TEM image
Co_THF_50°C_48h_**CNT$_1$** lxj041	0.21	95.0	/	/	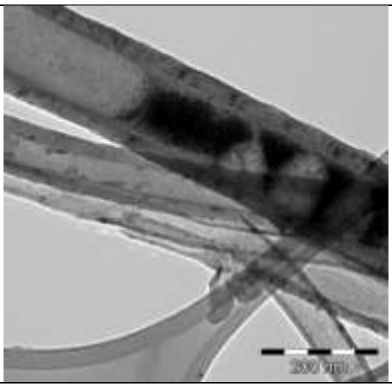
Fe_1BBA:2PPP_ Mes_150°C_48h_**CNT$_1$**; Order: BBA + PPP + Fe Fast adding rate **Lxj062**	0.25	94.4	54.7	100.6	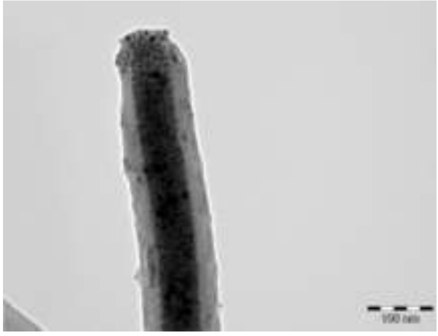
Co_1.2LA:1.2HDA_ Ani_150°C_48h_**CNT$_1$**; Order: LA + HDA + Co Slow adding rate **Lxj065b**	0.42	189.8	100.8	121	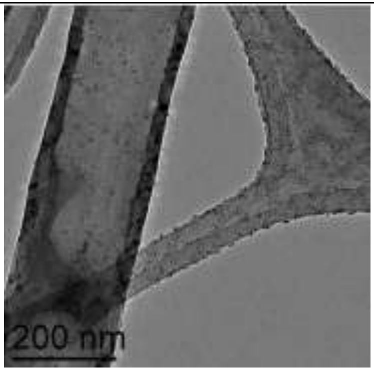

Fe_1BBA:2PPP_ Mes_150°C_48h_**CNT$_1$**; Order: BBA + PPP + Fe Slow adding rate **Lxj102**	0.5	188.4	109.4	201.2	
Co_Tol_100°C_48h_ **CNT$_2$**; lxj125	0.084	38	/	/	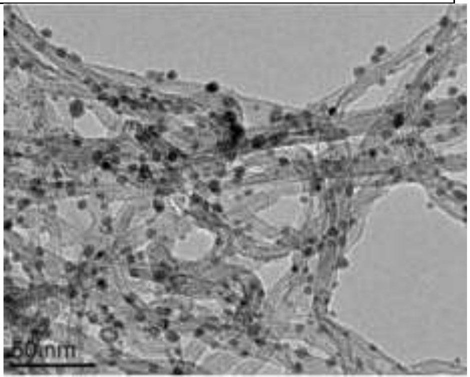
Fe_Tol_100°C_48h_ **CNT$_2$**; lxj127	0.1	37.7	/	/	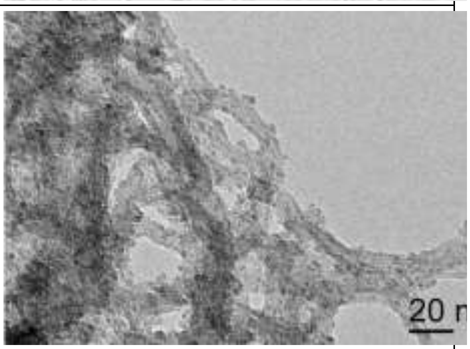
Fe_4BBA_Tol_100°C_48h **_CNT$_2$;** Slow adding rate lxj129	0.1	37.7	87.2	/	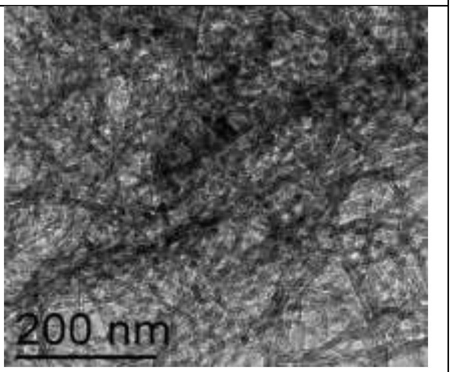

Fe_4PPP_Tol_100°C_48h_**CNT$_2$;** Slow adding rate lxj130	0.1	37.7	/	80.4	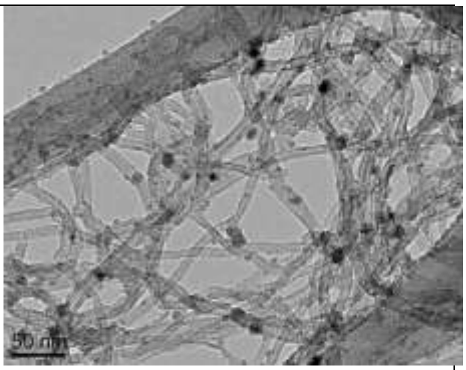
Co_4BBA_Tol_100°C_48h_**CNT$_2$;** Slow adding rate lxj131	0.1	45.2	87.2	/	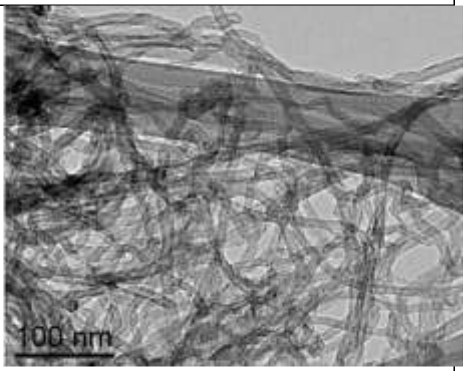
Co_4PPP_Tol_100°C_48h_**CNT$_2$;** Slow adding rate lxj132	0.1	45.2	/	80.4	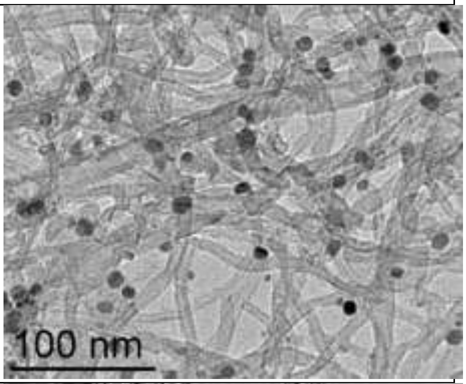
Co_2BBA_2PPP_Tol_100°C_48h_**CNT$_2$;** Order: BBA + PPP + Co Slow adding rate lxj145	0.1	45.2	43.6	40.2	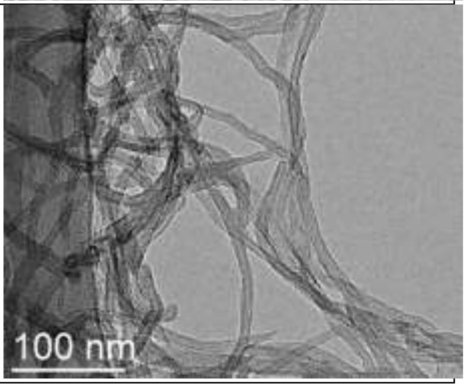

Co_BBA_PPP_Tol_100°C _48h_**CNT₂;** Order: BBA + PPP + Co Slow adding rate lxj146	0.084	38	21.8	20.1	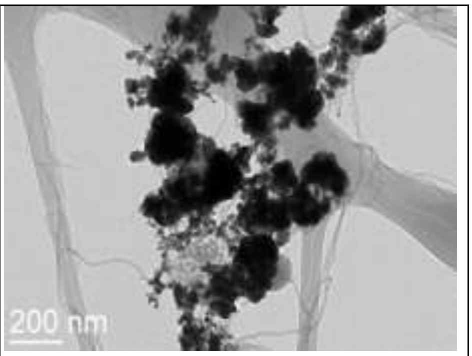

VII. Polymerization of isoprene on the confined iron nanoparticles

VII.1 Atom transfer radical polymerization

VII.1 Polymerization with initiator

VII.1.1 Study of polymerization with various monomer/initiator ratios

In a Schlenk tube, CuBr (43 mg, 0.3 mmol) and bipyridine (117 mg, 0.75 mmol) were dissolved in 3 ml of DMF (solution A). The mixture was maintained under stirring for 30 min. A brick red solution was obtained. In another Schlenk tube, 12-bromododecanoic acid (41.8 mg, 0.15 mmol) was dissolved in 6mL of isoprene (monomer/initiator ratio = 400) (Solution B). The solution B was then added to the solution A, and the mixture was magnetically stirred at room temperature. After 24 hours, the white precipitate was washed with 10 mL of methanol and washing was repeated at least 3 times to remove by-products and Cu complexes from the reaction.

Other three reactions were also performed, where isoprene amounts were kept constant while the amount of 12-bromododecanoic acid varied with different monomer/initiator ratio, which were respectively 200, 800 and 1200. The obtained polymers were dried and weighed.

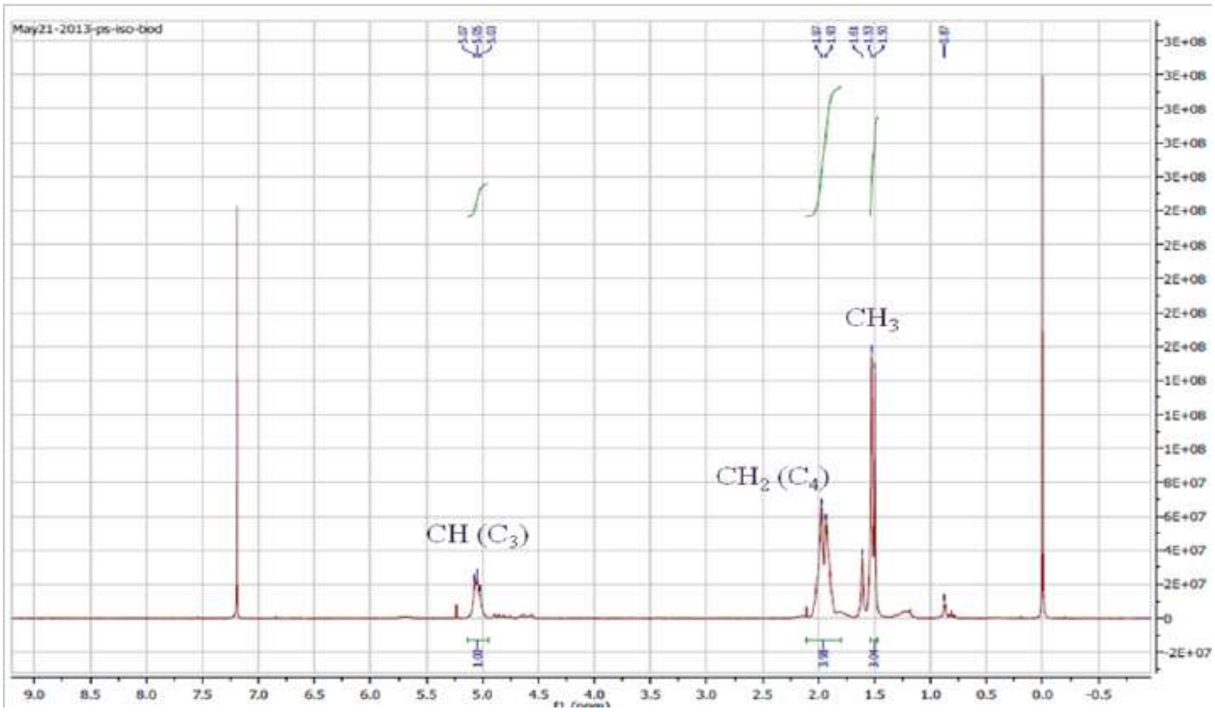

Figure V.1: NMR ^{1}H of polyisoprene in CDCl$_3$.

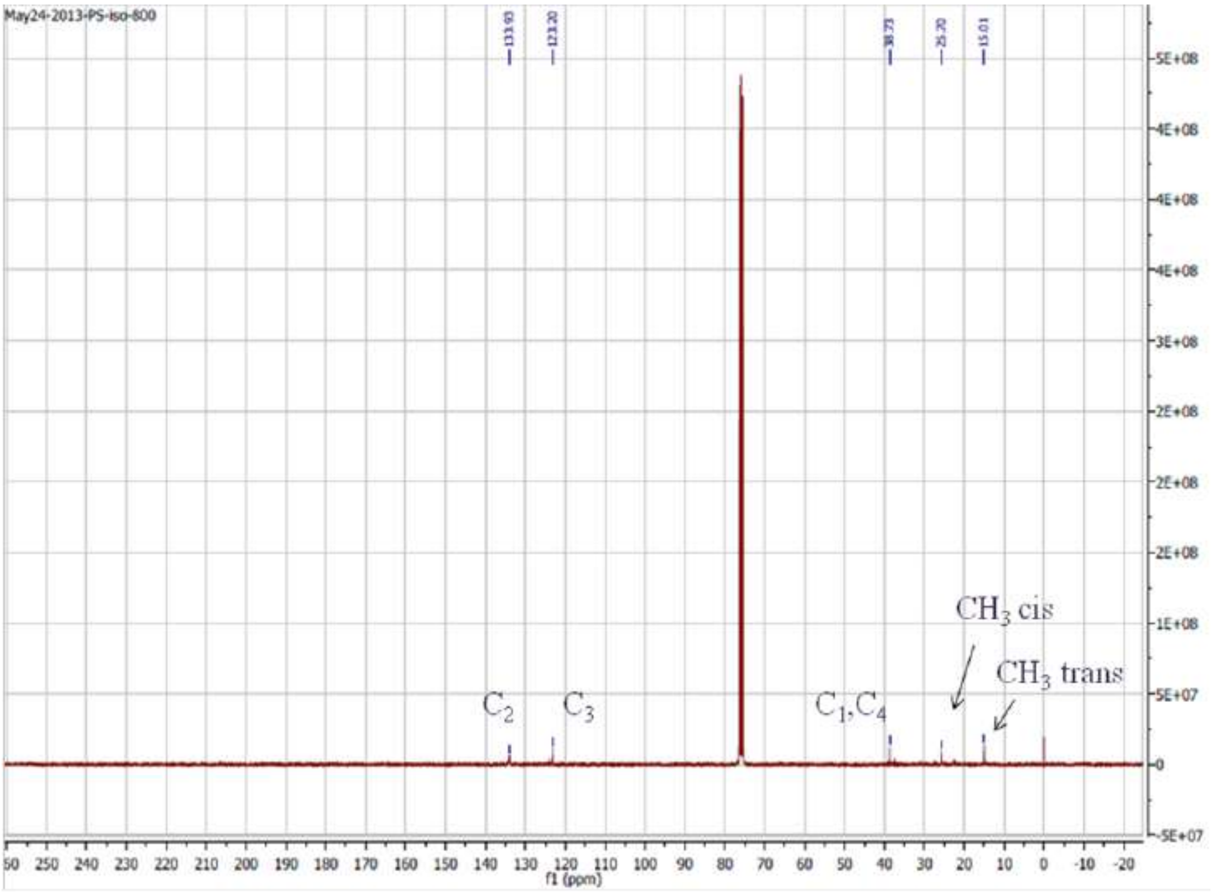

Figure V.2: NMR ^{13}C of polyisoprene in $CDCl_3$.

VII.1.2 Study of polymerization under different reaction temperature and reaction time

A series of polymerizations was performed with a constant monomer/initiator ratio of 400 but under three different temperature (30°C, 50°C and 70°C). For the latter two reactions, the solution was refluxed due to the low boiling point of isoprene (34°C).

Another series of polymerizations was carried out during different reaction time (1h, 3h and 6h). The obtained polymers were then dried and weighed.

VII.1.3 Polymerization with the initiator-modified Fe NPs and with the CNT-confined initiator-modified Fe NPs

Similarly to the polymerization with the initiator, at first CuBr (43 mg, 0.3 mmol) and bipyridine (117 mg, 0.75 mmol) were dissolved with 3 mL of DMF in a Schlenk tube. A suspension of 1 mg of the initiator-modified Fe NPs in 3 mL of isoprene was then added to the Schlenk flask. The colloidal solution was magnetically stirred at room temperature for 12 hours. A TEM grid was prepared with a diluted solution of the mixture in toluene. Due to the small amount of the added NPs before the reaction, nearly no solid was obtained in the end, which cannot be used for further study.

The polymerization with the CNT-confined surface-initiated Fe NPs followed the same general procedureIn this case, 10 mg of the CNTs containing confined surface-initiated Fe NPs was used instead of the NPs in the previous one. Finally, the black solid was washed with 10 mL of methanol and repeated for 3 times.

VII.2 Polymerization through a polymerization Fe complex

VII.2.1 Synthesis of Fe catalyst

Under argon, a mixture of 63.5 mg $FeCl_2$ (0.5 mmol) and two equivalents of ligand ($C_{17}H_{14}N_2$) (1) (246 mg, 1 mmol) was stirred in ethanol (5mL) at room temperature for 6 h. Then, 20 mL of diethyl ether were added to precipitate the complex that was collected by filtration, washed several times with diethyl ether, and dried under reduced pressure. The desired iron complex was obtained as a brown powder with a yield 86% (266 mg).

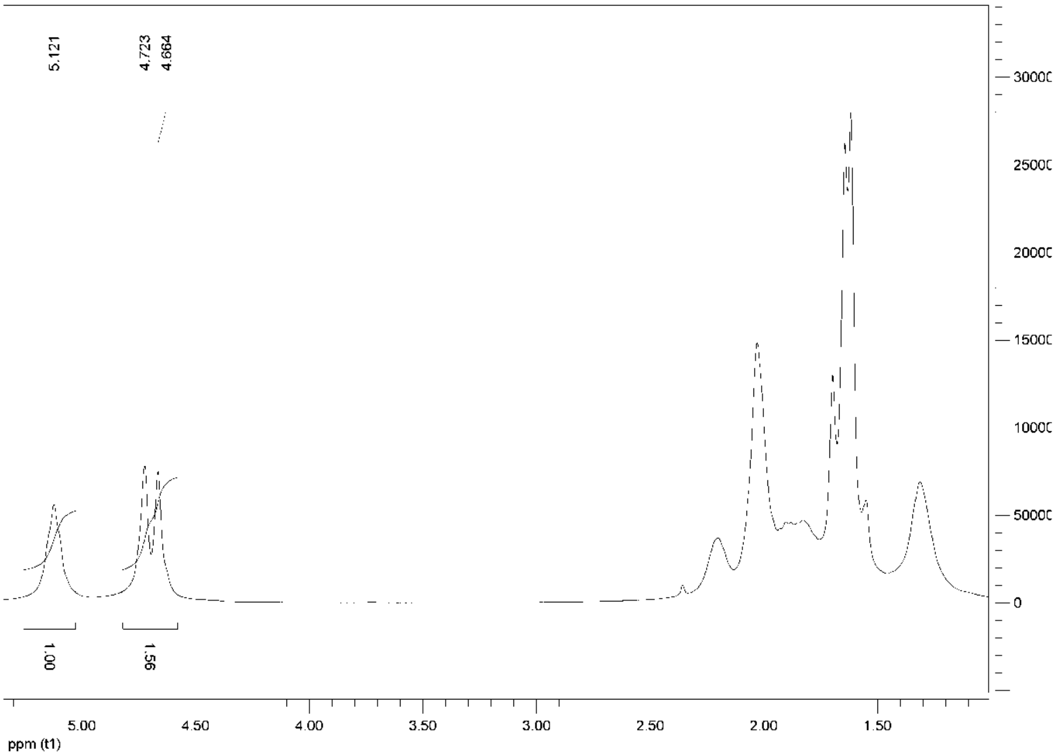

Figure V.3: NMR ^1H of Fe complex in $CDCl_3$.

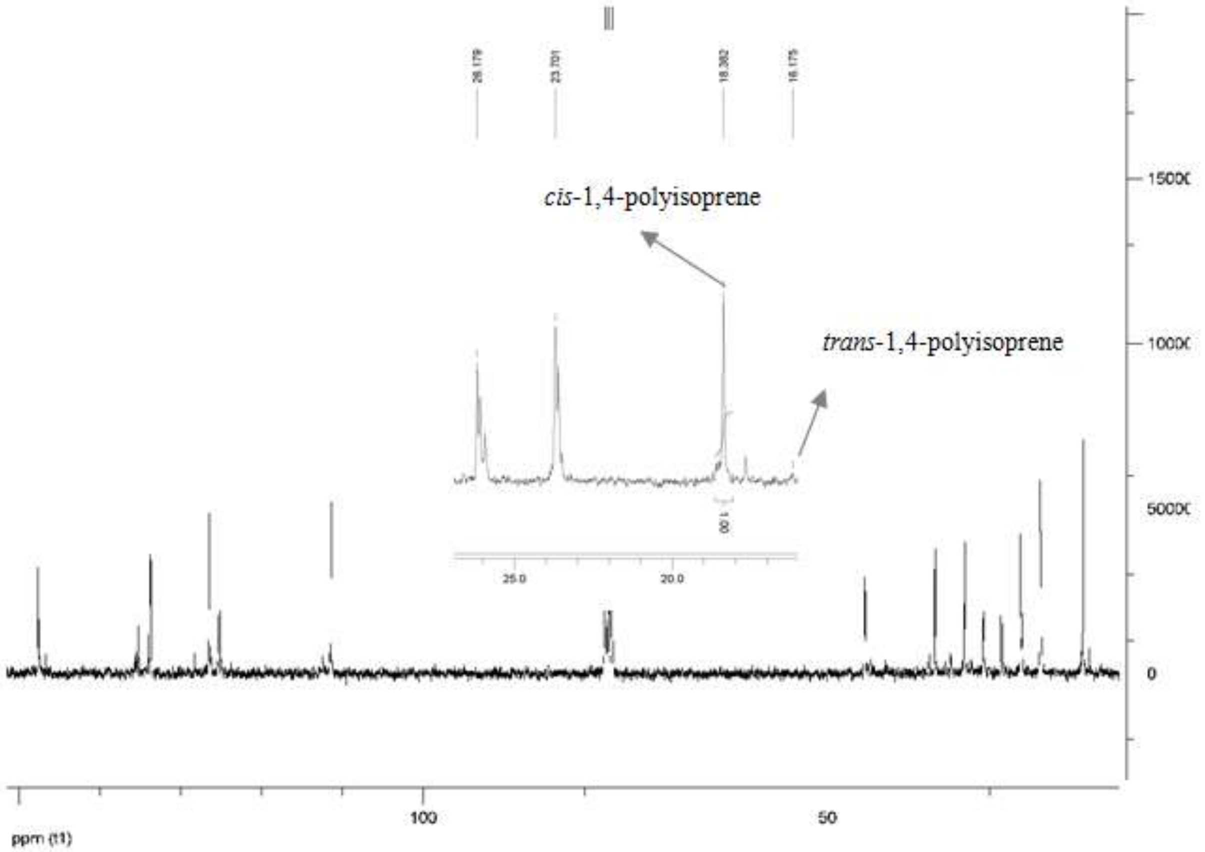

Figure V.4: NMR ^{13}C of Fe complex in $CDCl_3$.

VII.2.2 Functionalization of theFe NPs with the Fe complex

see **V.3.3**

VII.2.3 Isoprene polymerization using the iron particles supported catalyst

The supported catalyst (10 mg FeNP@Fe or 20 mg FeNP@Fe@CNT), 1 mL isoprene, 2 mL $Al(^{i}Pr)_3$ (0.02 M in toluene), 20 mg trityltetrakis(pentafluorophenyl)borate and 100 mL toluene were added into a Schlenk tube. The reaction mixture was intensively stirred for 30 min at 25°C. Then toluene was removed under reduced pressure. Finally, the black solids were conserved in the freezer of the glove-box.

VIII. Pt-based magnetic alloys and confinement

In this section, all the starting solution were prepared with slow addition rate and the addition order (acid + Pt + amine + M) (M= Co or Fe) unless otherwise stated.

VIII.1 Pt-based magnetic NPs in the absence of CNTs

The NPs were synthesized in order to be introduced in the CNTs by the *ex situ* suspension method. In the reaction "Pt_1_0.84Co_2BBA_2PPP_Tol_100°C_24h", 0.2 mmol of BBA (43.6 mg) was dissolved in 2 mL of toluene, and then this solution was transferred to a Fischer-porter tube. 0.1 mmol of $[Pt(CH_3)_2(COD)]$ (33.3 mg) was dissolved in 1.5 mL of toluene, and then the Pt solution was added dropwise (1.5 mL in 2 min) to the Fischer-porter tube under stirring, After 5min, a solution of 0.2 mmol of PPP (40.2 mg) in 1.5 mL of toluene was fast added. After 5min, a solution of 0.084 mmol of $[Co\{N(SiMe_3)_2\}_2(THF)]$ (38 mg) in 1.5 mL of toluene was added dropwise (1.5 mL in 2 min) into the tube under stirring. After preparation the starting solution was charged with H_2 The thermal reduction was then performed as described in part V.

In the reaction with Pt_2 $[Pt(acac)_2]$, all the procedure was as same as that with $[Pt(CH_3)_2(COD)]$, except 0.1 mmol of $[Pt(acac)_2]$ (40.1 mg) was dissolved in 2.5 mL of toluene.

The M_xPt_y NPs were isolated from the colloidal solution by adding pentane (a volume equal to the initial solution), and the supernatant was removed. The precipitate was washed 3 times with an equal to the initial solution volume of pentane and kept in the glove-box for further study. TEM grids were prepared with the dilution of the final colloidal solution in toluene.

Table V.8: Synthesis of MPt (M= Co or Fe) NPs (Pt_1=$Pt(CH_3)_2(COD)$; Pt_2= $Pt(acac)_2$) NPs.

Ref	Pt (mg)	M (mg)	Acid (mg)	Amine (mg)	TEM image
Pt_1_0.84Co_1BBA_1PPP_ Mes_150°C_24h; Lxj076	33.3 (0.1 mmol)	38	21.8	20.1	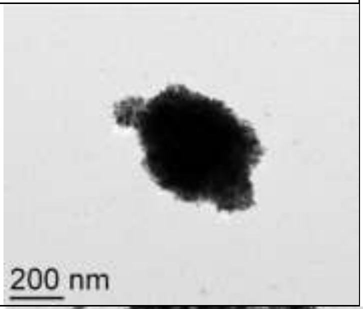
Pt_1_0.84Co_2BBA_2PPP_ Mes_150°C_24h; Lxj081	33.3 (0.1 mmol)	38	43.6	40.2	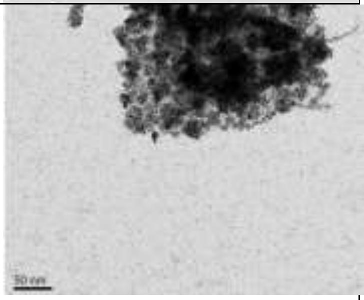
Pt_1_0.84Co_2BBA_2PPP_ Tol_100°C_24h; Lxj084	33.3 (0.1 mmol)	38	43.6	40.2	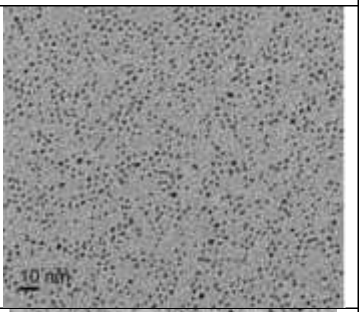
Pt_1_0.84Co_2BBA_2PPP_ Tol_100°C_48h; Lxj096	33.3 (0.1 mmol)	38	43.6	40.2	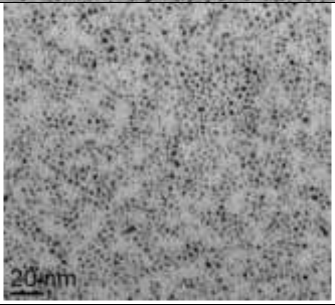
Pt_1_0.84Co_2BBA_2PPP_ Tol_100°C_24h; BBA + PPP + Co +Pt_1 Lxj098	33.3 (0.1 mmol)	38	43.6	40.2	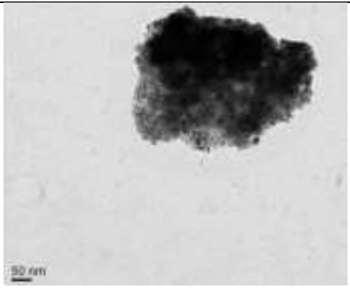

Pt$_1$_2.52Co_1BBA_1PPP_Mes_150°C_24h; Lxj101	33.3 (0.1 mmol)	114	21.8	20.1	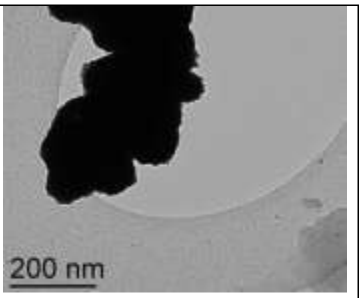
Pt$_1$_Fe_2BBA_2PPP_Tol_100°C_24h; Lxj208	33.3 (0.1 mmol)	37.7	43.6	40.2	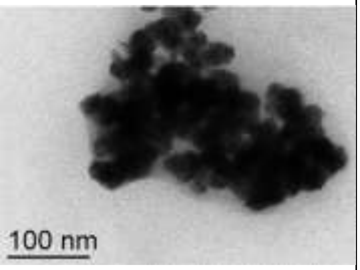
Pt$_2$_Fe_2BBA_2PPP_Tol_100°C_24h; Lxj215	40.1 (0.1 mmol)	37.7	43.6	40.2	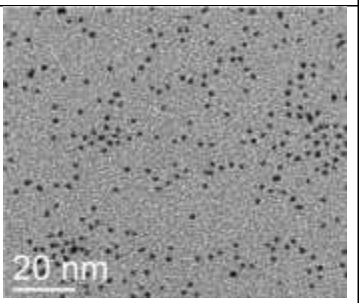
Pt$_2$_Co_2BBA_2PPP_Tol_100°C_24h; Lxj230	40.1 (0.1 mmol)	45.2	43.6	40.2	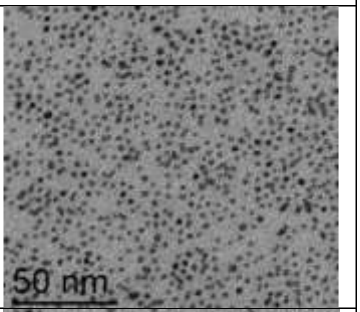
Pt$_2$_Fe_2BBA_2PPP_Tol_100°C_24h; Lxj215	80.2 (0.2mmol)	75.4	87.2	80.4	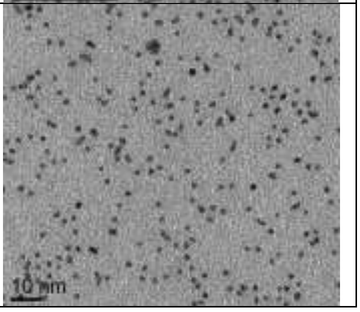

VIII.2 Pt-based magnetic nanostructures within the f-CNTs

As in the previous section, all the starting solutions were prepared with slow addition rate. For all reactions the addition order was the same unless otherwise mentioned in Table V.9 and V.10. For each reaction, the entire volume was fixed to 10 mL. The starting solution was prepared as described in the previous section VIII.1. Then it was transferred to a Fischer-Porter tube where a suspension of CNTs (30 mg) in 3 mL of slovent (toluene or mesitylene), sonicated for 20 min, is contained. Finally, the H_2 charging and thermal reduction followed the same procedure as in part V.

The CNT-templated NWs and the CNT-confined NPs were isolated from the colloidal solution by decanting and removing the supernatant. Then, the precipitate was washed first with the equal to the initial solution volume of toluene 3 times, and then washed with pentane 3 times. Finally, the sample was kept in the glove-box. TEM grids were prepared with the dilution of the colloidal solution. HRTEM and STEM-EDX samples were prepared with the dried sample by re-dispersing it in toluene with ultra-sonication and deposited on TEM grids.

The conditions for the preparation of CoPt and FePt magnetic nanostructures confined within the f-CNTs are given on Table V.9 and V.10, respectively.

Table V.9: CoPt nanostructure presented inside or outside the CNTs.

<table>
<tr><td colspan="4">(1equivalent= 0.1 mmol)</td></tr>
<tr><td>Ref</td><td>precursors</td><td>ligands</td><td>Reaction conditions</td></tr>
<tr><td rowspan="2">lxj122</td><td>1Pt</td><td>2BBA</td><td rowspan="2">Tol_100ºC_24h</td></tr>
<tr><td>0.84Co</td><td>2PPP</td></tr>
<tr><td colspan="3">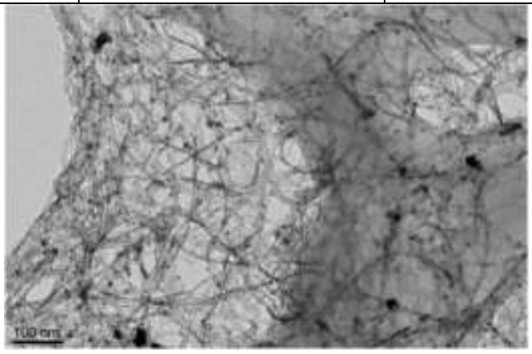 </td><td>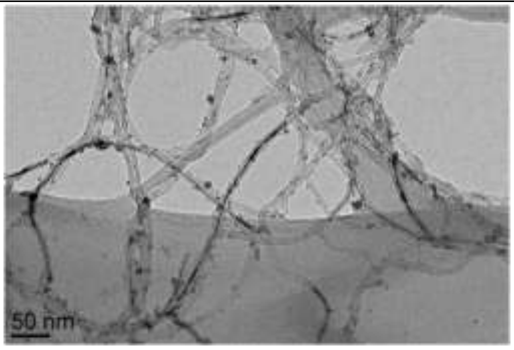 </td></tr>
<tr><td rowspan="2">lxj126</td><td>1Pt</td><td>/</td><td rowspan="2">Tol_100ºC_48h</td></tr>
<tr><td>/</td><td>/</td></tr>
<tr><td colspan="3">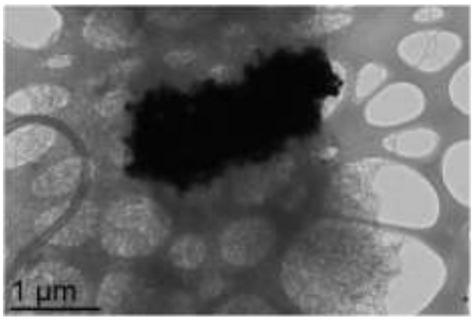 </td><td>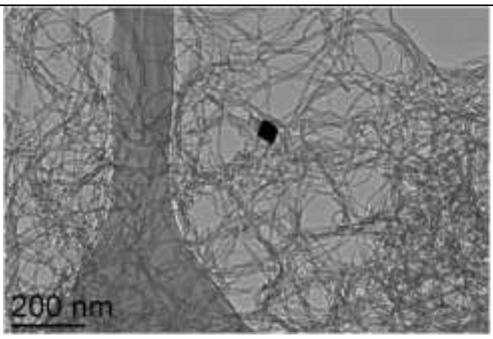 </td></tr>
<tr><td rowspan="2">lxj133</td><td>1Pt</td><td>4BBA</td><td rowspan="2">Tol_100ºC_48h</td></tr>
<tr><td>/</td><td>/</td></tr>
<tr><td colspan="3">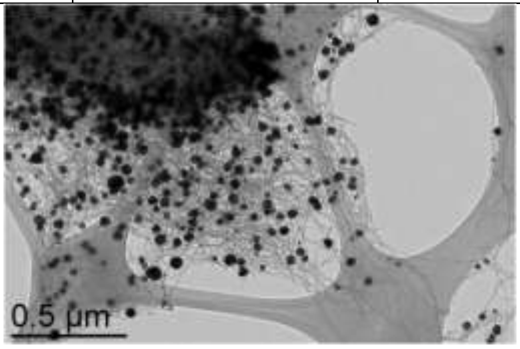 </td><td>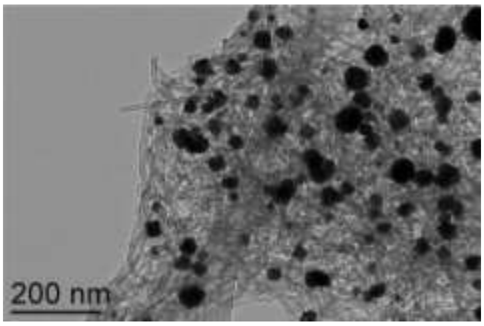 </td></tr>
<tr><td colspan="3"></td><td></td></tr>
</table>

<table>
<tr><td rowspan="2">lxj134</td><td>1Pt</td><td>/</td><td rowspan="2">Tol_100ºC_48h</td></tr>
<tr><td>/</td><td>4PPP</td></tr>
<tr><td colspan="3">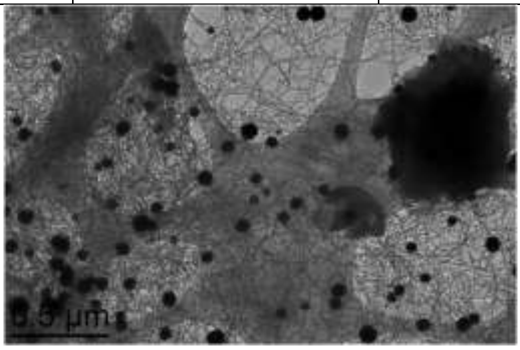 </td><td>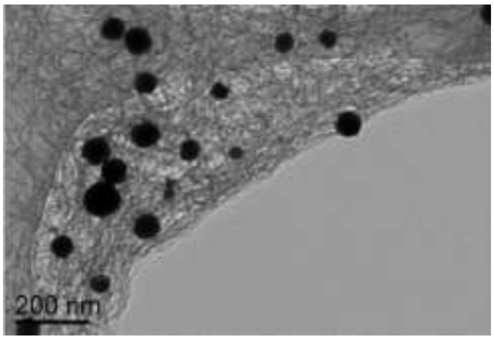 </td></tr>
<tr><td rowspan="2">lxj136</td><td>1Pt</td><td>2BBA</td><td rowspan="2">Tol_100ºC_48h</td></tr>
<tr><td>0.84Co</td><td>2PPP</td></tr>
<tr><td colspan="3">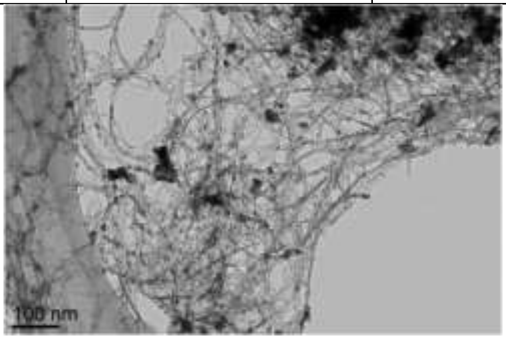 </td><td>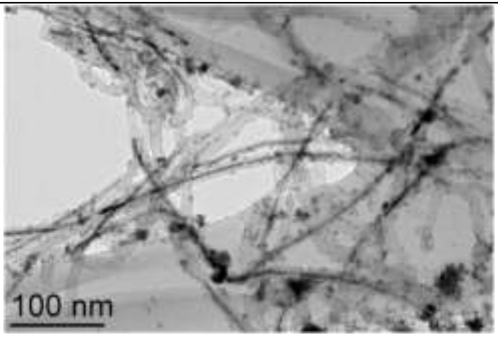 </td></tr>
<tr><td rowspan="2">lxj144</td><td>1Pt</td><td>2BBA</td><td rowspan="2">Tol_100ºC_48h</td></tr>
<tr><td>/</td><td>2PPP</td></tr>
<tr><td colspan="3">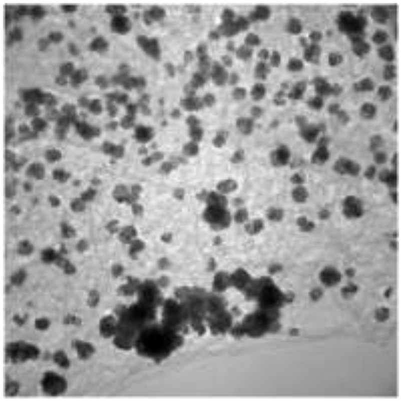</td><td>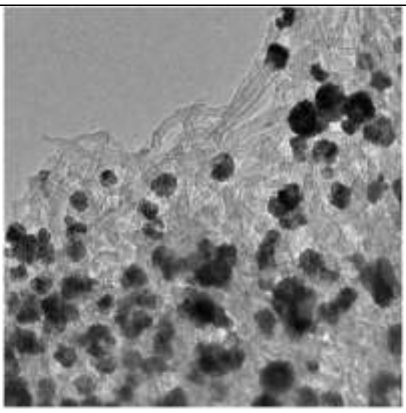</td></tr>
<tr><td rowspan="2">lxj150</td><td>1Pt</td><td>BBA</td><td rowspan="2">Tol_100ºC_48h</td></tr>
<tr><td>/</td><td>PPP</td></tr>
</table>

<table>
<tr><td colspan="3">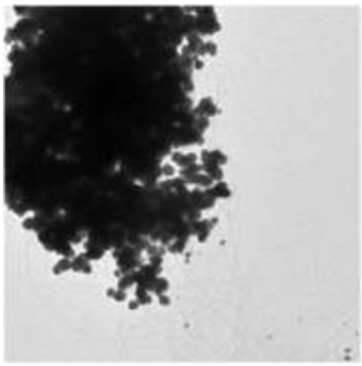</td><td>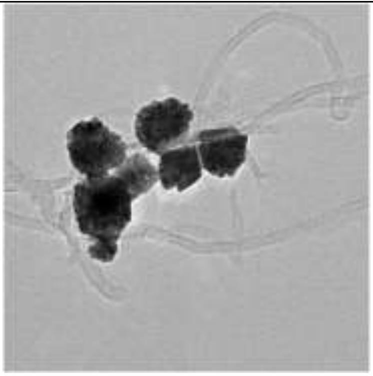</td></tr>
<tr><td rowspan="2">lxj153</td><td>1Pt</td><td>2BBA</td><td rowspan="2">Tol_100ºC_24h</td></tr>
<tr><td>0.84Co</td><td>2PPP</td></tr>
<tr><td colspan="3">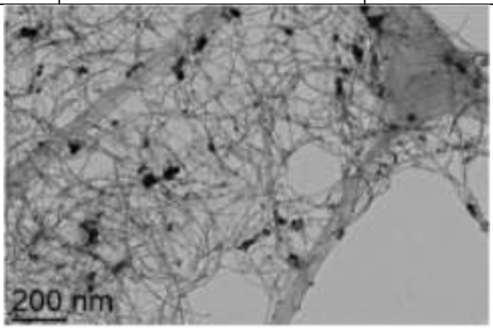 </td><td>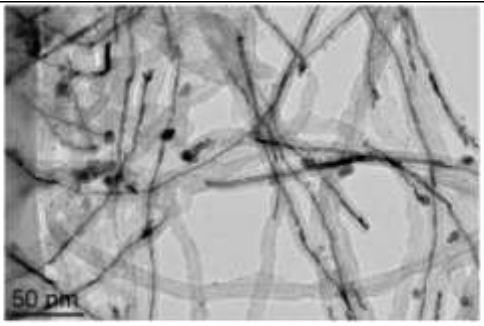 </td></tr>
<tr><td rowspan="2">lxj157</td><td>1Pt</td><td>2LA</td><td rowspan="2">Tol_100ºC_24h</td></tr>
<tr><td>0.84Co</td><td>2HDA</td></tr>
<tr><td colspan="3">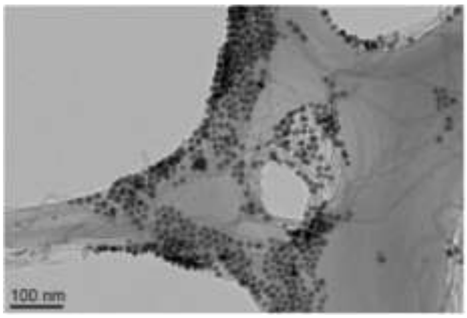 </td><td>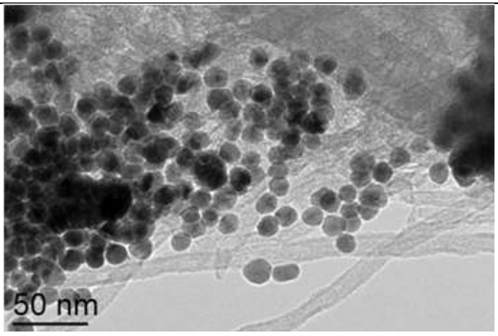 </td></tr>
<tr><td rowspan="2">lxj160</td><td>1Pt</td><td>2BBA</td><td rowspan="2">Tol_100ºC_24h</td></tr>
<tr><td>1.7Co</td><td>2PPP</td></tr>
<tr><td colspan="3">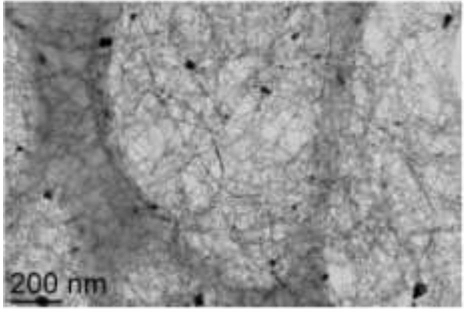 </td><td>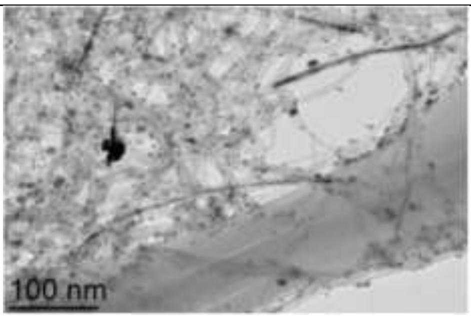 </td></tr>
</table>

<table>
<tr><td rowspan="2">lxj161</td><td>1Pt</td><td>2BBA</td><td rowspan="2">Tol_100ºC_1h,3h</td></tr>
<tr><td>0.84Co</td><td>2PPP</td></tr>
<tr><td colspan="3">1h
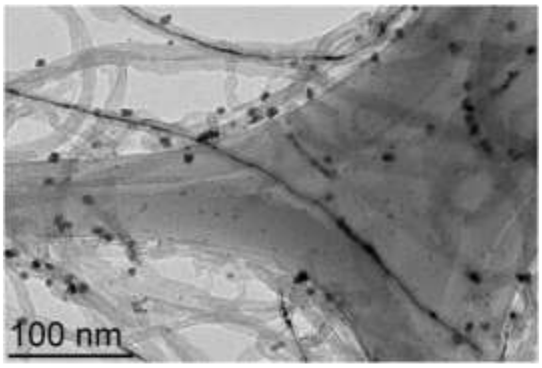
 </td><td>3h
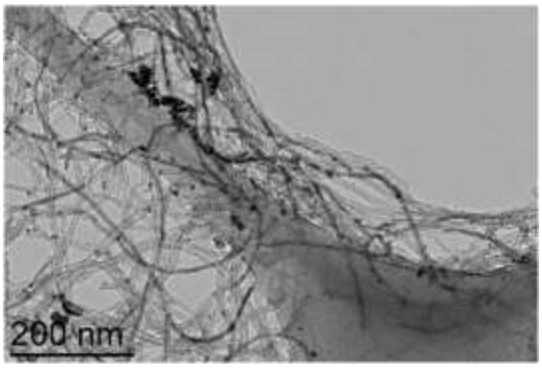
 </td></tr>
<tr><td rowspan="2">lxj162</td><td>1Pt</td><td>2BBA</td><td rowspan="2">Tol_100ºC_24h
Order: BBA+Co+PPP+Pt</td></tr>
<tr><td>0.84Co</td><td>2PPP</td></tr>
<tr><td colspan="3">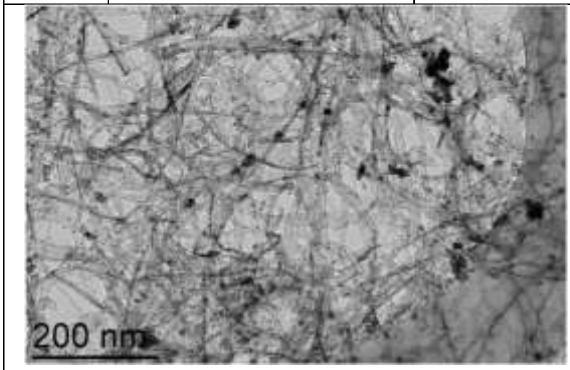
 </td><td>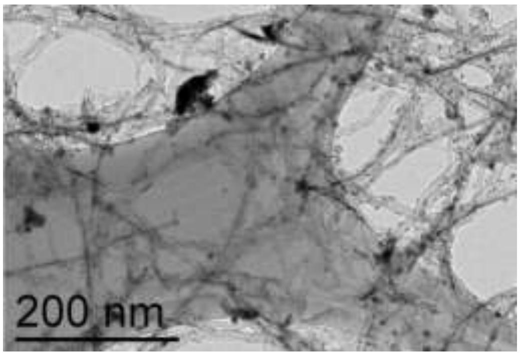
 </td></tr>
<tr><td rowspan="2">lxj164</td><td>1Pt</td><td>2BBA</td><td rowspan="2">Tol_120ºC_24h</td></tr>
<tr><td>0.84Co</td><td>2PPP</td></tr>
<tr><td colspan="3">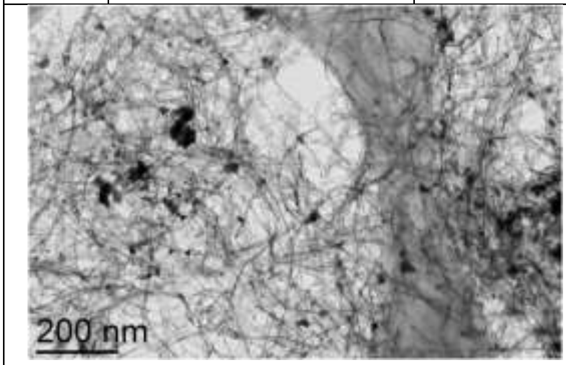
 </td><td>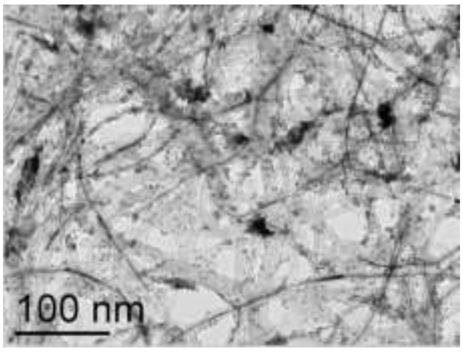
 </td></tr>
<tr><td rowspan="2">lxj172</td><td>1Pt</td><td>2BBA</td><td rowspan="2">Tol_100ºC_24h (fast Co addition)</td></tr>
<tr><td>0.84Co</td><td>2PPP</td></tr>
</table>

<table>
<tr><td colspan="3">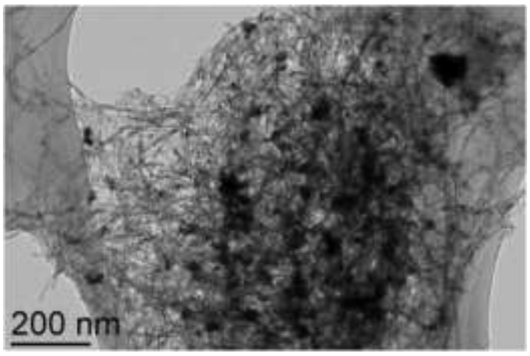 </td><td>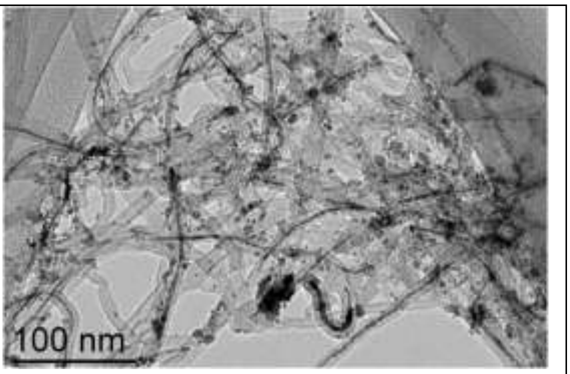 </td></tr>
<tr><td rowspan="2">lxj173</td><td>1Pt</td><td>2BBA</td><td rowspan="2">Tol_150ºC_24h</td></tr>
<tr><td>0.84Co</td><td>2PPP</td></tr>
<tr><td colspan="3">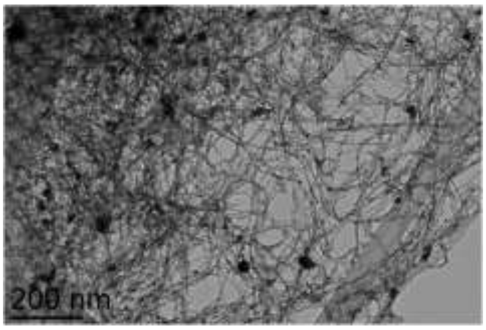 </td><td>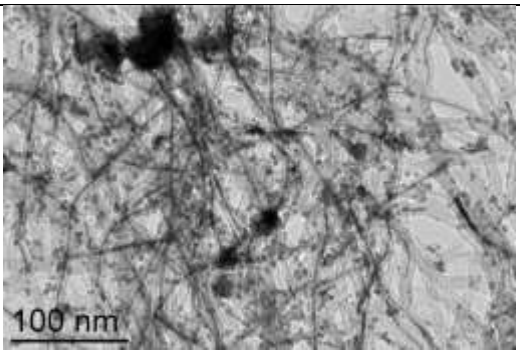 </td></tr>
<tr><td rowspan="2">lxj174</td><td>1Pt</td><td>2BBA</td><td rowspan="2">Tol_100ºC_24h</td></tr>
<tr><td>1Co(COD)(COT)</td><td>2PPP</td></tr>
<tr><td colspan="3">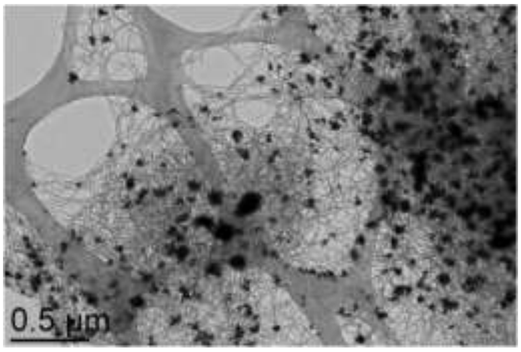 </td><td>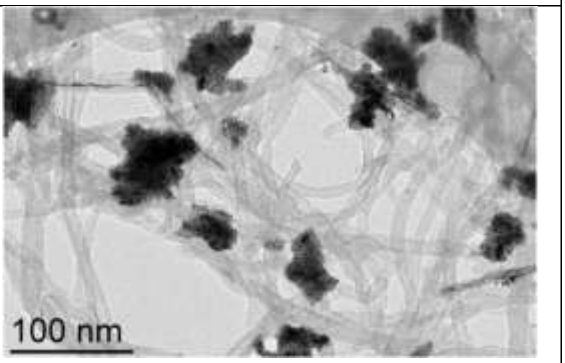 </td></tr>
<tr><td rowspan="2">lxj176</td><td>1Pt</td><td>2BBA</td><td rowspan="2">Tol_100ºC_24h (stock solution long kept)</td></tr>
<tr><td>0.84Co</td><td>2PPP</td></tr>
</table>

<table>
<tr><td colspan="3">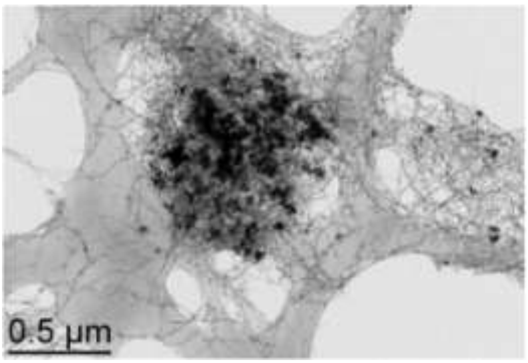 </td><td>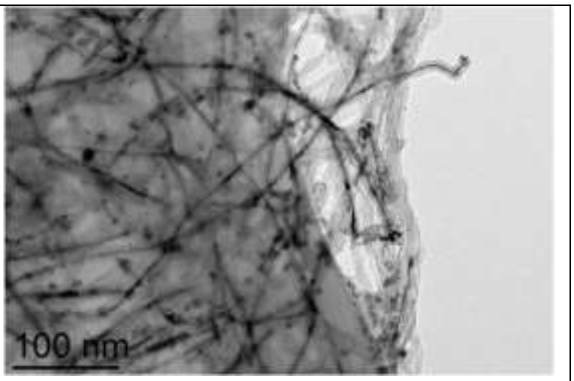 </td></tr>
<tr><td rowspan="2">lxj180</td><td>1Pt</td><td>2BBA</td><td rowspan="2">Tol_100ºC_24h</td></tr>
<tr><td>1Co</td><td>2PPP</td></tr>
<tr><td colspan="3">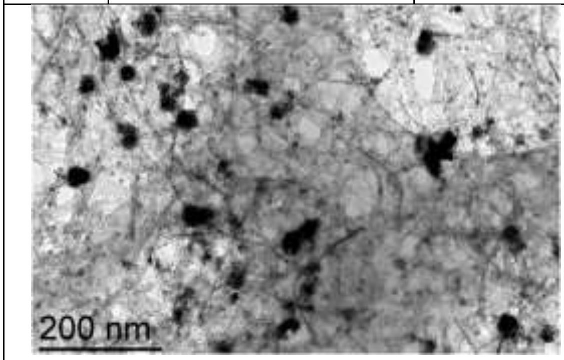 </td><td>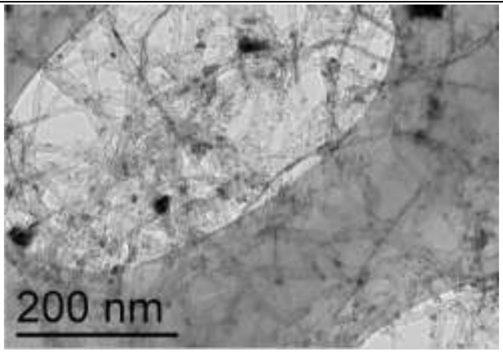 </td></tr>
<tr><td rowspan="2">lxj188</td><td>1Pt</td><td>2BBA</td><td rowspan="2">Tol_100ºC_24h ;Tubes pre-washed by Co solution</td></tr>
<tr><td>1Co</td><td>2PPP</td></tr>
<tr><td colspan="3">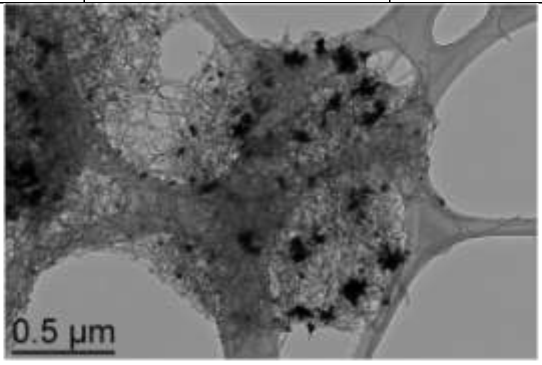 </td><td>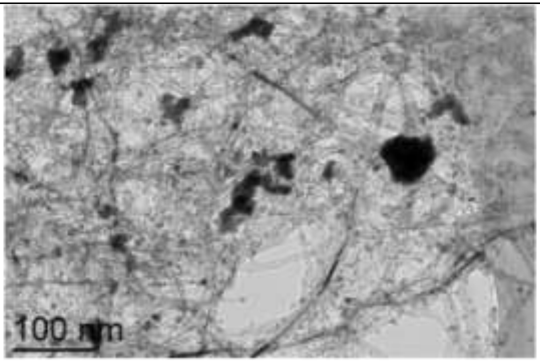 </td></tr>
<tr><td rowspan="2">lxj189</td><td>1Pt</td><td>2BBA</td><td rowspan="2">Tol_100ºC_24h</td></tr>
<tr><td>1Co</td><td>/</td></tr>
</table>

<table>
<tr><td colspan="3">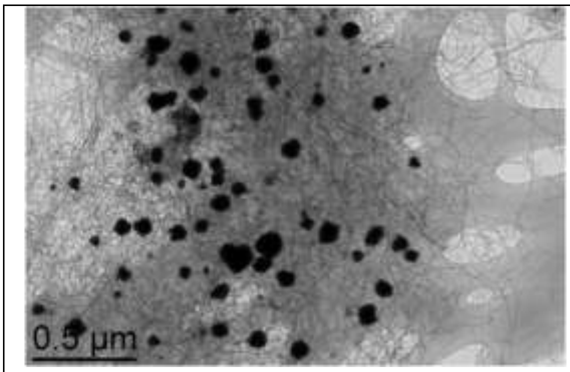 </td><td>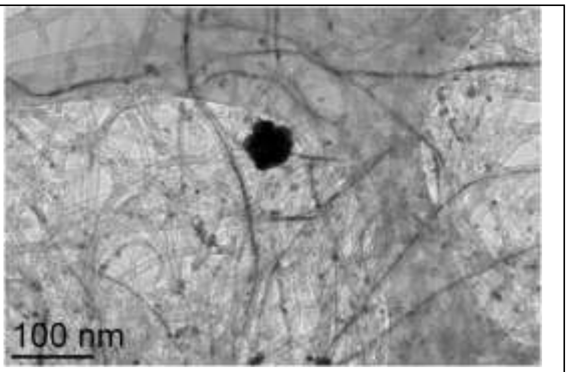 </td></tr>
<tr><td rowspan="2">lxj190</td><td>1Pt</td><td>2BBA</td><td rowspan="2">Tol_100ºC_24h</td></tr>
<tr><td>1Co(COD)(COT)/2HMDS</td><td>2PPP</td></tr>
<tr><td colspan="3">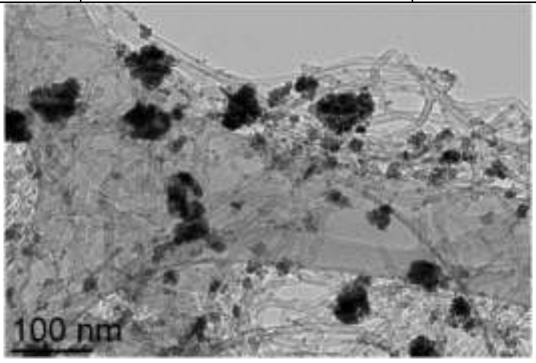 </td><td>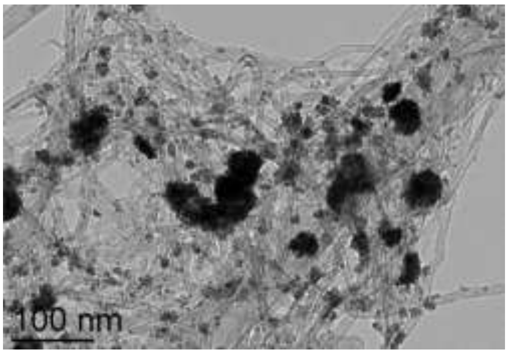 </td></tr>
<tr><td rowspan="2">lxj192</td><td>1Pt</td><td>/</td><td rowspan="2">Tol_100ºC_24h</td></tr>
<tr><td>1Co</td><td>/</td></tr>
<tr><td colspan="3">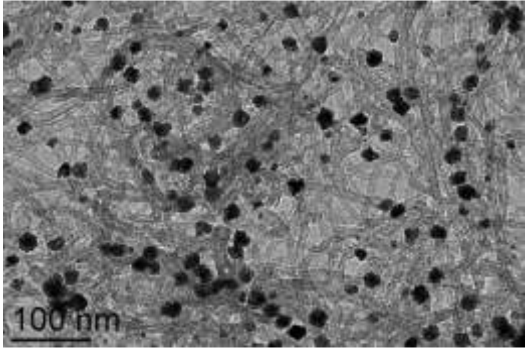 </td><td>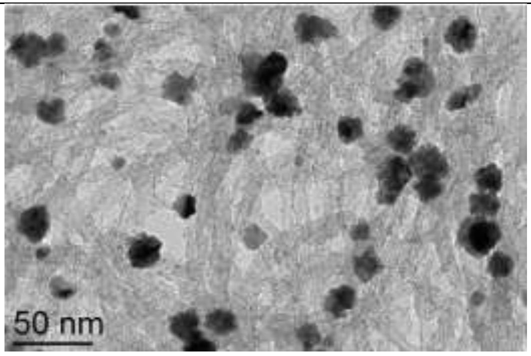 </td></tr>
<tr><td rowspan="2">lxj233</td><td>1Pt(acac)$_2$</td><td>2BBA</td><td rowspan="2">Tol_100ºC_24h; **CNT$_3$**</td></tr>
<tr><td>1Co</td><td>2PPP</td></tr>
</table>

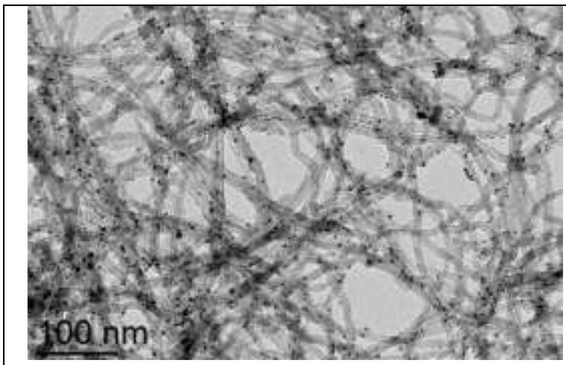100 nm	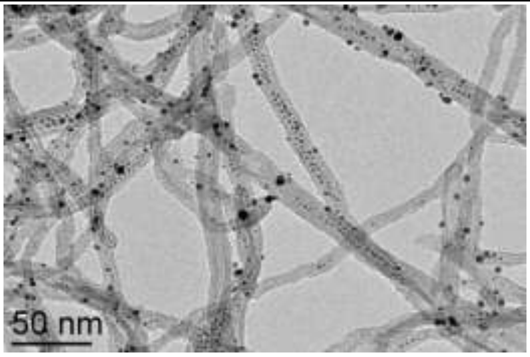50 nm

Table V.10: FePt nanostructure presented inside or outside the CNTs.

<table>
<tr><td colspan="4">(1equivalent= 0.1 mmol)</td></tr>
<tr><td>Ref</td><td>precursors</td><td>ligands</td><td>Reaction conditions</td></tr>
<tr><td rowspan="2">lxj158</td><td>1Pt</td><td>2BBA</td><td rowspan="2">Tol_100ºC_24h</td></tr>
<tr><td>1Fe</td><td>2PPP</td></tr>
<tr><td colspan="3">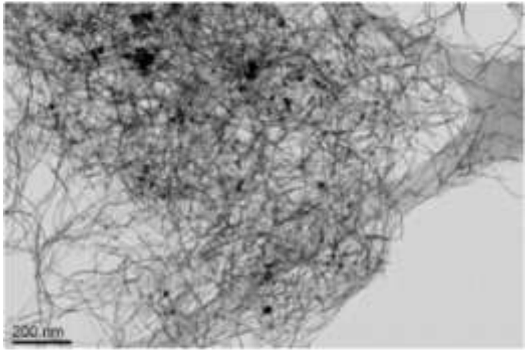 </td><td>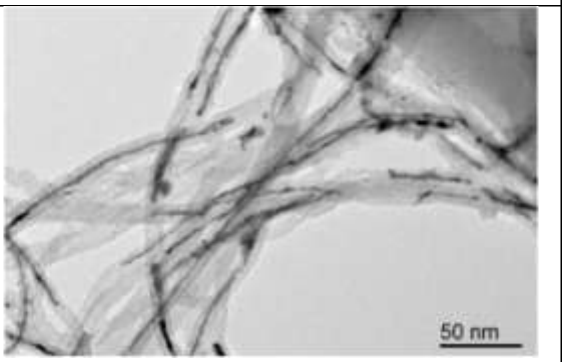 </td></tr>
<tr><td rowspan="2">lxj175</td><td>0.5Pt</td><td>2BBA</td><td rowspan="2">Tol_100ºC_24h</td></tr>
<tr><td>1.5Fe</td><td>2PPP</td></tr>
<tr><td colspan="3">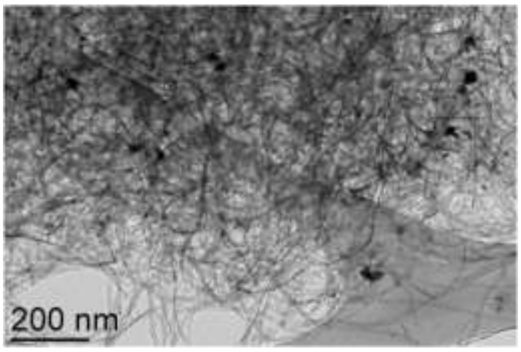 </td><td>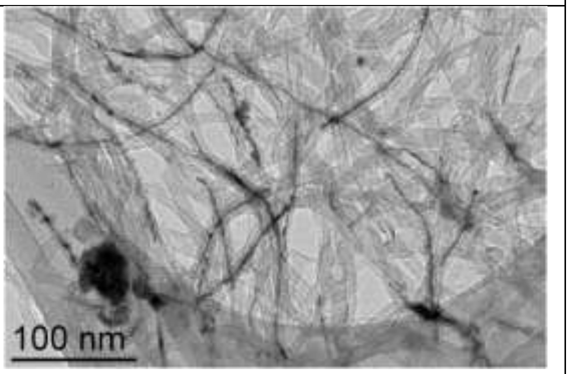 </td></tr>
<tr><td rowspan="2">lxj177</td><td>1Pt</td><td>2BBA</td><td rowspan="2">Tol_100ºC_24h</td></tr>
<tr><td>1Fe</td><td>/</td></tr>
<tr><td colspan="3">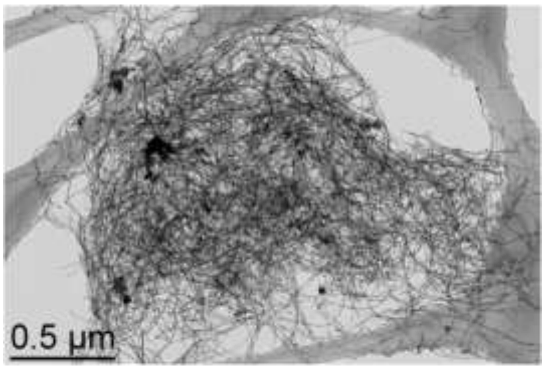 </td><td>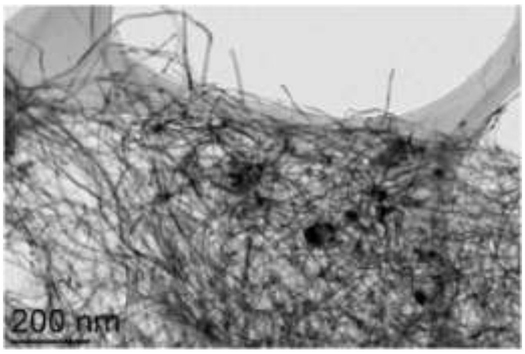 </td></tr>
</table>

<table>
<tr><td rowspan="2">lxj179</td><td>1Pt</td><td>/</td><td rowspan="2">Tol_100ºC_24h</td></tr>
<tr><td>1Fe</td><td>2PPP</td></tr>
<tr><td colspan="3">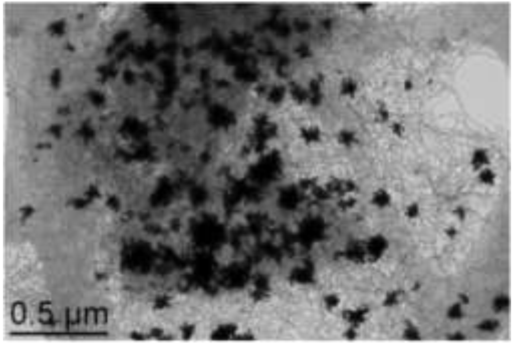
</td><td>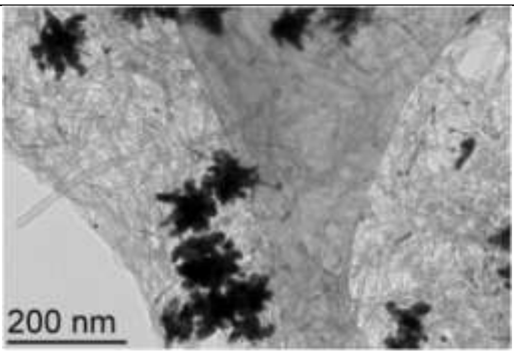
</td></tr>
<tr><td rowspan="2">lxj182</td><td>1Pt</td><td>2BBA</td><td rowspan="2">Mes_150ºC_24h</td></tr>
<tr><td>1Fe</td><td>2PPP</td></tr>
<tr><td colspan="3">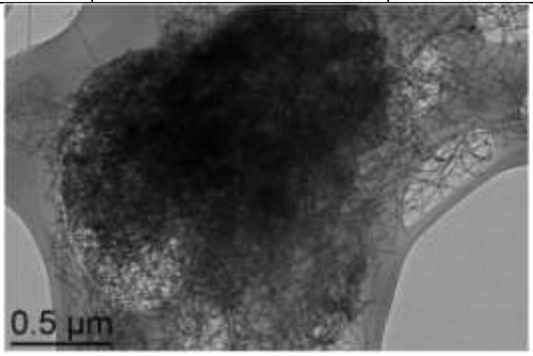
</td><td>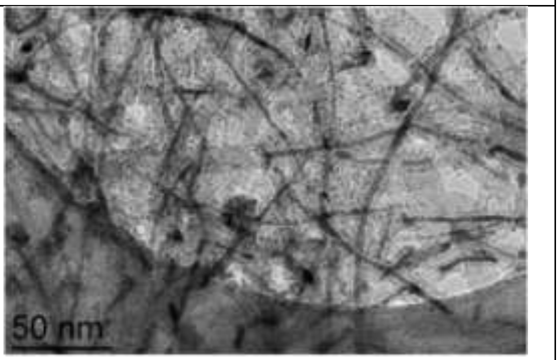
</td></tr>
<tr><td rowspan="2">lxj183</td><td>1Pt</td><td>4BBA</td><td rowspan="2">Tol_100ºC_24h</td></tr>
<tr><td>2Fe</td><td>4PPP</td></tr>
<tr><td colspan="3">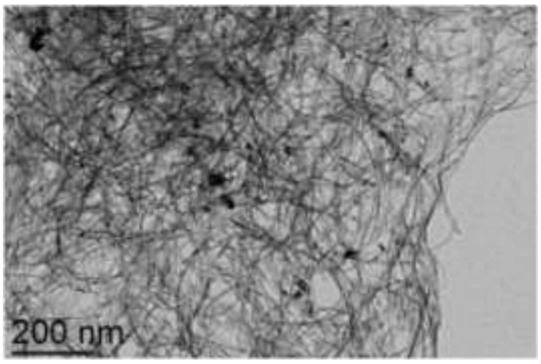
</td><td>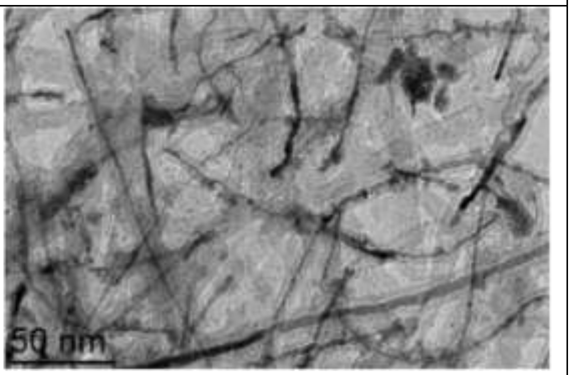
</td></tr>
<tr><td colspan="3"></td><td></td></tr>
</table>

<table>
<tr><td rowspan="2">lxj185</td><td>1Pt</td><td>2BBA</td><td rowspan="2">Tol_100ºC_24h double CNTs</td></tr>
<tr><td>1Fe</td><td>2PPP</td></tr>
<tr><td colspan="3">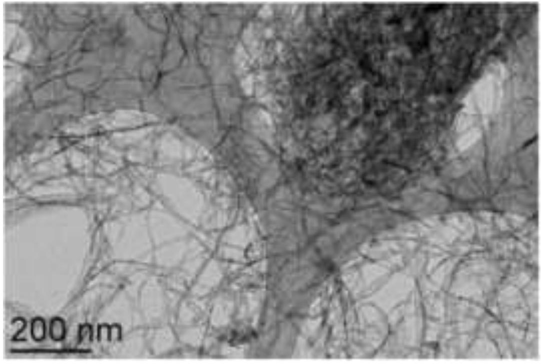 </td><td>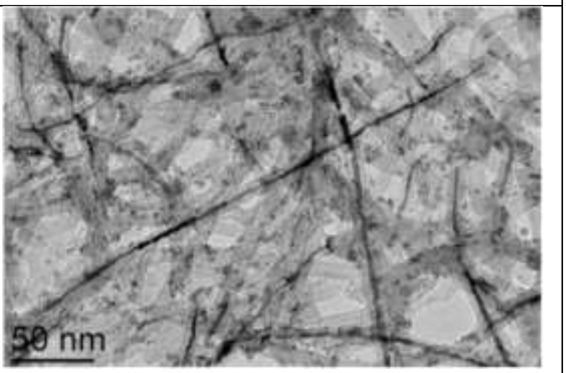 </td></tr>
<tr><td rowspan="2">lxj197</td><td>1Pt</td><td>2BBA</td><td rowspan="2">Tol_100ºC_24h</td></tr>
<tr><td>1Fe</td><td>/</td></tr>
<tr><td colspan="3">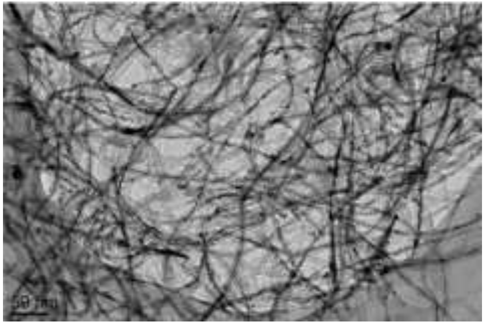 </td><td>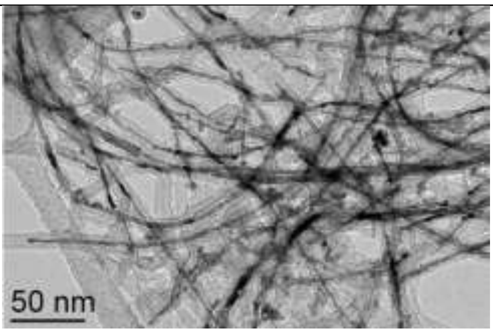 </td></tr>
<tr><td rowspan="2">lxj198</td><td>1Pt(dba)$_2$</td><td>2BBA</td><td rowspan="2">Tol_100ºC_24h</td></tr>
<tr><td>1Fe</td><td>2PPP</td></tr>
<tr><td colspan="3">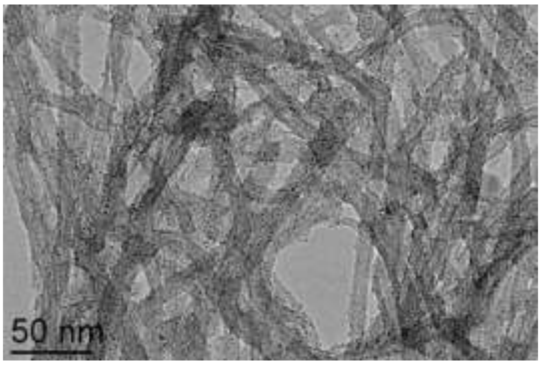 </td><td>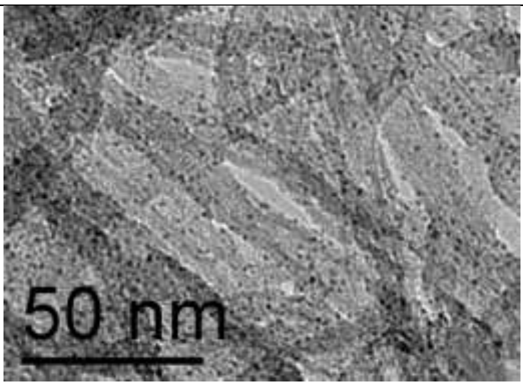 </td></tr>
<tr><td colspan="3"></td><td></td></tr>
</table>

<table>
<tr><td rowspan="2">lxj199</td><td>1Pt</td><td>2BBA</td><td rowspan="2">Tol_100ºC_24h</td></tr>
<tr><td>1Fe</td><td>/</td></tr>
<tr><td colspan="3">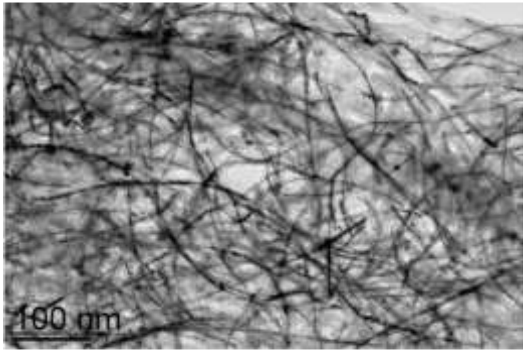 </td><td>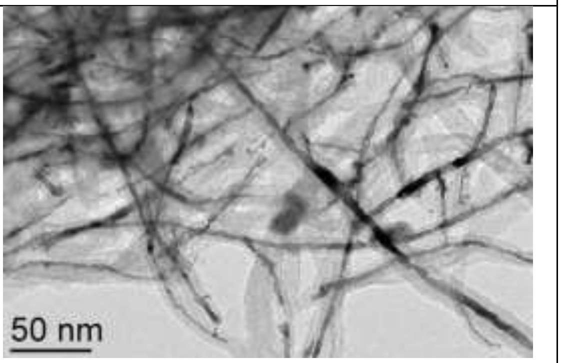 </td></tr>
<tr><td rowspan="2">lxj201</td><td>1Pt</td><td>2BBA</td><td rowspan="2">Tol_100ºC_24h ;Tubes pre-washed by Fe solution</td></tr>
<tr><td>/</td><td>/</td></tr>
<tr><td colspan="3">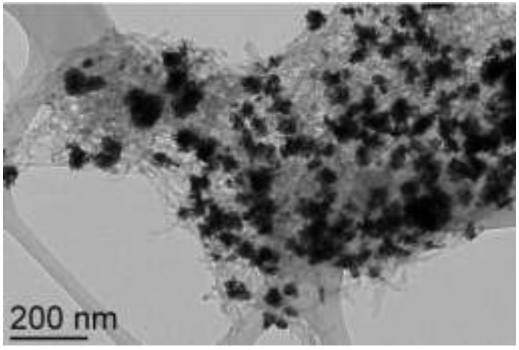 </td><td>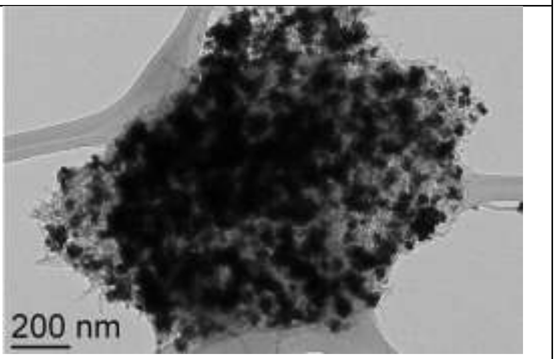 </td></tr>
<tr><td rowspan="2">lxj205</td><td>1Pt</td><td>1BBA</td><td rowspan="2">Tol_100ºC_24h</td></tr>
<tr><td>1Fe</td><td>/</td></tr>
<tr><td colspan="3">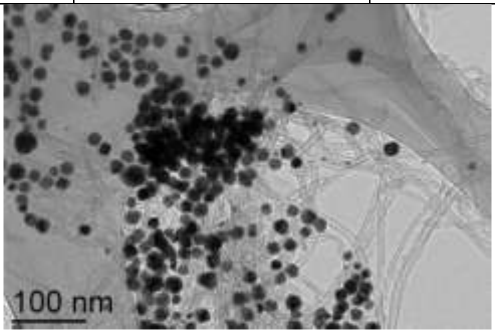 </td><td>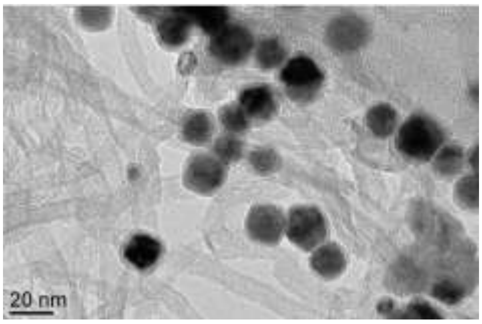 </td></tr>
<tr><td colspan="3"></td><td></td></tr>
</table>

<table>
<tr><td rowspan="2">lxj206</td><td>1Pt</td><td>1BBA</td><td rowspan="2">Tol_100ºC_24h</td></tr>
<tr><td>1Fe</td><td>2PPP</td></tr>
<tr><td colspan="3">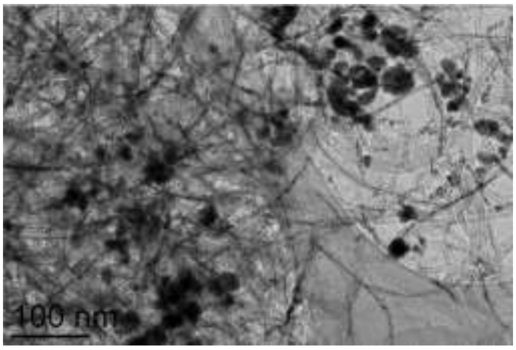 </td><td>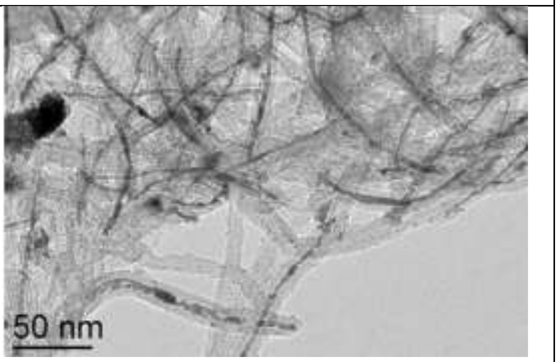 </td></tr>
<tr><td rowspan="2">lxj209</td><td>1Pt(acac)2</td><td>2BBA</td><td rowspan="2">Tol_100ºC_24h</td></tr>
<tr><td>1Fe</td><td>2PPP</td></tr>
<tr><td colspan="3">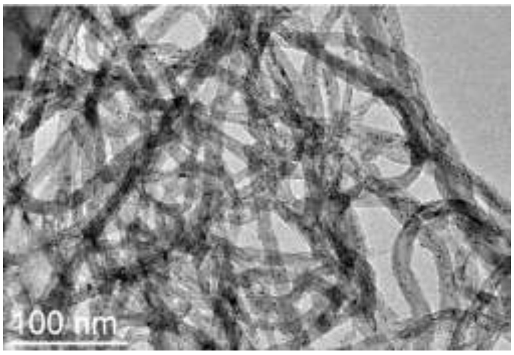 </td><td>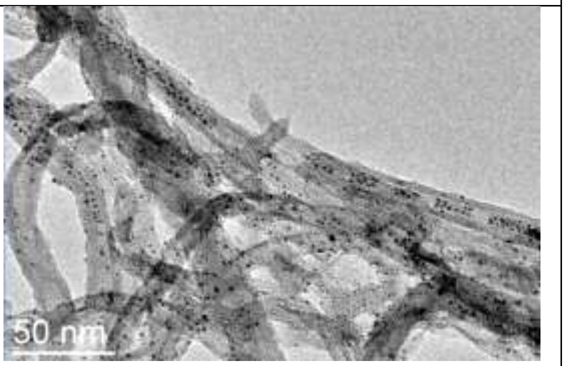 </td></tr>
<tr><td rowspan="2">lxj212</td><td>1Pt</td><td>1BBA</td><td rowspan="2">Mes_150ºC_24h</td></tr>
<tr><td>1Fe</td><td>/</td></tr>
<tr><td colspan="3">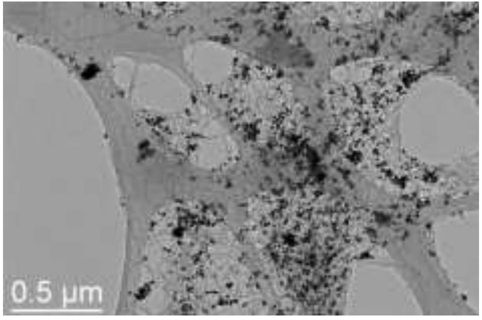 </td><td>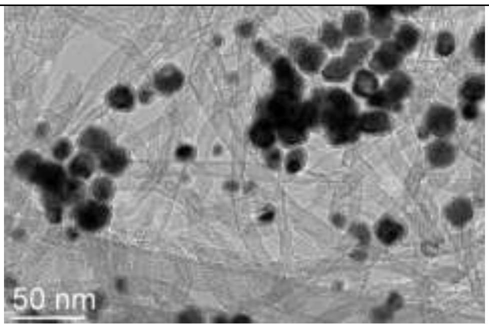 </td></tr>
<tr><td colspan="3"></td><td></td></tr>
</table>

<table>
<tr><td rowspan="2">lxj213</td><td>1Pt(acac)$_2$</td><td>2BBA</td><td rowspan="2">Mes_150ºC_24h</td></tr>
<tr><td>1Fe</td><td>2PPP</td></tr>
<tr><td colspan="3">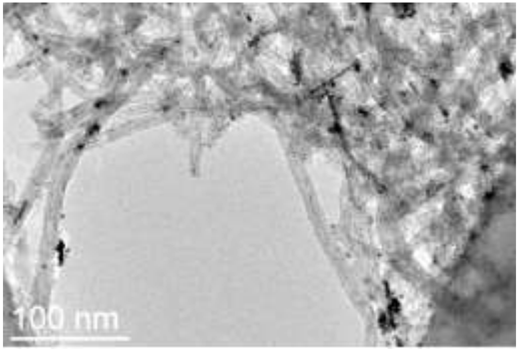 </td><td>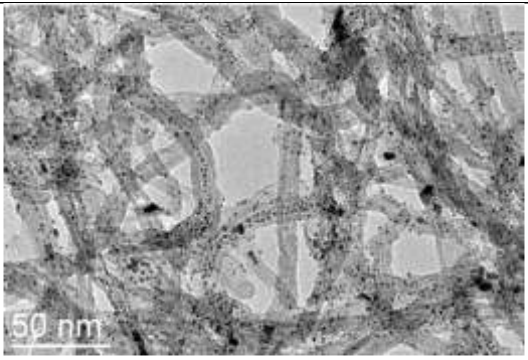 </td></tr>
<tr><td rowspan="2">lxj217</td><td>1Pt(acac)$_2$</td><td>2BBA</td><td rowspan="2">Tol_100ºC_24h; CNT$_3$</td></tr>
<tr><td>1Fe</td><td>2PPP</td></tr>
<tr><td colspan="3">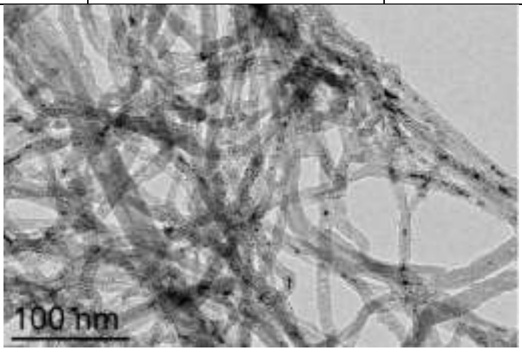 </td><td>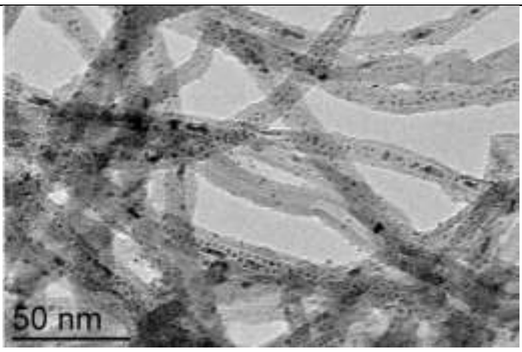 </td></tr>
</table>

1. L. Zhang, E. Yue, B. Liu, P. Serp, C. Redshaw, W.-H. Sun, J. Durand, *Catal. Commun.*, **2014**, *43*, 227–230.

Appendix II- Analysis techniques

PART A. Analysis techniques

I. Transmission Electron Microscopy (TEM)

Electron microscopy is a powerful analytical tool for the study of nanomaterials. We will describe briefly the operation principles of the the transmission electron microscope (TEM) (conventional and high resolution).

I.1 Transmission Electron Microscopy (TEM)

Transmission Electron Microscopy is a basic characterization technique in the nanoscale materials domain. This technique is routinely employed in order to investigate the size the shape and the organization of the synthesized nanocrystals . In the following Figure A.1 a schematic representation of an electron microscope (TEM) illustrating its different parts is provided.

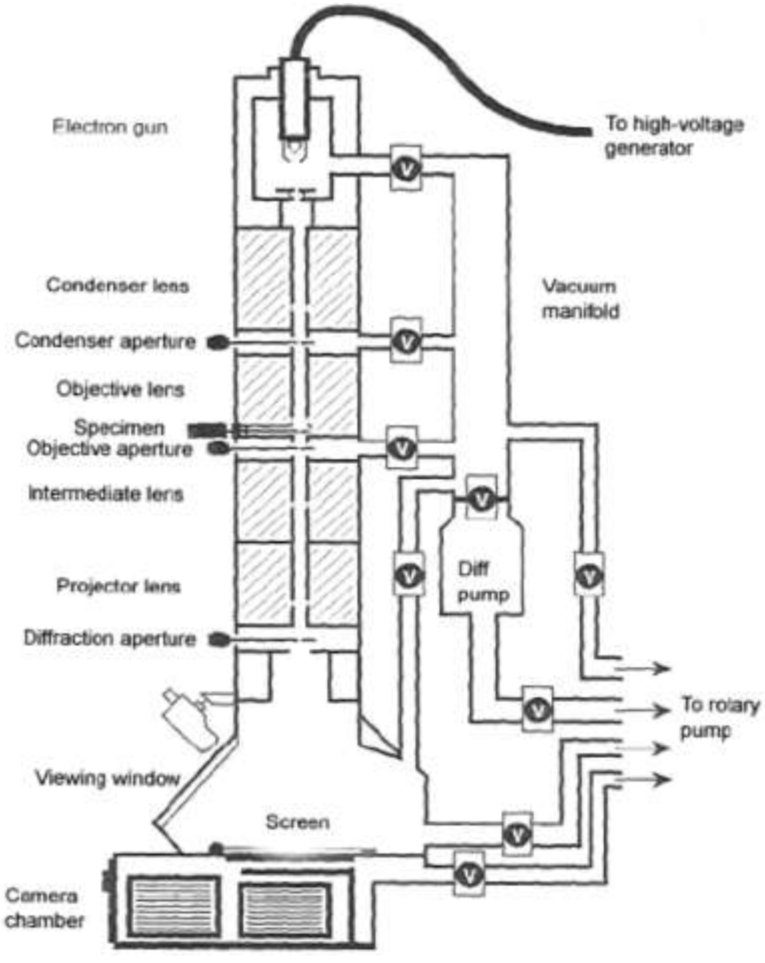

Figure A.1: Schematic representation of a Transmission Electron Microscope.

The gun of the microscope is the element where the electron beam is generated. The electrons in a TEM are emitted by a thermal cathode. They are accelerated by a tension which is typically between 100 and 300 kV. One intermediate electrode, the Wehnelt, generates a repulsive field for the electrons and makes the beam approach its axis. Every point of the extremity of the filament emits in all directions. In this way the electrons pass from a common surface of diameter d_0, that constitutes the geometric source of the beam.

A schematic representation of an electron gun is presented in the following Figure A.2.

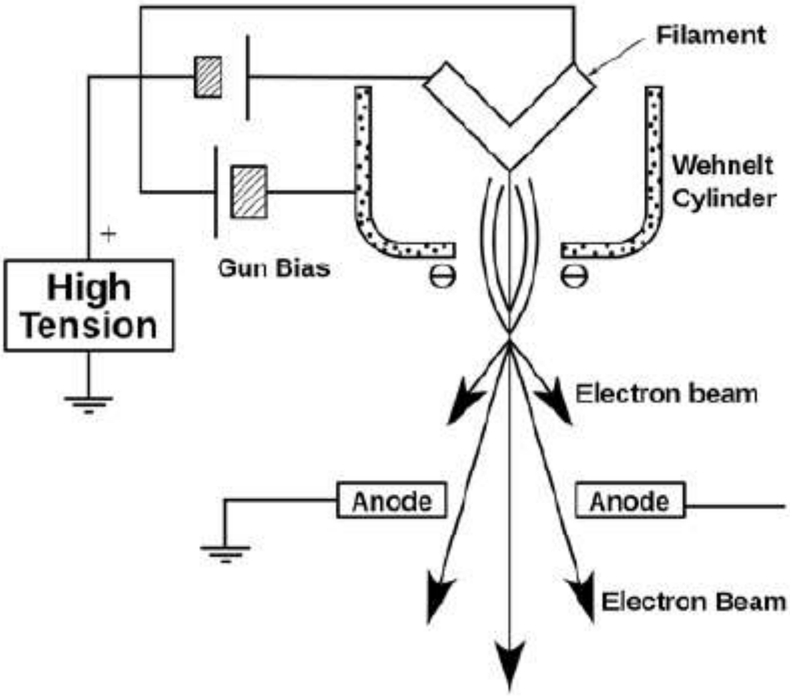

Figure A.2: Schematic representation of an electron gun.

The electrons after exiting the gun follow a guided path by the electromagnetic lenses. The optical properties of these lenses are analogous to the properties of glass lenses. A current passing from a copper coil generates a magnetic field that is canalized by soft magnets. This results in a helical movement of the electrons. There are three types of electromagnetic lenses: i) the condenser lenses that focus the beam on the object; ii) the objective lens that gives a first image of the object and determines the resolution of the image; iii) the projection lenses that transfer the image given by the objective lens to the fluorescent screen or the camera.

Another group of the microscope elements is the apertures. The apertures are essential parts for the function of the microscope. The different apertures as seen in the Figure A.1 above are:

i) The condenser aperture that limits the electron beam before it contacts the object; ii) The opening or contrast aperture that is found in the focal plane of the objective lens; iii) The selective aperture that is found in the image plane of the objective lens and allows the selection of one part of the image in order to perform a diffraction diagram.

Image Formation

The lenses that are placed after the objective lens permit the variation of the projection system. It is possible to obtain an image or a diffraction diagram. These two modes are described below:

Image mode

The focus on the image plane of the objective (Gauss plane) is performed. The spherical aberration is reduced by placing an aperture in the focal plane before the objective lens. The user can thus choose between the images in bright field mode or in dark field mode. These two modes are obtained as a function of the position of the aperture with respect to the diffraction diagram.

1. Bright Field mode

The aperture is centered directly to the beam. The non-diffracted rays of electrons contribute to the formation of the image and appear bright, while the other parts that are diffracted appear dark. The grey level of the dark parts depends on the zone orientation of the crystallized parts. This mode is the most conventional mode and gives mostly information about the size and the shape of the objects.

2. Dark Field mode

The aperture is centered on the diffracted beam of the crystal. Only the rays that correspond to the selected reflection contribute to the image formation. In this way, the crystal appears bright in a dark background. In dark field mode we can get some information about the location of various crystalline phases in our sample.

Diffraction mode

The projection system is focused on the backward focal plane of the objective lens, known as Fourier plane. In the absence of the contrast aperture, a diffraction diagram is observed. It represents a plane section of the reciprocal diffraction network. The diffraction pattern obtained is useful for the determination of the crystalline phase of the materials and their orientation with respect to the beam axis.

I.2 High Resolution Transmission Electron Microscopy (HRTEM)

In conventional electron microscopy, the image contrast, named as amplitude contrast is obtained while the images are produced by one beam: the transmitted beam or a diffracted beam by the sample. The phase relations between the different beams are masked. The image resolution is limited by the objective aperture used in order to select one beam. In HRTEM, the opening of the aperture is larger and this way more electrons participate in the formation of the image. Their phase relation is preserved.

The image is the result of the interference of the transmitted beam with one or more diffracted beams. The collected intensity in the image mode is a function of amplitude and of the relative phases of the different beams. This mode allows the gathering of information on the periodicity of the crystalline lattice. The phase contrast imaging requires that the object is oriented in the same way as the optical axis of the microscope, or in other words parallel to a high symmetry crystal axis (zone axis). The incident beam is thus diffracted by the crystal planes that contain this axis. It is thus possible that under certain conditions that depend on the object and the experiment, representative images of the crystalline lattice are obtained following the observation axis.

II. Magnetometry

II.1 SQUID

The Superconducting Quantum Interference Device (SQUID) is considered as the most sensitive sensor for measuring the magnetic flux of a sample.

Two phenomena of superconductivity, the Josephson effect (tunneling) and the flux quantization are the base for the operation principle of the SQUID as a flux to voltage converter. SQUID can be used to measure almost every physical quantity that can be converted to magnetic flux with high sensitivity over a wide range of temperature and under applied magnetic fields that reach several Tesla.

The main parts of a SQUID magnetometer are the superconducting magnet, the superconductive detection coil, the SQUID which is connected to the superconducting coil and a superconducting magnetic shield.

The superconducting magnet is a solenoid made of superconducting materials that should be kept at low temperature. This magnet is able of producing magnetic fields of more than 10 T.

The superconducting coil is a single superconducting wire that is placed in the interior of the solenoid magnet and encloses the sample. The geometry of this coil is adjusted so that it can serve as a second-order gradiometer.

The SQUID is usually a thin film that functions as an extremely sensitive current-to-voltage-converter. The measurement of the magnetic moment is performed by moving the sample in the interior of the superconducting coil. The magnetic moment of the sample induces an electric current in the coil and this current is converted to voltage by the SQUID. A variation of the magnetic flux in the coil will result in a variation of the voltage produced by the SQUID. This variation is proportional to the magnetic moment of the sample.

Finally, the superconducting magnetic shield is the part of the magnetometer used to protect it from the fluctuations of the ambient magnetic field present in the place of the equipment. The main parts of a SQUID magnetometer are presented schematically in the following Figure A.3.

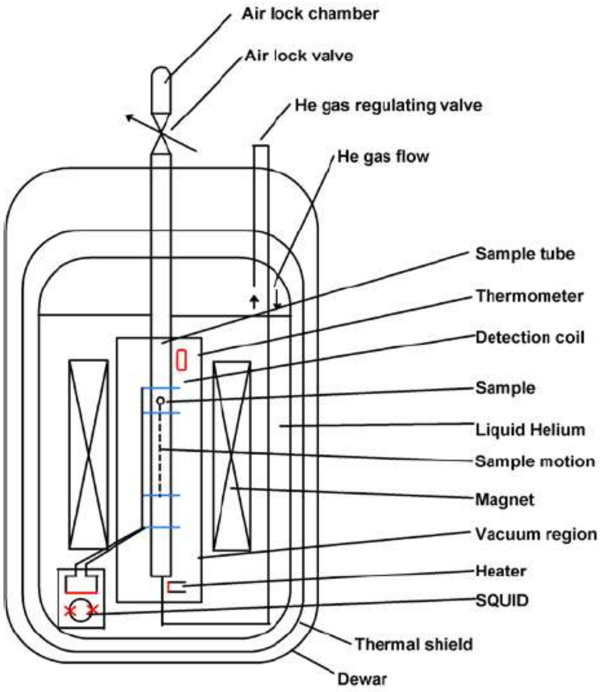

Figure A.3: Schematic representation of a SQUID magnetometer.

The SQUID magnetometer is considered as the most accurate and sensitive magnetometer available.

II.2 VSM

The Vibrating Sample Magnetometer (VSM) is a widely used instrument for measuring the magnetic properties of materials. It was invented by Simon Foner in 1956. Like SQUID magnetometers the VSM is characterized by high sensitivity in a wide range of temperature and under applied magnetic fields of several Tesla.

The principle of the VSM is based on the Faraday's law of induction that tells us that an electric current can be produced by a varying magnetic field. In fact, the sample vibrates in a uniform magnetic field produced by the electromagnet of the magnetometer in a sinusoidal motion. The sample as in the case of SQUID is placed in a pick-up coil. Because of its motion, the sample can cause a sinusoidal electric current by induction to the coil. The frequency of the current is equal to the frequency of the motion while its intensity is proportional to the magnetization of the sample.

A schematic representation of a VSM and its different components is given in the following figure.

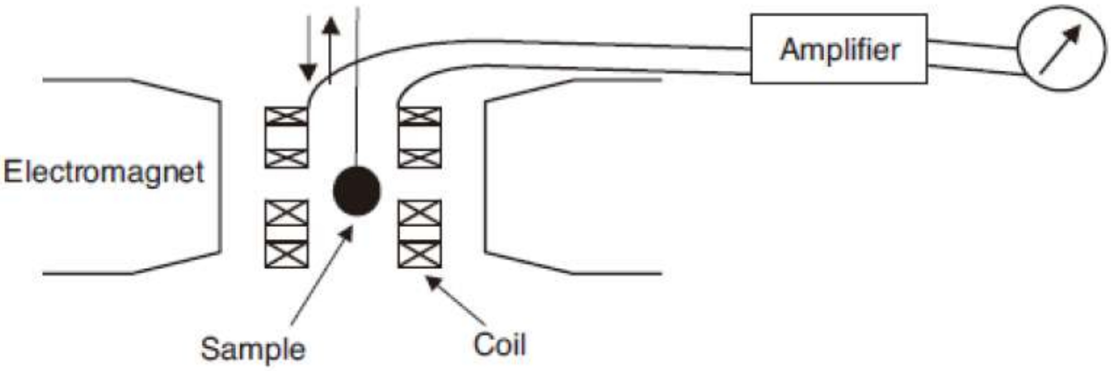

Figure A.4: Schematic representation of a VSM.

While the VSM is not as sensitive as the SQUID magnetometer, it is more rapid in its measurements due to the fast movement (vibration) of the sample giving in this way the possibility of having more experimental points for a certain time period.

III. UV-vis spectroscopy

UV-vis spectroscopy is the spectroscopic technique that studies the phenomena related to the absorption of light that is characterized by a wavelength (λ) that is typically in the UV-vis region and sometimes in the near IR (about 200-1100 nm).

The molecular species of a solution can undergo electron transitions from lower to higher energy levels upon irradiation with light. Since the energy levels of the molecules are discrete the light should have an energy corresponding to the energy difference between these levels in order to cause the transition. UV-vis light can interact with the electrons and induce their transition.

For solutions in general we accept that the law of Lambert and Beer is applicable. This law describes the absorption (A) as a function of the concentration (c) and the optical path of the solution (l). The A is defined as the logarithm of I_0/I, where I is the intensity of the light.

$$A = \log (I_0/I)$$

According to the Lambert-Beer law, $A=\varepsilon\ c\ l$, where ε is the molar extinction which is constant for a particular substance at a particular wavelength and temperature. This means that A is proportional to the concentration for a given l and for a certain substance.

The UV-vis spectrophotometer measures the intensity of the light passing through the sample and compares it to the intensity of the light before interaction with the sample. The basic parts of a spectrophotometer are the light source, the sample chamber and its holder, the monochromator in order to separate the different wavelengths and the detector. A UV-vis spectrophotometer is schematically presented in the following figure.

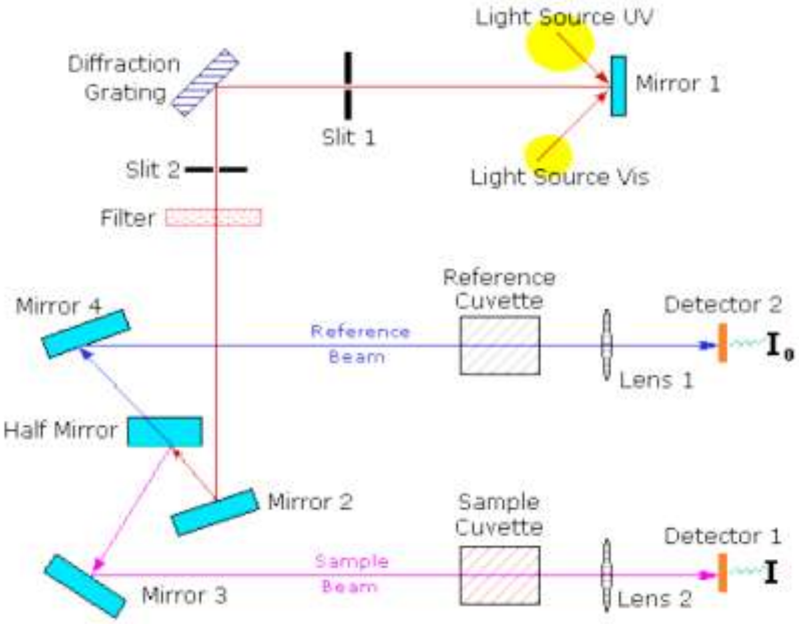

Figure A.5: Schematic representation of the functioning of a UV-vis spectrophotometer.

A spectrophotometer can be of single or double-beam. In the case of the single beam instruments the whole beam passes through the sample and the comparison with the incident light intensity is performed by removing the sample. A double-beam spectrophotometer operates by splitting the initial beam to two equivalent beams before passing through the sample. One beam is used as the reference while the other passes through the sample. The two intensities, depending on the instrument, can be measured at the simultaneously if two detectors are present, or alternatively by the use of a beam chopper.

The information obtained from the UV-vis spectra is helpful for identifying chemical compounds. It can also inform on the structure of metal complexes, since electronic transitions depend on the molecular symmetry.

IV. Fourier Transfer-InfraRed spectroscopy (FT-IR)

FT-IR spectroscopy was developed in the 1970s and provided a great improvement to the analysis by Infrared spectroscopy. Sensitivity, speed and improved data processing are the key advantages of this technique compared to the conventional IR spectroscopy, which is limited by several factors (presence of water vapor, CO_2 etc…).

The basic components of an FT-IR spectrometer are the IR source that generates the infrared radiation, the interferometer that modulates this radiation, by performing an optical inverse

Fourier transform on the entering IR radiation, and the detector of the reflected by the sample radiation.

The most important part of the FT-IR spectrometer is the interferometer. This part is typically a Michelson-type plane mirror interferometer (Figure A.6).

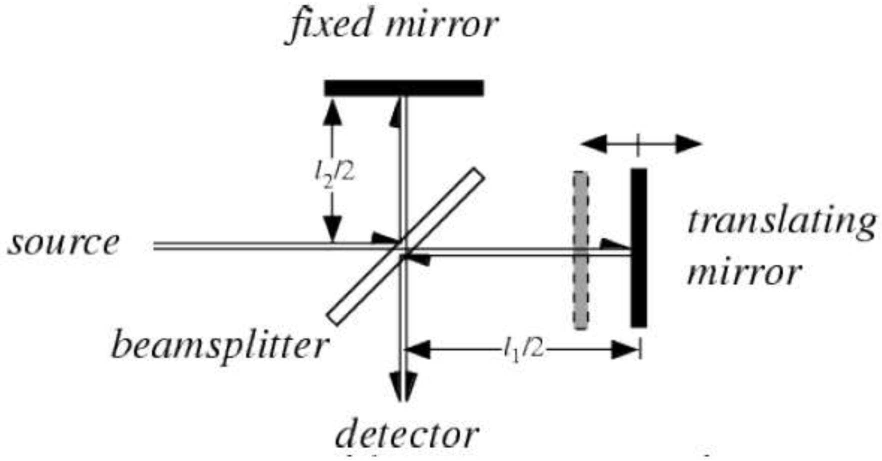

Figure A.6: Schematic representation of the main components of an FT-IR spectrophotometer.

The infrared radiation upon being collimated is separated by a beam splitter. Half of the radiation is transmitted and the other half is reflected. Both transmitted and reflected beams are reflected back to the beam splitter by mirrors. Thus, one half of the infrared radiation that finally goes to the sample has first been reflected from the beam splitter to the moving mirror, and then back to the beam splitter. The other half of the infrared radiation going to the sample has first passed through the beam splitter and then reflected from the fixed mirror back to the beam splitter. When these two optical paths are reunited, interference occurs at the beam splitter because of the optical path difference caused by the scanning of the moving mirror.

The optical path length difference between the two optical paths of a Michelson interferometer is two times the displacement of the moving mirror. The interference signal measured by the detector as a function of the optical path length difference is called the interferogram. A typical interferogram produced by the interferometer is shown in Figure A.7. The graph shows the intensity of the infrared radiation as a function of the displacement of the moving mirror. At the peak position, the optical path length is exactly the same for the radiation that comes from the moving mirror as it is for the radiation that comes from the fixed mirror.

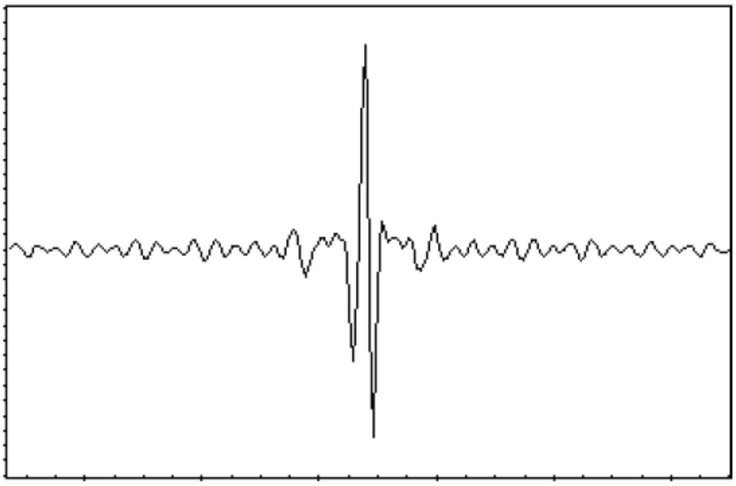

Figure A.7: Interferogram produced by the FT-IR interferometer.

The spectrum can be computed from the interferogram by performing a Fourier transform. The Fourier transform is performed by the same computer that ultimately performs the quantitative analysis of the spectrum. A FT-IR spectrum is presented in the following Figure A.8.

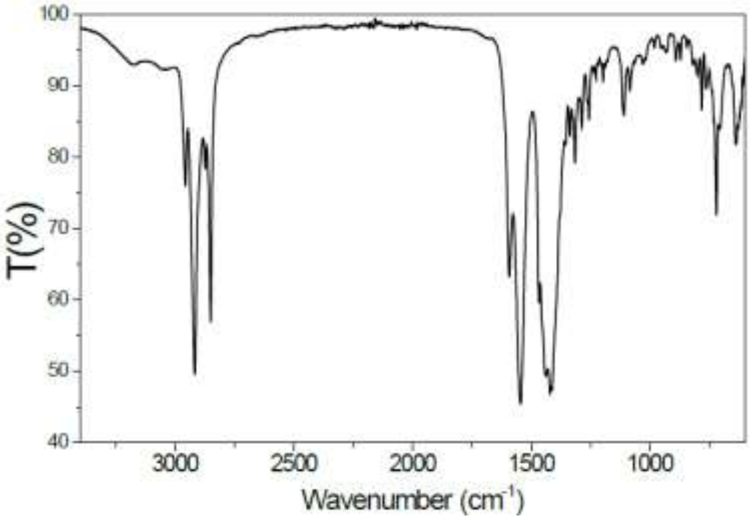

Figure A.8: FT-IR spectrum.

Typically, the FT-IR spectroscopy measures the vibration frequency of various bonds that occurs upon irradiation by the IR beam. This frequency is correlated to the chemical bond strength which is characteristic of the nature of the chemical bonds. The intensity of the peaks and the energy that they correspond to depends on the symmetry of the vibration and the bond strength. By examining a spectrum, depending on the complexity of the system we can detect the presence of functional groups, such as –COOH or –SH etc. as well as the coordination of certain groups to metal centers. The symmetry of the vibration is crucial since symmetric vibrations are not visible by IR spectroscopy. Only the vibrations corresponding to a modification of the polarization of molecule during vibration are visible.

V. X-Rays Diffraction (XRD)

X-Rays Diffraction (XRD) is widely used for the characterization of crystalline materials. It is based on the interactions between the X-rays and the crystals of the material following the law of Bragg. A unique diffraction pattern is produced by each material.

When an X-ray of a wavelength λ interacts with a crystalline material at an angle θ it can be reflected (diffracted) as shown in Figure A.9. The reflected beam with the maximum intensity will be the one that is in phase with the incident beam. For this to happen, the distance d between the planes has to be such as given b the Bragg's law:

$$n\lambda=2d\ \sin\theta \text{ (Bragg's law)}$$

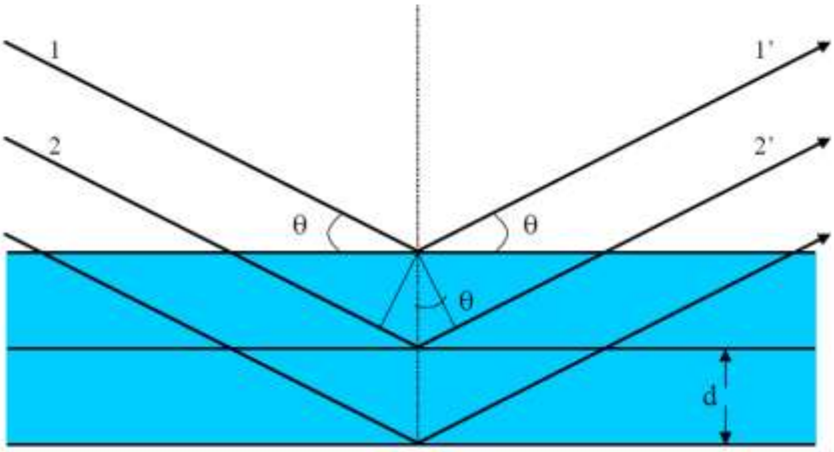

Figure A.9: Diffraction of X-rays from a crystal displaying planes separated by a distance d.

The different *d-spacings* of the crystal are defined by the indices of the crystal unit cell (*h, k, l*). Therefore, the possible 2θ angles where diffraction can happen are defined by the crystal structure of the material (typically n is considered as 1). The intensity of the diffracted patterns depends on the electron density along the diffraction planes of the crystal and thus from the nature of the atoms (heavy atoms diffract more).

The different parts of an XRD instrument are the X-rays source, the Kβ filter, the sample stage and the X-rays detector. A typical X-rays diffractometer setup is presented in the following figure.

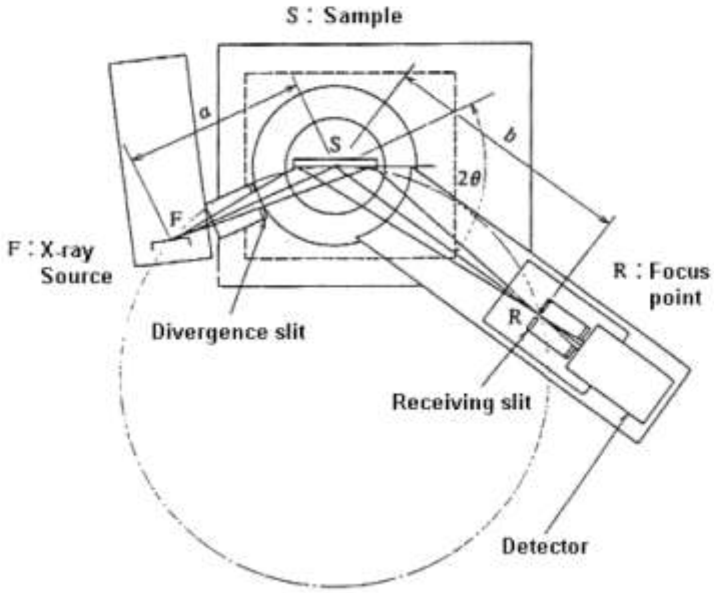

Figure A.10: Schematic representation of the setup of a typical X-Rays diffractometer.

At the X-rays source electrons are accelerated at the cathode and result in the generation of X-rays at the cathode by inelastic interactions with the nuclei. Typically, materials like Mo or Co are used as the anode. For example X-rays of 1.78890 Å for Co (Ka1) or 0.70926 Å for Mo are generated.

XRD is a very powerful technique for the identification of the crystalline phases, the characteristics of the lattice and the relative content of a sample in each phase. Additional analysis can lead also to the calculation of the crystallite size along certain crystallographic directions.

VI. Wide Angle X-rays Scattering (WAXS)

Wide Angle X-ray Scattering (WAXS) is a technique that is often used to determine the crystalline structure of materials. This technique has been greatly developed and adapted to the determination of the crystal structure of small nanoparticles. Since it is a technique that studies Bragg peaks scattered to wide angles it refers to sub-nanometer distances.

Typically, for a WAXS experiment, the sample is placed at a short distance from the detector and so the scattering angles measured are large enough. The scattering intensity is plotted as a function of the *2θ* angle. The angle of scattering depends on the interplanar distances (d-spacing) of the crystalline material that is measured. The intensity of the d-space pattern is proportional to the number of electrons present in the imaginary planes. Also, the shape of the peaks depends on the crystallite size. Small crystallites typically produce broad diffraction patterns while big crystallites produce fine peaks.

The different parts of WAXS diffractometer are presented schematically in the figure below.

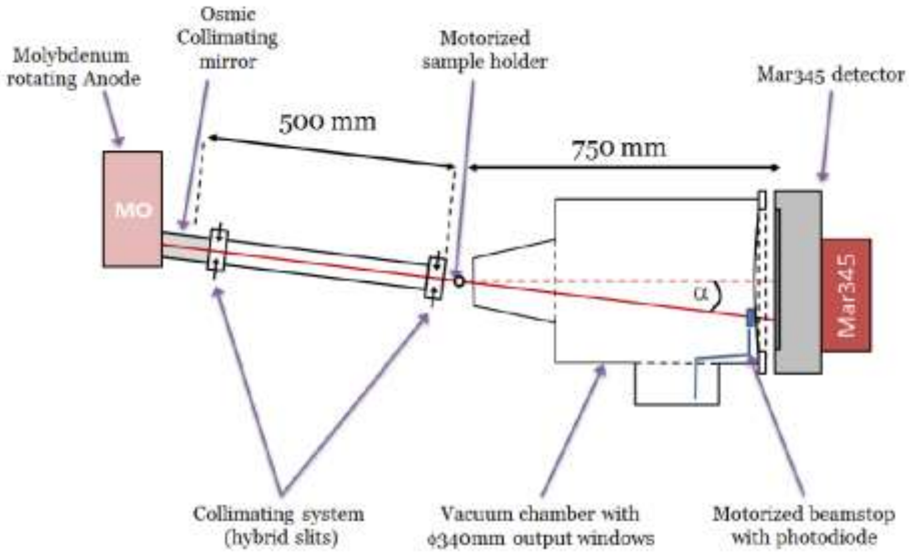

Figure A.11: Schematic representation of a WAXS setup.

VII. Nuclear Magnetic Resonance (NMR) spectroscopy

Nuclear Magnetic Resonance (NMR) spectroscopy is one of the most powerful techniques in molecular chemistry for analysis and characterization. NMR is a physical phenomenon in which certain nuclei when they are present in a magnetic field absorb and reemit electromagnetic radiation. The energy of the radiation depends on the magnetic field and the nucleus. This phenomenon is observed only for nuclei that have an odd number of protons and/or neutrons. The most commonly studied nuclei by NMR are ^{1}H, ^{13}C, ^{31}P, ^{19}F, ^{14}N, ^{29}Si, and ^{35}Cl. These nuclei have a nuclear spin that is These nuclei have a nuclear spin that is different than zero and depends on the number of protons and neutrons. For example the ^{1}H has a spin S=1/2 while deuterium ^{2}H has S=1.

However, all the nuclei of the same nuclide do not resonate at exactly the same frequency. This is the reason chemists can obtain useful information by the NMR spectroscopy. The presence of nuclei in different chemical environment causes a different shielding from the magnetic field. This difference can be observed by NMR spectroscopy and it depends mainly on their near chemical environment. For example a proton of a carboxyl group is less shielded compared to a proton of methyl group, since this shielding depends on the electron density around the proton.

The protons of tetramethylsilane (TMS) are used as a reference. The shift is measured in ppm from the:

$$\delta=(\upsilon-\upsilon_0)/\ \upsilon_0 \times 10^6 \text{ (ppm)}$$

Apart from the shielding, other phenomena such as spin-spin coupling and spin relaxation can give valuable information on the number and the nature of nuclei that interact through chemical bonds, or even through space. A combination of several complementary NMR techniques often allows a detailed elucidation of a molecular structure. Unfortunately the NMR is easily applicable only on non-magnetic molecules.

Today, most of the NMR spectroscopy is based on Fourier Transform (FT) analysis since it made it easier and more efficient. For solution NMR spectroscopy special solvents need to be used that is typically deuterated solvents like toluene-d^8.

A typical NMR spectrometer is presented schematically in the following figure.

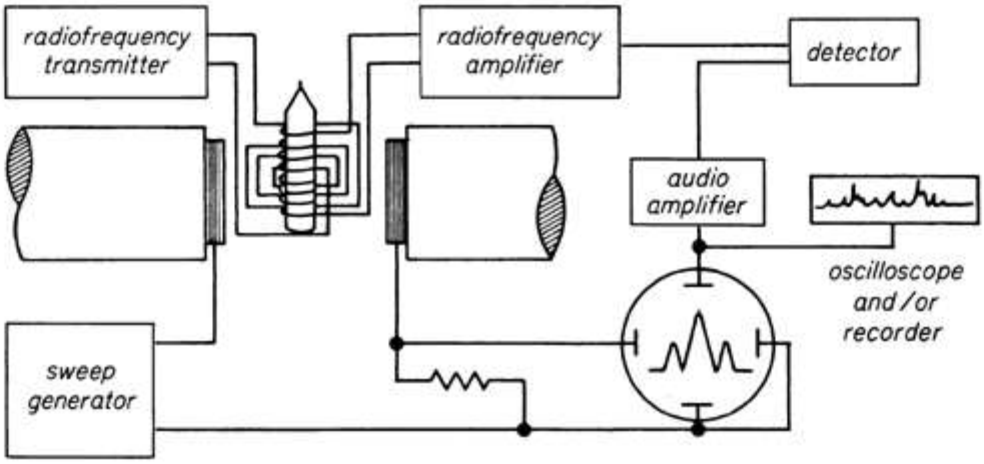

Figure A.12: Simple schematic representation of an NMR spectrophotometer.

PART B. Magnetic metallic nanoparticle synthesis and their magnetic characterization

I. Magnetic metallic nanoparticles (MMNPs) synthesis

Metallic magnetic nanoparticles (MMNPs) of the 3d series and their alloys are among the most important targets in nanoscience research with applications ranging from ultra-high density magnetic recording to multifunctional magnetic probes and transport media for biomedicine (1). Up to now, studies based on magnetic oxides are more numerous; however MMNPs possess better magnetic properties than those of oxides because they combine a high magnetization, which guarantees a more efficient response to magnetic field stimuli, and a tuneable anisotropy, which may be optimized depending on the target application.

Two basic pathways, “top-down” and “bottom-up”, have been used for NPs synthesis. In contrary to the “top-down” pathway in which nano-objects with relatively broad size distribution are obtained, the chemical “bottom-up” synthesis has drawn a great interest since the last three decades. In this technique, growth of NPs is achieved by decomposition of molecules, and NPs are stabilized by stabilizing agents that interact with the surface of NPs and prevent them from agglomeration.

In this thesis, we chose the synthesis method based on the “organometallic” approach developed by Chaudret *et al.* (2-6), which schematic outline is presented in Figure B.1. Briefly, an organometallic precursor or coordination compound undergoes thermal decomposition and/or reduction in an organic solvent under heating and H_2 pressure in the presence of surfactants. During the reaction the starting precursor is decomposed and the first seeds of NPs are generated, through nucleation of what we call “active monomers”. These are high energy entities (naked or under-coordinated metal atoms, few-atom clustes etc. The NPs grow either through atom by atom addition of monomers to the seeds or by coalescence of seeds between them or both. The control of the nucleation and growth, which are the main steps in the process of NPs synthesis, can be achieved by controlling reaction parameters such as the nature and amount of surfactant, the temperature, the pressure, the concentrations etc. This approach allows synthesizing size and shape controlled MMNPs and their alloys free from any native oxide.

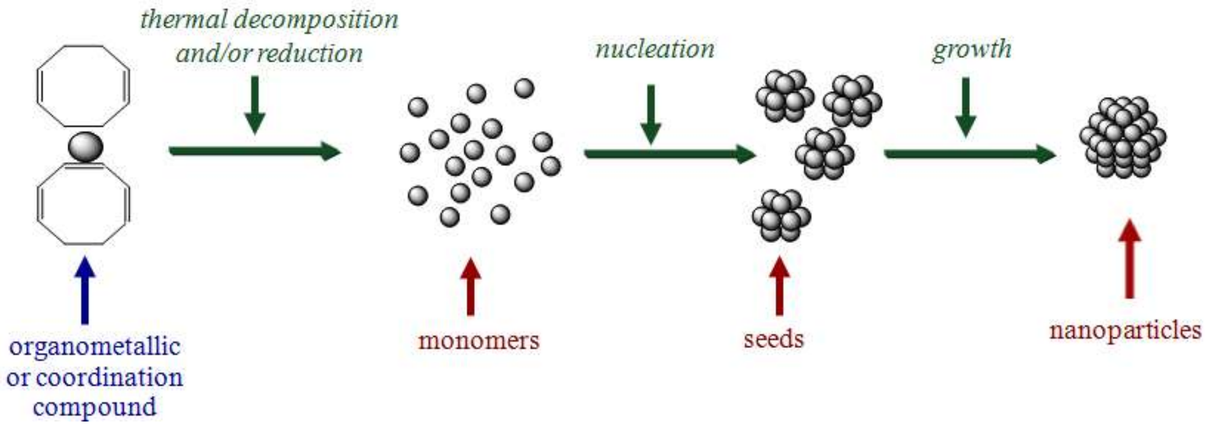

Figure B.1: Schematic representation of the organometallic approach for synthesis of MMNPs.

II. Magnetic properties of nanoparticles

II.1 Critical size and monodomain configuration of magnetic nanoparticles

Iron, cobalt and nickel are ferromagnetic 3d transition materials. Bulk magnetic materials consisting of these ferromagnetic elements present a magnetization when deposited in an applied magnetic field. This magnetization increases when the applied field strength is increased, until a limit value, known as saturation magnetization (*Ms*). These bulk magnetic materials can be imaginably divided into many magnetic domains, proposed by Weiss (7), which allows reducing of the total system energy. The self-organization of the multi-domains drives global magnetic moment to zero in the bulk material. These domains are considered as small areas where atomic magnetic spins are aligned, and they are separated by interfaces, called domain walls. The formation of domain walls and the size of the domains result from the magnetostatic energy and the domain wall interfacial energy. The magnetostatic energy increases with increasing domain volume and the domain wall interfacial energy increases with increasing domain wall interface area. The balance between these two energies decides the size of the domains for a given magnetic material. When the size of the material decreases until a critical size, the energy needed for creating a domain wall becomes larger than the magnetostatic energy of a single domain, and in this case as well as below this critical size the system retains its monodomain configuration (Figure B. 2).

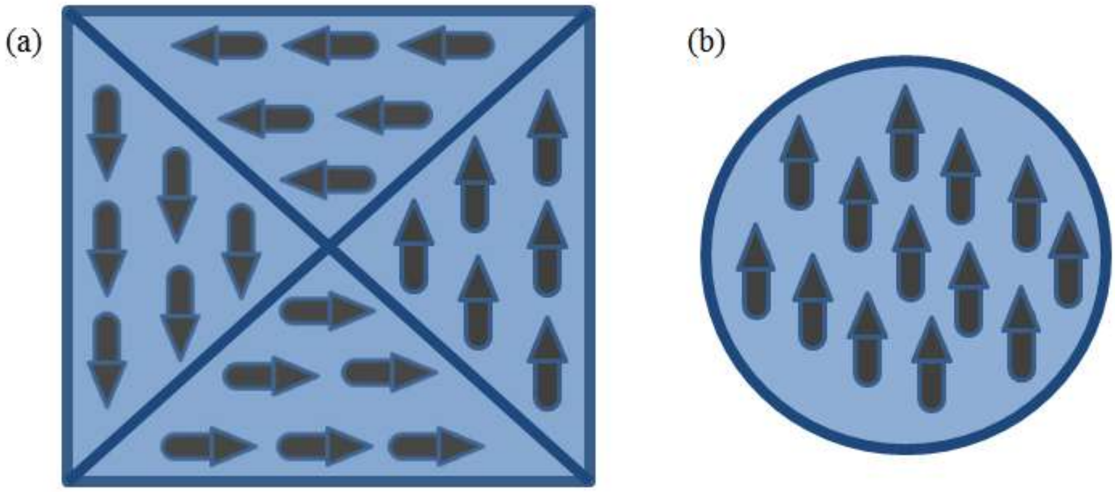

Figure B.2: Schematic representation of (a) a multidomain and (b) a monodomain configuration.

II.2 Superparamagnetism

The global magnetic moment of a monodomain particle can be modelled as a macrospin aligned along an easy axis given by an uniaxial effective anisotropy (K). In absence of external applied field, the magnetic moment of monodomain particles can fluctuate between two positions, up and down with respect to the easy axis. The energy barrier between these two opposite positions is equal to KV, where V is the particle volume.

Néel described this fluctuation of magnetic moment between these two positions (8). As the size of the particle decreases to a level where KV becomes comparable to the thermal energy k_BT (k_B is Boltzmann's constant and T is temperature), the magnetic moment fluctuates spontaneously from one direction to another, and in this case the particle is considered as superparamagnetic. He also introduced the relaxation constant τ_N that characterizes the average time of rotation of magnetic moment, defined by the following equation:

$$\tau_N = \tau_0 \exp(KV/k_BT)$$

where τ_0 is the limited relaxation time with an order of 10^{-9}s. When the measurement time $\tau_M < \tau_N$, the magnetic moment of the particle is considered as blocked. In contrary, when $\tau_M > \tau_N$, the magnetic moment of the particle is superparamagnetic. The temperature at which $\tau_M = \tau_N$, the temperature here is defined as the blocking temperature (*T_B*), which is the temperature where the transition of blocked/superparamagnetic takes places.

II.3 Magnetic characterization

The magnetic properties of materials can be studied by measurements performed with SQUID (superconducting quantum interference device) or VSM (vibrating sample magnetometer). Two main kinds of static properties can be evaluated, from evolutions of the magnetization with respect a) to temperature and b) to the external applied field.

II.3a Evolution of magnetization through temperature

A ZFC/FC measurement is used to study the magnetic behavior, size distribution of NPs and magnetic interaction between them. In detail, the sample is cooled under zero-field until 2K. The sample is then measured while the temperature is increased up to room temperature (300K) under a weak magnetic field (10 Oe). Then, it is cooled under the same amplitude magnetic field while its magnetization is recorded. A typical ZFC/FC curve is presented in Figure B.3. At the beginning of the ZFC curve, the particles have a magnetization close to zero due to their random orientation. As the temperature increases more particles get aligned to the magnetic field. However, when the temperature is larger than T_B the particles become randomly oriented as a result of the increased thermal energy. The curve displays a maximum at T_B. The FC curve is almost identical to the ZFC curve for temperatures that are higher than T_B but for lower temperatures the particles continue to be aligned and the thermal energy effect is limited. In this way the FC curve presents its maximum at the lowest temperature.

T_B found by a ZFC/FC curve corresponds to the mean T_B of all the particles in the sample, and it defines the blocked and superparamagnetic domains. The width of the peak on ZFC curve reflects directly the size distribution of NPs. If a sample has a large size distribution, its peak on ZFC curve will be large.

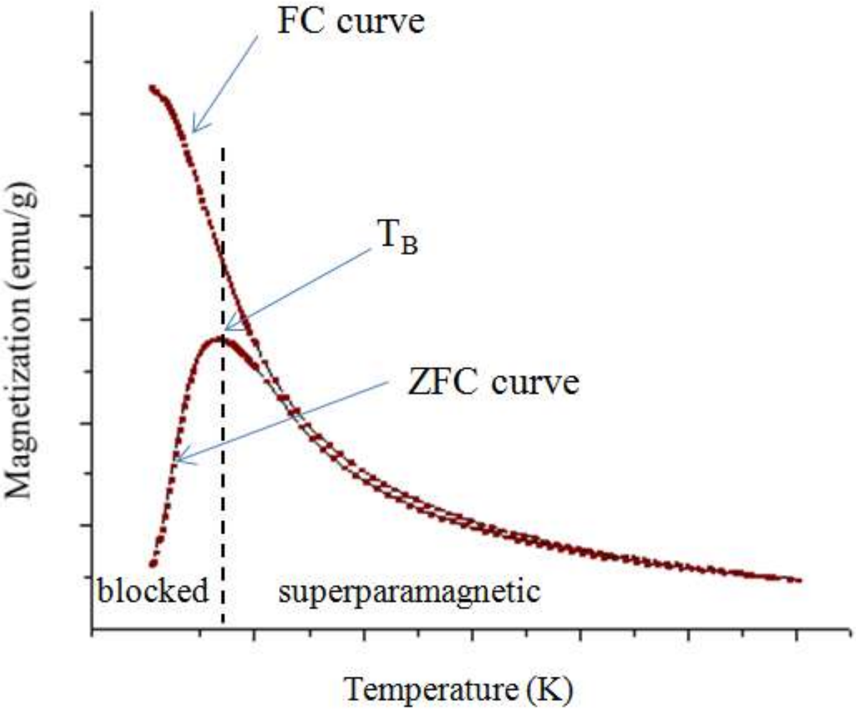

Figure B.3: a ZFC/FC curve presenting *T_B*.

Interaction effects between NPs can contribute to T_B modification. In most cases, in a sample with constant volume, if NPs proportion is increased, NPs will have stronger interactions due to the shorter distance among them, which results in a shifted T_B towards high temperature (9).

II.3b Evolution of magnetization through external applied field

The magnetic properties of NPs can be well analyzed by a hysteresis loop that measures the change of magnetic moment (*M*) over the strength of an applied magnetic field (*H*) (Figure B.4a). In the absence of an external field (center point), the magnetization of each particle points at random directions and the overall magnetic moment is zero. When an external magnetic field is applied, the magnetization of the particles aligns along the field direction. When the field is strong enough, all the particles have been aligned along the field and the magnetization of the sample is said to be saturated; the corresponding moment is called the saturation moment (*Ms*). Reducing the strength of the field leads to a smaller magnetic moment. When the external field drops to zero, the ferromagnetic particles retain a considerable degree of magnetization with a net measurable moment: the remnant magnetic moment (*Mr*). To demagnetize the particles, the external field must be reversed and increased to a value where the total moment is zero. This value is called the coercivity (*Hc*). If the particles are superparamagnetic, the magnetization of each particle undergoes thermal fluctuation. As soon as the field is removed, the overall moment is randomized to zero, leaving no remnant magnetic moment. The coercive field in this case is zero (Figure B.4b).

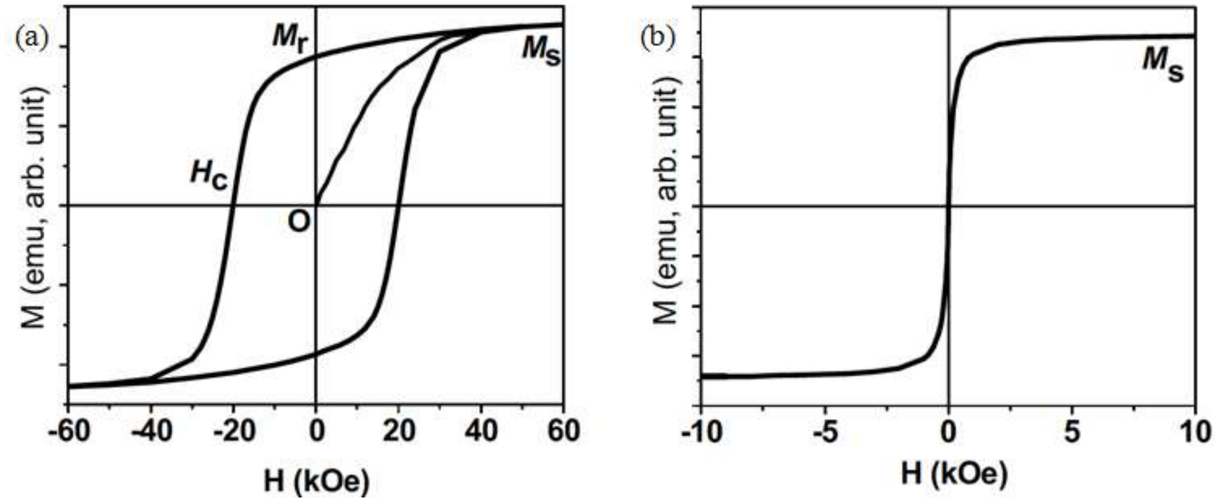

Figure B. 4: Schema of the hysteresis loops of (a) ferromagnetic NPs and (b) superparamagnetic NPs (10).

For magnetic recording applications, the *Mr* must be the higher possible in order to have an intense signal, and a large *Hc* is vital for the long-time conservation of the magnetic information. In contrary, the superparamagnetic property is very useful for biomedical applications since they present no *Mr* in the absence of external field at room temperature (Pourquoi il ne faut pas avoir une magnetization dans ce cas??).

II.3c Exchange bias effect

oxidation may cause a shift, called the exchange bias effet (11), of the hysteresis loop across the magnetic field *H* axis due to interactions at the interface between ferromagnetic core and antiferromagnetic shell. An example is given for Co@CoO in Figure III.21. Exchange bias can contribute to an increase of the effective magnetic anisotropy of the NPs, indicating that oxidation of a MMNPs occurs.

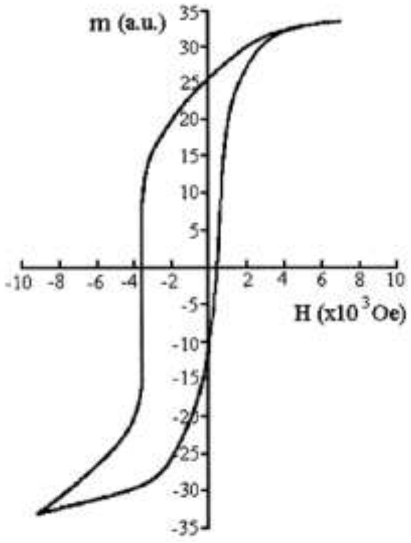

Figure B.5: Hysteresis loop of Co@CoO particles at 77K after field cooling (FC) (11).

1. Y-W. Jun, J-W. Seo, J. Cheon, *Acc. Chem. Res.*, **2008**, *41*, 179-189.
2. F. Dumestre, B. Chaudret, C. Amiens, M. Respaud, P. Fejes, P. Renaud, P. Zurcher, *Angew. Chem. Int. Ed.,* **2003**, *42*, 5213-5216.
3. C. Desvaux, C. Amiens, P. Fejes, Ph. Renaud, M. Respaud, P. Lecante, E. Snoeck, B. Chaudret, *Nature Mater.,* **2005**, *4*, 750-753.
4. F. Wetz, K. Soulantica, A. Falqui, M. Respaud, E. Snoeck, B. Chaudret, *Angew. Chem. Int. Ed.*, **2007**, *46*, 7079-7081.
5. J. Maynadie, A. Salant, A. Falqui, M. Respaud, E. Shaviv, K. Soulantica, B. Chaudret, *Angew. Chem., Int. Ed.,* **2009**, *48*, 1814–1817.
6. L.M. Lacroix, S. Lachaize, A. Falqui, M. Respaud, B. Chaudret, *J. Am. Chem. Soc.*, **2009**, *131*, 549.
7. P. Weiss, *J. Phys.*, **1907**, *6*, 661.
8. *Compt. Rend.*, **1949**, *228*, 64.
9. S. Sankar, A. E. Berkowitz, *Phys. Rev. B*, **2000**, *62*, 14273.
10. S. Sun, *Adv. Mater.*, **2006**, *18*, 393–403.
11. J. Nogués, I.K. Schuller, *J. Magn. Magn. Mater.*, **1999**, *192*, 203-232.